Physical Modelling of the Movement of Geological Fluids in the Earth's Crust with Application to Magma Transport, Storage and Degassing

Thierry Menand

To cite this version:

Thierry Menand. Physical Modelling of the Movement of Geological Fluids in the Earth's Crust with Application to Magma Transport, Storage and Degassing. Volcanology. Université Blaise Pascal - Clermont-Ferrand II, 2013. tel-03099400

HAL Id: tel-03099400
https://theses.hal.science/tel-03099400

Submitted on 6 Jan 2021

Université Blaise Pascal - Clermont-Ferrand II

UFR Sciences et Technologies
École Doctorale des Sciences Fondamentales

numéro d'ordre : 374

Mémoire présenté en vue de l'obtention de l'Habilitation à Diriger des Recherches

Spécialité : **Volcanologie**

par

Thierry Menand

Maître de conférences, Chaire d'excellence mixte UBP - IRD
Laboratoire Magmas et Volcans
UMR Université Blaise Pascal – CNRS – IRD

Physical Modelling of the Movement of Geological Fluids in the Earth's Crust with Application to Magma Transport, Storage and Degassing

Date et lieu de soutenance : 21 janvier 2013, Laboratoire Magmas et Volcans

Composition du jury :

Claude JAUPART - Professeur à l'Université Paris-Diderot et l'IPGP	Rapporteur
Steve SPARKS - Professeur à l'Université de Bristol, Royaume Uni	Rapporteur
Tim DRUITT - Professeur à l'Université Blaise Pascal	Rapporteur
Virgine PINEL - Chargé de recherche IRD à l'Université de Savoie	Examinateur
Andy HARRIS - Professeur à l'Université Blaise Pascal	Responsable tutélaire

Contents

Foreword and Acknowledgement

In 2000, having successfully defended my PhD on the transport of magma in dykes at the Institut de Physique du Globe de Paris (IPGP), I decided to tackle a different research topic and to spend some time abroad. This lead me to the University of Cambridge where I joined the BP Institute for Multiphase Flow (BPI) as a postdoc and delved into porous flows. During three years, I discovered a new environment, with stronger links with the industry than in France, and a new type of research. However, three years later, the lure of volcanology was too strong, and when Steve Sparks offered me to join his group as a postdoc at the Univeristy of Bristol, I jumped on the opportunity. There I went back to investigating magma transport, and I broadened my research interests to magma degassing, the formation of plutons and magma chambers. I can easily say these seven years in Bristol were among the happiest of my research career. For a decade, I discovered and learned to love a new country, before returning to France in 2010 when I got a Lectureship at the Laboratoire Magmas et Volcans (LMV) in Clermont-Ferrand.

During my research career, I have been fortunate enough to meet and work with great people and collaborators, to whom I would like to express my gratitude: Claude Jaupart and my PhD supervisor Steve Tait (both at IPGP), Andy Woods, Charlotte Gladstone and Mats Nigam (all from the BPI); Steve Sparks, Jeremy Phillips, Catherine Annen, Janine Kavanagh, Richy Brown, Jess Trofimovs, Oleg Melnik, Antonio Costa, Lena Melekhova, Jo Gottsmann, Alison Rust, Madeleine Humphreys, Jon Blundy and a fantastic cohort of PhD students and postdocs at the University of Bristol that would be too long to list without forgetting someone; Michel de Saint Blanquat from the Univeristé Paul Sabatier in Toulouse introduced me to the Henry Mountains in Utah; Andy Bunger from CSIRO invited me recently down under and I hope our recent and fruitful collaboration will continue. Finally, I would also like to thank my colleagues at LMV for welcoming me and I look forward to exciting present and future collaborations.

Chapter 1

A Short Introduction

My research interests revolve essentially around the physical modelling of geological fluid flows in the Earth's crust. My approach is not to try to reproduce natural phenomena but rather to identify the physical processes that govern these geological flows. To achieve this is, I use a combination of small-scale, analogue, laboratory experiments, analytical and numerical modelling. My aim is to identify governing scaling laws and upscale them to geological conditions to discuss their range of validity and implications for natural systems.

Over the years, I have delved into three different strands of research, which I will introduce and summarise in the following separate chapters:

In Chapter 2, I present my work on porous fluid flows, which includes the fracturing of porous media induced by fluid flows, the effect of thermal inertia on the morphology and dynamics of porous flows, mechanical dispersion, and the development of Rayleigh-Taylor instabilities;

Chapter 3 deals with the degassing of volcanic systems and associated magma dynamics, with applications to the passive degassing of basaltic volcanoes, modelling the impact of volcanism on the performance of underground nuclear waste repositories, the diffusion of volatiles from rhyolitic melt inclusions and its potential use as a magmatic geospeedometer;

In Chapter 4, various aspects of magma transport and storage are presented including the transport of magma through the Earth's crust in dykes, how dykes can assist continental rifting, how dyke swarms could form, the formation of sills and their role in the formation and growth of plutons and magma chambers.

Each chapter is followed by a list of selected publications, before I finally present in Chapter 5 the different projects I envisage to conduct over the next years.

Chapter 2

Porous Flows (1998, 2000–2003; Cambridge)

(Funding: *Schlumberger Cambridge Research*, and *Isaac Newton Trust Research Fellowship*)

The displacement of fluids through porous rocks occur in a wide range of geophysical, environmental and industrial applications. It is fundamental for the recharge of geothermal and hydrocarbon reservoirs (Grant et al., 1982; Lake, 1989), for contaminant dispersal through the groundwater (Bear, 1972), in controlling mineral reactions in permeable rocks (Phillips, 1991), as well as the repeated intrusion of sea water into aquifers in coastal environments. These displacements can also have a strong impact on the integrity of the surrounding solid matrix.

My interest in this strand of research started during my PhD when I had the opportunity in 1998 to join and do an internship in the Geomechanics Group at Schlumberger Cambridge Research. There I worked for three months on the fracturing and disintegration of porous media induced by fluid flowing through their pores. This first experience was then followed in 2000 by a postdoc at the University of Cambridge, BP Institute for Multiphase Flow where I focused on various aspects of miscible displacements in porous media.

Most porous flows of geological interest occur at low Reynolds numbers (which expresses the ratio of inertial to viscous forces), that is the average flow velocity u through the pores is slow enough that the Reynolds number $Re = (\rho u d)/\mu << 1$, where ρ is the density of the fluid, μ is its dynamic viscosity, and d is the average size of the pores. In this particular case, porous flows are governed by Darcy's law, which states that the transport velocity, referred to as the Darcy velocity, is proportional to the pressure gradient:

$$\boldsymbol{u} = -\frac{k}{\mu}\left(\nabla p + \Delta\rho g\right) \boldsymbol{z}. \tag{2.1}$$

$\boldsymbol{u}$ is the velocity vector, z is a unit vector directed vertically upward, k is the permeability of the medium, and fluid flows through the pores of the solid matrix owing to a pressure gradient, which can be split into a non-hydrostatic component, ∇p, and a hydrostatic component, $\Delta\rho g$, that arises when the density of the fluid differs from that of the solid matrix by an amount $\Delta\rho = \rho_{solid} - \rho_{fluid}$. Equation (2.1) is referred to as the transport or Darcy velocity. It corresponds to the average macroscopic velocity with which the fluid moves through the entire porous medium. It is an average flux per unit area of the medium, i.e. pores plus grains. However, the fluid actually flows through the pores only, and so travels at the interstitial speed $\boldsymbol{u}/\phi$ where $\boldsymbol{u}$ is the transport (Darcy) velocity and ϕ is the porosity of the matrix.

Despite its simplicity, Darcy's law accounts for a great variety of flows. A key parameter is the medium permeability k, which has the dimensions of a surface area, and so can be viewed as the pore cross section area. The permeability is a scalar if the porous medium is isotropic or a tensor if the medium is instead anisotropic, such as rocks made of strata each characterised by different porosity and permeability for instance. More refined and complex treatment are needed to account for fractured porous media where both the intrinsic permeability of the medium and that of its fractures will affect the flow. Also, strictly speaking, equation (2.1) is only valid for the case of a porous rock saturated with one fluid. However, this expression can be extended to the case of simultaneous flow of two immiscible fluids by considering the effective permeability and viscosity as those of the phase that is considered, for instance $\boldsymbol{u} = -(k_1/\mu_1)(\nabla p + \Delta\rho g)z$ for fluid phase 1. The effective permeability k_1 will then depend on the structure of the porous medium involved, and more specifically on the permeability of that medium to a single-phase fluid completely saturating it.

Equation (2.1) gives the velocity field for a fluid flowing through a porous medium, provided the properties of both the fluid and medium are known as well as the pressure gradient the fluid is subjected to. However these conditions can change, which in turn will affect the fluid flow. This could happen in a variety of different ways. One possibility is that the permeability of the porous medium is modified, which could occur because of some reactive transport, either increasing or decreasing locally the matrix permeability, or because of fracturing. Another possibility is that the properties of the fluid are altered such that the pressure gradient changes as well. This will be the case if the density of the fluid changes for instance. I investigated some aspects of these two mechanisms: fracturing and density change.

2.1 Fluid-induced fracturing

Fracturing and disintegration of a porous medium can occur because of increased pore pressure. This is as much an important issue in academic research, both fundamental and applied, as it is for the hydrocarbon industry. When extracting low-viscosity hydrocarbons, high-production flow rates, although economically desirable, can lead to substantial erosion of unconsolidated formations, a phenomenon referred to as solid-particle co-production, which represents a major production and safety hazard. Conversely, the solid-particle co-production from unconsolidated formations stemming from the exploitation of highly viscous hydrocarbons at low flow rate induces an increase of the permeability of these formations and thus of their economic viability. An additional side effect is that solid-particle co-production affects and usually diminishes the stability of the host rock formation. This hazard echoes the wider issue of slope instability induced by increased pore pressure.

At the rock formation scale, porous flow usually involves several phases: one or several fluids (liquid, gas or both) present or flowing through the pores, and the solid grains of the matrix. In the late 1990s, the processes and mechanisms that lead to fracturing and disintegration of poorly-consolidated rocks were not well understood, when such formations host potentially large hydrocarbon reservoirs. One particular issue was whether capillary forces between the fluid and solid phases could play a role and perhaps even impede the co-production of solid particles in the weakest formations. The aim of my internship at the Geomechanics Group at Schlumberger Cambridge Research was to test this hypothesis by means of laboratory analogue experiments.

In these experiments, a viscous hydrocarbon fluid, was made to flow through a water-wet sand pack of cylindrical geometry. Water was both giving some cohesion to the sand pack, and simulating the presence of brine in natural formation. The fluid flowed at a constant volumetric flow rate from the outer perimeter of the sand pack to its centre, where it was collected through a hole whose diameter was much smaller than that of the sand pack; the overall geometry was designed to simulate, at the laboratory scale, the extraction of interstitial hydrocarbons through a production well. It was observed that at very low flow rates, the fluid would flow without disturbing the sand pack. At higher flow rates, however, sand grains at the centre of the sand pack, near the experimental well, were observed to separate from each other leading to erosion of the well. This erosion was only transitory, however. It always followed an increase in the fluid flow rate, and ultimately a steady state would be achieved after the well had eroded to a greater stable diameter.

The hypothesis was made that the observed erosion could be induced by the viscous drag exerted by the flowing fluid on the sand grains, which would tend to haul them out of position, and resisted by the capillary forces exerted by the water film wetting the sand grains. A scaling analysis was then made to test this hypothesis. First, all sand grains were assumed to be identical rigid spheres, arranged in a cubic packing, and saturated with the viscous fluid. These approximations allowed the geometry of the pores to be simplified and allowed the average size of pores to be related to the diameter of the spherical grains, which then allowed simple expressions for the capillary force and the fluid viscous drag to be derived.

In the case of constant fluid flow rate, balancing the capillary forces and viscous drag reveals the existence of an optimum or critical well radius below which the viscous drag exceeds the capillary forces and above which the opposite holds. To first order, this critical radius compared well with the diameter of the eroded experimental well. Moreover, this simple scaling analysis explains qualitatively the experimental observations: i) sand co-production starts once the viscous drag on the grains becomes greater than the capillary forces; and ii) the sand co-production stops once the eroded well reaches a critical radius for which the balance between capillary forces and viscous drag is restored.

At a geological scale, however, flow rate is rarely constant, whether during industrial hydrocarbon production or for natural flows. Solid co-production and flow rate will therefore be interdependent, and the conditions for potential fracturing and disintegration of the porous medium will vary and depend on the strength of the fluid flow.

This first experience whetted my appetite for porous flows by highlighting the important role played by the forces driving fluid flow. After my PhD, I decided to delve into the displacement of miscible fluids in porous media, and more specifically on the effects of temperature and mixing on the fluid driving forces.

2.2 Thermal inertia

Many natural and industrial situations involve the invasion of a porous medium by some fluid, which results in the displacement of the fluid that originally saturated the porous medium. In many cases, the buoyancy force induced by the density difference between the formation and displacing fluids controls the rate and pattern of flow through the permeable rock. The density of the fluids, hence the buoyancy force, depend on the composition and the temperature of the fluids. However, in most cases, the composition and temperature of both fluids are different, which has a profound impact on the flow.

When a fluid flows through a formation initially saturated with a fluid of different temperature and composition, a thermal and compositional stratification develops as the properties of the injected fluid adjusts to that of the formation fluid. This stratification arises because solute and heat do not travel at the same rate through the porous medium. As stated earlier, the compositional (solute) front travels with the interstitial speed $\boldsymbol{u}/\phi$. Heat, on the other hand, is transferred between the invading fluid and the whole rock matrix: as the injected fluid migrates through the pores, it exchanges heat with both the formation fluid and porous medium. As a result the thermal front travels with the speed $\Gamma\boldsymbol{u}$ where $\Gamma = (\rho C_p)_{liq}/\left(\overline{\rho C_p}\right)$ has value close to one and is the ratio of the specific heat of the liquid to the average specific heat of the liquid and porous matrix (Woods and Fitzgerald, 1993; Barenblatt, 1996; Turcotte and Schubert, 2002). Therefore heat travels at a rate that is $\phi\Gamma$ times that of the fluid interstitial speed. In many cases, this factor $\phi\Gamma$ is smaller than unity, which results in the development of a compositional front, that separates the invading and formation fluids, and a thermal front that lags behind and through which the invading fluid adjusts its temperature to that of the porous medium (Fig. 2.1). This lagging of the thermal front behind the compositional front is referred to as thermal inertia.

The initial composition and temperature of the invading fluid relative to those of the original formation fluid determine the density difference between the two

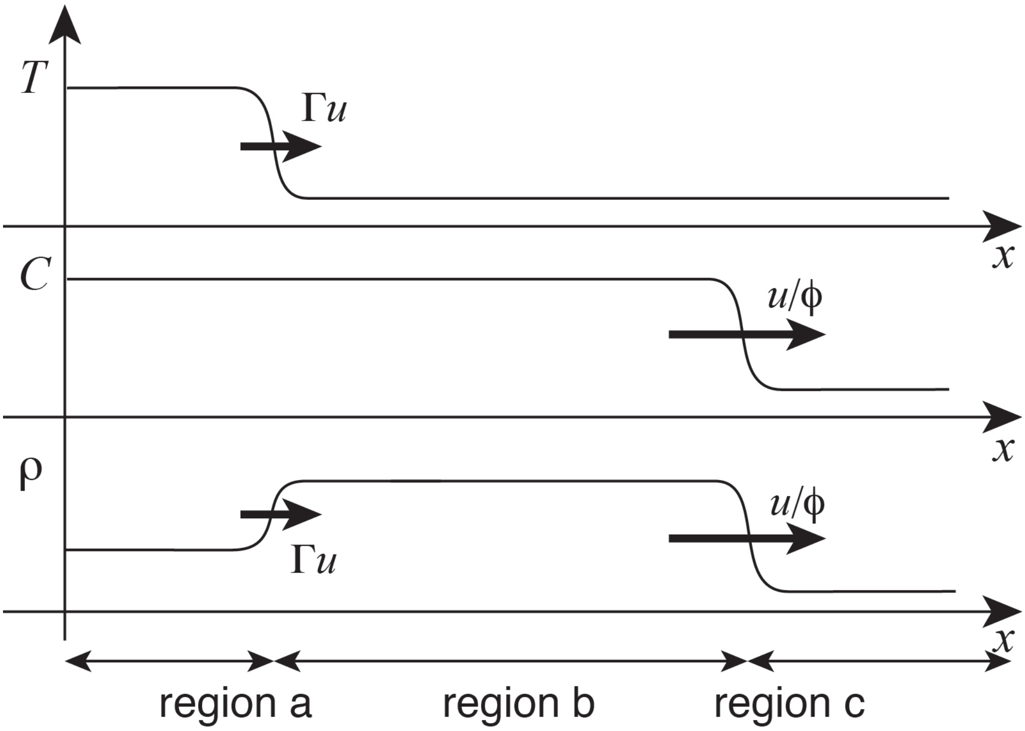

Figure 2.1: Diagram illustrating the spatial distribution of the temperature T, the composition C, and the resulting density ρ as a fluid of one temperature and composition is injected into a bead pack saturated with a fluid of different temperature and composition. The spatial decoupling of the thermal and fluid fronts creates three regions in which the fluid has different density: near the source (region a), between the thermal and compositional fronts (region b) and in the original formation fluid (region c).

fluids and so the initial buoyancy force acting on the flow. However, as the flow proceeds and thermal inertia operates, the density difference, hence the buoyancy, changes as the invading fluid crosses the thermal front. This has a profound effect on the dynamics and pattern of buoyancy-driven porous flows as illustrated in Fig. 2.2. This figure shows photographs of four different analogue experiments where a saline solution was injected at a constant rate into a bead pack saturated with an aqueous solution of different salinity and temperature. The bead pack, made of millimetre-size glass beads, had a porosity $\phi = 0.40 \pm 0.01$ and a specific heat ratio

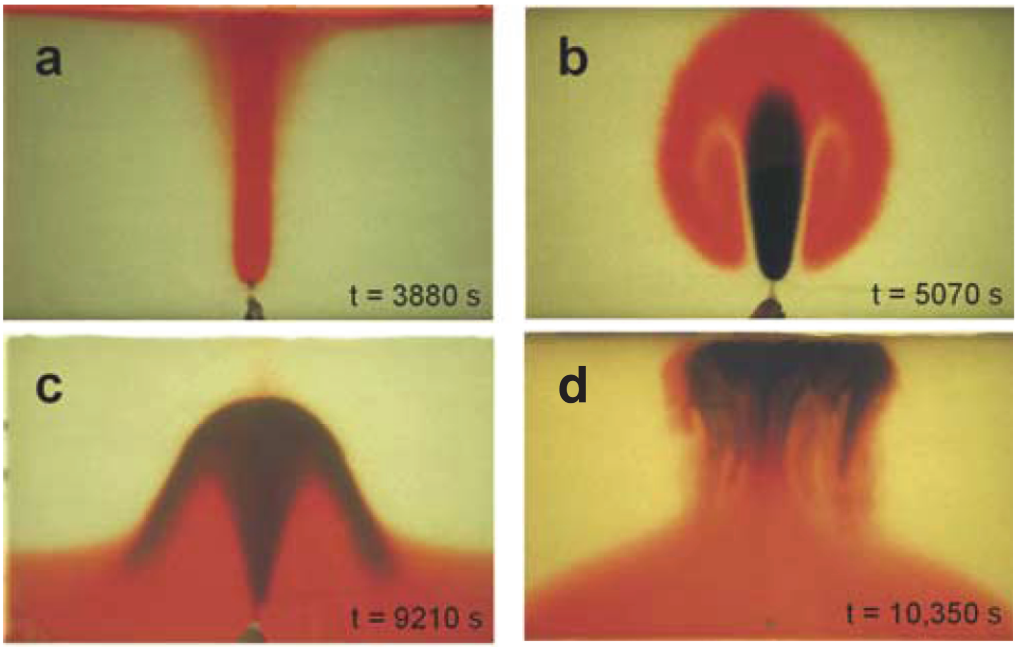

Figure 2.2: Photographs illustrating four different flow patterns that arise owing to different injection conditions (Menand et al., 2003). The injected and formation fluids have different temperature and composition, and the injected fluid is initially dyed red and then black to reveal the evolving flow pattern. (a) The fluid injected at the base of the bead pack has a smaller NaCl concentration than the formation fluid, but the same temperature; its buoyancy stays constant through time. (b) The fluid injected at the base of the bead pack has the same composition, but is hotter that the formation fluid; as the fluid crosses the thermal front it becomes neutrally buoyant. (c) The fluid injected at the base of the bead pack has a greater NaCl concentration but is hotter than the formation fluid, so that initially it is of smaller density; as the fluid crosses the thermal front, its buoyancy is reversed because of a greater NaCl concentration than the ambient fluid. (d) The fluid injected at the top of the bead pack has a greater NaCl concentration but is hotter than the formation fluid so that, as in (c), it is initially less dense than the formation fluid; the buoyancy of the injected fluid evolves as in (c) but the injection configuration leads to a strikingly different flow pattern. In each case, the bead pack is 50 cm high, 80 cm large and only 3 cm thick so that the flow can be approximated as two-dimensional.

$\Gamma \simeq 1.7$, so that the thermal front propagated at approximately two-third the fluid interstitial speed. The bead pack was much thinner than its two other dimensions, and the flow could be approximated as two-dimensional. The key aspect of these experiments is that the initial composition and temperature of the invading fluid were different for all cases, but its initial buoyancy was identical: the invading fluid was initially buoyant because of a deficit in NaCl concentration, a higher injection temperature, or a combination of both concentration and temperature difference. These experiments reveal how the separation of the compositional and thermal fronts evolves through time, and how this leads to a buoyancy increase, decrease or even reversal for the invading fluid (Fig. 2.2). Thus these experiments show that the pattern and dynamics of the flow depend on the nature (compositional and thermal) more than the actual value of the buoyancy of invading fluids.

These experiments are limited to two dimensions when in nature flow is essentially three-dimensional, although to some extent it can be locally restricted or confined to two-dimensional strata. In principle, numerical modelling could resolve the issue and deal with three-dimensional flow. However, one difficult aspect in the case of miscible fluids is that of the inevitable mixing of the two fluids that occurs in the pore space as one displaces the other. Numerical modelling could deal with such a mixing but this would require considerable computing power to account for a wide range of scales, from that of the individual pores to that of the entire formation. One way to circumvent this difficulty is to establish macroscopic mixing laws at a scale that is larger than that of the pores, which would then be more easily dealt with numerically. This requires a relationship between mixing at the pore-scale and the flow conditions.

2.3 Mixing and the development of Rayleigh-Taylor instability

When a fluid migrates through a porous formation already saturated with another fluid, if both fluids have identical physical properties, such as density and viscosity, then the heterogeneities of the permeable formation will dictate the behaviour of the fluid interface, i.e. the mixing between both fluids (Phillips, 1991). Tracer dispersion is often used to map out such heterogeneities, whereby tracer is injected into the underground flow and its concentration is then measured some distance away from the point of injection. However, the presence of multiple, tortuous pathways in a porous medium leads to mechanical and dynamical dispersion of the flow (Bear, 1972). This dispersion is usually characterized by a coefficient of mechanical dispersion, D, which depends on both the geometrical structure of the porous matrix and the structure of the fluid flow, as well as fluid molecular diffusion. Additionally, fluid dispersion has been shown to be affected by density and viscosity contrasts (Jiao and Hötzl, 2004; Wood et al., 2004). Quantifying this dependency is important because dispersion-induced mixing will affect the local density contrast between invading and formation fluids and thus the overall flow behaviour. Dispersion could also act against or delay the onset of buoyancy-driven, Rayleigh-Taylor instability.

Analogue experiments were therefore carried out to quantify the effect of density difference on mechanical dispersion both in gravitationally stable and unstable flows, and to determine how this process relationship affects the spatial and time development of Rayleigh-Taylor instability (Menand and Woods, 2005). An aqueous solution was injected at a constant rate through a 15-cm wide, 23-cm high and 1-cm thick homogeneous, isotropic bead pack made of 1.5 mm glass beads and saturated with an aqueous solutions of different density. The injected and ambient fluids were both aqueous solutions with variable amounts of NaCl to control their respective density. As shown earlier, flows in porous media at low Reynolds number are governed by Darcy's law (equation 2.1), which can be written as the sum of a velocity induced by a non hydrostatic pressure gradient $u_s = -k/\mu \nabla p$, that is a background-flow velocity, and a velocity associated with the gravitational force $u_g = -k/\mu \Delta\rho g$. The NaCl concentration of the injected and ambient fluids controlled the density difference between the two fluids hence the gravity-driven velocity u_g, whereas a pump independently controlled the background-flow velocity u_s. Experiments were carried out over a range of background-flow and gravity-driven velocities as well as total Darcy velocity u under both potentially stable and unstable conditions.

When there is no density difference between the invading and ambient fluids, a diffusive mixing zone develops at the interface between the two fluids. However sharp this interface is initially, diffusive mixing occurs between the fluids owing to fluid dispersion, and as the invading fluid migrates through the porous bead pack the width of this mixing zone at the interface grows as $\sqrt{Dt}$ where t is time. When both fluids have differing densities and flow occurs in a stable configuration (the densest fluid lies above the lightest), diffusive dispersion at the fluid interface still occurs but it is decreased by the stable density difference: flow proceeds as in the tracer case but with a reduced dispersion coefficient D.

When flow occurs in an unstable configuration, its pattern and behaviour are markedly different with the development of Rayleigh-Taylor instability. Two dispersive regimes are successively observed (Fig. 2.3). Initially, the fluid interface grows diffusively with a diffusion coefficient D that is increased by the mixing taking place at the fluid front. Then an advective regime develops whereby Rayleigh-Taylor unstable fingers emerge from the mixing zone and propagate at a greater, constant speed proportional to the gravity-driven velocity u_g. It is also observed that the wavelength of these unstable fingers scales with the width of the mixed interface at the onset of the Rayleigh-Taylor instability. These unstable experiments show that as flow proceeds, mixing at the interface grows and thus reduces locally the density difference between invading and ambient fluids, which delays the onset of gravitaty-driven instability. Unstable fingers emerge when their propagation velocity becomes greater than the diffusive growth rate of the mixed interface. A

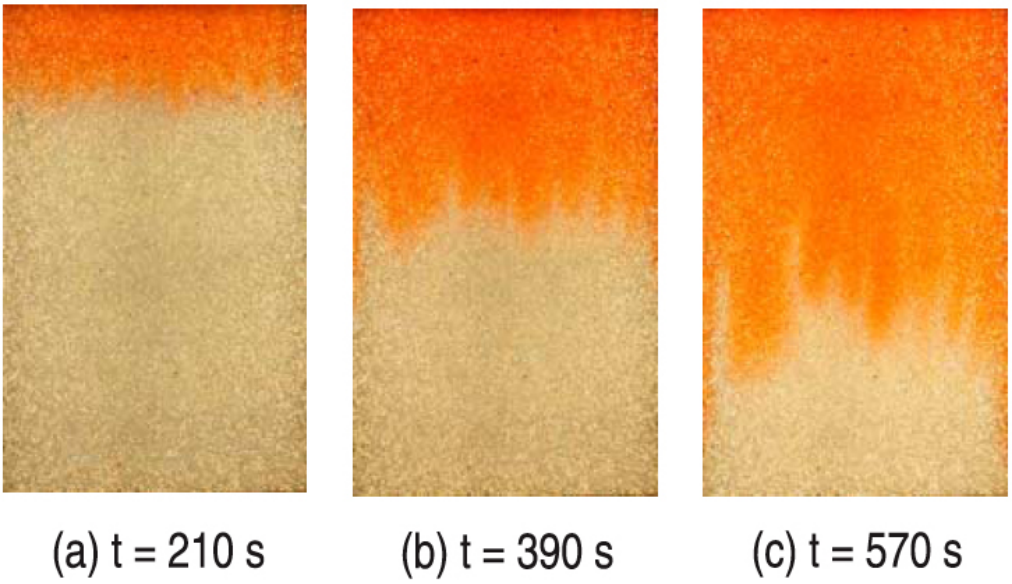

(a) t = 210 s (b) t = 390 s (c) t = 570 s

Figure 2.3: The development of unstable fingers as dense salty water (red) migrates from top to bottom through a porous bead pack saturated with lighter fresh water (Menand and Woods, 2005). The bead pack has a porosity $\phi = 0.39 \pm 0.01$ and a permeability $k = (1.9 \pm 0.1)\ 10^{-9}$ m^2. The onset of the Rayleigh-Taylor instability is delayed by the mechanical dispersion that takes place at the interface between the two fluids: (a) initially, the mixing zone at the fluid interface grows diffusively; (b) later on, unstable fingers emerge from the mixed interface; (c) these unstable fingers migrates with a constant velocity proportional to the gravity-driven velocity u_g and with a wavelength that scales with the width of the mixed interface.

consequence is that higher imposed background flow rates lead to higher mechanical dispersion of the interface and thus wider fluid interface. In turn, this leads to a larger delay in the development of the Rayleigh-Taylor instability with a larger wavelength.

Fluid dispersion is affected by both the density contrasts between invading and ambient fluid and the relative strength of the background flow, which in turn determines the onset and wavelength of Rayleigh-Taylor instability. When applied to homogeneous and uniform geological settings, these results suggest that mechanical dispersion suppresses the onset of Rayleigh-Taylor instability until a mixed zone 1–2 m thick has developed. The wavelength of the instability would then be expected to be of the order of centimetres to metres depending on the relative value of background-flow and gravity-driven velocities (Menand and Woods, 2005).

Bibliography

Barenblatt, G. I. (1996). *Scaling, self-similarity, and intermediate asymptotics*. Cambridge University Press.

Bear, J. (1972). *Dynamics of fluids in porous media*. Dover Publications.

Grant, M. A., I. G. Donaldson, and P. F. Bixley (1982). *Geothermal Reservoir Engineering*. Academic.

Jiao, C.-Y. and H. Hötzl (2004). An experimental study of miscible displacements in porous media with variation of fluid density and viscosity. *Transp. Porous Media 54*, 125–144.

Lake, L. W. (1989). *Enhanced Oil Recovery*. Prentice-Hall.

Menand, T., A. Raw, and A. W. Woods (2003). Thermal inertia and reversing buoyancy in flow in porous media. *Geophys. Res. Lett. 30(6)*(1291), doi:10.1029/2002GL016294.

Menand, T. and A. W. Woods (2005). Dispersion, scale, and time dependence of mixing zones under gravitationally stable and unstable displacements in porous media. *Water Resour. Res. 41*(W05014), doi:10.1029/2004WR003701.

Phillips, O. M. (1991). *Flow and reactions in permeable rocks*. Cambridge University Press.

Turcotte, D. L. and G. Schubert (2002). *Geodynamics. Applications of Continuum Physics to Geological Problems* (second ed.). Cambridge: CambridgeUniversity Press.

Wood, M., C. T. Simmons, and J. L. Hutson (2004). A breakthrough curve analysis of unstable density-driven flow and transport in porous media. *Water Resour. Res. 40*(W03505), doi:10.1029/2003WR002668.

Woods, A. W. and S. D. Fitzgerald (1993). The vaporization of a liquid front moving through a hot porous rock. *J. Fluid Mech. 251*, 563–579.

2.4 Selected publications

1. **Menand, T.,** Raw, A. and Woods, A. W. (2003) Thermal inertia and reversing buoyancy in flow in porous media. *Geophys. Res. Lett.* **30** (6), 1291, 10.1029/2002GL016294.

2. **Menand, T.** and Woods, A. W. (2005) Dispersion, scale, and time dependence of mixing zones under gravitationally stable and unstable displacements in porous media. *Water Resour. Res.* **41**, W05014, 10.1029/2004WR003701.

GEOPHYSICAL RESEARCH LETTERS, VOL. 30, NO. 6, 1291, doi:10.1029/2002GL016294, 2003

Thermal inertia and reversing buoyancy in flow in porous media

Thierry Menand, Alan Raw, and Andrew W. Woods
BP Institute for Multiphase Flow, University of Cambridge, Cambridge, UK

Received 17 September 2002; revised 4 December 2002; accepted 17 January 2003; published 21 March 2003.

[1] The displacement of fluids through porous rocks is fundamental for the recharge of geothermal and hydrocarbon reservoirs [*Grant et al.*, 1982; *Lake*, 1989], for contaminant dispersal through the groundwater [*Bear*, 1972] and in controlling mineral reactions in permeable rocks [*Phillips*, 1991]. In many cases, the buoyancy force associated with density differences between the formation fluid and the displacing fluid controls the rate and pattern of flow through the permeable rock [*Phillips*, 1991; *Barenblatt*, 1996; *Turcotte and Schubert*, 2002]. Here, using new laboratory experiments, we establish that a striking range of different flow patterns may develop depending on whether this density contrast is associated with differences in temperature and/or composition between the two fluids. Owing to the effects of thermal inertia in a porous rock, thermal fronts lag behind compositional fronts [*Woods and Fitzgerald*, 1993; *Turcotte and Schubert*, 2002], so that two zones of different density develop in the region flooded with injected fluid. This can lead to increasing, decreasing or even reversing buoyancy in the injected liquid; in the latter case it may then form a double-flood front, spreading along both the upper and lower boundary of the rock. Recognition of these different flow regimes is key for predicting sweep efficiency and dispersal patterns in natural and engineered flows, and offers new opportunities for the enhanced recovery of natural resources in porous rocks. *INDEX TERMS:* 1832 Hydrology: Groundwater transport; 1884 Hydrology: Water supply; 1829 Hydrology: Groundwater hydrology; 3665 Mineralogy and Petrology: Mineral occurrences and deposits. **Citation:** Menand, T., A. Raw, and A. W. Woods, Thermal inertia and reversing buoyancy in flow in porous media, *Geophys. Res. Lett.*, *30*(6), 1291, doi:10.1029/2002GL016294, 2003.

1. Introduction

[2] When a fluid of temperature $T + \Delta T$ and composition $C + \Delta C$ migrates through a porous layer initially saturated with fluid of temperature T and composition C, thermal and compositional fronts develop across which the properties of the injected fluid adjusts to that of the formation fluid. The compositional front travels with the interstitial speed, u/ϕ, where u is the transport (Darcy) velocity and ϕ the porosity of the matrix. However, heat is transferred between the invading fluid and the rock matrix, causing the thermal front to travel with the slower speed Γu where $\Gamma = (\rho C_p)_{liq}/\overline{(\rho C_p)} \sim O(1)$ is the ratio of the specific heat of the liquid to the average specific heat of the liquid and porous matrix [*Woods and Fitzgerald*, 1993; *Barenblatt*, 1996; *Turcotte and Schubert*, 2002]. This separation of the two fronts results in three regions of different density (Figure 1a). Near the source, the fluid retains the temperature and composition of the injected solution $\rho(T + \Delta T, C + \Delta C)$ (region a); ahead of the thermal front, but still within the injected solution, the fluid temperature has adjusted to that of the rock, and so the density has value $\rho(T, C + \Delta C)$ (region b); finally, in the original formation fluid, the density has value $\rho(T, C)$ (region c). These three regimes may be clearly seen in a simple draining experiment (Figure 1b) in which a fresh, hot aqueous solution, dyed in red, drains at a constant rate through a fine-bead pack initially saturated with a cold, saline aqueous solution. The successive positions of both the fluid front (compositional signal) and the temperature front (thermal signal) have been measured during the experiment (Figures 1b and 1c) and are in very good accord with the theoretical prediction.

2. Impact of the Thermal Inertia on Buoyancy Driven Flows in Porous Media

[3] In flows driven by the gravitational force associated with the difference in density between the injected and original fluid, the spatial decoupling of the thermal and compositional signals in the migrating fluid is crucial. To illustrate this we present three laboratory experiments (A, B and C) in which a dyed aqueous solution was injected from a point source at the base of a bead pack initially saturated with an aqueous solution of different density. In all experiments, the injected fluid is approximately 0.5% less dense than the fluid originally in the bead pack. However, the injected fluid had three different temperatures and compositions denoted by points A ($\Delta T = 0$°C, $\Delta C = -0.75$ wt%), B ($\Delta T = 19$°C, $\Delta C = 0$) and C ($\Delta T = 33.5$°C, $\Delta C = 0.75$ wt%) in Figure 2. As the three injected fluids migrate through the porous layer, the temperature of the injected fluid adjusts to that of the porous layer and hence their densities evolved in very different ways (Figure 2). Fluid A remains at the same temperature and hence density; fluid B cools to the temperature of the bead pack and the density adjusts to the density of the formation fluid; fluid C cools until its temperature matches that of the formation, at which point it has become dense relative to the formation fluid. These different density structures lead to very different flooding patterns as shown in Figures 3a to 3c.

[4] In case A, fluid of the same temperature as the fluid in the bead pack, but smaller composition, was injected from below. This produced a buoyant plume with no change in density of the source fluid (Figure 2, point A). As the flow evolved, there was a small amount of mixing in the head of the flow, but subsequently a sharp, nearly parallel-sided plume developed (Figure 3a). In case B, fluid of the same composition as the fluid in the bead pack, but higher temperature, was injected from below. As this fluid migrated upwards, the thermal front lagged behind the

0094-8276/03/2002GL016294$05.00

injected fluid so that neutrally buoyant fluid was supplied to the head of the plume (Figure 2, point B). This neutrally buoyant fluid then displaced the formation fluid radially outwards (Figure 3b), leading to a much larger head structure than in the saline experiment (Figure 3a). Meanwhile, the continuing injection of hot fluid heated up the porous layer to form a focused hot plume behind the head. Heat transferred from this plume to the surrounding porous matrix produced a zone of heated ambient fluid beside the source. This ambient fluid also ascended, producing the clear halo around the hot plume of injected fluid (Figure 3b). In case C, the injected fluid was hot but relatively saline compared to the formation fluid. As it displaced the formation fluid and cooled down, the density of the injected fluid actually became larger than the formation fluid, owing to the greater initial composition (Figure 2, point C). This change in the sign of the density of the injected fluid led to a more complex flow pattern. Initially, the injected fluid was of smaller density than the formation fluid, and so it ascended upwards. However, once it had cooled down, the density difference became controlled by the compositional difference, so that the injected fluid became relatively dense. It then descended back to the base of the bead pack, and spread laterally as a relatively dense compositional gravity current (Figure 3c). The continuing injection produced a growing fountain of hot fluid above the source and supplied the laterally spreading dense current.

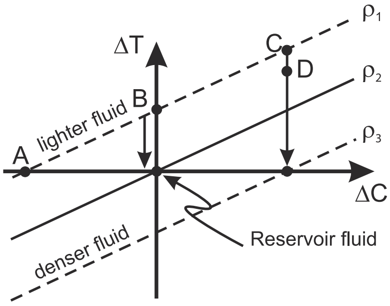

Figure 2. A Temperature-Composition phase diagram for an aqueous solution of NaCl illustrating curves of constant density, $\rho_1 < \rho_2 < \rho_3$. The different initial conditions for the experiments A-D are shown by solid circles. Arrows indicate how the density of the injected fluid evolves as it moves through the bead pack and its temperature adjusts to that of bead pack.

[5] In the case of reversing buoyancy, a fourth, different flow regime, case D, may develop and this is shown in Figure 3d. Here, relatively hot but saline fluid (Figure 2, point D) was injected from the top of the bead pack rather than the base of the bead pack. Initially, the relatively buoyant fluid spread laterally along the upper surface of the formation. However, as the fluid migrated through the

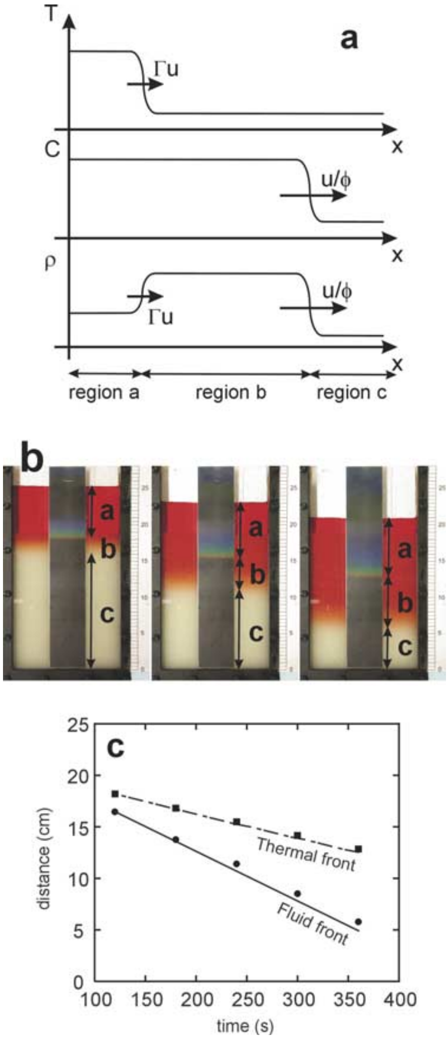

Figure 1. (opposite) (a) Diagram illustrating the spatial distribution of (i) temperature, T; (ii) composition, C and (iii) density, ρ as fluid of one temperature and composition is injected into a bead pack saturated with fluid of different temperature and composition. The spatial decoupling of the thermal and fluid fronts creates three regions in which the fluid has different density: near the source (region a), between the thermal and compositional fronts (region b) and in the original formation fluid (region c). (b) Photographs from an experiment in which hot, fresh water dyed red drained downwards at a constant rate through a bead pack initially saturated with cold, saline water. The bead pack has porosity 0.4 ± 0.01, has dimensions 15 cm wide, 19 cm high, 1 cm deep, and is made of ballotini 425–600 μm in diameter. The specific heat ratio for this experiment including the thermal mass of the bead pack and cell walls, which are in equilibrium with the fluid, is $\Gamma \approx 1.7$. The flow rate was 0.3 cm^3 s^{-1}. The advancing front of fresh water is shown by the red dye front, while the yellow horizontal line on the liquid crystal strip illustrates the leading edge of the thermal front. (c) The location of the dye front and the thermal front measured during the experiment are indicated by circles and squares respectively. The solid line indicates the location of the dye front as predicted by a pure volume displacement, indicating that there is little dispersive mixing across the compositional front. The dashed line indicates the location of the thermal front Γut. Both are in excellent accord with the data.

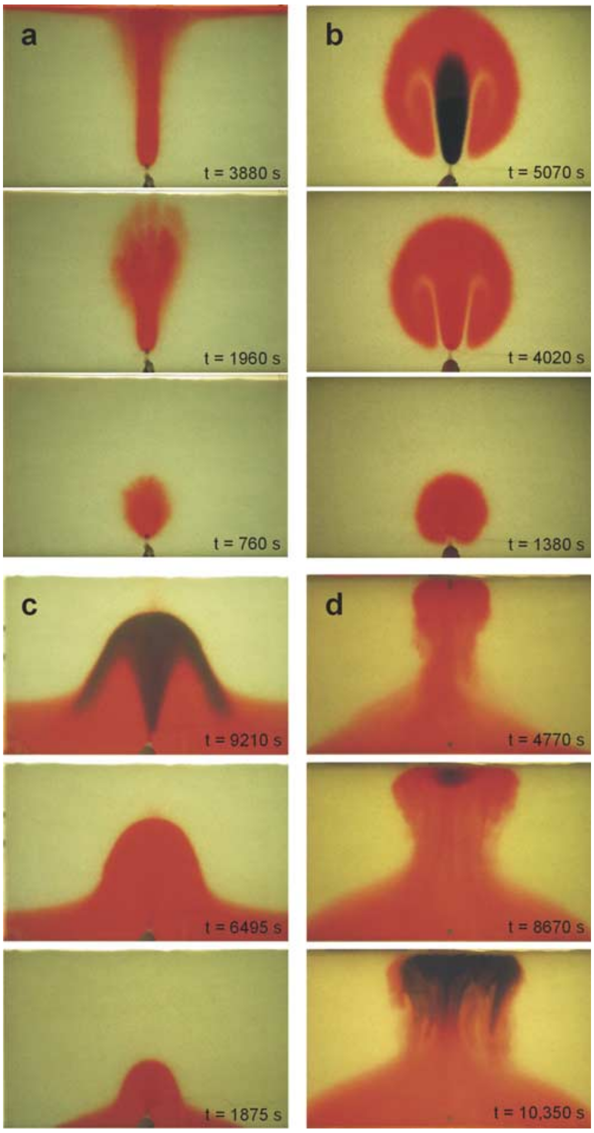

Figure 3. Four sequences of photographs illustrate the flow patterns that arise when fluid of one temperature and composition, dyed red, is continuously injected from a point source into a porous layer saturated with fluid of different temperature and composition. The initial conditions are shown in Figure 2. In the experiments, darker dye is added to the red injected fluid after some time to reveal the evolving flow pattern. (a) The fluid injected at the base of the bead pack has smaller composition than the formation fluid, but the same temperature; (b) The fluid injected at the base of the bead pack has the same composition, but is hotter that the formation fluid; (c) The fluid injected at the base of the bead pack has greater composition but is hotter than the formation fluid, but so that initially it is of smaller density; (d) The fluid injected at the top of the bead pack has greater composition but is hotter than the formation fluid so that, as in (c), it is initially of smaller density.

hot thermal front and cooled, the greater composition of the injected fluid caused it to become dense relative to the formation (Figure 2, point D), and the fluid sank to the base of the layer. Here, a compositionally-driven dense current spread out along the base of the layer. Meanwhile, the continuing injection of fluid led to a gradual lateral spreading of the hot thermal front along the upper surface of the porous layer, thereby forming a double-flood front (Figure 3d).

3. Conclusion

[6] This rich variety of flow patterns resulting from the separation of the thermal and compositional fronts may be key for accurate prediction of (i) the dispersal of contaminants injected into permeable sub-surface rocks, especially in evaluating risks of sub-surface storage of nuclear waste; (ii) the dispersal of reacting fluids over geological timescales, which may control the spatial distribution of diagenetic reactions and hence mineral deposits; and, (iii) the sweep pattern in high permeability geothermal or hydrocarbon reservoirs in which there are often significant temperature and compositional contrasts between the injected and formation water. These complex thermo-solutal transport effects introduce new challenges for theoretical models of dispersion and transport, since the flow structures identified herein are controlled by thermal boundary layers located in the interior of the flow domain and which are therefore hard to resolve accurately. However, the fundamental process of buoyancy reversal can lead to injected fluids spreading along both the upper and lower boundaries of a permeable rock; as with our experiments. If the injected fluid is engineered appropriately, this could result in substantially enhanced oil recovery from high temperature sub-surface hydrocarbon reservoirs or layered reaction zones within a reacting permeable matrix.

[7] **Acknowledgments.** This work was supported by the BP Institute for Multiphase Flow. T. Menand was also supported by a Newton Trust Fellowship.

References

Barenblatt, G. I., *Scaling, Self-Similarity, and Intermediate Asymptotics*, 386 pp., Cambridge Univ. Press, New York, 1996.

Bear, J., *Dynamics of Fluids in Porous Media*, 764 pp., Dover, Mineola, N.Y., 1972.

Grant, M. A., I. G. Donaldson, and P. F. Bixley, *Geothermal Reservoir Engineering*, 369 pp., Academic, San Diego, Calif., 1982.

Lake, L. W., *Enhanced Oil Recovery*, 550 pp., Prentice-Hall, Old Tappan, N.J., 1989.

Phillips, O. M., *Flow and Reactions in Permeable Rocks*, 285 pp., Cambridge Univ. Press, New York, 1991.

Turcotte, D. L., and G. Schubert, *Geodynamics*, 456 pp., Cambridge Univ. Press, New York, 2002.

Woods, A. W., and S. D. Fitzgerald, The vaporization of a liquid front moving through a hot porous rock, *J. Fluid Mech.*, *251*, 563–579, 1993.

T. Menand, A. Raw, and A. W. Woods, BP Institute for Multiphase Flow, University of Cambridge, Madingley Rise, Madingley Road, Cambridge CB3 0EZ, U.K. (thierry@bpi.cam.ac.uk; alan@bpi.cam.ac.uk; andy@bpi.cam.ac.uk)

WATER RESOURCES RESEARCH, VOL. 41, W05014, doi:10.1029/2004WR003701, 2005

Dispersion, scale, and time dependence of mixing zones under gravitationally stable and unstable displacements in porous media

T. Menand

Centre for Environmental and Geophysical Flows, Department of Earth Sciences, University of Bristol, Bristol, UK

A. W. Woods

BP Institute for Multiphase Flow, University of Cambridge, Cambridge, UK

Received 1 October 2004; revised 21 February 2005; accepted 10 March 2005; published 18 May 2005.

[1] We report on an experimental study of the mixing of two miscible fluids in a porous medium driven by either a gravitationally stable or unstable linear displacement flow. A solution of a given NaCl concentration was injected at a constant rate into a homogeneous bead pack saturated with an aqueous solution of different NaCl concentration. The position and width of the fluid interface were recorded using digital image analysis. Our results highlight the strong interplay between gravity and mechanical dispersion. For stable flows, at low Péclet number Pe, the dispersion coefficient increases with Pe, whereas for Pe >500, it becomes constant. Although similar regimes are observed with pure mixing, the stabilizing effect of gravity reduces significantly the dispersion coefficient by a factor of 2–4, even for density contrasts as low as 0.07%. For unstable flows, gravitational instability is delayed by mechanical dispersion. The ratio of the gravitational to background fluid velocity, *G*, controls the initial diffusive growth of the mixing zone and the time at which the instability subsequently arises. The wavelength of the instability scales with the width of the diffusive mixing zone at onset of instability and its subsequent linear convective growth rate is one fourth of the unstable gravity speed. For natural porous flows, mechanical dispersion can suppress the onset of gravitational instability until the mixing zone is 1–2 m thick. The width of this mixed zone then controls the length scale of the unstable fingers.

Citation: Menand, T., and A. W. Woods (2005), Dispersion, scale, and time dependence of mixing zones under gravitationally stable and unstable displacements in porous media, *Water Resour. Res.*, *41*, W05014, doi:10.1029/2004WR003701.

1. Introduction

[2] Miscible displacements in porous media occur in a wide range of geophysical, environmental and industrial applications. Examples include miscible displacements in oil reservoirs, the migration of pollutants through aquifers and the repeated intrusion of sea water into aquifers in coastal environments. A crucial issue in these applications is the characterization of the zone in which the displacing fluid mixes with the original fluid. If both fluids have identical physical properties, such as density and viscosity, then the heterogeneities of the permeable rock dictate the behavior of the interface [*Phillips*, 1991]. Tracer dispersion is often used to map out such heterogeneities; tracer is injected into the underground flow and its concentration is then measured at some distance from the point of injection. However, in many cases the properties of the displacing and displaced fluids differ and this can lead to flow instabilities.

[3] Study of flow instabilities in porous media started 50 years ago when *Hill* [1952] showed that both density and viscosity contrasts can either trigger or suppress the development of instabilities in homogeneous porous media. This experimental and analytical work was followed by theoretical studies which showed how negative density gradients or positive viscosity gradients favor Rayleigh-Taylor and Saffman-Taylor instabilities respectively, whereas opposite gradients prevent them [*Saffman and Taylor*, 1958; *Chuoke et al.*, 1959; *Chandrasekhar*, 1961].

[4] Factors that act against the onset of instability are dispersion, in the case of miscible displacements, and surface tension, in the immiscible case, which both tend to suppress the smallest wavelengths. Molecular diffusion is generally too small a parameter to affect flow instability. However, the presence of multiple pathways in a porous medium leads to natural dispersion of the flow. This dispersion is usually characterized by a coefficient *D*, the coefficient of mechanical dispersion, which depends on both the geometrical structure of the porous matrix and the structure of the fluid flow. As a result, this flow dispersion is difficult to quantify: models require some assumption on how fluid mixing occurs in the pores; for example if it occurs along capillaries or at the pore junctions, one gets rather different relationships between the dispersion coefficient and the mean flow velocity *u* [*Taylor*, 1953; *Scheidegger*, 1954; *Aris*, 1956; *De Josselin de Jong*,

0043-1397/05/2004WR003701$09.00

1958; *Saffman*, 1959, 1960; *Bear*, 1972]. Hydrodynamic dispersion depends generally on both molecular diffusion D_o and the flow field [*Pfannkuch*, 1963]. The Péclet number Pe = ua/D_o, where the length scale a is typically the grain size of the medium, characterizes the strength of convection relative to molecular diffusion. In the tracer case, where displacing and displaced fluids have identical density, it has been observed experimentally that the coefficient of mechanical dispersion increases continuously with Pe from a value close to that of molecular diffusion for flows at extremely low Péclet number to values that are several orders of magnitude greater when the flow regime reaches the limit for which Darcy's law applies [*Pfannkuch*, 1963].

[5] The dimensionless number that is usually used to described the occurrence of instability in variable density systems is the Rayleigh number Ra, the ratio of buoyancy to diffusion and dispersion. *Wooding* [1959] showed that the occurrence of instability was related to density differences and the average pore velocity but also that instability cannot develop if the Rayleigh number of the flow is less than a critical value Ra_c, below which the negative, and therefore potentially unstable, density gradient is resisted by viscous resistance and diffusion and the flow remains stable. However, this Rayleigh stability criteria gives only a threshold for the onset of instability but does not provide any information on the wavelength or the growth rate of the instability. *List*'s [1965] analysis and the work by *Schincariol and Schwartz* [1990] and *Schincariol et al.* [1994, 1997] showed that whether or not perturbations become unstable depends not only on the Rayleigh number of the system but also upon the perturbation wavelength, which must exceed some critical wavelength determined by the flow and the transport parameters; a system where a heavy fluid overlies a lighter one is always potentially unstable, but only perturbations with a wavelength greater than a critical wavelength will grow, while those below decay. These studies reveal also that (1) larger wavelengths grow at a larger rate and are thus more unstable, (2) the instability growth rate increases with density difference, and (3) the instability is enhanced by decreasing dispersivity; dispersion acts against instability.

[6] There is often difficulty in applying Rayleigh number concepts in a transient system, however, because of the difficulty in defining an unambiguous length scale and determining the dispersion associated with the flow [*Oostrom et al.*, 1992a; *Simmons et al.*, 2001]. Arguments based on dimensional analysis reveal that in a mixed convective system the Rayleigh number alone is not sufficient to characterize the instability of the system and that the ratio of free over forced convection must also be considered [*Oostrom et al.*, 1992a, 1992b; *Liu and Dane*, 1996]. Moreover, Rayleigh number concepts implicitly assume that mechanical dispersion is constant and independent of the convective flow velocity. Instead, the onset of instability has been shown to be dependent upon the dispersivity of the system, which depends on the convective flow velocity, particularly in mixed convective systems [*Schincariol et al.*, 1994].

[7] Recent studies have investigated how dispersivity is affected by density and viscosity contrasts [*Jiao and Hötzl*, 2004; *Wood et al.*, 2004]. The work by *Wood et al.* [2004] dealt specifically with gravitationally unstable flows and shows that unstable mixing increases as the density difference between fluids increases, as parameterized by the ratio of free over forced convection M. However, this work does not provide any quantitative information for the relationship that exists between this ratio M and the fluid mixing at the interface, other than the qualitative statement that mixing increases with M. This increase of mixing, induced by the development of unstable fingers could be interpreted as an increase in effective or apparent dispersion. However, as the authors state, additional experimental and theoretical development is required in order to explore the time and scale dependence of the mixing caused by unstable fingering. *Jiao and Hötzl* [2004] studied both stable and unstable displacements and measured the dispersion coefficient for various density or viscosity contrasts. Their results show that dispersion is reduced by stable density contrasts and is enhanced by unstable density contrasts whereas dispersion increases with the viscosity ratio, irrespective of the viscous stability of the flow. However, the authors have not developed quantitatively the process relationship as a function of dimensionless parameters such as the Péclet number and the ratio of free over forced convection, nor a complete description of the spatial and temporal scaling.

[8] The aim of the present paper is (1) to quantify the effect of density difference on mechanical dispersion both in gravitationally stable and unstable flows and (2) to determine how this process relationship affects the spatial and time development of instability in the latter case. As mentioned previously, several difficulties arise when one wants to apply Rayleigh number concepts in a transient system undergoing mixed convection with variable density. For these reasons, Rayleigh number calculations are not given in this paper. Instead, the dimensionless numbers presented here are limited to more easily quantified parameters such as the ratio of the gravitationally driven flow rate to the applied flow rate, referred to here as the gravity number, and the Péclet number that capture the key physical parameters, that is the density difference and the strength of advective flow.

[9] Flows in porous media at low Reynolds number are governed by Darcy's law which states that the transport velocity, or Darcy velocity, is proportional to the pressure gradient:

$$\mathbf{u} = -\frac{k}{\mu}\left(\nabla p + \Delta\rho g\right)\mathbf{z}. \qquad (1)$$

Here, $\mathbf{u}$ is the velocity vector, $\mathbf{z}$ is a unit vector directed vertically upward, k is the permeability of the medium, μ is the dynamic viscosity of the fluid, ∇p is the non hydrostatic pressure gradient and $\Delta\rho g$ is the pressure gradient induced by the density change experienced by the fluid $\Delta\rho$. The right hand side of this expression can be split into two terms $u_s = -k/\mu\nabla p$ and $u_g = -k/\mu\Delta\rho g$. u_s is the velocity associated with the non hydrostatic pressure gradient and can be seen as a source velocity created by an external imposed flow rate (the background flow), whereas u_g is the velocity scale associated with the gravitational force. We now introduce the gravity number G to represent the ratio of buoyancy to viscous forces:

$$G = \frac{k\,\Delta\rho\,g}{\mu\,u_s} = \frac{u_g}{u_s}. \qquad (2)$$

Increasing the background flow decreases the gravity number and thus the impact that gravity could have on the porous flow and in particular on instabilities. This should be the case particularly when the background flow is comparable to or greater than the gravitational flow, that is for $G \geq 1$. Moreover, this partition could in principle affect mechanical dispersion as well.

[10] Finally, by recognizing that the Rayleigh number can be expressed as the product of the Péclet and gravity numbers, we argue that the description of the system in term of its Péclet and gravity numbers provides a complete description of the mixing.

[11] Here, we report our study of the impact of the gravity number on the behavior of the mixing zone between two miscible fluids. This work is based on laboratory experiments in which a solution of a given NaCl concentration is injected, vertically and downward, at a constant rate into a homogeneous porous medium saturated with an aqueous solution of different NaCl concentration. Two series of experiments have been carried out. In the first series, the invading fluid is less saline and so it is lighter than the displaced fluid and the configuration is gravitationally stable. In the second series, the invading fluid is the more saline leading to a gravitationally unstable configuration. We first introduce the experimental apparatus and techniques that we developed to measure the evolution of the mixing zone. We then describe the experimental results.

2. Experimental Method

2.1. Setup

[12] Our porous medium is a 15 ± 0.1 cm wide, 23.5 ± 0.1 cm high and 1 ± 0.05 cm thick bead pack made of glass beads of size $a = 1.5$ mm, with porosity $\phi = 0.39 \pm 0.01$ and permeability $k = 1.9 \times 10^{-9} \pm 0.1 \times 10^{-9}$ m^2. A homogeneous and isotropic bead pack was achieved by slowly pouring the glass beads into the tank after the latter had been previously filled with the ambient fluid, either water or NaCl solution. This technique prevented the entrapment of air bubbles in the bead pack and thus ensured its saturation.

[13] The coefficient of molecular diffusion D_o of the aqueous solutions used in the experiments has been assumed to be 10^{-9} m^2 s^{-1} [*Phillips*, 1991]. The injected solution flows vertically downward and displaces the ambient solution at a constant rate; fluid drains out of the base of the bead pack at the same rate as it is injected at the top. This was achieved by using a double head peristaltic pump, one head being connected to the top of the bead pack and the other at its bottom, which ensured that both inflow and outflow were constant and identical during an experiment.

[14] Both the Péclet number and the gravity number have been systematically varied to assess their effect on the spreading of the fluid front (Figure 1). This was achieved by varying the flow rate of the pump and the density difference between the fluids. Pump limitations restricted the Péclet number to a minimum value of 15 whereas its maximum value was 4300. This latter number corresponds to a maximum Reynolds number of 10, usually considered as the upper limit of Darcy regime [*Nield and Bejan*, 1999]. NaCl concentrations between 0 and 20 wt% enabled a range of gravity number of 0–300. Details of experimental conditions are given in Table 1.

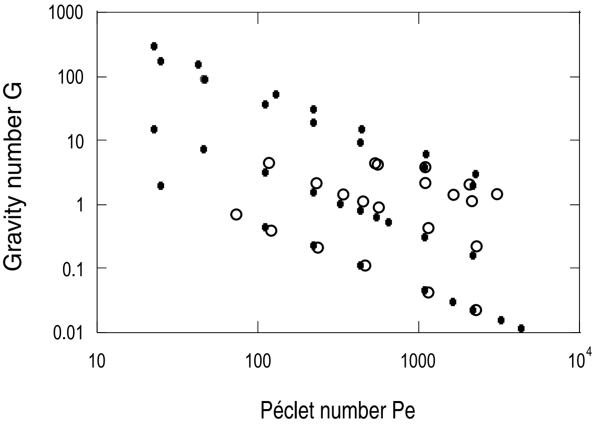

Figure 1. Range of gravity and Péclet numbers covered in the experiments. Dots refer to experiments in stable configurations and circles to experiments in unstable configurations.

[15] In the gravitationally unstable configurations, a 3 cm thick layer of fine glass beads (180–300 μm in diameter) was placed at the top of the bead pack in order to start the experiments with a horizontal, flat interface. The salty fluid was initially injected rapidly through this very low permeability layer and then the flow rate was lowered to the experimental rate as the fluid interface approached the bead pack. This technique delayed the growth of the gravitational instability sufficiently that the injected fluid enters the bead pack with a horizontal and flat interface.

[16] To follow the interface between the two fluids and measure the rate of dispersion, the injected solution was dyed red. The mass of dye used was low enough (5×10^{-2} wt%) to ensure that it does not affect the density difference between the two fluids. Digital photographs were taken at regular time intervals during an experiment with a Nikon Coolpix 995. The digital camera was placed at a distance of 1.5 m from the bead pack, which was illuminated by a projector 1.3 m behind it with a mask that ensured light was only transmitted through the bead pack.

2.2. Image Analysis

[17] Digital photographs were analyzed with the software MATLAB using the following procedure. Each digital photograph was first rotated to ensure they all had the same orientation. The portion containing the bead pack was then cropped, thus providing the image that was subsequently analyzed. When reading a colored image with MATLAB, each pixel of that image is assigned a red, green, and blue value between 0 and 255 according to the transmitted light intensity, so a simple way of defining a light intensity for each pixel is to add these values. This was done in several steps.

[18] Although great care was taken to ensure the light was as uniform as possible, spatial and temporal variation cannot totally be avoided. One of the best ways to correct the lighting nonuniformity is to subtract a photograph of the bead pack that had been taken just prior to the start of the experiment and that is used as a background image [*Schincariol et al.*, 1993]. This gave corrected red, green and blue values for each pixel.

Table 1. Experimental Details of the Experiments[a]

Stable Configuration				Unstable Configuration					Tracer Case		
Exp	$\bar{v}_s$, m s^{-1}	G	Pe	Exp	$\bar{v}_s$, m s^{-1}	G	Pe	Obs	Exp	$\bar{v}_s$, m s^{-1}	Pe
1	3.1×10^{-5}	7.6	46	35	1.5×10^{-3}	0.2	2265	S	56	6.2×10^{-5}	93
2	7.4×10^{-5}	3.2	110	36	7.6×10^{-4}	0.4	1142	S	57	1.2×10^{-4}	183
3	1.5×10^{-4}	1.6	218	37	3.8×10^{-4}	0.9	566	T	58	2.2×10^{-4}	330
4	2.2×10^{-4}	1.1	326	38	2.3×10^{-4}	1.5	343	T	59	5.6×10^{-4}	840
5	2.9×10^{-4}	0.8	433	39	3.0×10^{-4}	1.1	457	T	60	2.5×10^{-3}	3750
6	3.6×10^{-4}	0.6	541	40	1.5×10^{-4}	2.2	232	U	61	2.8×10^{-5}	42
7	4.3×10^{-4}	0.5	648	41	7.5×10^{-5}	4.3	116	U	62	1.3×10^{-3}	1890
8	7.2×10^{-4}	0.3	1079	42	3.7×10^{-4}	4.3	551	U	63	1.5×10^{-5}	23
9	1.4×10^{-3}	0.2	2154	43	3.6×10^{-4}	4.3	544	U	64	9.7×10^{-6}	15
10	1.4×10^{-3}	0.02	2154	44	7.3×10^{-4}	2.1	1099	U			
11	1.1×10^{-3}	0.03	1616	45	1.1×10^{-3}	1.4	1639	T			
12	7.2×10^{-4}	0.05	1079	46	1.4×10^{-3}	1.1	2163	T			
13	2.9×10^{-4}	0.1	433	47	7.3×10^{-4}	3.9	1095	U			
14	1.5×10^{-4}	0.2	218	48	1.4×10^{-3}	2.1	2065	U			
15	7.4×10^{-5}	0.5	110	49	2.0×10^{-3}	1.4	3075	S			
16	2.9×10^{-3}	0.01	4306	50	4.9×10^{-5}	0.7	74	T			
17	2.2×10^{-3}	0.02	3230	51	8.0×10^{-5}	0.4	120	T			
18	7.4×10^{-5}	39	110	52	1.6×10^{-4}	0.2	236	S			
19	3.1×10^{-5}	93	46	53	3.1×10^{-4}	0.1	466	S			
20	1.5×10^{-4}	20	218	54	7.7×10^{-4}	0.04	1155	S			
21	2.9×10^{-4}	9.8	433	55	1.5×10^{-3}	0.02	2263	S			
22	7.2×10^{-4}	4.0	1079								
23	1.4×10^{-3}	2.0	2154								
24	2.8×10^{-5}	161	42								
25	1.5×10^{-5}	306	22								
26	8.6×10^{-5}	53	129								
27	1.5×10^{-4}	31	218								
28	2.9×10^{-4}	16	439								
29	7.4×10^{-4}	6.2	1106								
30	1.5×10^{-3}	3.0	2250								
31	3.1×10^{-5}	91	47								
32	1.6×10^{-5}	174	25								
33	1.5×10^{-5}	16	22								
34	1.6×10^{-5}	2.1	25								

[a] Exp, Experiment; Obs, Observations; S, stable interface; T, transition; U, unstable interface.

[19] Red, green, and blue values do not vary with the dye concentration in the same way however: both the blue and green values increase with dye concentration while the red value decreases with increasing dye concentration. Therefore an intensity profile was defined by adding the blue and green profiles and subtracting the red one. This intensity varies linearly with dye concentration provided the latter does not exceed 0.5 g/L (Figure 2), higher concentration leading to intensity saturation.

[20] In order to estimate the vertical mixing of the fluids, the dye intensity values for each horizontal row of pixels were averaged. This provided a very high resolution, horizontally averaged vertical profile of the dye intensity. In order to reduce the noise in this profile associated with subbead-scale scattering of light, the signal was then filtered by using the average intensity of each set of nine adjacent data points to represent the dye intensity at the central point of each set of nine data points; this leads to a very smoothly varying profile of dye intensity.

[21] Finally, we used the fact that dye concentration at both ends of the bead pack is fixed: dye concentration has value 1 at the source, provided that the fluid interface has progressed sufficiently into the bead pack, typically more than 2 cm, and has value 0 at the bottom of the bead pack. Therefore, for each image, the average intensity value at the source and at the bottom of the bead pack were used to normalize the intensity profile of that image. The normalized profile of dye concentration was then identified with this normalized intensity profile.

[22] This simple method gives results that are reproducible within 5% (the difference between two intensity profiles calculated from two photographs taken in quick succession). Its resolution depends mainly on the capacity of the digital camera. For the study described in this paper, images were acquired at a resolution of 7 pixels per mm.

[23] Repeating this procedure for digital photograph taken at successive times, enabled us to follow the time

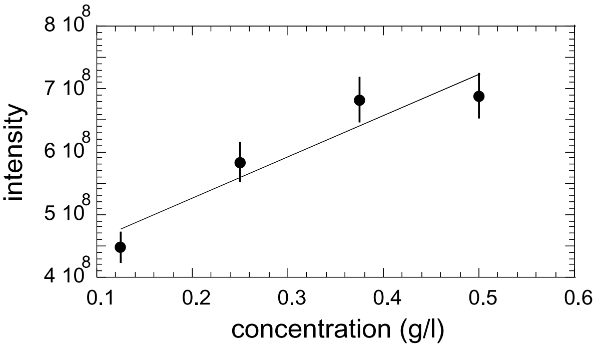

Figure 2. Variation of light intensity with dye concentration.

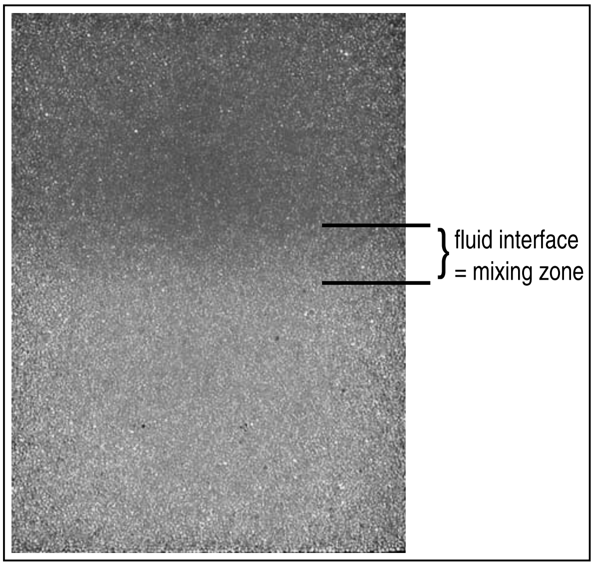

Figure 3. Photograph of experiment 4 at time t = 405 s after start of injection. The mixing zone is 3.1 cm thick. See color version of this figure at back of this issue.

evolution of the interface between the red injected solution and the ambient one, and to measure the spreading of the mixing zone by mechanical dispersion.

3. Experiments With a Gravitationally Stable Configuration

[24] In this series of experiments, fresh red water displaced a NaCl solution at a constant rate and G and Pe have been varied over five and three orders of magnitude respectively (Figure 1). We also report tracer experiments, for which the displacing fluid was identical to the displaced fluid except for its small dye content. These tracer experiments serve as a reference.

[25] In the stable configuration, the interface between the two fluids, characterized by a zone with various shades of pink, remains horizontal during the whole displacement (Figure 3) and becomes thicker as it flows through the bead pack. The concentration of the injected fluid along the bead pack is obtained from each photograph. In the pure tracer dispersion case, as the injected fluid invades a porous medium and disperses the ambient fluid, the mixing zone at the fluid interface spreads according to the dispersion equation [*Bear*, 1972]. We now investigate whether the concentration of injected fluid $C(x, t)$ in our experiments also varies along the flow direction from $C(0, t) = 1$ at the top of the bead pack, $x = 0$, to $C(H, t) = 0$ at the bottom, $x = H$, according to the relation

$$C(x,t) = \frac{1}{2}\, erfc\left(\frac{x - x_{\mathrm{int}}(t)}{w(t)/\sqrt{2}}\right). \tag{3}$$

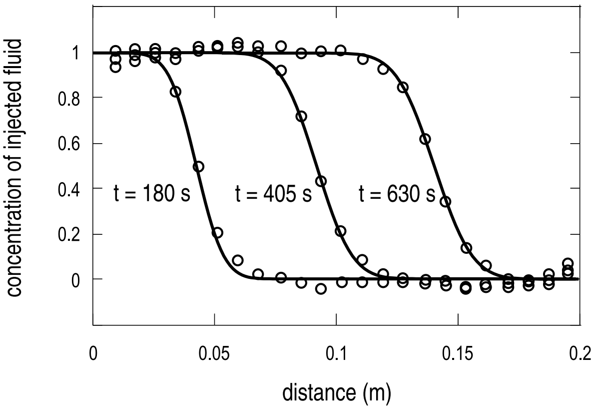

Figure 4. Concentration profiles (circles) at three different times during experiment 4. Fits are equation (3).

Here, the position $x_{\mathrm{int}}(t)$ of the interface is calculated by a pure volume displacement: $x_{\mathrm{int}} = \bar{v}_s\, t = u_s t/\phi$, where the interstitial velocity (or mean pore velocity) is obtained by dividing the source flow rate Q by the effective cross-sectional area ϕA of the bead pack. The width $w(t)$ of the interface is usually taken as the distance that separates concentrations $C = 0.8413 \simeq 0.84$ and $C = 0.1587 \simeq 0.16$ [*Fried and Combarnous*, 1971; *Bear*, 1972]. We find that in the stable displacement experiments, the actual concentration profile is in very good accord with the theoretical model equation (3) as shown on Figure 4. By fitting the concentration profiles obtained from the photographs with equation (3), we can determine the width of the mixing zone at different times and measure its evolution during each experiment. In a stable configuration, we expect the mixing zone to spread diffusively and therefore to grow as

$$w(t) = 2\sqrt{2\, D_L\, t}, \tag{4}$$

where D_L is the longitudinal coefficient of mechanical dispersion [*Fried and Combarnous*, 1971]. This coefficient controls the growth of the mixing zone and therefore characterizes the spreading of the interface as it travels through the bead pack. For each experiment, D_L has been calculated by fitting the time evolution of the width $w(t)$ with equation (4). The coefficients of mechanical dispersion D_L for these stable experiments are shown on Figure 5 as a

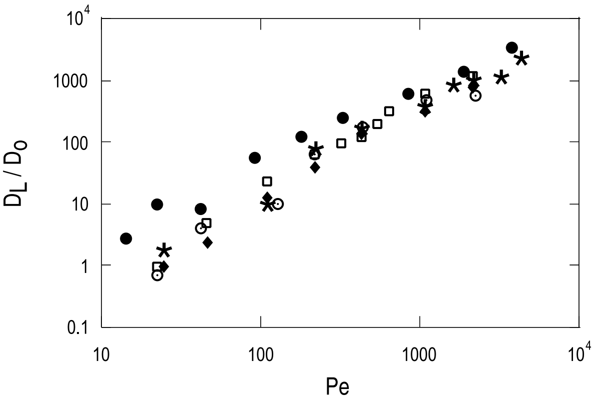

Figure 5. Normalized dispersion coefficient as a function of Péclet number. Each symbol corresponds to a density contrast: dots, tracer case (no density contrast); stars, 0.07%; squares, 0.5%; diamonds, 0.7%; dotted circles, 1.4%.

function of Pe where they have been normalized by the coefficient of molecular diffusion D_o. Coefficients calculated from tracer experiments are also reported on Figure 5 for comparison.

[26] In the tracer case, several regimes have been experimentally observed [*Pfannkuch*, 1963; *Fried and Combarnous*, 1971; *Bear*, 1972], which correspond to different mixing mechanisms. Two end-member mixing models for mechanical dispersion in porous media have been derived. In the first model, mechanical dispersion occurs mainly across the individual channels that connect pores and as a result D_L is proportional to $\bar{v}_s^2$ [*Taylor*, 1953; *Aris*, 1956]. In the other model, it is assumed that mixing occurs on the contrary within the pores, that is at the junctions of the channels, which leads to a dependence of D_L on $\bar{v}_s$ [*Bear*, 1972]. According to these models, $(a\ \bar{v}_s)$ arises as a natural dispersion scale and, therefore a natural graphic representation of mechanical dispersion is illustrated by plotting $D_L/(a\ \bar{v}_s)$ as a function of Pe [see also *Perkins and Johnston*, 1963]. It then appears that for Péclet numbers greater than 5–10 mechanical dispersion becomes more important than, although influenced by, molecular diffusion and $D_L/(a\ \bar{v}_s) \simeq 0.5\ \mathrm{Pe}^m$ with $0 < m < 0.2$. This regime corresponds to a fluid mixing which is intermediate to that predicted by Taylor's and Bear's models. The pure mechanical dispersion regime occurs at higher Péclet numbers, typically $\mathrm{Pe} > 10^2–10^3$, where $D_L/(a\ \bar{v}_s) \simeq 1.8 \pm 0.4$. This latter regime corresponds to Bear's model where all the mixing occurs within pores.

[27] We have normalized the coefficients of mechanical dispersion for both tracer and stable experiments by $(a\ \bar{v}_s)$ and plotted them as a function of the Péclet number on Figure 6. Scalings reported in the literature for tracer case have also been drawn for comparison. Our dispersion coefficients appear to be systematically of lower value than those from the literature, even when comparing tracer case values. This might reflect the use of regular, round glass beads in contrast to most other studies which have used less regular materials, such as sand [*Pfannkuch*, 1963]. However, the key point here is that Figure 6 clearly shows that mechanical dispersion is decreased significantly by gravity. For the tracer case, we observe that the two different regimes of mechanical dispersion are characterized by a change of scaling at Pe ~ 300:

$$D_L/(a\bar{v}_s) \simeq 0.07\,\mathrm{Pe}^{0.45} \quad \text{for Pe} < 300, \tag{5}$$

$$D_L/(a\bar{v}_s) \simeq 0.8 \pm 0.1 \quad \text{for Pe} > 300, \tag{6}$$

whereas, despite some scattering, we observe for stable experiments that the two regimes are characterized by two different scalings with transition at Pe ~ 500:

$$D_L/(a\bar{v}_s) \simeq (0.005 \pm 0.0025)\,\mathrm{Pe}^{0.7\pm0.3} \quad \text{for Pe} < 500, \tag{7}$$

$$D_L/(a\bar{v}_s) \simeq 0.4 \pm 0.1 \quad \text{for Pe} > 500. \tag{8}$$

In the high Péclet number regime, gravity halves $D_L/(a\ \bar{v}_s)$ compared with the tracer case. In the low Péclet number regime, dispersion coefficients get even smaller and are only approximatively 1/4 of the tracer values, even for very low density contrasts. However, given the scattering of the data, measured dispersion coefficients in the stable experiments do not seem to differ markedly from one another despite a gravity number spanning two orders of magnitude at a given Péclet number (Figure 1).

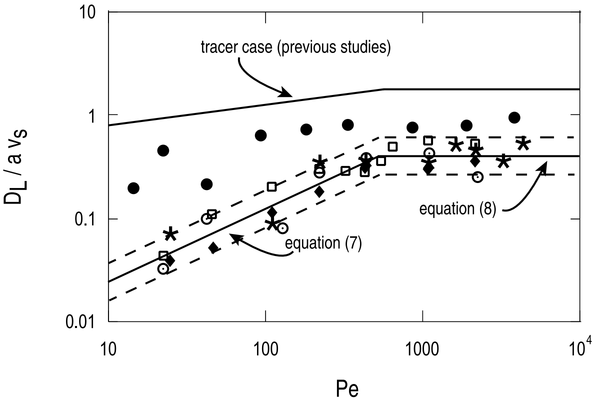

Figure 6. $D_L/(a\ \bar{v}_s)$ versus Pe. Symbols are the same as on Figure 5. Solid curves are tracer case scalings reported in the literature [*Pfannkuch*, 1963; *Fried and Combarnous*, 1971; *Bear*, 1972] and our scalings (equations (7) and (8)). Dashed curves represent the uncertainties on our scalings.

[28] Density contrasts act on perturbations of the fluid front. In a homogeneous medium, perturbations of the fluid front arise owing to (1) the fluid flowing faster at the center of pores than close to the surface of grains, (2) changes in pore cross section along the flow path and (3) local flow directions, induced by the tortuosity of the medium, that differ both from one pore to another and from the mean flow direction. Our results indicate that density contrasts as small as 0.07% (corresponding to a concentration difference in NaCl of 0.1 wt%) are able to oppose such perturbations and thus to decrease significantly the spreading of the front by dispersion that would be expected in the tracer case. Perhaps more surprisingly, our results also seem to indicate that higher density contrasts, even 200 times as high, are not more effective in suppressing such perturbations and hence do not reduce the dispersion relative to flows with lower density contrasts. This may indicate that there is some irreducible dispersive mixing associated with the tortuous flow which cannot be suppressed by gravity, that is, perturbations of the fluid front induced by the tortuous flow seem to be always present that cannot be suppressed by gravity forces. For dispersion to be even more reduced would require the further reduction of these perturbations but it seems that the tortuous pathways of the flow creates always some perturbations of the fluid front and that although gravity forces will tend and oppose such perturbations these ever present multiple tortuous pathways ensure that some perturbations will always be created and lead to some irreducible mixing.

4. Experiments With a Gravitationally Unstable Configuration

[29] In this series of experiments, red NaCl solution displaced fresh water downward at a constant rate and G

and Pe have been varied over two orders of magnitude (Figure 1).

4.1. Observations

[30] Although the starting configuration of this series of experiments is unstable, it was observed that the flow did not develop any instability for a certain range of initial conditions and that the fluid interface remained horizontal, whereas the flow developed unstable fingers for other initial conditions.

[31] Indeed, for small gravity numbers, the flow appeared to be very similar to the flow started from a gravitationally stable configuration, maintaining a flat fluid interface that widened as it flowed through the porous medium. For large gravity numbers, the flow developed unstable thin fingers of red fluid that intruded into the layer of lighter fluid, 5 to 7 fingers being typically observed initially although up to 12 tiny fingers have been observed at the onset of some experiments. As the flow carried on, the number of fingers seemed to decrease as the fingers widened and some of them merged. Typically, 4 to 5 of them remained at the end of the experiments, defined as the time at which the fingers reached the base of the experimental tank. These sinking red fingers were separated by channels of white, lighter fluid that were gradually flushed downward by the continuing flow from above. Moreover, these channels of light fluid were generally thicker than the dense sinking fingers. Such a feature has also been observed in the case of Rayleigh-Taylor instability in a Hele-Shaw cell rather than a porous medium [*Lewis*, 1950], but in the present porous case the tip of the light channels appear less rounded. Finally, it was noticed that the upper part of the bead pack, flushed by the dense red solution and lying above the channels of light fluid, was not uniform; instead, it was in fact interspersed with darker red regions, above the red fingers, and lighter red or pink-colored regions, above the white channels, in which some of the pores still contained light fluid (Figure 7).

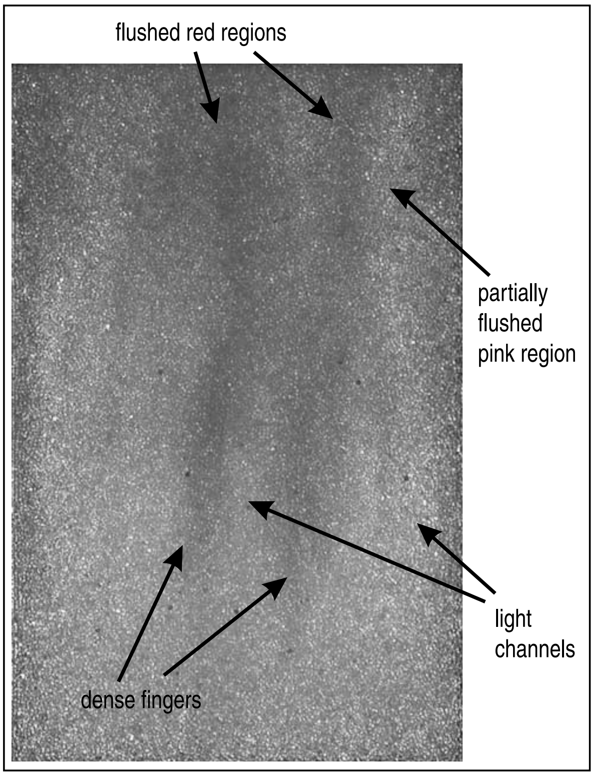

Figure 7. Photograph of experiment 47. Dense, red, salty fingers, separated by white channels of fresh water, are fed from regions flushed by the invading fluid. Between these regions the beads have only been partially flushed, as revealed by its lighter color, and some of the pores are still containing the initial fresh water. See color version of this figure at back of this issue.

4.2. Analysis

[32] Although we observe that unstable fingers seem to develop only when the gravity number is greater than 1, this does not necessarily mean that fingers do not develop at smaller gravity number. Although, previous works suggest that unstable fingering will be observed only if the density contrast is high enough to overcome viscous and dispersion resistance, it has also been observed in laboratory experiments that instabilities require some time before they develop [*Schincariol and Schwartz*, 1990]. Therefore unstable fingers might not be observed if they have not had time to develop on the time and length scales of the experiments.

[33] Moreover, the spectrum of unstable wavelengths is function of the density contrast and the dispersion, which both evolve with time as the flow proceeds [*Schincariol et al.*, 1994]. The initial development of the instability is damped by mechanical dispersion: in the case of disturbances with shorter wavelength, dispersion is increasingly more efficient at smoothing out or eliminating the fingers or perturbations before they have a chance to grow while it also reduces the density difference that drives the instabilities. Furthermore, instability growth rate increases with density difference [*Schincariol et al.*, 1994]. Therefore, as the density contrast is reduced by dispersion, instability growth rate would be expected to be reduced as well. Since mechanical dispersion increases with the advection rate, thus for smaller gravity numbers, the onset of instability would be delayed owing to its smaller growth rate. This is consistent with the fact that for small gravity number experiments we did not observe fingers, at least over the length of our tank.

[34] Provided that the density difference is high enough and that unstable fingers could develop ultimately, we expect the mixing zone to spread diffusively at early times, growing like $t^{1/2}$, but subsequently it will develop fingers and grow convectively like t owing to the advection of these unstable fingers. In order to quantify the effective dispersion coefficient for these experiments, we modified the methodology used for the stable regime because of the finger zone which developed progressively during each experiment.

[35] At time t, the fluid interface is centered at position $x_{\mathrm{int}}(t)$ and we can define the function $f(x)$ as

$$\begin{cases} f(x) = 1 - C(x,t), & 0 < x < x_{\mathrm{int}}(t), \\ f(x) = C(x,t), & H > x > x_{\mathrm{int}}(t), \end{cases} \tag{9}$$

where H is the height of the bead pack. We find that $f(x)$ is not symmetric, particularly when unstable fingers have fully

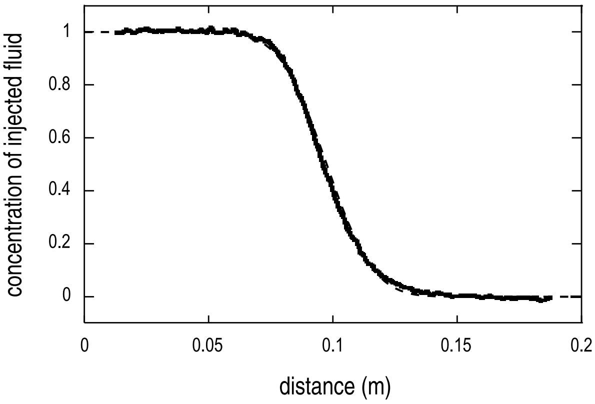

Figure 8. Concentration profile during experiment 35 at t = 59 s (G = 0.2, Pe = 2265). The measured profile is represented by the solid curve, and the dashed curve corresponds to the diffusive equation (3).

developed. Moreover, the concentration profiles obtained from the digital photographs contain some noise, owing to the diffraction of light by the individual grains of the bead pack, that tends to induce negative values of the function $f(x)$ as it gets closer to $x = 0$ and $x = H$, instead of fading away to zero (equation (9)). As a result, calculating the standard deviation of the function f would be meaningless. Instead, we have identified the width of the mixing zone with the interquartile distance ID of this function. This distance is defined as ID = $x_{3/4} - x_{1/4}$, where one quarter of the integral of the function f lies at the right of $x_{3/4}$ and one quarter at the left of $x_{1/4}$:

$$\int_0^{x_{1/4}} f(x)\mathrm{d}x = \frac{1}{4}\int_0^H f(x)\mathrm{d}x, \text{ and } \int_0^{x_{3/4}} f(x)\mathrm{d}x = \frac{3}{4}\int_0^H f(x)\mathrm{d}x. \tag{10}$$

Although in a sense this choice for determining a width of the function f is arbitrary, ID can be calculated for any function f and in the pure tracer dispersion case it corresponds to half the width $w(t)$ of the concentration profile given by equation (3). Therefore we have defined the width of the mixing zone that develops in a gravitationally unstable configuration as $w = 2$ ID(t). The results derived for the stable regime are therefore directly comparable to the analysis of the dispersive mixing in the unstable regime prior to the onset of convective fingering.

4.2.1. Diffusive Regime

[36] As mentioned above, in experiments with low gravity number ($G < 1$), the source velocity u_s is much greater than the buoyancy velocity u_g and any potential gravitational instability is therefore expected to have not enough time to fully develop over the length and time scales of the experiment; during the course of an experiment, mechanical dispersion suppresses the growth of unstable fingers, which remain confined within the diffusive mixing zone, so that the fluid front remains planar in an analogous fashion to the gravitationally stable case. As a consequence, the mixing zone in fact obeys the dispersion equation and the variation of the injected fluid concentration along the bead pack may be represented by equation (3) (Figure 8). When $G \simeq 1$, a transition appears: the interface remains fairly flat at the beginning of the experiment and subsequently unstable fingers develop (Figure 15). During the initial stage of these experiments, the mixing zone obeys the dispersion equation, as in experiments carried out at lower gravity numbers

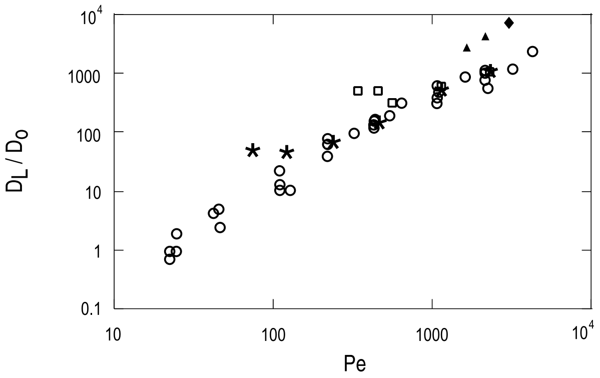

Figure 9. Normalized dispersion coefficient D_L/D_o versus Pe. Open circles are stable configurations; other symbols are unstable configurations that display a diffusive regime: stars, density contrast of 0.07%; squares, 0.7%; triangles, 3.5% and diamonds, 7%.

[37] In this diffusive regime, as for gravitationally stable flows, the mixing zone grows like $t^{1/2}$ and a coefficient of mechanical dispersion can be calculated. Figure 9 represents D_L/D_o as a function of the Péclet number, and Figure 10 shows $D_L/(a\ \bar{v}_s)$ versus Pe. On both Figures 9 and 10, coefficients obtained from the stable experiments are also shown for comparison. Both Figures 9 and 10, particularly Figure 10, show that both the Péclet number and the gravity number impact mechanical dispersion in unstable flows, even though it behaves diffusively. For small gravity number, the normalized mechanical dispersion $D_L/(a\ \bar{v}_s)$ calculated in unstable configurations has value similar to that in stable configurations. However, for G larger than approximately 0.4, it becomes significantly higher, up to one order of magnitude higher, than in stable ones. This is observed even for density contrasts as low as 0.07%.

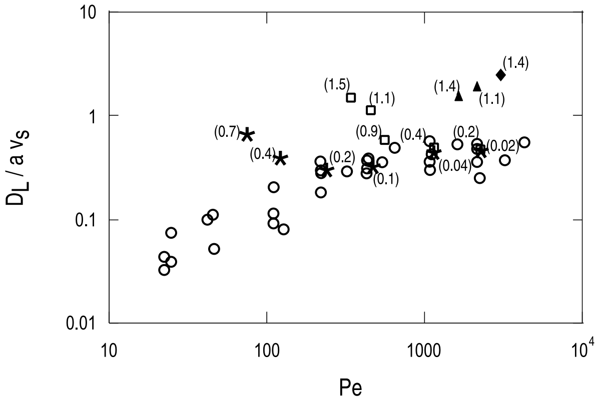

Figure 10. $D_L/(a\bar{v}_s)$ versus Pe. Symbols are the same as on Figure 9. Values of G are in parentheses for unstable configurations.

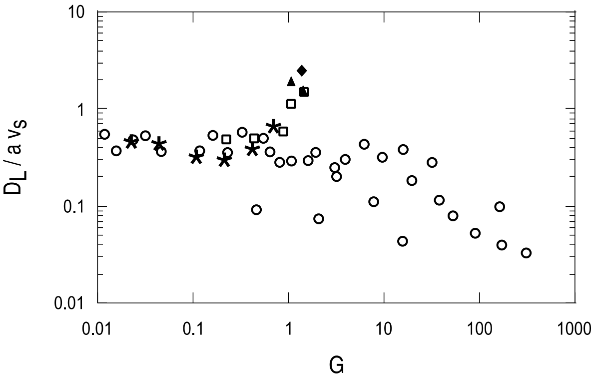

Figure 11. $D_L/(a\bar{v}_s)$ versus G. Symbols are the same as on Figure 9.

[38] However, the impact of gravity on mechanical dispersion in unstable configurations is better seen when $D_L/(a\ \bar{v}_s)$ is presented as a function of G rather than Pe, as shown on Figure 11, where all data collapse on the same curve. This is in striking contrast to the stable case where the control parameter appears to be the Péclet number rather than G, even though gravity does reduce the mechanical dispersion compared to that found for the pure tracer dispersion. Figure 11 identifies two different scalings depending on the value of the gravity number:

$$D_L/(a\,\bar{v}_s) \simeq 0.4 \pm 0.1 \quad \text{for } G < 0.2, \tag{11}$$

$$D_L/(a\,\bar{v}_s) \simeq (1.2 \pm 0.2)\,G^{1.2\pm0.5} \quad \text{for } G > 0.2. \tag{12}$$

For gravity numbers lower than approximately 0.2, $D_L/(a\ \bar{v}_s)$ appears to remain constant at a value identical to that measured in the diffuse regime. This suggests that for gravity numbers lower than approximately 0.1, dispersion is sufficiently large to prevent the development of instability in the bead pack; despite being gravitationally unstable, the fluid interface remains flat and grows diffusively. The dispersion coefficient depends then only on the background flow as parameterized through the Péclet number. For gravity numbers greater than approximately 0.2, we observe that, although the fluid interface still grows diffusively, G is sufficiently large to enhance the dispersion and $D_L/(a\ \bar{v}_s)$ appears to increase as $G^{1.2}$.

[39] As will be shown below, for values of G greater than 1.5, the mixing zone grows linearly with time owing to the advection of unstable fingers. For intermediate values of G, between 0.2 and 1.5, the flow is at the transition between these two regimes: the mixing zone appears to grow initially diffusively and then subsequently advectively. This is during the initial seemingly diffusive growth that $D_L/(a\ \bar{v}_s)$ appears to increase as $G^{1.2}$. Therefore this nearly linear scaling presumably reflects the fact that the flow is at that transition between the two regimes with the mixing zone switching to an advective growth controlled by the finger velocity and thus by G.

4.2.2. Convective Regime

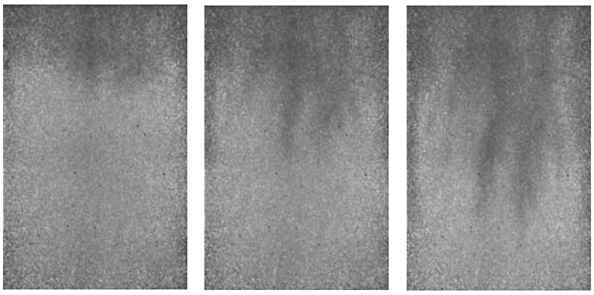
(a) t = 75 s (b) t = 105 s (c) t = 135 s

Figure 12. Convective regime (experiment 47, G = 3.9, Pe = 1095). See color version of this figure at back of this issue.

[40] Ultimately, unstable fingers are observed to develop at the interface (Figure 12) and emerge from the diffusive mixing zone so that unstable convection is established. This distorts the concentration profile, which can no longer be modeled by the simple diffusive equation (3) (Figure 13).

[41] The fingers appear to propagate at a constant velocity. This velocity has been measured by following the progression of the point on the horizontally averaged concentration profile that corresponds to fluid containing 5% of the injected solution. This value is sufficiently large to be accurately measured but sufficiently small that it is located near the average position of the tips of the fingers.

[42] We expect that the velocity of the fingers, in the linear convective regime, should scale with the gravity number. Indeed, in Figure 14, $\mathrm{v}_{\mathrm{finger}}$ measured in the reference frame of the laboratory, normalized by $\bar{v}_s$, has been plotted as a function of G. All data collapse on the linear relationship

$$\mathrm{v}_{\mathrm{finger}}/\bar{v}_s = 1 + 0.25\,G, \tag{13}$$

so that in the moving frame of reference of the fluid front

$$\mathrm{v}_{\mathrm{finger}} = 0.25\,v_g. \tag{14}$$

The reduction in the finger velocity by the factor α = 0.25 is presumably a result of the intermediate density of the mixed

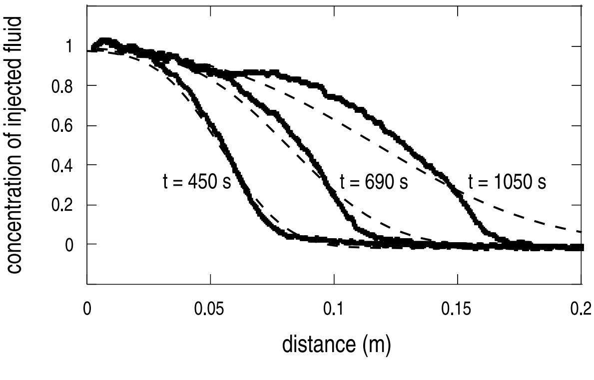

Figure 13. Evolution of the concentration profile in the convective regime (experiment 41, G = 4.3, Pe = 116). The emergence and growth of unstable fingers at the interface distort the concentration profile (thick solid curve). The dashed curve is the diffusive equation (3) for comparison.

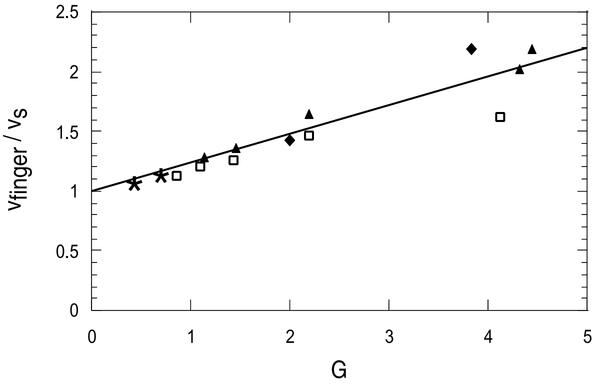

Figure 14. Nondimensional finger velocity $v_{\rm finger}/\bar{v}_s$ versus gravity number G for all experiments started from an unstable configuration. Symbols are the same as on Figure 9. Fit is equation (13).

zone which is the initial source of fluid for the descending fingers.

4.2.3. Transition Between Regimes

[43] In experiments carried out at gravity numbers close to unity, the transition between the diffusive and linear convective regimes is observed. As shown on Figures 15 and 16, the interface is horizontal in the early stage of the experiments and, as a result, the mixing zone behaves diffusively and grows like $t^{1/2}$; subsequently the interface becomes unstable and develops fingers, which leads to the linear convective growth of the mixing zone.

[44] We expect instabilities to develop when the growth rate of unstable fingers becomes greater than the rate of spread of the mixing zone owing to mechanical dispersion. This argument is similar to that for the onset of thermal convection, which arises when its growth rate overcomes that of conduction over the thickness over which the temperature difference is effective. This arguments can be expressed as

$$v_{\rm finger} > \frac{{\rm d}w}{{\rm d}t} = \left(\frac{2D_L}{t}\right)^{1/2}. \tag{15}$$

Combining this condition with the finger velocity measured experimentally (14) and the dispersion scalings (11) and (12), we find that instability does not develop until $t > t_c = 2D_L/(\alpha\, v_g)^2$ with

$$t_c = \frac{0.8a^2}{\alpha^2 D_0\, \mathrm{Pe}}\, G^{-2} \quad \text{for } G < 0.2, \tag{16}$$

$$t_c = \frac{2.4a^2}{\alpha^2 D_0\, \mathrm{Pe}}\, G^{-0.8} \quad \text{for } G > 0.2. \tag{17}$$

As shown on Figure 17, the theoretical transition time (17) compares well with the transition time measured experimentally ($G \geq 0.4$ in all transition experiments).

[45] Finally, when unstable fingers develop, they emerge from the mixing zone, which grew previously owing to mechanical dispersion. *Schincariol et al.* [1994] have shown that dispersion is increasingly more efficient at smoothing out the perturbations with the shortest wavelength and their experiments reveal that the critical wavelength for onset of instability increases as the density difference is reduced. Therefore, as the mixing zone grows owing to dispersion, the density contrast is reduced, which increases the critical

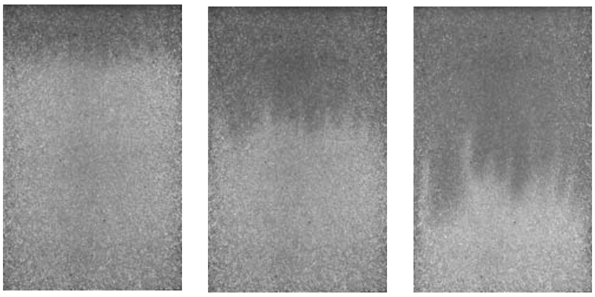
(a) t = 210 s (b) t = 390 s (c) t = 570 s

Figure 15. Transition between an initial diffusive regime (Figure 15a) and a subsequent linear convective regime (Figure 15c) (experiment 39, G = 1.1, Pe = 457): (a) t = 210 s, (b) t = 390 s, and (c) t = 570 s. See color version of this figure at back of this issue.

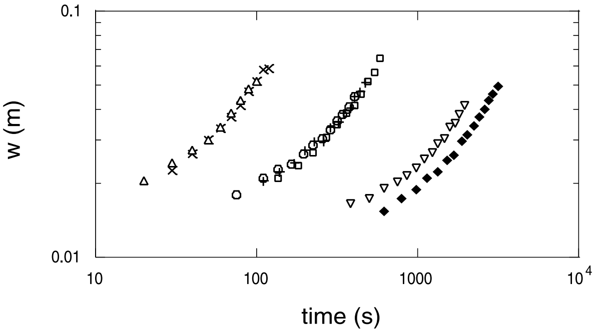

Figure 16. Width of the mixing zone w as a function of time showing the transition between initial diffusive regime, where $w \propto t^{1/2}$, and later linear convective regime, where $w \propto t$. Each symbol corresponds to an experiment: circles, 37; squares, 38; pluses, 39; crosses, 45; triangles, 46; diamonds, 50; inverted triangles, 51.

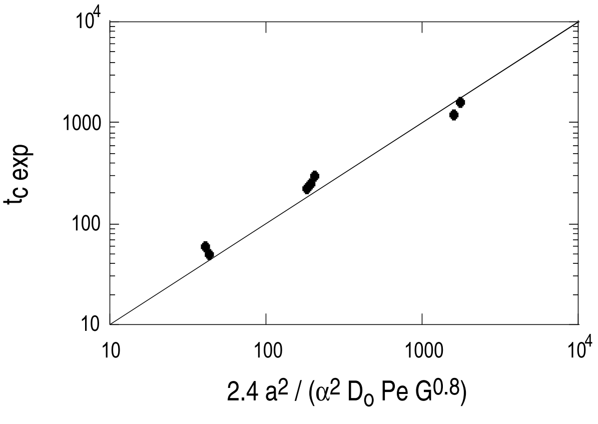

Figure 17. Experimental transition time $t_{c\rm exp}$ compared with the theoretical transition time 2.4 $a^2/(\alpha^2\, D_0\, G^{0.8}\, \mathrm{Pe})$.

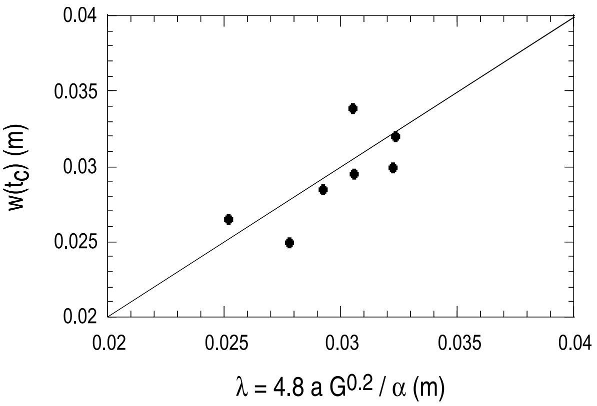

Figure 18. Experimental width of the mixing zone at transition time, $w(t_c)$, compared with the theoretical wavelength of instability $4.8a\ G^{0.2}/\alpha$.

wavelength for instability. Since the thickness of the mixing zone and the critical wavelength for instability both increase as the dispersion increases, we make the assumption that dispersion will favor the emergence of an instability in which the wavelength scales with the thickness of the mixing zone at the onset of instability, $\lambda \sim w(t_c)$. We therefore expect λ to scale like $4\ D_L/(\alpha\ v_g)$ and using dispersion scalings (11) and (12), we get

$$\lambda \sim \frac{1.6a}{\alpha G} \quad \text{for } G < 0.2, \tag{18}$$

$$\lambda \sim \frac{4.8a}{\alpha} G^{0.2} \quad \text{for } G > 0.2. \tag{19}$$

Figure 18 shows that λ (equation (19)) is close indeed to the experimental values of the interface thickness measured at the transition between regimes, thereby verifying our initial assumption. Also, these theoretical length scales correspond to 4–6 initial fingers, a value close to the average number of observed fingers in these experiments.

4.3. Discussion and Comparison With Previous Theoretical Descriptions

[46] We have found that the onset of the fingering instability occurs when the growth rate of the unstable fingers is larger than that of the mixing zone by dispersion and that the size of the fingers scales with the width of the mixed zone, which can be expressed as a function of the gravity number G by the equations (18) and (19). In particular, we have found that the wavelength λ associated with the emergence of instabilities tends to infinity as G tends to zero (equation (18)). Also, we find that λ is weakly dependent on G but tends to the value $4.8\ a/\alpha \simeq 19\ a$, which is determined by the grain size of the porous medium, for large values of G (equation (19)). These findings are consistent with the works by *Schincariol et al.* [1994] and *Simmons et al.* [2001]. They found that the critical wavelength corresponding to the first instance of instabilities seems to asymptote to infinity for very small density differences and to a small constant value for large density differences.

[47] Our experimental results have also implications for the use and the validity of Rayleigh numbers Ra in stability criteria. Usually, a flow is assumed unstable if Ra becomes larger than a critical value Ra_c. Linear stability analysis gives the value $\text{Ra}_c = 4\pi^2 = 39.48$ [*Nield and Bejan*, 1999], although the pioneering work of *Wooding* [1959] gives also $\text{Ra}_c = 3.39$. The Rayleigh number associated with a porous flow is $\text{Ra} = \Delta\rho g k h/\mu D$. As mentioned earlier, the length scale h is difficult to define unambiguously. However, the thickness of the mixing zone (equation (4)) seems the most appropriate since it represents the distance over which the effective density difference has an influence, in which case $\text{Ra} = \frac{8\Delta\rho g k}{\mu}\sqrt{t/D}$. Therefore the onset of instability can be understood by evaluating the Rayleigh number of the mixing layer, and observing that this increases with time until exceeding the critical value for stability, hence the mixing layer becoming unstable. The key physics is that at a critical thickness, the convective transport of fluid within the mixing layer becomes faster than the diffusive transport and hence fingers develop.

5. Geological Implications

[48] In the uniform porous medium used in our laboratory experiments, with vertical displacement flows, the unstable gravitational fingers developed vertically while the gravitationally stable interface remained horizontal. In a more natural geological environment, heterogeneities such as layers of lower permeability will certainly affect the flow and may distort fluid-fluid interfaces. However, assuming a uniform porous medium we can estimate the timescale and the wavelength associated with the development of gravitational instability. Baring in mind these are highly idealized settings, they nevertheless enable to illustrate how the interplay between gravity and dispersion could prevent or delay unstable mixing.

[49] An example of miscible displacement through porous rocks occurs following the injection of seawater in hydrocarbon reservoirs, a technique that is widely used to enhance the productivity of offshore oil reservoirs. Usually, the density of seawater differs noticeably from that of connate water and density contrasts as high as 10% can be observed. As seawater is injected from a well, it flows preferentially along layers of high permeability, from which it also seeps through the neighboring layers of lower permeability. Knowledge about the development of unstable fingers is key for the hydrocarbon industry as they can have a strong impact on the sweep efficiency. For instability to be prevented over the thickness h of a porous layer, h has to be smaller than the distance the fluid front would need to travel for instability to occur, that is $h < \bar{v}_s\ t_c$. For porous layers 1–10 m thick, with a grain size of ~1 mm, this requires $G < 10^{-2}$–10^{-1}. Expressing this condition as a function of injected flux Q per unit width of porous layer, we require $k\Delta\rho g h/(\mu Q) < 10^{-2}$–$10^{-1}$. Taking $k = 10^{-14}$ m^2, $\mu = 10^{-3}$ Pa s and $\Delta\rho = 100$ kg m^{-3}, we would expect instability to be prevented by mechanical dispersion if seawater is injected at flux Q higher than 10^{-7}–10^{-5} m^2 s^{-1} or 0.05–5 bbl day^{-1} m^{-1}.

[50] An example of a geological miscible, porous displacement is the repeated invasion and retreat of

seawater into carbonate layers originally saturated with fresher water of lower magnesium content, a mechanism which leads to the dolomitization of the carbonate rocks [*Phillips*, 1991]. Again, we would expect mechanical dispersion to be able to prevent or delay the onset of gravitational instability if $G < 10^{-2}$–10^{-1}. For a background flow driven by a head Δh, this corresponds to $(\Delta\rho/\rho)$ $(h/\Delta h) < 10^{-2}$–10^{-1}. Seawater contains typically 3.5 wt% NaCl but this concentration can increase by a factor of 5 or even 10 when halite deposits form [*Phillips*, 1991]. This gives a range of density contrasts $\Delta\rho/\rho \sim 10^{-2}$–$10^{-1}$. As a result, instability would not develop if the relative head $\Delta h/h$ that drives the background flow is greater than unity. Thus mechanical dispersion might be able to prevent or delay instability only in layers thinner than a meter or so.

[51] Our experiments suggest that when gravitational instability develops, its wavelength scales with the thickness of the fluid front. In homogeneous porous rocks with grain size ~1 mm, equations (18) and (19) indicate that this wavelength would be of centimeter to meter scale depending on the value of G. For gravity number greater than ~0.2 the initial instability wavelength is weakly dependent on G and should be approximately constant with value ~3 cm. For lower value of G however, the wavelength scales as $1/G$ and it is therefore expected to have greater value for smaller density contrasts. For example, a gravity number of 10^{-2} would give $\lambda \sim 60$ cm.

6. Conclusion

[52] We have investigated the behavior of the mixing zone between two miscible fluids in a porous medium when the flow starts from either a stable or an unstable configuration. Our experimental results highlight the strong interplay that exists between gravity and mechanical dispersion.

[53] In stable configurations, our results show different scalings: at low Péclet number, the dispersion coefficient increases with Pe whereas for Péclet numbers higher than 500, a pure mechanical dispersion regime is achieved and the dispersion coefficient remains constant. Although a similar transition in scalings is observed in the pure tracer dispersion case, our results show that gravity decreases significantly the degree of mixing of the fluids by reducing the dispersion coefficient by a factor of 2 to 4, depending on the Péclet number, even for density contrasts as low as 0.07%.

[54] In the case of flows starting from an unstable configuration, we observe that the Rayleigh-Taylor instability is damped by mechanical dispersion until the time at which the speed of the dispersing front has fallen to a value equal to that of the unstable gravity driven fingers. At the onset of the fingering instability the size of the fingers scales with the width of the mixed zone. During the dispersive regime, for gravity number lower than 0.2, mixing does not appear to be affected by gravity and is characterized by a constant coefficient of dispersion. For higher values of G, mechanical dispersion scales as $D_L \sim \mathrm{Pe}\ G^{1.2}$. In turn, this controls the initial diffusive growth of the mixing zone and therefore the time at which the instability subsequently arises as well as its wavelength.

[55] When applied to homogeneous and uniform geological settings, these results would suggest that mechanical dispersion suppresses the onset of Rayleigh-Taylor instability until a mixed zone 1–2 m thick has developed. The wavelength of the instability would be expected to have value of order centimeter to meter depending on the value of G.

[56] **Acknowledgments.** This work was supported by the BP Institute for Multiphase Flow. T. Menand was also supported by a Newton Trust Fellowship. Reviews by an anonymous referee and an anonymous Associate Editor have greatly improved the manuscript.

References

Aris, R. (1956), On the dispersion of a solute in a fluid flowing through a tube, *Proc. R. Soc. London*, *235*, 67–77.

Bear, J. (1972), *Dynamics of Fluids in Porous Media*, Dover, Mineola, N. Y.

Chandrasekhar, S. (1961), *Hydrodynamic and Hydromagnetic Stability*, Clarendon, Oxford, U. K.

Chuoke, R. L., P. van Meurs, and C. van der Poel (1959), The instability of slow, immiscible, viscous liquid-liquid displacements in permeable media, *Trans. Inst. Min. Metall. Pet. Eng.*, *216*, 188–194.

De Josselin de Jong, G. (1958), Longitudinal and transverse diffusion in granular deposits, *Eos Trans. AGU*, *39*, 67–74.

Fried, J. J., and M. A. Combarnous (1971), Dispersion in porous media, *Adv. Hydrosci.*, *7*, 169–282.

Hill, M. A. (1952), Channelling in packed columns, *Chem. Eng. Sci.*, *1*, 247–253.

Jiao, C.-Y., and H. Hötzl (2004), An experimental study of miscible displacements in porous media with variation of fluid density and viscosity, *Transp. Porous Media*, *54*, 125–144.

Lewis, D. J. (1950), The instability of liquid surfaces when accelerated in a direction perpendicular to their planes. II, *Proc. R. Soc. London*, *202*, 81–96.

List, E. J. (1965), The stability and mixing of a density-stratified horizontal flow in a saturated porous medium, *Rep. KH-R-11*, Calif. Inst. of Technol., Pasadena.

Liu, H. H., and J. H. Dane (1996), A criterion for gravitational instability in miscible dense plumes, *J. Contam. Hydrol.*, *23*, 233–243.

Nield, D. A., and A. Bejan (1999), *Convection in Porous Media*, Springer, New York.

Oostrom, M., J. S. Hayworth, J. H. Dane, and O. Güven (1992a), Behavior of dense aqueous phase leachate plumes in homogeneous media, *Water Resour. Res.*, *28*(8), 2123–2134.

Oostrom, M., J. H. Dane, O. Güven, and J. S. Hayworth (1992b), Experimental investigation of dense solute plumes in an unconfined aquifer model, *Water Resour. Res.*, *28*(9), 2315–2326.

Perkins, T. K., and O. C. Johnston (1963), A review of diffusion and dispersion in porous media, *Soc. Pet. Eng. J.*, *3*, 70–84.

Pfannkuch, H. O. (1963), Contribution à l'étude des déplacements de fluides miscibles dans un milieux poreux, *Rev. Inst. Fr. Pet.*, *18*(2), 215–270.

Phillips, O. M. (1991), *Flow and Reactions in Permeable Rocks*, Cambridge Univ. Press, New York.

Saffman, P. G. (1959), A theory of dispersion in porous medium, *J. Fluid Mech.*, *6*, 321–349.

Saffman, P. G. (1960), Dispersion due to molecular diffusion and macroscopic mixing in flow through a network of capillaries, *J. Fluid Mech.*, *7*, 194–208.

Saffman, P. G., and G. Taylor (1958), The penetration of a fluid into a porous medium or Hele-Shaw cell containing a more viscous liquid, *Proc. R. Soc. London*, *245*, 312–329.

Scheidegger, A. E. (1954), Statistical hydrodynamics in porous media, *J. Appl. Phys.*, *25*, 994–1001.

Schincariol, R. A., and F. W. Schwartz (1990), An experimental investigation of variable density flow and mixing in homogeneous and heterogeneous media, *Water Resour. Res.*, *26*(10), 2317–2329.

Schincariol, R. A., E. E. Herderick, and F. W. Schwartz (1993), On the application of image analysis to determine concentration distributions in laboratory experiments, *J. Contam. Hydrol.*, *12*, 197–215.

Schincariol, R. A., F. W. Schwartz, and C. A. Mendoza (1994), On the generation of instabilities in variable density flow, *Water Resour. Res.*, *30*(4), 913–927.

Schincariol, R. A., F. W. Schwartz, and C. A. Mendoza (1997), Instabilities in variable density flows: Stability and sensitivity analyses for homogeneous and heterogeneous media, *Water Resour. Res.*, *33*(1), 31–41.

Simmons, C. T., T. R. Fenstemaker, and J. M. Sharp Jr. (2001), Variable-density groundwater flow and solute transport in heterogeneous porous media: Approaches, resolutions and future challenges, *J. Contam. Hydrol.*, *52*, 245–275.

Taylor, G. I. (1953), Dispersion of soluble matter in solvent flowing slowly through a tube, *Proc. R. Soc. London*, *219*, 186–203.

Wood, M., C. T. Simmons, and J. L. Hutson (2004), A breakthrough curve analysis of unstable density-driven flow and transport in porous media, *Water Resour. Res.*, *40*, W03505, doi:10.1029/2003WR002668.

Wooding, R. A. (1959), The stability of a viscous liquid in a vertical tube containing porous material, *Proc. R. Soc. London, Ser. A*, *252*, 120–134.

T. Menand, Centre for Environmental and Geophysical Flows, Department of Earth Sciences, University of Bristol, Queen's Road, Bristol BS8 1RJ, UK. (t.menand@bristol.ac.uk)

A. W. Woods, BP Institute for Multiphase Flow, University of Cambridge, Madingley Rise, Madingley Road, Cambridge CB3 0EZ, UK. (andy@bpi.cam.ac.uk)

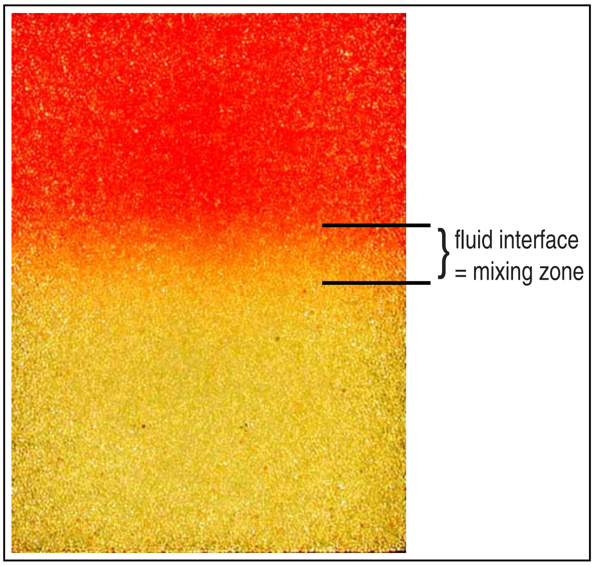

Figure 3. Photograph of experiment 4 at time t = 405 s after start of injection. The mixing zone is 3.1 cm thick.

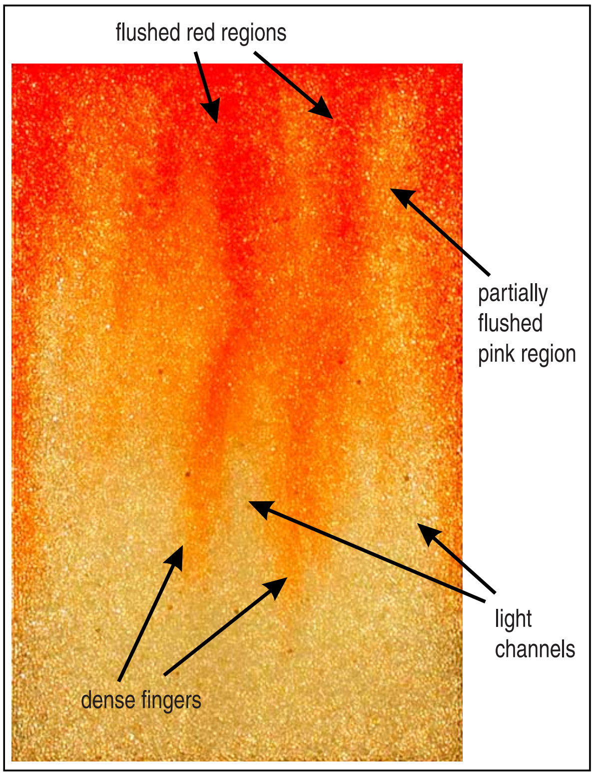

Figure 7. Photograph of experiment 47. Dense, red, salty fingers, separated by white channels of fresh water, are fed from regions flushed by the invading fluid. Between these regions the beads have only been partially flushed, as revealed by its lighter color, and some of the pores are still containing the initial fresh water.

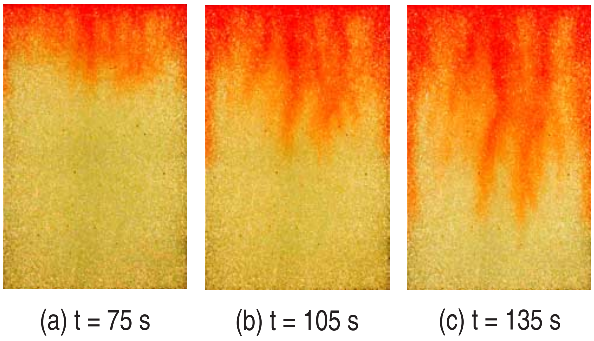
(a) t = 75 s (b) t = 105 s (c) t = 135 s

Figure 12. Convective regime (experiment 47, G = 3.9, Pe = 1095).

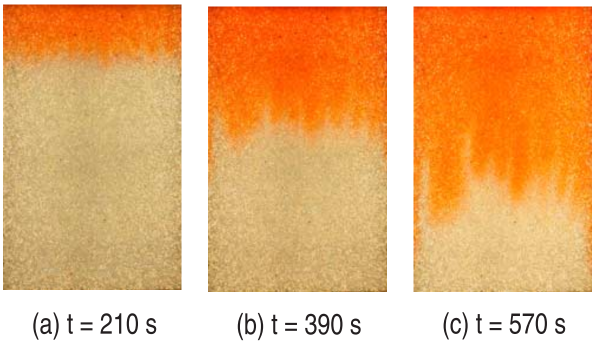
(a) t = 210 s (b) t = 390 s (c) t = 570 s

Figure 15. Transition between an initial diffusive regime (Figure 15a) and a subsequent linear convective regime (Figure 15c) (experiment 39, G = 1.1, Pe = 457): (a) t = 210 s, (b) t = 390 s, and (c) t = 570 s.

Chapter 3

Magma Degassing (2003–2008; Bristol)

(Fundings: *Center for Nuclear Waste Regulatory Analyses*, and *Leverhulme Trust*)

In 2003, I moved to the University of Bristol, UK, as a Research Associate where I started working on magma degassing, focusing essentially, but not exclusively, on basaltic systems.

3.1 Control exerted by the geometry of the plumbing system on basaltic passive degassing

Magma degassing exerts a fundamental control on the eruptive style of volcanoes. The effusive behaviour of basaltic volcanoes is commonly characterised by a relatively mild and fairly continuous degassing, whereas silicic volcanoes exhibit more violent eruptions owing to constrained and thus more powerful and sporadic degassing. Yet, although the duration and cyclicity of these two eruption styles are different, the initial dissolved gas content does not vary significantly between either style. Basaltic magmas typically contain 1–3 wt.% volatiles, although dissolved water contents as high as 6 wt.% have been measured in arc basalts (Sisson and Layne, 1993), whereas silicic magmas contain 4–6 wt.% volatiles (e.g. Wallace, 2001). The observed difference between basaltic and silicic eruptive styles implies a more efficient gas exsolution and separation in less silicic magmas owing to lower viscosity.

Another feature of basaltic volcanoes is that many emit vast amounts of gas while erupting relatively little, if any, degassed lava. Furthermore, some of these volcanoes have been persistently degassing for years to millennia. This requires a physical gas separation from the magma that remains efficient over very long periods of time. Mass balance requires that large amounts of magma must be processed during gas separation. This could imply growth of the volcanic plumbing system whereby influx of fresh, gas-bearing magma is stripped of its volatiles and degassed magma is then stored at shallow depth. Alternatively, long-lived degassing could be achieved by a recirculation of magma between shallow parts of volcanic plumbing system, where over-saturated volatiles are extracted, and deeper parts of the system where degassed magma is recycled.

The main control on gas separation in basaltic magmas is their low viscosity, which allows more efficient extraction than from more viscous silicic magmas (e.g. Vergniolle and Jaupart, 1990; Phillips and Woods, 2001). However, gas separation does not simply result from gas bubbles rising more rapidly than the magma on ascent; this mechanism would require centimetre-scale bubbles, usually associated with fragmented flows hence at or very near the conduit surface. Alternative and physically viable mechanisms include bubble coalescence (Sparks, 2003), convection processes within volcanic conduits (Stevenson and Blake, 1998) and foam development in reservoirs (Jaupart and Vergniolle, 1989). All these mechanisms are intimately linked to the geometry and degree of connectivity of the volcanic plumbing systems, which often involve a complex network of interconnected subunits, from vertical conduits to horizontal dykes and sills and other sub-reservoirs of less well-defined geometry.

Analogue experiments were carried out to study how the geometry and connectivity of the plumbing system affects the circulation of magma, and how this circulation impacts gas separation. The investigation was restricted to the geometry of a vertical conduit connected to a horizontal magma body to identify the key physical principles that govern gas separation in magmatic systems. To this end, two interconnected glass tubes simulated a vertical conduit connected to a horizontal intrusion with a closed end. The tubes were filled with various mixtures of golden syrup, water and NaCl. Their respective concentrations determined the density and viscosity of the mixture, while gas bubbles were produced either by electrolysis (Menand and Phillips, 2007a) or by aerating the mixture (Menand and Phillips, 2007b). The presence of these bubbles (up to 40 vol.%) increased the bulk viscosity and decreased the bulk density of the mixture. Whether the bulk bubbly mixture was forced to rise in the vertical conduit or staid still instead, the presence of the bubbles was the catalyst for an exchange flow between the vertical conduit and the horizontal arm, whose timescale was controlled by the viscosity of the bulk mixture, the bubble size and the side arm dimensions.

Irrespective of the flow rate in the vertical tube and for bubble content up to 40 vol.%, the same fluid-flow processes were observed as illustrated in Fig. 3.1. At the beginning of the experiments, the presence of the bubbles in the vertical conduit decreases the bulk density of the mixture, which creates a density difference between the bubbly fluid in the vertical conduit and the fluid originally at rest in the horizontal side arm. In turn, this density difference drives an exchange flow between the two tubes (Fig. 3.1A). The time-scale associated with this exchange is long enough that bubbles in the horizontal side arm have time to rise, separate from the fluid, and accumulate at its top. This separation is coupled with the accumulation of degassed, hence bubble-free fluid at the base of the side arm (Fig. 3.1B). Ultimately, a steady state is reached whereby the influx of bubbly fluid into the side arm is balanced by the outward flux of lighter foam and denser degassed fluid, which are respectively reinjected up the conduit toward the surface, and recycled at depth in the vertical section (Fig. 3.1C). The structure of the fluid stratification in the side arm is then fixed, with the thickness of both the foam and the layer of degassed fluid remaining constant.

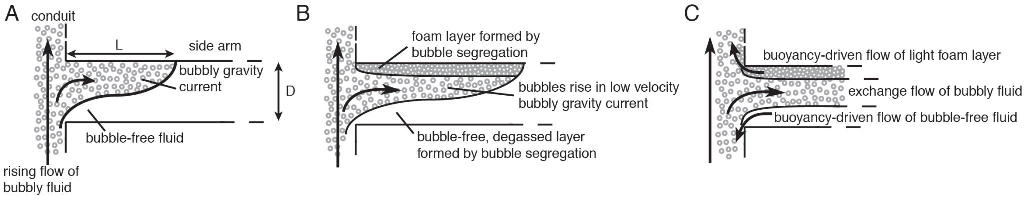

Figure 3.1: Schematic illustration of the control exerted by the geometry of a volcanic plumbing system on gas separation, and of the exchange flow that develops between a vertical conduit and a horizontal side arm of length L and thickness D. Arrows indicate flow directions. A) The bubble-rich fluid originally present in the vertical conduit is less dense than the bubble-free fluid in the side arm, which induces a bubbly gravity current that intrudes the side arm. B) As this bubbly gravity current spreads, bubbles rise and separate from the carrying liquid to form a bubble-rich foam at the upper surface of the side arm. C) A steady exchange flow is ultimately established between the vertical conduit and the side arm.

The length and time scales of the gas separation are controlled by the rise of bubbles in the horizontal intrusion and the rate at which the gas-rich foam flows out of the side arm. Once a steady-state is reached, the height of the gas-rich foam h can be written as the product of a characteristic height H and a shape function $f(x)$:

$$h(x) = H\,f(x), \tag{3.1}$$

where

$$f(x) = \left(\frac{x}{L} - \frac{x^2}{4\,L^2}\right)^{1/4}, \tag{3.2}$$

and

$$H = \left[\frac{c\,(1-c)^2\,d^2\,L^2}{\epsilon\,(1-\epsilon)^{5/2}\,(\epsilon - c)}\right]^{1/4} \tag{3.3}$$

at low volumetric gas fraction c (less than 0.1), or

$$H = \left[\frac{c\,(1-c)^{7/2}\,d^2\,L^2}{\epsilon\,(1-\epsilon)^{5/2}\,(\epsilon - c)}\right]^{1/4} \tag{3.4}$$

at higher volumetric gas fraction (Menand and Phillips, 2007a,b; Menand et al., 2008). d is the characteristic size of gas bubbles, L is the length of the intrusion, ϵ

is the gas fraction of the foam, and the variable x is the position along the intrusion with origin at the junction with the conduit.

The time scales to reach steady-state are the time taken by bubbles to rise, following Stokes' law, to the top of the intrusion

$$T_b = \frac{12\,\mu_l\, D}{\rho_l\, g\, d^2}, \tag{3.5}$$

and the time taken by the foam to develop a steady-state height

$$T_f = \frac{12\,\mu_l\, L^{1/2}}{\rho_l\, g\, d^{3/2}} \left[\frac{\epsilon^3}{c^3\,(1-\epsilon)^{5/2}\,(\epsilon - c)}\right]^{1/4}. \tag{3.6}$$

D is the height or thickness of the intrusion, μ_l and ρ_l are the viscosity and density of the liquid phase, respectively, and g is the gravitational acceleration. These time scales correspond to low volumetric gas fractions ($c < 0.1$). They should be multiplied by a factor $1/(1-c)^{7/2}$ and $1/(1-c)^{21/8}$), respectively, at higher gas fractions. Whether the gas separation processes reported here operate also in nature depends on the cooling and solidification of the intrusion. A conservative estimate for this time scale is obtained by considering cooling and solidification by conduction (Turcotte and Schubert, 2002):

$$T_s = \frac{D^2}{16\,\kappa\,\lambda^2}. \tag{3.7}$$

A typical value for magma thermal diffusivity is $\kappa = 5\ 10^{-7}$ m^2 s^{-1}, and the dimensionless constant λ depends on the temperature difference between the magma and surrounding rocks and is typically in the range 0.5–0.75 (Turcotte and Schubert, 2002). This time scale T_s is a lower estimate because if the intrusion were connected to an active conduit, the solidification time would be larger as any exchange flow would mean both mass and heat are exchanged, keeping the intrusion hotter than in the purely conductive scenario. Comparison of these time scales suggests that more efficient gas separation occurs in sills than in horizontal dykes. Both time scales associated with gas separation, T_b and T_f, increase with magma viscosity and intrusion size, but the cooling and solidification time scale T_s appears to be the most sensitive to intrusion size. As a result, gas separation could be efficient within large intrusions with magmas of basaltic to intermediate composition as well as within smaller, basaltic intrusions (Menand and Phillips, 2007a).

This gas-separation process is essentially the same as that of Jaupart and Vergniolle (1989). However, it is shown here that gas separation by foam accumulation is not restricted to occurring solely in magmatic reservoirs; any non-vertical elements of volcanic plumbing systems can also act as strong gas segregators. This model of gas separation has also implications for the generation of gas-rich and gas-poor magmas and their eruptive behaviour. For low magma supply rates at a persistent volcano, very efficient gas separation is expected, inducing episodic degassing and pulse-like activity that erupt relatively gas-poor magmas, because separation rates are larger than overall magma supply rate. At higher magma supply rates, gas separation is expected to be less effective, leading to stronger explosions erupting gas-rich as well as gas-poor magmas. These general physical principles for gas separation in shallow horizontal intrusions can be applied to Stromboli, and their implications are all consistent with independent field data. Gas separation at Stromboli is likely to occur in a shallow reservoir of sill-like geometry at 3.5 km depth with bubbles of exsolved gas 0.1–1 mm in diameter. The transition between Strombolian activity erupting gas-poor, highly porphyritic magmas and violent explosions that erupt also gas-rich, low porphyritic magmas would correspond to a critical magma supply rate on the order of 0.1–1 m^3 s^{-1} (Menand and Phillips, 2007a).

3.2 Impact of magmatism on nuclear waste repository performance

The previous investigation of the control exerted by the geometry of a magmatic plumbing system on the degassing and movements of basaltic magmas in that system has also been applied to an engineering problem, namely the impact a basaltic dyke would have on the performance of the potential nuclear waste repository at Yucca Mountain in Nevada, USA.

Until recently, Yucca Mountain was a proposed site for a potential underground nuclear waste repository (the program has now been closed). However, regulations require repository developers to consider various natural hazards when evaluating repository performance. The proposed site for the Yucca Mountain repository is located within a historically geologically active basaltic volcanic field with six Quaternary basaltic volcanoes located within 20 km, whose activity has been characterised by Strombolian bursts to violent Strombolian eruptions as well as effusions of lavas. Based on probabilities estimated for repository disruption by future basaltic volcanism (e.g. 1.8×10^{-8}, Bechtel SAIC Company, LLC (2007); 1.0×10^{-6}, Smith and Keenan (2005)) and the potential risks for this natural hazard, performance assessments should evaluate the consequences of a basaltic dyke intersecting the drifts and tunnels of the potential repository, which might damage the emplaced waste packages and waste form, and could transport radioactive material to the biosphere (NRC, 2005).

There is almost no precedent for a volcanic eruption interacting with an underground storage facility of the kind envisaged for radioactive waste repositories. These facilities generally consist of a network of tunnels or drifts. Some designs require the drifts to remain empty apart from their inventory of radioactive waste containers, at least up to the time the repository is permanently closed (i.e. on the order of several hundred years in some cases). Thus, the generic processes that might occur if magma erupts into empty drifts have been a prominent topic of study.

Previous work at the University of Bristol (Lejeune et al., 2009) focused on laboratory analogue experiments that investigated the transient dynamics of how gas-bearing and gas-free fluids similar to magmas could suddenly decompress into subsurface openings, which can accelerate and fragment the fluids. Following the initial transient decompression of gas-bearing magma into the drift, the flow would likely adjust to a steady state within seconds to hours depending on whether magma flow is diverted along the drift or is limited to the main dyke if access drifts are backfilled with crushed rocks (Woods et al., 2002; Dartevelle and Valentine, 2005). At shallow crustal depths typical for repository drifts (< 500 m), magma volatiles are very likely to exist as exsolved bubbles. For instance, initial water contents of basalts that have erupted in the vicinity of Yucca Mountain range from 1.9–4.6 wt.% (Nicholis and Rutherford, 2004), and at a depth of 300 m a basaltic magma with 4.6 wt.% initial water will have exsolved 3.8 wt.% of its water (Holloway and Blank, 1994), which would correspond to volumetric gas fractions in the range of 70–90% at that depth (Menand et al., 2008), provided no gas loss occurred before magma reach the repository drifts level.

The gas separation processes described in the previous section (3.1) could also occur at these high volumetric gas fractions (Menand and Phillips, 2007b; Menand et al., 2008). For the potential Yucca Mountain repository geometry, the time required for steady-state gas separation ranges from hours to hundreds of years depending on the average size of exsolved gas bubbles and on the viscosity of degassed magmas, which depends strongly on the degree of water exsolution, cooling and crystallisation. The steady-state flux Q_{ex} associated with gas separation ranges from 1 m^3 s^{-1} for the less viscous magmas, to 10^{-8} m^3 s^{-1} for the most viscous degassed magmas. These flux values are strongly dependent on the average exsolved bubble diameter. The relative proportion of erupted degassed magma will depend on the value of the magma supply rate relative to the value of Q_{ex}. If magma is supplied at a rate higher than Q_{ex}, then gassy as well as degassed magmas are expected to be violently erupted; if the supply rate is lower, then mainly degassed magma would be erupted by milder episodic Strombolian explosions generated by the repeated collapse of the foam accumulated at the top of drifts (Menand et al., 2008, 2009).

3.3 Diffusion of water in hourglass melt inclusions: a magmatic geospeedometer

In parallel to the work on the passive degassing of basaltic systems described in the previous sections, I also worked on the diffusion of water in imperfectly trapped melt inclusions, also called hourglass inclusions, and its use as a magmatic geospeedometer. Indeed, a major challenge in physical volcanology is to obtain direct, in situ measurements of ascent velocity during explosive volcanic eruptions. The ascent rate of magma controls the height and strength of the eruption column and thus determines the physical dispersal of tephra. Magma ascent velocity is also a key parameter in numerical conduit-flow models. Melt inclusions permit direct, independent measurements of ascent velocity from erupted materials.

Melt inclusions in phenocrysts are now routinely used to measure the pre-eruptive volatile contents, and hence crystallisation pressures, of volatile-saturated magmas (e.g. Dunbar and Hervig, 1992; Blundy and Cashman, 2001; Wallace, 2005). However, not all melt inclusions are perfectly trapped within the host phenocryst. Some are elongate tubes connected to the external melt, allowing them to exchange chemical components, including volatiles, with the matrix (Anderson, 1991). Others have ruptured and vesiculated during ascent. However, these imperfections can be exploited to obtain information about the timescale over which components have been exchanged by diffusion with the matrix, and thus offer insights into the degassing history of the magma. For example, Anderson (1991) used the variation of bubble volumes and H_2O concentrations in imperfectly trapped hourglass inclusions in quartz (similar features are also called melt tubes, melt pockets, reentrant inclusions) to infer decompression rates during the eruption of the Bishop Tuff.

We developed at Bristol University a new technique for using syn-eruptive volatile diffusion in imperfectly trapped melt inclusions to obtain a direct estimate of such ascent velocities, and we applied this technique to melt inclusions from the May 18th, 1980 Plinian eruption of Mount St Helens, Washington, USA (Humphreys et al., 2008). In this study we showed there is a negative, linear correlation between melt H_2O concentrations measured by SIMS analysis and greyscale intensity of glass in back-scattered electron images (Fig. 3.2). Greyscale intensity profiles, extracted using image-processing software, can therefore be calibrated against H_2O measured at discrete points by ion microprobe. An advantage of this new technique is that concentration profiles can be determined in melt tubes that are otherwise too small to analyse directly, with a spatial resolution ($\leq 1\ \mu$m) that is considerably better than that obtainable by ion microprobe or FTIR.

The time taken to produce the measured H_2O concentration profiles was estimated by calculating the time required to establish such profiles by diffusion. The tubular melt inclusions were approximated as cylindrical tubes whose lengths are much larger than their radii so that diffusion occurred mainly along the inclusion length, consistent with the geometry of melt tubes observed in transmitted light on other similar samples. Diffusion perpendicular to the tube axis was neglected because the diffusivity of H_2O within plagioclase is low compared with the melt. The model assumed that the outer end of each tube underwent instantaneous dehydration, with 1-D diffusion of H_2O occurring along the melt tube towards its open end, in the time taken to ascend to the fragmentation horizon and quench. The concentration of H_2O remaining at fragmentation (C_f) was measured directly from the concentration profile and was defined as the concentration at the open

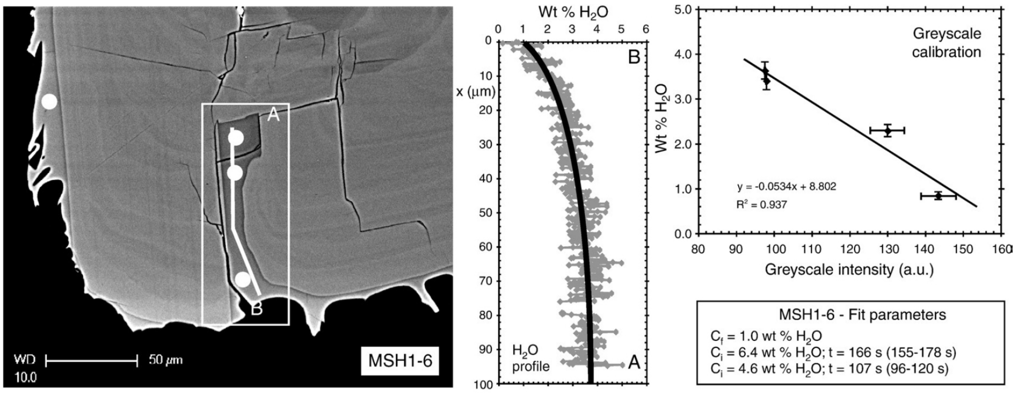

Figure 3.2: H_2O diffusion profile for a tubular (hourglass) inclusion in a plagioclase from Mount St Helens (Humphreys et al., 2008). *Left*: BSE image showing a strongly zoned plagioclase crystal, the melt tube (highlighted by white box) and other inclusions, and matrix glass filaments used in the calibration. The spots mark the positions of SIMS analyses. *Centre*: H_2O diffusion profile constructed from BSE image. The model fits use the H_2O diffusivity of Nowak and Behrens (1997). The break in the profile at $x \sim 80\ \mu$m is where the profile crosses a crack in the glass (see BSE image). *Right*: Calibration of wt.% H_2O from SIMS measurements against greyscale intensity from the BSE image, used to construct the profile.

end of the tube, close to vesicle walls, consistent with petrological observations that matrix glasses contain 0.5–2.2 wt.% H_2O. The initial magma H_2O content was constrained by petrological information to be in the range 4.6–6.4 wt.%, and was assumed to be the initial concentration in the inclusions (C_i). However, this could not be constrained further because none of the tubes was sufficiently long that the initial concentration was preserved in the diffusion profile. Consequently, the diffusion times produced by the model were not unique: for a given final value of H_2O concentration C_f, different initial H_2O concentration C_i could fit the data equally well, and the calculated diffusion times would increase with C_i. For this reason, we performed calculations using the extreme likely values of C_i, 4.6 and 6.4 wt.%, in order to give lower and upper bounds, respectively, on time. The final pressure used in the model was the pressure at fragmentation, calculated from the C_f of the H_2O-saturated melt using (Newman and Lowenstern, 2002). We assumed a pre-eruptive temperature of 880 °C, ignored latent heat effects, and assumed that the magma underwent closed-system, isothermal degassing during ascent in the conduit, with equilibrium maintained between melt and vapour.

H_2O diffusivity in rhyolitic melts depends on H_2O concentration in the glass as well as temperature and pressure. We therefore used the generalised form of Fick's second law:

$$\frac{\partial C}{\partial t} = \frac{\partial}{\partial x}\left(D(C)\frac{\partial C}{\partial x}\right) \tag{3.8}$$

where C is H_2O concentration (wt.%), D is diffusivity, x is distance and t is time. This cannot be solved analytically, and a 1-D finite element model was built using the commercially available finite element software Comsol Multiphysics. The model calculated the evolution of H_2O concentration with time, in a semi-infinite system, as a function of distance with the following initial and boundary conditions: $C = C_i$ for all x at $t = 0$, $C = C_f$ in $x = 0$ for $t > 0$, and $\partial C/\partial x = 0$ at the closed end of the melt inclusion ($x = L$). Best fits to the data were determined by a least-square algorithm, which focused on the regions of the concentration profiles showing the strongest changes in gradient (i.e., excluding most of the non-hydrated part of the experimental sample profiles). The best fits provided the best estimates of the time taken to produce the measured concentration profiles, and the uncertainties on these time estimates were determined using a moving, variable-length, block bootstrap technique as described by Efron and Tibshirani (1993). Other bootstrapping techniques usually assume that all data points are independent. However, because D_{H_2O} depends on H_2O concentration, adjacent data points along the concentration profiles are dependent over a length-scale which depends on the H_2O concentration at that point. For every data point we therefore used a block length l, such that $l = (D_{H_2O}\Delta t)^{1/2}$, where D_{H_2O} is the H_2O diffusivity at that data point, and Δt is the timestep between two successive theoretical concentration profiles (typically 10 s). With this technique, data more than a block length apart are assumed to be nearly independent (Efron and Tibshirani, 1993). This procedure gives a 99% confidence interval for each time estimate.

Our technique was first applied to experimentally hydrated glass chips in order to determine the nature of the relationship between BSE intensity and H_2O concentration, assess the ability of previously published empirical H_2O diffusivity relationships to fit the data, and to test the accuracy of our technique. The H_2O diffusivity model of Nowak and Behrens (1997) was found to give the best fit to the synthetic concentration profiles, and the best estimate of the time duration of the experiments. This diffusivity model was then used to fit the H_2O concentration profiles measured in the melt inclusions from Mount St. Helens. Our model produced good fits to the data, indicating very rapid ascent times of between 102 and 166 s, which correspond to mean magma ascent velocities of 37–64 m/s, or mean decompression rates of 0.9–1.6 MPa s^{-1}, in agreement with previous estimates from petrological studies (Anderson, 1991) and numerical modelling (Papale et al., 1998). This new technique is applicable to any fresh pumice sample containing phenocrysts with melt inclusion tubes.

Bibliography

Anderson, A. T. (1991). Hourglass inclusions: Theory and application to the Bishop Rhyolitic Tuff. *Am. Mineral. 76*(3-4), 530–547.

Bechtel SAIC Company, LLC (2007). Characterize framework for igneous activity at Yucca Mountain, Nevada, ANL-MGR-GS-000002, Rev. 3. Las Vegas, Nevada: Bechtel SAIC Company, LLC.

Blundy, J. and K. Cashman (2001). Ascent-driven crystallisation of dacite magmas at Mount St. Helens. *Contrib. Mineral. Petrol. 140*, 631–650.

Dartevelle, S. and G. Valentine (2005). Early-time multiphase interactions between basaltic magma and underground openings at the proposed Yucca Mountain radioactive waste repository. *Geophysical Research Letters 32*(L22311), doi: 10.1029/2005GL024172.

Dunbar, N. and R. Hervig (1992). Petrogenesis and volatile stratigraphy of the Bishop Tuff - Evidence from melt inclusion analysis. *J. Geophys. Res. 97*, 15,129–15,150.

Efron, B. and R. Tibshirani (1993). *An introduction to the bootstrap*. Chapman & Hall.

Holloway, J. R. and J. G. Blank (1994). Application of experimental results to C-O-H species in natural melts. In M. R. Carroll and J. R. Holloway (Eds.), *Volatiles in Magmas*, Number 30 in Mineralogical Society of America, Reviews in Mineralogy, pp. 187–230.

Humphreys, M. C. S., T. Menand, J. D. Blundy, and K. Klimm (2008). Magma ascent rates in explosive eruptions: Constraints from h2o diffusion in melt inclusions. *270*, 25–40.

Jaupart, C. and S. Vergniolle (1989). The generation and collapse of a foam layer at the roof of a basaltic magma chamber. *J. Fluid Mech. 203*, 347–380.

Lejeune, A.-M., A. W. Woods, R. S. J. Sparks, B. E. Hill, and C. B. Connor (2009). Intrusion dynamics for volatile-poor basaltic magma subsurface nuclear installations. In N. Chapman, C. Connor, and L. Connor (Eds.), *Volcanism, Tectonism, and the Siting of Nuclear Facilities*, pp. 429–451. Cambridge University Press.

Menand, T. and J. C. Phillips (2007a). Gas segregation in dykes and sills. *J. Volcanol. Geotherm. Res. 159*, 393–408.

Menand, T. and J. C. Phillips (2007b). A note on sas segregation in dykes and sills at high gas fractions. *J. Volcanol. Geotherm. Res. 162*, 185–188.

Menand, T., J. C. Phillips, and R. S. J. Sparks (2008). Circulation of bubbly magma and gas segregation within tunnels of the yucca mountain repository. *Bull. Volcanol. 70*, 947–960.

Menand, T., J. C. Phillips, R. S. J. Sparks, and A. W. Woods (2009). Modelling impacts of volcanism on repository performance. In N. Chapman, C. Connor, and L. Connor (Eds.), *Volcanism, Tectonism, and the Siting of Nuclear Facilities*, pp. 406–428. Cambridge University Press.

Newman, S. and J. B. Lowenstern (2002). VolatileCalc: a silicate melt-H_2O-CO_2 solution model written in Visual Basic for excel. *Computers & Geosciences 28*, 1–8.

Nicholis, M. G. and M. J. Rutherford (2004). Experimental constraints on magma ascent rate for the Crater Flat volcanic zone hawaiite. *Geology 32*, 489–492.

Nowak, M. and H. Behrens (1997). An experimental investigation on diffusion of water in haplogranitic melts. *Contributions to Mineralogy and Petrology 126*, 365–376.

NRC (2005). Integrated issue resolution status report NUREG-1762, 1(1). Washington, DC: US Nuclear Regulatory Commission.

Papale, P., A. Neri, and G. Macedonia (1998). The role of magma composition and water content in explosive eruptions. 1. Conduit ascent dynamics. *J. Volcanol. Geotherm. Res. 87*, 75–93.

Phillips, J. C. and A. W. Woods (2001). Bubble plumes generated during recharge of basaltic magma reservoirs. *Earth Planet. Sci. Lett. 186*, 297–309.

Sisson, T. W. and G. D. Layne (1993). H2O in basalt and basaltic andesite glass inclusions from four subduction-related volcanoes. *Earth Planet. Sci. Lett. 117*, 619–635.

Smith, E. I. and D. L. Keenan (2005). Yucca mountain could face greater volcanic threat. *EOS Trans. AGU 86(35)*, doi:10.1029/2005EO350001.

Sparks, R. S. J. (2003). Dynamics of magma degassing. In C. Oppenheimer, D. M. Pyle, and J. Barclay (Eds.), *Volcanic Degassing*, Volume 213 of *Geol. Soc. London Spec. Publ.*, pp. 5–22.

Stevenson, D. S. and S. Blake (1998). Modelling the dynamics and thermodynamics of volcanic degassing. *Bull. Volcanol. 60*, 307–317.

Turcotte, D. L. and G. Schubert (2002). *Geodynamics. Applications of Continuum Physics to Geological Problems* (second ed.). Cambridge: CambridgeUniversity Press.

Vergniolle, S. and C. Jaupart (1990). Dynamics of degassing at Kilauea Volcano, Hawaii. *J. Geophys. Res. 95*, 2793–2809.

Wallace, P. J. (2001). Volcanic SO2 emissions and the abundance and distribution of exsolved gas in magma bodies. *J. Volcanol. Geotherm. Res. 108*, 85–106.

Wallace, P. J. (2005). Volatiles in subduction zone magmas: concentrations and fluxes based on melt inclusion and volcanic gas data. *J. Volcanol. Geotherm. Res. 140*, 217–240.

Woods, A., S. Sparks, O. Bokhove, A. LeJeune, C. Connor, and B. Hill (2002). Modeling magma-drift interaction at the proposed high-level radioactive waste repository at Yucca Mountain, Nevada, USA. *Geophysical Research Letters 29*(1641), doi: 10.1029/2002GL014665.

3.4 Selected publications

1. **Menand, T.** and Phillips, J. C. (2007a) Gas segregation in dykes and sills. *J. Volcanol. Geotherm. Res.*, **159**, 393–408.
2. **Menand, T.** and Phillips, J. C. (2007b) A note on gas segregation in dykes and sills at high gas fractions. *J. Volcanol. Geotherm. Res.*, **162**, 185–188.
3. Humphreys, M. C. S., **Menand, T.**, Blundy, J. D. and Klimm, K. (2008) Magma ascent rates in explosive eruptions: Constraints from H_2O diffusion in melt inclusions. *Earth Planet. Sci. Lett.*, **270**, 25–40.
4. **Menand, T.**, Phillips, J. C. and Sparks, R. S. J. (2008) Circulation of bubbly magma and gas segregation within tunnels of the potential Yucca Mountain repository. *Bull. Volcanol.*, **70**, 947–960.
5. **Menand, T.**, Phillips, J. C., Sparks, R. S. J., and Woods, A. W. (2009) Modeling the flow of basaltic magma into subsurface nuclear facilities. In: Chapman, N., Connor, C. and Connor, L. (Eds.), *Volcanic and Tectonic Hazard Assessment for Nuclear Facilities*, Chap. 17, Cambridge University Press. ISBN-13: 9780521887977.

Available online at www.sciencedirect.com
ScienceDirect

Journal of Volcanology and Geothermal Research 159 (2007) 393–408

Journal of volcanology and geothermal research

www.elsevier.com/locate/jvolgeores

Gas segregation in dykes and sills

Thierry Menand *, Jeremy C. Phillips

Department of Earth Sciences, Centre for Environmental and Geophysical Flows, University of Bristol, Wills Memorial Building,
Queen's Road, Bristol BS8 1RJ, UK

Received 24 January 2006; received in revised form 29 June 2006; accepted 8 August 2006

Abstract

Many basaltic volcanoes emit a substantial amount of gas over long periods of time while erupting relatively little degassed lava, implying that gas segregation must have occurred in the magmatic system. The geometry and degree of connectivity of the plumbing system of a volcano control the movement of magma in that system and could therefore provide an important control on gas segregation in basaltic magmas. We investigate gas segregation by means of analogue experiments and analytical modelling in a simple geometry consisting of a vertical conduit connected to a horizontal intrusion. In the experiments, degassing is simulated by electrolysis, producing micrometric bubbles in viscous mixtures of water and golden syrup. The presence of exsolved bubbles induces a buoyancy-driven exchange flow between the conduit and the intrusion that leads to gas segregation. Bubbles segregate from the fluid by rising and accumulating as foam at the top of the intrusion, coupled with the accumulation of denser degassed fluid at the base of the intrusion. Steady-state influx of bubbly fluid from the conduit into the intrusion is balanced by outward flux of lighter foam and denser degassed fluid. The length and time scales of this gas segregation are controlled by the rise of bubbles in the horizontal intrusion. Comparison of the gas segregation time scale with that of the cooling and solidification of the intrusion suggests that gas segregation is more efficient in sills (intrusions in a horizontal plane with typical width:length aspect ratio 1:100) than in horizontally-propagating dykes (intrusions in a vertical plane with typical aspect ratio 1:1000), and that this process could be efficient in intermediate as well as basaltic magmas. Our investigation shows that non-vertical elements of the plumbing systems act as strong gas segregators. Gas segregation has also implications for the generation of gas-rich and gas-poor magmas at persistently active basaltic volcanoes. For low magma supply rates, very efficient gas segregation is expected, which induces episodic degassing activity that erupts relatively gas-poor magmas. For higher magma supply rates, gas segregation is expected to be less effective, which leads to stronger explosions that erupt gas-rich as well as gas-poor magmas. These general physical principles can be applied to Stromboli volcano and are shown to be consistent with independent field data. Gas segregation at Stromboli is thought likely to occur in a shallow reservoir of sill-like geometry at 3.5 km depth with exsolved gas bubbles 0.1–1 mm in diameter. Transition between eruptions of gas-poor, high crystallinity magmas and violent explosions that erupt gas-rich, low crystallinity magmas are calculated to occur at a critical magma supply rate of 0.1–1 $m^3\ s^{-1}$.

Keywords: gas segregation; persistent volcanism; sills; volcanic gas fluxes; magma evolution; Strombolian activity

---

1. Introduction

Magma degassing provides a fundamental control on the eruptive style of volcanoes. The activity of Kilauea, Hawaii, is characterized by short-lived, intense fire-

---

* Corresponding author.
E-mail addresses: T.Menand@bristol.ac.uk (T. Menand), J.C.Phillips@bristol.ac.uk (J.C. Phillips).

doi:10.1016/j.jvolgeores.2006.08.003

fountaining and longer-lived gentle effusion of lava. In contrast, explosive activity such as the May 18th 1980 eruption of Mt. St. Helens is characterized by intense degassing in the volcanic conduit, leading to explosive fragmentation of silicic magma to form a Plinian eruption column and pyroclastic density currents. Although the duration and cyclicity of these two eruption styles are different, the initial dissolved gas content does not vary significantly between either style. Basaltic magmas typically contain 1–3 wt.% volatiles, although dissolved water contents as high as 6 wt.% have been measured in arc basalts (Sisson and Layne, 1993), whereas silicic magmas contain 4–6 wt.% volatiles (e.g., Wallace, 2001). Petrological, theoretical and analogue experimental studies suggest that the rate of degassing, and not the absolute volatile abundance, is of primary importance in controlling eruptive style (Sparks et al., 1994; Sparks, 2003). Processes that may affect the rate of degassing include ascent rate and nucleation. Degassing rate can also be strongly influenced by processes of gas segregation within the sub-surface magma.

Many basaltic volcanoes emit a substantial amount of gas while erupting relatively little, if any, degassed lava. Examples include Kilauea in Hawaii (Francis et al., 1993), Mount Etna (Allard, 1997) and Stromboli in Italy (Francis et al., 1993), Erta'Ale in Ethiopia (Le Guern et al., 1979), Nyiaragongo in Zaire (Le Guern, 1987), Masaya in Nicaragua (Stoiber et al., 1986) and Mount Erebus in Antarctica (Kyle et al., 1990). These volcanoes have been persistently degassing for years to millennia, which requires a physical separation of volatiles from the magma that must remain efficient over very long periods of time. Mass balance requires that large amounts of magma must be processed during gas segregation. This would imply growth of the volcanic plumbing system whereby influx of new, gas-bearing magma is stored at shallow depth where it degases. Alternatively, long-lived degassing can be achieved by a recirculation of magma between shallow parts of volcanic plumbing system, where over-saturated volatiles can be extracted, and deeper parts of the system where degassed magma can be recycled. Regardless of the precise mechanism, gas segregation must occur so that exsolved volatiles are physically decoupled and separated from the melt.

The main control on gas segregation is that the lower viscosity of mafic magmas allows the development of bubbly suspensions from which bubbles can escape more rapidly than from more viscous silicic melts (Vergniolle and Jaupart, 1990; Phillips and Woods, 2001). The process of gas segregation, however, does not simply result from gas bubbles rising more rapidly than the magma on ascent; even in very low viscosity basalts (~1 Pa s) with typical ascent speeds on the order of 0.1–1 m s^{-1}, centimetric-scale bubbles are required for bubble rise speeds to exceed magma ascent speeds. In explosive basaltic eruptions, larger bubbles (>1 cm) are observed in scoriae. These large bubbles are usually associated with fragmented flow in conduits where gas velocities exceed typical rise velocities, although they may also be able to expand at atmospheric pressure after fragmentation, suggesting that during the flow they were probably much smaller. However, this centimetric scale bubble size is at least one order of magnitude larger than typical bubble diameters in basaltic lavas, intrusions, and scoriae (Sarda and Graham, 1990; Cashman and Mangan, 1994; Sparks, 2003), suggesting that alternative mechanisms of gas segregation must be considered.

Rates of degassing in excess of those due to independent ascent of equilibrium-sized bubbles include bubble coalescence (Sparks, 2003), convection processes in conduit (Stevenson and Blake, 1998) and foam development in reservoirs (Jaupart and Vergniolle, 1989). A simple plumbing system with a single vertical conduit connected to a single deeper reservoir is usually assumed in process models. Volcanic plumbing systems, however, often involve a complex geometry of interconnected subunits, from vertical conduits to horizontal dykes and sills and other sub-reservoirs of less well-defined geometry. For example, flank eruptions are usually fed by dykes propagating laterally from a summit conduit (Woods and Cardoso, 1997; Acocella and Neri, 2003), although such eruptions can involve a more complex degree of connectivity (Acocella and Neri, 2003; Andronico et al., 2005). Seismic studies of Kilauea volcano, Hawaii, suggest a three dimensional, interconnected plumbing system (Ryan et al., 1981; Ryan, 1988) with a complex plexus of sills and dykes beneath Halemaumau (Dawson et al., 2004). Evidence for complex plumbing systems also is apparent from geochemical studies, which suggest multistage magma ascent and degassing during the volcanic activity at, for example, Mt. St. Helens in 1980 (Berlo et al., 2004).

The geometry and degree of connectivity of the plumbing system could provide an important control on magma movement in the system and thus on gas segregation processes in basaltic magmas. Here we investigate 1) how the geometry and connectivity of the plumbing system affects the circulation of magma and 2) how this circulation impacts gas segregation. We restrict our investigation to the geometry of a vertical conduit connected to a horizontal magma body. This simple geometry enables the identification of the key physical principles that govern gas segregation in more complex magmatic plumbing systems. In Section 2 we describe laboratory

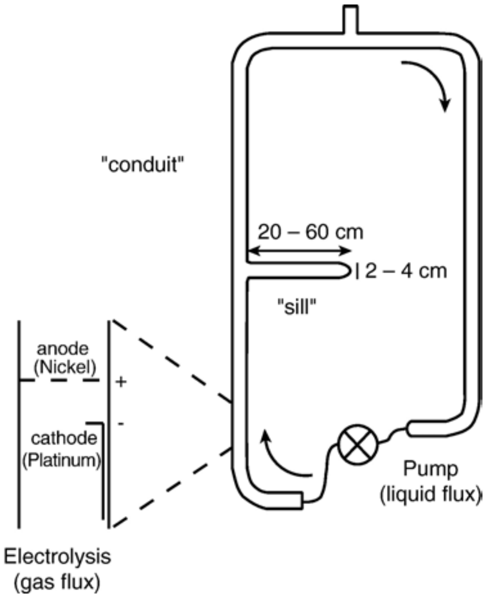

Fig. 1. Schematic diagram of the apparatus.

analogue experiments investigating bubble segregation in idealized geometry, and in Section 3 we develop mathematical models for transient and steady-state flow driven by gas segregation process. In Section 4 we discuss the implications and limitations of our work in detail, before concluding in Section 5.

2. Analogue experiments

2.1. Setup and calibration

We have carried out a series of analogue laboratory experiments to investigate gas segregation in a simple geometry consisting of two interconnected glass tubes that simulated a vertical conduit connected to a horizontal intrusion with a closed end. Both ends of the vertical glass tube are connected to a peristaltic pump to form a recirculating flow loop (Fig. 1). The internal diameter of the vertical tube was 4 cm, whereas the length and the diameter of the horizontal side arm were varied.

The solutions used as a magma analogue were various mixtures of golden syrup, water and Sodium Chloride (NaCl). Density, ρ_l, and viscosity, μ_l, of these Newtonian solutions were varied by changing the relative amount of water and golden syrup. Density was measured by weighing a known volume, and the viscosity was measured using a Haake RV20 viscometer. Properties of the experimental mixtures are summarised in Table 1.

Small bubbles were produced by electrolysis (Fig. 1) of the viscous NaCl solution to simulate magma degassing by cooling and crystallisation (Cardoso and Woods, 1996; Phillips and Woods, 2002). An electrolysis cell was set up into the vertical tube using a 20 mesh nickel gauze with wire diameter 180 μm as the cathode and a platinum wire as the anode. The nickel gauze was positioned across the vertical tube below its junction with the horizontal side arm, and the platinum wire was situated 5 cm above. A 35 V power supply drove the electrolysis cell. Bubble size distributions were measured by pressing samples of the mixtures between two glass plates 0.5 mm apart. Bubbles rose and collected on the upper glass plate, and a digital image was taken through a microscope at 4× magnification. A typical image contained approximately 150 bubbles. The mean bubble diameter, d, was measured for different golden syrup:water:NaCl mass ratios, and one standard deviation was used as a measure of the bubble size distributions. Mean bubble diameters of 25±10 μm and 35± 21 μm were measured for mixture mass ratios of 45:45:10 and 60:30:10, respectively. These values were used together with the solution viscosity to calculate the bubble rise speed using Stokes law and showed that bubbles rose at an average speed of 0.06 mm s^{-1} and 0.03 mm s^{-1} in the 45:45:10 and 60:30:10 mixtures, respectively. The low viscosity of 30:60:10 mixtures meant that most of the bubbles escaped during the sample preparation, preventing any reliable measurement.

The gas flux produced by electrolysis was calibrated by installing the anode and cathode in the vertical tube without a side arm, but connected to a 1 mm diameter capillary tube at the upper end. The tube was filled with a golden syrup:water:NaCl mixture. The fluid was not circulated by the pump during the calibration measurements. Gas produced by electrolysis drove a liquid film up this tube, and recording of its successive positions enabled the gas flux to be estimated. As shown in Fig. 2, these experimental measurements enable the gas production rate Q_g to be related to electric current intensity I by the linear relationship $Q_g = (1.43 \pm 0.03) \times 10^{-7} \times I$ m^3 s^{-1}, where I is expressed in Ampere.

The volumetric gas fraction, c, produced by electrolysis was calibrated by weighing known volumes of

Table 1
Properties of golden syrup (GS), water and Sodium Chloride (NaCl) mixtures

GS:water:NaCl (mass ratio)	ρ_l (kg m^{-3})	μ_l (mPa s)
30:60:10	1187.6±0.4	3.4±0.1
45:45:10	1257.6±0.4	11±1
60:30:10	1325.9±0.4	43±3

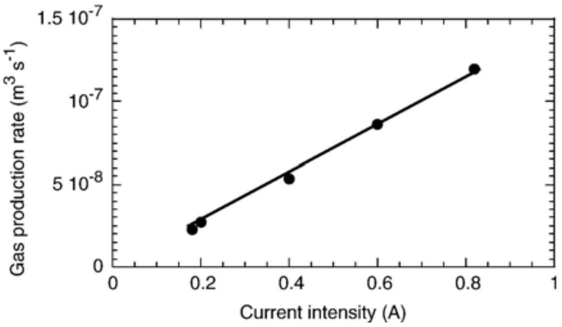

Fig. 2. Gas production rate Q_g as a function of electric current intensity *I*. The uncertainty on the measurements is represented by the symbol size. The black line represents the linear regression $Q_g = (1.43 \pm 0.03) \times 10^{-7} \times I$ m^3 s^{-1} ($R^2 = 0.99914$).

bubble-free liquid and bubbly fluid. The ratio of the measured mass of bubbly fluid, m_b, to that of the bubble-free liquid, m_o, is the volumetric fraction of liquid so that $c = 1 - m_b / m_o$ (bubble mass is negligible and the density of degassed and non-degassed liquids is similar). This procedure was repeated for different electric current intensities. Electric current intensity in the range 0–0.5 amp gives gas fractions in the range 0–5 vol.%. These measurements, however, lead to high systematic uncertainties of typically 1–2 vol.%. It was therefore decided to use the gas fraction as a fitting parameter when comparing model and experiments, provided the fitting values are concordant with the gas production rates. Because gas production rate increases linearly with electric current intensity (Fig. 2) and gas fraction is proportional to gas production rate, the gas fraction also must increase linearly with electric current intensity.

At the start of an experiment, the apparatus was filled with golden syrup:water:NaCl mixture and all gas bubbles introduced by the filling process were removed. The experiment was initiated by setting the peristaltic pump to a desired flow rate. The electrolysis cell was then switched on, and the desired gas flux was set independently of the liquid flux. Experimental duration was measured from the time that the electrolysis cell was switched on, and the position of the interface between the bubbly liquid, the foam layer and bubble-free liquid was measured as the experiment proceeded.

2.2. Observations

We have investigated a range of liquid and gas flow rates from the case of no fluid flow (i.e., bubbles rose through and separated from the liquid in the vertical tube) to that of a fluid flow rate 80 times larger than the gas flux (i.e., bubbles were carried by and rose at the same speed as the liquid).

Irrespective of the flow rate in the vertical tube, the same fluid-flow processes were observed. At the beginning of the experiments, the electrolysis creates bubbles that rise up the vertical conduit. These bubbles decrease

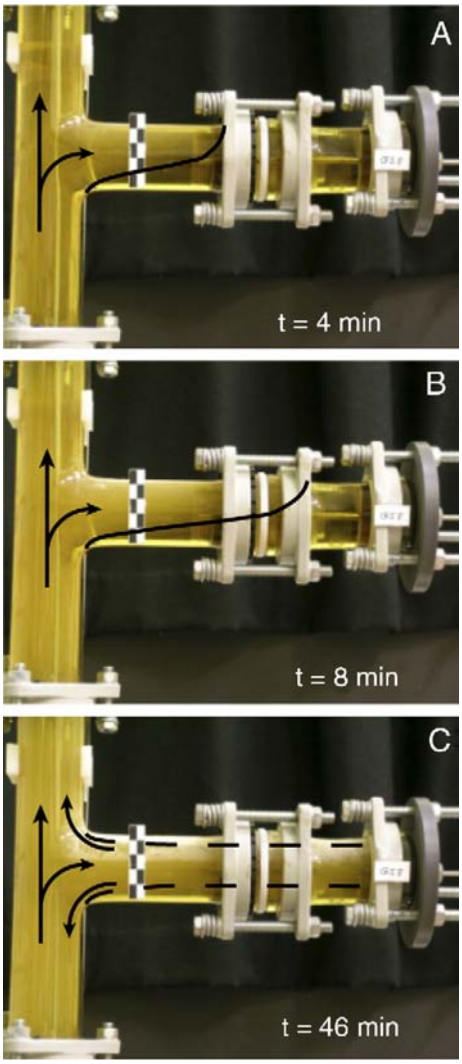

Fig. 3. Establishment of a steady-state exchange flow (golden syrup:water:NaCl mixture ratio is 60:30:10, no fluid flow, $Q_g = 2.9 \times 10^{-8}$ m^3 s^{-1}). Black rectangles on ruler are 1 cm high and 5 mm wide. Arrows indicate flow directions. (A) time = 4 min; the bubble rich mixture can clearly be seen as the opaque fluid in the vertical tube and the initial part of the side arm, and the black curve indicates the position of the interface between bubbly and bubble-free liquids. (B) time = 8 min; the interface has propagated further into the side arm and a more opaque foam is visible at the upper surface of the side arm. (C) time = 46 min; a steady exchange flow is established between the vertical tube and the side arm. Dashed curves show the approximate thickness of the upper foam layer and the lower degassed liquid layer.

the bulk density of the mixture, which creates a density difference between the bubbly fluid rising in the vertical conduit and the bubble-free fluid originally at rest in the horizontal side arm. In turn, this density difference drives an exchange flow between the two tubes (Fig. 3A). The time-scale associated with this exchange is long enough that bubbles in the horizontal side arm have time to rise, segregate from the fluid, and accumulate at its top. This segregation is coupled with the accumulation of degassed fluid at the base of the side arm (Fig. 3B). Ultimately, a steady state is reached whereby the influx of bubbly fluid into the side arm is balanced by the outward flux of lighter foam and denser degassed fluid, which are respectively reinjected up the conduit toward the surface, and recycled at depth in the vertical section (Fig. 3C). The structure of the fluid stratification in the side arm is then fixed, with the thickness of both the foam and the layer of degassed fluid remaining constant.

3. Model

3.1. Transient exchange flow

Before modelling the gas segregation in the side arm, let us focus on the buoyancy-driven exchange flow set up between the rising bubbly fluid with density ρ_b, and the initially bubble-free fluid with density ρ_l in the horizontal arm of thickness D. Modelling this transient exchange flow will allow us to determine how the length, L, of the intruding bubbly current evolves with time, and therefore the areal extent of the bubbly source for gas segregation. Fig. 4 shows a schematic diagram of the transient flow.

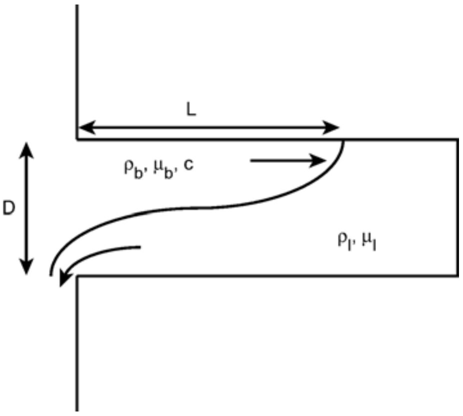

Fig. 4. Schematic illustration of the transient exchange flow between the vertical tube and the horizontal side arm.

We treat the inflowing bubbly flow as a viscous gravity current. After an initial adjustment, we assume that the pressure distribution in the bubbly current becomes hydrostatic because of negligible vertical accelerations. Excess pressure driving the exchange flow comes from the density difference between the bubbly fluid and the bubble-free fluid, $\Delta\rho=\rho_l-\rho_b$, and is balanced by viscous dissipation. Density of the bubbly fluid is a function of the liquid density, the gas bubble density ρ_g and the gas fraction c: $\rho_b=c\rho_g+(1-c)\rho_l$. Therefore, the density difference that drives the flow is $\Delta\rho=c(\rho_l-\rho_g)$, which because $\rho_l \gg \rho_g$ simplifies to

$$\Delta\rho = c\rho_l. \tag{1}$$

The viscosity of the bubbly fluid, μ_b, can be estimated from the viscosity of the bubble-free fluid, μ_l, and the volumetric gas fraction, c, in the current. Several expressions for the dependence of effective viscosity on gas volume fraction exist, depending on the value of the volumetric gas fraction, and some of these are based on experimental measurements (Wallis, 1969). For our experimental gas fractions (typically less than 0.1), the viscosity of the bubbly fluid may be approximated as

$$\mu_b = \mu_l(1+c). \tag{2}$$

This expression is based on theory and validated by experiments (Wallis, 1969; Jaupart and Vergniolle, 1989). For these low gas fractions, viscosities of the bubbly current and the bubble-free fluid only differ by a few percent. As a result, the advance of the current is resisted by viscous dissipation occurring within as well as around the bubbly current (Huppert, 1982). The exact mathematical treatment of the problem is thus complex, but we can use arguments based on dimensional analysis to find how the current length varies as a function of the other relevant variables.

The bubbly current length, L, depends on the side arm diameter, D; the gravitational pressure gradient, $\Delta\rho gD/L$, where g is the gravitational acceleration; the viscosity of the bubbly fluid, μ_b; bubble-free fluid, μ_l; and time, t:

$$L = L\left(\frac{\Delta\rho g D}{L}, D, \mu_b, \mu_l, t\right). \tag{3}$$

Dimensional analysis yields the following three dimensionless groups

$$\Pi_1 = \frac{L}{D}, \quad \Pi_2 = \frac{\mu_l}{\mu_b}, \quad \Pi_3 = \frac{\Delta\rho g D t}{\mu_b}, \tag{4}$$

such that $\Pi_1=\Phi(\Pi_2,\Pi_3)$ where Φ is an unknown function that needs to be defined (Barenblatt, 1996). Thus, the length of the current can be expressed as

$$L = D\ \Phi\left(\frac{\mu_l}{\mu_b},\frac{\Delta\rho g D t}{\mu_b}\right). \tag{5}$$

We do not know the form of function Φ but can use the following physical argument to estimate it. The fluid current is driven by the gravitational pressure gradient; the current would not exist if there were no density difference between the bubbly and bubble-free fluids. This density difference depends on the volumetric gas fraction c (Eq. (1)), thus, L must be directly proportional to $\Delta\rho$, and therefore proportional to the dimensionless group $\Delta\rho g D t/\mu_b$. We now make the assumption that the dependence of L on the density difference follows a power law, which is a common assumption when using dimensional analysis. That is, the dimensionless group $\Delta\rho g D t/\mu_b$ can be raised to some power α, from which we get the following expression for the current length:

$$L = D\left(\frac{\Delta\rho g D t}{\mu_b}\right)^{\alpha} F\left(\frac{\mu_l}{\mu_b}\right). \tag{6}$$

The time dependence t^{α} of the current length does not depend on the viscosity ratio μ_l/μ_b (Eqs. (5) and (6)). Therefore, this time dependence should remain the same whatever the viscosity ratio is, and we can choose the viscosity ratio to simplify the problem and determine α. In the particular case of a gravity current that is much more viscous than the surrounding fluid, advance of the current is resisted mainly by internal viscous dissipation (Huppert, 1982). Thus, the buoyancy-viscous balance that governs the current flow is

$$\frac{\Delta\rho g D}{L} \sim \mu_b \frac{L}{D^2 t} \tag{7}$$

and the length of the current increases with time as $L \sim (\Delta\rho g D^3 t/\mu_b)^{\frac{1}{2}}$. This time dependence of L is independent of the viscosity ratio, so we expect L to increase with time similarly in the general case:

$$L(t) = \left(\frac{\Delta\rho g D^3 t}{\mu_b}\right)^{\frac{1}{2}} F\left(\frac{\mu_l}{\mu_b}\right) \tag{8}$$

where F is an unknown function of the viscosity ratio μ_l/μ_b.

We use the experiments to test the time dependence of the bubbly current given by Eq. (8). There is a maximum distance, $L_{\max}$, that the current can travel, which corresponds to the point where all bubbles have risen to the top of the side arm. Because of low bubble concentrations, bubble interactions can be neglected, and bubbles rise according to Stokes law with constant velocity $v_b=(\Delta\rho_g g d^2)/(12\mu_l)$, where $\Delta\rho_g$ is the difference between the density of the pure liquid and the gas bubble, $\Delta\rho_g=\rho_l-\rho_g$, and d is the bubble diameter [the numerical constant 12 at the denominator differs from the usual constant 18 because of constant stress condition at the bubble surface between the inner gas and the outer liquid, whereas the constant 18 should arise in the case of a rigid sphere on which surface a no slip condition applies (Batchelor, 1967)]. Because $\rho_l \gg \rho_g$, the density difference can be approximated by $\Delta\rho_g=\rho_l$ and bubbles rise at speed

$$v_b = (\rho_l g d^2)/(12\mu_l). \tag{9}$$

The maximum distance that bubbles can rise is the diameter, D, of the side arm, so the maximum time that bubbles take to reach the top of the side arm is $T_b=D/v_b=12\mu_l D/(\rho_l g d^2)$. Therefore, the maximum current length is:

$$L_{\max} = L(T_b) = \left[\frac{12\mu_l \Delta\rho D^4}{\mu_b \rho_l d^2}\right]^{\frac{1}{2}} F\left(\frac{\mu_l}{\mu_b}\right). \tag{10}$$

Substituting Eq. (1) for $\Delta\rho$ and (2) for μ_b, the maximum current length becomes

$$L_{\max} = \frac{D^2}{d}\left(\frac{12c}{1+c}\right)^{\frac{1}{2}} F\left(\frac{\mu_l}{\mu_b}\right). \tag{11}$$

Evolution of the bubbly current length in the experiments was measured by recording the successive positions of the tip until advance ceased. For each

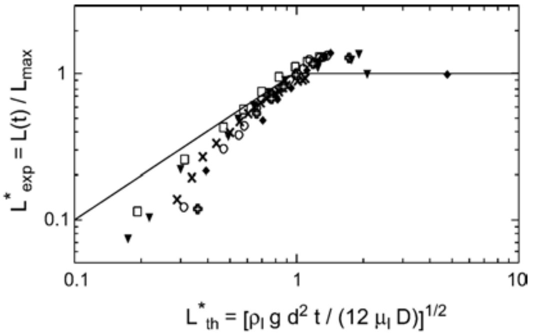

Fig. 5. The experimental dimensionless current length $L^*=L(t)/L_{\max}$ compared with the theoretical dimensionless length $[\rho_l g d^2 t/(12\mu_l D)]^{1/2}$. Beyond one, L^* is constant according to theory as shown by the solid line. Each set of symbols corresponds to measurements from a single experiment: squares, $Q_g=(5.7\pm0.1)\times10^{-8}$ m^3 s^{-1} and $\mu_l=8$ mPa s; inverted triangles, $Q_g=(2.9\pm0.1)\times10^{-8}$ m^3 s^{-1} and $\mu_l=39$ mPa s; Xs, $Q_g=(2.7\pm0.1)\times10^{-8}$ m^3 s^{-1} and $\mu_l=42$ mPa s; open circles, $Q_g=(7.7\pm0.2)\times10^{-8}$ m^3 s^{-1} and $\mu_l=8$ mPa s; open crosses, $Q_g=(5.7\pm0.1)\times10^{-8}$ m^3 s^{-1} and $\mu_l=9$ mPa s; and diamonds, $Q_g=(3.6\pm0.1)\times10^{-8}$ m^3 s^{-1} and $\mu_l=7$ mPa s.

experiment, the length of the current has been non-dimensionalised on the maximum length, $L_{\max}$, attained by the current, allowing comparison over a range of conditions. This approach enables us to eliminate the unknown function *F*. Fig. 5 shows the experimental dimensionless current length as a function of the theoretical dimensionless length $L^* = L(t)/L_{\max} = [\rho_l g d^2 t/(12\mu_l D)]^{1/2}$. After an initial adjustment phase, the data collapse onto the theoretical relationship up to the point where the current has reached its maximum length. Beyond this point, L^* remains equal to unity as the bubbly current has ceased to propagate. In the adjustment phase, data are quite scattered, and in some experiments the measured length needs to reach almost 60% of the theoretical maximum length before the measured length follows the theoretical relationship. However, the adjustment phase is shorter for most experiments. Close examination of the data reveals that the initial mismatch appears proportional to the velocity scale in the vertical conduit (either the average fluid velocity imposed by the pump or the bubble rise speed when no fluid was circulated by the pump). This suggests that the initial spread of the bubbly gravity current is controlled, in some way, by the vertical movement of bubbly fluid up the conduit. Fig. 5 shows, however, that ultimately the bubbly current is controlled by the segregation of the bubbles from the fluid as they rise and accumulate at the top of the horizontal arm; the advance of the bubbly gravity current is then described by L^*.

3.2. Gas segregation and foam development

We now consider the bubble segregation that occurs in the bubbly current. This problem is similar to that investigated by Jaupart and Vergniolle (1989) and we shall base our analysis on their model.

We approximate the foam as a long and thin viscous gravity current, in which the vertical acceleration is negligible and pressure is hydrostatic (Fig. 6). Thus, the flow is driven by the horizontal gradient of the hydrostatic pressure and resisted by the viscous stresses. The foam, however, is much more viscous than the underlying fluid because of a high gas content, ϵ, that is approximately 70% by volume. Foam viscosity, μ_f, is well approximated by the relationship (Jaupart and Vergniolle, 1989)

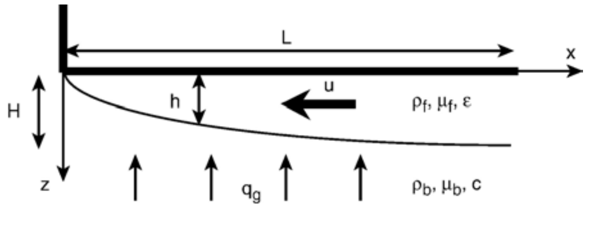

Fig. 6. Schematic illustration of the flow of foam.

$$\mu_f = \mu_l (1-\epsilon)^{-5/2}. \tag{12}$$

Using this expression, a foam with 70 vol.% bubbles is approximately 20 times more viscous than the underlying fluid. Therefore, the main viscous dissipation that resists the flow occurs within the foam and the shear stress at the interface between the foam and the bubbly fluid can be neglected (Huppert, 1982). Consequently, the problem allows analytical treatment.

The horizontal flow is governed by the momentum equation

$$\Delta\rho_f g \frac{\partial h}{\partial x} = \mu_f \frac{\partial^2 u}{\partial z^2} \tag{13}$$

where *x* is the horizontal distance from the entrance of the side arm and *z* the vertical distance from its top. $\Delta\rho_f$ is the density difference between the bubbly fluid ($\rho_b = c\rho_g + (1-c)\rho_l$) and the foam ($\rho_f = \epsilon\rho_g + (1-\epsilon)\rho_l$), such that $\Delta\rho_f = (\epsilon - c)(\rho_l - \rho_g)$. Because $\rho_g \ll \rho_l$, this simplifies to $\Delta\rho_f = (\epsilon - c)\rho_l$. Integrating the momentum Eq. (13) with the two boundary conditions of (i) no slip at the top of the side arm, $u(z=0)=0$, and (ii) no shear stress at the interface, $\frac{\partial u}{\partial z} = 0$ for $z = h$, gives the foam velocity, *u*, as

$$u = \frac{\Delta\rho_f g z}{2\mu_f}(z-2h)\frac{\partial h}{\partial x}. \tag{14}$$

Mass conservation for gas in the foam layer can be expressed as

$$\frac{\partial h}{\partial t} = q - \frac{\partial}{\partial x}\int_0^h u dz. \tag{15}$$

The left hand term represents the vertical growth of the foam thickness. It is balanced on the right by two terms: the gas flux per unit area, *q*, that is supplied by the underlying bubbly current, and a second term representing the outward flux of foam per unit area into the vertical conduit that represents the lateral extend of the foam, which is controlled by the foam velocity *u*. In the bubbly current, the rise of bubbles is characterised by the rise speed, v_b, (9) so the vertical gas flux per unit area that feeds the foam is $q = c v_b/\epsilon$. Using the foam velocity (14) to integrate the foam mass balance (15), we get

$$\frac{\partial h}{\partial t} = q + \frac{\Delta\rho_f g}{12\mu_f}\frac{\partial^2 h^4}{\partial x^2}. \tag{16}$$

This equation is non-dimensionalised using the scales $x = Lx'$, where L is the length of the underlying bubbly current, $h = Hh'$, and $t = Ht'/q$, with $H = [(12\mu_f qL^2)/(\Delta\rho_f g)]^{1/4}$ and where the primes denote dimensionless variables:

$$\frac{\partial h'}{\partial t'} = 1 + \frac{\partial^2 h'^4}{\partial x'^2}. \tag{17}$$

We seek the steady-state shape of the foam, $\frac{\partial h'}{\partial t'} = 0$. Integrating this equation twice with the boundary conditions of (i) zero foam thickness at the entrance of the side arm, $h'(x'=0)=0$, and (ii) no lateral foam flux at the end of the side arm, $\frac{\partial h'}{\partial x'} = 0$ for $x'=1$, gives

$$h'(x') = \left(x' - \frac{x'^2}{2}\right)^{1/4}. \tag{18}$$

Therefore, expressed in dimensional variables, the height of the foam, h, can be written as the product of a characteristic height, H, and a shape function, $f(x)$:

$$h(x) = Hf(x), \tag{19}$$

where

$$H = \left[\frac{12\mu_f qL^2}{\Delta\rho_f g}\right]^{1/4}, \tag{20}$$

and

$$f(x) = \left(\frac{x}{L} - \frac{x^2}{4L^2}\right)^{1/4}. \tag{21}$$

From Eq. (20), the characteristic foam height can be simplified further by recalling that $\Delta\rho_f = (\epsilon - c)\rho_l$, $q = cv_b/\epsilon$ and by using Eq. (9) for v_b and (12) for μ_f:

$$H = \left[\frac{cd^2L^2}{\epsilon(1-\epsilon)^{5/2}(\epsilon - c)}\right]^{1/4}. \tag{22}$$

This two-dimensional analysis does not account for the cap-like geometry of the foam in the cylindrical side arm used in the experiments; the foam is assumed to have a constant thickness over its entire width, perpendicular to the direction of flow (i.e., Fig. 6). Consequently, at a given position along the side arm, for a given foam flux per area perpendicular to the flow, the predicted foam height is underestimated by the theory (i.e., dotted rectangle in Fig. 7). Because the foam has in fact a cap-like cross section, it requires a greater height to accommodate the same flux (i.e., striped area in Fig. 7). To compare the model with the experiments, the theoretical height was increased so that it gives the same foam flux in both the theoretical model and the experiments (Fig. 7).

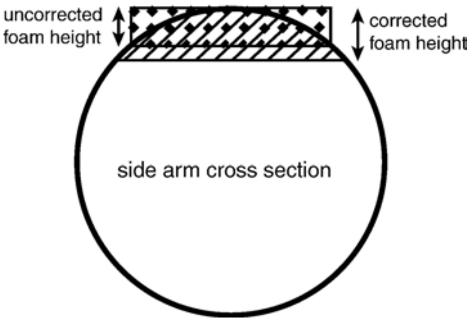

Fig. 7. Illustration showing how the theoretical foam height was corrected. For a given foam flux, hence area perpendicular to the flow, the two-dimensional analysis underestimates the foam height (dotted rectangle); for the same foam flux, the cap-like foam is in fact thicker because of its shape (striped area). The theoretical height was increased such that both dotted rectangle and stripped cap have identical areas, ensuring identical foam flux in both model and experiment.

To calculate the foam height, we also need to know the foam gas fraction, ϵ. Stable foams typically contain approximately 70 vol.% of gas (Jaupart and Vergniolle, 1989). This value is likely to be a lower bound in our experiments, however, because the fine bubbles produced by electrolysis tend to coalesce and create centimetric to decimetric long bubbles of free gas phase floating on top of the foam. Observation indicates that the foam gas fraction in the experiments is therefore more likely to be in the range $\epsilon = 0.7$–0.9.

For each experiment, the steady-state foam thickness was measured from a digital photograph at different positions along the tube, with an uncertainty of ±1 mm. The gas fraction, c, in the bubbly layer was used as a fitting parameter when comparing experimental and theoretical steady-state foam thicknesses (see Section 2.1). The foam height is also very sensitive to the foam gas fraction, ϵ, because it is close to unity (Eq. (22)). Fig. 8 shows the foam thickness measured along the side arm in three experiments that differ by their electrolysis electric current intensities, and hence gas fraction, c. In all three experiments, the theoretical thickness predicted by the model is shown for a foam gas fraction $\epsilon = 0.7$ and $\epsilon = 0.9$. Our simple foam model is in good agreement with the data. Unrealistically high bubbly gas fractions, however,

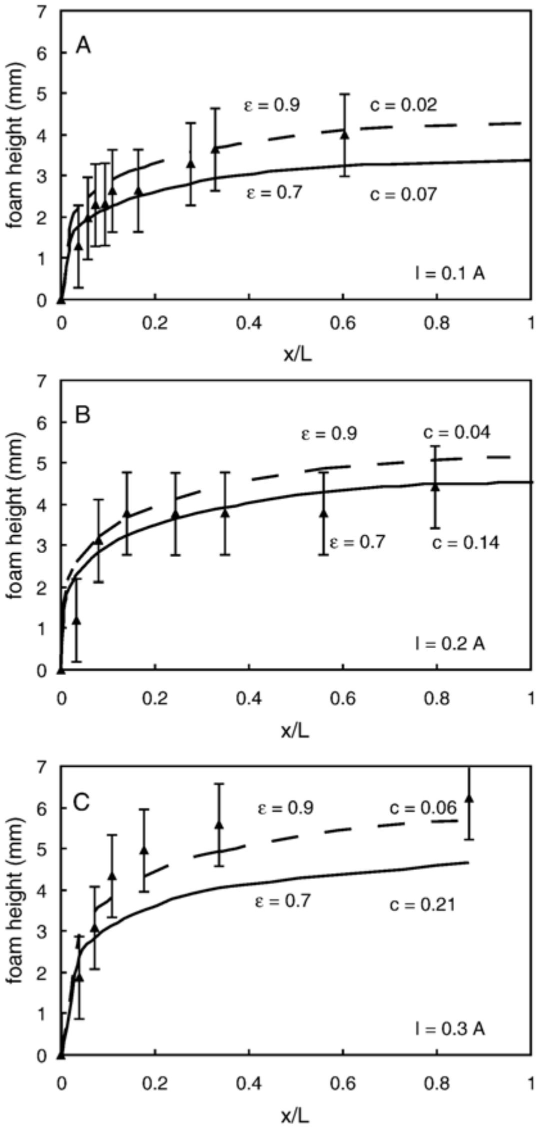

Fig. 8. Variation of the steady-state foam height along the side arm in three different experiments with a 45:45:10 golden syrup:water:NaCl mixture ratio and no fluid flow. (A) current intensity $I=0.1$ A, (B) $I=0.2$ A, (C) $I=0.3$ A. The solid line shows the prediction of the theoretical model for a foam gas fraction $\epsilon=0.7$ and a bubbly gas fraction $c=0.7\times I$. The dashed line shows the prediction for a foam gas fraction $\epsilon=0.9$ and a bubbly gas fraction $c=0.2\times I$.

are required if the foam is assumed to contain 70 vol.% gas (Fig. 8B and C). More realistic values are obtained if instead the foam gas fraction is higher, in accord with the experimental observations.

We have implicitly assumed that the flow of rising fluid in the vertical conduit has no effect on the exchange flow and gas segregation that occur in the side arm. Fig. 9 shows that this assumption is indeed correct. Foam thickness was measured in three experiments that differ by their vertical conduit fluid flux, Q_l, only: $Q_l=0$, $Q_l=9Q_g$ and $Q_l=79Q_g$, with $Q_g=2.9\times10^{-8}$ m^3 s^{-1} in all three experiments. Within the experimental errors, the foams that developed in these three experiments have identical thickness even though the fluid flux varied over two orders of magnitude in the vertical conduit.

Finally, the lateral extent of the foam will be larger than the underlying bubbly current length, $L_{\max}$, if the side arm is longer than $L_{\max}$. In this case, as bubbles accumulate at the top of the side arm, the foam tip opposite the vertical conduit rests against a bubble-free fluid of higher density. The foam will therefore flow towards the closed end of the side arm until ultimately reaching a constant thickness. The steady-state foam thickness is then described by Eqs. (19)–(21) between the entrance of the side arm and $x=L_{\max}$, and will have value $h(x=L_{\max})$ away from the entrance.

4. Implications and limitations

4.1. Time scales

To apply this model of gas segregation to magma degassing, the time scale needs to be smaller than that of magma cooling and solidification. Two time scales arise in our model: a bubble time scale, T_b (for bubbles to rise over the thickness of the horizontal intrusion), and a foam time scale, T_f (to establish a steady-state foam). Cooling and solidification of magma occur over a time scale T_s.

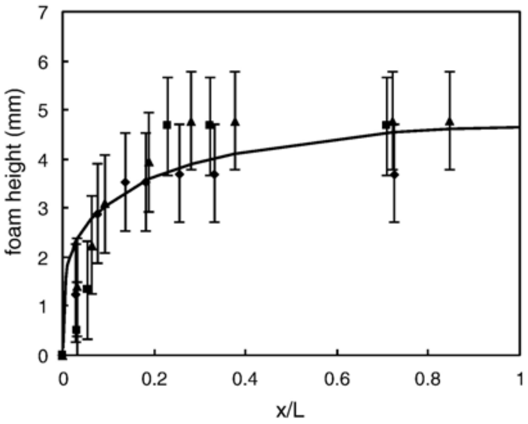

Fig. 9. Foam heights for three different experiments with a 60:30:10 golden syrup:water:NaCl mixture ratio. Each symbol corresponds to a fluid flux in the vertical conduit: triangles, no fluid flux; diamonds, $Q_l=9Q_g$; squares, $Q_l=79Q_g$. Q_g is the same in all experiments. The solid line shows the model prediction with a gas fraction $c=0.06$ in the bubbly layer and a gas fraction $\epsilon=0.8$ in the foam.

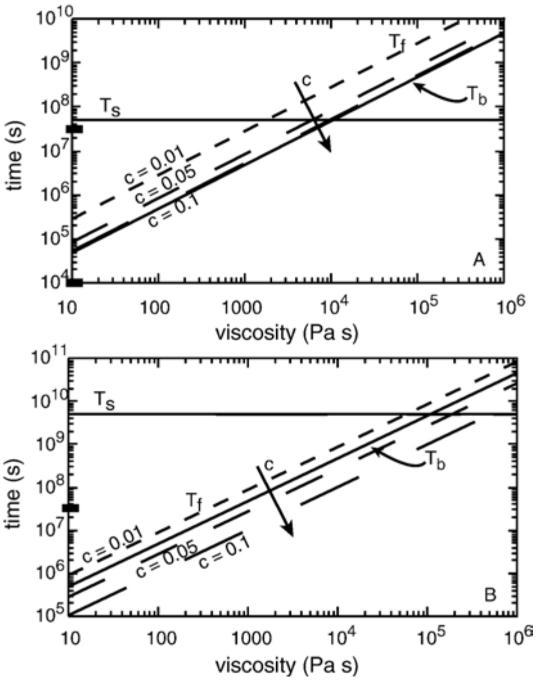

Fig. 10. The different time scales as a function of magma viscosity for different sill sizes. (A) sill thickness $D=10$ m and length $L=1$ km; (B) $D=100$ m and $L=10$ km. The horizontal solid curve represents the solidification time T_s, the slanted solid curve represents the bubble rise time T_b and the dashed curves represent the foam time T_f for different volumetric gas fractions: short dashes, $c=0.01$; medium dashes, $c=0.05$; long dashes, $c=0.1$. Magma density $\rho_l=2700$ kg m^{-3} and gas bubbles are 1 mm in diameter in all calculations. Thick black ticks on time axis represent 1 day ($\simeq 9\ 10^3$ s) and 1 year ($\simeq 3\ 10^7$ s).

Bubbles rise in the laminar regime according to Stokes law, so

$$T_b = \frac{12\mu_l D}{\rho_l g d^2}. \tag{23}$$

T_f is obtained by dividing the characteristic foam thickness H (Eq. (22)) by the foam velocity scale q,

$$T_f = \frac{12\mu_l L^{1/2}}{\rho_l g d^{3/2}}\left[\frac{\epsilon^3}{c^3(1-\epsilon)^{5/2}(\epsilon-c)}\right]^{1/4}. \tag{24}$$

Throughout our calculations we assume a foam gas fraction $\epsilon=0.7$. Although foams in our experiments have higher gas fraction, a value of 0.7 is a generally accepted value for generic foams and thus seems a reasonable value for magmatic systems (Jaupart and Vergniolle, 1989). The horizontal intrusion is assumed to cool down by conduction. As magma cools and solidifies at the walls, latent heat is released that warms up the interior of the intrusion. The exact and detailed treatment of this problem is described in Turcotte and Schubert (1982), from which the time needed to cool and solidify an intrusion of thickness, D, by conduction is

$$T_s = \frac{D^2}{16\kappa\lambda^2}. \tag{25}$$

Magma thermal diffusivity $\kappa=5\ 10^{-7}$ m^2 s^{-1} and the dimensionless constant λ, which depends on the temperature difference between the magma and surrounding rocks and is typically in the range 0.5–0.75 (Turcotte and Schubert, 1982). Throughout our calculations, we assume $\lambda=0.5$. T_s is a lower estimate; if the intrusion were connected to an active conduit, the solidification time would be larger as any exchange flow would mean both mass and heat are exchanged, keeping the intrusion hotter than in the purely conductive scenario.

Fig. 10 shows the three time scales as a function of magma viscosity for sills with a thickness:length aspect ratio of 1:100. All three time scales increase with the intrusion size, but T_s is more sensitive to size than T_b and T_f. In consequence, efficient gas segregation in smaller sills would require magmas of relatively lower viscosity than in larger intrusions. The foam time scale decreases with increasing volumetric gas fraction, c, so gas segregation is favoured in magmas with higher volumetric gas fraction. The time scales also are strongly sensitive to the bubble size (Fig. 11). An order of magnitude change in bubble diameter affects T_b and T_f by two orders of magnitude (Eqs. (23) and (24)).

Using the exsolved gas fraction $c=0.01$–0.1 and bubbles 1 mm in diameter as reasonable values for

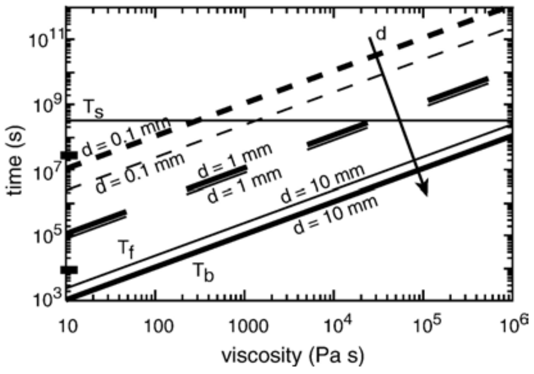

Fig. 11. The different time scales as a function of magma viscosity and bubble diameter d for a sill 25 m thick and 2.5 km long. The horizontal solid curve represents the solidification time T_s, the slanted thick curves represent the bubble rise time T_b, and the slanted thin curves represent the foam time T_f for different bubble diameters: short dashes, $d=0.1$ mm; long dashes, $d=1$ mm; solid curves, $d=10$ mm. Volumetric gas fraction $c=0.1$ in all calculations. Thick black ticks on time axis represent 1 day ($\simeq 9\ 10^3$ s) and 1 year ($\simeq 3\ 10^7$ s).

shallow magmatic degassing, efficient gas segregation in a sill 10-m thick and 1-km long would require magmas of viscosity lower than 10^3–10^4 Pa s, whereas in a sill 100-m thick and 10-km long, gas segregation would remain efficient with magma viscosity as high as 10^5 Pa s. Recalling that T_s is a lower estimate for the solidification time, gas segregation by foam formation in sills is a supportable process for intermediate as well as basaltic magmas.

We expect gas segregation to be more efficient in sills than in horizontally-propagating dykes. Dykes typically have a thickness:length aspect ratio of 1:1000 whereas the sill aspect ratio is usually 1:100, reducing T_s by a factor of 100. Bubble rise time also is substantially increased for a dyke. Both effects reduce gas segregation efficiency. Our analysis, however, does not account for two processes that both would increase the solidification time scale. The first one is the advection of heat induced by any exchange flow between an active vertical conduit and the horizontal dyke. The second is bubble convection, which has not been considered for any geometry (see Section 4.4). Consequently, the solidification time scale would be longer and gas segregation could occur in dykes containing magmas of low viscosity.

4.2. Implications for gas segregation

Different eruptive scenarios can be envisaged depending on the values of supply rate, Q_s, exchange rate asssociated with gas segregation, Q_{ex}, foam layer return flow, Q_g, and degassed magma return flow, Q_D (Fig. 12). We infer from our experiments that gas segregation processes and rates in an intrusion will be independent of moderate changes in magma supply rate because the exchange of magma and gas between the conduit and the horizontal intrusion is predominantly driven by the gas segregation that occurs in the latter. Thus, the exchange rate does not depend on the magma supply rate. If magma supply rate is low and $Q_{\mathrm{ex}} > Q_s$, then effective gas segregation can occur in the intrusion and can lead to episodic Strombolian eruptions of relatively gas-poor magma (Q_D) driven by the rise of expanding foam packets and slugs up the conduit. If the magma supply rate is sufficiently large that it exceeds the exchange rate, $Q_s > Q_{\mathrm{ex}}$, then there will be ineffective gas segregation suggestive of stronger explosions driven mainly by the deep supply in fresh magma and therefore erupting gas-rich (Q_s) as well as gas-poor (Q_D) magmas.

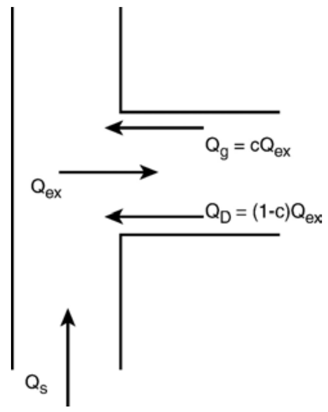

Fig. 12. Schematic illustration of an exchange flow of bubbly and degassed magma driven by steady-state gas segregation. In a system with supply rate Q_s, an exchange rate Q_{ex} of bubbly fluid entering the intrusion is balanced by an exsolved gas return rate Q_g and a degassed magma return rate Q_D: $Q_{\mathrm{ex}} = Q_g + Q_D$.

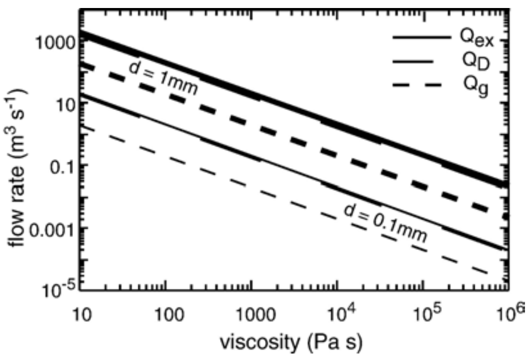

Fig. 13. Exchange flow rate Q_{ex} (solid curves), exsolved gas return rate Q_g (short dashed curves) and degassed magma return rate Q_D (long dashed curves) as a function of magma viscosity. Thick lines corresponds to an average bubble diameter $d = 1$ mm, thin lines to a diameter $d = 0.1$ mm. We assume an intrusion 2.5 km long and wide, and a volumetric gas fraction $c = 0.1$.

As illustrated in Fig. 12, the steady-state volumetric flux of bubbly fluid entering an intrusion, Q_{ex}, is balanced by an outward gas flux, or foam layer return flow, Q_g, and a degassed magma return rate, Q_D, so that $Q_{\mathrm{ex}} = Q_g + Q_D$. A proportion, c, of Q_{ex} is made of exsolved gas, $Q_g = cQ_{\mathrm{ex}}$. By mass balance, $Q_D = (1 - c)Q_{\mathrm{ex}}$. The gas return flux is $Q_g = Acv_b/\epsilon$, where A is the interface area between the bubbly fluid and the foam in the intrusion. Assuming A is similar to the surface area of the intrusion, $A \sim L^2$, and using Eq. (9) for the bubble rise speed, it follows that

$$Q_{ex} = \frac{\rho_l g d^2 L^2}{12\mu_l \epsilon}, \tag{26}$$

$$Q_D = \frac{(1-c)\rho_l g d^2 L^2}{12\mu_l \epsilon}, \tag{27}$$

$$Q_g = \frac{c\rho_l g d^2 L^2}{12\mu_l \epsilon}. \tag{28}$$

These fluxes are shown in Fig. 13 as function of magma viscosity for two different bubble diameters, $d=0.1$ mm and $d=1$ mm.

We expect a transition between Strombolian activity when $Q_s < Q_{\text{ex}}$ and more explosive eruptions when $Q_s > Q_{\text{ex}}$ to occur when both fluxes are comparable,

$$Q_s \sim Q_{\text{ex}} = \frac{\rho_l g d^2 L^2}{12\mu_l \epsilon}. \tag{29}$$

As shown on Fig. 13, the transition to more explosive eruptions would require a much higher supply rate with low viscosity magmas than with more viscous magmas; low viscosity produces very effective gas segregation. Bubble size has also a strong effect and will increase with decreasing pressure, which also increases Q_{ex}. Thus, we expect gas segregation processes to become more important at lower pressure (i.e., shallower depths).

4.3. Stromboli volcano

We can apply these general principles to degassing and eruption processes at Stromboli volcano, Italy. Stromboli has been experiencing continuous phases of activity for millenia (Allard et al., 1994). Persistent activity consists of mild explosions occurring every tens of minutes associated with a more quiescent, continuous open-conduit degassing from the summit craters, while extruding very little basalt. Between 1980 and 1993, the time-averaged gas mass flux has been estimated at $6–12 \times 10^3$ t/day ($350–680$ m^3 s^{-1}). The associated flux of degassed magma, Q_D, estimated from measured SO_2 flux, was $0.3–0.6$ m^3 s^{-1}, which is two orders of magnitude greater than the observed magma eruption rate of approximately 2.5×10^{-3} m^3 s^{-1} (Allard et al., 1994). This degassing is predominantly quiescent (Allard et al., 1994).

Normal Strombolian activity erupts highly porphyritic (HP) black scoriae, lapilli, ash, and occasionally lava with approximately 50 vol.% crystals (Francalanci et al., 1999; Métrich et al., 2001). This normal activity is punctuated by more violent and paroxysmal eruptions that eject crystal-poor (<5 vol.% phenocrysts) and highly vesiculated pumices and scoriae that are referred to as low porphyritic (LP), in addition to crystal-rich, dense HP scoriae identical to the products of normal activity (Francalanci et al., 1999; Métrich et al., 2001). Petrological evidence reveals that LP products represent fresh, crystal-poor, gas-rich magma that feeds the plumbing system and HP products are the stored and differentiated form of the fresh magma (Francalanci et al., 1999).

Thermal and gas budget balances indicate that the plumbing system of Stromboli has been in steady state for millenia (Giberti et al., 1992; Allard et al., 1994; Harris and Stevenson, 1997). CO_2- and H_2O- rich magma is continuously supplied from a deep reservoir into the crystal-rich shallow plumbing system where it undergoes crystallization driven by decompression and volatile loss at low pressure (Métrich et al., 2001). Pressure estimates from fluid inclusions in restitic quartzite nodules suggest a three stage plumbing system with (i) a deep reservoir at about 11 km depth (~290 MPa), (ii) a shallow reservoir at about 3.5 km depth (~100 MPa) and (iii) a near-surface reservoir (Vaggelli et al., 2003; Francalanci et al., 2004). The latter corresponds to the location of shallow explosive activity about 250 m below the surface (Chouet et al., 1997; Ripepe et al., 2001; Chouet et. al., 2003), whereas the 3.5-km-deep reservoir is envisaged as the crystal-rich HP body ($\rho_l = 2700$ kg m^{-3}, $\mu_l = 1.4 \times 10^4$ Pa s) that is continuously renewed by deeper volatile-rich LP magma (2.4–2.8 wt.% H_2O, $\rho_l = 2500$ kg m^{-3}, $\mu_l = 15–20$ Pa s) (Métrich et al., 2001). Brittle deformation of CO_2-rich fluid inclusions suggests rapid ascent of the gas-rich magma from a deep to a shallow reservoir, implying a high magma flow rate. Fast ascent and injection of gas-rich magma into the 3.5-km-deep reservoir has been proposed to cause the more violent explosions at Stromboli (Vaggelli et al., 2003).

We apply the general principles of gas segregation and generation of gas-rich and degassed magma identified in our experiments to these processes at Stromboli. The geometry of the shallow reservoir at 3.5 km is not well-constrained, mainly because the seismicity is restricted to very shallow depths (<1 km) (Chouet et al., 2003), and there is poor knowledge of the internal structure of the volcano (Chouet et al., 1997). Nevertheless, 3.5 km corresponds approximately to the transition to crustal basement, where a lithological discontinuity is expected (Vaggelli et al., 2003), which is favourable to the formation of a sill-like reservoir. Analysis of Sr isotope ratios of scoriae and lavas from Stromboli enabled Francalanci et al. (1999) to estimate the volume of this shallow reservoir at approximately 0.3–0.04 km^3. We calculate the reservoir dimensions assuming two bounding geometries: (i) a disk-like sill with a thickness:length aspect ratio of 1:100, whose volume would require an average thickness $D=25$ m and diameter $L=2.5$ km, and (ii) an equant body with diameter $D=500$ m. The true geometry of the Stromboli shallow reservoir is likely to lie in between these two end members.

Estimating *a priori* bubble sizes in the range 0.1–1 mm, which is reasonable for shallow basaltic systems (Sarda and Graham, 1990; Cashman and Mangan, 1994), time scales have been calculated for the sill-like geometry (Fig. 11) and the equant body (Fig. 14) using Eqs. (23)–(25). Recalling that T_s is a lower estimate for the solidification time, Figs. 11 and 14 show that, regardless of the shallow chamber geometry, sufficient time is present for gas segregation to occur at Stromboli (gas-poor magma viscosity $\sim 10^4$ Pa s) with bubble diameters in the range 0.1–1 mm. In comparison, Francalanci et al. (1999) estimated the average magma residence time in the shallow reservoir at $\tau \sim 19 \pm 12$ years (i.e., $6 \pm 4 \times 10^8$ s). In our model, we assume that gas segregation occurs on a time scale shorter than the magma residence time. Although this is not a severe restriction for the sill-like geometry, because the residence time is comparable to the solidification time (Fig. 11), gas segregation in an equant body of gas-poor magma would only be possible with bubble diameters ~1 mm or larger (Fig. 14).

The average magma residence time and volume estimated by Francalanci et al. (1999) for the shallow reservoir enable us to calculate an exchange flow rate of order $Q_{\mathrm{ex}} \sim V/\tau \sim 0.07$–$0.5\ \mathrm{m}^3\ \mathrm{s}^{-1}$. This rate is in the range given by Giberti et al. (1992) ($\sim 0.06\ \mathrm{m}^3\ \mathrm{s}^{-1}$ estimated from thermal and gas budget balances) and Allard et al. (1994) (0.3–0.6 $\mathrm{m}^3\ \mathrm{s}^{-1}$ estimated from measured SO2 flux). Assuming $\rho_l = 2700\ \mathrm{kg\ m}^{-3}$, $\mu_l = 1.4 \times 10^4$ Pa s, and $\epsilon = 0.7$ in Eq. (26), these exchange rates would imply an average bubble diameter $d \sim 0.2$–0.6 mm in a sill 2.5 km long and $d \sim 1$–3 mm in an equant reservoir. These values are in the bubble size range measured in lapilli from Stromboli (Lautze and Houghton, 2005) and are within the range of acceptable sizes for gas segregation to occur on time scale shorter than the magma residence time.

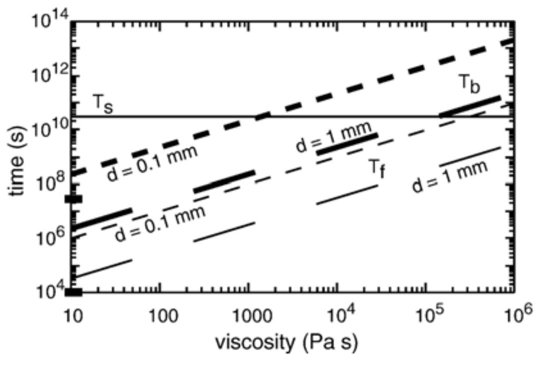

Fig. 14. The different time scales as a function of magma viscosity for an equant reservoir 500 m in diameter. The horizontal solid curve represents the solidification time T_s, the slanted thick curves represent the bubble rise time T_b and the slanted thin curves represent the foam time T_f for different bubble diameters: short dashes, $d = 0.1$ mm; long dashes, $d = 1$ mm. Volumetric gas fraction $c = 0.1$. Thick black ticks on time axis represent 1 day ($\simeq 9\ 10^3$ s) and 1 year ($\simeq 3\ 10^7$ s).

We would expect normal, episodic Strombolian degassing for a magma supply rate smaller than the exchange rate, and more violent eruptions at higher supply rates. Using our model with bubble sizes consistent with gas segregation in the Stromboli shallow reservoir, we expect the transition between these two eruptive regimes to occur at a supply rate on the order of 0.1–1 $\mathrm{m}^3\ \mathrm{s}^{-1}$ (Fig. 13). Landi et al. (2004) estimated the eruption rate of gas-rich material during violent recent eruptions at Stromboli at $\sim 30\ \mathrm{m}^3\ \mathrm{s}^{-1}$, implying that Q_s exceeded Q_{ex} by two orders of magnitude, in accord with our model principles.

Although our experimental work was not expressly designed to study degassing and generation of gas-poor and gas-rich magmas at a specific volcano, we have shown that the general physical principles governing gas segregation in shallow horizontal intrusions can be applied to Stromboli volcano. Model implications, in terms of the bubble sizes of exsolved gas in the shallow chamber, the fluxes of gas-poor and gas-rich magmas generated by gas segregation as well as the different eruptive regimes determined by the relative values of supply rate and exchange flow, are all consistent with a variety of independent field data.

4.4. Limitations of our analysis

Two processes that have not been accounted for in our analysis are bubble convection and thermal convection. Bubble convection effects arise as the concentration of bubbles increases. Although it is difficult to predict the onset of bubbly convection in shallow magmatic systems, and consequently laminar bubble rise is considered to be a reasonable regime, we now consider the convective regime for completeness.

Bubbly convection occurs in suspensions of uniformly-distributed bubbles when the characteristic gas bubble size d is large enough that three-dimensional inertial effects become important and bubbles are entrained in each other's wake. This is thought to occur when $d > 4\sqrt{\sigma/(\rho_l g)}$ (Wallis, 1969), where σ is the coefficient of surface tension between gas and liquid, of density ρ_l. For most magmas, $\sigma = 0.3$–0.4 kg s^{-2} (e.g., Williams and McBirney, 1979), and three-dimensional inertial effects are expected to be important for centimetric gas bubbles, or larger, but not for bubbles of smaller size. However, the departure from a uniform bubbly pattern can also occur due to the characteristics of the production of the gas bubbles and their interaction with the overall flow dynamics (Wallis, 1969). This effect is difficult to assess, but the associated convective velocity scale has been observed experimentally to be typically greater than laminar rise speed (e.g., Cardoso and Woods, 1999; Phillips and Woods, 2001). We note, however, that both the bubble time scale, T_b, and the foam time scale, T_f, are inversely proportional to bubble rise speed (see Section 4.1). As convecting gas bubbles are expected to rise faster than in the laminar regime, both time scales will thus decrease by the same amount. Therefore, steady-state gas segregation will be established more rapidly. This also implies that the range of magma viscosity over which gas segregation could occur is increased (see Figs. 10 and 11). Regardless of the time needed for gas segregation to occur, the same physical principles apply whether bubbles rise in a laminar or turbulent suspension, with laminar analysis leading to conservative modelling of the bubble rise and therefore of the time needed to establish steady-state gas segregation.

In deriving the cooling and solidification time scale (25), we assumed that a horizontal sill cools down by conduction. However, the impact of thermal convection in the sill also needs to be considered. Conditions for thermal convection in a sill are reached when the Rayleigh number, Ra, exceeds approximately 2000 (Sparks et al., 1984). The Rayleigh number is defined by

$$Ra = \frac{\beta \rho_l g \Delta T D^3}{\mu_l \kappa}, \tag{30}$$

where β is the volumetric coefficient of thermal expansion of the magma (2×10^{-5} K^{-1}; Annen et al., 2006) and ΔT is the temperature difference between the magma and the surrounding rocks. Application of Eq. (30) with a magma viscosity of 10^5 Pa s and a temperature difference of 1 °C shows that the Rayleigh number exceeds 2000 for any sill thicker than 6 m. This indicates that thermal convection can be attained in relatively thin sills even with relatively small thermal gradients accross the magma layer, as recognised in previous studies (e.g., Sparks et al., 1984; Annen et al., 2006). However, magma cooling and crystallisation induce exsolution of gas bubbles, which decreases the density and increases the viscosity of the magma. Cardoso and Woods (1999) have calculated the evolution of the Rayleigh number as the melt cools and becomes volatile saturated. Their study shows that the magnitude of the Rayleigh number, and thus the intensity of the convection, increases by a factor of 10–100 as a result of the bubble production. Convection in a horizontal intrusion will therefore be driven predominantly by gas bubbles. As shown above, we expect steady-state gas segregation to be established more rapidly than in the pure conductive case. We stress again that regardless of the time needed for gas segregation to occur, whether bubble suspension is laminar or turbulent, the same physical principles for gas segregation apply, as captured by the present laminar analysis.

Finally, our analysis of gas segregation was restricted to horizontal intrusions, whereas real plumbing systems will involve more complex geometries with elements departing from being perfectly vertical or horizontal. These geometries will affect the extent over which gas segregation processes occur; a downward inclined sill would limit the intrusion of bubbly material, whereas an upward inclined intrusion would enhance the storage and thus gas segregation efficiency. However, gas segregation as described in this paper is a dynamic process. Therefore, the key physical principles that govern gas segregation will hold regardless of the real geometry of the system.

5. Conclusion

Gas segregation in plumbing systems of persistent volcanoes has been investigated by means of analogue experiments in the specific case of low exsolved volumetric gas concentrations in a vertical conduit connected to a single horizontal intrusion. These experiments show that the presence of horizontal intrusions can lead to strong gas segregation effects in volcanic plumbing systems.

Gas segregation is driven by an exchange flow between the conduit and the horizontal intrusion because of the presence of exsolved bubbles. Bubbles rise and accumulate as foam at the top of the intrusion, thereby segregating bubbles from the fluid. Bubble segregation is coupled with the accumulation of denser degassed fluid at the base of the intrusion. Steady state is ultimately reached, whereby any influx of fluid from the conduit and into the intrusion is balanced by an outward flux of lighter foam and denser degassed fluid. The length and time scales of this gas segregation are controlled by the rise of bubbles in the horizontal intrusion.

The comparison of time scales for gas segregation processes with that of the cooling and solidification of the intrusion suggests that more efficient gas segregation occurs in sills than in horizontal dykes. All time scales associated with gas segregation increase both with magma viscosity and intrusion size. However, the cooling and solidification time scale appears to be the most sensitive to intrusion size. This suggests that gas segregation could be efficient within large intrusions with magmas of basaltic to intermediate composition as well as within smaller, basaltic intrusions.

Our analysis has also implications for the generation of gas-rich and gas-poor magmas by gas segregation processes in persistent plumbing systems. For a low magma supply rate at a persistent volcano, very efficient gas segregation is expected, inducing episodic degassing and pulse-like activity that erupt relatively gas-poor magmas, because segregation rates are larger than overall magma supply rate. At higher magma supply rates, gas segregation is expected to be less effective, leading to stronger explosions erupting gas-rich as well as gas-poor magmas.

The general physical principles governing gas segregation in shallow horizontal intrusions can be applied to Stromboli, and their implications are all consistent with independent field data. Gas segregation at Stromboli is likely to occur in a shallow reservoir of sill-like geometry at 3.5 km depth with bubbles of exsolved gas 0.1–1 mm in diameter. The transition between Strombolian activity erupting gas-poor, highly porphyritic magmas and violent explosions that erupt also gas-rich, low porphyritic magmas would correspond to a critical magma supply rate on the order of 0.1–1 m^3 s^{-1}.

Our analysis of gas segregation in the conduit plumbing system was restricted to horizontal dykes and sills. The effect of more complex geometries should be addressed in future studies. Although the key physical principles that govern gas segregation are not expected to differ, the system geometry affects the extend over which gas segregation processes occur, and in turn their efficiency.

Acknowledgements

This work benefited from fruitful discussions with Brittain Hill, Steve Sparks, AndyWoods, Andrew Hogg and Gary Matson. The authors acknowledge Steve Sparks for his helpful comments and suggestions on an earlier version of this manuscript, and Brittain Hill for his thorough review of a previous version of the manuscript. We thank Alain Burgisser and an anonymous reviewer for their reviews and comments. This paper was prepared to document work performed by the Center for Nuclear Waste Regulatory Analyses (CNWRA) and its contractors for the U.S. Nuclear Regulatory Commission (NRC) under Contract No. NRC-02-02-012. The activities reported here were performed on behalf of the NRC Office of Nuclear Material Safety and Safeguards, Division of High Level Waste Repository Safety. This paper is an independent product of the CNWRA and does not necessarily reflect the view or regulatory position of the NRC.

References

Acocella, V., Neri, M., 2003. What makes flank eruptions? The 2001 Etna eruption and its possible triggering mechanisms. Bull. Volcanol. 65, 517–529.

Allard, P., 1997. Endogenous magma degassing and storage at Mount Etna. Geophys. Res. Lett. 24, 2219–2222.

Allard, P., Carbonnelle, J., Métrich, N., Loyer, H., Zettwoog, P., 1994. Sulphur output and magma degassing budget of Stromboli volcano. Nature 368, 326–330.

Andronico, D., Branca, S., Calvari, S., Burton, M., Caltabiano, T., Corsaro, R.A., Del Carlo, P., Garfì, G., Lodato, L., Miraglia, L., Murè, F., Neri, M., Pecora, E., Pompilio, M., Salerno, G., Spampinato, L., 2005. A multi disciplinary study of the 2002–03 Etna eruption: insights into a complex plumbing system. Bull. Volcanol. 67, 314–330.

Annen, C., Scaillet, B., Sparks, R.S.J., 2006. Thermal constraints on the emplacement rate of a large intrusive complex: The Manaslu leucogranite, Nepal Himalaya. J. Petrol. 47, 71–95.

Barenblatt, G.I., 1996. Scaling, Self-Similarity, and Intermediate Asymptotics. Cambridge University Press.

Batchelor, G.K., 1967. An Introduction to Fluid Dynamics. Cambridge University Press.

Berlo, K., Blundy, J., Turner, S., Cashman, K., Hawkesworth, C., Black, S., 2004. Geochemical precursors to volcanic activity at Mount St. Helens, USA. Science 306, 1167–1169.

Cardoso, S.S.S., Woods, A.W., 1996. Interfacial turbulent mixing in stratified magma reservoirs. J. Volcanol. Geotherm. Res. 73, 157–175.

Cardoso, S.S.S., Woods, A.W., 1999. On convection in a volatile-saturated magma. Earth Planet. Sci. Lett. 168, 301–310.

Cashman, K.V., Mangan, M.T., 1994. Physical aspects of magma degassing II. Constraints on vesiculation processes from textural studies of eruptive products. Mineral. Soc. Am., Rev. Mineral. 30, 447–478.

Chouet, B., Saccorotti, G., Martini, M., Dawson, P., De Luca, G., Milana, G., Scarpa, R., 1997. Source and path effects in the wave fields of tremor and explosions at Stromboli Volcano, Italy. J. Geophys. Res. 102, 15,129–15,150.

Chouet, B., Dawson, P., Ohminato, T., Martini, M., Saccorotti, G., Giudicepietro, F., De Luca, G., Milana, G., Scarpa, R., 2003. Source mechanisms of explosions at Stromboli Volcano, Italy, determined from moment-tensor inversions of very-long-period data. J. Geophys. Res. 108 (B1), 2019. doi:10.1029/2002JB001919.

Dawson, P., Whilldin, D., Chouet, B., 2004. Application of near real-time radial semblance to locate the shallow magmatic conduit at Kilauea Volcano, Hawaii. Geophys. Res. Lett. 31, L21606. doi:10.1029/2004GL021163.

Francalanci, L., Tommasini, S., Conticelli, S., Davies, G.R., 1999. Sr isotope evidence for short magma residence time for the 20th century activity at Stromboli volcano, Italy. Earth Planet. Sci. Lett. 167, 61–69.

Francalanci, L., Tommasini, S., Conticelli, S., 2004. The volcanic activity of Stromboli in the 1906–1998 AD period: mineralogical, geochemical and isotope data relevant to the understanding of the plumbing system. J. Volcanol. Geotherm. Res. 131, 179–211.

Francis, P., Oppenheimer, C., Stevenson, D., 1993. Endogenous growth of persistent active volcanoes. Nature 366, 554–557.

Giberti, G., Jaupart, C., Sartoris, G., 1992. Steady-state operation of Stromboli volcano, Italy: constraints on the feeding system. Bull. Volcanol. 54, 535–541.

Harris, A.J.L., Stevenson, D.S., 1997. Magma budgets and steady-state activity of Vulcano and Stromboli. Geophys. Res. Lett. 24, 1043–1046.

Huppert, H.E., 1982. The propagation of two-dimensional and axisymmetric viscous gravity currents over a rigid horizontal surface. J. Fluid Mech. 121, 43–58.

Jaupart, C., Vergniolle, S., 1989. The generation and collapse of a foam layer at the roof of a basaltic magma chamber. J. Fluid Mech. 203, 347–380.

Kyle, P.R., Meeker, K., Finnegan, D., 1990. Emission rates of sulfur dioxide, trace gases and metals from Mount Erebus, Antarctica. Geophys. Res. Lett. 17, 2125–2128.

Landi, P., Mètrich, N., Bertagnini, A., Rosi, M., 2004. Dynamics of magma mixing and degassing recorded in plagioclase at Stromboli (Aeolian Archipelago, Italy). Contrib. Mineral. Petrol. 147, 213–227.

Lautze, N.C., Houghton, B.F., 2005. Physical mingling of magma and complex eruption dynamics in the shallow conduit at Stromboli volcano, Italy. Geology 33, 425–428.

Le Guern, F., 1987. Mechanism of energy transfer in the lava lake of Niragongo (Zaire), 1959–1977. J. Volcanol. Geotherm. Res. 31, 17–31.

Le Guern, F., Carbonnelle, J., Tazieff, H., 1979. Erta'Ale lava lake: heat and gas transfer to the atmosphere. J. Volcanol. Geotherm. Res. 6, 27–48.

Métrich, N., Bertagnini, A., Landi, P., Rosi, M., 2001. Crystallization driven by decompression and water loss at Stromboli volcano (Aeolian Islands, Italy). J. Petrol. 42, 1471–1490.

Phillips, J.C., Woods, A.W., 2001. Bubble plumes generated during recharge of basaltic magma reservoirs. Earth Planet. Sci. Lett. 186, 297–309.

Phillips, J.C., Woods, A.W., 2002. Suppression of large-scale magma mixing by melt-volatile separation. Earth Planet. Sci. Lett. 204, 47–60.

Ripepe, M., Ciliberto, S., Della Schiava, M., 2001. Time constraints for modeling source dynamics of volcanic explosions at Stromboli. J. Geophys. Res. 106, 8713–8727.

Ryan, M.P., 1988. The mechanics and three-dimensional internal structure of active magmatic systems: Kilauea Volcano, Hawaii. J. Geophys. Res. 93 (B5), 4213–4248.

Ryan, M.P., Koyanagi, R.Y., Fiske, R.S., 1981. Modeling the three dimensional structure of macroscopic magma transport systems: application to Kilauea volcano, Hawaii. J. Geophys. Res. 86, 7111–7129.

Sarda, P., Graham, D., 1990. Mid-ocean ridge popping rocks: implications for degassing at ridge crests. Earth Planet. Sci. Lett. 97, 268–289.

Sisson, T.W., Layne, G.D., 1993. H_2O in basalt and basaltic andesite glass inclusions from four subduction-related volcanoes. Earth Planet. Sci. Lett. 117, 619–635.

Sparks, R.S.J., 2003. Dynamics of magma degassing. In: Oppenheimer, C., Pyle, D.M., Barclay, J. (Eds.), Volcanic Degassing. Geol. Soc. London Spec. Publ., vol. 213, pp. 5–22.

Sparks, R.S.J., Huppert, H.E., Turner, J.S., 1984. The fluid dynamics of evolving magma chambers. Philos. Trans. R. Soc. Lond., A 310, 511–534.

Sparks, R.S.J., Barclay, J., Jaupart, C., Mader, H.M., Phillips, J.C., 1994. Physical aspects of magma degassing I. Experimental and theoretical constraints on vesiculation. Mineral. Soc. Am., Rev. Mineral. 30, 413–445.

Stevenson, D.S., Blake, S., 1998. Modelling the dynamics and thermodynamics of volcanic degassing. Bull. Volcanol. 60, 307–317.

Stoiber, R.E., Williams, S.N., Huebert, B.J., 1986. Sulfur and halogen gases at Masaya Caldera Complex, Nicaragua: Total flux and variations with time. J. Geophys. Res. 91 (B12), 12,215–12,231.

Turcotte, D.L., Schubert, G., 1982. Geodynamics. Applications of Continuum Physics to Geological Problems. John Wiley & Sons, New York.

Vaggelli, G., Francalanci, L., Ruggieri, G., Testi, S., 2003. Persistent polybaric rests of calc-alkaline magmas at Stromboli volcano, Italy: pressure data from fluid inclusions in restitic quartzite nodules. Bull. Volcanol. 65, 385–404.

Vergniolle, S., Jaupart, C., 1990. Dynamics of degassing at Kilauea Volcano, Hawaii. J. Geophys. Res. 95, 2793–2809.

Wallace, P.G., 2001. Volcanic SO_2 emissions and the abundance and distribution of exsolved gas in magma bodies. J. Volcanol. Geotherm. Res. 108, 85–106.

Wallis, G.B., 1969. One-dimensional Two-phase Flow. McGraw-Hill Book Company.

Williams, H., McBirney, A.R., 1979. Volcanology. Freeman Cooper, San Francisco.

Woods, A.W., Cardoso, S.S.S., 1997. Triggering basaltic volcanic eruptions by bubble-melt separation. Nature 385, 518–520.

Available online at www.sciencedirect.com

ScienceDirect

Journal of Volcanology and Geothermal Research 162 (2007) 185 – 188

Journal of volcanology and geothermal research

www.elsevier.com/locate/jvolgeores

Addendum

A note on gas segregation in dykes and sills at high volumetric gas fractions

Thierry Menand *, Jeremy C. Phillips

Department of Earth Sciences, Centre for Environmental and Geophysical Flows, University of Bristol,
Wills Memorial Building, Queen's Road, Bristol BS8 1RJ, UK

Received 2 November 2006; received in revised form 16 February 2007; accepted 1 March 2007
Available online 14 March 2007

Abstract

The model of gas segregation in volcanic systems developed by Menand and Phillips [Menand, T., Phillips, J.C., 2007. Gas segregation in dykes and sills. J. Volcanol. Geotherm. Res. 159, 393–408] show that non-vertical elements of the plumbing systems, such as dykes and sills, act as strong gas segregators and can explain the persistent degassing displayed by many basaltic volcanoes as well as their associated eruptive characteristics. However, this model is based on laboratory experiments carried out at low volumetric gas fractions $<10\%$. We present additional laboratory experiments which show that the processes governing gas segregation at high volumetric gas fractions are identical to those occurring at low gas fractions, except that higher gas fractions lead to an increase of the viscosity of the bubbly fluid and thus increase the time scales associated with gas segregation. We show that the theory developed by Menand and Phillips [Menand, T., Phillips, J.C., 2007. Gas segregation in dykes and sills. J. Volcanol. Geotherm. Res. 159, 393–408], originally valid at low volumetric gas fractions, can be extended to high gas fractions, at least as high as 40% by volume.

Keywords: gas segregation; persistent volcanism; dykes; sills; Strombolian activity

1. Introduction

Menand and Phillips (2007) have recently developed a model of gas segregation in volcanic plumbing systems, which shows that non-vertical elements of the plumbing systems, such as dykes and sills, can act as strong gas segregators. The model suggests that very effective gas segregation occurs at low magma supply rates and induces episodic degassing of relatively gas-poor magmas, whereas higher magma supply rates lead to less effective gas segregation and thus to stronger explosions of gas-rich as well as gas-poor magmas. This model was successfully applied to Stromboli volcano, Italy, and suggests a critical magma supply rate of 0.1–1 $m^3 s^{-1}$ for the transition between Strombolian degassing and a more explosive regime in which bubbly magma supplied from depth is erupted before much gas segregation can take place (Menand and Phillips, 2007).

Menand and Phillips (2007) investigated gas segregation in the simple geometry of a vertical conduit connected to a horizontal magma body by means of analogue experiments with two interconnected glass tubes, with both ends of the vertical glass tube being connected to a peristaltic pump to form a recirculating flow loop. Degassing involving low volumetric gas fractions ($<10\%$) was simulated by electrolysis, producing micrometric bubbles in viscous mixtures of water and golden syrup. The presence

---

DOI of original article: 10.1016/j.jvolgeores.2006.08.003.

* Corresponding author.

E-mail address: T.Menand@bristol.ac.uk (T. Menand).

doi:10.1016/j.jvolgeores.2007.03.002

of exsolved bubbles induces a buoyancy-driven exchange flow between the conduit and the horizontal intrusion, whereby bubbly fluid flows from the conduit into the intrusion as a viscous gravity current. This exchange flow is slow enough that bubbles in the intrusion have time to rise, segregate from the fluid and accumulate as foam at its top, with corresponding accumulation of degassed fluid at its base. Ultimately a steady state is reached whereby influx of bubbly fluid into the intrusion is balanced by outward flux of lighter foam and denser degassed fluid back into the conduit. The length scale of the intrusion of bubbly fluid into the horizontal intrusion and the time scale of the gas segregation that occurs are both controlled by the rise of bubbles within the horizontal intrusion.

However, this model of gas segregation is derived from laboratory experiments that have been carried out at low volumetric gas fractions (typically less than 10% by volume). Consequently, this model of gas segregation might not be directly applicable to other volcanic systems involving higher volumetric gas fractions, as higher bubbly gas fractions might not necessarily lead to stronger exchange flow characterized by higher Reynolds number. Instead higher bubbly gas fractions could impede the strength of the exchange flow because (1) the difference in density between the bubbly fluid, now with a higher bubbly gas fraction, and the foam would decrease, and (2) a higher gas fraction would increase the viscosity of the intruding bubbly magma.

Consequently, additional laboratory analogue experiments were carried out in order to better understand whether and how gas segregation operates at high volumetric gas fractions and to assess the range of gas fractions over which the model of gas segregation described by Menand and Phillips (2007) is valid. In Section 2 we describe the technique used to generate volumetric gas fractions as high as 40 percent and present the result of the analogue experiments. In Section 3 we extend the mathematical model of Menand and Phillips (2007) to high gas fractions before concluding in Section 4.

2. Analogue experiments

2.1. Setup

The experiments reported in the present paper were carried out in the same apparatus as that described by Menand and Phillips (2007): a vertical dyke interconnected to a horizontal intrusion was simulated by two interconnected glass tubes 4 cm in diameter. The technique used to generate bubbles was different, however, to obtain higher volumetric gas fractions. We used the aeration technique described by Llewellin et al. (2002) whereby golden syrup was aerated with air using a Mondomix aerator. Pure golden syrup (density ρ_l= 14391±1 kg m^{-3}, measured by weighing a known volume) was used as the liquid phase in order to obtain the highest volumetric gas fraction. Using this method we could generate polydisperse bubble suspensions with volumetric gas fraction $c=0.35\pm0.05$. The bubble size distribution was measured using the technique described by Menand and Phillips (2007). Bubble diameters range from 2 to 500 μm with a mean diameter of 30±33 μm. We note, however, that the largest bubbles account for most of the gas volume: 50% of the total gas volume is contained in bubbles larger than 250 μm and bubbles larger than 125 μm represent 80% of the total gas volume. Once aerated, the bubbly mixture was poured into the tubes, and so the bubbles were initially evenly distributed throughout the conduit and the side arm. The mixture was then left to evolve without imposing any fluid movement.

2.2. Observations

The same fluid-flow processes were observed in these high gas fraction experiments as in the low gas fraction experiments reported by Menand and Phillips (2007). These are shown in Fig. 1, taken 4 days after the start of an experiment, to ensure that a steady-state had been fully established. Bubbles in the horizontal side arm are observed to rise and segregate from the fluid, accumulating as a foam at the top of the side arm, and creating a layer of degassed liquid at its base. A steady state is

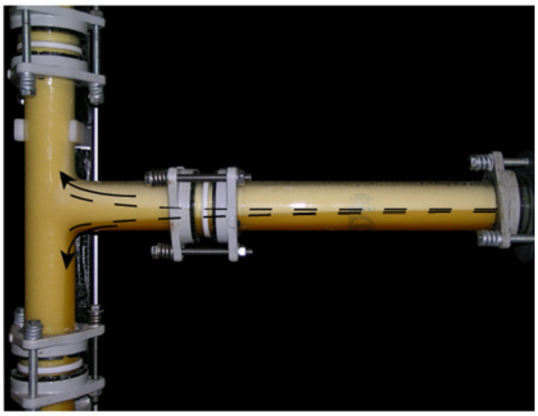

Fig. 1. Establishment of a steady-state exchange flow between the vertical tube and the side arm at high volumetric gas fraction. The liquid phase is pure golden syrup and the mixture contains 40% of gas in volume. Dashed curves show the approximate thickness of the upper white foam layer and the lower darker degassed liquid layer. Arrows show outward flow directions (the arrow indicating the inward flow of bubbly material from the conduit into the side arm is omitted for clarity).

reached whereby influx of bubbly fluid from the vertical conduit into the side arm is balanced by outward flux of lighter foam and denser degassed liquid.

3. Steady-state gas segregation

Experiments carried out at low gas fractions suggest that fluid movement in the vertical conduit does not have any influence on gas segregation in the side arm (Menand and Phillips, 2007). Further, we expect the static starting configuration of the experiments at high gas fractions not to affect the steady-state segregation and that segregation at high gas fractions to be controlled by the rise of bubbles in the side arm.

The rising velocity of a single bubble through a fluid of viscosity μ is given by the Stokes velocity $v_s=(\Delta\rho\, g\, d^2)/(12\ \mu)$, where d is the bubble diameter and $\Delta\rho$ is difference between the density of the fluid and that of the bubble gas. Here, individual bubbles rise through the ambient bubbly mixture, so the bulk density and the bulk viscosity, μ_b , of the bubbly mixture are the appropriate continuous phase properties for calculating the Stokes velocity. Neglecting the density of the gas relative to that of the fluid, ρ_l , we obtain $\Delta\rho=(1-c)\rho_l$ and so:

$$v_b=\frac{(1\text{-}c)\rho_l g d^2}{12\mu_b}. \tag{1}$$

The bubbly mixture in the high gas fraction experiments described here is polydisperse with bubble diameters ranging from 2 to 500 μm. However, we note that 50% of the total gas volume is accounted for by the largest bubbles, with diameters in the range 250–500 μm. We therefore expect these bubbles to rise the fastest and thus to be the bubble population that dominates gas segregation. Consequently, we have taken $d=375$ μm as the average bubble diameter that controls the bubble rise velocity v_b.

Establishing an expression for the viscosity of the bubbly mixture μ_b is more problematic. In principle, the mixture viscosity can be estimated from the viscosity of the fluid phase, μ_l , and the volumetric gas fraction, c. Several expressions for the dependence of effective viscosity on gas volume fraction exist, depending on the value of the volumetric gas fraction, and some of these are based on experimental measurements (Wallis, 1969; Llewellin and Manga, 2005). The mixture viscosity also depends on the tendency of bubbles to deform owing to viscous stresses induced by flow, relative to their tendency to remain spherical owing to interfacial stresses, and the rapidity of this response (Llewellin and Manga, 2005). For steady flows involving spherical bubbles, the commonly accepted relationship is $\mu_b=\mu_l/(1-c)$ (Llewellin and Manga, 2005). However, Llewellin and Manga (2005) describe this relation as a minimum viscosity model. They also derive a maximum viscosity model where the mixture viscosity $\mu_b=(1+9c)\mu_l$ based on the study of Llewellin et al. (2002), which used aerated golden syrup similar to our mixtures with volumetric gas fraction c in the range 0 to 0.5. As pointed out by Llewellin and Manga (2005), the true mixture viscosity will be somewhere between these two models. We also note that for higher volumetric gas contents, the behavior of the bubbly mixture becomes closer to that of a foam, and that for gas fractions as high as 70% by volume its viscosity is better approximated by the relationship (Jaupart and Vergniolle, 1989)

$$\mu_b=\mu_l(1\text{-}c)^{-5/2}. \tag{2}$$

In the range $c=0$ to $c=0.5$, Eq. (2) lies in between the minimum and maximum viscosity models introduced by Llewellin and Manga (2005) and so we assume here that the viscosity of our bubbly mixtures is adequately approximated by Eq. (2). Using this viscosity model, we obtain a bubble rising velocity

$$v_b=\frac{(1\text{-}c)^{7/2}\rho g d^2}{12\mu_l}. \tag{3}$$

We calculate the time needed for bubbles to rise and accumulate as a foam in the side arm by dividing the side arm diameter (the maximum distance bubbles can rise) by

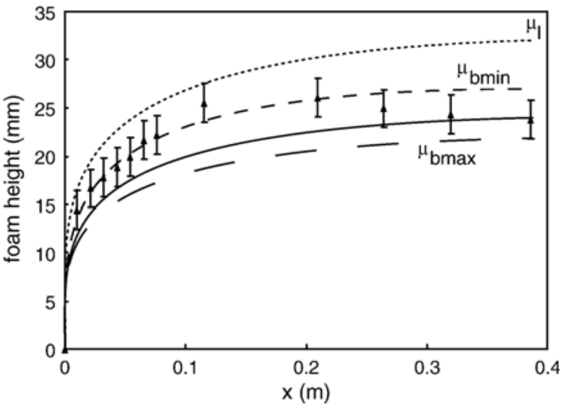

Fig. 2. Variation of the steady-state foam height along the side arm in a high gas fraction experiment. The solid line shows the prediction of the theoretical model for a foam volumetric gas fraction $\epsilon=0.8$ a bubbly volumetric gas fraction $c=0.35$ and the viscosity model (Eq. (2)). The dashed lines show the predictions for two other limiting viscosity models (see text): $\mu_{b\min}=\mu_l/(1-c)$ (short dashes) and $\mu_{b\max}=(1+9c)\mu_l$ (long dashes). The dotted line shows the foam height that would be predicted if the viscosity of the pure fluid μ_l was considered instead of that of the bulk mixture, as in the very low vesicularity case (Menand and Phillips, 2007).

the rising bubble velocity (Eq. (3)). For a volumetric gas fraction $c = 0.35$ and an average bubble diameter $d = 375$ μm, steady state in a side arm 4 cm in diameter is reached in 14 h as shown on Fig. 1 (using the smallest bubble velocity derived from the maximum viscosity model, steady state should be achieved in 20 h).

We tested the analysis derived for gas segregation at low gas fractions by Menand and Phillips (2007) by calculating the height of the foam that develops at the top of the side arm (using Eqs. (19−21) of Menand and Phillips, 2007). Fig. 2 compares the theoretical foam height with the experimental foam height, measured from the experiment shown in Fig. 1, and shows very good agreement between theory and data. We conclude that the theory developed by Menand and Phillips (2007), originally valid at low volumetric gas fractions, can be extended to high volumetric gas fractions, at least up to 40% by volume.

4. Conclusion

Our experiments show that the processes governing gas segregation at high volumetric gas fractions are identical to those occurring at low gas fractions, as described by Menand and Phillips (2007), except that higher gas fractions lead to an increase of the viscosity of the bubbly fluid and thus increase the time scales associated with gas segregation.

We have shown that this is the case for volumetric gas fractions up to 40% by volume. At higher volumetric gas fractions, however, bubbly fluid would behave like a foam. Whether the gas segregation processes described here would also operate in this case requires further investigation. Indeed, gas segregation might then become negligible because of the viscosity increase and smaller density difference between the bubbly mixture and any foam potentially built from gas segregation. However, such high gas fractions would also increase the propensity of the whole bubbly fluid to collapse (Jaupart and Vergniolle, 1989). This would lead to strongly explosive behavior as exemplified by Stromboli, Italy, or Kilauea, Hawaii.

Acknowledgment

We thank Alain Burgisser and an anonymous reviewer for their reviews and comments.

References

Jaupart, C., Vergniolle, S., 1989. The generation and collapse of a foam layer at the roof of a basaltic magma chamber. J. Fluid Mech. 203, 347–380.

Llewellin, E.W., Manga, M., 2005. Bubble suspension rheology and implications for conduit flow. J. Volcanol. Geotherm. Res. 143, 205–217.

Llewellin, E.W., Mader, H.M., Wilson, S.D.R., 2002. The rheology of a bubbly liquid. Proc. R. Soc. Lond. A 458, 987–1016.

Menand, T., Phillips, J.C., 2007. Gas segregation in dykes and sills. J. Volcanol. Geotherm. Res. 159, 393–408.

Wallis, G.B., 1969. One-dimensional Two-phase Flow. McGraw-Hill Book Company.

Earth and Planetary Science Letters 270 (2008) 25–40

Contents lists available at ScienceDirect

Earth and Planetary Science Letters

journal homepage: www.elsevier.com/locate/epsl

Magma ascent rates in explosive eruptions: Constraints from H_2O diffusion in melt inclusions

Madeleine C.S. Humphreys [a],*, Thierry Menand [b], Jon D. Blundy [b], Kevin Klimm [b]

[a] Department of Earth Sciences, University of Cambridge, Downing Street, Cambridge, CB2 3EQ, UK
[b] Department of Earth Sciences, University of Bristol, Queens Road, Bristol, BS8 1RJ

ARTICLE INFO

Article history:
Received 15 October 2007
Received in revised form 13 February 2008
Accepted 29 February 2008
Available online 12 March 2008

Editor: C.P. Jaupart

Keywords:
H_2O
diffusion
melt inclusions
Plinian
ascent rate
Mount St. Helens

ABSTRACT

The pre-fragmentation velocity of magma ascending during explosive volcanic eruptions remains difficult to quantify. Here we present a new technique for using syn-eruptive volatile diffusion in imperfectly trapped melt inclusions to obtain a direct estimate of such ascent velocities. H_2O diffusion profiles are obtained from back-scattered electron images of synthetic, partially hydrated glasses and tube-shaped melt inclusions. The greyscale intensity of glass in the images shows a good negative linear correlation with melt H_2O concentration. Greyscale intensity profiles, extracted using image-processing software, can therefore be calibrated against H_2O measured at discrete points by ion microprobe. An advantage of the technique is that concentration profiles can be determined in melt tubes that are too small to analyse directly, with a spatial resolution (≤ 1 μm) that is considerably better than that obtainable by ion microprobe or FTIR. A finite element model, which incorporates previously published estimates of concentration-dependent H_2O diffusivity, is used to fit the resulting continuous concentration profiles. We apply the technique to tube-shaped melt inclusions from the May 18th, 1980 Plinian eruption of Mount St Helens, Washington, USA. The model produces good fits to the data, indicating very rapid ascent times of between 102 and 166 s, which correspond to mean ascent velocities of 37-64 m/s, or mean decompression rates of 0.9-1.6 MPa/s. These are in agreement with previous estimates from petrological studies and numerical modelling.

1. Introduction

A major challenge in physical volcanology is to obtain direct, in situ measurements of ascent velocity during explosive volcanic eruptions. The ascent rate of magma controls the height and strength of the eruption column and thus determines the physical dispersal of tephra. Magma ascent velocity is also a key parameter in numerical conduit-flow models. Previous studies have attempted to estimate magma ascent velocity through petrological methods (Anderson, 1991; Castro et al., 2005; Toramaru, 2006; Liu et al., 2007) or numerical modelling (e.g. Papale et al., 1998; Proussevitch and Sahagian, 2005). Alternative methods use reconstruction of ballistics or the volumes of erupted magma to determine discharge rates, and thus infer ascent velocities (e.g. Wilson et al., 1980; Carey and Sigurdsson, 1985, 1989; Carey et al., 1990). Such reconstruction methods are rather indirect, while numerical models require *a priori* assumptions to be made about the magmatic system. In contrast, petrological methods permit direct, independent measurements of ascent velocity from erupted materials.

Melt inclusions in phenocrysts are now routinely used to measure the pre-eruptive volatile contents, and hence crystallisation pressures, of volatile-saturated magmas (e.g. Dunbar and Hervig, 1992; Blundy and Cashman, 2001; Wallace, 2005). Studies of melt inclusions have shown that dome-forming eruptions typically undergo H_2O-saturated, polybaric crystallisation (e.g. Sisson and Layne, 1993; Geschwind and Rutherford, 1995; Blundy and Cashman, 2001; Humphreys et al., 2008) while magmas may undergo almost no crystallisation during a Plinian eruption (e.g. Blundy and Cashman, 2005). Not all melt inclusions are perfectly trapped within the host phenocryst. Some are elongate tubes connected to the external melt (see Fig. 1, Blundy and Cashman, 2005), allowing them to exchange chemical components, including volatiles, with the matrix (Anderson, 1991; Humphreys et al., 2008). Others have ruptured and vesiculated during ascent. However, these imperfections can be exploited to obtain information about the timescale over which components have been exchanged by diffusion with the matrix, and thus offer insights into the degassing history of the magma. For example, Anderson (1991) used the variation of bubble volumes and H_2O concentrations in imperfectly trapped "hourglass" inclusions in quartz (similar features are also called melt tubes, melt pockets, re-entrant inclusions) to infer decompression rates during the eruption of the Bishop Tuff. Castro et al. (2005) measured mm-scale variations in H_2O across interbanded obsidian-pumice samples, using Fourier transform infra-red spectroscopy (FTIR), to obtain timescales of vesiculation. Liu et al. (2007) also used FTIR measurements of the quenched CO_2 and H_2O concentrations in quartz-hosted inclusions to estimate the timescale of volatile diffusion into the external melt, and thus the ascent time. However, their method is limited for melt inclusions because of size constraints - the diffusion profile is defined

---

* Corresponding author. Tel.: +44 1223 333433.
E-mail address: mcsh2@cam.ac.uk (M.C.S. Humphreys).

0012-821X/$ – see front matter © 2008 Elsevier B.V. All rights reserved.
doi:10.1016/j.epsl.2008.02.041

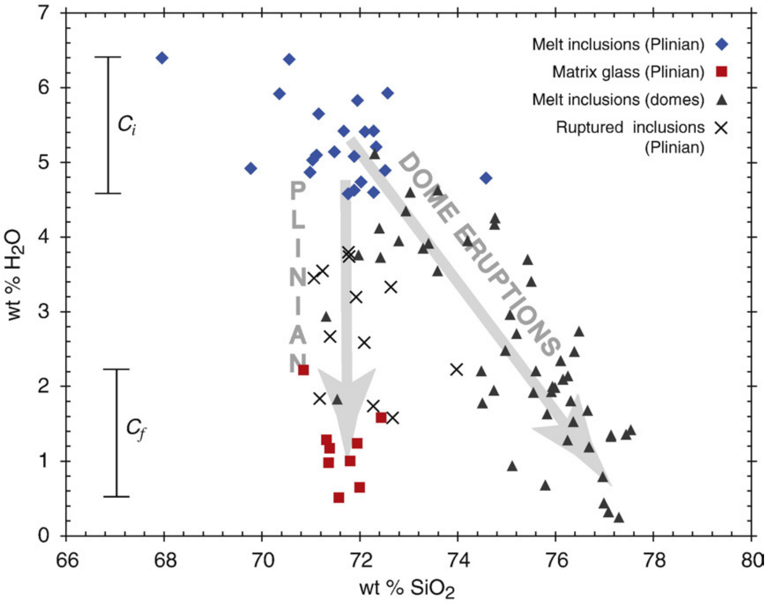

Fig. 1. Major-element composition of melt inclusions from Mount St. Helens, after Blundy andCashman (2005). Melt inclusions from dome-forming eruptions follow a trend of increasing SiO_2 with decreasing H_2O, consistent with H_2O-saturated decompression crystallisation. In contrast, melt inclusions from the 1980 Plinian eruption were trapped at high pressures prior to decompression crystallisation, and cluster at low SiO_2, with 4.6 – 6.4 wt.% H_2O. This forms the basis for our estimate of C_i. Plinian matrix glasses have low H_2O but are not any more evolved because there was no time for decompression crystallisation during the eruption. The H_2O contents of matrix glasses reflect the pressure of fragmentation and form the basis of our estimate of C_f. Ruptured melt inclusions from the Plinian eruption have leaked H_2O during ascent and therefore lie part way between the pristine inclusions and the matrix glasses.

only by 3-4 measured points. Here, we present a novel technique for measuring continuous H_2O diffusion profiles in plagioclase-hosted melt tubes. We anticipate that this technique will be suitable for any phenocryst phase where melt tubes are formed, and is therefore applicable to a wide range of magma compositions.

2. Approach

This study takes a two-pronged approach. First, we extracted a series of synthetic H_2O diffusion profiles from back-scattered electron (BSE) images of experimentally hydrated glass chips. This was done in order to determine the nature of the relationship between BSE intensity and H_2O concentration; to assess the ability of previously published, empirical H_2O diffusivity relationships to fit the data; and to test the accuracy of our technique. Second, we applied the technique to tube-shaped melt inclusions in pumices from Mount St. Helens volcano, USA. A series of concentration profiles was produced from SEM photographs of melt tubes, by calibrating the greyscale intensity of back-scattered electron images against H_2O measured by ion probe. The resolution of the images allowed us to measure the shape of the diffusion profiles accurately, even in tubes which would have been too small to analyse by ion probe or FTIR. Using finite-element modeling, we were able to fit the diffusion profiles and thus determine magma ascent velocities during the Plinian eruption of 1980.

3. Geological background

3.1. The May 18th, 1980 eruption of Mount St. Helens

In the weeks leading up to 18th May, 1980, there was an increase in seismic activity at Mount St. Helens, followed by phreatic explosions and deformation on the NE side of the volcano. This was interpreted as intrusion of a cryptodome into the summit region (Moore and Albee, 1981; Cashman, 1992). At 0832 PDT on 18th May, a magnitude 5 earthquake triggered failure of the north flank of the volcano, resulting in a debris avalanche of >2 km^3 (Voight et al., 1981), followed by a lateral blast which devastated an area of over 500 km^2 (Kieffer, 1981; Eichelberger and Hayes, 1982). The cloud that lifted off the blast/ surge region reached 25 km in height (Sparks et al., 1986). Nine hours of sustained Plinian activity followed, with an eruption column reaching a mean height of 16 km (Carey and Sigurdsson, 1985; Carey et al., 1990). Tephra were dispersed to the east-northeast, producing a tephra fall deposit of ~1.3 km^3 (Rose and Hoffman, 1982).

The eruption has been separated into four phases on the basis of variations in sedimentary features of the fall deposits (Criswell, 1987; Carey et al., 1990). Average magma discharge rates during the Plinian activity are thought to have fluctuated between $\sim 5.0 \times 10^6$ and 4.4×10^7 kg s^{-1}, based on eruption column heights (Carey et al., 1990). The highest average magma discharge rate, 4.4×10^7 kg s^{-1}, occurred during the period of co-ignimbrite plumes and pyroclastic flows which formed unit B3 (Criswell, 1987). Modelling of pyroclast dispersion suggests that exit velocities at the vent reached 200 m s^{-1} or more (Carey and Sigurdsson, 1985). The magma fragmentation depth (the point at which the magma moves from a continuous liquid phase to a continuous gas phase) was estimated at 500-600 m depth or 13-16 MPa (Carey and Sigurdsson, 1985).

3.2. Petrological information from melt inclusions

Melt inclusions are droplets of magmatic liquid that become trapped within growing crystals. Quenched to glass, they can provide information about pre-eruptive conditions within the magma. For example, incompatible trace-element concentrations can be used to determine the degree of crystallinity of the magma; dissolved volatile contents can be used to infer the depth of storage through known solubility relationships; and for plagioclase-hosted inclusions, the composition of the host and coexisting inclusion can be used to determine pre-eruptive magma temperatures (Blundy et al., 2006).

Table 1
Normalised, anhydrous compositions of average Mount St Helens matrix glass and average plagioclase-hosted melt inclusions, from Blundy and Cashman (2005)

	Avg MSH matrix glass (n=9)	±1σ	Avg MSH plag-hosted melt inclusion (n=29)	±1σ	AOQ (Nowak and Behrens, 1997)	Lipari obsidian (Nielsen and Sigurdsson, 1981)
SiO_2	71.68	0.81	71.94	1.12	76.14	75.27
TiO_2	0.36	0.04	0.34	0.1		0.08
Al_2O_3	14.79	0.33	14.76	0.85	13.53	12.93
FeO	2.39	0.30	2.1	0.4		1.59
MgO	0.56	0.06	0.58	0.12		0.00
CaO	2.40	0.18	2.22	0.47		0.73
Na_2O	5.84	0.37	5.94	0.5	4.65	4.13
K_2O	1.97	0.15	2.12	0.14	5.68	5.27
Total	100.0		100.0		100.0	100.0

'AOQ' is the composition used for the H_2O diffusivity experiments of Nowak and Behrens (1997). Lipari obsidian was used in our synthetic diffusion experiments, also normalised to anhydrous.

Detailed studies of melt inclusions from Mount St. Helens (Rutherford et al., 1985; Blundy and Cashman, 2001, 2005; Berlo et al., 2004; Blundy et al., 2006, in press;) have allowed the evolution of the magma and plumbing system at the volcano to be assessed. Our current understanding is briefly summarised here from Blundy et al. (in press) and Blundy and Cashman (2005). In samples of dome-rock, plagioclase-hosted melt inclusions are rhyodacite to rhyolite in composition, and define major-element trends that are oblique to those of the whole-rocks. The inclusions contain up to 6.7 wt.% H_2O, and H_2O concentrations decrease with increasing fractionation as defined by K_2O, SiO_2 and incompatible trace element concentrations. Matrix glasses plot at the low-H_2O end of this trend. These features are consistent with closed-system crystallisation of H_2O-saturated magma, in response to decompression and exsolution of H_2O.

Melt inclusions from the 1980 Plinian eruption follow a rather different chemical trend to that of subsequent dome-forming eruptions. Major element variation is very limited, and in particular SiO_2 and K_2O contents do not show a consistent increase with decreasing H_2O (Fig. 1; Blundy and Cashman, 2005). Matrix glasses have lost H_2O, but otherwise have very similar compositions to the melt inclusions (see Table 1; Rutherford et al., 1985; Blundy and Cashman, 2005). This is consistent with syn-eruptive degassing of H_2O, during which there was insufficient time for crystallisation to occur, thus preventing any change in SiO_2 or K_2O. The H_2O contents of unruptured melt inclusions thus represent C_i, the volatile concentration in the magma prior to ascent (4.6 – 6.4 wt.% H_2O; Fig. 1). Matrix glasses give C_f, the H_2O content after fragmentation and quenching (0.5 – 2.2 wt.% H_2O; Fig. 1). Because the magma at Mount St Helens is H_2O-saturated (Blundy and Cashman, 2005), we can use the solubility of H_2O in rhyolite (Newman and Lowenstern, 2002), combined with experimental data (Rutherford et al., 1985) to constrain the range of pressures at which the magma resided prior to the eruption (137 - 230 MPa), and at which fragmentation occurred (9 - 33 MPa). For this we assume negligible CO_2 concentration in the vapour, and a pre-eruptive temperature of 880 °C (Blundy et al., 2006).

3.3. Tube melt inclusions

The shape of plagioclase-hosted melt inclusions depends primarily on the mode of trapping. Inclusions trapped during simple crystal growth are typically euhedral (or "negative-crystal" shaped) whereas inclusions trapped in old, corroded cores of partially dissolved crystals are typically highly irregular (Humphreys et al., 2008). Tube-shaped inclusions may be common (Anderson, 1991; Thomas et al., 2003; Blundy and Cashman, 2005; Humphreys et al., 2008). These inclusions have not been completely sealed off from the surrounding matrix and may consequently exchange chemical components with the matrix as it evolves. During an explosive eruption there will only be time for diffusive exchange of components with very high diffusivities (e.g. H_2O and Li). In this study we use the diffusive exchange of H_2O along the melt tubes to determine the duration of ascent.

4. Experimental and analytical methods

4.1. Experimental methods

The experiments were designed to achieve partial hydration of the initially anhydrous rhyolite. Dehydration experiments were also attempted, but these consistently resulted in micro-vesicular products without simple diffusion profiles. Similar problems were reported by Zhang and Behrens (2000).

The experimental starting materials were glass cylinders, 2.9 mm in diameter and 2-4 mm in length, cored from a single block of Lipari obsidian, LIPRF (generously donated by D.K. Bailey), using a diamond-coring device. The obsidian glass (Table 1) was homogeneous and contained ~ 0.25 wt.% H_2O prior to hydration. In each experiment, a single glass cylinder (~40-100 mg) was loaded into a gold capsule 3 mm in diameter, together with 10-20 wt.% H_2O added by micro-syringe. A small amount (~1 mg) of finely ground powder of the same Lipari obsidian was also added to each capsule in an attempt to minimise dissolution of the glass cylinder during the experiment. The loaded capsule was frozen using wet tissues and liquid N_2 and arc-welded. Capsules were re-weighed after welding to ensure no H_2O loss.

Experiments were carried out at the University of Bristol, in hydrothermal cold-seal apparatus equipped with rapid-quench capability, described in more detail in Carroll and Blank (1997). The pressure vessel was first pressurised and then externally heated. The temperature of the vessel was controlled by a thermocouple inserted into a small hole, 5 mm from the sample. The final sample temperature was calibrated against the outer temperature, with an error of ±5 °C. Once the vessel was at temperature the sample was inserted into the hot spot by means of a magnetic ring and filler rod. Pressure was adjusted manually to minimise fluctuations during sample insertion, and throughout the run to within 10 MPa. All experiments were designed to be super-liquidus; conditions ranged from 150 to 200 MPa and 855-905 °C, with run durations of 20 to 80 min (Table 2). No allowance was made for the small amount of time (typically in the range tens of seconds) needed to heat the sample up to the run temperature. One run, LIPRF6, was first held at 150 MPa for 4 h to ensure full hydration, and then further pressurised to 200 MPa for 40 min; however the run product broke on mounting and no clear concentration gradient could be discerned on the BSE image.

Table 2
Run conditions for glass hydration experiments

Run	t_{exp} (min)	P (MPa)	T (°C)	Measured H_2O_i (wt.%)	Measured H_2O_f (wt.%)	t_{model} (min)	+	-	Modelled C_i	Modelled C_f	Eqm H_2O (NL 2002)
LIPRF - starting material				0.23±0.02							
LIPRF2	20	200	857	0.23	5.6	15.5	0.7	0.3	0.23	6.2	5.9
LIPRF3	80	200	859	0.19	5.0	102.7	5.7	5.6	0.5	5.5	5.9
LIPRF5	67	150	899	0.25	5.4	100	8.7	5.3	0.53	5.4	4.8
LIPRF7	20	150	901	0.21	4.8	22.3	4.6	1.6	0.2	5.2	4.8

Measured H_2O values are from SIMS. "Eqm H_2O" indicates H_2O predicted from solubility relationships (Newman and Lowenstern, 2002). Modelled C_i and C_f are the values used in fitting.

At the end of each experiment, the sample was quickly withdrawn into the water-cooled nut below the pressure vessel using the magnetic ring. The pressure in the line was reduced at the same time to ensure a near-isobaric quench. The fO_2 during the run was controlled by the material forming the pressure vessel (Nimonic 105) and is ~1 log unit above the Ni-NiO buffer (Fabbrizio et al., 2006). After quenching, samples were extracted and weighed to verify that no leakage had occurred during the run. The capsules were then pierced to check if excess vapour was present; this was true for all runs except LIPRF2, which did not appear to liberate H_2O on puncture. However, the weights of this capsule before and after the run agreed to within 0.2 mg, suggesting vapour saturation. Samples were extracted from their gold capsules, mounted longitudinally in resin and polished to a depth close to the centre line of each glass cylinder. This was relatively straightforward as each glass cylinder had changed little in diameter in the course of a run. All run products were entirely glassy, with no sign of quench crystals.

4.2. Identification of melt inclusions

Individual plagioclase phenocrysts were hand-picked from pumices in two splits of a single sample, KVC518B, erupted on 18th May 1980 at Mount St. Helens. Both splits are described in Blundy et al. (in press), and represent a microlite-free pumice from pyroclastic flow deposits of the Plinian eruption. The crystals were mounted in resin and polished to expose melt inclusions. Inclusions zoned in H_2O content were identified using a JEOL JSM-820 SEM at the University of Cambridge, or a Philips XL30CP SEM at the University of Edinburgh Ion Microprobe Facility. Back-scattered electron images were taken of each inclusion.

4.3. Analytical methods

4.3.1. Electron probe micro-analysis (EPMA)

Melt inclusions and experimental run products were analysed for major elements using a CAMECA SX-100 five-spectrometer electron microprobe at the University of Cambridge, using methods described in Humphreys et al. (2006). The experimental glass chips were found to be homogeneous in terms of major elements, indicating that no major-element diffusion had occurred during the experiment. Thus the only cause of variations in mean atomic number, and hence BSE intensity, is H_2O content.

4.3.2. Secondary ion mass spectrometry (SIMS)

Points selected for use in BSE image calibration (see later) were analysed for $^{1}H^{+}$, $^{7}Li^{+}$, $^{9}Be^{+}$, $^{11}B^{+}$, $^{19}F^{+}$, and $^{47}Ti^{+}$ using a CAMECA ims4f secondary ion mass spectrometer at the University of Edinburgh. SRM610 was used as a primary trace element calibration standard. A 10.75 kV, 2 nA, O^{-} primary beam was accelerated onto the sample with a net impact energy of 14.5 kV. Secondary ions were extracted at +4.5 eV using a 75 V offset and 40 eV energy window. A pre-sputter period of approximately 2 min, with a 20 μm rastered beam, was used to clean the surface. For quantitative analysis, the ~15 μm focused beam was finely rastered to approximately 5 μm to minimise charging of the sample. The beam was manually aimed onto the melt inclusion or experimental glass. H_2O contents of the glass were derived from measured H^{+}/Si^{+}, using a daily working curve of H^{+}/Si^{+} vs. H_2O from well-calibrated hydrous glass standards (Blundy and Cashman, 2005). The working curves gave a straight line with $R^2 > 0.98$ (usually $R^2 \geq 0.997$). Errors on H_2O concentrations are typically less than 5% relative.

5. BSE profiles and calibration

Back-scattered electron (BSE) images of each experimental glass chip or inclusion were taken at the University of Edinburgh Ion Microprobe Facility using a Philips XL30CP SEM. Typical image resolution is 1424 × 1064 pixels. Contrast in the BSE signal is observed because the diffusion of H_2O produces variations in mean atomic number in the sample. The open-source software package *ImageJ* (Rasband, 2007) was used to extract a profile of greyscale intensity along a specified path in the inclusion. The scale of the BSE image was used to measure the length of the profile. To convert the greyscale intensity profile into a profile of H_2O concentration, H_2O was measured by SIMS at several points along each profile. For each equivalent point (~15 μm in diameter) on the image, *ImageJ* was used to obtain three measurements of greyscale intensity (1 σ of greyscale intensity ~3%). The average of the three measurements was plotted against wt.% H_2O. These data were fitted using a linear least squares relationship, with R^2 usually ~ 0.96 or better. Neighbouring melt inclusions and matrix glass filaments were also used in the calibration, providing that they were included in the same SEM image as the tube, i.e. under identical conditions of contrast and brightness, and had the same major element composition. This allowed profiles to be measured even along narrow tubes which were too small to be analysed directly by ion probe. Since there is little difference between matrix glass and melt inclusion compositions (Fig. 1; Rutherford et al., 1985; Blundy and Cashman, 2005), the effect of any slight variations in major element composition (between melt inclusions) on the back-scatter intensity was negligible.

Each BSE image was calibrated independently, since the absolute value of greyscale intensity depends on the contrast and brightness conditions used, in addition to the absolute variation in atomic number, field of view, and noise (Newbury, 1975; Reed, 2005). In practice, the quality of the polished surface is also of major importance in producing a clear image. The signal to noise ratio is determined by the accelerating voltage, beam current and scanning rate, as well as factors like the specification of the back-scatter detector. The standard deviation of the measured greyscale intensity at any point (and the vertical scatter on the resulting concentration profile) gives a measure of the precision of the profile, which is limited by the resolution of the image. The concentration profiles presented here have low precision but relatively high accuracy.

6. Modelling – overview and assumptions

H_2O diffusivity is dependent on H_2O concentration in the glass as well as temperature and pressure (e.g. Shaw, 1972; Delaney and Karsten, 1981; Zhang et al., 1991; Jambon et al., 1992; Nowak and Behrens, 1997; Zhang and Behrens, 2000). We therefore used the generalised form of Fick's second law:

$$\frac{\partial C}{\partial t} = \frac{\partial}{\partial x}\left(D(C)\frac{\partial C}{\partial x}\right) \tag{1}$$

where *C* is the concentration (wt.%), *D* is diffusivity, *x* is distance and *t* is time. This cannot be solved analytically, and a 1-D finite element model was built using the commercially available finite element software COMSOL Multiphysics. The model calculates the evolution of H_2O concentration with time, in a semi-infinite system, as a function of distance. The following initial and boundary conditions were applied:

$$C = C_i, \quad x, \quad t = 0 \quad C = C_f, \quad x = 0, \quad t > 0 \tag{2}$$

and

$$\frac{\partial C}{\partial x} = 0, \quad x = L \tag{3}$$

where C_i is the initial (homogeneous) H_2O concentration, C_f is the final H_2O concentration (fixed at the rim) and *L* is equivalent to the maximum length of the profile. Best fits to the data were determined by a least-square algorithm, which focused on the regions of the concentration profiles showing the strongest changes in gradient (i.e.,

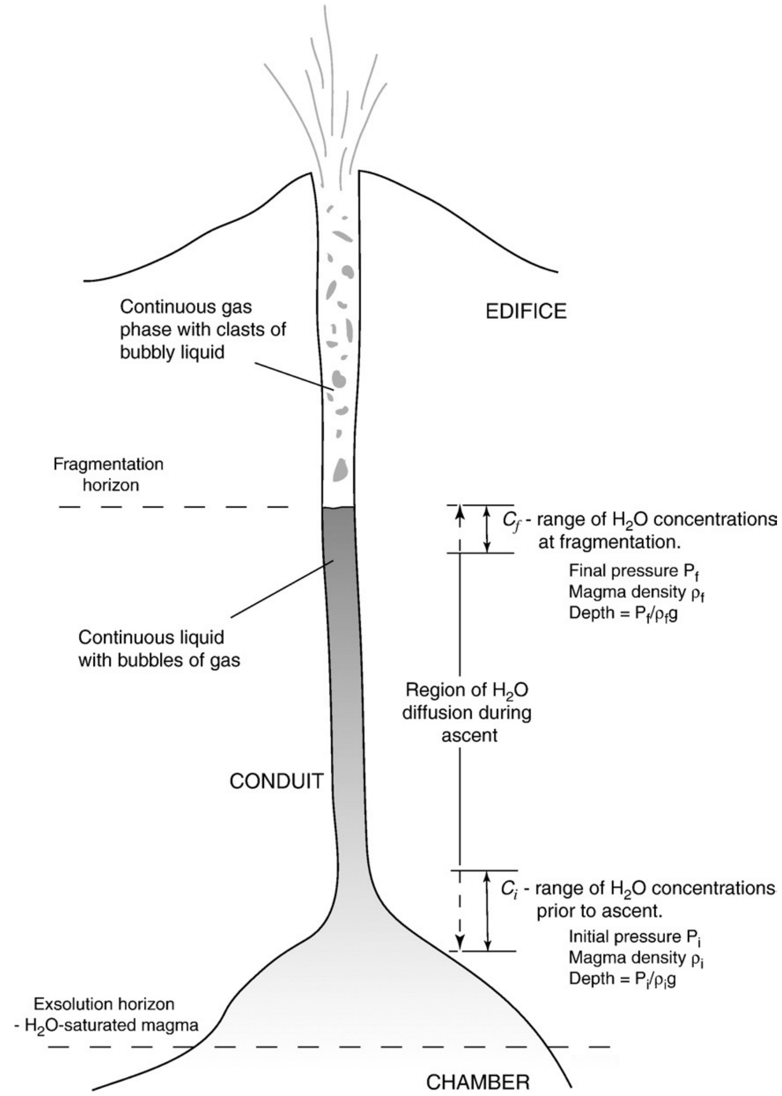

Fig. 2. Schematic figure outlining some of the processes occuring during Plinian eruptions and the assumptions made in the model. H_2O-saturated magma ascends from its storage region in the chamber, containing C_i wt.% dissolved H_2O and ~40% crystals. During ascent, H_2O vapour exsolves from the external melt into bubbles, H_2O diffuses along tube-shaped melt inclusions into the external melt. As ascent continues, the volume fraction of bubbles in the magma increases, until fragmentation occurs at ~75 vol.% bubbles and C_f wt.% H_2O. At fragmentation, the melt is quickly quenched to glass, preserving H_2O concentration profiles in partially diffused melt tubes.

excluding most of the non-hydrated part of the experimental sample profiles). We initially used H_2O diffusivity models from Nowak and Behrens (1997) and Zhang and Behrens (2000) to fit our synthetic concentration profiles. The model that gave the better fit to the data, and a better estimate of the time duration of the experiment, was then used to fit the H_2O concentration profiles measured in the melt inclusions from Mount St. Helens.

The best fits provided the best estimates of the time taken to produce the measured concentration profiles, for given values of C_i and C_f. The uncertainties on these time estimates were determined using a moving, variable-length, block bootstrap technique as described by Efron and Tibshirani (1993). Other bootstrapping techniques usually assume that all data points are independent. However, because D_{H_2O} depends on H_2O concentration, adjacent data points along the concentration profiles are dependent over a length-scale which depends on the H_2O concentration at that point. For every data point we therefore used a block length l, such that $l=(D_{H_2O}\Delta t)^{1/2}$, where D_{H_2O} is the H_2O diffusivity at that data point, and Δt is the timestep between two successive theoretical concentration profiles (typically 10 s). With this technique, data more than a block length apart are assumed to be nearly independent (Efron and Tibshirani, 1993). This procedure gives a 99% confidence interval for each time estimate.

6.1. Experimental diffusion profiles

For the experimental profiles, we assume instantaneous hydration of a finite space, corresponding in size to the radius of the glass cylinders. Diffusion of H_2O is assumed to occur radially within the glass cylinders, and perpendicular to their length. In practice this means that we can model diffusion in the cylinders as a 1-D process, since the diffusion profiles were measured sub-parallel to the radius of the cylinders. In cases where the polished surface did not coincide exactly with the centre-line of the cylinder, measured profile lengths were normalised to radial distance from the centre of the cylinder. The initial H_2O value (C_i) was derived from the measured H_2O

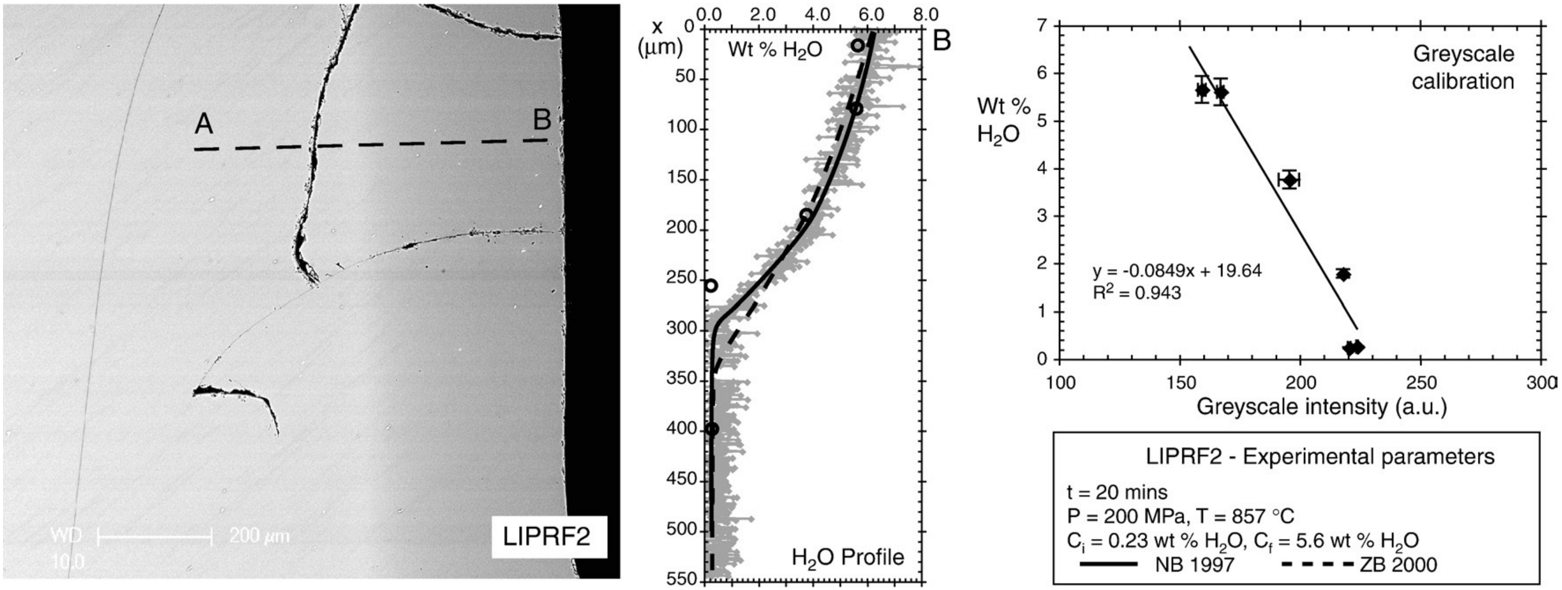

Fig. 3. Experimental run profile LIPRF2. *Left*: BSE image showing the region of the chip used in the profile (solid line). *Centre*: H_2O profile extracted from the BSE image (grey diamonds) with points measured by SIMS (spots) for comparison. *X* (μm) is measured from the BSE image and normalised to radial distance in the glass cylinder. Model fits use the H_2O diffusivity of Nowak and Behrens (1997; solid line) with that of Zhang and Behrens (2000; dashed line) for comparison. *Right*: Calibration of wt.% H_2O (from SIMS measurements) against greyscale intensity from the BSE image, used to construct the profile.

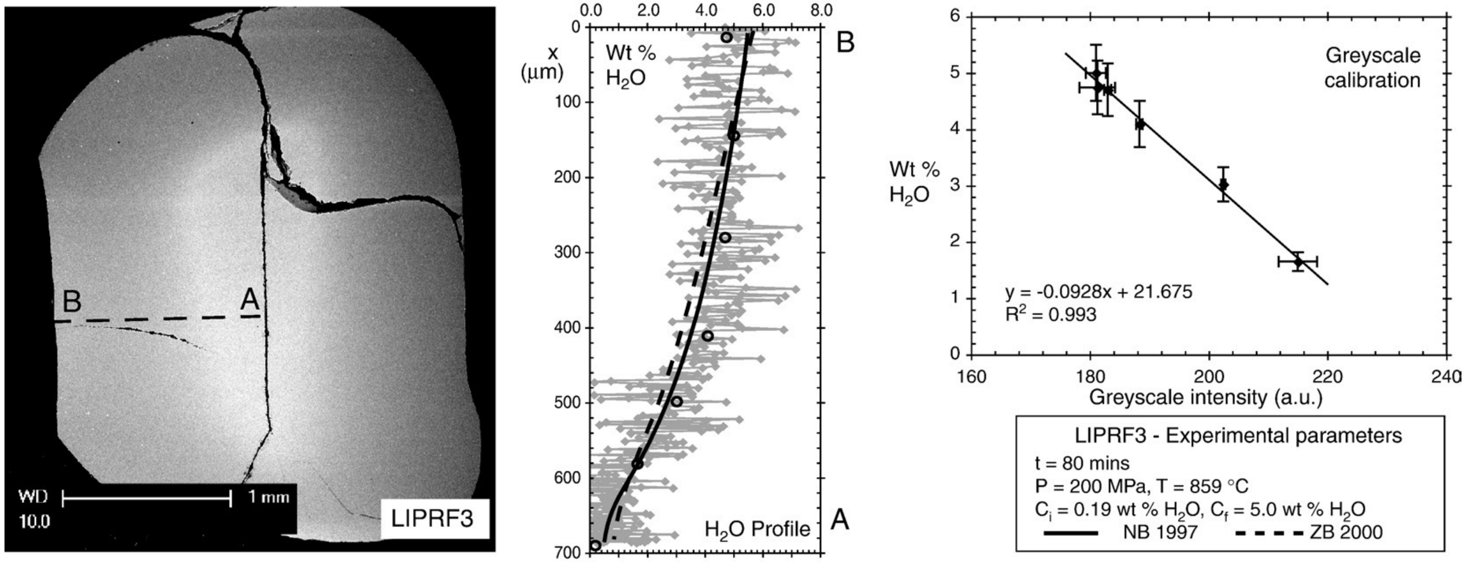

Fig. 4. Experimental run profile LIPRF3. *Left*: BSE image showing the region of the chip used in the profile (solid line). *Centre*: H_2O profile extracted from the BSE image (grey diamonds) with points measured by SIMS (spots) for comparison. *X* (μm) is measured from the BSE image and normalised to radial distance in the glass cylinder. Model fits use the H_2O diffusivity of Nowak and Behrens (1997; solid line) with that of Zhang and Behrens (2000; dashed line) for comparison. *Right*: Calibration of wt.% H_2O (from SIMS measurements) against greyscale intensity from the BSE image, used to construct the profile.

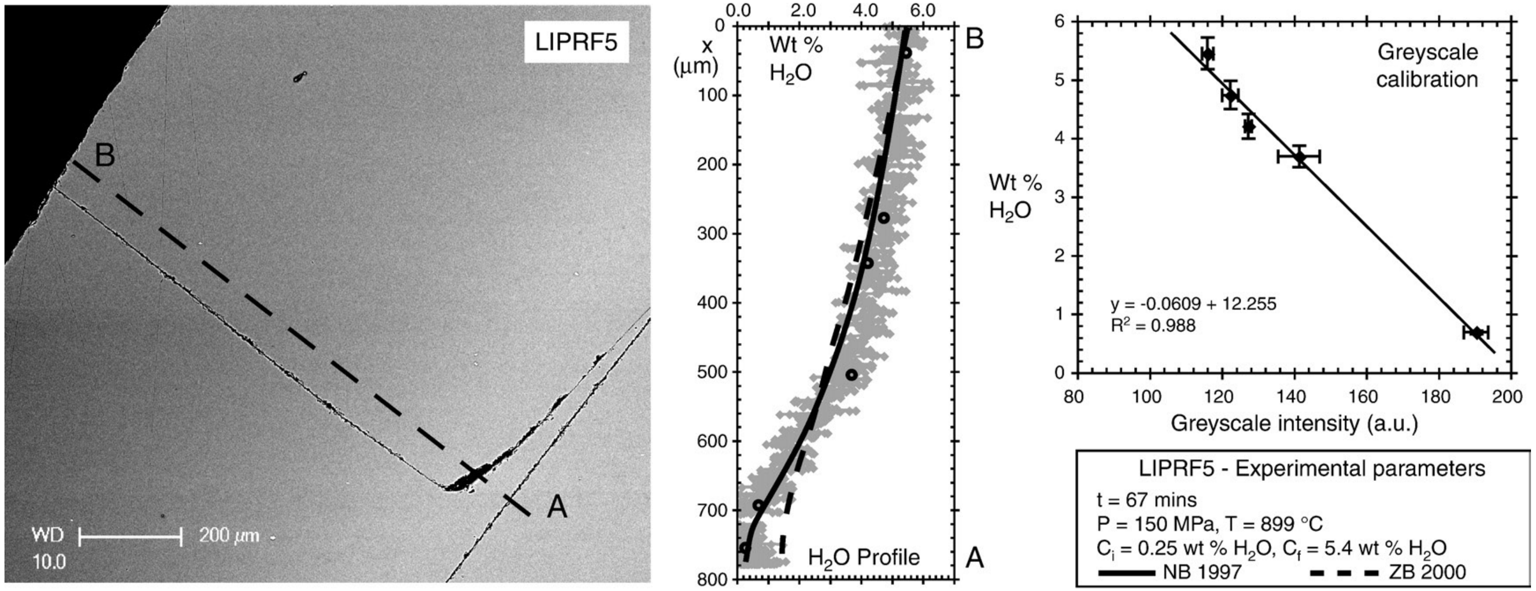

Fig. 5. Experimental run profile LIPRF5. *Left*: BSE image showing the region of the chip used in the profile (solid line). *Centre*: H_2O profile extracted from the BSE image (grey diamonds) with points measured by SIMS (spots) for comparison. *X* (μm) is measured from the BSE image and normalised to radial distance in the glass cylinder. Model fits use the H_2O diffusivity of Nowak and Behrens (1997; solid line) with that of Zhang and Behrens (2000; dashed line) for comparison. *Right*: Calibration of wt.% H_2O (from SIMS measurements) against greyscale intensity from the BSE image, used to construct the profile.

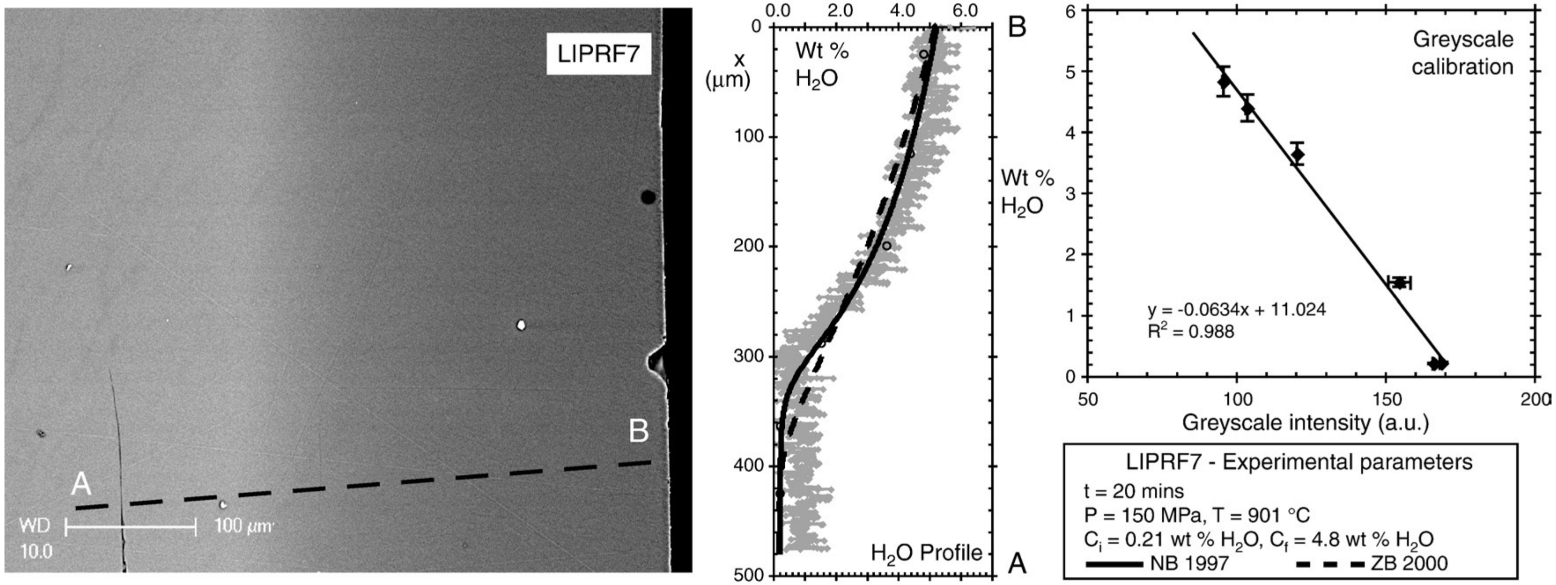

Fig. 6. Experimental run profile LIPRF7. *Left*: BSE image showing the region of the chip used in the profile (solid line). *Centre*: H_2O profile extracted from the BSE image (grey diamonds) with points measured by SIMS (spots) for comparison. *X* (μm) is measured from the BSE image and normalised to radial distance in the glass cylinder. Model fits use the H_2O diffusivity of Nowak and Behrens (1997; solid line) with that of Zhang and Behrens(2000; dashed line) for comparison. *Right*: Calibration of wt.% H_2O (from SIMS measurements) against greyscale intensity from the BSE image, used to construct the profile.

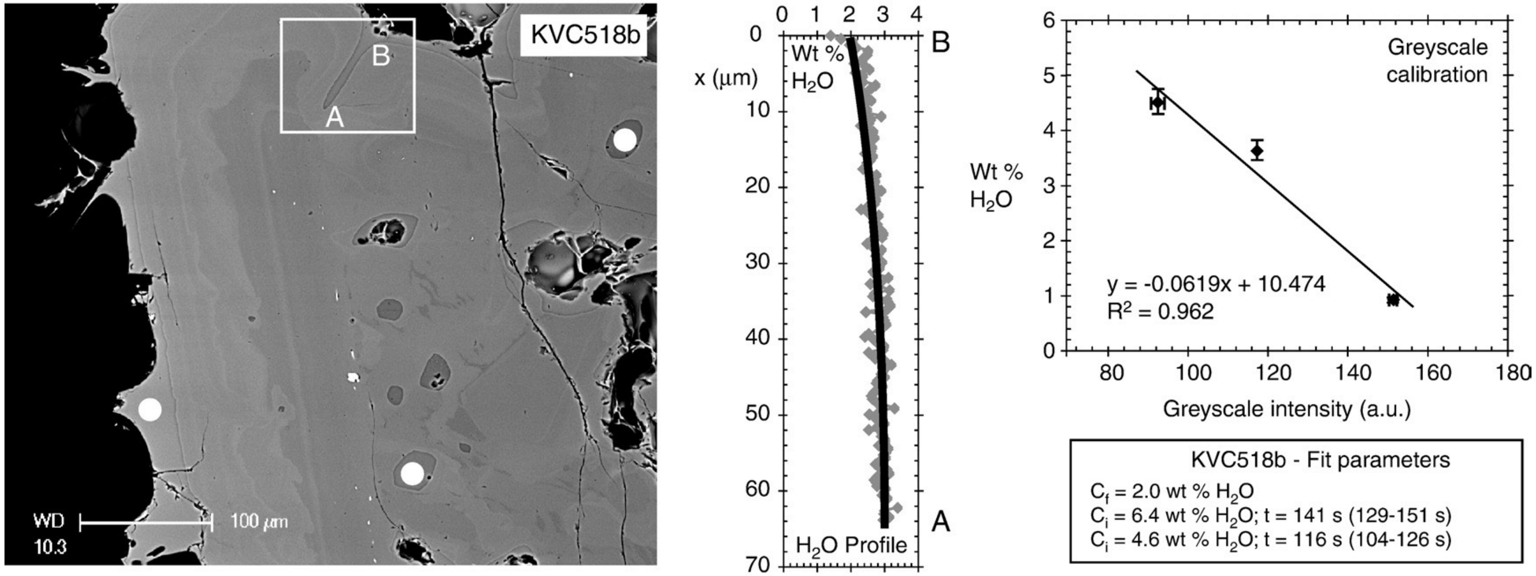

Fig. 7. H_2O diffusion profile for inclusion KVC518b. *Left*: BSE image showing strongly zoned plagioclase crystal, the melt tube (highlighted by white box) and other inclusions and matrix glass filaments used in the calibration. Spots mark the positions of SIMS analyses. The melt tube was too small to analyse directly. *Centre*: H_2O diffusion profile constructed from BSE image. Model fits use the H_2O diffusivity of Nowak and Behrens (1997). Right: Calibration of wt.% H_2O (from SIMS measurements) against greyscale intensity from the BSE image, used to construct the profile.

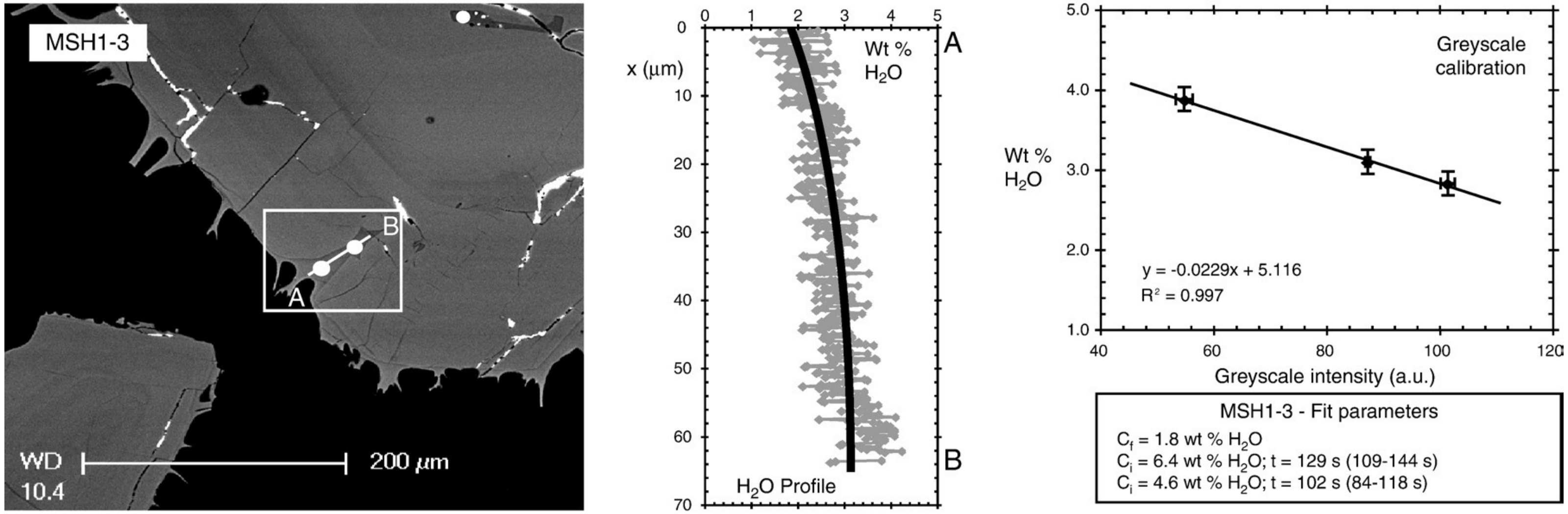

Fig. 8. H_2O diffusion profile for inclusion MSH1-3. *Left*: BSE image showing strongly zoned plagioclase crystal, the melt tube (highlighted by white box) and other inclusions used in the calibration. Spots mark positions of SIMS analyses. *Centre*: H_2O diffusion profile constructed from BSE image. Model fits use the H_2O diffusivity of Nowak and Behrens (1997). Break in the profile at $x \sim 65$ µm is where the profile crosses a crack in the glass (see text). Right: Calibration of wt.% H_2O (from SIMS measurements) against greyscale intensity from the BSE image, used to construct the profile.

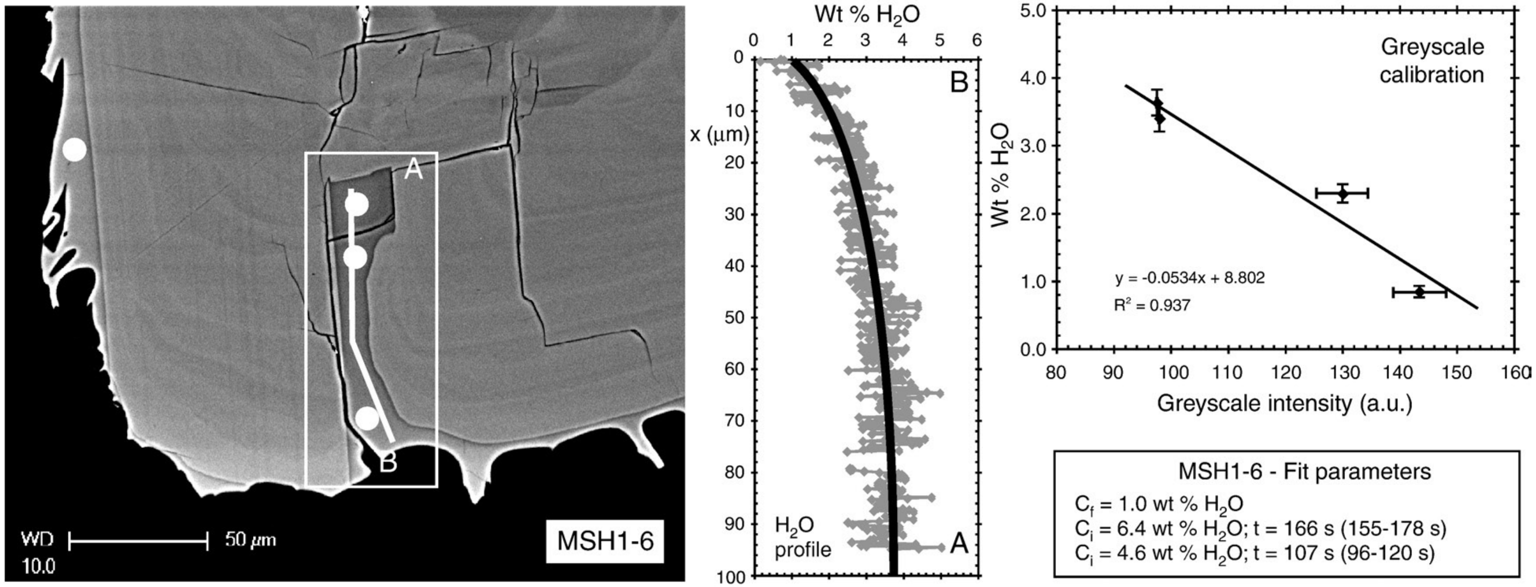

Fig. 9. H_2O diffusion profile for inclusion MSH1-6. *Left*: BSE image showing strongly zoned plagioclase crystal, the melt tube (highlighted by white box) and other inclusions and matrix glass filaments used in the calibration. Spots mark positions of SIMS analyses. *Centre*: H_2O diffusion profile constructed from BSE image. Profile has a slight dog-leg at approximately 55 μm. Model fits use the H_2O diffusivity of Nowak and Behrens (1997). Break in the profile at $x \sim 80$ μm is where the profile crosses a crack in the glass (see text). Right: Calibration of wt.% H_2O (from SIMS measurements) against greyscale intensity from the BSE image, used to construct the profile.

concentration in the undiffused core of the cylinder (0.20-0.25 wt.% H_2O). Boundary H_2O concentrations (C_f) were derived from the known P, T conditions of each experiment, and the H_2O concentration at the rim of the cylinder (Table 2).

6.2. Melt inclusion diffusion profiles

We assume that the melt inclusions can be approximated as cylindrical tubes whose lengths are much larger than their radii, so that diffusion occurs mainly along the length of the inclusion. This is consistent with the geometry of melt tubes observed in transmitted light on other similar samples. We also assume that diffusion perpendicular to the tube axis is negligible; this is reasonable because the diffusivity of H_2O within plagioclase is low compared with the melt. The model assumes that the outer end of each tube undergoes instantaneous dehydration, with 1-D diffusion of H_2O occurring along the melt tube towards its open end, in the time taken to ascend to the fragmentation horizon and quench (Fig. 2). The initial H_2O of the magma is constrained by petrological information to be in the range 4.6 - 6.4 wt.% H_2O (see section 2.3; Fig. 1), and we assume that this is equivalent to the initial concentration in the inclusions (C_i). This cannot be constrained further because none of the tubes is sufficiently long that the initial concentration is preserved in the diffusion profile. Consequently, the diffusion times produced by the model are not unique (see later). The concentration of H_2O remaining at fragmentation (C_f) is measured directly from the concentration profile and is defined as the concentration at the open end of the tube, close to vesicle walls. These values are consistent with petrological observations that matrix glasses contain 0.5 - 2.2 wt.% H_2O (see Fig. 1). The final pressure used in the model was the pressure at fragmentation, calculated from the C_f of the H_2O-saturated melt using Newman and Lowenstern (2002). We assume a pre-eruptive temperature of 880 °C, consistent with recent geothermometry (Blundy et al., 2006), and ignore latent heat effects. We assume that the magma undergoes closed-system, isothermal degassing during ascent in the conduit, with equilibrium maintained between melt and vapour.

7. Results

7.1. Experimental diffusion profiles

BSE images of the synthetic glass chips show clear concentration gradients parallel to the walls of the chips, manifest as changes in greyscale intensity (Figs. 3–6). This is consistent with diffusion of H_2O inward from the edge of the cylinder. Profiles LIPRF2 and LIPRF5 run across cracks in the glass chip, which are black in the greyscale image and translate to anomalously high H_2O concentrations. These anomalous points have been removed and are apparent as small gaps in the profiles. Bright rims are probably due either to topographic or compositional edge effects (Newbury, 1975). Excellent linear negative correlations of greyscale intensity and H_2O concentration were obtained for each chip (Figs. 3–6). Figs. 3–6 show the synthetic diffusion profiles with fits from Nowak and Behrens (1997) and Zhang and Behrens (2000). The best fits to the synthetic profiles were obtained using the expression of Nowak and Behrens (1997):

$$\begin{aligned}\log D_{H_2O} = &\left(-4.81 - 0.045.C_{H_2O} + 0.027.C_{H_2O}^2\right)\\ &-\left(3378 - 483.C_{H_2O} + 46.9.C_{H_2O}^2 + 47.5\right)/T\end{aligned} \tag{4}$$

where D_{H2O} is in $cm^2\ s^{-1}$, P is in kbar and T is in K. The modelled diffusion times are within a factor of 1.5 of the experimental run times (Table 2). We consider this to be reasonable given that the diffusivity model was calibrated for haplogranite melts (Nowak and Behrens, 1997; Table 1), and that the exact run duration is not precisely known because of the finite time taken for heating the sample after insertion into the bomb, and for quenching. The formula of Zhang and Behrens (2000) did not give comparable fits to the data (Figs. 3–6), in particular to the strong curvature of the concentration profiles. We therefore used Eq. (4) to model diffusion in the melt inclusions.

7.2. Melt inclusion diffusion profiles

The melt inclusions also show clear concentration gradients in BSE images. H_2O concentration again correlates well with greyscale intensity, giving robust H_2O diffusion profiles, although with a relatively high degree of scatter (Figs. 7–9). The scatter is derived from noise in the BSE image, and could be reduced by capturing higher resolution images. One profile (MSH1-3) shows an excursion to higher H_2O near the interior of the profile. This is an artefact derived from the BSE image, and could represent either topography from the walls of the inclusion, or interference from the crack that runs across it.

Values of C_f range from 1.0±0.6 to 2.0±0.5 wt.% H_2O. The maximum H_2O concentration observed in each inclusion ranges from 2.9 to 3.6± 0.5 wt.% H_2O, although the real initial H_2O concentration, C_i, is constrained by petrology to be 4.6 - 6.4 wt.% H_2O (see earlier). Diffusion was therefore sufficiently prolonged that $C(x=0)$ dropped below C_i. This means that the fits provided by the model are not unique: for a given value of C_f, different C_i can fit the data equally well, and the calculated diffusion times will vary with C_i. For this reason, we performed calculations using the extreme likely values of C_i, 4.6 and 6.4 wt.% H_2O, in order to give lower and upper bounds, respectively, on time.

Table 3
Results of diffusion modelling of melt tubes

A. Ascent times and decompression rates, C_i=4.6 wt.%

Inclusion	C_f (wt.%)	P_f (MPa)	Final depth (m)	C_i (1) (wt.%)	P_i (1) (MPa)	Initial depth (m)	ΔP (MPa)	Δdepth (m)	t (s)	+	-	Mean decomp. rate (MPa/s)	Mean ascent velocity (m/s)	+	-
KV518b-1	2.0	33	1328	4.6	137	5590	104	4262	116	10	12	0.9	37	4	3
MSH1-3	1.8	27	1101	4.6	137	5590	110	4489	102	16	18	1.1	44	9	6
MSH1-6	1.0	9	389	4.6	137	5590	128	5201	107	13	11	1.2	49	6	5

B. Ascent times and decompression rates, C_i=6.4 wt.%

Inclusion	C_f (wt.%)	P_f (MPa)	Final depth (m)	C_i (2) (wt.%)	P_i (2) (MPa)	Initial depth (m)	ΔP (MPa)	Δdepth (m)	t (s)	+	-	Mean decomp. rate (MPa/s)	Mean ascent velocity (m/s)	+	-
KV518b-1	2.0	33	1322	6.4	230	9380	197	8058	141	10	13	1.4	57	6	4
MSH1-3	1.8	27	1099	6.4	230	9380	203	8281	129	15	20	1.6	64	12	7
MSH1-6	1.0	9	400	6.4	230	9380	221	8980	166	12	11	1.3	54	4	4

Diffusion times are presented assuming variation of C_i between 4.6 wt.% (a) and 6.4 wt.% (b). Calculated depths use a density model which includes the effects of gas exsolution and 40% crystals. Bubble-free magma density is 2500 kg m^{-3}. Pressures are calculated from H_2O solubility at 880 °C, assuming negligible CO_2 (Newman and Lowenstern, 2002).

The model gives good fits to the data (Figs. 7–9), with C_f evaluated by eye. The model times range from 102 to 166 s, depending on the value of C_i used (Table 3). This is equivalent to decompression rates of 1.2 - 1.6 MPa/s. Because the magma is volatile-saturated (Blundy and Cashman, 2001, 2005), variations in C_i also relate to variations in pressure, and hence the distance ascended. For example, the calculations using 4.6 wt.% H_2O involve shorter times, but also shorter decompression paths, compared with those using 6.4 wt.% H_2O. The use of different C_i therefore does not strongly alter the ascent rate. Errors in fitting are estimated by evaluating the 99% confidence interval of the least square best fit, using the moving block bootstrap technique (section 6).

To convert pressure to depth, we use a magma density model (Wilson et al., 1980; Carey and Sigurdsson, 1985) which incorporates the effects of bubble exsolution and 40% pre-existing phenocrysts in a column of magma (Rutherford et al., 1985; Blundy and Cashman, 2005):

$$\rho = \left[\left(\frac{1-n}{\rho_m}\right) + \left(\frac{nRT}{P}\right)\right]^{-1} \tag{5}$$

where ρ_m is the bubble-free magma density (~2500 kg m^{-3}), n is the mass fraction of exsolved volatiles, R is the gas constant and P is the pressure. The ascent velocity (v) is then determined by:

$$v = \frac{1}{t}\left(\frac{P_i}{\rho_i g} - \frac{P_f}{\rho_f g}\right) \tag{6}$$

where g is the acceleration due to gravity (9.81 m s^{-2}), and t is the diffusion time. Density effects due to adiabatic expansion are neglected. Ascent rates calculated in this way range from 37 to 64 m s^{-1}, taking into account the possible variation in C_i (Table 3).

8. Discussion

8.1. Magma ascent rate, magma supply, and fragmentation depth

In our model, the concentration (C_f) of H_2O at the exit of the tube is inferred to be that in equilibrium with the external melt at the point of fragmentation, i.e. when diffusion effectively stopped (see below). Our measured C_f are in the range 1.0 - 2.0±0.5 wt.% H_2O, equivalent to fragmentation pressures of 9 to 33 MPa, or depths of approximately 400 - 1300 m. This agrees well with previous estimates of fragmentation pressure in Plinian eruptions: 40 MPa for the Bishop Tuff (Anderson, 1991), 15-20 MPa for a rhyolite with 4.5-6 wt.% H_2O (Papale et al., 1998) and for Mount St. Helens, 16 MPa (Carey and Sigurdsson, 1985). A review of conduit flow models gave fragmentation pressures of 12-28 MPa for H_2O-rich rhyolite at 850 °C (Sahagian, 2005). The calculated average magma ascent rate is 37 - 64 m s^{-1}, equivalent to a decompression rate of 0.9 - 1.6 MPa s^{-1}. This is considerably greater than ascent rates estimated using reconstructed eruption dynamics (~0.6 - 1 ms^{-1}, Scandone and Malone, 1985; Eichelberger, 1995), which was based on the nearly 4 h time interval between the initial landslide and the onset of the climactic phase of the eruption (Scandone and Malone, 1985; Criswell, 1987). This suggests that magma from the deep chamber was being erupted before the onset of the climactic phase (Criswell, 1987; Papale and Dobran, 1994). Our ascent rate is much less than the very high rate estimated from textural characteristics (140 MPa s^{-1}, Toramaru, 2006), although this value may reflect bubble nucleation during the passage of a shock wave (Toramaru, 2006). Our method agrees well with values calculated from other petrological methods and from numerical models. Anderson (1991) obtained decompression times of ~2 min by modelling rates of melt loss from hourglass inclusions in quartz from the Bishop Tuff. This is equivalent to ascent rates of 40 ms^{-1}, using an inferred fragmentation pressure of 40 MPa and ascent from 180 MPa (Anderson, 1991). From numerical models, Papale et al. (1998) obtained comparable magma velocities of approximately 15-20 ms^{-1} up to the point of fragmentation, for a rhyolite containing 6 wt.% H_2O.

Our model provides a robust method for measuring magma ascent rates in explosive volcanic eruptions. However, the calculated values represent the *mean* speed of the magma in the conduit. Ascent speeds increase sharply close to fragmentation (Papale et al., 1998), so the calculated values may slightly overestimate the magma velocity along the majority of the conduit length.

The radius of the magma conduit at Mount St. Helens is estimated to be ~25 - 40 m (Carey and Sigurdsson, 1985; Scandone and Malone, 1985; Pallister et al., 1992) or 17-33 m (Papale and Dobran, 1994). For a cylindrical conduit of radius 25 m, our calculated ascent velocity of 37 - 64 m s^{-1} indicates a magma supply rate of 7.3 - 12.6×10^4 m^3 s^{-1}. Assuming a magma density of 2500 kg m^{-3}, this equates to 1.8 – 3.1×10^8 kg s^{-1}. This is significantly greater than the values calculated by Scandone and Malone (1985) and Carey and Sigurdsson (1985) on the basis of tephra volumes (0.14×10^8 and 0.19×10^8 kg s^{-1} respectively). Fluctuations in column height indicate magma discharge rates up to 0.44×10^8 kg s^{-1} during eruption of co-ignimbrite plumes (Carey et al., 1990), while numerical modelling for crystal-free rhyolite with 4.5 - 6 wt.% H_2O predicts mass flow rates of 3 - 4×10^8 kg s^{-1} (Papale et al., 1998). Our estimate therefore seems high compared with field-based estimates, although it is consistent with the results of numerical modelling. This could be because (i) we use *mean* ascent speed to calculate magma supply rate, (ii) distal tephra volumes may be underestimated (Pyle, 1989) or (iii) our samples come from a period in the eruption which experienced particularly high discharge rates.

At decompression rates of >0.25 MPa s^{-1}, equilibrium cannot be maintained between vapour and melt (Gardner et al., 1999). Degassing is retarded, resulting in supersaturation of the melt, manifest as melt H_2O contents greater than the equilibrium concentration. For rhyolite ascending at ~ 1 ms^{-1}, the maximum supersaturation is reached some way below the surface, and H_2O levels fall back towards equilibrium values (Proussevitch and Sahagian, 2005). However, for ascent rates of 10 ms^{-1} or greater, the maximum supersaturation will occur at very shallow depths (Larsen and Gardner, 2004). This means that our calculations will tend to overestimate ascent speed.

8.2. Thermal variations during ascent

A key simplification in our model is the assumption of isothermal conditions up to the point of fragmentation, followed by instantaneous quenching. Estimated cooling rates in a Plinian eruption column are ~60-100 °C per second (Kaminski and Jaupart, 1997) due to entrainment and turbulent mixing of cold air from outside the column. An assumption of rapid quenching therefore seems reasonable, although cooling rates may differ between clasts of different diameters, or clasts which take differing trajectories through the column (Thomas and Sparks, 1992). However, magma-gas mixtures may undergo cooling prior to fragmentation during isentropic ascent, which is most likely to occur when velocity and gas expansion are high (Mastin and Ghiorso, 2001). For rhyolite magma initially at 200 MPa and 900 °C, modelling suggests that the temperature can drop to ~850 °C at 30 MPa, and to ~800 °C at 10 MPa (Mastin and Ghiorso, 2001). Thus the majority of cooling occurs during the final stages of ascent towards fragmentation. This adiabatic cooling would reduce H_2O diffusivity by about 25% at 850 °C, or about 40% at 800 °C. Significant undercooling during ascent would cause our model to underestimate the true diffusion time, and hence overestimate the ascent speed.

8.2.1. Diffusion blocking temperature

The H_2O concentration profiles in the melt tubes are effectively “frozen in” once D_{H_2O} has dropped below a critical temperature, at which diffusion becomes ineffective. At fragmentation, the melt still contains 1-2 wt.% H_2O. Using Eq. (4), D_{H_2O} drops to <0.1 μm^2 s^{-1} at ~ 400 °C (for 1 wt.% H_2O) or ~350 °C (for 2 wt.% H_2O). At cooling rates of 60-100 °C, this would take only 4-8 s. This suggests that little diffusive modification of the profiles occurred after fragmentation, and that the measured profiles accurately reflect concentration gradients at the point of fragmentation.

8.3. Gradual decompression

The 1980 eruption of Mount St Helens was triggered by a large landslide, which is estimated to have created a pressure drop of 12-20 MPa inside the conduit (Kieffer, 1981; Eichelberger and Hayes, 1982). This would have immediately reduced H_2O solubility throughout the magmatic system, by ~1 wt.% at 1 km depth, or ~0.4 wt.% at 5 km depth. Our model assumes an instantaneous drop in pressure from P_i to P_f, which simulates a pressure drop of ~100 MPa (C_i=4.6 wt.% H_2O) or ~200 MPa (C_i=6.4 wt.% H_2O). This simplification creates an artificially low H_2O diffusivity at the tube exit, and an artificially high driving force for diffusion. In terms of the modelled diffusion time, these effects may counteract each other; however a full treatment of different pressure profiles is beyond the scope of this study.

9. Conclusions

A new technique for obtaining continuous H_2O diffusion profiles from tube-shaped melt inclusions has been applied to plagioclase-hosted inclusions from the May 18th, 1980 eruption of Mount St. Helens. Diffusion profiles are extracted from greyscale variation on back-scattered electron images of the melt tubes. BSE greyscale intensity is calibrated against H_2O concentrations measured by ion probe. The model takes into account concentration-dependent diffusivity of H_2O and assumes instantaneous decompression and isothermal ascent. Modelled diffusion times were 102 - 166 s. Known initial and final magma pressures allow decompression rates to be quantified. Modelled decompression rates were 0.9 – 1.6 MPa s^{-1}, equivalent to an average ascent speed of 37 - 64 m s^{-1}. This new technique is applicable to any fresh pumice sample containing phenocrysts with melt inclusion tubes.

Acknowledgements

MCSH was supported by a Junior Research Fellowship from Trinity College, University of Cambridge. TM was supported by a Leverhulme Trust research grant, and JDB by a NERC Senior Research Fellowship. We are very grateful for the continuing excellent support of the staff at the NERC Ion Microprobe Facility, University of Edinburgh. We thank Chris Hayward (University of Cambridge) for assistance with electron probe analysis, and D.K. Bailey for providing the sample of Lipari glass used in experiments. The manuscript was improved by thorough and helpful reviews by Oded Navon, Fidel Costa and an anonymous reviewer.

References

Anderson, A.T., 1991. Hourglass inclusions: Theory and application to the Bishop Rhyolitic Tuff. Am. Mineral. 76, 530–547.

Berlo, K., Blundy, J., Turner, S., Cashman, K., Hawkesworth, C., Black, S., 2004. Geochemical precursors to volcanic activity at Mount St Helens, USA. Science 306, 1167–1169.

Blundy, J., Cashman, K., 2001. Ascent-driven crystallisation of dacite magmas at Mount St. Helens, 1980-1986. Contrib. Mineral. Petrol. 140, 631–650.

Blundy, J., Cashman, K., 2005. Rapid decompression-driven crystallization recorded by melt inclusions from Mount St. Helens volcano. Geology 33, 793–796.

Blundy, J., Cashman, K., Humphreys, M., 2006. Magma heating by decompression-driven crystallization beneath andesite volcanoes. Nature 443, 76–80.

Blundy, J., Cashman, K., Berlo, K., in press. Evolving magma storage conditions beneath Mount St. Helens inferred from chemical variations in melt inclusions from the 1980-1986 and current eruptions. USGS Professional Paper.

Carey, S., Sigurdsson, H., 1985. The May 18, 1980 eruption of Mount St. Helens 2. Modeling of dynamics of the Plinian phase. J. Geophys. Res. 90, 2948–2958.

Carey, S., Sigurdsson, H., 1989. The intensity of plinian eruptions. Bull. Volcanol. 51, 28–40.

Carey, S., Sigurdsson, H., Gardner, J.E., Criswell, W., 1990. Variations in column height and magma discharge during the May 18, 1980 eruption of Mount St. Helens. J. Volcanol. Geotherm. Res. 43, 99–112.

Carroll, M.R., Blank, J.G., 1997. The solubility of H_2O in phonolitic melts. Am. Mineral. 82, 549–556.

Cashman, K.V., 1992. Groundmass crystallization of Mount St. Helens dacite, 1980-1986: a tool for interpreting shallow magmatic processes. Contrib. Mineral. Petrol. 109, 431–449.

Castro, J.M., Manga, M., Martin, M.C., 2005. Vesiculation rates of obsidian domes inferred from H2O concentration profiles. Geophys. Res. Lett. 32, L21307.

Criswell, W., 1987. Chronology and pyroclastic stratigraphy of the May 18, 1980 eruption of Mount St. Helens. J. Geophys. Res. 92, 10237–10266.

Delaney, J.R., Karsten, J.L., 1981. Ion microprobe studies of water in silicate melts. Concentration-dependent water diffusion in obsidian. Earth Planet. Sci. Lett. 52, 191–202.

Dunbar, N.W., Hervig, R.L., 1992. Petrogenesis and volatile stratigraphy of the Bishop Tuff – Evidence from melt inclusion analysis. J. Geophys. Res. 97, 15129–15150.

Efron, B., Tibshirani, R.J., 1993. An introduction to the bootstrap. Chapman & Hall.

Eichelberger, J.C., 1995. Silicic volcanism: Ascent of viscous magmas from crustal reservoirs. Ann. Rev. Earth Planet. Sci. 23, 41–64.

Eichelberger, J.C., Hayes, D.B., 1982. Magmatic model for the Mount St. Helens blast of May 18, 1980. J. Geophys. Res. 87, 7727–7738.

Fabbrizio, A., Rouse, P.J., Carroll, M.R., 2006. New experimental data on biotite plus magnetite plus sanidine saturated phonolitic melts and application to the estimation of magmatic water fugacity. Am. Mineral. 91, 1863–1870.

Gardner, J.E., Hilton, M., Carroll, M.R., 1999. Experimental constraints on degassing of magma: isothermal bubble growth during continuous decompression from high pressure. Earth Planet. Sci. Lett. 168, 201–218.

Geschwind, C.-H., Rutherford, M.J., 1995. Crystallization of microlites during magma ascent: the fluid mechanics of 1980-1986 eruptions at Mount St Helens. Bull. Volcanol. 57, 356–370.

Humphreys, M.C.S., Kearns, S.L., Blundy, J.D., 2006. SIMS investigation of electron-beam damage to hydrous, rhyolitic glasses: Implications for melt inclusion analysis. Am. Mineral. 91, 667–679.

Humphreys, M.C.S., Blundy, J.D., Sparks, R.S.J., 2008. Shallow-level decompression crystallisation and deep magma supply at Shiveluch Volcano. Contrib. Mineral. Petrol 155, 45–61.

Jambon, A., Zhang, Y., Stolper, E.M., 1992. Experimental dehydration of natural obsidian and estimation of D_{H2O} at low water contents. Geochim. Cosmochim. Acta 56, 2931–2935.

Kaminski, E., Jaupart, C., 1997. Expansion and quenching of vesicular magma fragments in Plinian eruptions. J. Geophys. Res. 102 (B6), 12187–12203.

Kieffer, S.W., 1981. Fluid dynamics of the May 18 blast at Mount St. Helens. U.S. Geol. Surv. Prof. Pap. 1250, 379–400.

Larsen, J.F., Gardner, J.E., 2004. Experimental study of water degassing from phonolite melts: implications for volatile oversaturation during magmatic ascent. J. Volcanol. Geotherm. Res. 134, 109–124.

Liu, Y., Anderson, A.T., Wilson, C.J.N., 2007. Melt pockets in phenocrysts and decompression rates of silicic magmas before fragmentation. J. Geophys. Res. 112, B06204.

Mastin, L.G., Ghiorso, M.S., 2001. Adiabatic temperature changes of magma-gas mixtures during ascent and eruption. Contrib. Mineral. Petrol. 141, 307–321.

Moore, J.G., Albee, W.C., 1981. Topographic and structural changes, March-July 1980 – Photogrammetric data. *In* Lipman, P.W., Mullineaux, D.R., eds., The 1980 eruptions of Mount St. Helens, Washington. U.S. Geol. Surv. Prof. Pap. 1250, 123–134.

Nielsen, C.H., Sigurdsson, H., 1981. Quantitative methods for electron microprobe analysis of sodium in natural and synthetic glasses. Am. Mineral. 66, 547–552.

Newbury, D.E., 1975. Image formation in the scanning electron microscope. In: Goldstein, J.I., Jakowitz, H. (Eds.), Practical scanning electron microscopy. Plenum Press, New York.

Newman, S., Lowenstern, J.B., 2002. Volatile-Calc: a silicate melt-H_2O-CO_2 solution model written in Visual Basic for Excel. Comput. Geosci. 28, 597–604.

Nowak, M., Behrens, H., 1997. An experimental investigation on diffusion of water in haplogranitic melts. Contrib. Mineral. Petrol. 126, 365–376.

Pallister, J.S., Hoblitt, R.P., Crandell, D.R., Mullineaux, D.R., 1992. Mount St. Helens a decade after the 1980 eruptions: magmatic models, chemical cycles, and a revised hazards assessment. Bull. Volcanol. 54, 126–146.

Papale, P., Dobran, F., 1994. Magma flow along the volcanic conduit during the Plinian and pyroclastic flow phases of the May 18, 1980 Mount St. Helens eruption. J. Geophys. Res. 99, 4355–4373.

Papale, P., Neri, A., Macedonia, G., 1998. The role of magma composition and water content in explosive eruptions. 1. Conduit ascent dynamics. J. Volcanol. Geotherm. Res. 87, 75–93.

Proussevitch, A., Sahagian, D., 2005. Bubbledrive-1: A numerical model of volcanic eruption mechanisms driven by disequilibrium magma degassing. J. Volcanol. Geotherm. Res. 143, 89–111.

Pyle, D.M., 1989. The thickness, volume and grainsize of tephra fall deposits. Bull. Volcanol. 51, 1–15.

Rasband, W.S., 1997-2007. ImageJ, US National Institutes of Health, Bethesda, Maryland, USA. http://rsb.info.nih.gov/ij/.

Reed, S.J.B., 2005. Electron microprobe analysis and scanning electron microscopy in geology, Second ed. Cambridge University Press.

Rose Jr., W.I., Hoffman, M.F., 1982. The 18 May 1980 eruption of Mount St. Helens: The nature of the eruption, with an atmospheric perspective. Atmospheric affects and potential climatic impact of the 1980 eruptions of Mount St. Helens. NASA Conference Pulication, vol. 2240, pp. 1–14.

Rutherford, M.J., Sigurdsson, H., Carey, S., Davis, A., 1985. The May 18, 1980 eruption of Mount St. Helens 1. Melt composition and experimental phase equilibria. J. Geophys. Res. 90, 2929–2947.

Sahagian, D., 2005. Volcanic eruption mechanisms: Insights from intercomparison of models of conduit processes. J. Volcanol. Geotherm. Res. 143, 1–15.

Scandone, R., Malone, S.D., 1985. Magma supply, magma discharge and readjustment of the feeding system of Mount St. Helens during 1980. J. Volcanol. Geotherm. Res. 23, 239–262.

Shaw, H.R., 1972. Viscosities of magmatic silicate liquids – empirical method of prediction. Am. J. Sci. 272, 870–893.

Sisson, T.W., Layne, G.D., 1993. H_2O in basalt and basaltic andesite glass inclusions from four subduction-related volcanoes. Earth Planet. Sci. Lett. 117, 619–635.

Sparks, R.S.J., Moore, J.G., Rice, C.J., 1986. The initial giant umbrella cloud of the May 18th, 1980, explosive eruption of Mount St. Helens. J. Volcanol. Geotherm. Res. 28, 257–274.

Thomas, R.M.E., Sparks, R.S.J., 1992. Cooling of tephra during fallout from eruption columns. Bull. Volcanol. 54, 542–553.

Thomas, J.B., Bodnar, R.J., Shimizu, N., Chesner, C.A., 2003. Melt inclusions in zircon. Rev. Mineral. Geochem. 53, 63–87.

Toramaru, A., 2006. BND (bubble number density) decompression rate meter for explosive volcanic eruptions. J. Volcanol. Geotherm. Res. 154, 303–316.

Voight, B., Glicken, H., Janda, R.J., Douglass, P.M., 1981. Catastrophic rockslide avalanche of May 18. U.S. Geol. Surv. Prof. Pap. 1250, 347–377.

Wallace, P.J., 2005. Volatiles in subduction zone magmas: concentrations and fluxes based on melt inclusion and volcanic gas data. J. Volcanol. Geotherm. Res. 140, 217–240.

Wilson, L., Sparks, R.S.J., Walker, G.P.L., 1980. Explosive volcanic eruptions. 4. The control of magma properties and conduit geometry on eruption column behaviour. Geophys. J. R. Astron. Soc. 63, 117–148.

Zhang, Y., Behrens, H., 2000. H_2O diffusion in rhyolitic melts and glasses. Chem. Geol. 169, 243–262.

Zhang, Y., Stolper, E.M., Wasserburg, G.J., 1991. Diffusion in rhyolite glasses. Geochim. Cosmochim. Acta 55, 441–456.

Bull Volcanol (2008) 70:947–960
DOI 10.1007/s00445-007-0179-5

RESEARCH ARTICLE

Circulation of bubbly magma and gas segregation within tunnels of the potential Yucca Mountain repository

Thierry Menand · Jeremy C. Phillips ·
R. Stephen J. Sparks

Received: 1 December 2006 / Accepted: 11 October 2007 / Published online: 13 November 2007

Abstract Following an intersection of rising magma with drifts of the potential Yucca Mountain nuclear waste repository, a pathway is likely to be established to the surface with magma flowing for days to weeks and affecting the performance of engineered structures located along or near the flow path. In particular, convective circulation could occur within magma-filled drifts due to the exsolution and segregation of magmatic gas. We investigate gas segregation in a magma-filled drift intersected by a vertical dyke by means of analogue experiments, focusing on the conditions of sustained magma flow. Degassing is simulated by electrolysis, producing micrometric bubbles in viscous mixtures of water and golden syrup, or by aerating golden syrup, producing polydisperse bubbly mixtures with 40% of gas by volume. The presence of exsolved bubbles induces a buoyancy-driven exchange flow between the dyke and the drift that leads to gas segregation. Bubbles segregate from the magma by rising and accumulating as a foam at the top of the drift, coupled with the accumulation of denser degassed magma at the base of the drift. Steady-state influx of bubbly magma from the dyke into the drift is balanced by outward flux of lighter foam and denser degassed magma. The length and time scales of this gas segregation are controlled by the rise of bubbles in the horizontal drift. Steady-state gas segregation would be accomplished within hours to hundreds of years depending on the viscosity of the degassed magma and the average size of exsolved gas bubbles, and the resulting foam would only be a few cm thick. The exchange flux of bubbly magma between the dyke and the drift that is induced by gas segregation ranges from 1 m^3 s^{-1}, for the less viscous magmas, to 10^{-8} m^3 s^{-1}, for the most viscous degassed magmas, with associated velocities ranging from 10^{-1} to 10^{-9} m s^{-1} for the same viscosity range. This model of gas segregation also predicts that the relative proportion of erupted degassed magma, that could potentially carry and entrain nuclear waste material towards the surface, would depend on the value of the dyke magma supply rate relative to the value of the gas segregation flux, with violent eruption of gassy as well as degassed magmas at relatively high magma supply rates, and eruption of mainly degassed magma by milder episodic Strombolian explosions at relatively lower supply rates.

Keywords Yucca Mountain · Nuclear waste repository · Gas segregation · Magma circulation · Volcanic gas fluxes · Magma fluxes · Strombolian activity

Introduction

Future volcanic activity may disrupt the potential Yucca Mountain radioactive waste repository site during the next 10,000 years. Consequently, health and safety hazards that may result from future igneous activity must be quantitatively estimated. In addition, a broad range of models and data proposed by the US Department of Energy must be evaluated before potential licensing of the repository. A key component of the hazard analysis is understanding how rising basaltic magma may interact with subsurface repository structures, such as tunnels or drifts.

Editorial responsibility: D. Dingwell

T. Menand (✉) · J. C. Phillips · R. S. J. Sparks
Department of Earth Sciences, Centre for Environmental and Geophysical Flows, University of Bristol,
Bristol, UK
e-mail: t.menand@bristol.ac.uk

Previous work at the University of Bristol (Lejeune et al. 2007) has focused on laboratory experiments using analogue materials that simulate magma and drifts. These experiments investigated the transient dynamics of how gas-bearing and gas-free fluids similar to magmas could suddenly decompress into subsurface openings, which can accelerate and fragment the fluids. Following this work, new experiments have been developed to investigate the potential circulation of bubbly magma within drifts due to density variations caused by separation of bubbles.

Following intersection of rising magma with a drift, a pathway will likely be established to the surface. Magma will then flow through this pathway for days to weeks, affecting the performance of engineered structures located along or near the flow path. Convective circulations may occur in magma-filled structures due to gas exsolution and segregation. Different flow regimes may develop, depending on the flux of gas and magma through the system, the size of bubbles in the magma, the magma rheology and the geometry of flow system. The flux of magma through the potential dyke may drive a recirculating flow within a drift, which may result in significant mixing between magma in the drift and in the dyke. Conversely, there may be stagnant regions where the magma has a long residence time. Vapour bubbles also will exsolve or grow from the magma. If the bubble size is large, the bubble rise speed may be large compared to the flow within a drift, resulting in significant melt-bubble separation in the drift and the formation of a coalesced foam at the drift roof. Along with bubble rise, denser (i.e., degassed) magma may drain back into the dyke/conduit system and possibly be re-entrained into the ascending magma flow. These processes need to be quantified in order to evaluate the likely impacts on waste containment structures and effects on health and safety.

A series of experiments has been carried out to investigate convective circulation in magma-filled structures due to gas exsolution and segregation. This work considered magma rising towards the surface through a vertical dyke that intersects a drift and focused on the conditions of sustained magma flow. The aim of this work is to quantify (1) the time and length scales for bubble segregation and flow recirculation in the drift and (2) the fluxes associated with this gas segregation. The results of this work have been applied to gas segregation in the plumbing systems of basaltic volcanoes (Menand and Phillips 2007a). The present report applies these concepts and results to the particular geometries of the potential Yucca Mountain repository. We first review the different experimental methods that were used to explore the range of parameters relevant to Yucca Mountain. Then, we introduce the model we derived in analyzing the experimental data, before applying this model specifically to Yucca Mountain.

Analogue experiments

A volcanic eruption at the potential Yucca Mountain repository is likely to involve magma with a high volumetric gas fraction (Nicholis and Rutherford 2004; see section on the application to the potential Yucca Mountain repository). However, given the uncertainty on the gas volume fraction, experiments have been carried out over a range of gas fraction varying from a few percent up to 40 percent by volume. This resulted in two separate sets of experiments referred to as low and high gas fraction experiments, respectively.

Low gas fraction experiments

Setup and calibration

The geometry of a vertical dyke intersecting a drift was simulated at the laboratory scale by two interconnected glass tubes, both ends of the vertical glass tube being connected to a peristaltic pump to form a recirculating flow loop (Fig. 1). The internal diameter of the vertical tube was 4 cm, whereas the length and the diameter of the horizontal side arm have been varied.

The solutions used as a magma analogue were various mixtures of golden syrup, water and sodium chloride (NaCl). The density ρ_l and viscosity μ_l of these Newtonian solutions were varied by changing the relative amount of water and golden syrup. The density was measured by weighing a known volume and the viscosity was measured using a Haake RV20 viscometer. Degassing of the magma was simulated by electrolysis of the viscous NaCl solution. The electrolysis cell was situated in the vertical tube below its junction with the horizontal side arm. It produced micrometric bubbles, whose mean diameter d were mea-

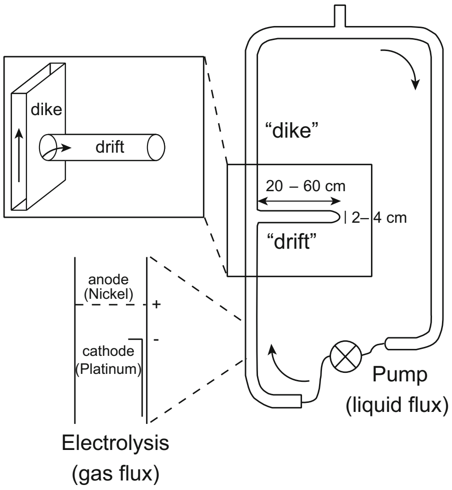

Fig. 1 Schematic diagram of the apparatus

sured from a digital image taken through a microscope at 4× magnification with one standard deviation used as a measure of the bubble size distributions. Electrolysis calibration gives a gas production rate Q_g proportional to current intensity I: $Q_g=(1.43\pm0.03)\times10^{-7}\times I$ m^3 s^{-1}, where I is expressed in Ampere. The reader is referred to Menand and Phillips (2007a) for a more detailed account of how these different measurements were carried out. The properties of the experimental mixtures and bubble sizes d are summarized in Table 1.

At the start of an experiment, the apparatus was filled with golden syrup:water:NaCl mixture and all gas bubbles introduced by the filling process were removed. The experiment was initiated by setting the peristaltic pump to a desired flow rate. The electrolysis cell was then switched on, and the desired gas flux was set independently of the liquid flux. The duration of the experiments was measured from the time that the electrolysis cell was switched on, and the position of the interface between the bubbly liquid, the foam layer and bubble-free liquid in the side arm was measured as the experiment proceeded.

Observations

A large range of liquid and gas flow rates has been investigated, from the case of no liquid flow (bubbles rose through and separated from the liquid in the vertical tube) to that of a liquid flow rate 80 times larger than the gas flux (bubbles were carried by and rose at the same speed as the liquid).

Over the range of experimental flow rates in the vertical tube, the same fluid-flow processes were observed (Fig. 2). At the beginning of the experiments, the electrolysis creates bubbles that rise up the vertical conduit. These bubbles decrease the bulk density of the mixture, which creates a density difference between the bubbly fluid rising in the vertical conduit and the bubble-free fluid originally at rest in the horizontal side arm. In turn, this density difference drives an exchange flow between the two tubes (Fig. 2a). The time-scale associated with this exchange is long enough that bubbles in the horizontal side arm have time to rise, segregate from the fluid and accumulate at its top as a foam. This segregation is coupled with the accumulation of degassed fluid at the base of the side arm (Fig. 2b). Ultimately, a steady state is reached whereby the influx of bubbly fluid into the side arm is balanced by the outward flux of lighter foam and denser degassed fluid, which are respectively reinjected up the conduit toward the surface and recycled at depth in the vertical section (Fig. 2c). The structure of the fluid stratification in the side arm is then fixed, with the thickness of both the foam and the layer of degassed fluid remaining constant.

High gas fraction experiments

Setup and calibration

These experiments differed from the low gas fraction experiments in the technique used to obtain higher volumetric gas fractions. The production of bubbles by electrolysis in golden syrup:water:NaCl mixtures is limited by the maximum electrical current intensity that drives the electrolysis and which is related to the amount of golden syrup present in the mixture. For low golden syrup contents, high electrical current intensity can be used but mixtures have a low viscosity, which allows bubbles to easily rise through the mixture and escape at its free surface in the upper part of the flow loop. Higher golden syrup contents result in higher mixture viscosity and, consequently, bubbles stay longer in suspension in the mixtures. However, higher golden syrup contents decreased the maximum electrical current intensity that can be used to drive the electrolysis cell and hence the bubble production rate. In practice, only volumetric gas fractions lower than 10% could be generated with the electrolysis technique.

In order to achieve higher volumetric gas fractions, we used the aeration technique described by Llewellin et al. (2002). Pure golden syrup was aerated with air using a

Table 1 Properties of golden syrup (GS), water and sodium chloride (NaCl) mixtures and bubbles created by electrolysis

GS:water:NaCl (mass ratio)	ρ_l (kg/m^3)	μ_l (mPa s)	d (µm)	Rising velocity (mm/s)
Low gas fraction experiments				
30:60:10	1,187.6±0.4	3.4±0.1	–	–
45:45:10	1,257.6±0.4	11±1	25±10	0.06
60:30:10	1,325.9±0.4	43±3	35±21	0.03
High gas fraction experiments				
100:0:0	1,439±1	46,700±400	30±33	–
			375	–

The low viscosity of 30:60:10 mixtures prevented any reliable measurement (Menand and Phillips, 2007a). The lower bubble diameter for the high gas fraction experiments is the average measured value of the bubble diameter distribution and the higher diameter is the value used in the analysis (see section on the application to the potential Yucca Mountain repository).

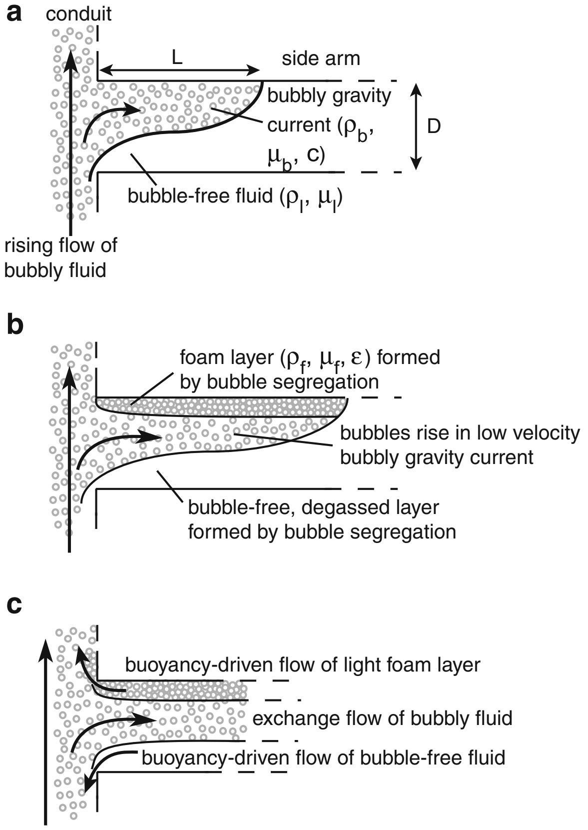

Fig. 2 Schematic illustration of the transient exchange flow between the vertical tube and the horizontal side arm. *Arrows* indicate flow directions. **a** The bubble rich mixture originally present in the vertical conduit is less dense than the bubble-free fluid in the side arm, so that a bubbly gravity current intrudes the side arm. **b** The bubbly gravity current has propagated further into the side arm and a bubble-rich foam has formed at the upper surface of the side arm. **c** A steady exchange flow is established between the vertical tube and the side arm

Mondomix aerator.. This technique provided polydisperse mixtures with volumetric gas fraction c=0.35±0.05. The bubble size distribution was measured by the same technique used for low gas fraction experiments. Bubble diameters range from 2 to 500 μm with a mean diameter of 30±33 μm (Table 1). However, the largest bubbles account for most of the gas volume, and Menand and Phillips (2007b) found that gas segregation processes are dominated by bubbles with the highest diameter. This will be important when modelling gas segregation, as explained in the modeling section.

The high viscosity of golden syrup at room temperature (47 Pa s) combined with the high gas fraction of the mixture created a very viscous bubbly mixture, which could not to be pumped by a peristaltic pump within the flow loop without coalescing the bubbles. Once aerated, the bubbly mixture was poured into the flow loop, and bubbles were therefore evenly distributed throughout the conduit and the side arm. The mixture was left to evolve without imposing any flow loop circulation.

Observations

Despite starting from a static condition (no fluid flow imposed), the same fluid-flow processes were observed. Bubbles in the horizontal side arm are observed to rise and segregate from the liquid, accumulating as a foam at its top and creating a layer of degassed liquid at its base, and a steady state is reached with influx of the bubbly liquid into the side arm balanced by outward flux of the lighter foam and the denser degassed fluid.

Model

Transient exchange flow in low gas fraction experiments

Before modelling the gas segregation that occurs in the side arm during low gas fraction experiments, we first focus on the buoyancy-driven exchange flow set up between the rising bubbly fluid, of density ρ_b, and the initially bubble-free fluid, of density ρ_l, in the horizontal arm of thickness D. This allows us to determine how the length L of the intruding bubbly current evolves with time, and therefore the areal extent of the bubbly source for gas segregation. Figure 2a shows a schematic diagram of the transient flow.

We treat the inflowing bubbly flow as a viscous gravity current. After an initial adjustment, we assume that the pressure distribution in the bubbly current becomes hydrostatic because of negligible vertical accelerations. The excess pressure driving the exchange flow comes from the density difference between the bubbly fluid and the bubble-free fluid, $\Delta\rho = \rho_l - \rho_b$, and is balanced by viscous dissipation. The density of the bubbly fluid is a function of the liquid density, the gas bubble density ρ_g and the volumetric gas fraction c: $\rho_b = c\rho_g + (1-c)\rho_l$. Since $\rho_l \gg \rho_g$, the density difference that drives the flow simplifies to

$$\Delta\rho = c\rho_l \tag{1}$$

The viscosity of the bubbly fluid μ_b can be estimated from the viscosity of the bubble-free fluid μ_l and the volumetric gas fraction c in the current. The experimental volumetric gas fraction was typically less than 0.1 so the viscosity of the bubbly fluid can be approximated as (Wallis 1969; Jaupart and Vergniolle 1989; Llewellin and Manga 2005)

$$\mu_b = \frac{\mu_l}{(1-c)}. \tag{2}$$

For these low volumetric gas fractions, the viscosities of the bubbly current and the bubble-free fluid differ by a few percent only. As a result, the advance of the current is resisted by viscous dissipation occurring within, as well as around, the bubbly current (Huppert 1982). The exact mathematical treatment of the problem is thus complex, but we can use arguments based on dimensional analysis to find how the current length varies as a function of the other relevant variables. The details of these mathematical scaling arguments are given in Menand and Phillips (2007a) and only the main findings are reported here.

From these scaling arguments, we find that the length L of the bubbly current increases with time as

$$L(t) = \left(\frac{\Delta\rho g D^3 t}{\mu_b}\right)^{\frac{1}{2}} F\left(\frac{\mu_l}{\mu_b}\right) \tag{3}$$

where F is an unknown function of the viscosity ratio μ_l/μ_b.

The experiments were used to test the time dependence of the bubbly current given by Eq. 3. There is a maximum distance $L_{\max}$ the current can travel, which corresponds to the point at which all bubbles have risen to the top of the side arm. Due to low bubble concentrations, bubble interactions can be neglected and bubbles of diameter d would rise according to Stokes' law with constant velocity $v_s = \left(\rho_l - \rho_g\right) g d^2 \Big/ (12\mu_l)$. Although bubble interaction and convection will certainly arise at high bubble concentration, the use of Stokes' law leads to conservative modelling of the bubble rise and thus time-scale over which gas segregation processes occur (Menand and Phillips 2007a). The numerical constant 12 at the denominator differs from the usual constant 18 because of constant stress condition at the bubble surface between the inner gas and the outer liquid; the constant 18 should arise in the case of a rigid sphere on which surface a no slip condition applies (Batchelor 1967). However, the upward movement of bubbles results in a downward countercurrent flow of liquid. The Stokes' velocity v_s is relative to the liquid velocity, and, therefore, the true upward velocity of rising bubbles is $(1-c)v_s$. Moreover, bubbles are rising through the bubbly mixture, so the Stokes' velocity should be modified and use the mixture viscosity (2) instead of the pure fluid viscosity. Since$\rho_l \gg \rho_g$, the density difference can be approximated by $\Delta\rho_g = \rho_l$ and bubbles rise at speed

$$v_b = (1-c)^2 \left(\rho_l g d^2\right) \Big/ (12\mu_l). \tag{4}$$

The maximum distance that bubbles can rise is the diameter D of the side arm so the maximum time that bubbles take to reach the top of the side arm is $T_b = D/v_b = 12\mu_l D \Big/ \left[\rho_l g d^2 (1-c)^2\right]$. Therefore, the maximum current length is $L_{\max} = L(T_b)$ and making use of Eqs. 1 for $\Delta\rho$ and 2 for μ_b, the maximum current length becomes

$$L_{\max} = \frac{D^2}{d}\left(\frac{12c}{1-c}\right)^{\frac{1}{2}} F\left(\frac{\mu_l}{\mu_b}\right). \tag{5}$$

Menand and Phillips (2007a) measured the evolution of the bubbly current length in the experiments by recording the successive positions of its tip until its arrest. For each experiment, the length of the current was non-dimensionalised on the maximum length $L_{\max}$ attained by the current, so that experiments over a range of conditions could be compared: $L^*(t) = L(t)/L_{\max} = \left[\rho_l g d^2 (1-c)^2 t/(12\mu_l D)\right]^{\frac{1}{2}}$. Menand and Phillips (2007a) found that after an initial adjustment phase, the data collapse onto the theoretical relationship $L^*(t)$ up to the point where the current has reached its maximum length, at which point L^* remains equal to unity as the bubbly current has ceased to propagate. In the adjustment phase, data are quite scattered. In some experiments the measured length needs to reach almost 60% of the theoretical maximum length before the measured length follows the theoretical relationship, but the adjustment phase is shorter for most experiments. Close examination of the data reveals that the initial mismatch appears proportional to the velocity scale in the vertical conduit (either the average fluid velocity imposed by the pump or the bubble rise speed when no fluid was circulated by the pump). This suggests that the initial spread of the bubbly gravity current is controlled, in some way, by the vertical movement of bubbly fluid up the conduit. We expect an entry effect whereby the exact characteristics of the adjustment phase are related to the particular geometry of the junction. However, this effect should be localised at the entrance and limited to a length of the side arm of the order of its diameter, as it appears to be the case in the experiments. Ultimately, the experimental data show that the bubbly current is controlled by the segregation of the bubbles from the fluid as they rise and accumulate at the top of the horizontal arm, and that the advance of the bubbly gravity current is then described by L^* (Fig. 5, Menand and Phillips 2007a).

Steady-state gas segregation in low gas fraction experiments

We now consider the bubble segregation that occurs in the bubbly current. This problem is similar to that investigated by Jaupart and Vergniolle (1989) and our analysis is based on their model.

We approximate the foam as a long and thin viscous gravity current, in which the vertical acceleration is negligible, pressure is hydrostatic and side-wall drag is negligible (Fig. 2b and c). Thus, the flow is driven by the horizontal gradient of the hydrostatic pressure and resisted by the viscous stresses. However, the foam is much more viscous than the underlying fluid because of the high foam volumetric gas fraction ε, typically ~ 70% by volume, and the foam viscosity μ_{f} is well approximated by the relationship (Jaupart and Vergniolle 1989)

$$\mu_{\mathrm{f}} = \mu_{\mathrm{l}}(1-\varepsilon)^{\frac{-5}{2}}. \tag{6}$$

Stable foams contain typically around 70% of gas by volume (Jaupart and Vergniolle 1989). However, this is likely to be a lower bound in our experiments because the fine bubbles produced by electrolysis tend to coalesce into centimetric to decimetric bubbles at the top of the foam. The foam volumetric gas fraction ε in the experiments is therefore more likely to lie in the range ε=0.7–0.9. Over this range, and using Eq. 6, the foam in our experiments is 20–320 times more viscous than the underlying fluid. Therefore, the main viscous dissipation that resists the flow occurs within the foam and the shear stress at the interface between the foam and the bubbly fluid can be neglected (Huppert 1982). Consequently, the problem allows analytical treatment, the details of which are given in Menand and Phillips (2007a).

Menand and Phillips (2007a) integrate the momentum equation for the foam flow, with the two boundary conditions of (a) no slip at the top of the side arm and (b) no shear stress at the interface, to give the foam velocity, which in conjunction with mass conservation for the gas in the foam layer determines the steady-state shape of the foam layer. The thickness h can be written as the product of a characteristic thickness H and a shape function $f(x)$:

$$h(x) = Hf(x), \tag{7}$$

where

$$H = \left[\frac{c(1-c)^2 d^2 L_{\max}^2}{\varepsilon(1-\varepsilon)^{\frac{5}{2}}(\varepsilon - c)}\right]^{\frac{1}{4}}, \tag{8}$$

and

$$f(x) = \left(\frac{x}{L_{\max}} - \frac{x^2}{4L_{\max}^2}\right)^{\frac{1}{4}}. \tag{9}$$

The two-dimensional analysis does not account for the cylindrical geometry of the side arm; both foam and fluid are assumed to have a constant thickness over the entire width perpendicular to the direction of flow. Consequently, the predicted foam thickness is underestimated by the theory because the foam has in fact a cap-like cross section and thus requires a greater depth to achieve a given area perpendicular to the flow. In order to compare the model with the experiments, the theoretical thickness was increased so that it gives the same foam area in both the theoretical model and the experiments, following the method described by Menand and Phillips (2007a).

For each experiment, the steady-state foam thickness was measured from a digital photograph at different position along the tube, with an uncertainty of ±1 mm. The experimental foam thickness measured along the side arm was compared with the theoretical thickness predicted by the model for different volumetric gas fraction c, and our simple foam model was shown to be in good agreement with the data (Fig. 8, Menand and Phillips 2007a).

Our model implicitly assumes that the flow of rising fluid in the vertical conduit has no effect on the exchange flow and gas segregation that occur in the side arm. Comparison of experimental foam thickness with our theoretical model for three different experiments that differ by their net vertical conduit liquid flux, Q_{l}, only (Q_{l}=0, Q_{l}=9 Q_{g} and Q_{l}=79 Q_{g}, with identical gas flow rate Q_{g} in all three experiments) shows that this is indeed the case: within the experimental errors, the foam that developed in these three experiments has identical thickness even though the fluid flux varied over two orders of magnitude in the vertical conduit (Fig. 9, Menand and Phillips 2007a).

If the side arm is longer than the maximum lateral extent of the bubbly current $L_{\max}$, the lateral extent of the foam will be larger than the underlying bubbly current length $L_{\max}$. In this case, as bubbles accumulate at the top of the side arm, the foam tip opposite the vertical conduit rests against a bubble-free fluid of higher density. The foam will, therefore, flow towards the closed end of the side arm until it reaches the closed end. The steady-state foam thickness will then described by Eqs. 7, 8 and 9 between the entrance of the side arm and $x = L_{\max}$, and will have a value of $h(x = L_{\max})$ away from the entrance.

Finally, we note that this two-dimensional analysis neglects the drag exerted by the side walls of the horizontal arm. Taking full account of this effect would require a detailed three-dimensional analysis of the exchange flow and gas segregation that takes place in the cylindrical side arm. However, this added complication to the analysis does not seem necessary based on the good agreement between the experimental measurements, that reflect any drag occurring in the cylindrical side arm, and our two-dimensional analysis. This good agreement between model and experiments gives confidence that the present analysis correctly captures the key physical principles that control exchange flow and gas segregation in the cylindrical side arm. We also note that our model does not consider non-newtonian effects which might become important for bubble-rich foams with large bubble contents.

Steady-state gas segregation in high gas fraction experiments

Experiments carried out at low gas fractions suggest that fluid flow in the vertical conduit does not affect gas segregation in the side arm. Further, we expect the static starting not to affect the steady-state segregation and that segregation at high volumetric gas fractions to be controlled by the rise of bubbles in the side arm.

As explained in the section on the transient exchange flow in low gas fraction experiments, the bubble rise velocity v_b is relative to the fluid velocity within the mixture: $v_b = (1-c)\rho_l g d^2 / (12\mu_b)$. Experiments carried out at high gas fractions differ from those involving low gas fractions in two aspects. First, they involve polydisperse bubbly mixtures with bubble diameters ranging from 2 to 500 μm. However, 50% of the total gas volume is accounted for by the largest bubbles, with diameter in the range 250–500 μm, and an average bubble diameter d= 375 μm can be taken as that controlling the average bubble rise velocity v_b through the bubbly mixture (Menand and Phillips 2007b). Second, the high volumetric gas fraction strongly increases the viscosity of the bubbly mixture. For gas fractions in the range c=0 to c=0.5, Menand and Phillips (2007b) show that the viscosity of the experimental bubbly mixtures is best approximated by the expression

$$\mu_b = \mu_l (1-c)^{\frac{-5}{2}}. \tag{10}$$

This equation is consistent with Eq. 6, which is valid for foams (Jaupart and Vergniolle 1989), and gives slightly higher viscosities than Eq. 2 at lower bubble concentrations. Using the viscosity model (10), we obtain a bubble rising velocity

$$v_b = \frac{(1-c)^{\frac{7}{2}} \rho_l g d^2}{12\mu_l}. \tag{11}$$

The analysis derived for gas segregation at low volumetric gas fractions was tested by calculating the thickness of the foam that develops at the top of the side arm in high gas fraction experiments with the bubble rising velocity (Eq. 11). Comparison of this theoretical foam thickness with the experimental foam thickness shows very good agreement between theory and data, and we conclude that the theory developed for low volumetric gas fractions can be extended to high gas fractions, at least as high as 40% by volume (Menand and Phillips 2007b).

Application to the potential Yucca Mountain repository

Geometry of the repository and value of the model parameters

The proposed site for the Yucca Mountain repository is located within a historically geologically active basaltic volcanic field with six Quaternary basaltic volcanoes located within 20 km, whose activity has been characterized by Strombolian bursts to violent Strombolian eruptions as well as effusions of lavas. The geology and eruptive sequence of this volcanic field have been studied in detailed by Valentine et al. (2006) and Valentine et al. (2007) and Table 2 only summarises the geometry of the repository and the value of the parameters used in our model.

The diameter D and length L of the repository are based on the values reported in the 2004 DOE report on dyke-drift interactions (BSC 2004); we use here an average length of repository drifts, 500 m, and assume a dyke intersects the drifts at one of their extremities. [The width of dykes erupting at Yucca Mountain would likely be on the order of a meter based on the composition of the magma erupted at Lathrop Wells (Nicholis and Rutherford 2004), which is typical of that of mafic dykes in general and of mafic dykes in southern Nevada in particular (Valentine and Krogh 2006; Valentine et al. 2006; Valentine et al. 2007).]

Nicholis and Rutherford (2004) determined the magma composition of a hawaiite from the Crater Flat volcanic zone near Yucca Mountain and measured an initial water content of up to 4.6 wt.%. At this initial water content, the magma density is 2,750 kg m^{-3} (following Lange 1994). The viscosity of the magma is a crucial parameter in our model that will strongly depend on the degree of water

Table 2 Value of the potential Yucca Mountain repository geometry and parameters of the gas segregation model

Parameter	Value	Source
Repository geometry		
D	5.5 m	BSC (2004)
L	500 m	BSC (2004)
Magma properties		
Water content	1.9–4.6 wt.%	Nicholis and Rutherford (2004)
Bubbly gas fraction c	50–70 vol.%	control parameter
Foam gas fraction ε	70 vol.%	Jaupart and Vergniolle (1989)
Bubble diameter d	100 μm–5 mm	control parameter
Density ρ_l	2,750 kg m^{-3}	Lange (1994); Nicholis and Rutherford (2004)
Viscosity μ_l	10–10^5 Pa s	control parameter
Thermal diffusivity κ	5×10^{-7} m^2 s^{-1}	Turcotte and Schubert (1982)
Thermal constant λ	0.5	Turcotte and Schubert (1982)
Temperature	970°C	Nicholis and Rutherford (2004)
Surface tension σ	0.3 kg s^{-2}	Vergniolle and Jaupart (1990)

exsolution, cooling and crystallisation. We estimate a range of viscosity by using the composition and temperature (970°C) of Nicholis and Rutherford (2004) with the models of Shaw (1972), for a wet basalt with 4.6 wt.% water, and Giordano and Dingwell (2003, 2004), for a dry (degassed) basalt. We obtain viscosities of 10 Pa s and 1.5×10^5 Pa s, respectively. These latter estimates give only the viscosity of the melt, however, and the viscosity of the magma will be larger if it contains crystals. However, as will be shown in the section on time scales, we note that efficient gas segregation in magmas with viscosities larger than 10^5 Pa s requires bubbles that are nearly centimetric in size. These bubble sizes seem unrealistic and we therefore limit the range of explored viscosity to 10–10^5 Pa s.

We estimate that the foam that would develop from gas segregation would have a volumetric gas fraction similar to that of stable foams or ε=0.7. Although foams in our experiments have higher volumetric gas fraction, a value of 0.7 is a generally accepted value for generic foams and thus seems a reasonable value for magmatic systems (Jaupart and Vergniolle 1989). The fate of the foam depends on the coefficient of surface tension σ between the melt and the gas in the bubbles, and Vergniolle and Jaupart (1990) report an average value for basaltic melts of 0.3 kg s^{-2}.

We also investigate a range of average exsolved bubble diameter for shallow magmatic degassing between d= 100 μm and d=5 mm, that is typical of the bubble diameters observed in basaltic rocks (Sarda and Graham 1990; Cashman and Mangan 1994; Sparks 2003).

Finally, owing to high initial water content, basaltic magmas in the Yucca Mountain region are expected to have a high volumetric gas fraction, particularly at the low depth and pressure of the repository. At an average repository depth of 300 m (BSC 2004), the lithostatic pressure is 7 MPa with an average rock density of 2,400 kg m^{-3} (BSC 2004). The magma pressure may be greater or less than lithostatic during eruption, but this cannot be quantified without knowing the detailed dynamics of the eruption. Assuming a basalt solubility of 3×10^{-6} $Pa^{1/2}$ and an initial water content of 4.6 wt.% water, the amount X of exsolved water is 3.8 wt.% at the depth of the repository. We assume that exsolved water vapour follows the perfect gas law $P = \rho_g RT \big/ M$, where M=18 g/mol is the molar mass of water, R=8.31 J mol^{-1} K^{-1} is the universal gas constant, T is the temperature of the magma (1,273 K; Table 2), and ρ_g is the density of the water vapour at these pressure and temperature. This gives us a gas density of 12.2 kg/m^3. The volumetric gas fraction c is obtained from the exsolved mass fraction using the following equation: $\frac{(1-c)}{c} = \frac{\rho_g}{\rho_l}\frac{(1-X)}{X}$. For a magma density of 2,750 kg/m^3 (Table 2), this expression gives a volumetric gas fraction c = 0.9. We note, however, that such a volumetric gas fraction is much higher than the generally accepted value of 0.7 for generic foams. As will be shown in the following section, this suggests an unstable collapse regime will result within the entire drift (Jaupart and Vergniolle 1989). Alternatively, any gas loss during magma flow from a deeper source up to the depth of the repository will reduce the volumetric gas fraction c. Therefore, we investigate a range of volumetric gas fraction c=0.5 to c=0.7. (According to Eqs. 8, 12 and 15, the foam height and time scale cannot be calculated at a volumetric gas fraction equal to the volumetric foam fraction, c=ε =0.7. In this case, a bubbly fraction c=0.69 is used to calculate values for the foam height and time scale.)

Length scales

According to our model, the intrusion of bubbly magma into a drift is limited to a maximum length $L_{\max}$ (Eq. 5). Although Eq. 5 was derived from experiments with low bubbly volumetric gas fraction, it can be seen from Eq. 3 that the viscosity of the mixture enters only the function F (its explicit contribution in the square root of Eq. 3 is cancelled by its implicit contribution within t=T_b) and therefore that Eq. 5 is also valid at high volumetric gas fraction. F is an a priori unknown function of the viscosity ratio μ_l/μ_b. However, as discussed in the modelling section, for the high volumetric gas fractions likely to characterise conditions at the potential Yucca Mountain repository, the viscosity of the bubbly magmas is better approximated by Eq. 10. With a volumetric gas fraction c in the range 0.5–0.7, the viscosity ratio $\mu_l/\mu_b = (1-c)^{5/2} \approx 0.1$ and the function F has value of order 10^{-1} (Matson and Hogg, personal communication, 2006). Consequently, $L_{\max}$ ranges from about 100 km, for an average bubble diameter 100 μm, to about 2 km, for bubble 5 mm in diameter, and the bubbly current is expected to invade the entire length of the drift.

The steady-state characteristic foam thickness is then given by Eq. 8, modified to take into account the bubbly fluid viscosity (Eq. 10) and the bubble rise velocity (Eq. 11):

$$H = \left[\frac{c(1-c)^{\frac{7}{2}}d^2L^2}{\varepsilon(1-\varepsilon)^{\frac{5}{2}}(\varepsilon-c)}\right]^{\frac{1}{4}}. \tag{12}$$

However, H is limited by the way bubbles are packed in the foam and how they respond to this packing; as the foam grows, bubbles deform and, eventually, can coalesce leading to the collapse of the foam. Therefore, there is a maximum, critical thickness H_c the foam can sustain before collapsing. If the steady-state characteristic foam thickness H is smaller than the critical thickness H_c, then the foam is stable and has thickness H. If instead $H > H_c$, then the foam structure collapses when it reaches H_c (Jaupart and Vergniolle, 1989). This foam collapse occurs as a result of bubble packing. Foam collapse occurs when this packing generates deformation that can not be resisted by surface tension anymore. As such, foam collapse can occur in static foams. The critical thickness depends mainly on the coefficient of surface tension σ between the melt and the gas trapped in bubbles and on the bubble diameter with no dependence upon viscosity (Jaupart and Vergniolle 1989):

$$H_{\mathrm{c}} = \frac{4\sigma}{\varepsilon \rho_{\mathrm{l}} g d}. \tag{13}$$

Figure 3 represents the steady-state foam thickness H (Eq. 12) that can develop in a 500 m long drift as a function of the bubble diameter d and the volumetric gas fraction c. The maximum thickness the foam can reach is H_{c} (Eq. 13). If the theoretical steady-state thickness H is greater than H_{c}, then the foam will never reach steady-state but instead collapse and rebuilt periodically, releasing pockets of low viscosity gas in the process. Assuming a volumetric gas fraction c in the range 0.5–0.69 (H tends towards infinity when the volumetric gas fraction c tends towards that of the foam, ε=0.7, but, as discussed below, this is not critical given the fate of the foam), the maximum foam thickness cannot exceed approximately 60 cm. However, this requires bubbles about 100 μm in diameter or smaller. Bubbles would presumably be bigger because of the shallow depth of the repository, however, leading to foam collapse at smaller thickness. In the case of magma containing bubbles 1 mm in diameter, the maximum foam thickness will be about 6 cm, which is several orders of magnitude lower than the steady-state thickness the foam would reach if no collapse were to occur. Therefore, magma with the properties considered typical for the Yucca Mountain region would likely form an unstable foam collapse regime, with the foam being unable to reach a steady-state thickness but instead experiencing repeated collapse as it accumulates at the top of the drift.

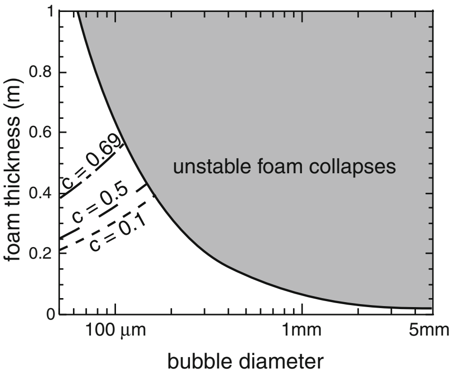

Fig. 3 Foam thickness H (Eq. 12) as a function of bubble diameter d and volumetric gas fraction c. Foam usually collapses unless bubbles are smaller than 100 μm in diameter and the volumetric gas fraction is less than 0.7

Time scales

Two time scales arise in our model. There is first a bubble time scale T_{b} for bubbles to rise over the drift diameter D. Bubbles rise in the laminar regime according to Stokes' law, so

$$T_{\mathrm{b}} = \frac{12\mu_{\mathrm{l}} D}{\rho_{\mathrm{l}} g d^2 (1-c)^{7/2}}. \tag{14}$$

Second, there is a foam time scale T_{f} to establish a steady-state foam, which is obtained by dividing the characteristic foam thickness H (Eq. 12) by the foam velocity scale $c v_{\mathrm{b}}/\varepsilon$,

$$T_{\mathrm{f}} = \frac{12\mu_{\mathrm{l}} L^{\frac{1}{2}}}{\rho_{\mathrm{l}} g d^{\frac{3}{2}}} \left[\frac{\varepsilon^3}{c^3 (1-c)^{\frac{21}{2}} (1-\varepsilon)^{\frac{5}{2}} (\varepsilon - c)} \right]^{\frac{1}{4}}. \tag{15}$$

However, the foam thickness H is presumably not larger than a few cm and thus does not represent more than a small fraction of a drift diameter. Therefore, this means that the time needed to reach maximum foam thickness, before collapse, is much smaller than the steady-state foam time T_{f} and, consequently, the time scale associated with the building of foam in a drift is the bubble time scale T_{b} (Eq. 14). Calculations of the foam time scale T_{f} are, nevertheless, given for completeness.

Gas segregation occurs within a drift if these two time scales are smaller than the time scale for cooling and solidification of the magma, T_{s}. Analysing how magma cools and solidifies in a drift should take into account the presence of nuclear waste canisters and their engineered barrier system, both in terms of their geometry and their thermal properties, and how magma would flow around them. Such an analysis would require 3-D computational modelling coupling mass, momentum and heat transfer. Such complex modelling, however, is beyond the scope of this paper. Instead, the aim of the paper is to assess whether magma circulation and gas segregation have the potential to develop within drifts, and the worst case scenario would be that where engineered barrier system does not have any effect in preventing such circulation and segregation. Therefore, our thermal analysis will neglect the presence of engineered barrier system and instead consider the cooling and solidification problem of a simple cylindrical magma-filled drift.

A magma-filled drift will cool down by conduction and crystallise, releasing latent heat in the process. Following Turcotte and Schubert (1982), the time needed to cool down and solidify a magma-filled drift of thickness D by conduction is

$$T_s = \frac{D^2}{16\kappa\lambda^2}, \qquad (16)$$

where κ is the magma thermal diffusivity and the thermal constant λ depends on the temperature difference between the magma and surrounding rocks (Turcotte and Schubert 1982). T_s is a lower estimate, however; the solidification time will certainly be larger as any exchange flow between a dyke and a drift would mean both mass and heat are exchanged, keeping the drift hotter than in the conduction-only scenario.

Figure 4 shows the three time scales as a function of magma viscosity, bubble size and volumetric gas fraction. Larger bubbles decrease both the bubble and the foam time scales and thus increase the viscosity range over which gas segregation can occur. Depending on the volumetric gas fraction, gas segregation with bubbles 100 µm in diameter requires very fluid magmas, with viscosity less than 10 Pa s, whereas 5 mm bubbles enable gas segregation to occur with magma viscosity as high as 10^3–10^4 Pa s. However, given that T_s is only a lower estimate, gas segregation and magma recirculation within a drift would occur presumably with degassed magmas of higher viscosity.

Depending on the viscosity of the degassed magma, average bubble diameter and volumetric gas fraction, and recalling that the time scale associated with the building of the foam is the bubble time scale, the time scale associated with gas segregation ranges from a day to tens of years (Fig. 4).

Although our model does not account for any magma quenching on the wall of a drift, it can be demonstrated that quenching is not a significant factor. First, on the time scale of magma emplacement and circulation into a drift the change in cross-section is negligible and so will not affect the results. For example a chilled margin of 2 cm thickness reduces the cross-section by 1.6% in a 5 m diameter drift. Second, the eruption of basalt lava through a 10 cm diameter borehole with a length of over 1 km during the 1977 eruption of Krafla volcano, Iceland (Larsen et al. 1979) demonstrates empirically that basalt magma can flow along a hole that has a cross-sectional area two orders of magnitude smaller than a repository drift, and that quenching is not a major factor provided the time scale of the flows being considered are much shorter than the solidification time scale. Thus cooling to form a quenched layer is not a significant factor, so that the gas segregation model reported here, which does not take account of cooling, is not invalidated.

Fluxes and velocities associated with gas segregation

As illustrated in Fig. 5, a steady-state gas segregation between a dyke and a drift would be characterised by a balance between a volumetric flux Q_{ex} of bubbly fluid entering the drift and outward volumetric fluxes of gas, Q_g, and degassed magma, Q_D, so that $Q_{ex}=Q_g+Q_D$. A proportion c of Q_{ex} is made of exsolved gas, $Q_g=cQ_{ex}$. By mass balance, $Q_D=(1-c)Q_{ex}$. The gas return flux $Q_g = Acv_b/\varepsilon$, where $A \sim DL$ is the interface area between the bubbly fluid and the foam in the drift. Using Eq. 11 for the bubble rise speed, it follows that

$$Q_{ex} = \frac{(1-c)^{\frac{7}{2}}\rho_l g d^2 DL}{12\mu_l\varepsilon}, \qquad (17)$$

$$Q_D = \frac{(1-c)^{\frac{9}{2}}\rho_l g d^2 DL}{12\mu_l\varepsilon}, \qquad (18)$$

$$Q_g = \frac{c(1-c)^{\frac{7}{2}}\rho_l g d^2 DL}{12\mu_l\varepsilon}. \qquad (19)$$

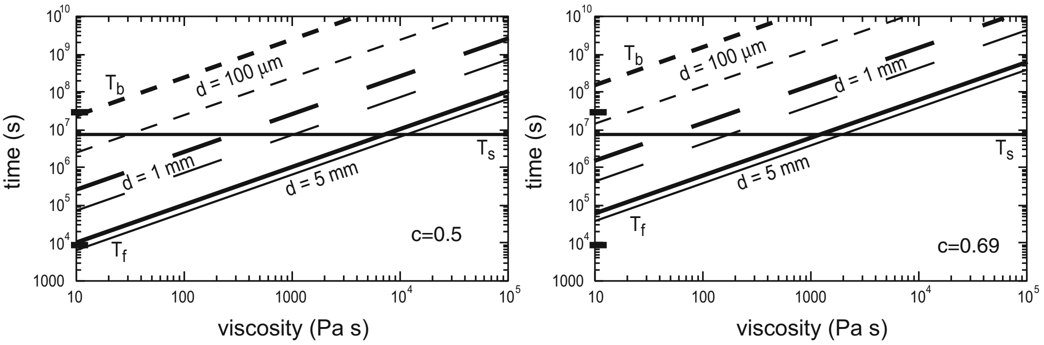

Fig. 4 The different time scales as a function of magma viscosity for two volumetric gas fractions, c=0.5 and c=0.69. The horizontal solid curve represents the solidification time T_s. Slanted thick and thin curves represent the bubble rise time T_b and the foam time T_f, respectively, for different bubble diameters: *short dashes*, d=100 µm; *long dashes*, d=1 mm; *solid curves*, d=5 mm. Thick black ticks on time axis represent 1 day (9×10^3 s) and 1 year (3×10^7 s)

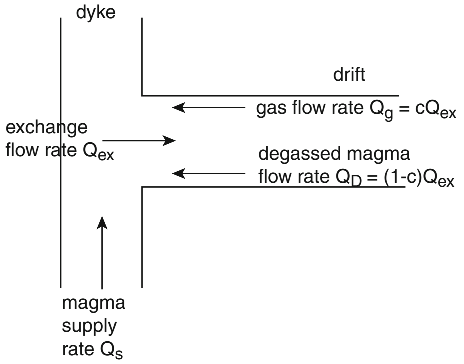

Fig. 5 Schematic illustration of the exchange flow of bubbly and degassed magma driven by steady-state gas segregation. For a dyke with supply rate Q_s, an exchange rate Q_{ex} of bubbly fluid entering the drift is balanced by an exsolved gas return rate Q_g and a degassed magma return rate Q_D: $Q_{ex}=Q_g+Q_D$

Figure 6 shows these fluxes vary strongly with magma viscosity and bubble diameter, ranging from 10^{-8} to 1 m^3 s^{-1} in the parameter ranges considered for Yucca Mountain. So, unless gas segregation involves suspensions of large bubbles in low viscosity magmas, these fluxes are much lower than typical magma ascent rates (~1 m^3/s).

The associated depth-averaged velocities u are obtained by dividing the fluxes (Eqs. 17, 18, and 19) by the characteristic cross section area $S_i \approx DH_i$ of the specific layer i that is considered, where H_i is the thickness of that layer (foam, bubbly fluid or degassed layer). The thicknesses of the bubbly and degassed fluids depend on the viscosity ratio μ_l/μ_b, which determines the viscous dissipation associated with the exchange flow. For a volumetric gas fraction c=0.5–0.7, the viscosity ratio $\mu_l/\mu_b \approx 0.1$ and the bubbly layer thickness H_b and the degassed layer thickness H_D are approximately equal (Matson and Hogg, personal communication, 2006). Thus, by mass balance $H_b \approx H_D = (D-H)/2 \approx D/2$ (since $H \ll D$), which gives us the cross section areas $S_b \approx S_D = \pi D^2/8$. The foam thickness H is much smaller than the diameter of a drift. Moreover, we found that the Yucca Mountain system would very likely be in an unstable foam collapse regime, so the maximum thickness the foam can reach before collapsing is H_c (Eq. 13). Simple geometrical considerations show that the cross section area S_f of very thin ($H_c \ll D$) cap-like foam is well approximated by $S_f \approx \left[H_c^3(D-H_c)\right]^{\frac{1}{2}}$. Depth-averaged velocities in foam, bubbly fluid and degassed layers are obtained by dividing the fluxes (Eqs. 17, 18, and 19) by their respective cross section areas:

$$u_{ex} = \frac{2(1-c)^{\frac{7}{2}}\rho_l g d^2 L}{3\pi\mu_l \varepsilon D}, \tag{20}$$

$$u_D = \frac{2(1-c)^{\frac{9}{2}}\rho_l g d^2 L}{3\pi\mu_l \varepsilon D}, \tag{21}$$

$$u_g = \frac{c(1-c)^{\frac{7}{2}}\rho_l g d^2 DL}{12\mu_l \varepsilon \left[H_c^3(D-H_c)\right]^{\frac{1}{2}}}. \tag{22}$$

These velocities are shown in Fig. 7 as function of magma viscosity, bubble diameter and volumetric gas fraction. It appears that, although these three fluxes have similar values for a given average bubble diameter, associated velocities differ by 1 to 3 orders of magnitude since the foam thickness represents typically only 1 percent of the drift diameter. Consequently, foam velocities have much higher value than bubbly and degassed magma velocities. We note, however, that the current model treats

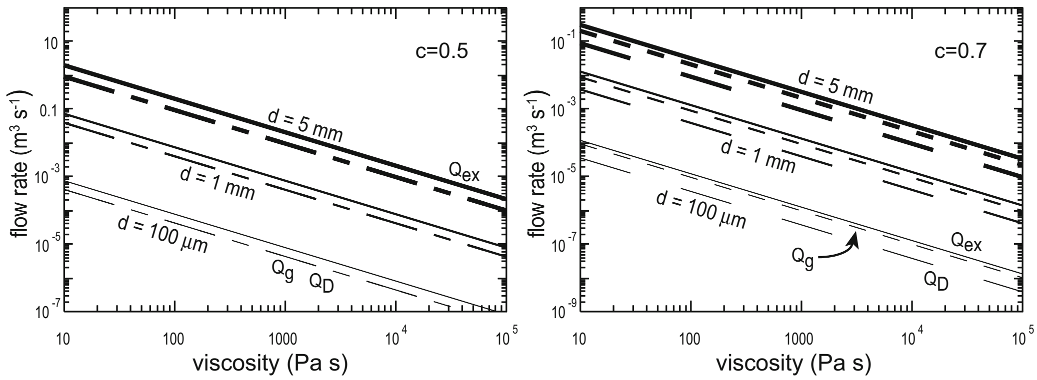

Fig. 6 Exchange flow rate Q_{ex} (*solid curve*), exsolved gas return rate Q_g (*short dashed curve*) and degassed magma return rate Q_D (*long dashed curve*) as a function of magma viscosity for different bubble diameters and volumetric gas fractions. Q_g and Q_D have same values when volumetric gas fraction c=0.5. Note the change of flow rate scale between the two graphs

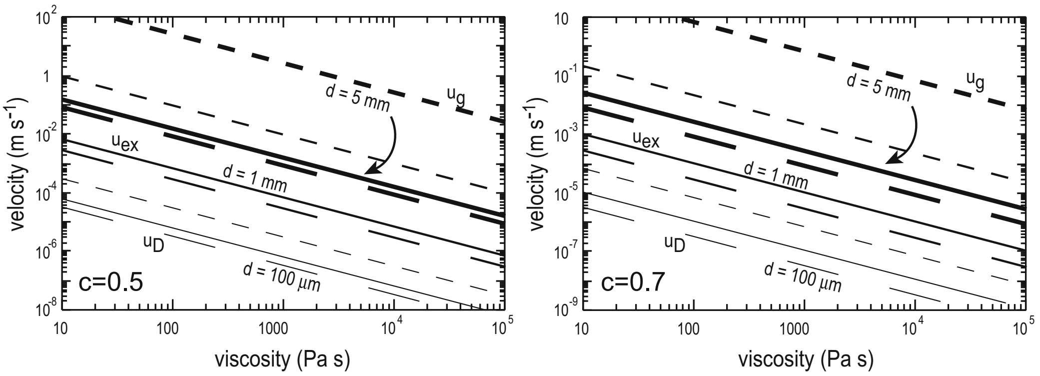

Fig. 7 Depth-averaged velocity of the bubbly layer u_{ex} (*solid curve*), the foam layer u_g (*short dashed curve*) and the degassed magma layer u_D (*long dashed curve*) as a function of magma viscosity and for different average bubble diameters (*thin curves*, d=100 µm; *medium thickness*, d=1 mm; *thick curves*, d=5 mm) and volumetric gas fractions. Note the change of velocity scale between the two graphs

the foam flow as a viscous gravity current, which is valid for low Reynolds numbers only, and consequently will break down at high foam velocities.

More importantly, both fluxes and associated averaged velocities vary inversely proportionally to magma viscosity and increase as the square of the average bubble diameter. Comparatively, the effect of the volumetric gas fraction is negligible in the framework of the present model. It is therefore crucial to constrain as far as possible the petrological evolution magmas will undertake as they rise and interact with drifts in order to get the best estimate for their viscosity and the size of their exsolved gas bubbles.

Implications for potential eruptions

We infer from our experiments that gas segregation in the drift will be independent of moderate changes in the dyke magma supply rate. However, different eruptive scenarios can be envisaged depending on the values of supply rate Q_s, exchange rate Q_{ex} associated with gas segregation, foam layer return flow Q_g and degassed magma return flow Q_D. If $Q_{ex} > Q_s$ then we have strong segregation in the drift leading to episodic Strombolian eruptions of relatively gas-poor magma (Q_D) driven by foam collapse; if $Q_s > Q_{ex}$, there will be ineffective segregation suggestive of stronger explosions erupting gas-rich (Q_s) as well as gas-poor (Q_D) magmas. This prediction of the model is in agreement with the observation at Stromboli, Italy, of more violent eruptions occurring at higher supply rate and with estimations of the critical magma supply rate between the two eruptive regimes (Menand and Phillips 2007a). This has strong implications for the amount of degassed magma generated by gas segregation that could be entrained towards the surface.

We expect a transition between Strombolian activity when $Q_s < Q_{ex}$ and more explosive eruptions when $Q_s > Q_{ex}$ to occur when both fluxes are comparable, $Q_s \sim Q_{ex}$ (Eq. 17).

As shown on Fig. 6, the transition to more explosive eruptions would require a much higher supply rate with low viscosity magmas than with more viscous magmas; low viscosity produces very effective gas segregation. The critical magma supply rate, which delimits a Strombolian eruptive regime that erupts mainly degassed magma from a more explosive regime that erupts degassed as well as gas-rich magma, ranges from 10^{-4} to 1 m^3 s^{-1}, for $\mu_l \sim 10$ Pa s, to about 10^{-8} to 10^{-4} m^3 s^{-1}, for $\mu_l \sim 10^5$ Pa s, depending on the average bubble size (Fig. 6).

Limitations of the model

Our experiments show that the processes governing gas segregation at high and low volumetric gas fractions are identical except that higher gas fractions lead to an increase of the viscosity of the bubbly fluid and thus increase the time scales associated with gas segregation. We have shown that this is the case for volumetric gas fractions as high as 40% by volume but could not investigate higher gas fractions because of the difficulty of generating these high gas fractions experimentally. We assume that gas segregation involving gas fractions as high as 60–70% would be controlled in a way similar to that identified in our experiments. At higher volumetric gas fractions, however, the bubbly fluid would behave like a foam. Although it could be argued that gas segregation might then become negligible because of the viscosity increase and of the negligible density difference between the bubbly fluid and any foam potentially built from gas segregation, such high gas fractions would also increase the propensity of the whole bubbly fluid to collapse (section on the gas segregation length scales; Jaupart and Vergniolle 1989). This could lead to strongly explosive behaviour. Assessing this possibility is particularly important given the high volumetric gas fraction likely to be present within magmas that could interact with the potential Yucca Mountain repository and should be addressed in future studies.

Our experiments and analysis are also limited to the case of horizontal drifts. Although gas segregation would also occur in non-horizontal drifts, the exact arrangement or geometry of drifts would certainly affect the overall pattern of magma circulation induced by gas segregation. This could have strong implications for the potential mobilization of nuclear waste by magma movement and should be assessed in future studies.

Conclusion

In the event of a vertical dyke intersecting the potential Yucca Mountain repository, convective circulation in horizontal magma-filled structures could occur owing to gas exsolution and segregation. Gas segregation in a magma-filled drift has been investigated by means of analogue experiments with focus on the conditions of sustained magma flow. These experiments reveal how gas segregation is driven by an exchange flow between the vertical dyke and the horizontal drift due to the presence of exsolved gas bubbles.

The length and time scales of this gas segregation are controlled by the rise of bubbles in the drift. For the potential Yucca Mountain repository geometry, the time required for steady-state gas segregation ranges from hours to hundreds of years depending on the average size of exsolved gas bubbles and on the viscosity of degassed magmas, which depends strongly on the degree of water exsolution, cooling and crystallisation.

The flux Q_{ex} associated with gas segregation ranges from 1 $\mathrm{m}^3\ \mathrm{s}^{-1}$, for the less viscous magmas, to 10^{-8} $\mathrm{m}^3\ \mathrm{s}^{-1}$, for the most viscous degassed magmas. These values of flux are strongly dependent on the average exsolved bubble diameter. Associated depth-averaged velocity u_{ex} ranges from 10^{-1} to 10^{-9} $\mathrm{m\ s}^{-1}$ for the same viscosity range. The relative proportion of erupted degassed magma depends on the value of the magma supply rate relative to the value of Q_{ex}. If magma is supplied at a rate higher than Q_{ex}, then gassy as well as degassed magmas are expected to be violently erupted; if the supply rate is lower, then mainly degassed magma would be erupted by milder episodic Strombolian explosions generated by the repeated collapse of the foam accumulated at the top of drifts.

Our analysis neglects the presence of engineered barrier system which adds additional thermal mass to the problem and thus a more complex cooling system which is coupled to the complex flow of magma around canisters. Assessing how this could affect gas segregation within drifts will require three-dimensional computational modelling that couples mass, momentum and heat transfer. Future studies should also address the petrological evolution of magmas as they rise and interact with drifts and their content. This evolution determines their viscosity and the size of their exsolved gas bubbles, which in turn control strongly the fluxes and average velocities associated with gas segregation. Furthermore, better constraints on magma viscosity are crucial in order to estimate more accurately the heat transfer and cooling rates during and after gas segregation, and thus the duration of magma exchange flow within repository drifts.

Acknowledgements This work benefited from fruitful discussions with Brittain Hill, Andy Woods, Andrew Hogg and Gary Matson, and from the thorough reviews of Steve Green and Stuart Stothoff of a previous version of the manuscript. We thank Steve Lane for his very useful review and comments. This report was prepared to document work performed by the Center for Nuclear Waste Regulatory Analyses (CNWRA) and its contractors for the US Nuclear Regulatory Commission (NRC) under Contract No. NRC-02-02-012. The activities reported here were performed on behalf of the NRC Office of Nuclear Material Safety and Safeguards, Division of High Level Waste Repository Safety. This report is an independent product of the CNWRA and does not necessarily reflect the view or regulatory position of the NRC.

References

Batchelor GK (1967) An introduction to fluid dynamics. Cambridge University Press, Cambridge

BSC (2004) Dike/drift interactions (MDL-MGR-GS-000005). NV: Bechtel SAIC Company, Las Vegas, NV

Cashman KV, Mangan MT (1994) Physical aspects of magma degassing II. Constraints on vesiculation processes from textural studies of eruptive products. Rev Miner 30:447–478

Giordano D, Dingwell DB (2003) Non-Arrhenian multicomponent melt vicosity: a model. Earth Planet Sci Lett 208:337–349

Giordano D, Dingwell DB (2004) Erratum to‘non-Arrhenian multicomponent melt vicosity: a model.’ Earth Planet Sci Lett 221:449

Huppert HE (1982) The propagation of two-dimensional and axisymmetric viscous gravity currents over a rigid horizontal surface. J Fluid Mech 121:43–58

Jaupart C, Vergniolle S (1989) The generation and collapse of a foam layer at the roof of a basaltic magma chamber. J Fluid Mech 203:347–380

Lange RA (1994) The effect of H_2O, CO_2 and F on the density and viscosity of silicate melts. Rev Miner 30:331–369

Larsen G, Grönvold K, Thorarinsson S (1979) Volcanic eruption through a geothermal borehole at Námafjall, Iceland. Nature 278:707–710

Lejeune A-M, Woods AW, Sparks RSJ, Hill BE, Connor CB (2007) The decompression of volatile-poor basaltic magma from a dike into a horizontal subsurface tunnel. In: Connor C, Chapman N, Connor L (eds) Volcanism, tectonism, and siting nuclear facilities. Cambridge University Press (accepted)

Llewellin EW, Manga M (2005) Bubble suspension rheology and implications for conduit flow. J. Volcanol Geotherm Res 143:205–217

Llewellin EW, Mader HM, Wilson SDR (2002) The rheology of a bubbly liquid. Proc R Soc Lond A 458:987–1016

Menand T, Phillips JC (2007a) Gas segregation in dykes and sills. J Volcanol Geotherm Res 159:393–408

Menand T, Phillips JC (2007b) A note on gas segregation in dykes and sills at high volumetric gas fractions. J Volcanol Geotherm Res 162:185–188

Nicholis MG, Rutherford MJ (2004) Experimental constraints on magma ascent rate for the Crater Flat volcanic zone hawaiite. Geology 32:489–492

Sarda P, Graham D (1990) Mid-ocean ridge popping rocks: implications for degassing at ridge crests. Earth Planet Sci Lett 97:268–289

Shaw HR (1972) Viscosities of magmatic silicate liquids: an empirical method of prediction. Am J Sci 272:870–893

Sparks RSJ (2003) Dynamics of magma degassing. In: Oppenheimer C, Pyle DM, Barclay J (eds), Volcanic degassing, vol. 213, Geol. Soc. London Spec. Publ., pp 5–22

Turcotte DL, Schubert G (1982) Geodynamics. Applications of continuum physics to geological problems. Wiley, New York

Valentine GA, Krogh KEC (2006) Emplacement of shallow dikes and sills beneath a small basaltic volcanic center—the role of pre-existing structure (Paiute Ridge, southern Nevada, USA). Earth Planet Sci Lett 246:217–230

Valentine GA, Krier DJ, Perry FV, Heiken G (2007) Eruptive and geomorphic processes at the Lathrop Wells scoria cone volcano. J Volcanol Geotherm Res 161:57–80

Valentine GA, Perry FV, Krier D, Keating GN, Kelley RE, Cogbill AH (2006) Small-volume basaltic volcanoes: eruptive products and processes, and posteruptive geomorphic evolution in Crater Flat (Pleistocene), southern Nevada. Geol Soc Amer Bull 118:1313–1330

Vergniolle S, Jaupart C (1990) Dynamics of degassing at Kilauea Volcano, Hawaii. J Geophys Res 95:2793–2809

Wallis GB (1969) One-dimensional two-phase flow. McGraw-Hill, New York

17

Modeling the flow of basaltic magma into subsurface nuclear facilities

T. Menand, J. C. Phillips, R. S. J. Sparks and A. W. Woods

Worldwide, a consensus is developing among countries using nuclear power that deep, geologic disposal of spent nuclear fuel and high-level radioactive waste is the safest long-term option (National Research Council, 1990, 2001; EPA, 2001). The geologic medium acts as a component of a multiple barrier system (including the waste form and engineering components) designed to isolate the waste from the biosphere. Regulations in many countries, therefore, require repository developers to consider various natural hazards when evaluating repository performance. Among the hazards considered is the potential for igneous activity at the site and surrounding area (Long and Ewing, 2004). For example, in the United States, regulations governing the geologic disposal of high-level radioactive waste at the potential Yucca Mountain, Nevada, repository require inclusion of risk (i.e. probability and consequence) in assessments of the safety of the repository system. Based on probabilities estimated for repository disruption by future basaltic volcanism (e.g. 1.8×10^{-8}: Bechtel SAIC Company, LLC, 2007; 1.0×10^{-6}: Smith and Keenan, 2005) and the potential risks for this natural hazard, performance assessments should evaluate the consequences of a basaltic volcano intersecting the drifts and tunnels of the potential repository, which might damage the emplaced waste packages and waste form, and could transport radioactive material to the biosphere (NRC, 2005).

There is almost no precedent for a volcanic eruption interacting with an underground storage facility of the kind envisaged for radioactive waste repositories. These facilities generally consist of a network of tunnels or drifts. Some designs require the drifts to remain empty apart from their inventory of radioactive waste containers, at least up to the time the repository is permanently closed (i.e. on the order of several hundred years in some cases). Thus, the generic processes that might occur if magma erupts into empty drifts have been a prominent topic of study. Because no such events have occurred and analogues such as eruptions into natural caves have not yet been identified, the assessment of igneous disruption will need to rely largely on non-empirical information. In general, such assessments may consider the limited empirical evidence of volcanic and intrusive processes; knowledge of the properties of erupting magmas that help constrain the dynamics of these processes; laboratory experiments designed to elucidate how multiphase fluids interact with drifts; and finally, development of models. Because of the complexity of the processes and current state of the art in representing those processes, a comprehensive approach to assessing igneous consequences that integrates knowledge from each of these sources is appropriate.

This chapter focuses on modeling with an emphasis on the use of analog laboratory experiments that are designed to either (i) test theories and numerical models or (ii) gain insights into processes in circumstances where numerical models are either poorly understood or too complex. To develop representative models, we considered results from volcanological studies of eruption behavior and products. We also incorporated the physical properties of magma when choosing relevant analog fluids and addressing scaling issues.

17.1 Magma properties and fluid dynamics relevant to magma–drift interaction

17.1.1 Physical properties of magmas

The magma properties that exert the strongest control on flow dynamics are the magma density ρ and viscosity μ, both of which decrease with increasing temperature. Typical basalt eruption temperatures range from 1000–1300 °C (Kilburn, 2000; Francis and Oppenheimer, 2004), and over this range of temperatures the density and viscosity of natural, dry basaltic melts range between 2600 and 2800 $\mathrm{kg\,m^{-3}}$ and between 1 and 1000 Pa s at atmospheric pressure, respectively (Murase and McBirney, 1973; Kilburn, 2000; Spera, 2000; Francis and Oppenheimer, 2004).

Magma typically consists of three phases: melt (liquid), crystals (solid) and bubbles (gas). The temperature dependence of the melt viscosity can be described by several models; the simplest is the Arrhenian model $\mu = \mu_0 \exp(E^*/RT)$, where μ_0 is the melt viscosity at infinite temperature, E^* is the melt activation energy, R is the universal gas constant and T is the temperature in Kelvin. According to this model, melt composition mainly affects the activation energy E^*, and Shaw (1972) estimated the activation energy from the partial molar coefficients of SiO_2. Although melts with high silica content do not exactly follow the Arrhenian temperature–viscosity relationship (Hess and Dingwell, 1996), it is usually necessary to employ the simpler Arrhenian model of Shaw (1972) for petrologic purposes (Spera, 2000), which is a good approximation for low-viscosity basalts (Giordano and Dingwell, 2003).

Small amounts of dissolved volatiles can have important effects on the density, viscosity and crystallization of melts and magmas, which will strongly influence the ability of magmas to flow. Of all the volatile species, water is the most abundant and accounts for the largest variations in density and, more importantly, viscosity. Basaltic magmas typically contain 1–4 wt.% volatiles, although dissolved water contents as high as 6 wt.% have been measured in arc basalts (Sisson and Layne, 1993); and water contents up to 4.6 wt.% have been estimated for the Lathrop Wells basalts near the proposed site for the high-level radioactive waste repository at Yucca Mountain, Nevada (Nicholis and Rutherford, 2004; Valentine *et al.*, 2007). Dissolved water contents of 3 wt.% will lower the density of basaltic melts by 5 wt.% (Lange, 1994; Wallace and Anderson, 2000) and lower the melt viscosity of basalts by two orders of magnitude (Shaw, 1972; Giordano and Dingwell, 2003). Water is not the only volatile species, however. Carbon dioxide is also present in magmas, but the amounts of dissolved CO_2 are typically one to two orders of magnitude less than those of water. Furthermore, the effect of CO_2 on melt density and viscosity is smaller than for water: Wallace and Anderson (2000) report that adding 3 wt.% of CO_2 to a basaltic melt will decrease its density by $\approx 3\%$. Contrary to water, dissolved CO_2 appears to have a minimal effect on melt viscosity. This effect depends on the speciation of CO_2, and dissolved CO_2 can increase melt viscosity slightly if the CO_2 is dissolved as carbonate (Lange, 1994). Dissolved CO_2 in melts can also have important indirect effects on melt viscosity because dissolved CO_2 lowers the solubility of water (Holloway and Blank, 1994).

The presence of exsolved gas bubbles and crystals also has a strong influence on magma density and viscosity. Crystals act to increase both magma viscosity and density. Estimating the speciation and volume fraction of different crystal phases present in the melt requires modeling the thermal and decompression history of the magma. This is a complex process using an incomplete understanding of the phase behavior, particularly the solubility of CO_2 in basalts. Therefore a more typical approach in recent studies has been to investigate a wide range of magma viscosities that will account for the ranges of temperatures, compositions and crystal contents that characterize basaltic magmas.

The presence of exsolved gas bubbles also significantly affects the density of magmas, which decreases linearly with the volumetric concentration c of the bubbles: $\rho \sim \rho_l(1-c)$ where ρ_l is the density of pure melt. The effect of bubbles on magma viscosity is more complex as it depends on the tendency of bubbles to deform under viscous stresses induced by flow, relative to their tendency to remain spherical as a result of interfacial stresses, and the rapidity of this response (Llewellin and Manga, 2005). For steady flows involving spherical bubbles, the commonly accepted empirical relationship at low volumetric fractions ($< 10\%$) for viscosity of the bubbly mixture, μ_b, as a function of bubble content and melt viscosity, μ_l, is $\mu_b = \mu_l/(1-c)$ (Llewellin and Manga, 2005; Menand and Phillips, 2007b). For higher bubble contents, viscosity appears to be better approximated by the relationship $\mu_b = \mu_l(1-c)^{-5/2}$ (Jaupart and Vergniolle, 1989; Menand and Phillips, 2007b).

An important consideration in the eruption of water-rich basalts is the crystallization that is principally related to the change in liquidus temperatures of the main stable mineral phases. Degassing-induced crystallization and the consequent rheological changes are key to understanding conduit flows and lava extrusions in andesite eruptions (Cashman, 1992; Melnik and Sparks, 1999). This is likely to be the case for wet basalt eruptions, too, although there is less supporting research. The viscosity increases dramatically as groundmass crystals form from degassing basalt, and the crystal content may become so high that the rheology can become non-Newtonian. For example, wet trachybasalt with a liquidus at 950−1000 °C (Nicholis and Rutherford, 2004) tends toward the solidus at one atmosphere pressure. The effects of degassing on crystallization and viscosity will be counteracted by the latent heat of crystallization (Blundy *et al.*, 2006) such that the temperature will be above the solidus in the fully degassed and decompressed state at one atmosphere. Fifty percent crystallization will increase the temperature by ≈ 100 °C based on the latent heat of crystallization of plagioclase as the dominant groundmass mineral. Thus, the eruption temperature of trachybasalt should be ∼ 1050−1100 °C. The rheology of such magmas can be compared to the field rheological measurements of Etna trachybasalt lava (Pinkerton and Sparks, 1978), which is ∼ 10^5 Pa s with ≈ 50% total crystal content at 1070 °C.

At lower pressures, gases become less soluble in magmas, leading to an increase in gas exsolution and magma crystallinity. Additionally, gas bubbles expand as the magmatic pressure decreases, so the controls exerted by bubbles and crystals on magma properties become more significant at lower pressures, and these effects will be especially important at the typically shallow depths (∼ 500 m) of radioactive waste repositories. The exsolved gas mass fraction n varies with pressure according to the solubility law (based on Henry's law),

$$n(P) = n_0 - sP^{1/2} \tag{17.1}$$

where n_0 is the total gas mass fraction, P is pressure and s is the solubility constant for water in basalt, with a value $3 \times 10^{-6}\,\mathrm{Pa}^{1/2}$ (Holloway and Blank, 1994). In general, the gas pressure will not be equal to the bulk flow pressure or to the surrounding rock lithostatic pressure. Exsolving gas bubbles are overpressured with respect to the surrounding fluid due to surface tension, viscous resistance, and inertia, as gas bubbles expand in ascending magma due to diffusion and decompression (Sparks, 1978; Sparks *et al.*, 1994). In basalt magmas, overpressures due to surface tension and inertia are typically negligible but overpressures due to viscous resistance can be significant in very fast explosive flows. Additionally, the bulk flow pressure is initially determined by the pressure in the source chamber but decreases due to frictional losses in the magma flow. Thus, gas pressure evolves during magma ascent, which in turn determines volatile exsolution and depends on the detailed dynamics of the eruption (Massol *et al.*, 2001). A common approach is to assume that pressure is lithostatic, but magma pressures that deviate significantly from lithostatic are likely. For example, a dike typically requires internal pressure that exceeds lithostatic pressure and the tensile strength of the surrounding rock to propagate (Lister and Kerr, 1991), whereas an explosive eruption through an open conduit can result in large underpressures (e.g. Mason *et al.*, 2006). Significant disequilibrium is also possible for fast flows so that kinetics have to be taken into account. If flows are at equilibrium, however, the solubility law given by (17.1) can be used for any pressure assumption.

17.1.2 Magma flow dynamics

Magma ascends through the Earth's crust by means of dikes, which are sheet-like igneous intrusions typically several centimeters to meters or tens of meters (rarely several hundreds of meters) in thickness and several kilometers (rarely several hundreds of kilometers) in extent (Pollard, 1987). The present study considers a 1 m-width and a 1–10 km lateral extension as reasonable average dimensions for basaltic dikes (Lister and Kerr, 1991; Rubin, 1995). Magma fluxes can range from 1 $\mathrm{m^3\,s^{-1}}$, an average replenishment rate for the summit reservoir at Kilauea volcano, Hawaii (Rubin and Pollard, 1987), to 10^6 m^3 s^{-1}, such as may be appropriate to very high volumetric flow flood basalt eruptions (Swanson *et al.*, 1975; Wilson and Head, 1981). An average magma flux of 10^3 m^3 s^{-1} would correspond to an average magma ascent rate of 1 m s^{-1} through a 1 m-wide, 1 km-long dike.

Magma ascent through dikes is mainly driven by magma buoyancy, initially determined by magma composition and ultimately controlled by volatile exsolution, which becomes the dominant control at shallower depths. A key fluid dynamical parameter for magma flow is the Reynolds number, $Re = \rho u L/\mu$, which represents the ratio of viscous to inertial forces (u is the flow velocity and L is a typical length scale such as dike thickness). Magma flow is laminar if $Re << 10$, and the flow is considered to become turbulent when the Reynolds number exceeds a critical value of ~ 1000 (Lister and Kerr, 1991). In most cases, magma flow is laminar with a Reynolds number of ~ 1 for basaltic magma with viscosity of 1000 Pa s and density of 2750 kg m^{-3} flowing at a rise velocity of 1 m s^{-1} in a 1 m-wide dike. However, flows that involve magmas of much lower viscosity or higher magma ascent rates, such as during flood basalt eruptions, may become turbulent (Huppert and Sparks, 1985).

An important question is whether exsolved volatile bubbles are uniformly distributed throughout the magma, forming a uniform bubbly mixture, or whether phase separation occurs, which would strongly modify the flow behavior. Two-phase flow regimes range, in order of increasing bubble content and flow explosivity, from: bubbly flows; to slug flows, where bubbles coalesce into larger gas pockets; to annular flows, where gas flows in the center of a dike or conduit while the fluid phase flows on its periphery; to dispersed flows, where fragmented magma is carried by gas flow (Wallis, 1969; Jaupart, 2000; Slezin, 2003; Figure 17.1). Although magma flow will evolve through these different regimes as the bubble content increases, how magma flows change from one regime to another is still not fully understood. The different two-phase flow regimes depend on various parameters that include, but are not restricted to, bubble contents, flow rates, and flow geometries (Wallis, 1969). A reasonable assumption is to consider that deeper in a basaltic system, bubbles are well mixed due to low volumetric concentration, the relatively small size of the bubbles, the relatively low viscosity of basaltic melts, and the effects of magma convection (Phillips

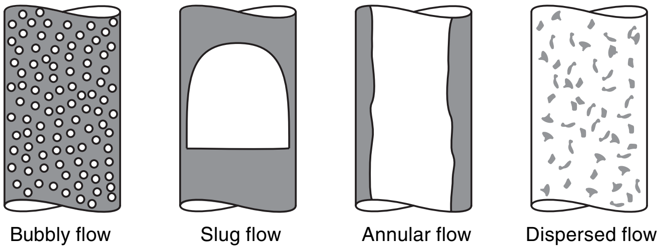

Fig. 17.1 The different flow regimes experienced by two-phase flows, going from bubbly flow to dispersed flow as both gas content and flow explosivity increase.

and Woods, 2001). As we shall show, the geometry of the magmatic system provides a strong control on bubble segregation from the melt, so an appropriate starting condition is to assume exsolved gas bubbles are uniformly distributed throughout the melt.

17.2 Modeling magma–repository interaction

17.2.1 Transient flows

The initial interaction with repository drifts involves the transient case where a magma-filled dike propagates and intersects a drift; however, it is unknown whether this magma will be degassed. Degassed lava emerges early in some basaltic eruptions and can be associated with simultaneous explosive activity. As mentioned previously, gas segregation processes are not understood well enough to determine whether the magma that first flows into a drift will be degassed. Thus, both end-member cases should be considered to bound possible interactions. Lejeune *et al.* (Chapter 18, this volume) consider the degassed case through laboratory experiments and theoretical analysis. Here we consider the explosive end-member where the magma and gas have not segregated.

An explosive flow is expected for the interaction of rapidly decompressing gas-rich magma rising in a dike with an underground drift structure. Repository drifts are usually proposed to be maintained at atmospheric pressure (Rosseau *et al.*, 1999), while at the potential Yucca Mountain repository depths of 200–300 m, the magma pressure just behind the tip of a dike is estimated to be typically 10–20 MPa, based on the lithostatic pressure and the fluid pressure required to drive a fracture at the dike tip (Pollard, 1987; Lister and Kerr, 1991; Woods *et al.*, 2002). When the dike intersects the drift, the magma will rapidly decompress, and at the relatively high water contents measured for Lathrop Wells basalts of up to 4.6 wt.% (Nicholis and Rutherford, 2004), this decompression will be explosive (Blackburn *et al.*, 1976), assuming that the gas has been retained during ascent.

A quantitative model of the process of magma decompression into a subsurface horizontal drift was proposed by Woods *et al.* (2002). On decompression, volatile exsolution within the magma in the dike and the drift will cause the magma to expand and accelerate, and if this process occurs sufficiently rapidly, the magma will fragment into a two-phase mixture of vesicular magma and gas. Woods *et al.* (2002) modeled this flow as a one-dimensional homogeneous mixture of magma and gas in a coordinate frame that was continuous for the flow from the dike into the drift (Figure 17.2). The cross-sectional area was assumed to vary smoothly between the dike and drift, and the flow was assumed to remain isothermal during volatile exsolution due to the high thermal inertia of the magma.

The motion of the magma–gas mixture can be described in terms of its averaged velocity, u, and averaged density, ρ, at position x, at pressure P and at time, t, leading to the equation for the conservation of momentum,

$$\rho\left(\frac{\partial u}{\partial t}+u\frac{\partial u}{\partial x}\right)=-\frac{\partial P}{\partial x}-fu-\rho g G(x) \tag{17.2}$$

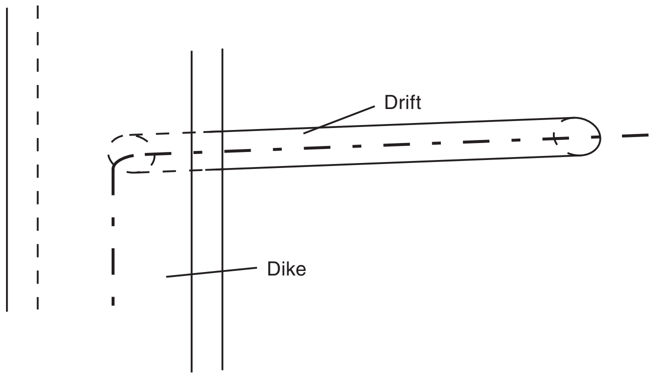

Fig. 17.2 The coordinate frame used in the one-dimensional simulations of Woods *et al.* (2002).

where f is a drag coefficient, g is the acceleration due to gravity and $G(x)$ has value 1 in the vertical dike and 0 in the horizontal drift. The terms on the left-hand side describe the inertia of the magma–gas mixture, and the terms on the right-hand side represent the pressure gradient in the flow, the resistance to motion due to flow against the walls of the dike or drift, and the buoyancy forces, respectively. The drag coefficient was parameterized as

$$f = \frac{\alpha\mu}{D^2} + \frac{2C\rho|\mu|}{D} \tag{17.3}$$

where α is a coefficient with value 12 for a two-dimensional dike and 8 for a cylindrical drift, D is dike width or drift diameter and C is the turbulent-drag coefficient. The first term on the right-hand side is the viscous drag, and the second term is the turbulent drag.

The equation of conservation of momentum was coupled with an equation for mass conservation,

$$\frac{\partial(A(x)\rho)}{\partial t} + \frac{\partial(A(x)\rho u)}{\partial x} = 0 \tag{17.4}$$

where $A(x)$ is the cross-sectional area of the dike or drift, and an equation for the bulk density of the magma–gas mixture (based on the perfect gas law),

$$\frac{1}{\rho} = \frac{n(P)RT}{P} + \frac{(1-n(P))}{\rho_l} \tag{17.5}$$

where $R = 462\,\mathrm{J\,kg^{-1}\,K^{-1}}$ is the gas constant for H_2O, T is the (constant) temperature, and $n(P)$ is the exsolved gas mass fraction given by the solubility law (17.1).

For their model simulations, Woods *et al.* (2002) assumed basaltic values $\mu = 10\,\mathrm{Pa\,s}$, $\rho = 2600\,\mathrm{kg/m^{-3}}$, a water content of 2 wt.% and $C = 0.01$. The results of a typical simulation for a dike intersecting a drift and remaining open are shown in Figure 1 in Woods *et al.* (2002). Initially, the magma–gas mixture rapidly expands as a rarefaction wave propagates back into the dike through the magma, and volatiles are exsolved. The expanding mixture accelerates along the drift, reaching speeds of tens to hundreds of meters per second, with the density decreasing as the pressure falls. Air is displaced and compressed ahead of the magma–gas mixture, and as a result, a shock forms in the air and moves down the drift at speeds of several hundreds of meters per second. If the drift is closed at its ends, then the shock is reflected when it reaches the end of the drift, increasing its amplitude by an order of magnitude. The reflected shock recompresses the magma–gas mixture, and a region of higher pressure, up to a few MPa, is formed in the drift. If the drift is open ended, the flow adjusts to a steady regime within seconds once the drift system is completely filled (Woods *et al.*, 2002).

Dartevelle and Valentine (2005) further investigated the eruption scenario proposed by Woods *et al.* (2002) using the GMFIX multiphase numerical model (Dartevelle, 2004). This model allowed the properties of each phase (pyroclasts and gas) to be determined in a two-dimensional Cartesian frame with full time-dependence, relaxing the assumption of homogeneous flow made by Woods *et al.* (2002). The results of a simulation corresponding to the intersection of an overpressurized dike containing basalt with 1 wt.% water with a drift at atmospheric pressure are shown in their Figure 1 (Dartevelle and Valentine, 2005). About $30-35\%$ of the magma-gas mixture flows into the drift, forming a shock that propagates into the drift at speeds of about $200\,\mathrm{m\,s^{-1}}$. The following flow forms a low-density current that flows along the drift roof at speeds of about $120\,\mathrm{m\,s^{-1}}$. If the end of the drift is closed, the shock is reflected and weakens through interaction with the following gas flow before interacting with the current of pyroclasts and ash at a time of 1.10 s. On reaching the closed end of the drift, the current is concentrated in density and reflected to form a dense current that flows along the base of the drift. When the dense return flow reaches the dike, some of the material is entrained into the rising flow and reaches the surface, while some is recirculated back into the drift.

Both Woods *et al.* (2002) and Dartevelle and Valentine (2005) investigated scenarios where there are secondary openings in the drift due to the presence of a further dike and found that there is little difference to the flow patterns and velocities and pressures generated. Both studies show the generation of high-speed shocks due to the initial decompression of the magma–gas mixture into the drift, although the shock amplification on reflection from the closed end of the drift observed by Woods *et al.* (2002) is not recognized in the simulations of Dartevelle and Valentine (2005). The formation of high-pressure regions in the magma–gas flow has important implications for the potential disruption of waste containers and transport of small fragments of spent nuclear fuel, as discussed further in Section 17.2.3.

We are aware that other models have been presented in various reports on igneous consequences at Yucca Mountain by different panels and bodies. We have not referred to this work, which has not been subject to peer review. However, the results of such studies all confirm that fast explosive flows will occur if volatile-rich basaltic magma is rapidly decompressed into tunnels or drifts.

The only reported natural example of the interaction of basalt with an analogous man-made structure occurred as an eruption along a geothermal borehole during the 1977 Krafla eruption (Larsen *et al.*, 1979). The borehole was 10 cm in diameter and 1138 m in length. The eruption involved an explosive Strombolian jet, lasted 20 minutes and erupted a volume of 26 m^3. In the context of potential repository interactions, this example is important because it shows that basalt magma can flow along a hole that has a cross-sectional area two orders of magnitude smaller than a radioactive waste repository drift. This case shows that cooling during magma flow to form a quenched layer is not significant, so models that do not account for cooling reasonably simulate the pertinent processes.

17.2.2 Steady-state flows

Following the initial transient decompression of the gas-bearing magma into the drift, the flow will adjust to a steady state within seconds to hours depending on whether magma flow is diverted along the drift or is limited to the main dike if access drifts are backfilled with crushed rocks (Woods *et al.*, 2002; Dartevelle and Valentine, 2005). If steady-state magma flow is established in the drift, Woods *et al.* (2002) calculated that magma will flow past the waste containers with steady speeds of $\sim 10\,\mathrm{m\,s^{-1}}$. Waste containers will experience considerable thermal stress from the magma and gradually heat by thermal conduction and, for times greater than $\approx 1000\,\mathrm{s}$ (based on diffusion of heat into the waste containers), they will become deformable and may break open. If the end of the drift remains closed, magma flow will be limited to the drifts directly intersected by the main dike; but basaltic magma will nevertheless fill the drift. In both cases, magma pressure in the repository will ultimately decrease to be close to lithostatic (Woods *et al.*, 2002).

This latter result is consistent with observations of natural volcanic systems. It is commonly observed that many basaltic eruptions tend to become less explosive with time. Initial basaltic eruptions occur explosively along fissures, typically in Strombolian-style fire fountains. Within hours to a few days, activity focuses onto a progressively restricted number of vents along the fissures; tephra plumes form, along with subordinate volumes of lava (Thorarinsson, 1969; Fedotov and Markhinin, 1983; Macdonald *et al.*, 1983). There is a general tendency for such eruptions to become less explosive with time and for lava to become an increasingly dominant product. However, observations of eruptions such as Eldfell volcano (Iceland) in 1973 show that even at the very beginning of an eruption, explosive flow of gas rich magma and discharge of degassed lava occur simultaneously. The interaction of a dike with an underground drift is therefore likely to involve magma flow of decreasing intensity. Basaltic magma can fill the drift, and subsequent magma circulation will depend on processes of gas segregation within the drift (Menand and Phillips, 2007a). Moreover, as the eruption proceeds, magma flow can be sustained for days to weeks in the vertical dike; for example, the great Tolbachik basaltic fissure eruption of 1975–1976 lasted for more than one and a half years (Fedotov and Markhinin, 1983). Over these timeframes, the dike may increase in size and change from a planar cross-section to a more circular cross-section owing to mechanical and thermal erosion as well as solidification of the dike in areas away from the focused flow (Macdonald *et al.*, 1983; Bruce and Huppert, 1990).

At shallow crustal depths (< 500 m) typical for repository drifts, magma volatiles are very likely to exist as exsolved bubbles. For instance, initial water contents of basalts that have erupted in the vicinity of Yucca Mountain range from 1.9 wt.%–4.6 wt.% (Nicholis and Rutherford, 2004) and at a depth of 300 m, a basaltic magma with 4.6 wt.% initial water will have exsolved 3.8 wt.% of its water (Holloway and Blank, 1994), which would correspond to volumetric gas fractions in the range of 70–90% at that depth in equilibrium (Menand *et al.*, 2008). The presence of exsolved bubbles as well as the amount of water that remains dissolved will strongly affect the density and viscosity of the basalts. Furthermore, there may be a range of bubble volumetric contents depending on exsolution at greater depths and gas loss during ascent. The amount of exsolved gas in magma within the drift will determine the nature and strength of magma circulation in the drift.

Menand and Phillips (2007a; 2007b) investigated gas segregation in a magma-filled drift intersected by a vertical dike using analog experiments. The apparatus consisted of a glass recirculating flow loop with a vertical mounting section (to simulate the vertical dike) connected to a horizontal section (to simulate the drift; Figure 1 in Menand and Phillips (2007a)). Electrolysis of the recirculating flow was used to simulate low volumetric gas fractions ($< 10\%$), producing micrometric bubbles in viscous mixtures of water and golden syrup. These low gas fractions correspond to the situation where magma has lost a large proportion of its gases at some depth greater than that of the repository, or during the latest waning stages of an eruption. To simulate higher volumetric gas contents, golden syrup was aerated before its injection into the recirculating flow loop, leading to volumetric gas fractions as high as 40%.

The experiments of Menand and Phillips (2007a) at low gas fractions ($< 10\%$) show that exsolved bubbles induce a buoyancy-driven exchange flow between the dike and the drift, whereby bubbly fluid flows from the dike into the drift as a viscous gravity current (Figure 17.3; Figure 3 in Menand and Phillips, 2007a). This exchange flow is slow enough that bubbles in the drift have time to rise, segregate from the fluid, and accumulate as foam at the top of the drift in conjunction with the accumulation of degassed fluid at the base of the drift. The maximum distance $L_{\max}$ that the gravity current can travel corresponds to the point where all bubbles have risen to the top of the side arm,

$$L_{\max} = \frac{D^2}{d}\left(\frac{12c}{1-c}\right)^{\frac{1}{2}} F(c) \tag{17.6}$$

where D is the drift diameter, d is the average bubble diameter, c is the volumetric bubble concentration, and F is a function of c which has a value ~ 0.1 (Menand *et al.*, 2008). Ultimately, a steady state is reached, whereby influx of bubbly fluid into the drift is balanced by outward flux of lighter foam and denser degassed fluid back into the dike. Moreover, gas segregation processes and rates appear to be independent of moderate changes in magma supply rates in the dike.

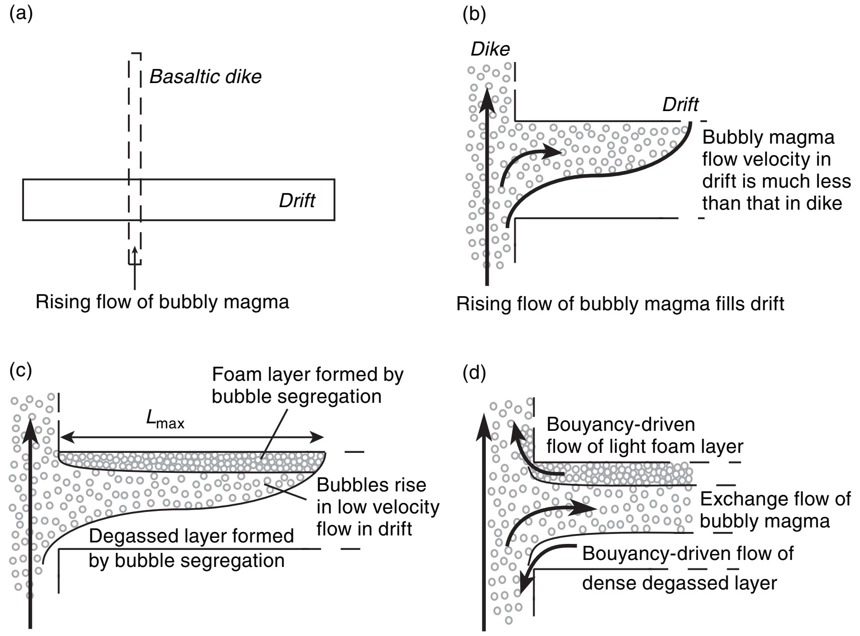

Fig. 17.3 Schematic illustration of magma flow in an interconnecting dike and drift. (a) System geometry. (b) Initial condition with the drift filling with bubbly magma from the dike. (c) Bubble segregation within the drift leads to the formation of a foam layer at the top of the drift and a degassed layer at its floor. (d) Steady-state exchange flows set up by bubble segregation.

The laboratory experiments at high gas fractions showed that the same processes occurred as for lower volumetric gas fractions, with the increased viscosity and reduced density contrast increasing the timescale for gas segregation (Menand and Phillips, 2007b; Menand *et al.*, 2008). The amount of foam that collects at the top of the drift is determined by the balance between the amount of bubbles rising from the bubbly fluid within the drift and the outward flux of foam that leaves it; the steady-state foam thickness $h(x)$ can be written as the product of a characteristic thickness H and a shape function $f(x)$, $h(x) = Hf(x)$, with

$$H = \left[\frac{c(1-c)^{\frac{7}{2}} d^2 L_{\mathrm{max}}^2}{\epsilon(1-\epsilon)^{\frac{5}{2}}(\epsilon - c)}\right]^{\frac{1}{4}} \qquad f(x) = \left(\frac{x}{L_{\mathrm{max}}} - \frac{x^2}{4L_{\mathrm{max}}^2}\right)^{\frac{1}{4}} \tag{17.7}$$

where ϵ is the volumetric gas fraction of the foam and x is the position along the foam (the origin is fixed at the dike–drift junction). The foam thickness is limited by the packing of the bubbles in the foam: as the foam thickness increases, bubbles deform and can coalesce, leading to the collapse of the foam. The maximum, critical thickness H_{c} the foam can sustain before collapsing is (Jaupart and Vergniolle, 1989; Menand *et al.*, 2008)

$$H_c = \frac{4\sigma}{\epsilon \rho_l g d} \tag{17.8}$$

where σ is the surface tension between the melt and the gas trapped in the bubbles of the foam. The steady-state foam thickness H described by (17.7) can develop only if it is smaller than the critical thickness H_c. If this is not the case, accumulation of bubbles at the top of the drift will lead to repeated collapse of the foam.

Two timescales are associated with this gas segregation process, and both are controlled by the rise of bubbles within the drift. The first one is the time needed by the bubbles to rise the diameter of the drift, D, and accumulate as the foam

$$T_b = \frac{12\mu_l D}{\rho_l g d^2 (1-c)^{\frac{7}{2}}} \tag{17.9}$$

The second timescale is the time needed for the steady-state foam to fully develop

$$T_f = \frac{12\mu_l L^{\frac{1}{2}}}{\rho_l g d^{\frac{3}{2}}} \left[\frac{\epsilon^3}{c^3 (1-c)^{\frac{21}{2}} (1-\epsilon)^{\frac{5}{2}} (\epsilon - c)} \right]^{\frac{1}{4}} \tag{17.10}$$

Gas segregation occurs in the drift if these two timescales are smaller than the timescale for cooling and solidification of the magma, T_s. Menand and Phillips (2007a; 2007b) based their calculations on cooling by pure conduction so that

$$T_s = \frac{D^2}{16\kappa\lambda^2} \tag{17.11}$$

where κ is the magma thermal diffusivity and the thermal constant, λ, depends on the temperature difference between the magma and surrounding rocks (Turcotte and Schubert, 1982).

Gas segregation leads to a steady-state recirculation of fluid in the drift with exchange of bubbly fluid with foam and degassed fluid, and this recirculation is characterized by a volumetric flux

$$Q = \frac{(1-c)^{\frac{7}{2}} \rho_l g d^2 D L}{12\mu_l \epsilon} \tag{17.12}$$

Up-scaled to the potential Yucca Mountain repository conditions, the results suggest that steady-state gas segregation would occur within hours to hundreds of years depending on the viscosity of the degassed magma, $10-10^5$ Pa s, and the average size of exsolved gas bubbles, 0.1–1 mm (right-hand plot of Figure 4 in Menand *et al.*, 2008). For comparison, Menand *et al.* (2008) give a solidification timescale by pure conduction of about 3 months for a 5 m-diameter drift; note that this estimate will be a lower bound due to circulation in the drift and replenishment with hotter magma as the eruption proceeds.

Using (17.12), Menand *et al.* (2008) calculated the fluxes that would be associated with gas segregation in a 5 m-diameter drift for different magma viscosities (right-hand plot of Figure 6 in Menand *et al.*, 2008). These range from 1 $\mathrm{m^3\,s^{-1}}$ for the less viscous magmas to $10^{-8}\,\mathrm{m^3\,s^{-1}}$ for the most viscous degassed magmas. Gas segregation is likely to be in an unstable foam collapse regime, with the foam accumulated by gas segregation at the top of the drift reaching a few centimeters in thickness before its collapse due to bubble coalescence (Jaupart and Vergniolle, 1989; Menand *et al.*, 2008). The relative proportion of erupted degassed magma, which could potentially transport radioactive waste material towards the surface, depends on the value of the dike magma supply rate relative to the value of the gas segregation flux; with violent eruption of gas-rich as well as degassed magmas at relatively high magma supply rates, and eruption of mainly degassed magma by milder episodic Strombolian explosions at relatively lower supply rates (Menand and Phillips, 2007a). Menand *et al.* (2008) calculated that, depending on the average size of exsolved gas bubbles, the critical magma supply rate delimiting these two eruptive regimes would range from $10^{-4}-1\,\mathrm{m^3\,s^{-1}}$ for magma viscosity of ≈ 10 Pa s to $10^{-8}-10^{-4}\,\mathrm{m^3\,s^{-1}}$ for magma viscosity of $\approx 10^5$ Pa s.

Menand and Phillips (2007a) also applied these general principles to degassing and eruption processes at Stromboli volcano, Italy. The results and their implications are consistent with a variety of independent field data. Gas segregation at Stromboli likely occurs in a shallow reservoir of sill-like geometry at a 3.5 km depth with bubbles of exsolved gas 0.1–1 mm in diameter. Menand and Phillips (2007a) also calculated that the transition between Strombolian activity, erupting gas-poor, highly porphyritic magmas, and violent explosions that also erupt gas-rich, low porphyritic magmas would correspond to a critical magma supply rate of $\sim 0.1-1\,\mathrm{m\,s^{-1}}$.

If magma flows along the drift, either because the drift is open-ended or because magma pressure in the repository is able to drive open a new fracture in the surrounding rocks, steady-state flow will be characterized by speeds of $\sim 10\,\mathrm{m\,s^{-1}}$ (Woods *et al.*, 2002; Dartevelle and Valentine, 2005), which corresponds to steady-state fluxes of $\sim 100\,\mathrm{m^3\,s^{-1}}$ in a 5 m diameter drift. These fluxes are at least two orders of magnitude greater than fluxes induced by gas segregation processes. In this scenario, gas segregation processes are unlikely to affect the flow as they would occur on timescales much longer than those needed for magma to flow along the drift. Therefore, the steady-state flow pattern would depend on the magma supply rate from the dike.

17.2.3 Magma flow dynamics and cooling within repository drifts

As magma flows up the dike and along the drift, heat will be advected by the flowing magma and will simultaneously be lost by conduction into the colder surrounding rocks and waste containers. Competition between heat advection and conduction can affect magma dynamics, as investigated quantitatively by Bruce and Huppert (1989; 1990) and Petford *et al.* (1993). During the initial stage of magma flow up a dike, magma cools in response to the lower temperature of the surrounding rock walls. Subsequently, the continual supply of magma transfers heat into the solid walls. Magma cooling within the dike is typically confined to a thin thermal boundary layer adjacent to the dike walls, and the width of this thermal boundary layer increases with the length of the dike (Carrigan, 2000). Whether the dike becomes blocked or remains open is determined by the balance between the rate of solidification of the magma (dike closure) and that of melting of the walls (dike opening). These rates are in turn controlled by the magnitude of the latent heat (released during solidification and consumed during melting) as well as the difference between the heat supplied to the walls by the thermal boundary layer and that conducted into the surrounding rocks. Bruce and Huppert (1989; 1990) and Petford *et al.* (1993) showed that a critical width

$$w_c = 1.5 \left[\frac{c_{\text{heat}}(T_w - T_\infty)^2}{L_{\text{heat}}(T_m - T_w)} \right]^{\frac{3}{4}} \left(\frac{\mu \kappa H_{\text{dike}}}{\Delta \rho g} \right)^{\frac{1}{4}}$$

exists, where c_{heat} is the specific heat, L_{heat} is the latent heat, T_m is the initial magma temperature, T_w is the temperature of the walls, T_∞ is the far field temperature of the rocks, H_{dike} is the dike length, and $\Delta\rho$ is the density difference between magma and rocks. If the dike is thinner than this critical width, it will solidify before it can transport a significant volume of magma to the surface. When applied to basaltic dikes, these analyses show that dikes must be thicker than ~ 0.5 m if they are to reach the surface before solidifying completely; this prediction agrees with field observations (Wada, 1994; Kerr and Lister, 1995; Wada, 1995). Three-dimensional analyses suggest that magma flowing through an initially long surface fissure will tend to localize to a number of isolated vents (Bruce and Huppert, 1989; 1990), as observed during basaltic fissure eruptions.

Insights about the cooling of magma as it flows within a drift can be obtained from studies of horizontal igneous intrusions (sills) and lava tubes. Holness and Humphreys (2003) observed that rocks surrounding the Traigh Bhàn na Sgùrra sill on the Isle of Mull, Scotland, displayed thermal aureoles up to 4 m thick around that sill, which taken in conjunction with the spatial distribution of crystals within the sill demonstrate that progressive focusing of magma flow into the wider parts of the sill was sustained for up to five months. Lava tubes, which form when the lava flow surface solidifies as a crust while hot lava continues to flow beneath, are a common feature of basaltic lava flow fields. If the flow rate is sufficiently high, lava can thermally erode its way into the surrounding solidified lavas (Francis and Oppenheimer, 2004). Lava tubes can extend significant distances because lava is well insulated by the tube crust and loses very little heat by conduction or radiation. Lava tubes up to 20 m in diameter and > 100 km in length have been observed in Queensland, Australia; these would have enabled the lava flow fields to develop over several months to years despite involving overall effusion rates perhaps as low as $10\ \text{m}^3\ \text{s}^{-1}$ (Stephenson *et al.*, 1998). The Krafla borehole eruption also shows that cooling may not be a major factor in the initial filling of a tunnel.

Precise assessment of magma cooling while flowing in a drift partially obstructed by waste containers is difficult because of the complex three-dimensional geometry of the flow field. Nevertheless, a conservative estimate can be made by assuming conductive cooling of the magma through the wall of the drift, which gives about three months for magma to solidify by conduction (Menand *et al.*, 2008). This estimate is comparable to the timescales associated with lava flows within sills and lava tubes and suggests that magma could remain fluid for several months, at least in some part of the drift. For comparison, based on the diffusion of heat into metal waste containers, Woods *et al.* (2002) calculated that the waste containers will become deformable and may break open for times $\gtrsim 1000\,\mathrm{s}$ ($< 1\,\mathrm{h}$). Improved estimates for potential magma cooling rates within repository drifts and their effect on flow dynamics, if warranted, would require three-dimensional numerical simulations.

If transient or steady magma flow occurs through radioactive waste repository drifts, possible consequences include the generation of waste container motion due to drag exerted by the flowing magma, heating and possible disruption of the waste containers, and transport of the container contents. Woods *et al.* (2002) estimate the drag force acting on the waste containers

$$F_\mathrm{d} = C_\mathrm{d}\rho u^2 A \tag{17.13}$$

where A is the area of the face of the container perpendicular to the flow direction, and C_d is the drag coefficient, which is order unity for these flow conditions. For steady flow conditions, Woods *et al.* (2002) estimated the ratio of the drag force to container weight to be typically of order or smaller than $0.1-1.0$, suggesting that the containers may be displaced down the drift. However, the flow is too weak to keep the containers in suspension, and any container motion is likely to be relatively slow. Later calculations of the flow conditions following the intersection of a basaltic dike with a repository drift conducted by Dartevelle and Valentine (2005) were made with smaller dike widths and resulted in much lower flow velocities than those calculated by Woods *et al.* (2002). In Dartevelle and Valentine's calculations, the drag force was insufficient to generate waste container motion; furthermore, because the waste containers will be placed in a line along the length of the repository drift, only the first container will feel the drag force estimated by Woods *et al.* (2002). Subsequent containers will feel a lower drag force in the wake flow behind the first container – the same effect exploited by the formations adopted by migrating birds and racing cyclists.

To the extent that waste containers can be disrupted by the combined effects of magma flow and heat transfer, waste container contents can possibly be transported in the magma flow through the drifts and to the surface. Although the exact contents of waste containers will vary, current models typically assume that the waste material is spent nuclear fuel that has been fragmented by disruptive processes in the size range $10-500$ microns (CRWMS M&O, 2000) with a density of $\approx 10\,000\,\mathrm{kg\,m^{-3}}$. Erosive transport of small particles by turbulent stream flows has been widely studied in sedimentology, and the key parametric relationship between the Shields number θ (ratio of shear stress acting on a particle to its weight) and particle Reynolds number (the ratio of inertial to viscous forces acting on a particle in the flow) has been empirically determined for turbulent flow conditions (Figure 2 in Miller *et al.*, 1977). However, until recently, there has been little study of particle transport under viscous flow conditions, as would be appropriate for magma flow.

The experimental and theoretical studies of Charru *et al.* (2004) provide a framework for estimating the transport properties of small particles in a uniformly sheared viscous flow. The experiments were conducted in a rotating annular viscous flow, to achieve steady flow over long times and under conditions in which the secondary velocity generated by centrifugal forces was negligible compared to plane Couette flow in the channel. Direct observations showed that small particle motion took the form of a series of saltation "flights," whose duration τ was found to be independent of shear rate γ, $\tau \approx 15\, d_\mathrm{p}/v_\mathrm{S}$, where d_p is the particle diameter and v_S is the Stokes settling speed of the particle. The mean particle velocity $\bar{u}$ was found to depend linearly on the shear rate, $\bar{u} \approx 0.1\, \gamma d_\mathrm{p}$. The particle flow rate Q_p was found to have a quadratic dependence on shear rate,

$$Q_\mathrm{p} \approx 0.1\gamma(0.47/d_\mathrm{p})(\theta - 0.12). \tag{17.14}$$

Erosive transport of small particles by fluid flow is a complex process that depends on interaction of the particles and fluid, and the particles with each other. Further work is required to understand the flow conditions representative of potential magma–waste repository interaction and particle transport under these conditions. However, the scaling arguments presented here form a fundamental framework for estimating transport properties of high-density particles in viscous magma flow. This can be illustrated with simple estimates for magma properties for basalts in the Yucca Mountain region (density of 2750 kg m^{-3}, viscosity of 10 Pa s, 70 vol.% of degassed bubbles 1 mm in diameter), assuming in this example that the magma flow pattern corresponds to flow through a circular cross-section drift. The presence of waste containers in the drift will complicate the flow patterns (e.g. create local eddies that can affect Couette flow dynamics), but the principles illustrated here should hold. For a maximum average velocity of degassed magma in a 5 m-diameter and 1 km-long drift of about 10^{-3} m s^{-1} (using (17.12) for the flux) and assuming a standard Poiseuille flow profile for viscous flow in a cylindrical cross-section (Schlichting, 1960), the maximum shear rate 0.1 m above the base of the drift is approximately 7.5 s^{-1}. Using the range of particle sizes and densities for fragments of spent nuclear fuel given previously, the maximum Shields number is $\sim$ 2 for this viscous flow (Charru *et al.*, 2004), corresponding to a particle flow rate of $\sim$ 1500 particles per unit drift width per second, (17.14). This particle flow rate is estimated for the largest fragments of spent nuclear fuel 500 μ in diameter. Particle transport from potentially disrupted waste containers will be limited by the volume of particles available to the flow.

Concluding remarks

The models discussed here provide some first-order constraints on the interaction of basaltic magma with an open-drift system that is the basis for some potential radioactive waste repositories. A first-order conclusion is that potentially intersected drifts rapidly will be filled by magma. This will be the case irrespective of whether the magma is explosive due to the exsolution and expansion of gases or degassed as a consequence of as yet poorly understood gas segregation processes during ascent. Lejeune *et al.* (Chapter 18, this volume) have presented the degassed end-member, and we present the explosive case. At typical eruption rates of monogenetic basaltic eruptions ($10-1000\,\mathrm{m}^3\,\mathrm{s}^{-1}$), a drift can be filled in a few tens of seconds for the explosive case and a few tens of minutes for the degassed case. Although the magma will form a thin quench on contact with the drift walls and containers, estimates of cooling timescales indicate that these effects are small and will not inhibit the filling of the drifts. This view is verified by the observation that basalt flowed along a geothermal borehole for hundreds of meters despite having a volume-to-surface area ratio that is two orders of magnitude smaller than a repository drift.

Characterizing container disruption is complex. In addition to considering the state of magma upon entry into a drift, disruption is also dependent on the design and properties of container materials, particularly in relation to response to impacts and heating. Such considerations go well beyond the scope of this paper, but some inferences can be made. Container failure could occur due to prolonged heating and pressure effects. Heating weakens the containers, making them more likely to fail, and the interior pressure of the container is expected to increase due to heating of the gases. Simultaneously, the pressure in the surrounding magma after a drift has been filled may increase substantially to lithostatic values or above. For example, if an eruption is occurring, the magma-static pressure at a 300 m-deep repository would be above 8 MPa for a column of degassed magma. In response to the combined thermal and mechanical stresses, the container might be deformed or broken open, and the contents of the affected containers might be released and transported to the surface by entrainment in the erupting column.

If a subvolcanic conduit developed through a drift, waste that is directly entrained in the erupting conduit could be transported to the surface. Two additional scenarios have been investigated that consider the ability of magma to entrain waste from drifts potentially intersected by a dike. Woods *et al.* (2002) described a "dogleg" scenario in which the dike intersects a drift and a secondary fracture develops in a new location along the drift so that once the magma breaches the surface, the magma flows along the drift to connect the inlet dike with the outlet dike. Here, a second scenario is considered where the original supply dike continues to the surface and there is convective exchange between the magma in the drift and the magma flowing up the dike.

In this alternative scenario, Menand and Phillips (2007a; 2007b) infer from their experiments that, independently of moderate changes in the dike magma supply rate, gas segregation processes will occur in the drift and lead to a convective exchange of gas-rich foam and degassed magma flowing out of the drift and back into the dike with bubbly magma from the dike. Using the potential Yucca Mountain repository geometry as an example, flows will likely be in an unstable collapse regime with the gas-rich foam experiencing repeated collapse as it accumulates at the top of the drift. The length and timescales of the gas segregation processes are controlled by the rise of bubbles in the drift. The time required for steady-state gas segregation is estimated to range from hours to hundreds of years, depending on the average size of exsolved gas bubbles; and on the viscosity of degassed magmas, which depends strongly on the degree of water exsolution, cooling and crystallization. The associated magma flux is estimated to range from $1\,\mathrm{m}^3\,\mathrm{s}^{-1}-10^{-8}\,\mathrm{m}^3\,\mathrm{s}^{-1}$, depending on the magma viscosity and the size of exsolved gas bubbles. The relative proportion of erupted degassed magma depends on the value of the dike magma supply rate relative to that of the gas segregation flux. If magma is supplied at a higher rate, then gas-rich as well as degassed magmas are expected to be violently erupted; if the supply rate is lower, then mainly degassed magma would be erupted by milder episodic Strombolian explosions generated by the repeated collapse of the foam accumulated at the top of drifts.

A related matter is whether a potential magma flow could transport very dense waste particles. Based on estimates of magma fluxes in the initial stages of basaltic volcanic eruptions, it is unlikely that significant transport of intact waste containers would occur, regardless of whether the flow is unidirectional along the drift (Woods *et al.*, 2002; Dartevelle and Valentine, 2005) or recirculates within the drift (Menand and Phillips, 2007a; 2007b). In the event of waste-container disruption, estimates suggest that small fragments of spent nuclear fuel of the size and density used in current design calculations might be transported along the drift in a viscous saltation regime. Two-phase flows of this type have not been widely studied, although recent interest has established the key principles and identified transport regimes (e.g. Charru *et al.*, 2004). As outlined in this chapter, precise estimates of potential magma transport dynamics for laminar Couette flows will not become available until the exact configuration of disrupted waste containers and drift geometry can be better constrained, but the first-order estimates presented here suggest that even modest magma shear rates can initiate erosive motion of dense waste fragments along the base of a drift, irrespective of the precise geometric details. For the scenario of volcanic activity potentially interacting with a repository drift, the calculations indicate magma flows are capable of transporting small waste fragments along the drift and into the erupting conduit, with the possibility that this material could be subsequently transported to the surface and dispersed in explosive eruptions or effusive flows.

Further lines of investigation

The presence of engineered barrier systems and their additional thermal mass will likely affect the flow of magma within drifts and thus the thermal evolution of the system. Assessing how waste containers and barrier systems may affect heat transfer into the containers and the cooling rate of magma, as well as gas segregation processes within drifts, is complex and may warrant three-dimensional computational modeling.

Confidence in models for potential magma–drift interaction processes would benefit from improved knowledge of the petrological evolution of magmas in the shallow subsurface during dynamic eruptions (see Spera and Fowler, Chapter 8, this volume). This evolution will affect magma viscosity and the size of exsolved gas bubbles, which in turn will exert a strong influence on the fluxes and average velocities associated with gas segregation and convective exchange flow. Constraining the petrological evolution of magmas will improve estimates of the heat transfer and cooling rates during and after gas segregation, and thus the duration of potential magma exchange flow within drifts.

Further reading

White (1979) provides a particularly clear introduction to fluid mechanics with applications to engineering problems including flow in ducts, flow around immersed bodies and calculations of drag coefficients for various flow configurations. Analytical techniques for the treatment of two-phase flow problems as well as practical applications can be found in Wallis (1969). Integrating observation, theory and experimental studies, Sparks *et al.* (1997) provide a technical and complete reference to physical volcanology using historical volcanologic events as case studies.

Acknowledgments

This work benefited from fruitful discussions with Chuck Connor, Brittain Hill, Andrew Hogg and Gary Matson. This chapter was prepared to document work performed by the Center for Nuclear Waste Regulatory Analyses (CNWRA) and its contractors for the US. Nuclear Regulatory Commission (NRC) under Contract No. NRC-02-07-006. The activities reported here were performed on behalf of the NRC Office of Nuclear Material Safety and Safeguards, Division of High-Level Waste Repository Safety. This chapter is an independent product of the CNWRA and does not necessarily reflect the view or the regulatory position of the NRC.

References

Bechtel SAIC Company, LLC (2007). Characterize framework for igneous activity at Yucca Mountain, Nevada, ANL-MGR-GS-000002, Rev. 3. Las Vegas, Nevada: Bechtel SAIC Company, LLC.

Blackburn, E. A., L. Wilson and R. S. J. Sparks (1976). Mechanism and dynamics of Strombolian activity. *Journal of the Geological Society of London*, **132**, 429–440.

Blundy, J., K. Cashman and M. Humphreys (2006). Magma heating by decompression-driven crystallization beneath andesitic volcanoes. *Nature*, **443**, 76–80.

Bruce, P. M. and H. E. Huppert (1989). Thermal control of basaltic fissure eruptions. *Nature*, **342**, 665–667.

Bruce, P. M. and H. E. Huppert. (1990). Solidification and melting along dikes by the laminar flow of basaltic magma. In: Ryan, M. P. (ed.) *Magma Transport and Storage*. New York, NY: John Wiley, 87–101.

Carrigan, C. R. (2000). Plumbing systems. In: Sigurdsson, H. *et al.* (eds.), *Encyclopedia of Volcanoes*. San Diego, CA: Academic Press, 219–235.

Cashman, K. V. (1992). Groundmass crystallization of Mount St Helens dacite, 1980–1986 – a tool for interpreting shallow magmatic processes. *Contributions in Mineralogy and Petrology*, **109**, 431–449.

Charru, F., H. Mouilleron and O. Eiff (2004). Erosion and deposition of particles on a bed sheared by a viscous flow. *Journal of Fluid Mechanics*, **519**, 55–80.

CRWMS M&O (2000). Miscellaneous waste-form FEPs, ANL-WIS-MD-000009 Rev **00** ICN 01. Las Vegas, NV: Civilian Radioactive Waste Management System, Management and Operating Contractor.

Dartevelle, S. (2004). Numerical modeling of geophysical granular flows: 1. A comprehensive approach to granular rheologies and geophysical multiphase flows. *Geochemistry, Geophysics, and Geosystems*, **5**, Q08003, doi:10.1029/2003GC000636.

Dartevelle, S. and G. A. Valentine (2005). Early-time multiphase interactions between basaltic magma and underground openings at the proposed Yucca Mountain radioactive waste repository. *Geophysical Research Letters*, **32**, L22311, doi:10.1029/2005GL024172.

EPA (2001). Background information document for 40 CFR 197: Public health and environmental radiation protection standards for Yucca Mountain, NV, EPA 402-R-01-004. US Environmental Protection Agency, Air and Radiation.

Fedotov, S. A. and Ye. K. Markhinin (eds.) (1983). *The Great Tolbachik Fissure Eruption: Geological and Geophysical Data 1975–1976*. Cambridge; New York: Cambridge University Press.

Francis, P. and C. Oppenheimer (2004). *Volcanoes*. Oxford: Oxford University Press.

Giordano, D. and D. B. Dingwell (2003). Viscosity of hydrous Etna basalt: implications for Plinian-style basaltic eruptions. *Bulletin of Volcanology*, **65**, 8–14.

Hess, K.-U. and D. B. Dingwell (1996). Viscosities of hydrous leucogranitic melts: a non-Arrhenian model. *American Mineralogist*, **81**, 1297–1300.

Holloway, J. R. and J. G. Blank (1994). Application of experimental results to C–O–H species in natural melts. In: Carroll, M. R. and J. R. Holloway (eds.) *Volatiles in Magmas*, Reviews in Mineralogy 30. Washington, DC: Mineralogical Society of America, 187–230.

Holness, M. B. and M. C. S. Humphreys (2003). The Traigh Bhàn na Sgùrra Sill, Isle of Mull: flow localization in a major magma conduit. *Journal of Petrology*, **44**, 1961–1976.

Huppert, H. E. and R. S. J. Sparks (1985). Cooling and contamination of mafic and ultramafic magmas during ascent through continental crust. *Earth and Planetary Science Letters*, **74**, 371–386.

Jaupart, C. (2000). Magma ascent at shallow levels. In: Sigurdsson, H. *et al.* (eds.), *Encyclopedia of Volcanoes*. San Diego, CA: Academic Press, 237–245.

Jaupart, C. and S. Vergniolle (1989). The generation and collapse of a foam layer at the roof of a basaltic magma chamber. *Journal of Fluid Mechanics*, **203**, 347–380.

Kerr, R. C. and J. R. Lister (1995). Comment on "On the relationship between dike width and magma viscosity" by Yutaka Wada. *Journal of Geophysical Research*, **100**(B8), 15 541.

Kilburn, C. R. F. (2000). Lava flows and flow fields. In: Sigurdsson, H. *et al.* (eds.), *Encyclopedia of Volcanoes*. San Diego, CA: Academic Press, 291–305.

Lange, R. A. (1994). Application of experimental results to C–O–H species in natural melts. In: Carroll, M. R. and J. R. Holloway (eds.), *Volatiles in Magmas*, Reviews in Mineralogy 30. Washington, DC: Mineralogical Society of America, 331–369.

Larsen, G., K. Grönvold and S. Thorarinsson (1979). Volcanic eruption through a geothermal borehole at Ná mafjall, Iceland. *Nature*, **278**, 707–710.

Lister, J. R. and R. C. Kerr (1991). Fluid-mechanical models of crack propagation and their application to magma transport in dikes. *Journal of Geophysical Research*, **96**, 10 049–10 077.

Llewellin, E. W. and M. Manga (2005). Bubble suspension rheology and implications for conduit flow. *Journal of Volcanology and Geothermal Research*, **143**, 205–217.

Long, J. C. S. and R. C. Ewing (2004). Yucca Mountain: Earth-science issues at a geologic repository for high-level nuclear waste. Ânnual Review of Earth and Planetary Sciences. **32**, 363–401.

Macdonald, G. A., A. T. Abbott and F. L. Peterson (1983). *Volcanoes in the Sea: The Geology of Hawaii*. Honolulu: University of Hawaii Press.

Mason, R. M., A. B. Starostin, O. E. Melnik and R. S. J. Sparks (2006). From Vulcanian explosions to sustained explosive eruptions: the role of diffusive mass transfer in conduit flow dynamics. *Journal of Volcanology and Geothermal Research*, **153**, 148–165.

Massol, H., C. Jaupart and D. W. Pepper (2001). Ascent and decompression of viscous vesicular magma in a volcanic conduit. *Journal Geophysical Research*, **106**(B8), 16 223–16 240.

Melnik, O. and R. S. J. Sparks (1999). Nonlinear dynamics of lava extrusion. *Nature*, **402**, 37–41.

Menand, T. and J. C. Phillips (2007a). Gas segregation in dikes and sills. *Journal of Volcanology and Geothermal Research*, **159**, 393–408.

Menand, T. and J. C. Phillips (2007b). A note on gas segregation in dikes and sills at high gas fractions. *Journal of Volcanology and Geothermal Research*, **162**, 185–188.

Menand T., J. C. Phillips and R. S. J. Sparks (2008). Circulation of bubbly magma and gas segregation within tunnels of the potential Yucca Mountain repository. *Bulletin of Volcanology*, **70**, 947–960.

Miller, M. C., N. I. McCave and P. D. Komar (1977). Threshold of sediment motion under unidirectional currents. *Sedimentology*, **24**, 507–528.

Murase, T. and A. R. McBirney (1973). Properties of some common igneous rocks and their melts at high temperatures. *Geology Society of America Bulletin*, **84**(11), 3563–3592.

National Research Council (US) and F. L. Parker (1990). *Rethinking high-level radioactive waste disposal: a position statement of the Board on Radioactive Waste Management, Commission on Geosciences, Environment, and Resources, National Research Council*. Washington, DC: National Academy Press.

National Research Council (US) (2001). *Disposition of High-Level Waste and Spent Nuclear Fuel: The Continuing Societal and Technical Challenges.* Washington, DC: National Academy Press.

Nicholis, M. G. and M. J. Rutherford (2004). Experimental constraints on magma ascent rate for the Crater Flat volcanic zone hawaiite. *Geology*, **32**, 489–492, doi:10.1130/G20324.1.

NRC (2005). Integrated issue resolution status report NUREG-1762, 1(1). Washington, DC: US Nuclear Regulatory Commission.

Petford, N., R. C. Kerr and J. R. Lister (1993). Dike transport in granitoid magmas. *Geology*, **21**, 845–848.

Pinkerton, H. and R. S. J. Sparks (1978). Field-measurements of the rheology of lava. *Nature*, **276**, 383–385.

Pollard, D. D. (1987). Elementary fracture mechanics applied to the structural interpretation of dikes. In: Hall, H. C. and W. F. Fahrig (eds.) *Mafic Dyke Swarms*, Special Paper 34. St. Johns, Newfoundland: Geologic Association of Canada, 5–24.

Phillips, J. C. and A. W. Woods (2001). Bubble plumes generated during recharge of basaltic magma reservoirs. *Earth and Planetary Science Letters*, **186**, 297–309.

Rosseau, J. P., E. M. Kwicklis and D. C. Giles (1999). Hydrogeology of the undersaturated zone, North Ramp Area of the Exploratory Studies Facility, Yucca

Mountain, Nevada, Water-Resources Investigations Report 98B4050. Denver, CO: US Geological Survey.

Rubin, A. M. (1995). Propagation of magma-filled cracks. *Annual Reviews of Earth Planetary Sciences*, **23**, 287–336.

Rubin, A. M. and D. D. Pollard (1987). Origin of blade-like dikes in volcanic rift zones. In: Decker, R. W. *et al.* (eds.) *Volcanism in Hawaii*, Professional Paper 1350(2). US Geological Survey, Volcano Hazards Team, 1449–1470.

Schlichting, H. (1960). *Boundary Layer Theory*. New York, NY: McGraw-Hill.

Shaw, H. R. (1972). Viscosities of magmatic silicate liquids: an empirical method of prediction. *American Journal of Science*, **272**, 870–893.

Sisson, T. W. and G. D. Layne (1993). H_2O in basalt and basaltic andesite glass inclusions from four subduction-related volcanoes. *Earth and Planetary Science Letters*, **117**, 619–635.

Slezin, Yu. B. (2003). The mechanism of volcanic eruptions (a steady state approach). *Journal of Volcanology and Geothermal Research*, **122**, 7–50.

Smith, E. I. and D. L. Keenan (2005). Yucca Mountain could face greater volcanic threat. *Eos, Transactions of the American Geophysical Union*, **86**(35), doi:10.1029/2005EO350001.

Sparks, R. S. J. (1978). The dynamics of bubble formation and growth in magmas: a review and analysis. *Journal of Volcanology and Geothermal Research*, **3**, 1–37.

Sparks, R. S. J., J. Barclay, C. Jaupart, H. M. Mader and J. C. Phillips (1994). Physical aspects of magma degassing I. Experimental and theoretical constraints on vesiculation. In: Carroll, M. R. and J. R. Holloway (eds.) *Volatiles in Magmas*, Reviews in Mineralogy 30. Washington, DC: Mineralogical Society of America, 413–445.

Sparks, R. S. J., M. I. Bursik, S. N. Carey *et al.* (1997). *Volcanic Plumes*. Chichester: John Wiley and Sons.

Spera, F. J. (2000). Physical properties of magma. In: Sigurdsson, H. *et al.* (eds.) *Encyclopedia of Volcanoes*. San Diego, CA: Academic Press, 171–190.

Stephenson, P. J., A. T. Burch-Johnston, D. Stanton and P. W. Whitehead (1998). Three long lava flows in north Queensland. *Journal of Geophysical Research*, **103**(B11), 27 359–27 370.

Swanson, D. A., T. L. Wright and R. T. Helz (1975). Linear vent systems and estimated rates of magma production and eruption for the Yakima Basalt on the Columbia Plateau. *American Journal of Science*, **275**, 877–905.

Thorarinsson, S. (1969). The Lakagigar eruption of 1783. *Bulletin of Volcanology*, **33**, 910–927.

Turcotte, D. L. and G. Schubert (1982). *Geodynamics: Applications of Continuum Physics to Geological Problems*. New York, NY: John Wiley and Sons.

Valentine, G. A., D. J. Krier, F. V. Perry and G. Heiken (2007). Eruptive and geomorphic processes at the Lathrop Wells scoria cone volcano. *Journal of Volcanology and Geothermal Research*, **161**, 57–80.

Wada, Y. (1994). On the relationship between dike width and magma viscosity. *Journal of Geophysical Research*, **99**(B9), 17 743–17 755.

Wada, Y. (1995). Comment on, "On the relationship between dike width and magma viscosity". *Journal of Geophysical Research*, **100**(B8), 15 543–15 544.

Wallace, P. and A. Anderson (2000). Volatiles in magmas. In: Sigurdsson, H. *et al.* (eds.), *Encyclopedia of Volcanoes*. San Diego, CA: Academic Press, 149–170.

Wallis, G. B. (1969). *One-dimensional Two-phase Flow*. New York, NY: McGraw-Hill.

White, F. M. (1979). *Fluid Mechanics*, International Student Edition. Tokyo: McGraw-Hill Kogakusha.

Wilson, L. and J. W. Head (1981). Ascent and eruption of basaltic magma on the Earth and Moon. *Journal of Geophysical Research*, **86**, 2971–3001.

Woods, A. W., S. Sparks, O. Bokhove *et al.* (2002). Modeling magma-drift interaction at the proposed high-level radioactive waste repository at Yucca Mountain, Nevada, USA. *Geophysical Research Letters*, **29**(13), 1641, doi:10.1029/2002GL014665.

Chapter 4

Magma Transport and Storage in the Crust (1995–present; IPGP, Bristol, UBP)

(Funding: *Allocation de recherche du Ministère de la Recherche et de l'Éducation Nationale*, *Leverhulme Trust*, *CNRS-INSU* and *Chaire d'excellence mixte UBP-IRD*)

In parallel to these studies on porous flows and magma degassing, I pursued the work on magma intrusions I started during my PhD and I developed a research programme to address the formation of plutons and magma chambers.

A major process of evolution of the Earth's lithosphere is the upward transport of magma by the creation and propagation of dykes from zones of partially molten rocks in the upper mantle to the surface. Forty years ago, Weertman (1971a,b) proposed that water-filled cracks could self-propagate through glaciers owing to their buoyancy once they had reached a critical size, and suggested that magma-filled dykes could propagate through the Earth's crust by the same mechanism. His reasoning was that smaller water-filled cracks would not have enough (negative) buoyancy, hence overpressure, to overcome the strength of ice whist larger cracks would have enough buoyancy to do so. According to Weertman (1971a,b), propagating liquid-filled cracks would maintain a constant length by fracturing the surrounding solid at their leading tip whilst at the same time closing at their trailing tip. Later, this seminal work was extended to dyke propagation, and refined to account for the primarily elastic deformation of crustal rocks and their fracturing, as well as the viscous flow of magma and its buoyancy (Spence and Sharp, 1985; Spence and Turcotte, 1985; Emerman et al., 1986; Spence et al., 1987; Spence and Turcotte, 1990) until Lister and Kerr (1991) seemingly nailed the problem. Their work summarises nicely two previous, more mathematical papers (Lister, 1990b,a), and discuss the problem of dyke propagation in terms of the pressure scales involved during dyke propagation.

Lister and Kerr (1991) identified four different pressure scales that tend to drive or resist dyke propagation: an elastic pressure scale, P_e, that characterises the elastic deformation of the rocks surrounding the dyke; a buoyancy scale, P_b, associated with de density difference $\Delta\rho$ between magma and host rocks; the viscous pressure drop induced by the flow of viscous magma along the dyke, P_v; and a resistance pressure scale, P_f, related to the rock fracture toughness K_c. These different pressures scale as follows:

$$P_e \sim \frac{E}{2(1-\nu^2)}\frac{w}{l} \qquad P_b \sim \Delta\rho g h \qquad P_v \sim \frac{\mu u l}{w^2} \qquad P_f \sim \frac{K_c}{\sqrt{L}}. \tag{4.1}$$

E and ν are the rock Young's modulus and Poisson's ratio, respectively, w is the dyke thickness, l is the smallest of its other two dimensions (height h or breadth), g is the gravitational acceleration, μ is the magma viscosity, u is the average magma flow velocity, and L is the dyke length. Comparing these resisting and driving pressure scales, based on laboratory measurements on rock samples (Atkinson, 1984) and scaling analysis, Lister and Kerr (1991) showed that once a dyke has been initiated and has grown to a small critical length, dyke propagation would be mainly driven by buoyancy and resisted by the viscous pressure drop induced by magma flow within the dyke, and that rock resistance to fracture would be comparatively negligible. Moreover, this scale analysis shows that a steady-state propagating dyke would develop a thick near-tip, head region that gradually tapers off behind (away from the tip) to a much thinner tail region. The size of the head region is defined by a balance between the elastic, buoyancy and fracture pressures, and often referred to as the buoyancy length:

$$L_b \sim \left(\frac{K_c}{\Delta\rho g}\right)^{2/3}. \tag{4.2}$$

However, fracture resistance only affects the dyke shape near its tip, not its dynamics. These are determined by magma flow in the tail region of the dyke (away from the tip, at a distance greater than the effective buoyancy length) which adjusts its width w_{tail} elastically to balance the viscous pressure drop induced by magma flowing owing to its buoyancy gradient:

$$w_{tail} \sim \left(\frac{\mu u}{\Delta\rho g}\right)^{1/2}. \tag{4.3}$$

Rubin (1995b) considered the case of dykes propagating laterally away from their feeding source. If the driving force comes from the overpressure present in the source, Rubin (1995b) showed dyke propagation would be controlled by a balance between this excess source pressure ΔP_0 and the viscous pressure drop induced by magma flow. Dykes would thus propagate with a velocity

$$u \sim \frac{(1-\nu^2)^2}{E^2}\frac{\Delta P_0^3}{\mu} L. \tag{4.4}$$

One notes that in the case of a constant excess source pressure, this velocity would increase exponentially.

In parallel, the thermal aspects of dyke propagation were first addressed by Bruce and Huppert (1989, 1990) for basaltic dykes, and then by Petford et al. (1993, 1994), who extended the approach to felsic magmas, as well as Rubin (1993b,a, 1995a). These studies revealed the exsitence of a critical dyke width w_c below which dykes will ultimately freeze solid before they could propagate far, and above which melting of the host rock by the hot, flowing magma would cause dykes to widen by thermal erosion and ensure further propagation. This critical width w_c is determined by a balance between heat advected along the dyke by inflowing magma and heat conducted way by the surrounding colder host rocks:

$$w_c = 1.5 \left(\frac{S_m}{S_\infty^2} \right)^{3/4} \left(\frac{\mu \kappa H}{\Delta \rho g} \right)^{1/4}, \tag{4.5}$$

where $S_m = L/[C_p(T_0 - T_f)]$, $S_\infty = L/[C_p(T_f - T_\infty)]$, L is the latent heat of the magma, C_p is its specific heat capacity, T_0, T_f and T_∞ are the initial magmatic temperature, the magma freezing temperature and the far-field temperature of the crust, respectively, and κ is the magma thermal diffusivity (e.g. Petford et al., 1993). These thermal considerations enable to explain the observed relationship that dykes containing more viscous magmas tend also to be thicker (Wada, 1994; Kerr and Lister, 1995; Wada, 1995).

Yet In spite of this extensive study carried out over the years, we could not answer some key questions of geological importance when I started my PhD. For instance, what determines the flux of magma carried by a dyke? Dyke propagation is likely to be initially pressure-driven close to the source when dykes are of small vertical extent before buoyancy could then become the driving force. However, the analysis of Rubin (1995b) showed pressure-driven dykes would tend to propagate with accelerating velocity whereas buoyancy driven dykes would tend to propagate steadily (Lister and Kerr, 1991). How would such a transition operate?

Additional questions I have tried to address since pertain to the fate of dykes and the conditions for magma storage: Why does the vast majority of dykes stall in the crust and never reach the surface? Which mechanisms are involved and what are their timescales? Answering these questions is key if we are to understand the inner workings and development of magmatic and volcanic systems.

4.1 Gelatine as a crustal analogue for modelling magma intrusions

Most of my work on magma intrusions involves laboratory-scale experiments where a solid of gelatine is used as an analogue for crustal rocks and is intruded by a fluid that simulates a magmatic intrusion.

During my PhD, I demonstrated that indeed gelatine solids deform and behave at the laboratory scale like elastic, brittle solids (including rocks), that is the Young's modulus E of a solid of gelatin and its fracture toughness K_c follow the theoretical relationship expected for such solids, $K_c \sim \sqrt{2\gamma_s E}$ where γ_s is the energy required to create a unit surface area. The best fit through the data was $K_c = 0.97\ E^{0.55}$ (Menand and Tait, 2002). This relationship enables an experimentalist to calculate the fracture toughness of a gelatin solid from the measurement of its Young's modulus in a nondestructive manner.

More recently, I refined this relationship with Katherine Daniels, a Bristol PhD student I co-supervise with Steve Sparks, and Janine Kavanagh from Monash University. We also studied in detail how the Young's modulus of gelatine evolves with time, as a function of the volume and concentration of gelatine used for its preparation (Kavanagh et al., 2012). As shown in Fig. 4.1, we find gelatine Young's

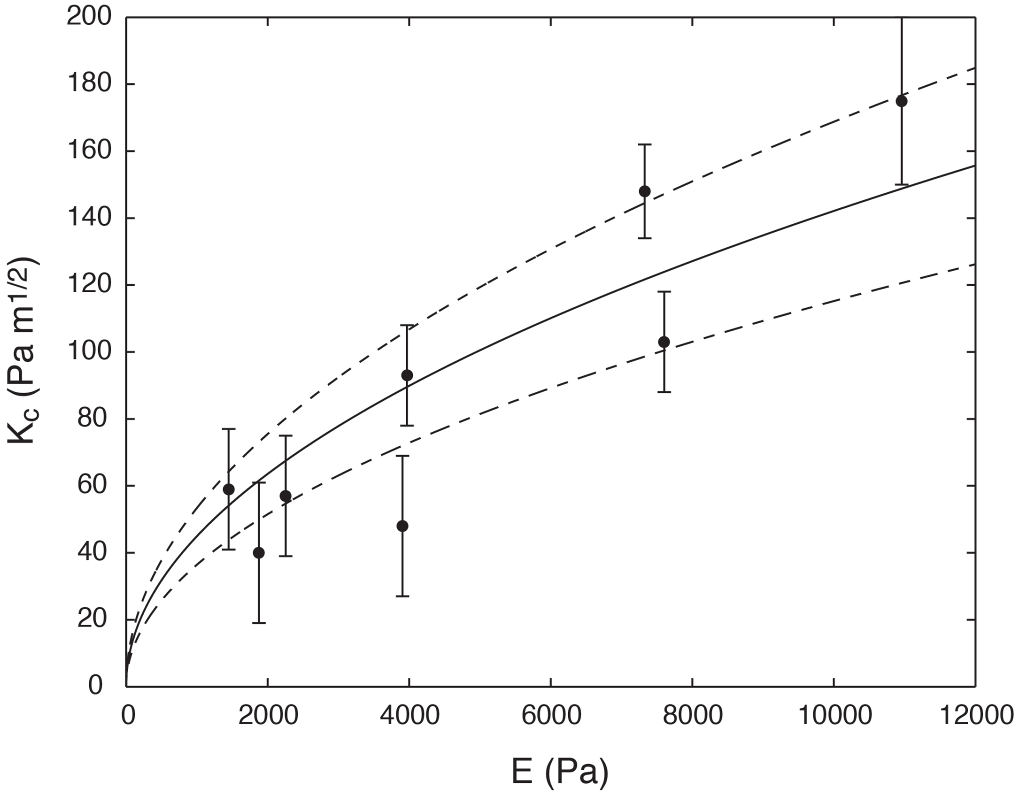

Figure 4.1: The fracture toughness K_c of gelatine solids as a function of their Young's modulus E. The continuous curve is the best fit through the data: $K_c = (1.4 \pm 0.1)\sqrt{E}$, with the 95% confidence limits (dashed lines). This shows gelatine solids behave like ideal elastic, brittle solids and rocks; their fracture toughness K_c and Young's modulus E follow the theoretical relationship expected for such solids: $K_c = \sqrt{2\gamma_s E}$ with a best estimate for the gelatine surface energy $\gamma_s = 1.0 \pm 0.2$ J m^{-2} (Menand and Tait, 2002; Kavanagh et al., 2012).

modulus and fracture toughness are best fit by the following relationship:

$$K_c = (1.4 \pm 0.1)\ \sqrt{E}, \tag{4.6}$$

where the best estimate for the gelatine surface energy is

$$\gamma_s = 1.0 \pm 0.2\ \text{Jm}^{-2}. \tag{4.7}$$

We also found gelatine Young's modulus E increases continuously with time towards a plateau value E_∞, which correlates linearly with gelatine concentration:

$$E = E_\infty\left(1 - e^{-t/\tau}\right) \quad \text{with} \quad E_\infty = 6000c_{gel} - 7800, \tag{4.8}$$

where the gelatine concentration c_{gel} is expressed in wt.% and E_∞ in kPa ($R^2 = 0.9992$).

Finally, we demonstrated that analogue experiments that use solids of gelatine to simulate the propagation of magmatic intrusions in the elastic crust, such as dykes or sills, are adequately scaled geometrically, kinematically and dynamically when carried out at 5–10 °C and with gelatine concentrations of 2-5 wt.% (Kavanagh et al., 2012).

4.2 Magma transport in dykes

4.2.1 Propagation of a single dyke

Dynamics of a buoyant dyke fed by a source with constant excess pressure

During my PhD, I wanted to address two questions: what determines the flux of magma carried by a dyke? and how does dyke propagation change from being initially pressure-driven to buoyancy-driven later on?

Up to the mid-1990s, most theoretical studies neglected the fracture resistance of rocks when dealing with dyke propagation, mainly motivated by laboratory measurements on rock samples (Atkinson, 1984). Based on scaling analysis, Lister and Kerr (1991) showed that the pressure associated with the strength of rocks should be negligible in comparison with the other pressure scales, especially magma viscous pressure drop. However, field estimations give values 10^2–10^3 times greater than those measured in the laboratory (e.g. Delaney and Pollard, 1981; Reches and Fink, 1988). Moreover, it is difficult to believe that fracturing is negligible from the very beginning of the propagation in the case of flawless solids. Hence the question: how may a dyke grow from a regime where the fracture resistance of rocks would be significant to a regime where it could be neglected?

I therefore used laboratory experiments to study the propagation of a fissure fed by a reservoir under a constant pressure. Fracturing processes are very difficult to handle in numerical models whereas they are always present in laboratory experiments using gelatine (Takada, 1990; Lister and Kerr, 1991). In these experiments, aqueous solutions were injected under constant source pressure in gelatine solids, care being taken to start fissure propagation from a well-characterized initial condition, and the fissure velocity and injection rate were measured rather than being imposed (Menand and Tait, 2002).

The results allowed evaluation of how the different driving and resistive pressures evolved during fissure propagation and highlight the influence of the fracture resistance of the host solid. Two propagations regimes were successively observed (Fig. 4.2). In an initial transient propagation regime, the elastic pressure generated by the fissure was balanced by the fracture pressure; the fissure propagated radially with decreasing velocity and increasing injection rate, controlled by the source conditions. Subsequently, buoyancy overcame the source pressure as the driving force, and vertical steady state propagation was established. The fissure developed a bulbous head whose size was controlled by a balance between buoyancy pressure and fracture pressure, hence equal to the buoyancy length L_b (equation 4.2). The steady-state values of velocity, flux, and strain energy release rate were established at the transition between the two regimes and so reflected the source conditions. Thus contrary to being negligible, rock fracture resistance would play a significant role in determining the transition between regimes hence the subsequent steady-state propagation velocity and magma flux.

An implication of this model is that greater horizontal dyke cross section reflects larger source pressure, and that dykes propagating from shallow magma chambers are unlikely to attain steady state. Additionally, these experiments place constraints on the mechanics of time-dependent failure of the solid as a process that resists fissure propagation: propagation velocity scales with the square of the height of the fissure head, and fracture toughness of rocks would be length-scale dependent rather than a material property.

Additional experiments investigated the effect of syn-propagation degassing on dyke dynamics (Menand and Tait, 2001).

Influence of syn-propagation gas exsolution

As silicate magmas ascend towards the Earth's surface, the reduction of pressure causes dissolved volatile components to exsolve and form gas bubbles. At the tip of a vertically oriented fissure, pressure is lowest because there is least rock overburden. In addition, the high viscosities of magmatic liquids implies large head losses as the fissure tapers to vanishing thickness (Barenblatt, 1962; Lister, 1990b). As the fissure propagates towards the surface, ambient pressure decreases, driving

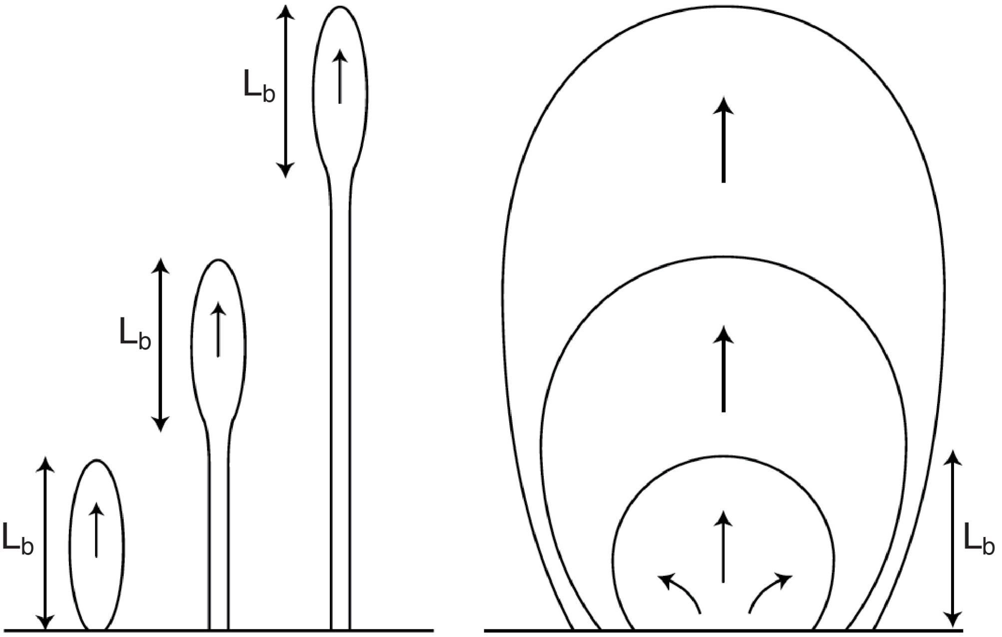

Figure 4.2: Schematic illustration of the fissure propagation regimes in cross section (left) and in plane (right) views. Propagation is initially transient, driven by the excess source pressure, and the fissure adopts a penny-shaped geometry. Once the fissure reaches a height L_b, steady, buoyancy-driven propagation regime is achieved and the fissure propagates mainly vertically with a bulbous head of length L_b (Menand and Tait, 2002).

further exsolution and expansion of the volatiles. Moreover, because of the no-slip boundary condition at the dyke wall, magma near the dyke wall moves more slowly than at the tip and, from mass balance, magma near the dyke centre moves faster than the tip. This means that fresh magma that has not been degassed is always being transported into the low-pressure region, where it should turn into foam. The subsequent lowering of magma density provides a buoyancy force that tends to keep it there. Intense shearing in this region may cause the foam to break down and allow the gas to collect into a separate pocket at the tip, which grows during propagation. This process is certainly complex but it is likely bubbles do not need to move significant distances with respect to the surrounding magma to feed the gas pocket. (Lister, 1990b) had shown theoretically, in the framework of a steadily propagating fissure with a fixed volume of gas at its tip, that the fissure tends to pinch off between the gas and the following liquid. Laboratory experiments were thus performed to look at the transient propagation of a liquid-filled crack with a gas pocket at its tip that grows with time.

The apparatus used for these experiments was essentially the same as before, except that to simulate exsolution and expansion of volatiles at the crack tip, air was continuously injected into the liquid-filled fissure some time after it began to propagate. The air collected at the fissure tip and formed a pocket that grew continuously as the fissure propagated (Fig. 4.3). As magma analogue, aqueous solutions of four different viscosities were used: 1, 41, 126 and 342 mPa s, achieved by dissolving small amounts (less than 0.5 wt.%) of hydroxyethylcellulose.

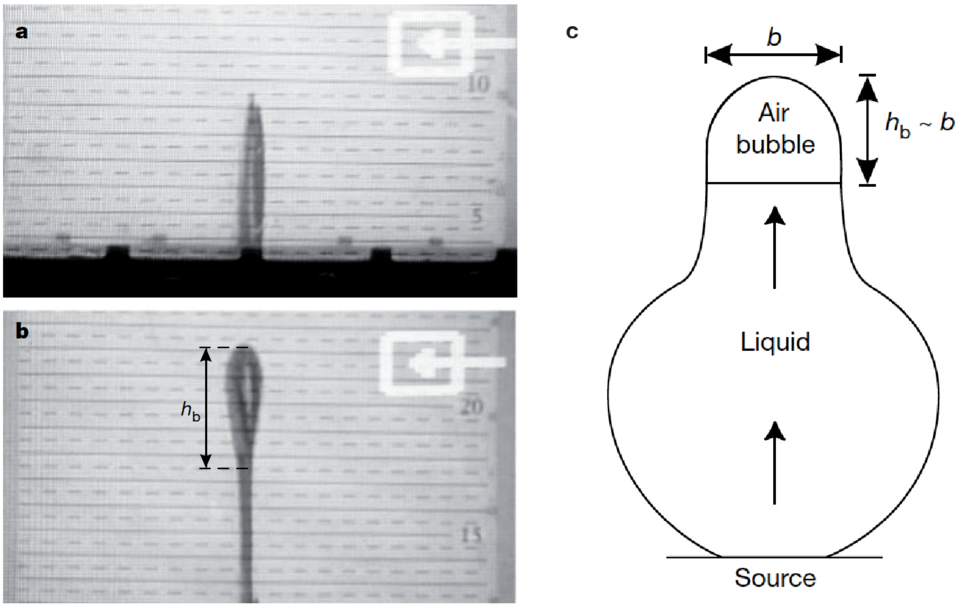

Figure 4.3: Propagation of a liquid-filled fissure with a growing gas pocket at its tip. (a) Initially the fissure propagates owing to the reservoir overpressure. (b, c) As the injected air accumulates at the tip it dramatically deforms the crack and dictates its width (b) as well as its breadth (c). From that point, the dynamics of the fissure are entirely controlled by that of the air pocket (Menand and Tait, 2001).

After the injection of air into the fissure, a bubble formed at its tip. When it became higher than about 2 cm, the shape of the crack was deformed markedly in both vertical cross-sections (Fig. 4.3b, c). When this happened, it was also observed that the fissure velocity (which was the bubble velocity) increased abruptly while the liquid injection rate stayed constant, indicating that the crack was closing. Having both a closing crack and an accelerating air bubble indicated that the bubble could separate from the liquid. This dynamic behaviour of the fissure was observed irrespective of the liquid viscosity. However, the liquid injection rate, which was not imposed but rather evolved naturally, was observed to decrease with the liquid viscosity. The transition from fissure dynamics determined by those of the liquid phase to fissure dynamics controlled by those of the gas phase occured when the gas pocket had enough buoyancy to overcome the fracture resistance of the surrounding solid.

These experiments provide a phenomenological model for the intense explosions of relatively short duration that frequently precede large explosive and effusive volcanic eruptions, by as much as weeks to months in the case of very viscous magmas. These explosions are intense but of short duration, and contain variable amounts (sometimes only very little) of juvenile magmatic component. The experiments provide a phenomenological model whereby fast-moving, gas-rich pockets reaching the surface ahead of the main liquid-filled fissure could be the origin of these precursor eruptions. In the experiments, the period of time between the beginning of precursor events and the main eruption, as well as the volume of erupted gas, depends mainly on liquid viscosity. One general prediction of the model is that precursor activity should be shorter in the case of basaltic volcanoes than for silicic ones. This seems to be supported by accounts of the Paricutin eruption, which indicate that gas and fine ash emissions began only hours before the main magma conduit reached the surface (Foshag and Gonzalez, 1956), a time period considerably shorter than the weeks to months typical of silicic eruptions such as that of Mount Pinatubo in 1991 (Newhall and Punongbayan, 1996).

Influence of cooling and inelastic deformation

To leading order, rocks are assumed to deform elastically around dykes during their propagation. But to which extent is this a valid approximation?

Solidified dykes are the end result of the flow of pressurized magma through fractures, recording magma transport through the crust. Crustal rocks are usually assumed to deform mainly elastically around propagating dykes, except for inelastic deformation taking place near their very tip. Furthermore, it is usually assumed these regions of inelastic deformation are minute compared to the size of dykes, so that inelastic deformation can be neglected when evaluating their overall shape. Thus the shape of a preserved solidified dyke is often used to calculate the pressure in the crack at the time of solidification, on the basis that this shape reflects a simple elastic deformation control with fixed overpressure. However, most studies report only the maximum thickness of dykes and use this maximum opening to infer magma overpressure at the time of emplacement, as opposed to using the entire shape of the dykes.

Recently, Katherine Daniels (Bristol PhD student) and Janine Kavanagh from Monash University tested these assumptions by measuring precisely the shapes of well-exposed examples of basaltic dykes from the Isle of Rum, Scotland, and Swartruggens kimberlite dyke swarm from Helam Mine, South Africa (Daniels et al., 2012). The thickness of these dykes was measured at regular intervals along their length; only dykes with crack tips exposed at both ends were selected for measurement. The elastic model of Pollard and Muller (1976) predicts the two-dimensional shape of a fluid-filled fracture subjected to both an internal overpressure and a remote stress gradient. This model was used to fit the field data in order to assess the extent to which elastic deformation can adequately describe dyke shape.

Dyke thickness measurements from the two data sets were analysed using the model of Pollard and Muller (1976). Best overpressure and gradient estimates for the Rum and Swartruggens were determined by minimizing the least-squares misfit between the model and the observations. Overpressures and stress gradients estimated from the best-fit models were then used to generate a model to fit the shape of an observed solidified magma-filled crack. By interpreting the static shape, the assumption was made that the fluid-filled crack had reached a static equilibrium and that flow effects as solidification occurred could be neglected. It was found that the shapes of most of the dykes differ from that expected from elastic theory, and that the difference is statistically significant. Most dykes appear too thin at their centre and too thick and blunt at their tip. As a result, elastic models overestimate both the magma pressures and regional stress gradients that opened these dykes. Furthermore, irrespective of the goodness of fit, most estimated values are implausibly high. Average calculated overpressure of ~ 700 MPa and stress gradient of ~ 600 MPa/m are much larger than independent estimates based on rock strength, particularly for the small-scale basaltic dykes on Rum.

As illustrated in Fig. 4.4, dyke shape can be explained by a combination of host-rock inelastic deformation prior to and coeval with magma emplacement, which would induce blunt dyke tips, and by magma chilling at the dyke tapering edges, which would prevent its closure as magma pressure declines during emplacement; this sequence provides the most complete explanation for the mismatches between the data and the model (Daniels et al., 2012). The permanent wedging of the dyke edges due to chilling has implications for crustal magma transport, since this would prevent dykes from closing fully and thus would enable them to act as open conduit for longer, as well as strain response in the crust due to dyke emplacement. However, care should be taken when extrapolating the observations from the dykes measured from the Swartruggens swarm and on Rum. Because the mean observed dyke thickness was less than 1 m, it should not automatically be assumed that our analysis will apply to larger dykes.

Dyke interactions with pre-existing faults

Another limitation of current dyke propagation models is that most if not all of them assume surrounding rocks are devoid of faults. Yet, it is likely both faults and propagating dykes interact with each other as suggested by geophysical and field observations (e.g. Cayol et al., 2000; Gudmundsson et al., 2008). These interactions might play an important role in the transport of magma through the crust, especially in monogenetic volcanic fields. These are characterized by numerous volcanic centers, each typically resulting from a single eruption. Therefore magma must be transported from source to surface at different places yet within the same field, which raises the question of the relative importance of 1) the self-propagation of magma through pristine rock, and 2) the control exerted by pre-existing fractures.

To address this issue, Nicolas Le Corvec came over to Bristol in 2010 as part

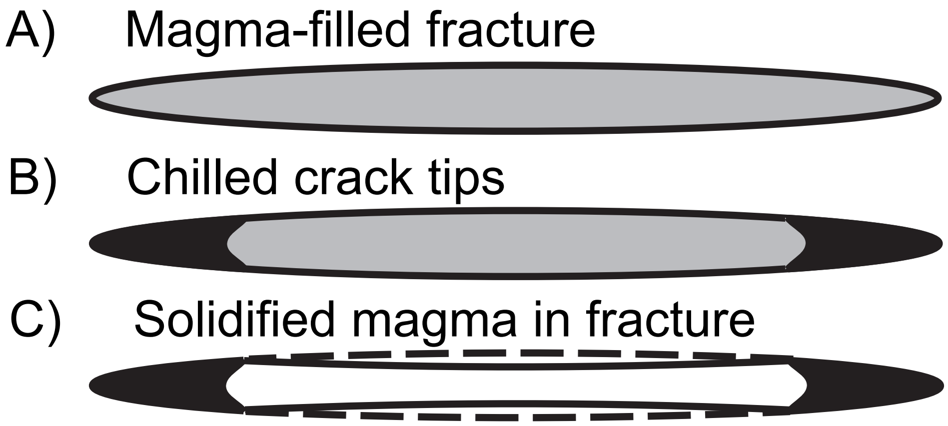

Figure 4.4: Schematic illustration of the impact of cooling on preserved dyke geometry, presented as three time steps in the evolution of a horizontal section through the dyke. (A) Magma intrudes a fracture, and (B) cooling ensues at the dyke margins. (C) Chilled fracture tip magma props the fracture open as the overpressure reduces, preventing crack closure and creating the observed dyke profile (solid line) with a thinner center and thicker tips. The dashed line in C indicates the expected profile of a pressurized magma-filled fracture in an elastic media. (Daniels et al., 2012).

of his PhD at the University of Auckland on the physical controls on monogenetic basaltic volcanism. He carried out a series of analogue experiments to constrain the interaction of a propagating dyke with pre-existing fractures. These experiments involved the injection of air (an analogue for buoyant magma) into a 40-cm-wide cubic gelatine solid, which was previously cut into its upper part to simulate pre-existing fractures. The number of pre-existing fractures, the volume of the dykes, their distance from the fractures and that separating fractures were systematically varied to assess their influence on potential dyke-fracture interactions. Moreover, the influence of two different stress fields was also tested: hydrostatic stress conditions and an extensional stress environment.

The initial stress field of a solidified gelatine solid is hydrostatic (Takada, 1990). Because gelatine solids have too weak a tensile strength, a tensile deviatoric stress cannot be applied directly to them. Instead, a compressive load can be imposed on their upper surface, and by imposing a no-displacement boundary condition on two opposite vertical sides of the gelatine and a free-surface boundary condition on the two other vertical sides, this vertical load translates into a horizontal deformation. Because gelatine solids are nearly incompressible ($\nu \simeq 0.5$), this horizontal deformation ϵ_x is directly related to the compressive vertical load σ_z (Le Corvec et al., submitted):

$$\epsilon_x = -\epsilon_z = \frac{3}{4}\frac{\sigma_z}{E}, \tag{4.9}$$

These experiments show that the volume of the dykes, the distance and angle between dykes and fractures as well as the distance separating adjacent pre-existing fractures and their dip all influence the dyke trajectory, and thus whether a dyke interacts and exploits a pre-existing fracture (Fig. 4.5). Dyke geometry and dynamics are also affected by both the presence of the fractures and the dyke volume; dykes propagating in between fractures tend to decelerate. The natural length-scale in these experiments is the buoyancy length L_b of the dykes. Interaction between a dyke and a fracture is observed when they are separated by a distance smaller than $\sim 0.5\, L_b$ or when adjacent fractures are separated by less than $\sim L_b$. Lower fracture dip increases the likelihood for interaction. The presence of pre-existing fractures affects also the dynamics of dykes by decreasing their ascent velocity, although this decrease is rather small (less than 10%). The experiments do not reveal any evidence for a potential effect of the stress regime on the mechanics and dynamics of the dykes (Le Corvec et al., submitted).

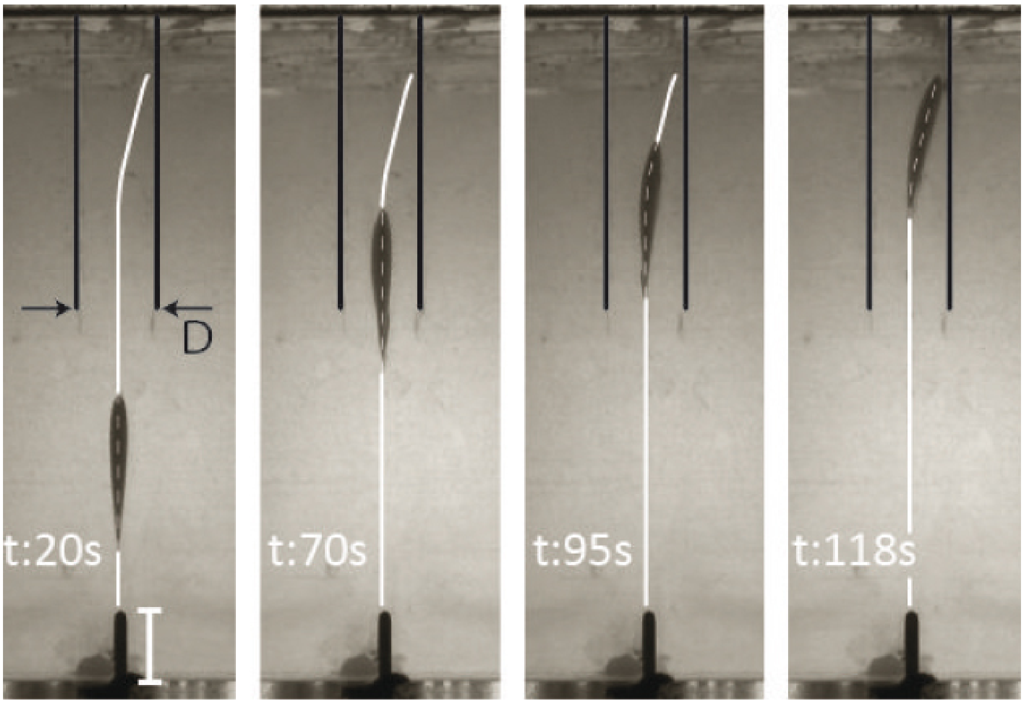

Figure 4.5: Successive photographs of a dyke rising in between two pre-existing fractures (black lines). Upon entering the region bounded by the fractures, the dyke modifies its trajectory (white curve) and ultimately intersects one of them. The vertical white scale at the bottom of each photograph is 5 cm long, and the stress field was hydrostatic (Le Corvec et al., submitted).

Uspcaled to magmatic conditions, interactions are expected for dykes and fractures separated by less than about 200 m, and dykes with a volume less than about 10^{-2} km^3 would experience a small velocity decrease. This study shows how the presence of pre-existing crustal fractures can influence the direction of propagation and the dynamics of dikes, and thus help magma to erupt at different places within a volcanic field. These heterogeneities should therefore be considered when studying the transport of magmas in the upper parts of the crust.

4.2.2 Repeated dyke intrusions: rifts and swarms

However, dykes rarely occur as single entities, and I am interested in understanding the spatial and temporal relationship of repeated dyke injection in the same crustal region. I have investigated this relationship at two different geological scales: the repeated injection of dykes into the Dabbahu-Manda-Harraro segment of the Red Sea Rift in Afar (regional scale); and the formation of giant dyke swarms (crustal scale).

Rifts

The emplacement of magma in dykes is an effective mechanism for releasing the tensional stress which builds up at divergent plate margins, and can lead to both fissure eruptions and normal faulting. In sub-aerial magmatic rifted margins, for example the East African Rift, the crust slowly spreads via the processes of dyke injection, normal faulting and volcanic eruption to form new oceanic crust. However, whether faulting, stretching or magma intrusion dominate the extension remains ambiguous (Bastow and Keir, 2011). The magmatic activity that started in Afar, Ethiopia, with a large dyke intrusion in September 2005 and has involved fourteen other intrusions since then offers the opportunity to study continental break up first-hand. The majority of the strain at the Afar triple junction is accommodated by magma intrusion (Ebinger and Casey, 2001). This is supported by the observation that repeated dyke injections can produce the morphology of the recently intruded Dabbahu-Manda-Harraro segment of the Red Sea Rift in Afar (Wright et al., 2006), and that magma intrusion, not faulting due to ductile stretching, is taking place in this part of Ethiopia (Bastow and Keir, 2011). However, the thermal structure, and by inference the strength, of an extending plate over time is poorly constrained.

The main part of Katherine Daniels' PhD at Bristol University was thus devoted to modelling the thermal evolution of a spreading rift margin where dykes are intruded repeatedly, which was then applied to the geological setting of the actively spreading Main Ethiopian and Red Sea rifts. Katherine developed a thermal conduction model that simulates the repetitive intrusion of basalt dykes into a rift by solving the heat-flow equation, incorporating the latent heat of fusion, both in one and two dimensions. This requires to define a relationship $X(T)$ between melt fraction and temperature, and Katherine defined a linear piece-meal relationship using both MELTS and Rhyolite-MELTS with the composition of samples of recently erupted basalt (2007–2009) collected from Afar (Ferguson et al., 2010).

The model was run for multiple injection of basaltic dykes at constant temperature, each instantaneously intruded into a basaltic crust, sequentially and at a constant rate. The case of intra-accretion, where each successive dyke is emplaced through the centre of the previous one, was considered with a dyke injection frequency ψ proportional to the spreading rate S of the rift: $S = 2w\psi$, i.e. spreading is entirely accommodated by dyke injections. The effect of injection frequency, geothermal gradient, and temperature and composition of the injected material on the thermal evolution of the crust were investigated.

The temperature of the intruded region rises gradually up to reaching the solidus after an incubation time t_c: prior to t_c, each dyke injection solidifies completely before the arrival of the next, and from time t_c onward melt starts accumulating in the intruded region. When considering the different parameters that were systematically varied, spreading rate has by far the largest effect on the thermal evolution of the intruded crust. Indeed, the time taken to reach a given isotherm some distance away from the rift axis is linearly correlated with the spreading rate: the spreading rate controls the rate at which heat is transported away from the injection locus, while diffusion of heat by conduction is comparatively minimal. Additionally, the spreading rate controls also the time taken to reach the solidus, the incubation time t_c, at the injection locus: t_c is found to scale like S^{-2}, i.e. t_c scales with the injection rate like ψ^{-2}. The model predicts also the extent of the region with potential melt and its evolution with time, and has been compared with data from MT surveys (Fig. 4.6) conducted by researchers at the Universities of Edinburgh and Addis Ababa. MT data are consistent with repeated dyke injections in the Manda Harraro-Dabbahu rift segment during 1 to 2 Ma (Fig. 4.6).

These results highlight the key control of the injection rate (here commensurate with the spreading rate) on the thermal evolution of the intruded rift. The model provides also an estimate of the time required to heat a rifting margin to the temperature for brittle-ductile transition and thus a constraint on the timescale over which the transition from continental rifting to sea floor spreading occurs.

This numerical modelling was complemented by analogue experiments designed to quantify the spatial relationship between successive dykes injected into a gelatine solid subjected to a remote tensile stress σ_y (this tensile stress was imposed as described in the previous section on dyke interactions with pre-existing faults). These experiments involved the repeated injection of a vegetable oil at a temperature above its solidification temperature of 31 °C (Galland et al., 2006) into a much colder gelatine solid. Each intrusion was let to solidify before the next injection of fluid was carried out. This allowed the spatial relationship between successive intrusions to be measured at the end of the experiments, and to relate them to the remote tensile stress σ_y, the initial distance d_s between successive fluid injections, the length of the experimental dykes $2a$, and their overpressure ΔP. This overpressure was derived from the shape and thickness of the dykes at the end of the experiment after excavating the intrusion out of the gelatine solid.

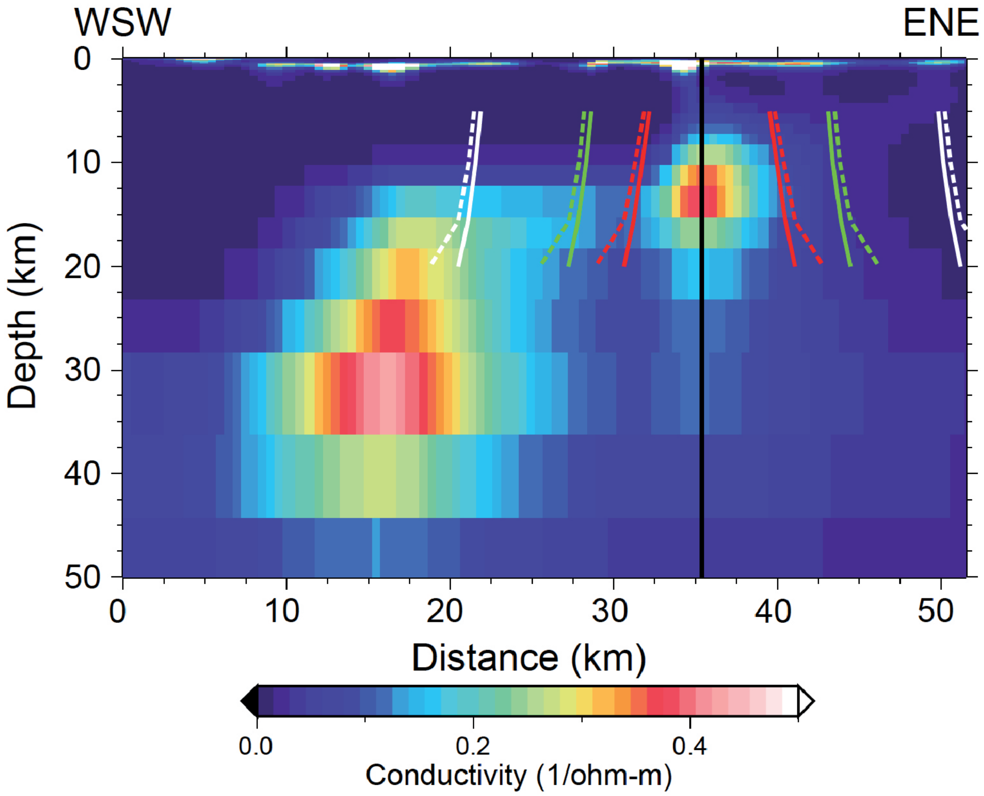

Figure 4.6: MT survey (WSW-ENE traverse line across the Manda Harraro-Dabbahu rift segment, Afar) compared with the numerical model results for S = 10 mm/yr. Three sets of four coloured lines show the model results after 500 ka (red lines), 1 Ma (green lines) and 2 Ma (white lines), and are symmetrical about the rift axis (solid black line). The sets of lines show the position of the solidus (solid lines) and the 600 °C isotherm (dashed lines), which represents the brittle-ductile transition (Daniels, 2012).

Each intrusion modifies locally the pre-existing, and initially tensile, stress field. As a result, a nearby subsequent intrusion would tend to orient itself according to this stress perturbation. Dimensionless analysis suggest that the rotation angle θ between two successive injections depends on two dimensionless ratios: the ratio of the distance separating the injections to the half-length of the first injection, d_s/a; and the ratio of the remote tensile stress to the overpressure of the first injection, $\sigma_y/\Delta P$:

$$\theta = f\left(\frac{d_s}{a}, \frac{\sigma_y}{\Delta P}\right). \tag{4.10}$$

The effect of both ratios should be independent. Analysis of the stress perturbation induced by a single intrusion suggests it should decay with distance d away from the intrusion as $1/[1 + d^2/(a^2\sqrt{\pi})]$. Furthermore, in the case of an intrusion with a fluid pressure much greater than the remote stress, we expect a second nearby intrusion to be strongly affected and to orient itself with a 90 degrees angle relative to the first one. In the opposite case, we expect the rotation angle θ to be zero.

Also, the fluid pressure must always remain positive (it can only be equal to zero at minimum). These considerations suggest the following relationship between rotation angle θ and distance and stress ratios:

$$\theta\left(\frac{\sigma_y}{\Delta P} \leq 1\right) = \frac{\frac{\pi}{2}\left(1 + \frac{\sigma_y}{\Delta P}\right)}{1 + \frac{d_s^2}{a^2\sqrt{\pi}}} \quad \text{and} \quad \theta\left(\frac{\sigma_y}{\Delta P} \geq 1\right) = 0. \tag{4.11}$$

As shown in Fig. 4.7, within uncertainty all measured experimental rotation angles follow the expected theoretical relationship given by equation (4.11).

The stress change caused by the opening of the September 2005 dyke in Afar has been estimated to be 30–80 MPa (Grandin et al., 2010; Hamling et al., 2010), while the tectonic force available for rifting has been estimated to be 4.2 Tera N/m (Bialas et al., 2010), which distributed over the thickness of the crust in Afar would correspond to a tensile stress of 170 MPa. Thus the magma overpressure associated with the opening of the September 2005 dyke would be in the range 200 to 250 MPa, hence correspond to a stress ratio $-\sigma_y/\Delta P$ of 0.68 to 0.85. Rotation angles between successive dyke injections have been estimated to range from $1°$

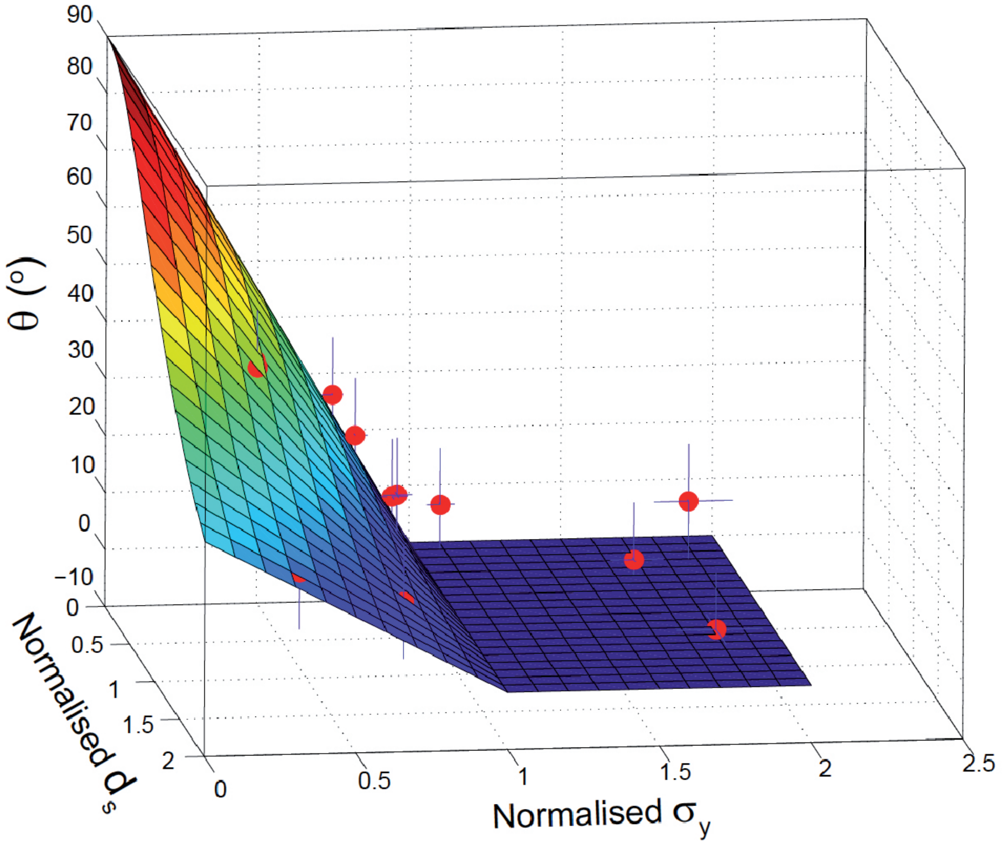

Figure 4.7: Rotation angle θ between successive injections as a function of normalised distance d_s/a and normalised stress $\sigma_y/\Delta P$. Within uncertainty all measured angles (red points) fall on the expected theoretical surface (equation 4.11).

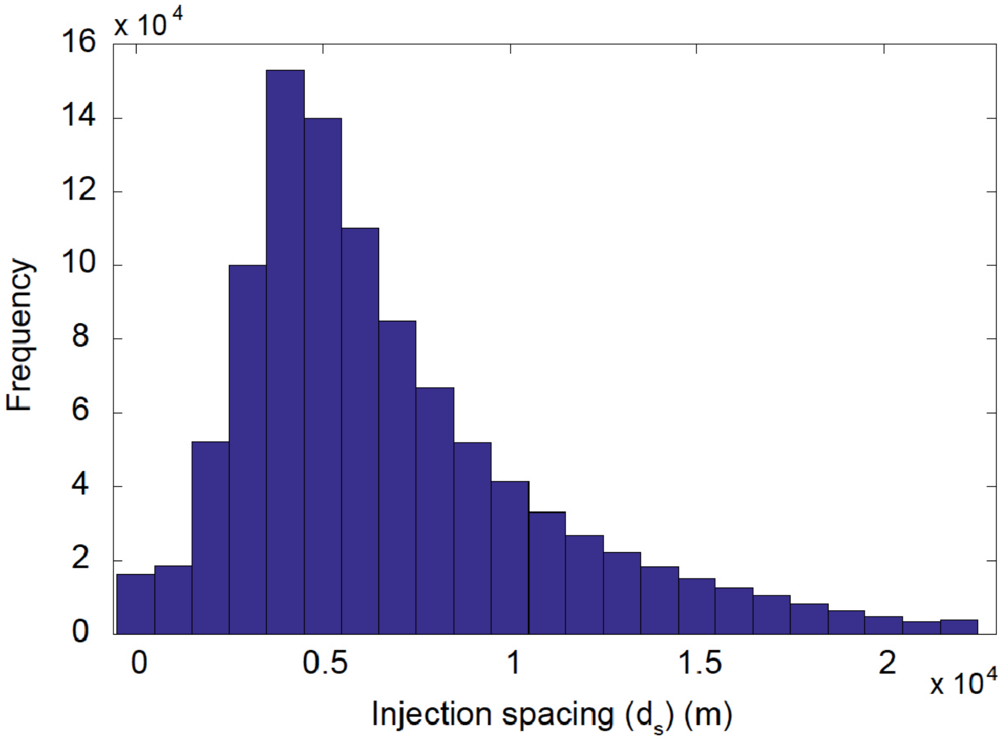

Figure 4.8: Histogram of the injection spacing d_s generated by Monte Carlo simulations for the range of rotation angles and stress ratios estimated for the recent Afar dyking sequence (Daniels, 2012).

to $16°$ from estimates of the dyke strikes. Using this range of rotation angles and stress ratios, a range of expected dyke spacings can be calculated. Fig. 4.8 shows the dyke spacing distribution that results from a Monte Carlo simulation that randomly drew a thousand values from the estimated ranges of rotation angles and stress ratios each. This distribution provides an estimate of the most likely injection spacing values that would be expected for the recent Afar dyking sequence. The most frequently occurring injection spacing is 4–5 km ($\sim 15\%$) whereas 80% of the generated spacings are ≤ 10 km. Thus for the range of stress ratios and rotation angles estimated in Afar, the vast majority of dyke intrusions are predicted to intrude within 10 km of the previous one and most frequently between 4 and 5 km, which would be consistent with MT data (Fig. 4.6).

Dyke swarms

As commonly observed, dykes often grow next to other dykes, evidenced by the widespread occurrence of dyke swarms made of several hundreds of individual, sub-parallel dykes originating from apparently a single source region. Dyke swarms appear to be ubiquitous and can be found over a wide variety of tectonic settings and length scales, from individual volcanic dyke systems, to mid-ocean ridges, to giant mafic dyke swarms that extend over hundreds to several thousands of kilometers in length (Ernst and Baragar, 1992, see also Fig. 4.9). In giant dyke swarms, dykes are observed to maintain a finite spacing from their neighbours that is tens to hundreds of times smaller than their length. Yet, in spite of their ubiquity, dyke swarms have been studied rather descriptively. As a result, field data that could inform about the mechanics and dynamics of dyke swarms remain scarce.

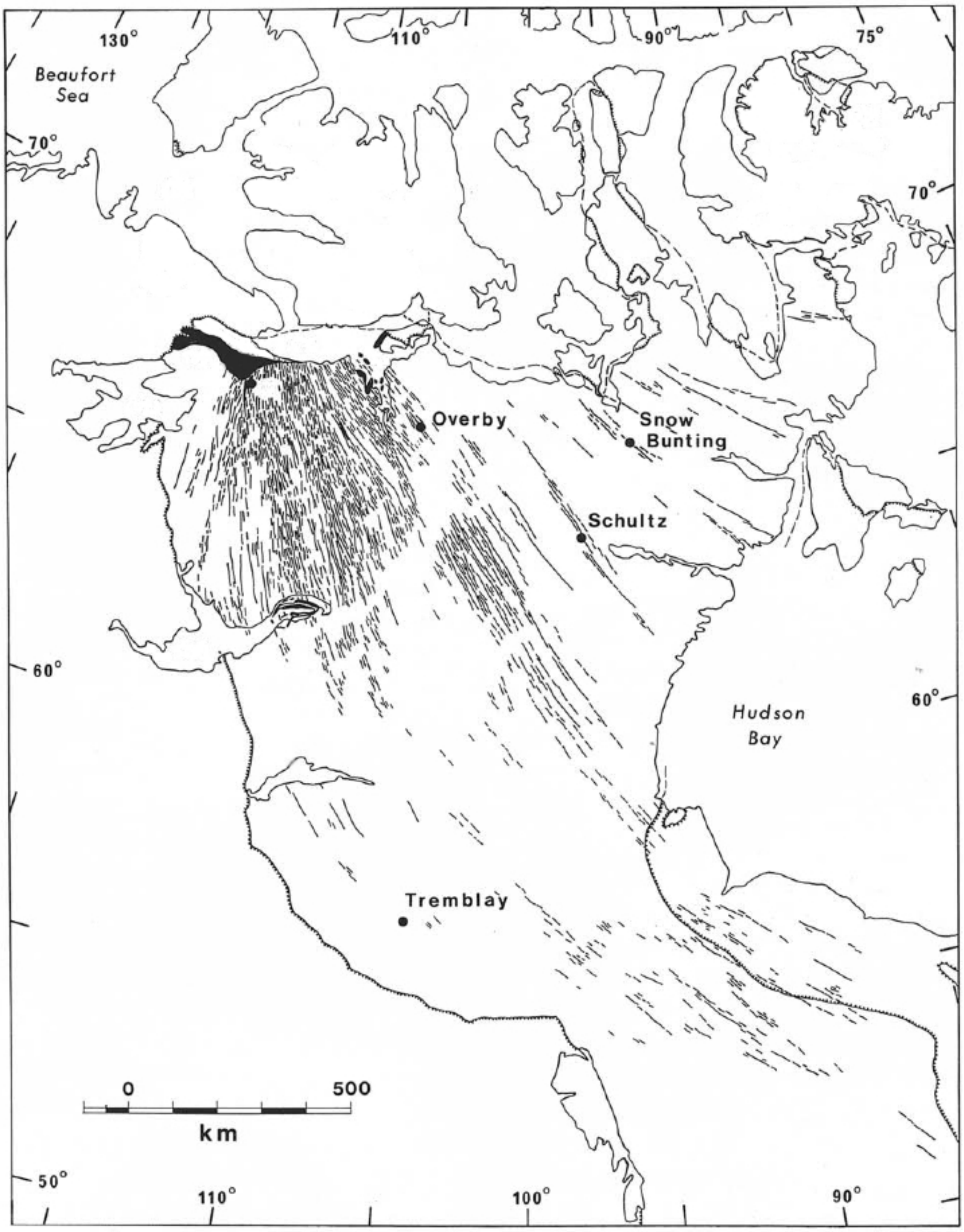

Figure 4.9: The 1270 Ma giant Mackenzie mafic dyke swarm in the northwestern Canadian Shield (after Le Cheminant and Heaman, 1989), whose dykes extend over more than 2,000 km with an average thickness of 30 m (Fahrig, 1987).

Furthermore, to date, mechanical models have not been able to clarify whether there exists an optimum, or natural spacing between the dykes. And yet, the existence of a natural spacing is at the heart of why dykes grow in swarms in the first place.

I developed a Finite Element Method (FEM) numerical model (using the Comsol Multiphysics software) to study the propagation of a swarm of identical, parallel and equally-spaced two-dimensional dykes away from a single source (Menand, to be submitted). In this model, dykes are modelled as edge-cracks and stress interactions between them are quantified by calculating the stress intensity factor K_I at their tip. In a first quasi-static case, the dynamics of the dykes were ignored and various dyke driving pressures were considered: buoyancy, a constant source overpressure, a remote tectonic stress or any combinations of these driving pressures. In a second case, dyke dynamics were accounted for by imposing a constant source overpressure and a linear pressure gradient along the dykes so that their overpressure was zero at the tip.

In both the quasi-static and dynamic cases, when the cracks are separated by a distance $2d$ that is greater than five times their length a, the stress intensity factor was found to be independent of the crack spacing, and thus could be expressed by the classical expression for a single crack with uniform load embedded in an infinite elastic medium (Tada et al., 2000): $K_I = \overline{\Delta P}\sqrt{a}$ for the static case ($\overline{\Delta P}$ is the average driving pressure over the entire length of the crack), and $K_I = \Delta P_0\sqrt{\pi a}$ for the dynamic case (ΔP_0 is the constant source excess pressure). That the stress intensity factor K_I does not dependent on the spacing indicates that cracks do not interact with one another when $2d > 5a$; in effect, although the cracks belong to the same swarm, they do not feel the presence of their neighbours. This provides also an *a posteriori* positive test of the numerical scheme, in that the computations retrieve the case of a single crack embedded in an infinite elastic solid.

When cracks are closer to each other such that $2d < 5a$, cracks do interact with each other and the previous expressions for K_I are no longer valid. In the quasi-static, it is found instead that the stress intensity factor at their tip can be expressed by a single relationship, irrespective of the exact type of crack loading (internal pressure, remote deviatoric stress, or buoyancy):

$$K_I = \left(\frac{3}{4}\Delta\rho g a + \Delta P_0 + \sigma_0\right)\sqrt{d}, \tag{4.12}$$

where $\Delta\rho$ is the density difference between the host rocks and the fluid in the crack, g is the gravitational acceleration, ΔP_0 is the constant source overpressure, and σ_0 the remote stress they experience. In the dynamic case, K_I can be expressed as

$$K_I = \frac{1}{\pi^{\frac{3}{2}}}\frac{\Delta P_0}{a}d^{\frac{3}{2}}. \tag{4.13}$$

As shown in Figure 4.10, equations (4.12) and (4.13) holds over 3 and almost 5 orders of magnitude, respectively. These results show that closer dykes will need

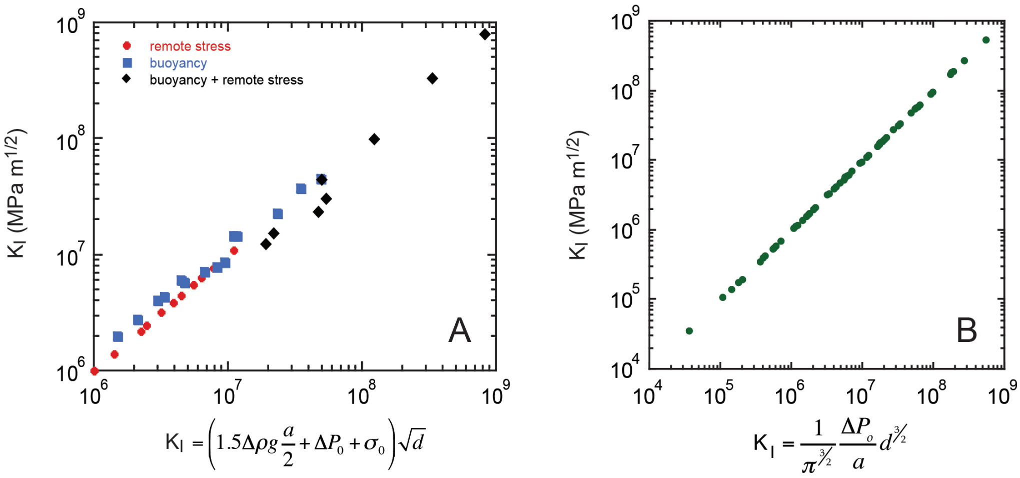

Figure 4.10: Stress intensity factor at the tip of two-dimensional edge-cracks separated by a distance $2d < 5a$. *Left*: quasi-static case. *Right*: dynamic case (Menand, to be submitted).

higher driving pressures to exceed a given rock fracture toughness K_c and propagate. Another result is that, everything else being equal, there exists a minimum dyke spacing below which the stress intensity factor K_I at the dyke tip will be smaller than the rock fracture toughness K_c hence precluding dyke propagation. This suggests that simultaneous dyke propagation in a swarm would be unstable, and would favour either the merging of adjacent dykes or the arrest of some of them so that dyke spacing is locally increased, which in turn would increase the stress intensity factor and so enable longer dykes to propagate. However, these expressions are only valid for two-dimensional dykes, for which the propagation length is much shorter than their breadth (their second larger dimensions).

With Andrew Bunger and Xi Zhang, both from CSIRO, Sandy Cruden, from Monash University, and Henry Halls, from the University of Toronto, we have developed another mechanical model for the horizontal propagation of multiple, closely-spaced blade-like dykes (Bunger et al., submitted). This model is not designed to solve analytically or numerically the governing equations for multiple dyke propagation. Rather, the model is used to derive appropriate scaling relationships for understanding the behaviour of the dominant terms in an energy balance. The ultimate aim is to determine whether a characteristic dyke spacing arises naturally from this energy balance.

We consider a model for an array of equally-spaced blade-like dykes that are propagating horizontally through brittle host rock. This model is justified for large dyke swarms that grow to be many times greater in length than the thickness of the crust. For the sake of simplicity, we assume the swarm is characterized by a single spacing between adjacent dykes, and we investigate how this spacing affects the propagation of the dykes; details of dyke initiation and early growth are not considered. Practically, the model is valid when the dyke length is at least 3 to 5 times greater than their height. When this is the case, it is valid to assume: 1) fluid flow to be unidirectional along the horizontal dyke-propagation direction, and 2) pressure to be uniform within each vertical planar cross section of the hydraulic fracture with the pressure and thickness related according to a local, plane strain condition. Both closely- and widely-spaced dykes are considered along with two limiting cases for the source condition: a constant source pressure (corresponding to an infinitely large and compressible source), and constant influx magma source (the case of a small, incompressible source).

We examine the model to find energetically optimal dyke spacings associated with both constant-pressure and constant-influx magma sources. Energy considerations indicate that for a constant-pressure source, the most energetically favourable condition amounts to maximizing Qp_0, where Q is the inlfux of magma leaving the source and feeding the dykes and p_0 is the constant source pressure. For the constant-influx source, the most energetically favourable situation is that which minimizing Qp, where p is the pressure in the source. In both case, the product Qp represents the net dyke propagation work rate and can be estimated from scaling analysis.

From this analysis we find that the constant-pressure source leads to an optimal spacing that is equal to the height of the blade-like dykes. The constant-influx source case, on the other hand, leads to two candidates for an optimal spacing, one which is expected to be around 0.3 times the dyke height and the other which is expected to be around 2.5 times the dyke height. We find also that for both constant-pressure and constant-influx sources, with time it becomes more advantageous energetically to initiate new dykes in between previous ones. Thus dyke spacing in a dyke swarm will decrease with time as more dykes are injected.

Comparison with measurements on dyke swarms in both Iceland and Canada lend initial support to our predictions, and we conclude that dyke swarms are indeed expected to have a natural spacing and that this spacing scales with, and is on the order of, the height of the blade-like dykes that comprise the swarm.

4.3 Formation of sills and magma storage in the crust

One must keep in mind that not all dykes lead to eruptions. In fact, the vast majority of dykes stall en route and remain trapped in the crust. Ratios of intrusive to extrusive magma volumes have been estimated to be of the order of 10:1 (Crisp, 1984; Shaw, 1985) whilst Gudmundsson et al. (1999) have calculated that the actual proportion of dykes reaching the surface in Iceland and Tenerife, Canary Islands, is only a few %. In many cases, those dykes which did not make it to the surface are associated with the formation or feeding of sub-horizontal sills (e.g.

Gudmundsson et al., 1999; Burchardt, 2008). Sills could therefore be envisaged as either arresting the advance of dykes or, conversely, forming as a result of dykes being prevented from propagating further. Repeated sill intrusion with evolution to laccolithic bodies (Pollard and Johnson, 1973) has also been proposed as a mechanism for forming crustal magma chambers and granite plutons (John, 1988; Hutton, 1992; Parsons et al., 1992).

Several models have been proposed for the arrest of dykes and associated sill formations: a buoyancy control, with sills emplacing at crustal levels where their magma becomes neutrally buoyant (Gilbert, 1877; Corry, 1988); a rheology control, where a rheology contrast between ductile rock layers and adjacent elastic, brittle strata would help stop feeder dykes and promote sill formation (Parsons et al., 1992); a rigidity control, as suggested by the many field studies showing that when sills intrude sedimentary sequences they commonly abut stiff rock layers, thus suggesting that these rigid layers could have arrested the vertical propagation of their feeder dyke and encouraged sill formation; or a stress control, because since igneous intrusions tend to propagate perpendicular to the least compressive stress (Anderson, 1951) sills should form when the least compressive stress is or becomes vertical.

We first tested the validity of the buoyancy and rigidity controls using analogue experiments with gelatine solids (Kavanagh et al., 2006). These experiments show that under lithostatic conditions the formation of sills requires the presence of interfaces. However, the presence of an interface is not sufficient. The experiments show that sills could only form when their feeder encountered an interface that separates a rigid layer that overlies a less rigid, lower layer (Fig. 4.11). In the opposite case, where a less rigid layer lies on top of a more rigid one, feeders would not intrude the interface between the two layers but would instead cross-cut that interface and carry on their propagation as vertical dykes (Kavanagh et al., 2006). Additionally, the properties of the interface itself can also have an important effect on whether a dyke would be deflected and intrude the interface (He and Hutchinson, 1989). This is supported by the analogue experiments of Kavanagh et al. (2006), who report instances where a dyke was expected to form a sill, because a rigid layer was overlying a less rigid layer, but instead was arrested by the interface without intruding the interface nor penetrating the upper layer; the interface was inferred to be too strong to be intruded by the dyke.

These experiments show also that contrary to dykes, sill dynamics are controlled by viscous dissipation of the fluid along their length (Kavanagh et al., 2006; Menand, 2008). If this interpretation is correct, this would have consequences for the size and shape of sills. Viscously-controlled dynamics would enable sills to propagate further and thus to grow thicker than dykes of similar magmas. These dynamics would also enable sills to propagate faster and thus to induce non-elastic deformations in surrounding rocks that could deviate them from the interface they originally follow. This could provide a mechanism for or assist the formation of concave saucer-shaped sills in sedimentary basins.

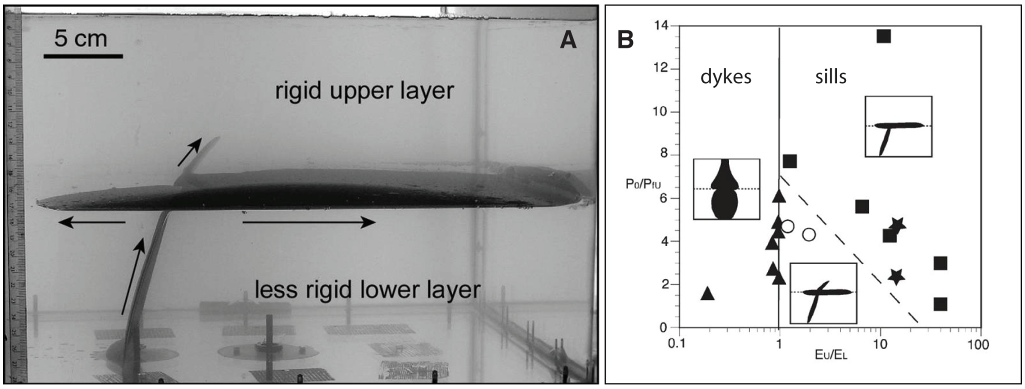

Figure 4.11: A) Photograph of a rigidity-controlled sill formation (Kavanagh et al., 2006). The rigidity modulus of the upper layer was 10% larger than that of the lower layer. The feeder dyke propagated from the injection point toward the interface, reached it and then intruded the interface as a sill in both opposite directions from the point where the dyke intersected the interface. Note the protruding dykelet that extended beyond the interface and into the more rigid upper layer; this dykelet was short-lived and stalled whilst the sill continued propagating. The arrows indicate flow directions. B) Rigidity contrasts (E_U/E_L) greater than unity are a prerequisite for sill formation.

Although these experiments were inconclusive regarding the role of neutrally buoyant levels, other studies suggest a neutral buoyancy alone is not expected to control sill formation, although it could arrest the vertical propagation of a rising buoyant dyke (Lister and Kerr, 1991; Pinel and Jaupart, 2004). However, overpressures large enough for sill intrusion could potentially develop provided high-density dykes manage to propagate far enough into low-density rocks (Taisne and Jaupart, 2009). Also, because a level of neutral buoyancy corresponds to the crustal level where a dyke is no longer buoyant and thus does not have any more internal vertical driving force, a dyke would become even more sensitive to horizontal compressive stress near its level of neutral buoyancy. So in principle, levels of magma neutral buoyancy could assist the formation of stress-controlled sills because, provided adequate stress conditions, levels of neutral buoyancy would represent advantageous horizons for sill emplacement.

How adequate stress conditions lead to sill formation was then investigated by Menand et al. (2010). Transition from dyke to sill is expected when the minimum compressive stress rotates from being horizontal, such as in extension tectonic environment, to being vertical, which would be the case in a horizontally compressive stress field. However, the orientation of an intrusion does not solely depend on the principal stress directions. It depends also on the magma overpressure, in that intrusions with higher overpressure need to propagate over greater distance before they can fully adjust their propagation to the principal directions (Mériaux and Lister, 2002). To quantify the conditions for the formation of stress-controlled sills, Menand et al. (2010) carried out analogue experiments where air was injected into a solid of gelatine that was then compressed laterally so that the minimum deviatoric compressive stress became vertical. The lateral deviatoric compressive stress was applied to the gelatine solid by inserting plastic sheets between the solid gelatine and the lateral walls of its container, thus imposing a horizontal deformation ϵ_x proportional to the thickness of these sheets hence a compressive lateral stress $\sigma_x = 4E\epsilon_x/3$ (E is the Young's modulus of the gelatine solid). Air acted as an analogue for buoyant magma. As shown in Fig. 4.12, air-filled cracks initially driven vertically by their buoyancy changed their trajectory and ultimately formed sills in response to the minimum compressive stress being vertical. But this trajectory re-adjustment was not instantaneous. Cracks of higher buoyancy required greater distances to re-orient themselves fully, and they could reach the surface in spite of the vertical minimum compressive stress, and therefore not form sills, if these distances happened to be larger than that separating the intrusions from the surface.

Applying dimensional analysis to their experimental data, Menand et al. (2010) related the vertical distance d the buoyant crack needed to propagate before turning into a sill to the buoyancy of the crack and the horizontal maximum deviatoric compressive stress σ_x. Upscaled to magmatic conditions over a range of reasonable geological values — tensile strength of homogeneous host rock T_s = 1–10 MPa, fracture toughness K_c = 1–1000 MPa m$^{1/2}$, density difference between dyke and host rock $\Delta\rho$ =100–500 kg/m^3, and σ_x = 0.1–100 MPa — the vertical distance d can be expressed as a function of T_s as

$$d \simeq \frac{T_s}{\Delta\rho g} \exp\left[(0.10 \pm 0.01)\left(\frac{T_s}{\sigma_x}\right)\right], \tag{4.14}$$

or as a function of K_c as

$$d \simeq \left(\frac{K_c}{\Delta\rho g}\right)^{2/3} \exp\left[(0.10 \pm 0.01)\frac{\left(\Delta\rho g K_c^2\right)^{\frac{1}{3}}}{\sigma_x}\right]. \tag{4.15}$$

In a homogeneous and elastic crust, and over this range of geological conditions, a dyke would have to travel a distance of the order of at least 200 m and in most cases of the order of 1 to 10 km to adjust to a vertical minimum compressive stress and turn into a sill. This distance is typically greater than the average thickness of lithological units, and therefore suggests that in most cases crustal heterogeneities and the distance between interfaces that are favourable to sill intrusions will play a larger role than remote tectonic stress rotation in determining where in the crust sills form, unless these favourable interfaces are several hundred meters or more apart.

This study has also implications for magma transport through dykes. The characteristic length-scale for stress-controlled sill formation is found to be typically greater (and in many instances much greater) than the average thickness of lithological units, in accord with previous studies (e.g. Dahm, 2000; Watanabe

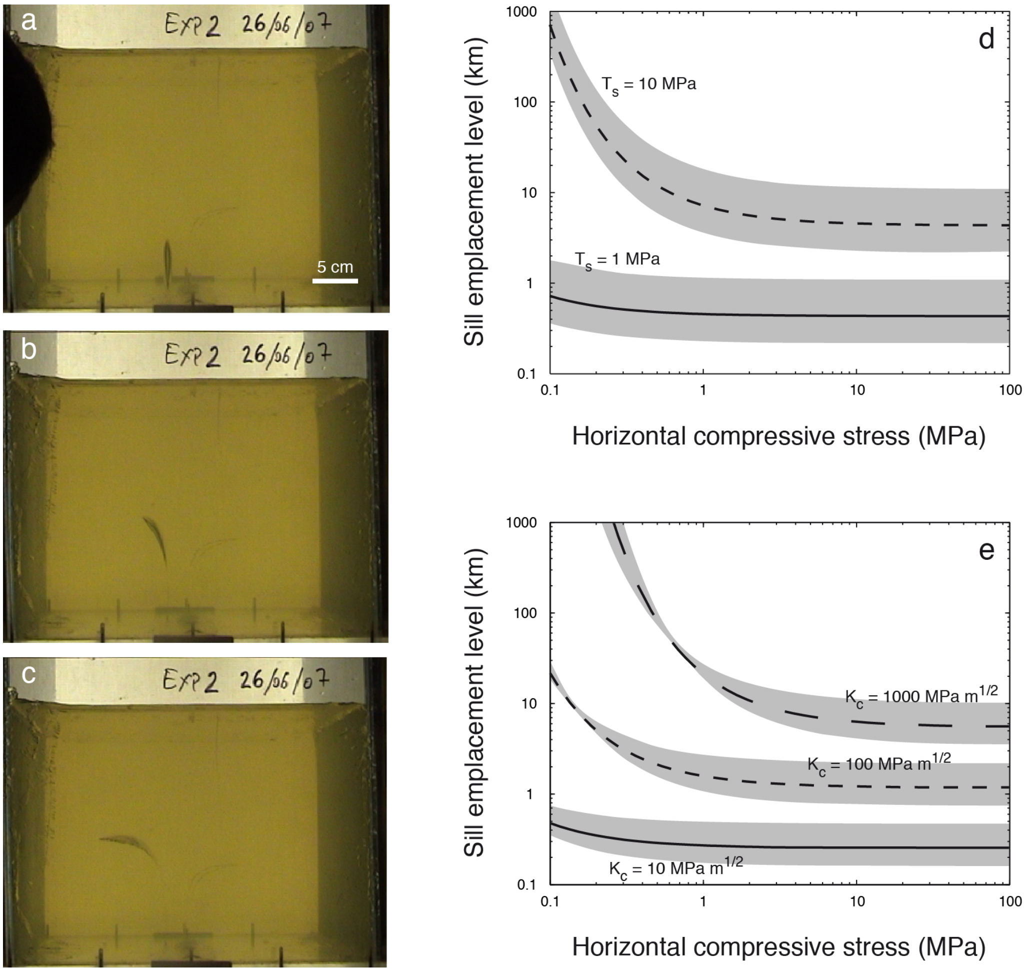

Figure 4.12: (a-c) Series of photographs of a stress-controlled sill formation (Menand et al., 2010). The ratio of initial crack buoyancy to horizontal compressive stress was 2.1. (a) The injection of air in the gelatine solid created a crack that was initially driven vertically by the air buoyancy. (b) The gelatine solid was compressed laterally, and so the crack experienced an additional horizontal compressive stress to which it reacted by changing its direction of propagation. (c) Ultimately, the crack rotated by 90° and formed a sill before coming to a stop. (d-e) Upscaling to magmatic conditions: the vertical distance a dyke has to propagate before turning into a sill is represented as a function of the ambient horizontal compressive stress for different rock tensile strengths T_s (equation 4.14) and fracture toughnesses K_c (equation 4.15); the grey areas represent a range of density differences between 100 and 500 kg/m^3.

et al., 2002). This therefore suggests that buoyant dykes would reach the surface even in a compressive hence *a priori* unfavourable tectonic environment if the characteristic length-scale for dyke-to-sill transition is greater than the distance that separates them from the surface. This contrasts with the field observations that only a few percentage of dykes reach the surface, and that not all the dykes that do not reach the surface turns into sills (Gudmundsson et al., 1999). In fact, this apparent contradiction would reinforce the point made by previous studies that crustal heterogeneities play an important role in controlling sill formation hence the fate of many dykes.

Reviewing these different mechanisms and the field evidence for rheology-controlled sills, Menand (2011) suggests that principal physical controls include rigidity contrasts, where sills form at the interface between soft strata overlaid by comparatively stiffer strata; rheology anisotropy, where sills form within the weakest ductile zones; and rotation of deviatoric stress, where sills form when the minimum compressive stress becomes vertical. Comparatively, the concept of neutral buoyancy is unlikely to play a leading control in the emplacement of sills, although it could assist their formation, whereas the efficiency of a stress-control would be strengthen by the presence of heterogeneous crustal layers, thus highlighting the dominant role played by crustal heterogeneities.

These mechanical considerations are key if we are to understand how intrusions can stall and magma be stored in some regions of the crust, and by extension the thermal evolution of these crustal regions, that is the formation of plutons (*sensu lato*) and magma chambers. Indeed, an increasing number of geophyscial and geochronological data as well as geological observations is currently modifying our understanding of pluton construction. When plutons were initially envisaged as quasi-spherical bodies growing slowly and essentially by an overall inflation, they are now recognized as growing incrementally by the accretion of successive and relatively small magma pulses, over variable periods of time, from less than a century to millions of years, depending on geodynamic setting and source fertility. I suggest that the formation of a sill provides favourable rigidity anisotropy for the emplacement of subsequent sills so that plutons grow by over-accretion, under-accretion or even mid-accretion of successive sills (Menand, 2008, 2011). In accord with field data, this model predicts these plutons grow mainly by vertical expansion, representing the cumulative thickness of their internal sills, while maintaining a comparatively constant lateral extend. The model also predicts that the time-scale over which laccoliths form is essentially determined by the cumulative time between successive sill intrusions. In any case, pluton growth by small increments brings new challenges and has far-reaching implications. The evolution of magma bodies is related to the processes that control the timescale and the spatial distribution of the successive pulses. Depending on their emplacement rate and on their ability to amalgamate, repeated magma pulses can either rapidly solidify or ultimately build up an active magma chamber. Thus understanding how magma bodies grow has fundamental implications for the link between volcanism and plutonism as well as for magma differentiation and ultimately for our understanding of the growth and evolution of the Earth's crust. The concept of pluton incremental growth challenges our understanding as well as our field interpretations of the processes involved during pluton construction. Indeed, these processes and how they operate in governing the emplacement and growth of plutons, both in space and time, are still debated (Menand et al., 2011).

Bibliography

Anderson, E. M. (1951). *The Dynamics of Faulting and Dyke Formation with Applications to Britain (Second Edition)*. Oliver and Boyd Ltd., Edinburgh and London.

Atkinson, B. K. (1984). Subcritical crack growth in geological materials. *J. Geophys. Res. 89*, 4077–4114.

Barenblatt, G. I. (1962). The mathematical theory of equilibrium cracks in brittle fracture. *Adv. Appl. Mech. 7*, 55–129.

Bastow, I. D. and D. Keir (2011). The protracted development of the continent–ocean transition in Afar. *Nature Geoscience 4*, 248–250.

Bialas, R. W., W. R. Buck, and R. Qin (2010). How much magma is required to rift a continent? *Earth and Planetary Science Letters 292*, 68–78.

Bruce, P. M. and H. E. Huppert (1989). Thermal control of basaltic fissure eruptions. *Nature 342*, 665–667.

Bruce, P. M. and H. E. Huppert (1990). Solidification and melting along dykes by laminar flow of basaltic magma. In M. P. Ryan (Ed.), *Magma Transport and Storage*, pp. 87–101. John Wiley & Sons Ltd.

Bunger, A. P., T. Menand, A. Cruden, X. Zhang, and H. Halls (submitted). Analytical predictions for a natural spacing within dyke swarms. *Earth Planet. Sci. Lett.*.

Burchardt, S. (2008). New insights into the mechanics of sill emplacement provided by field observations of the Njardvik Sill, Northeast Iceland. *J. Volcanol. Geotherm. Res. 173*, 280–288.

Cayol, V., J. H. Dietrich, A. T. Okamura, and A. Miklius (2000). High magma storage rates before the 1983 eruption of Kilauea, Hawaii. *Science 288*, 2343–2346.

Corry, C. E. (1988). Laccoliths: mechanics of emplacement and growth. *Geol. Soc. Am. Spec. Pap. 220.*

Crisp, J. A. (1984). Rates of magma emplacements and volcanic output. *J. Volcanol. Geotherm. Res. 20*, 177–211.

Dahm, T. (2000). Numerical simulations of the propagation path and the arrest of fluid-filled fractures in the Earth. *Geophys. J. Int. 141*, 623–638.

Daniels, K. A. (2012). *Modelling magma transport: a study of dyke injection*. Ph. D. thesis, University of Bristol.

Daniels, K. A., J. L. Kavanagh, T. Menand, and R. S. J. Sparks (2012). The shapes of dykes: Evidence for the influence of cooling and inelastic deformation. *GSA Bulletin 124*, 1102–1112.

Delaney, P. T. and D. D. Pollard (1981). Deformation of host rocks and flow of magma during growth of Minette dikes and breccia-bearing intrusions near Ship Rock, New Mexico. *U. S. Geol. Surv. Prof. Pap.* (1202).

Ebinger, C. and M. Casey (2001). Continental breakup in magmatic provinces: An Ethiopian example. *Geology 29*, 527–530.

Emerman, S. H., D. L. Turcotte, and D. A. Spence (1986). Transport of magma and hydrothermal solutions by laminar and turbulent fluid fracture. *Phys. Earth Planet. Int. 41*, 249–259.

Ernst, R. E. and W. R. A. Baragar (1992). Evidence from magnetic fabric for the flow pattern of magma in the Mackenzie giant radiating dyke swarm. *Nature 356*, 511–513.

Fahrig, W. F. (1987). The tectonic settings of continental mafic dyke swarms: failed arm and early passive margin. In H. C. Halls and W. F. Fahrig (Eds.), *Mafic Dyke Swarms*, Number 34 in Geol. Assoc. Can. Spec. Pap., pp. 331–348.

Ferguson, D. J., T. D. Barnie, D. M. Pyle, C. Oppenheimer, G. Yirgu, E. Lewi, T. Kidane, S. Carn, and I. Hamling (2010). Recent rift-related volcanism in Afar, Ethiopia. *Earth Planet. Sci. Lett. 292*, 409–418.

Foshag, W. and J. Gonzalez (1956). Birth and development of Paricutin volcano. *U. S. Geol. Surv. Bull. D 965*, 355–485.

Galland, O., P. Cobbold, E. Hallot, J. de Bremond d'Ars, and G. Delavaud (2006). Use of vegetable oil and silica powder for scale modelling of magmatic intrusion in a deforming brittle crust. *Earth and Planetary Science Letters 243*, 786–804.

Gilbert, G. K. (1877). Geology of the Henry Mountains, Utah. *U.S. Geographical and Geological Survey of the Rocky Mountain Region*.

Grandin, R., A. Socquet, E. Jacques, N. Mazzoni, J.-B. De Chabalier, and G. C. P. King (2010). Sequence of rifting in Afar, Manda-Hararo rift, Ethiopia, 2005–2009: Time-space evolution and interactions between dikes from interferometric synthetic aperture radar and static stress change modeling. *Journal of Geophysical Research 115*(B10413), doi: 10.1029/2009JB000815.

Gudmundsson, A., N. Friese, I. Galindo, and S. L. Philipp (2008). Dike-induced reverse faulting in a graben. *Geology 36*, 123–126.

Gudmundsson, A., L. B. Marinoni, and J. Marti (1999). Injection and arrest of dykes: implications for volcanic hazards. *J. Volcanol. Geotherm. Res. 88*, 1–13.

Hamling, I. J., T. J. Wright, E. Calais, L. Bennati, and E. Lewi (2010). Stress transfer between thirteen successive dyke intrusions in Ethiopia. *Nature Geoscience 3*, 713–717.

He, M. Y. and J. W. Hutchinson (1989). Crack deflection at an interface between dissimilar elastic materials. *International Journal of Solids and Structures 25*(9), 1053–1067.

Hutton, D. H. W. (1992). Granite sheeted complexes: evidence for the dyking ascent mechanism. *Trans. R. Soc. Edinburgh: Earth Sci. 83*, 377–382.

John, B. E. (1988). Structural reconstruction and zonation of a tilted mid-crustal magma chamber: The felsic Chemehuevi Mountains plutonic suite. *Geology 16*, 613–617.

Kavanagh, J. L., T. Menand, and K. A. Daniels (2012). Gelatine as a crustal analogue: determining elastic properties for modelling magmatic intrusions. *Tectonophysics*, 10.1016/j.tecto.2012.09.032.

Kavanagh, J. L., T. Menand, and R. S. J. Sparks (2006). An experimental investigation of sill formation and propagation in layered elastic media. *Earth Planet. Sci. Lett. 245*, 799–813.

Kerr, R. C. and J. R. Lister (1995). Comment on "On the relationship between dike width and magma viscosity" by Yutaka Wada. *J. Geophys. Res. 100*, 15,541.

Le Cheminant, A. and L. Heaman (1989). Mackenzie igneous events, Canada: Middle Proterozoic hotspot magmatism associated with ocean opening. *Earth Planet. Sci. Lett 96*, 38–48.

Le Corvec, N., T. Menand, and J. Lindsay (submitted). Interaction of ascending magma with pre-existing crustal fractures in monogenetic basaltic volcanism: an experimental approach. *J. Geophys. Res.*.

Lister, J. R. (1990a). Buoyancy-driven fluid fracture: similarity solutions for the horizontal and vertical propagation of fluid-filled cracks. *J. Fluid Mech. 217*, 213–239.

Lister, J. R. (1990b). Buoyancy-driven fluid fracture: the effects of material toughness and of low-viscosity precursors. *J. Fluid Mech. 210*, 263–280.

Lister, J. R. and R. C. Kerr (1991). Fluid-mechanical models of crack propagation and their application to magma transport in dykes. *J. Geophys. Res. 96*, 10,049–10,077.

Menand, T. (2008). The mechanics and dynamics of sills in elastic layered media and their implications for the growth of laccoliths. *Earth Planet Sci. Lett. 267*, 93–99.

Menand, T. (2011). Physical controls and depth of emplacement of igneous bodies: A review. *Tectonophysics 500*, 11–19.

Menand, T. (to be submitted). Spatial distribution of dykes and magma transport in dyke swarms. *Geochem. Geophys. Geosyst.*.

Menand, T., K. Daniels, and P. Benghiat (2010). Dyke propagation and sill formation in a compressive tectonic environment.

Menand, T., M. de Saint-Blanquat, and C. Annen (2011). Emplacement of magma pulses and growth of magma bodies. *Tectonophysics 500*, 1–2.

Menand, T. and S. R. Tait (2001). A phenomenological model for precursor volcanic eruptions. *Nature 411*, 678–680.

Menand, T. and S. R. Tait (2002). The propagation of a buoyant liquid-filled fissure from a source under constant pressure: An experimental approach. *J. Geophys. Res. 107 (B11)*(2306), doi:10.1029/2001JB000589.

Newhall, C. G. and R. S. Punongbayan (1996). *Fire and Mud: Eruptions and Lahars of Mount Pinatubo, Philippines*. Philippine Institute of Volcanology and Seismology, Univ. Washington Press,.

Parsons, T., N. H. Sleep, and G. A. Thompson (1992). Host rock rheology controls on the emplacement of tabular intrusions: Implications for underplating of extending crust. *Tectonics 11*, 1348–1356.

Petford, N., R. C. Kerr, and J. R. Lister (1993). Dike transport of granitoid magmas. *Geology 21*, 845–848.

Petford, N., J. R. Lister, and R. C. Kerr (1994). The ascent of felsic magmas in dykes. *Lithos 32*, 161–168.

Pinel, V. and C. Jaupart (2004). Magma storage and horizontal dyke injection beneath a volcanic edifice. *Earth Planet. Sci. Lett. 221*, 245–262.

Pollard, D. D. and A. M. Johnson (1973). Mechanics of growth of some laccolithic intrusions in the Henry Mountains, Utah, II. Bending and failure of overburden layers and sills formation. *Tectonophysics 18*, 311–354.

Pollard, D. D. and O. H. Muller (1976). The effect of gradients in regional stress and magma pressure on the form of sheet intrusions in cross section. *J. Geophys. Res. 81*, 975–984.

Reches, Z. and J. Fink (1988). The mechanism of intrusion of the Inyo Dike, Long Valley Caldera, California. *J. Geophys. Res. 93*, 4321–4334.

Rubin, A. M. (1993a). Dikes vs. diapirs in viscoelastic rock. *Earth Planet. Sci. Lett. 119*, 641–659.

Rubin, A. M. (1993b). On the thermal viability of dykes leaving magma chambers. *Geophys. Res. Lett. 20*, 257–260.

Rubin, A. M. (1995a). Getting granite dikes out of the source region. *J. Geophys. Res. 100*, 5911–5929.

Rubin, A. M. (1995b). Propagation of magma-filled cracks. *Ann. Rev. Earth Planet. Sci. 23*, 287–336.

Shaw, H. R. (1985). Links between magma-tectonic rate balances, plutonism, and volcanism. *J. Geophys. Res. 90*, 11,275–11,288.

Spence, D. A. and P. Sharp (1985). Self-similar solutions for elastohydrodynamic cavity flow. *Proc. R. Soc. London 400*, 289–313.

Spence, D. A., P. W. Sharp, and D. L. Turcotte (1987). Buoyancy-driven crack propagation: a mechanism for magma migration. *J. Fluid Mech. 174*, 135–153.

Spence, D. A. and D. L. Turcotte (1985). Magma-driven propagation of cracks. *J. Geophys. Res. 90*, 575–580.

Spence, D. A. and D. L. Turcotte (1990). Buoyancy-driven magma fracture: a mechanism for ascent through the lithosphere and the emplacement of diamonds. *J. Geophys. Res. 95*, 5133–5139.

Tada, H., G. R. Irwin, and P. C. Paris (2000). *The Stress Analysis of Cracks Handbook*. New York: ASME.

Taisne, B. and C. Jaupart (2009). Dike propagation through layered rocks. *Journal of Geophysical Research 114*(B9), B09203.

Takada, A. (1990). Experimental study on propagation of liquid-filled crack in gelatin: shape and velocity in hydrostatic stress condition. *J. Geophys. Res. 95*, 8471–8481.

Wada, Y. (1994). On the relationship between dike width and magma viscosity. *J. Geophys. Res. 99*, 17,743–17,755.

Wada, Y. (1995). On the relationship between dike width and magma viscosity: reply. *J. Geophys. Res. 100*, 15,543–15,544.

Watanabe, T., T. Masuyama, K. Nagaoka, and T. Tahara (2002). Analog experiments on magma-filled cracks: Competition between external stresses and internal pressure. *Earth Planets Space 54*, 1247–1261.

Weertman, J. (1971a). Theory of water-filled crevasses in glaciers applied to vertical magma transport beneath oceanic ridges. *J. Geophys. Res. 76*, 1171–1183.

Weertman, J. (1971b). Velocity at which liquid-filled cracks move in the Earth's crust or in glaciers. *J. Geophys. Res. 76*, 8544–8553.

Wright, T., C. Ebinger, J. Biggs, A. Ayele, G. Yirgu, D. Keir, and A. Stork (2006). Magma-maintained rift segmentation at continental rupture in the 2005 Afar dyking episode. *Nature 442*, 291–294.

4.4 Selected publications

Underlined are the names of students I supervised.

1. **Menand, T.** and Tait, S. R. (2001) A phenomenological model for precursor volcanic eruptions. *Nature,* **411**, 678–680.
2. **Menand, T.** and Tait, S. R. (2002) The propagation of a buoyant liquid-filled fissure from a source under constant pressure: An experimental approach. *J. Geophys. Res.* **107** (B11), 10.1029/2001JB000589.
3. Kavanagh, J. L., **Menand, T.** and Sparks, R. S. J. (2006) An experimental investigation of sill formation and propagation in layered elastic media. *Earth Planet. Sci. Lett.* **245**, 799–813.
4. **Menand, T.** (2008) The mechanics and dynamics of sills in elastic layered media and their implications for the growth of laccoliths. *Earth Planet. Sci. Lett.*, **267**, 93–99.
5. **Menand, T.**, Daniels, K., and Benghiat, P. (2010) Dyke propagation and sill formation in a compressive tectonic environment. *J. Geophys. Res.* **115**, B08201, 10.1029/2009JB006791.
6. **Menand, T.**, de Saint-Blanquat, M. and Annen, C. (2011) Emplacement of Magma Pulses and Growth of Magma Bodies, Preface, *Tectonophysics*, **500**, 1-2.
7. **Menand, T.** (2011) Physical controls and depth of emplacement of igneous bodies: A review. *Tectonophysics*, **500**, 11-19.
8. Daniels, K. A., Kavanagh, J. L., **Menand, T.**, and Sparks, R. S. J. (2012) The shapes of dykes: Evidence for the influence of cooling and inelastic deformation. *Geological Society of America Bulletin*, **124**, 1102–1112.
9. Kavanagh, J. L., **Menand, T.**, and Daniels, K. A. (2012) Gelatine as a crustal analogue: Determining elastic properties for modelling magmatic intrusions. *Tectonophysics*, 10.1016/j.tecto.2012.09.032.

A phenomenological model for precursor volcanic eruptions

Thierry Menand* & Stephen R. Tait*

Laboratoire de Dynamique des Systèmes Géologiques, Institut de Physique du Globe de Paris, 4, place Jussieu, 75252 Paris cedex 05, France

Intense explosions of relatively short duration frequently precede large explosive and effusive volcanic eruptions—by as much as weeks to months in the case of very viscous magmas[1–6]. In some cases, such pre-eruption activity has served as a sufficient warning to those living in the vicinity to evacuate and avoid calamity[1]. Precursor events seem to be related to the formation of a magma pathway to the surface, but their precise interpretation is a long-standing puzzle. It has been inferred from theoretical studies that exsolution of volatiles might create an almost separate gas pocket at the tip of a propagating dyke[7–9]. Here we explain the role that such a process may have, using a laboratory study of the transient propagation of a liquid-filled crack with a gas pocket at its tip that grows with time. We show that once the gas pocket acquires sufficient buoyancy to overcome the fracture resistance of the host solid the dynamics of the gas pocket, rather than those of the liquid, determine the velocity of the crack tip. Furthermore, we find that the gas can ultimately separate from the liquid. We propose that fast-moving, gas-rich pockets reaching the surface ahead of the main liquid-filled fissure could be the origin of many precursor eruptions.

Precursory activity associated with a number of carefully monitored volcanic eruptions seems to fit into a general pattern. Quasi-continuous volcanogenic seismic tremor associated with sporadic explosions and gas emissions at the surface are observed during several weeks before the arrival of the main magma conduit. Explosions are intense but of short duration, and contain variable amounts (sometimes only very little) of juvenile magmatic component. This pattern occurs whether the eruption is ultimately an explosive plinian event[3–5,10–12] or dome-forming[6,13,14]. This activity may sometimes not be followed by a large eruption. Although the term 'precursory' seems inappropriate in such cases, this activity may well be part of the same fundamental pattern, but the main magma conduit stalls and never reaches the surface, remaining as a shallow intrusion. At Usu volcano, Japan, months of degassing from craters followed initial intense explosions on 31 March 2000, but at present the main magma conduit has not reached the surface, and seems unlikely now to do so. This pattern follows that of other eruptions at Usu during the last century, for example in 1943, when the lava dome Showa-Shinzan formed[15]. Precursory activity is thus a common prelude to large volcanic events. Here we provide a framework in which precursory activity can be interpreted. This can help ultimately to gain understanding of its expected timescale at a volcano of a given type, which is of obvious practical use for hazard assessment.

As silicate magmas ascend towards the Earth's surface, the reduction of pressure causes dissolved volatile components to exsolve and form gas bubbles. At the tip of a vertically oriented fissure, pressure is lowest because there is least rock overburden. In addition, the high viscosities of magmatic liquids implies large head losses as the fissure tapers to vanishing thickness[7,8]. As the fissure propagates towards the surface, ambient pressure decreases, driving further exsolution and expansion of the volatiles. Moreover, because of the no-slip boundary condition at the dyke wall, magma near the dyke wall moves more slowly than at the tip and, from mass balance, magma near the dyke centre moves faster than the tip. This means that fresh magma that has not been degassed is always being transported into the low-pressure region, where it should turn into foam. The subsequent lowering of magma density provides a buoyancy force that tends to keep it there. Intense shearing in this region may cause the foam to break down and allow the gas to collect into a separate pocket at the tip, which grows during propagation. The complex dynamics of this process go beyond the scope of our work; however, we infer that bubbles do not need to move significant distances with respect to the surrounding magma to feed the gas pocket. One theoretical investigation has shown, in the framework of a steadily propagating fissure with a fixed volume of gas at the tip, that the fissure tends to pinch off between the gas and the following liquid[8]. We performed laboratory experiments to look at the transient propagation of a liquid-filled crack with a gas pocket at its tip that grows with time.

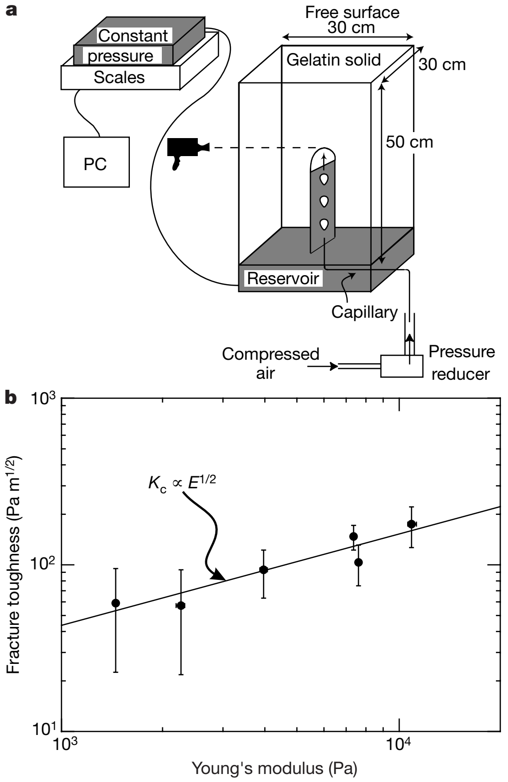

Figure 1 Experimental apparatus and rheology of gelatin. **a**, Gelatin was solidified in an acrylic tank under hydrostatic conditions. Liquid was then injected through the gelatin from a reservoir under constant overpressure. To simulate exsolution and expansion of volatiles at the crack tip, air was continuously injected into the liquid-filled fissure some time after it began to propagate. The air collected at the fissure tip. Dyed aqueous solutions of four different viscosities were used: 1, 41, 126 and 342 mPa s, achieved by dissolving small amounts (less than 0.5 wt%) of hydroxyethylcellulose. These low polymer concentrations allowed solution viscosities to be varied without affecting other properties. Propagation velocity was recorded by videotaping the experiment; liquid injection rate was monitored on a personal computer by measuring output from the reservoir. Experimental durations were less than 5 min, a time period short enough to consider the rheological behaviour of the gelatin to be purely elastic[24]. **b**, Relationship between Young's modulus E and fracture toughness K_c of the gelatin. E was calculated from the measured vertical deflection induced by a weight on the free surface of the gelatin. K_c was defined as the stress intensity factor at the tip of a fissure of known geometry and internal pressure distribution when gelatin is on the verge of failure.

---

* Present address: BP Institute for Multiphase Flow, University of Cambridge, Madingley Rise, Madingley Road, Cambridge CB3 0EZ, U.K. (T.M.); and TH Huxley School of Environment, Earth Science and Engineering, Imperial College of Science, Technology and Medicine, RSM Building, Prince Consort Road, London SW7 2BP, U.K. (S.R.T.).

Experimental apparatus and techniques are described in Fig. 1a. Young's modulus and fracture toughness have been measured independently *in situ* in our experimental apparatus. These conform to the expected theoretical relationship for a purely elastic solid[16,17] (Fig. 1b). This knowledge of the fracture toughness of the gelatin provides an important technical basis for the study. Figure 2 shows pictures of two different stages of an experiment. Initially the liquid-filled crack propagates vertically and radially owing to the reservoir overpressure (Fig. 2a). After we began to inject air into the fissure, a bubble formed at its tip. When it became higher than about 2 cm, the shape of the crack was deformed markedly in both vertical cross-sections (Fig. 2b, c). Moreover, the crack velocity (which is the bubble velocity) increased abruptly while the liquid injection rate stayed constant (Fig. 3), indicating that the crack is closing. Having both a closing crack and an accelerating air bubble indicates that the bubble may separate from the liquid. Liquid injection rate was a decreasing function of liquid viscosity (Fig. 3b).

The controlling influence of the air pocket on fissure propagation once it reached a critical height h_c is better seen on a graph of crack velocity as a function of the height of the air bubble h_b for heights greater than h_c (Fig. 4). Whatever the viscosity of the fluid and the injection rate of air, the crack velocity U is proportional to the square of the bubble height:

$$U \propto h_b^2 \qquad (1)$$

Such a relation has already been reported for buoyant cracks of constant volume filled with low-viscosity fluid[18], which emphasizes that in our experiments liquid viscosity had no function in governing velocity of the fissure tip once the air bubble reached its critical height h_c. We propose that h_c is the minimum height needed such that the air bubble can fracture the gelatin solid, on the basis of our knowledge of fracture toughness for gelatin.

In the framework of linear elastic fracture mechanics the intensity of the tensile stress concentration at the bubble tip owing to buoyancy of air is characterized by a stress intensity factor K_I (ref. 7). h_c is the height for which K_I reached the fracture toughness K_c of the gelatin solid, thought to be a material parameter independent of the loading or the velocity of the fissure. As K_I is almost exclusively due to the buoyancy of the air bubble[19], we obtain the following relation for h_c (ref. 7),

$$h_c = \left[\frac{4K_c}{3\rho_g g}\sqrt{\frac{2}{\pi}}\right]^{\frac{2}{3}} \qquad (2)$$

where ρ_g is the density of the gelatin solid and g the gravitational acceleration. The gelatin solids in our experiments had a fracture toughness $K_c \approx 54\ \mathrm{Pa\,m^{1/2}}$, which gives $h_c \approx 3$ cm, a value close to the 2 cm suggested by our observations. We conclude that once the bubble buoyancy overcomes the fracture resistance of the gelatin it controls the crack tip velocity.

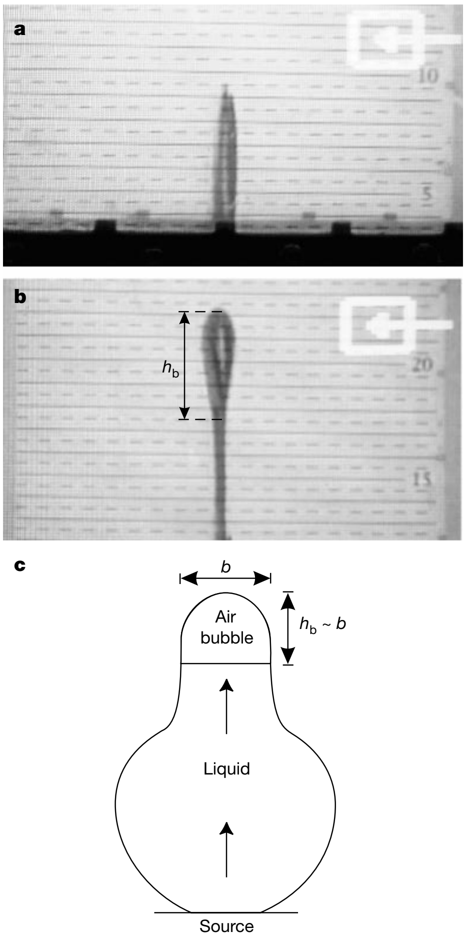

Figure 2 Photographs of an experiment. **a**, Initially the fissure propagates owing to the reservoir overpressure. **b**, **c**, As the injected air accumulates at the tip it dramatically deforms the crack and dictates its width (**b**) as well as its breadth (**c**).

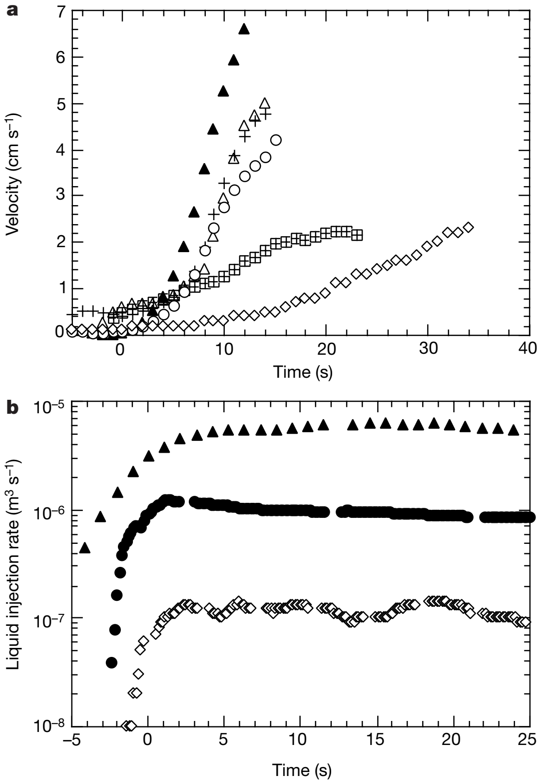

Figure 3 Time evolution of velocity and injection rate during propagation. **a**, **b**, The velocity (**a**) and the liquid injection rate (**b**) of the crack for different experiments as a function of time. The time origin corresponds to the moment at which the air bubble reached its critical height h_c. Each experiment corresponds to a given fluid viscosity. Diamond, 0.342 Pa s; filled circle, 0.126 Pa s; open circle, 0.041 Pa s; and other symbols, 10^{-3} Pa s.

The velocity of the fissure increases with the volume of the gas pocket; however, the velocity of the liquid is limited by the viscous pressure gradient inside the fissure tail, which balances and is therefore equal to liquid buoyancy. Assuming that the fissure tail has a steady-state horizontal elliptical cross-section and equating the kinematically determined tail width with the Poiseuille flow width, we obtain the fissure velocity u_s above which separation occurs between the gas pocket and the liquid:

$$u_s = \left[\frac{8q^2\Delta\rho g}{\eta\pi^2 b^2}\right]^{\frac{1}{3}} \approx \left[\frac{8q^2\Delta\rho g}{\eta\pi^2 h_b^2}\right]^{\frac{1}{3}} \qquad (3)$$

where q is the liquid flux, $\Delta\rho$ the difference between the density of the solid and the density of the liquid, η the liquid viscosity and b the breadth of the crack, which is approximately equal to the height of the gas pocket h_b (Fig. 2c). Once fissure velocity exceeds u_s, the gas pocket effectively separates from the liquid-filled fissure; a small quantity of liquid is generally carried along with the gas pocket because the viscosity of the liquid prevents clean separation of the phases.

The velocity at which the gas pocket will propagate once it has separated remains unknown. We have shown that gelatin is behaving as an elastic, brittle solid and that the stress intensity factor is greater than its fracture toughness. Furthermore, we find that crack tip velocity is a simple function of the height of the gas pocket. The fundamental control in this regime is presumably the mechanics of failure and crack propagation at the tip in response to the buoyancy force of the gas. Another possibility is that the velocity of the gas pocket is limited by the propagation of elastic waves in the solid and is comparable to the velocity of such waves. If the host solid is rock, these are of the order of km s^{-1}, considerably greater than those predicted by the regime observed in our experiments. Dyke velocity can be estimated by monitoring micro-seismic events due to cracking at its tip[20]. Therefore careful analysis of seismicity just before precursor eruptions could potentially resolve the issue. The precise mechanical interpretation, however, is not critical to our proposed model for precursor eruptions. The essential point is that the gas pocket will move faster—often considerably faster—than the main liquid-filled fracture, because liquid viscosity limits the velocity of the latter.

In our experiments, the period of time between the beginning of precursor events and the main eruption, as well as the volume of erupted gas, depends mainly on liquid viscosity; it controls u_s and thus the separation depth. For real magmas, however, the separation depth should also depend on volatile content and hence saturation pressure. The solid is fractured ahead of the liquid and is characterized by a lower fracture toughness; new gas pockets would need a lower critical height h_c to separate (equation (2)), and could potentially propagate at greater velocity[21,22]. New gas pockets forming at the tip of the liquid crack could possibly catch up with the first one. However, if a little magma is transported with the gas phase, it could aid in 'healing' the fractured rock after passage of the gas-rich phase; it seems probable that some magma would be left behind as the walls close behind the main gas pocket and could potentially freeze.

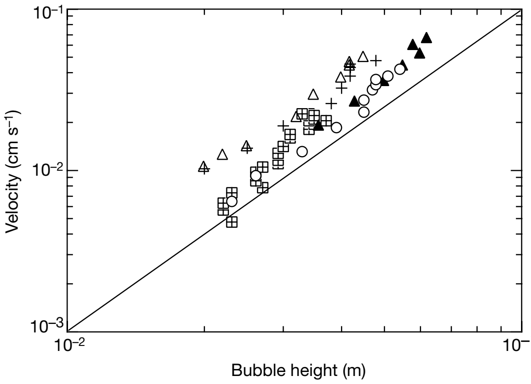

Figure 4 Crack velocity versus gas pocket height. The velocity of the air bubble as a function of its height for injected liquids of two different viscosities (1 mPa s and 41 mPa s) and different injection rates of air for a given fluid. The symbols are as in Fig. 3.

Further research, both observational and theoretical, is required to give more quantitative predictions. Nevertheless, this new framework provides a simple interpretation of precursor eruptions, and can be improved to give more precise estimates of the duration of precursor activity in specific cases. One general prediction is that precursor activity should be shorter in the case of basaltic volcanoes than for silicic ones. This seems to be supported by accounts of the Paricutin eruption, which indicate that gas and fine ash emissions began only hours before the main magma conduit reached the surface[23], a time period considerably shorter than the weeks to months typical of silicic eruptions. ☐

Received 11 December 2000; accepted 26 March 2001.

1. Heiken, G. & McCoy, F. Jr Caldera development during the Minoan eruption, Thira, Cyclades, Greece. *J. Geophys. Res.* **89,** 8441–8462 (1984).
2. Gardner, J. E., Carey, S. & Sigurdsson, H. Plinian eruptions at Glacier Peak and Newberry volcanoes, United States: implications for volcanic hazards in the Cascade Range. *Geol. Soc. Am. Bull.* **110,** 173–187 (1998).
3. Newhall, C. G. & Punongbayan, R. S. *Fire and Mud: Eruptions and Lahars of Mount Pinatubo, Philippines* (Philippine Institute of Volcanology and Seismology, Univ. Washington Press, 1996).
4. Foxworthy, B. L. & Hill, M. Volcanic Eruptions of 1980 at Mount St. Helens. The First 100 Days. *US Geol. Survey Prof. Pap.* **1249,** 1–125 (1982).
5. Lipman, P. W. & Mullineaux, D. R. The 1980 Eruption of Mount St. Helens. *US Geol. Survey Prof. Pap.* **1250,** 1–844 (1981).
6. Young, S. R. *et al.* Overview of the eruption of the Soufriere Hills volcano Montserrat, 18 July 1995 to December 1997. *Geophys. Res. Lett.* **25,** 3389–3392 (1998).
7. Barenblatt, G. I. The mathematical theory of equilibrium cracks in brittle fracture. *Adv. Appl. Mech.* **7,** 55–129 (1962).
8. Lister, J. R. Buoyancy-driven fluid fracture: the effects of material toughness and of low-viscosity precursors. *J. Fluid. Mech.* **210,** 263–280 (1990).
9. Rubin, A. M. Tensile fracture of rocks at high confining pressure: implications for dyke propagation. *J. Geophys. Res.* **98,** 15919–15935 (1993).
10. Daag, A. S. *et al.* in *Fire and Mud: Eruptions and Lahars of Mount Pinatubo, Philippines* (eds Newhall, C. G. & Punongbayan, R. S.) 409–414 (Philippine Institute of Volcanology and Seismology, Univ. Washington Press, 1996).
11. Harlow, D. H. *et al.* in *Fire and Mud: Eruptions and Lahars of Mount Pinatubo, Philippines* (eds Newhall, C. G. & Punongbayan, R. S.) 285–305 (Philippine Institute of Volcanology and Seismology, Univ. Washington Press, 1996).
12. White, R. in *Fire and Mud: Eruptions and Lahars of Mount Pinatubo, Philippines* (eds Newhall, C. G. & Punongbayan, R. S.) 307–327 (Philippine Institute of Volcanology and Seismology, Univ. Washington Press, 1996).
13. Aspinall, W. P. *et al.* Soufrière Hills eruption, Montserrat, 1995–1997: volcanic earthquake locations and fault plane solutions. *Geophys. Res. Lett.* **25,** 3397–3400 (1998).
14. Young, S. R. *et al.* Monitoring SO$_2$ emission at the Soufriere Hills volcano: implications for changes in eruptive conditions. *Geophys. Res. Lett.* **25,** 3681–3684 (1998).
15. Mimatsu, M. *Showa-Shinzan Diary* (Suda-Seihan, Sapporo, Japan, 1995).
16. Griffith, A. A. The phenomena of rupture and flow in solids. *Phil. Trans. R. Soc. Lond. A* **221,** 163–198 (1920).
17. Irwin, G. R. Analysis of stresses and strains near the end of a crack traversing a plate. *J. Appl. Mech.* **24,** 361–364 (1957).
18. Heimpel, A. M. & Olson, P. in *Magmatic Systems* (ed. Ryan, M. P.) 223–240 (Academic Press, San Diego, 1994).
19. Rubin, A. M. Dike ascent in partially molten rock. *J. Geophys. Res.* **103,** 20901–20919 (1998).
20. Einarsson, P. & Brandsdóttir, B. Seismological evidence for lateral magma intrusion during the July 1978 deflation of the Krafla volcano in NE-Iceland. *J. Geophys.* **47,** 160–165 (1980).
21. Takada, A. Experimental study on propagation of liquid-filled crack in gelatin: shape and velocity in hydrostatic stress condition. *J. Geophys. Res.* **95,** 8471–8481 (1990).
22. Koyaguchi, T. & Takada, A. An experimental study on the formation of composite intrusions from zoned magma chambers. *J. Volcanol. Geotherm. Res.* **59,** 261–267 (1994).
23. Foshag, W. & Gonzalez, J. Birth and development of Paricutin volcano. *U. S. Geol. Surv. Bull. D* **965,** 355–485 (1956).
24. Richard, R. Jr & Mark, R. Gelatin models for photoelastic analysis of gravity structures. *Exp. Mech.* **6,** 30–38 (1966).

Acknowledgements

We thank A. M. Rubin for comments and D. L. Sahagian. We also thank A. Agnon and C. Jaupart for discussions and G. Bienfait for help with experiments.

Correspondence and requests for materials should be addressed to T.M. (e-mail: thierry@bpi.cam.ac.uk).

JOURNAL OF GEOPHYSICAL RESEARCH, VOL. 107, NO. B11, 2306, doi:10.1029/2001JB000589, 2002

The propagation of a buoyant liquid-filled fissure from a source under constant pressure: An experimental approach

Thierry Menand
BP Institute for Multiphase Flow, University of Cambridge, Cambridge, UK

Stephen R. Tait
Department of Earth Sciences and Engineering, Imperial College of Science, Technology and Medicine, London, UK

Received 24 April 2001; revised 30 April 2002; accepted 24 June 2002; published 19 November 2002.

[1] We study the propagation of a buoyant liquid-filled fissure from a reservoir under constant pressure within the framework of linear elastic fracture mechanics. We conducted laboratory experiments by injecting aqueous solutions into gelatin solid: an analogue for elastic and brittle crustal rocks. Fissure velocity and injection rate of liquid were measured rather than being imposed. Our experimental results allow evaluation of how the different driving and resistive pressures evolved during fissure propagation and highlight the influence of the fracture resistance of the host solid. In an initial transient propagation regime, elastic pressure generated by the fissure is balanced by the fracture pressure; the fissure propagates radially with decreasing velocity and increasing injection rate, controlled by the source conditions. Subsequently, buoyancy overcomes the source pressure as the driving force, and vertical steady state propagation is established. The fissure develops a bulbous head and propagation is controlled by the balance in this head, between buoyancy pressure and fracture pressure. Even after this transition, the constant values of velocity, flux, and strain energy release rate reflect the source conditions. Our model suggests that greater horizontal dyke cross section reflects larger source pressure and that mafic dykes propagating from shallow magma chambers are unlikely to attain steady state. Moreover, our experiments place constraints on the mechanics of time-dependent failure of the solid as a process that resists fissure propagation: propagation velocity scales with the square of the height of the fissure head, and fracture toughness of rocks would be length scale dependent rather than a material property. *INDEX TERMS:* 5104 Physical Properties of Rocks: Fracture and flow; 8110 Tectonophysics: Continental tectonics—general (0905); 8145 Tectonophysics: Physics of magma and magma bodies; 8434 Volcanology: Magma migration; *KEYWORDS:* dyke, fissure propagation, analogue experiments, fracture resistance, rock failure, magma migration

Citation: Menand, T., and S. R. Tait, The propagation of a buoyant liquid-filled fissure from a source under constant pressure: An experimental approach, *J. Geophys. Res.*, *107*(B11), 2306, doi:10.1029/2001JB000589, 2002.

1. Introduction

[2] A major process of evolution of the Earth's lithosphere is the upward transport of magma by the creation and propagation of magma-filled cracks, or dykes, from zones of partially molten rocks in the upper mantle to the surface. At great depths and close to the mantellic source region magma percolates through a porous medium. Closer to the surface magma propagates by hydraulic fracturing. The latter transport mechanism is a complex problem mixing fracture mechanics, elasticity, and fluid dynamics. However, simplifications can be made: dykes may be idealized as planar sheets opening in mode I in brittle, elastic solid as the average strain associated with their emplacement, approximately their thickness to length aspect ratio, is typically of the order of 10^{-3} [*Pollard*, 1987]. Previous studies, mainly numerical, enabled us to understand separately the effects of the elasticity, the viscosity and the buoyancy of the fluid on crack propagation. Early studies presented static solutions for the equilibrium shape of fluid-filled cracks [e.g., *Pollard*, 1987]. Nevertheless, *Weertman* [1971a] showed that buoyant dykes are unstable and should move upwards. Studies that have taken into account the flow of liquid inside the fissure first focused on the coupling between elastic deformation and viscous flow and similarity solutions have been found when the injection rate is prescribed, whether the flow is laminar [*Spence and Turcotte*, 1985] or turbulent [*Emerman et al.*, 1986]. Solutions were also found for injection rates as a general power law in time [*Spence and Sharp*, 1985] and for propagation from a

0148-0227/02/2001JB000589$09.00

chamber with constant overpressure [*Spence and Sharp*, 1985; *Rubin*, 1993b, 1995a]. Subsequently, fluid buoyancy has been taken into account. *Spence et al.* [1987] and *Lister* [1990a] found solutions to the steady state case. According to *Lister* [1990a], the pressures associated with the elastic deformation and the strength of the host solid are only significant in the neighborhood of the fissure tip. The problem of the fissure shape far from its tip is thus simplified and *Spence and Turcotte* [1990] found solutions for fissures of constant volume. Similarity solutions have also been found for the lateral extent of a fissure that propagates vertically from a point source as well as its horizontal propagation in a stratified solid at the level of neutral buoyancy [*Lister*, 1990b]. *Lister and Kerr* [1991] applied these results to the propagation of magma-filled fractures and a comprehensive review of dyke propagation has been made by *Rubin* [1995b].

[3] Some experimental studies have also been carried out. However, it should be noted that few theoretical studies refer to them. All these experimental studies used a gel to simulate the elastic and brittle behavior of the Earth's crust. By injecting dyed water in gelatin, it has been shown that the direction of propagation is controlled by the stress field around the fissure which may be induced by topography [*Fiske and Jackson*, 1972] or by regional tectonics [*McGuire and Pullen*, 1989]. Further studies dealt with the effects on propagation direction of planar discontinuities in the host solid and spatial gradients in its elastic properties [*Pollard*, 1973], with formation of laccoliths [*Pollard and Johnson*, 1973; *Hyndman and Alt*, 1987], and linear elasticity has been applied to explain the shape of fluid-filled cracks in gelatin [*Maaløe*, 1987]. Following these static solutions, *Takada* [1990] seems to be the first to propose scaling laws by means of small-scale laboratory experiments. He found that fluid-filled fissures of constant volume propagate at a constant velocity which depends on the height of the fissures as well as on the difference of density between fluid and gelatin, contrary to fissures fed with a constant injection rate; in this latter case propagation velocity increases both with time and with injection rate. *Takada* [1990] also carried out experiments in which gelatin had been fractured prior to the propagation of a fluid-filled fissure. In those experiments, for which the strength of the gelatin was greatly reduced, crack velocities were observed to be two orders of magnitude greater than in experiments carried out with virgin gelatin but nonetheless were still lower by at least three orders of magnitude than velocity predicted by a Poiseuille flow, hence highlighting the role of the strength of gelatin. More recently, *Heimpel and Olson* [1994] put forward a new model for the propagation of cracks of constant volume, proposing notably that their speed might be limited by the transmission of information on the crack shape by elastic waves.

[4] Despite this intensive study we cannot answer some key questions of geological importance. For instance, what determines the flux of magma carried by a dyke? It is unlikely that a source can maintain a constant injection rate during fissure propagation. The few data on magma fluxes seem to indicate that the injection rate is not constant during the propagation of a dyke [*Brandsdóttir and Einarsson*, 1979; *Einarsson and Brandsdóttir*, 1980]. Furthermore, assuming a steady state boils down to not taking into account the initiation process. As a consequence the physical characteristics of the source are no longer linked to propagation and are excluded from the model. *Mériaux and Jaupart* [1998] studied crack propagation from a reservoir under constant overpressure and showed that the initial crack loading determines its subsequent propagation. However, these authors, like others, have neglected the fracture resistance of the solid. This was mainly motivated by laboratory measurements on rock samples [e.g., *Atkinson*, 1984]. Based on scaling analysis, it is shown that once a dyke has been initiated and has grown to a critical length, the pressure associated with the strength of rocks is negligible in comparison with the other pressure scales, especially magma viscous resistance [*Lister*, 1990b; *Lister and Kerr*, 1991]. However, field estimations give values 10^2-10^3 times greater than those measured in the laboratory [*Delaney and Pollard*, 1981; *Reches and Fink*, 1988]. Moreover, it is difficult to believe that fracturing is negligible from the very beginning of the propagation in the case of flawless solids. Hence we ask, how may a dyke grow from a regime where the fracture resistance of rocks would be significant to a regime where it could be neglected?

[5] We suppose in our study that magma cannot intrude the surrounding rock by hydraulic fracturing as long as the fracture resistance of the rock is not overcome. Similar to most studies on dyke propagation we base our analysis on linear elastic fracture mechanics. Therefore, we assume that a liquid-filled crack cannot propagate as long as the stress intensity factor K at its tip does not reach the fracture toughness K_c of the surrounding solid. One basic question is whether K_c is a material property independent of the crack dimensions and loading. This has been assumed in the vast majority of the literature on dykes, although *Rubin* [1993a] has argued that this vision may not be adequate for dykes at high confining pressure. We use this simplification in our initial approach but will return to this key issue in the light of our experimental results. We do not deal with the influence of the volatiles that could be present at the crack tip [*Barenblatt*, 1962]. A theoretical investigation of this effect has been made by *Lister* [1990a] and the hypothesis that such volatiles could be an origin for precursor volcanic eruptions has been experimentally investigated by *Menand and Tait* [2001]. Finally, because we concentrate on the mechanical aspects of the problem, we do not take into account thermal effects.

[6] Fracturing processes are very difficult to handle in numerical models whereas they are always present in laboratory experiments using gelatin [*Takada*, 1990; *Lister and Kerr*, 1991]. In this paper, we study with laboratory experiments the propagation of a fissure fed by a reservoir under a constant pressure. In these experiments, aqueous solutions are injected in gelatin solids simulating the elastic, brittle crust and care was taken to start fissure propagation from a well-characterized initial condition. We first introduce the experimental techniques that we developed to measure in situ Young's modulus and the fracture toughness of gelatin solids with which we characterize their rheology. We then present our experiments and propound a new model of fluid-filled fissure propagation. We conclude with a short discussion on our

results and the geological application and implications of our work.

2. Rheology of the Gelatin

[7] Gelatin is a clear, brittle, viscoelastic solid with a low shear modulus and a Poisson's ratio of nearly 0.5. It has been used in experimental studies of dyke propagation because its low shear modulus allows it to deform significantly under gravity at laboratory scale [e.g., *Fiske and Jackson*, 1972; *Maaløe*, 1987; *Takada*, 1990; *Heimpel and Olson*, 1994]. If it was assumed in these studies that gelatin behaves in an elastic, brittle manner, such an assumption however has never been carefully verified. Elasticity and brittleness are two different properties. However, *Griffith* [1920] and *Irwin* [1957] showed that they are not independent for elastic solids. In this ideal case, fracture toughness follows the relation

$$K_c = \sqrt{2\gamma_s E}, \tag{1}$$

where E is the Young's modulus of the elastic solid and γ_s is its surface energy which is thought to depend only on the temperature [*Griffith*, 1920]. Elastic solids of a similar composition at a given temperature should have surface energies of the same order of magnitude and therefore should differ only by their Young's modulus. We thus developed techniques to measure Young's modulus E and fracture toughness K_c of gelatin solids in situ in our experiments, which allowed us to verify relation (1) for gelatin.

[8] High-clarity, 200 bloom, acid, pigskin-derived gelatin in granular form was supplied by SKW Bio-Systems. The gelatin was prepared by dissolving the powder in distilled water. The solution was heated until complete dissolution of the gelatin at 60°C, after which 0.1% sodium hypochlorite was added to prevent fungal growth. The gelatin was then poured in two identical acrylic tanks; one to measure its Young's modulus and the other to measure its fracture toughness. The gelatin was left to solidify in these two tanks under hydrostatic conditions, horizontal strains are nil and Poisson's ratio $\nu = 0.5$, in an air-conditioned room at 20°C for 48 hours, timescale of gelification was approximately 1 day for the concentrations used, in order to ensure thermally homogeneous gelatin solids. A thin layer of silicon oil was poured on the gelatin surface in order to avoid evaporation during solidification, which would create a gradient of gelatin properties. Once the gelatin was solid both measurements of E and K_c were performed.

2.1. The Measurement of Young's Modulus

[9] We measured Young's modulus of the gelatin solid by putting a rigid, circular cylinder, made of duraluminum, on the surface of the gelatin. The radius of this object was small compared to the dimensions of the tank; the gelatin could thus be seen as a semiinfinite medium. The vertical deflection w created was then measured and Young's modulus was calculated by means of the following relation [*Timoshenko and Goodier*, 1970]:

$$E = \frac{M g (1 - \nu^2)}{2 a w}, \tag{2}$$

where M and a are the mass and radius of the cylindrical weight, g is the gravitational acceleration, and ν is the Poisson's ratio of the gelatin. The crucial point is to measure the deflection as accurately as possible. This was done by using a digital micrometer to determine the position of the top of the weight with respect to a reference position rigidly attached to the tank. This method allowed us to measure E with an error less than 2.5%. Solids of different Young's modulus were made by changing the concentration of gelatin. Note, however, that Young's modulus of a gelatin is not a constant but continuously increases with time as gelification continues. Thus, for each experiment, several measurements of Young's modulus were made and the experiment was carried out when the desired value of E was attained. Experimental durations were less than 5 min, a short time period when compared to the time evolution of Young's Modulus so it could be assumed to be constant during an experiment.

2.2. The Determination of the Fracture Toughness

[10] In the case of an edge crack embedded in a semi-infinite elastic solid, the stress intensity factor K at the crack tip may be expressed as [*Sneddon and Das*, 1971]

$$K = \alpha \overline{\Delta P} \sqrt{\pi h}, \tag{3}$$

$\overline{\Delta P}$ being the overpressure of the crack averaged over its height h. The overpressure of the crack is defined as the difference between the pressure in the crack and the stress in the solid in the absence of the crack. α is a dimensionless factor which is a function of boundary conditions, especially those at the surface of the semiinfinite solid, in the case of a crack embedded in an infinite elastic solid we would have $\alpha = 1$.

[11] We created a small edge crack in our gelatin by plunging a rigid, metallic blade, made of stainless steel, in the solution of gelatin before its solidification. Once the gelatin was solid, the blade was carefully removed. The fissure was then filled with water as well as the part of the tank that was free of gelatin. The tank was then turned over in order to have the water reservoir beneath the gelatin and the reservoir was fed in such a way that its pressure balanced exactly the weight of the gelatin. According to linear elastic fracture mechanics, once the stress intensity factor K at the tip of the fracture reaches the fracture toughness K_c of the solid the crack propagates. This was achieved by slowly increasing the crack overpressure: we injected some air into the crack by using compressed air going first through a pressure reducer and then through a small capillary positioned in the fissure. As air was injected into the crack, the excess water was bled from the reservoir in order to maintain a free surface condition at the interface between the reservoir and the gelatin. The experimental apparatus is schematically drawn in Figure 1. Measuring the height of air in the fissure, which gives us the crack overpressure at the onset of its propagation, and using equation (3) we calculated the stress intensity factor at the crack tip. The calculation requires determination of the factor α, which was done following the work of *Sneddon and Das* [1971] for an edge crack linked to a free boundary. We identified this

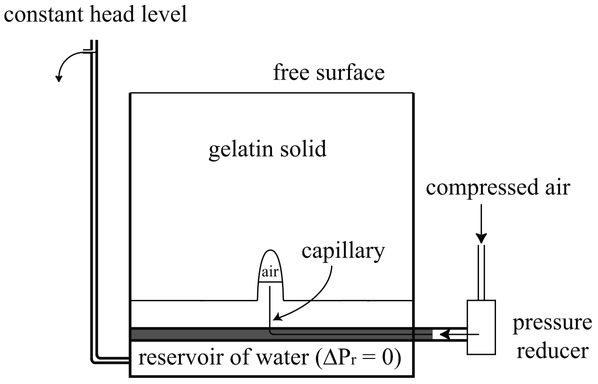

Figure 1. Schematic diagram of the experimental apparatus used for the determination of the gelatin fracture toughness. The excess of water is bled off the reservoir while air is injected in the crack insuring a free surface condition at the interface between the water reservoir and the gelatin solid.

stress intensity factor with the fracture toughness of the gelatin solid.

2.3. Relationship Between Young's Modulus and Fracture Toughness

[12] In the case of an edge crack embedded in a semi-infinite elastic solid, the stress intensity factor at the crack tip differs from the case of a crack in an infinite elastic solid by the factor α. However, we can still apply the approaches developed by *Griffith* [1920] and *Irwin* [1957]. Therefore, if our gelatin solids behave in a pure elastic manner they should obey relation (1). Figure 2 is a plot of K_c of our different gelatin solids as a function of their Young's modulus. The plain curve corresponds to the theoretical equation (1). The best fit through our data is

$$K_{c\,\mathrm{exp}} = 0.97 E^{0.55}\ \mathrm{Pa\ m}^{\frac{1}{2}}. \qquad (4)$$

Taking into account the error bars on K_c and E our data are in good agreement with the expected theoretical relation for pure elastic, brittle behavior. Furthermore, equation (4) enables us to calculate the fracture toughness of a gelatin solid from the measurement of its Young's modulus, the obvious advantage being the nondestructive determination of the latter. It also gives us the surface energy of the gelatin solids: $\gamma_s \simeq 1\ \mathrm{J\ m}^{-2}$.

3. Propagation of a Buoyant Fissure From a Reservoir Under Constant Overpressure

3.1. Experimental Method

[13] In this section we present the experimental apparatus that we used to study the propagation of a water-filled fissure from a reservoir under constant overpressure (Figure 3). Details of experimental conditions are given in Table 1. Gelatin was set under hydrostatic conditions in an acrylic tank 30 cm wide by 50 cm high. A rigid reservoir filled with dyed water was situated beneath the gelatin tank. The injection of water into the gelatin was allowed by a 5 mm wide and 20 cm long slit made in the undeformable roof of the reservoir. Furthermore, the reservoir was fed by an additional reservoir placed on a small elevator. This elevator enabled us to lift the additional reservoir in order to increase the reservoir overpressure. Once the small elevator was locked, the additional reservoir fed the main reservoir with a given head level. This header tank was large enough to maintain a constant head level during the propagation because the total volume of water injected in a crack was small, the maximum variation of the head level was 1–2 mm. Therefore the reservoir overpressure stayed constant during the crack propagation. We also measured the injection rate using scales placed on the small elevator and beneath the additional reservoir. The scales were linked to a PC, which recorded the mass of water lost by the reservoir and thus injected into the crack. This allowed us to measure the injection rate instead of imposing it. The propagation was videotaped in order to measure the crack tip velocity. The video camera was manually moved up on a vertical track to keep it level with the tip of the fissure.

[14] Inside the reservoir was a movable plate on which a 1 mm thick, 1.5 cm high, and 12 cm long metallic blade, made of stainless steel, was mounted. Before pouring the gelatin solution into its tank, we initially sealed the slit with the movable plate. This way, the metallic blade penetrated the slit in the reservoir roof. Once the gelatin was solid, the plate was carefully moved down. The metallic blade was thus taken out of the gelatin solid and created a small fissure filled with fluid from the reservoir. This technique enabled us to propagate the fissure from a well characterized linear source.

[15] Just prior to starting an experiment, the Young's modulus of the gelatin was measured by the technique described in section 2.1. The reservoir overpressure, initially nil, was slowly increased with the aid of the small elevator and the head level was maintained constant once the fissure started to propagate. The injection rate was then recorded and the propagation was videotaped.

3.2. Experimental Observations and Measurements

[16] When the fissure started to propagate, we observed in all experiments that the propagation was initiated from a

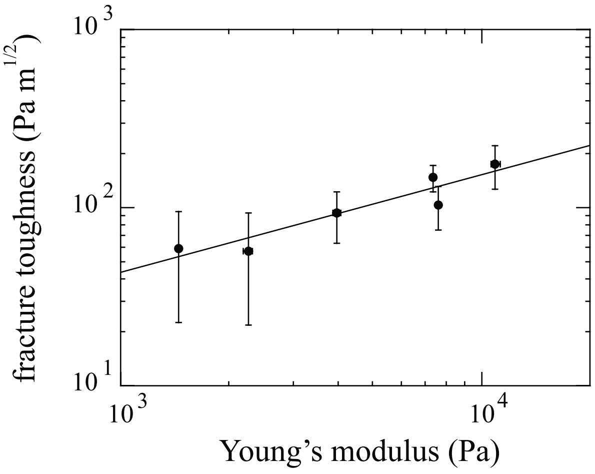

Figure 2. The fracture toughness K_c as a function of the Young's modulus E for different gelatin solids. Each point represents a gelatin solid. The plain curve represents the theoretical equation $K_c \propto \sqrt{E}$.

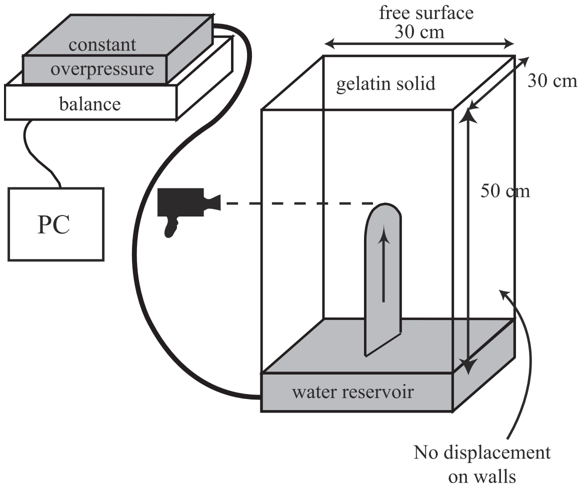

Figure 3. Schematic diagram of the experimental apparatus used for the propagation of a water-filled fissure from a reservoir under constant overpressure.

point of the linear source. Then, the source injection extended laterally and the fissure propagated radially in a nearly vertical plane. We also observed that the fissure had an approximately elliptical cross section, as expected for a pressurized cavity embedded in an elastic solid [*Sneddon*, 1946]. The form of the fissure during this early stage of the propagation is shown on Figure 4. Afterward, the propagation became mainly vertical and the shape of the fissure stretched out vertically. Moreover the fissure seemed to develop a head thicker than its tail. This was not easily observed because the fissure sometimes became slightly curved and was not along the axis of the camera, but it was particularly noted in experiments 19, 20, and 22. The transition between the initially radial and later vertical propagation occurred after typically 10–15 cm of propagation. Figure 5 shows the shape of the fissure after the transition. In almost all experiments we observed that during propagation in the uppermost part of the tank, after approximately 25–30 cm of propagation, the fissure deviated from vertical trajectory and followed a path that curved toward one side of the tank, presumably due to wall effects. We will restrict our description to the part of the fissure propagation, which is not affected by the walls of the tank.

[17] We measured the distance of propagation of the fissure and the mass of water injected into the fissure as functions of time, as shown on Figure 6 for experiment 24. Instantaneous velocity was calculated by differentiating a linear regression through the distance data for five fissure positions, the point on which the fit was centered and two either side. The instantaneous volumetric injection rate was calculated in the same manner from the mass data divided by the density of the fluid. Figure 7 is a plot of the velocity and the injection rate of the fissure as a function of its length for experiment 24, deduced from the data shown on Figure 6. The velocity data seem to be noisier than the injection rate data. This may be due to the measurement procedure that we used, the video camera was manually moved up, although we cannot rule out that this effect may be real and related to the dynamics of propagation. However, there are clearly two different regimes. This is particularly visible from the injection rate data, the transition between the two regimes occurring after about 10 cm of propagation in this case, experiment 24. The first regime was characterized by an increasing injection rate and a decreasing velocity. This implies that the fissure inflated and/or propagated laterally at the level of the source. It seems therefore that there is a correspondence between these velocity and injection rate measurements and the radial propagation we initially observed in the experiments. In the second regime, both the fissure velocity and the injection rate were essentially constant. This steady state was not imposed in our experiments but rather was naturally adopted by the system; we emphasize that this steady state was approached from a regime with an increasing flux and a decreasing velocity.

[18] Finally, in all experiments the flow inside the fissure was always laminar. In the case of a fissure of width w, which is filled with a liquid of density ρ and viscosity η, and that propagates at a velocity u, flow inside the fissure is turbulent if the Reynolds number $R_e = \frac{\rho u w}{\eta}$ exceeds a critical value of order 1000. Conversely, flow is laminar if $R_e \leq 1000$. In all experiments, the injected liquid was water, for which density and viscosity are 1000 kg m^{-3} and 10^{-3} Pa s, respectively, the velocity of propagation was always less than 1 cm s^{-1} and the fissure width was always less than 5 mm. As a consequence, the Reynolds number R_e was always less than 50.

3.3. The Different Pressure Scales

[19] In order to quantitatively analyze our observations, we follow *Lister* [1990b] and *Lister and Kerr* [1991] and define five different pressure scales. The geometry of the fissure that we use is shown on Figure 8. The height of the fissure is h, its breadth is $2b$, its thickness is $2w$ and we use the letter l when we refer to a length, h or $2b$, in a nonexplicit manner. There are three driving pressures. These are the elastic pressure scale required to open the fissure

$$P_e \sim \frac{E}{2(1-\nu^2)}\,\frac{w}{l}, \tag{5}$$

where l is the smallest of the height or the breadth of the fissure, the source overpressure ΔP_r and the hydrostatic, or buoyancy, pressure

$$P_h \sim \Delta\rho\, g\, h, \tag{6}$$

where $\Delta\rho$ is the difference between the density of the solid and the density of the liquid, so that the fluid overpressure is

Table 1. Details of the Experimental Conditions[a]

Experiment	ρ_g (kg m^{-3})	ρ_l (kg m^{-3})	η (Pa s)	E (Pa)	ΔP_r (Pa)
19[b]	1013.0	1000.6	10^{-3}	1525	749
20	1013.0	1000.0	10^{-3}	1581	327
21	1013.0	1000.3	10^{-3}	929	190
22	1024.9	1001.2	10^{-3}	5529	749
24	1024.6	1001.2	10^{-3}	7899	1133

[a] All experiments were dyed water injected in gelatin solid. ΔP_r corresponds to the reservoir overpressure needed to propagate the fissure. The overpressure was progressively increased until the fissure propagates except in experiment 19: ΔP_r has violently been imposed and fissure has immediately propagated.

[b] ΔP_r violently imposed.

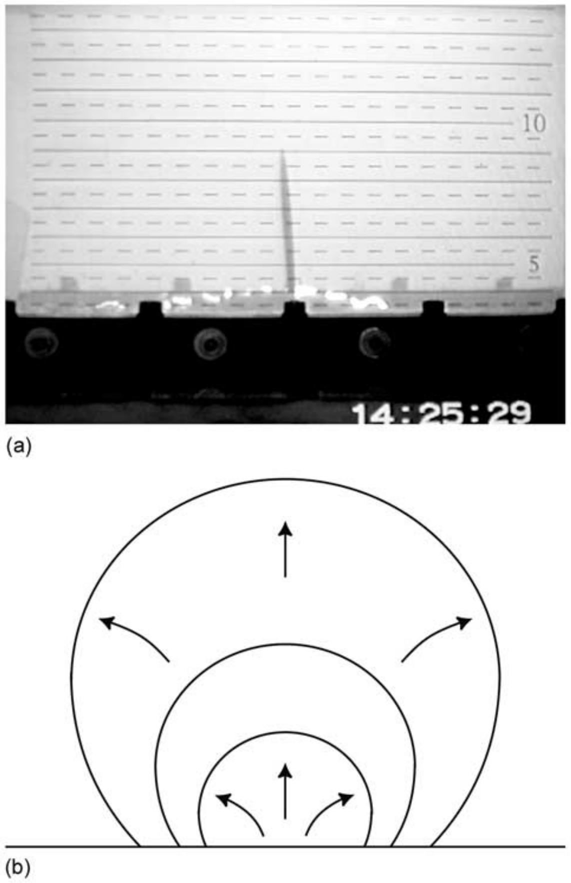

Figure 4. The shape of the fissure during the early stage of its propagation in experiment 22. The photo (a) taken after 9 cm of propagation shows the elliptical cross section of the fissure. The in plane view (b) is a schematic illustration of the radial propagation.

the sum of ΔP_r and P_h. The two other scales are resistive pressures. One is the viscous pressure drop

$$P_v \sim \frac{3\,\eta\,u\,l}{w^2}, \tag{7}$$

where η is the viscosity of the fluid, u the average velocity of the fluid inside the fissure, which is also the fissure velocity, and l the length of the fissure. The other is the fracture pressure

$$P_f \sim \frac{K}{\sqrt{\pi l}}. \tag{8}$$

This is the overpressure needed by the liquid to generate a stress intensity factor K at the crack tip, which should be at least equal to K_c for the host solid to be fractured.

[20] The elastic pressure (5) and the fracture pressure (8) are quasi-static from an elastic point of view, which means that they are not necessary valid for the dynamic problem of the propagation of a fissure. However, the use of these equations in the present study is justified by the fact that fissures propagated with velocities that were two orders of magnitude less than the velocities of elastic waves, hence propagated quasi-statically: in the range of the experimental conditions, shear wave velocities were approximately

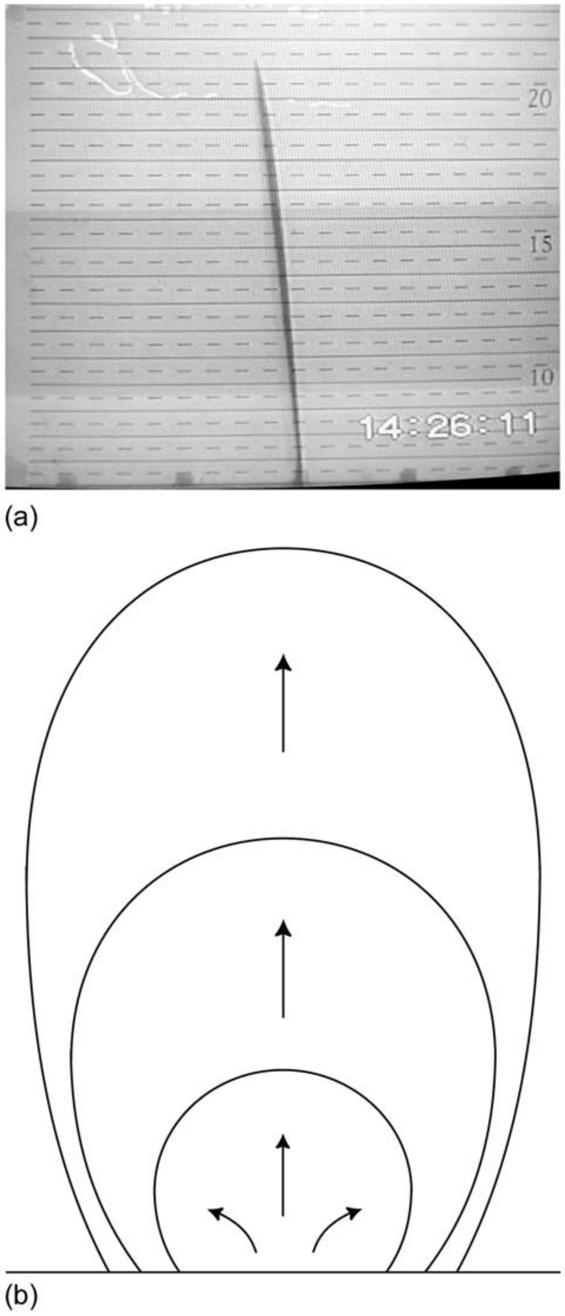

Figure 5. The shape of the fissure in cross section, in experiment 22, after 21 cm of propagation (a). The fissure seemed to develop a head thicker than its tail. Initially radial, the propagation became mainly vertical as schematically illustrated by the in plane diagram (b).

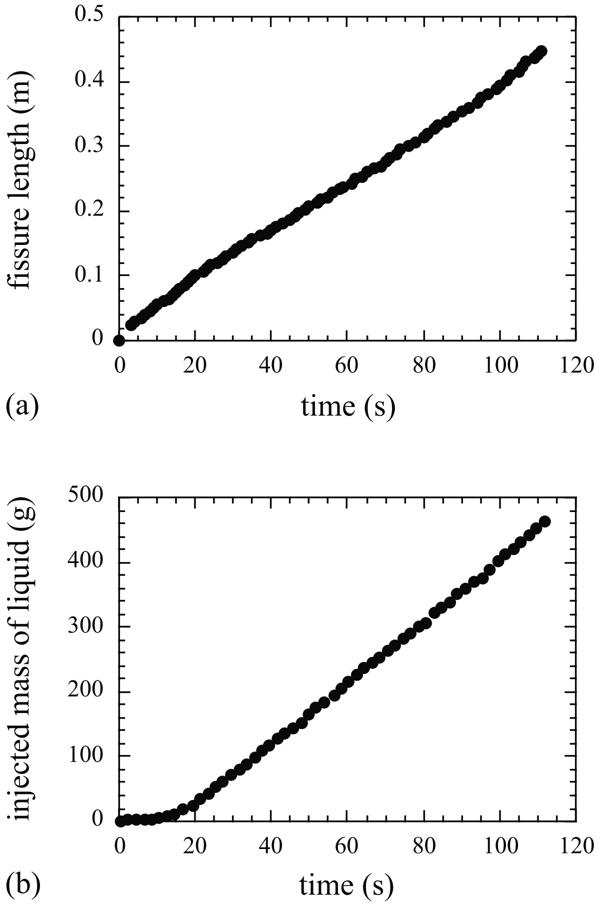

Figure 6. The distance of propagation of the fissure (a) and the mass of water injected in the fissure (b) as a function of time in experiment 24.

equal to 1 m s^{-1} while fissure velocities were always less than 1 cm s^{-1}.

3.4. Initial Propagation Regime

[21] We initially observed that the propagation was radial and in a vertical plane or nearly so, in short, there was no specific direction for fissure propagation. This suggests that the buoyancy pressure (6) was initially negligible compared with the other pressure scales. The initial height of the fissure was indeed small, 1.5 cm. Moreover, the fissure velocity was low as well as the viscosity of the injected liquid, water for which $\eta = 10^{-3}$ Pa s, suggesting that the viscous pressure drop (7) could be neglected as well.

[22] This can be shown quantitatively by comparing terms explicitly. The fissure was observed to have an ellipsoidal shape and to resemble "half a penny" so that its breadth was approximately equal to twice its height. Its basal width, $2w$, is thus easily expressed as a function of its volume V, which is known from the data of the mass of injected fluid:

$$2w = \frac{3\,V}{\pi\, l^2}. \tag{9}$$

It appears that, except in experiment 24, the basal width of the fissure remains nearly constant, influenced by the lower boundary condition of no displacement on the lower gelatin surface, as expected. In experiment 24, however, the fissure width appears to be proportional to the fissure length implying that the elastic pressure remains constant, as would be expected if slip occurred between the base of gelatin solid and the base of the tank. We assume that in this case, the gelatin adhered less well to the tank base than in the other experiments, although we were unable to check it independently. Equation (9) enables us to express the pressure scales as functions of V rather than w. Figure 9 represents the evolution of the four pressure scales (5)–(8) during the fissure propagation for the two boundary conditions: no displacement and slip displacements. It shows that the buoyancy pressure and the viscous pressure drop can be neglected during the initial propagation regime in both cases. Note that, in this transient regime, the viscous pressure drop stayed constant in most experiments and even decreased in the slip displacement case. This suggests that, initially, propagation occurred in a regime characterized by an approximate

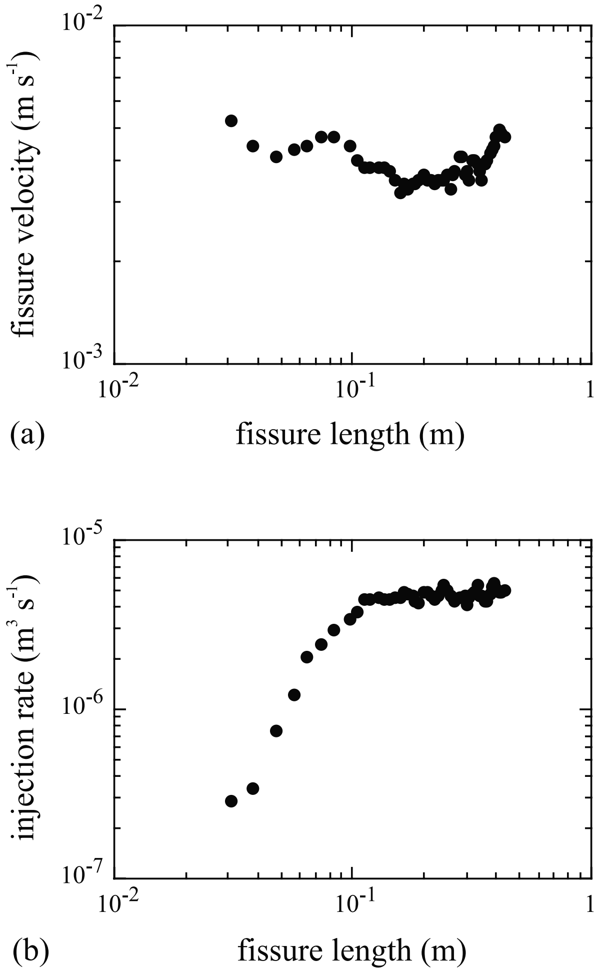

Figure 7. The velocity (a) and the injection rate (b) of the fissure as a function of its length in experiment 24.

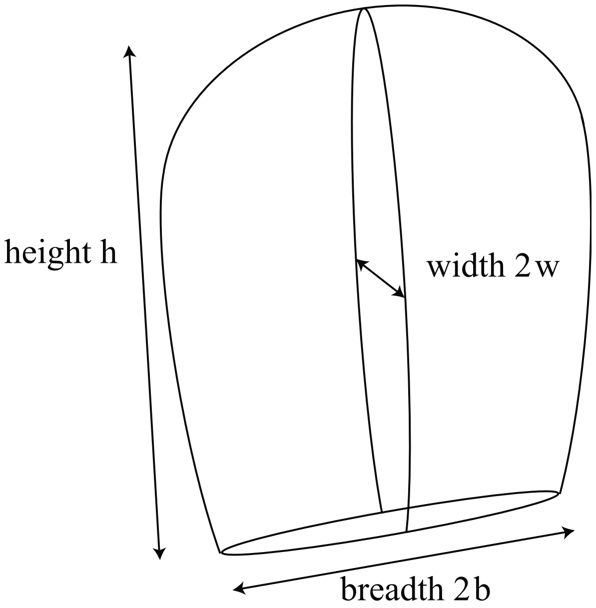

Figure 8. Schematic diagram of a fissure. The fissure has a height h, a breadth $2b$, and a thickness $2w$ such as $2w \ll 2b \leq h$.

balance between the elastic pressure (5) and the fracture pressure (8); as propagation was quasi-static, dilation of the fissure occurred much faster than propagation and during this initial regime the elastic pressure balanced the source overpressure while propagation was controlled by the stress intensity factor at the tip of the fissure:

$$\frac{E}{2(1-\nu^2)}\frac{w}{l} \sim \Delta P_r \sim \frac{K}{\sqrt{\pi l}}. \qquad (10)$$

[23] The quasi-static behavior of the fissure is not assumed but observed. The volume of the fissure V is function of the constant fissure width (equation (9)). By differentiating it with respect to time and dividing by the velocity $u = dl/dt$, we obtain the ratio of the flux $q = dV/dt$ over the crack velocity u as a linear function of the crack length. In experiment 24 however the elastic pressure rather than the fissure width was constant and V must be expressed as a function of the constant overpressure in the fissure ΔP_r before differentiating it with respect to time, by combining equations (9) and (10). We therefore obtain that

$$\frac{q}{u} = \beta \frac{V}{l}, \qquad (11)$$

with the numerical factor $\beta = 2$ for experiments 19–22 and $\beta = 3$ for experiment 24. Figure 10 shows that the experimentally measured ratios q/u follow the quasi-static relation (11).

[24] We therefore have observational evidence that the fissure is behaving quasi-statically, from an elastic point of view, even though it is propagating and even though the stress intensity factor at its tip K is larger than the fracture toughness K_c, as suggested by equation (10). Moreover, equation (10) implies that the rate of propagation of the fissure was being controlled in some way by time-dependent failure of the solid ahead of the tip. Before discussing the implications of this idea for dyke propagation we describe the propagation observed during the latter stages of experiments.

3.5. Steady State Regime

[25] After 10–15 cm of propagation we observed a new regime characterized by a constant fissure velocity and a constant injection rate. Furthermore, we observed that the propagation became mainly vertical which suggests that the buoyancy pressure had become an important driving force. Indeed, according to Figure 9, the buoyancy pressure P_h becomes comparable to the elastic pressure P_e at approximately this height. As the fissure propagated, the buoyancy

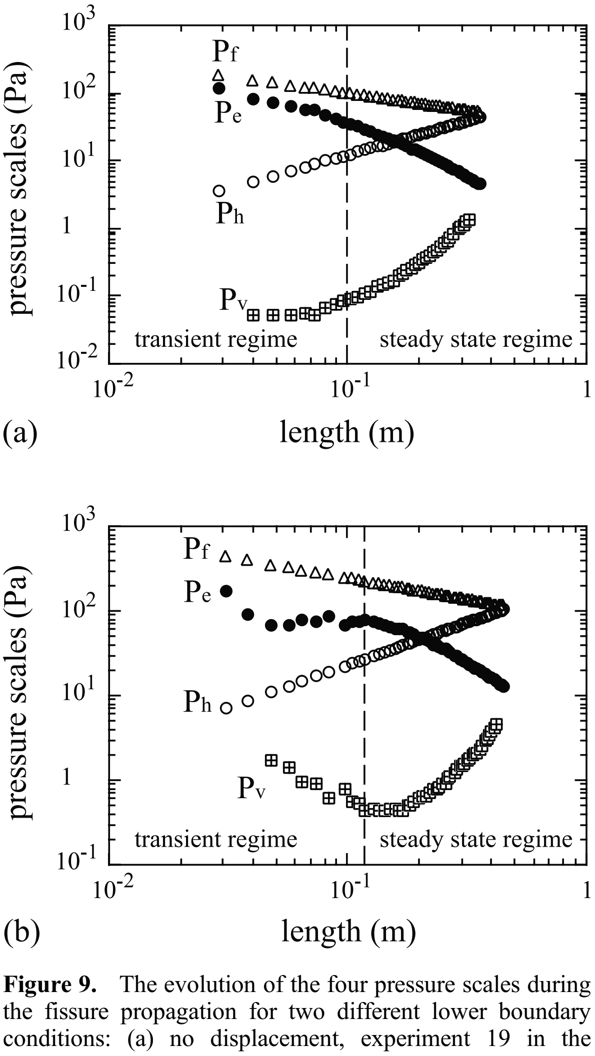

Figure 9. The evolution of the four pressure scales during the fissure propagation for two different lower boundary conditions: (a) no displacement, experiment 19 in the present case, and (b) slip displacements, experiment 24. In both cases, the stress intensity factor at tip of the fissure has been assumed to be equal to the fracture toughness of the solid during the whole propagation. The vertical dashed line separates the transient initial regime from the steady state one, as observed from the velocity and injection rate data.

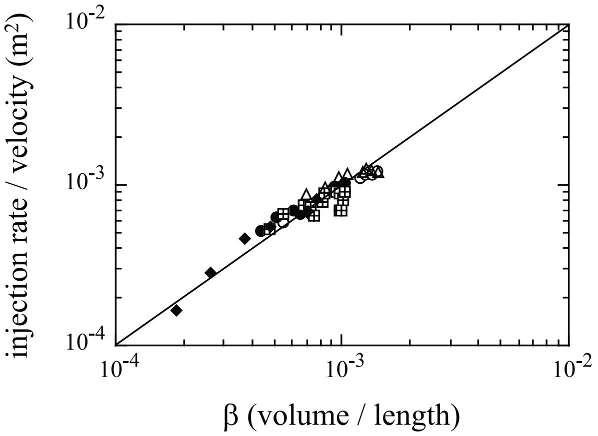

Figure 10. The ratio of the volumetric injection rate q over the crack velocity u as a function of the ratio of the volume of the fissure V over its length l. $\beta = 2$ for experiments 19–22 and $\beta = 3$ for experiment 24 in order to compare all the data on the same graph (see text). Each symbol represents an experiment: ○ 19, ● 20, ⊞ 21, △ 22, and ◆ 24. The plain curve is the theoretical relation $\frac{q}{u} = \beta\,\frac{V}{l}$.

increased. Ultimately, when the fissure reached a critical height

$$l_c \sim \frac{\Delta P_r}{\Delta\rho g}, \qquad (12)$$

the buoyancy pressure and the fissure overpressure were of the same order. Moreover, the viscous pressure drop P_v was negligible in comparison to the fracture pressure (Figure 9). It is therefore reasonable to assume that propagation was controlled subsequently by a balance between P_h and P_f:

$$\Delta\rho g\, l_c \sim \frac{K}{\sqrt{\pi l_c}}. \qquad (13)$$

This new balance explains the transition from a radial to a vertical propagation. We also observed qualitatively that the fissure developed a bulbous head although this was not practically possible to quantify. We propose that once the buoyancy pressure overcame the source pressure, the fissure developed a bulbous head of length l_c (equation (12)) that was connected to the source by a thinner tail and that the propagation was controlled by the balance which took place in this head between the buoyancy pressure and the fracture pressure. Figure 11 is a schematic illustration of such a propagation. At this point, the fissure head, in which elastic and buoyancy pressures are in balance, had a thickness

$$w_c \sim \frac{2(1-\nu^2)}{E}\Delta P_r\, l_c \sim \frac{2(1-\nu^2)}{E}\,\frac{\Delta P_r^2}{\Delta\rho g}. \qquad (14)$$

The fissure tail was thinner and viscous pressure drop is expected to be important there. Figure 9 shows that, in the steady state regime, it increased linearly with the height of the tail. So did the buoyancy pressure. Our interpretation is that the buoyancy balanced exactly the viscous pressure gradient as the tail of the fissure steadily lengthened and adjusted elastically its thickness w_s in order to maintain such a balance. According to *White* [1974], this thickness was

$$w_s = \left(\frac{4\eta q}{\pi b\,\Delta\rho g}\right)^{\frac{1}{3}}, \qquad (15)$$

where b is half the breadth of the fissure tail.

[26] At the transition between regimes, when the fissure had a height l_c, the buoyancy pressure generated a stress intensity factor K_t at the tip of the bulbous head. At the transition, both balances (10) and (13) should be approximately valid. By combining these two equations with the ratio q/u, used as a kinematic estimate for the cross-sectional area of the fissure $\pi w l_c$, we obtain that

$$l_c \sim \left[\frac{E}{2(1-\nu^2)\,\pi\,\Delta\rho g}\,\frac{q}{u}\right]^{\frac{1}{3}}, \qquad (16)$$

and

$$K_t \sim \left[\frac{E\,\Delta\rho g}{2(1-\nu^2)}\,\frac{q}{u}\right]^{\frac{1}{2}}. \qquad (17)$$

There is therefore a correspondence between a constant stress intensity factor at the fissure tip, which controls the fissure propagation, and the observed steady state propagation, with a constant ratio q/u. We propose that the steady state propagation was established by the constant head height l_c, and therefore the constant stress intensity factor K_t, that was determined at the transition between regimes. In this interpretation, the tail fed in a passive manner the steadily propagating fissure while the buoyancy pressure in its head overcame the fracture pressure and we suppose that the fracturing processes that controlled the propagation operated in a quasi-static manner.

4. Discussion

4.1. Results

[27] We have found that a buoyant liquid-filled crack fed by a reservoir under constant pressure can steadily propagate. The shape of the fissure in the steady state regime was the same as in the "viscous model [*Lister and Kerr*, 1991]." In fact, once the steady state regime is achieved, the head regime that we describe and the tail regime of the "viscous model" are exactly balanced, and hence we cannot tell the difference in a sense. That our model, controlled by fracture resistance of the host solid, and the "viscous model" give identical steady state regimes might seem a paradox. It is not: we show that we must take account of the transient regime through which the steady state is approached in order to know what the steady state will be. The "viscous model" determines what shape of crack is required to satisfy the assumed steady state propagation. This assumption means that the source is excluded, and thus we lose important information: we cannot say what kind of a geological source we are dealing with, at least not more than that it must be able to maintain a constant flux. We should therefore expect that in this steady state framework, the fracture toughness does not affect the rate of propagation, as the "viscous model" indeed shows.

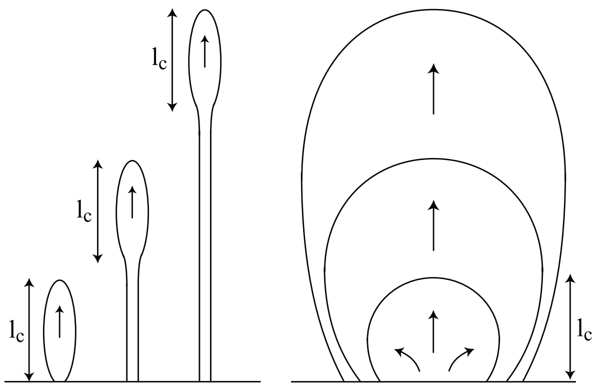

(a) (b)

Figure 11. Schematic illustration of the fissure propagation in the steady state regime in cross section (a) and in plane (b) views. Once the fissure reaches a height l_c, the hydrostatic pressure and the source pressure become comparable. Then, the fissure propagates mainly vertically and develops a bulbous head of length l_c. The propagation is controlled by the balance that takes place in the fissure head between the hydrostatic pressure and the fracture pressure.

[28] But this vision is too restrictive. At steady state the head and the tail must have the same speed, but different physical balances determine their respective velocities. We show that if the source is characterized by relatively constant pressure, which is reasonable physically, the speed of propagation in fact initially depends on the pressure in the source and the fracture toughness (Figure 9) and this also determines the speed of the head in the subsequent steady state. Once a dyke has reached a buoyancy-driven steady state, although the source is no longer directly "visible" (i.e., as in the "viscous regime"), the source is "remembered" in the following sense. The flux and velocity of the dyke transiently adjust in the fracturing regime to the steady state that is consistent with the source pressure and the fracture characteristics of the host as well as the density and viscosity of the liquid. Hence it is important geologically to characterize as well as possible this fracturing regime that we have shown to exist.

[29] However, the way fracturing processes operate at the fissure tip remains unclear. In our experiments, the viscosity of the liquid appears to exert no active control on the velocity of crack propagation. Propagation is controlled by time-dependent failure of the gelatin solid at the tip of the crack. The linear elastic fracture mechanics framework does not contain any timescale and thus cannot provide a model for propagation velocity; it only provides a threshold above which the solid fractures and thus crack propagation takes place. Nevertheless, our experiments provide some constraints on failure-controlled crack propagation. In the case of buoyant liquid-filled cracks of constant volume, it has been argued that, all else being equal, the velocity of cracks should be proportional to the square of their height [*Heimpel and Olson*, 1994, equation (8)]. Recently, it has been observed that fissures that have a growing gas pocket at their tip propagate with velocities proportional to the square of the height of the gas pocket, which is the fissure head [*Menand and Tait*, 2001]. There is no conceptual difference between this study and the steady state regime observed in our experiments; the tail of gas driven fissures does not play any role in the propagation, the latter being entirely controlled by the fissure head. We should therefore find that our fissures and those driven by gas are subject to the same fundamental control. Figure 12 shows that velocity data from both sets of experiments can indeed be correlated:

$$u \propto \Delta\rho\, l_c^2. \tag{18}$$

This relationship highlights that as l_c was determined by the source conditions, $l_c \sim \Delta P_r/(\Delta\rho g)$ and $\Delta P_r \sim K_c/\sqrt{\pi l_i}$, so was the crack velocity even in the steady state regime.

[30] We can illustrate this result in another way. In the steady state regime the stress intensity factor $K_t \sim \Delta P_r\sqrt{\pi\, l_c}$ was constant. The propagation being quasi-static, K_t may also be written as

$$K_t = \sqrt{G\,E}, \tag{19}$$

where G is the strain energy release rate during the steady propagation [*Lawn*, 1993] and, like K_t, stayed constant. At the onset of fissure propagation

$$K_c = \sqrt{2\,\gamma_s\,E} \sim \Delta P_r\sqrt{\pi\, l_i} = \text{constant}, \tag{20}$$

and combining equations (12), (19), and (20) we obtain

$$G \sim 2\,\gamma_s\,\frac{\Delta P_r}{\Delta\rho\, g\, l_i}. \tag{21}$$

Therefore the strain energy release rate G in the steady state regime was a function of γ_s and the ratio $\Delta P_r/(\Delta\rho g l_i)$. All our gelatin solids being characterized by the same surface energy γ_s, G in the steady state regime was thus determined by the ratio of the source overpressure and the buoyancy pressure in the initial fissure, that is to say by the initial source conditions.

[31] This result resembles that obtained by *Weertman* [1971a]: once the buoyancy pressure became nonnegligible and hence became the driving pressure, the length of the fissure head was determined. On the other hand, we found that the propagation was steady contrary to *Weertman* [1971b]. This difference comes from a discrepancy in his argument. Indeed, *Weertman* [1971b] assumed that the crack velocity was controlled by the fluid in the fissure, more specifically by the viscous pressure drop, but he also assumed that the crack had a constant volume. However, it is not possible to completely extract the fluid out of the crack tail as it closes. In other words, *Weertman* [1971b] took the fluid viscosity into account in the thicker part of the fissure to calculate its velocity but by assuming that the fissure could close to maintain a constant volume he implicitly neglected the viscosity in the thinner part of the fissure. In our work, we have shown that the viscosity affected only the thickness of the tail, which fed the fissure in a passive manner. The rate of propagation was seemingly entirely controlled by the fissure head and the mechanics of failure at its tip in response to its buoyancy.

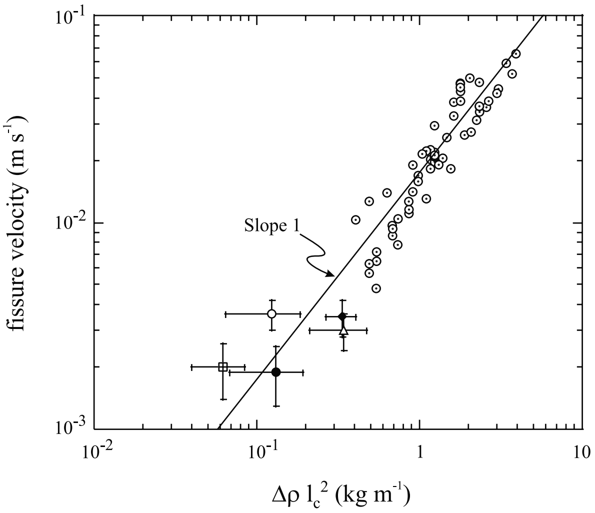

Figure 12. Fissure velocity scales with $\Delta\rho l_c^2$. Both liquid-filled fissures, same symbols as in Figure 10, and gas-driven fissures from the work of *Menand and Tait* [2001] identified by ⊙ are represented.

[32] The propagation was limited by the fracturing processes while the fissure overpressure remained constant during the initial regime. This would imply that the stress intensity factor K increased and became larger than the fracture toughness K_c:

$$K \sim \Delta P_r \sqrt{\pi l} \sim K_c \frac{\sqrt{l}}{\sqrt{l_i}} \geq K_c. \qquad (22)$$

If this is correct, then our experimental results show that a fissure may steadily propagate in a quasi-static manner even if the stress intensity factor at its tip is greater than the fracture toughness of the solid. In our experiments K_t could be up to 4 times greater than K_c. Note however that although K apparently increased during the initial propagation regime, we observed that the fissure slowed down. This suggests that the resistance to the propagation, performed by the fracturing processes, did not stay constant but increased as the fissure propagated, and hence that fracture resistance is not a material property but is length scale dependent.

4.2. Geological Application

[33] Is it possible to apply our model to dyke propagation? Answering this question requires knowledge of the fracture resistance of rocks. Our experiments suggest that time-dependent failure of the gelatin solid controls the propagation of fissures and one can argue that mechanics of time-dependent failure might be different for gelatin and rocks. However, when applied to dyke propagation, such complex mechanics are still not well understood as time-dependent failure depends on the deformation of rocks around the dyke tip, which in turn is affected by failure of rocks at the dyke tip [*Mériaux et al.*, 1999]. On the other hand, despite that linear elastic fracture mechanics does not provide any timescale, such a framework was nevertheless successful to explain the regimes we observed in our experiments. Moreover, we have shown that gelatin behaves as an elastic, brittle solid, which is the behavior thought to be relevant for rocks, at least to leading order. We therefore think that such a framework should be entertained for dyke propagation and briefly outline the geological implications, although these should be considered as preliminary at this stage.

[34] A typical value for the fracture toughness of rocks measured in laboratory is $K_c \approx 1$ MPa m^{12} [*Atkinson*, 1984] whereas estimations deduced from field measurements are two to three orders of magnitude greater [*Delaney and Pollard*, 1981; *Reches and Fink*, 1988]. By comparing P_v and P_f we see that these two pressure scales are comparable when a dyke has a length

$$l \sim \left(\frac{K w^2}{3\sqrt{\pi}\eta u}\right)^{\frac{2}{3}}. \qquad (23)$$

We may take for a typical mafic dyke from Hawaii a thickness $2w \sim 1$ m and a velocity $u \sim 1$ m s^{-1}. We therefore obtain that P_v and P_f are comparable when a Hawaiian dyke has a length $l \sim 60$ m if we take $K_c \approx 1$ MPa m^{12} or $l \sim 3.8$ km if we take $K_c \approx 500$ MPa m^{12}. Thus, this would suggest that, depending on the value of K_c, the resistive pressure may be the viscous pressure drop rather than the fracture pressure. However, several remarks may be made. First, the rock has to be fractured so that a dyke may propagate. If the rock has no weaknesses, in the light of the linear elastic fracture mechanics it is not possible to propagate a dyke as long as K_c has not been reached. If the rock is not fractured there is no propagation, which means $P_v \ll P_f$. Second, as previously mentioned, our experiments showed that in the case of a crack propagation initially controlled by a balance between P_e and P_f, the viscosity of the liquid acted on the propagation in a passive manner, affecting only the tail thickness. We therefore think that dyke propagation is not controlled by the viscous pressure drop but is rather controlled by the fracture resistance of the rocks. However, if rocks have weaknesses then things may be different. It has been observed that sometimes magma invades older fractures rather than propagating its own hydraulic fracture [*Delaney et al.*, 1986]. In those cases, the fracture resistance would be much lower and P_v may become the dominant resisting pressure scale. So the key question is: what is the real fracture resistance of rocks? It seems to be the key parameter for determining the propagation regime of a dyke.

4.3. Geological Implications

[35] Coupled with field measurements of dyke cross sections, our model enables us to estimate the source overpressure at the time of the emplacement of dykes and to infer whether they propagated in a steady state regime or not. We apply our model to two different magmatic systems: Hawaii and the MacKenzie Dyke Swarm, Canada. In the model framework, we have to make a number of assumptions. We first assume that the source pressure remains constant during dyke propagation. Moreover, although we are dealing with dykes that propagated toward the surface and in most cases reached it, we make the strong assumption that the surface did not have any effect on their propagation. Finally, we also assume that dykes have been

propagating in a steady state regime up to the surface. Such an assumption will be tested in order to infer the propagation regime of the dykes: if it is incompatible with the field measurements, then dykes would have been propagating in the initial transient regime.

[36] Combining equations (12) and (16), the source overpressure ΔP_r may be expressed as a function of the ratio q/u in the steady state regime:

$$\Delta P_r \sim \left[\frac{E\,(\Delta\rho g)^2}{2\,(1-\nu^2)\,\pi}\frac{q}{u}\right]^{\frac{1}{3}}. \qquad (24)$$

As q/u is a kinematic estimate for the fissure cross section $\pi w l$, it increases with the length of the fissure during the transient regime and is therefore greater in the steady state. Hence, substituting measured cross sections of dykes, assumed to have reached steady state propagation, into equation (24) enables us to infer a minimum value for the overpressure ΔP_r in the magmatic source that fed those dykes. Moreover, equation (16) enables us to estimate the transition height between the transient and steady state regimes from the measurements of these dyke cross sections. Figure 13 represents the dyke cross section as a function of the source overpressure (equation (24)) and of the critical height for the transition between regimes (equation (16)), we use E = 40 GPa, ν = 0.25 and $\Delta\rho$ = 300 kg m^{-3} as typical values for the Earth's crust and for the density contrast between rock and magma. Typical cross sections for dykes from Hawaii and the MacKenzie Dyke Swarm, shown as ellipses, have been drawn as well. Table 2 gives the estimations of dyke cross sections, source overpressures and transition heights (equations (16) and (24)) for Hawaii and the MacKenzie Dyke Swarm.

[37] The magma chamber in Hawaii is thought to be about 1.5 km below the surface [*Ryan et al.*, 1981; *Rubin and Pollard*, 1987]. This depth is comparable to our transition height estimation. However, our density contrast may be an overestimation for that between magma and rocks close to the surface. This would increase the transition height and thus suggests that Hawaiian dykes fed by shallow regions of the magma chamber may be unlikely to attain the steady state regime. Equation (24) estimates the source overpressure to be between about 40 and 100 bars. These values are close to those given by *Rubin and Pollard* [1987]. However, an overestimation of the density contrast would also lead to an underestimated source overpressure suggesting that ΔP_r would therefore be greater than 100 bars.

[38] In the Canadian shield, the MacKenzie Dyke Swarm is more than 2000 km long and 500 km wide with a mean dyke thickness of 30 m. It is thought to appear 1.27 Ga ago because of a giant mantellic plume [*Fahrig*, 1987; *LeCheminant and Heaman*, 1989] the head of which would have measured 1000 km in diameter [*Ernst and Baragar*, 1992]. According to *Ernst and Baragar* [1992] the flow in dykes was vertical above the plume head and horizontal around it. Although such a plume would have strongly thinned the lithosphere, this thinning remains unknown and a comparison with our transition height estimation is therefore difficult. However, the presence of sills [*LeCheminant and Heaman*, 1989] as well as the indication of horizontal flow [*Ernst and Baragar*, 1992] suggest that the propagation was dominated by the overpressure in the plume head rather than by the buoyancy of the magma. Vertical dykes would have therefore propagated in a non-steady state regime and our estimations of transition height and source overpressure would be underestimated. This would suggest an enormous overpressure in the plume head, more than 1500 bars, at the time of the swarm emplacement. If we have overestimated dyke cross sections, because we considered dykes that propagated laterally and not vertically, our model would still predict overpressures of several hundreds of bars. Another possibility is that a giant mantellic plume such as this one would have dramatically modified the thermal structure of the lithosphere and, as a result, its stiffness would have been strongly reduced. In that case, our estimated source overpressure would be lowered.

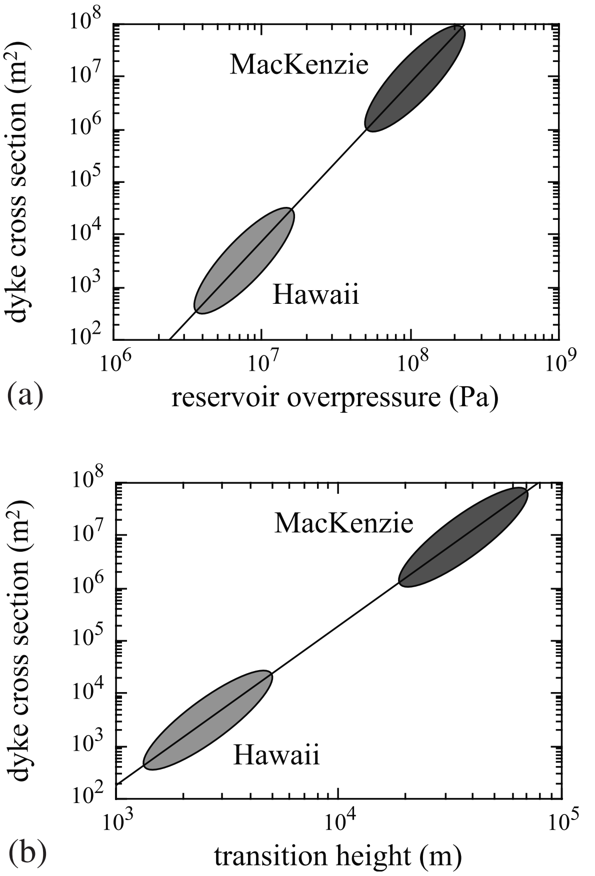

Figure 13. Dyke cross section as a function of (a) source overpressure (equation (24)) and (b) transition height (equation (16)). E = 40 GPa, ν = 0.25, and $\Delta\rho$ = 300 kg m^{-3}. Ellipses are estimations of typical dyke cross sections estimated for Hawaii and MacKenzie Dyke Swarm.

[39] Are such overpressures realistic? We have assumed that dyke initiation and propagation are controlled by the fracture toughness of rocks, which is thought to be independent of the dimensions of the dykes as well as their loading. This seems to be in contradiction with our results that suggest a greater source overpressure is needed to create a greater geological object, such as a giant dyke swarm, and therefore that fracturing processes depend on a length scale.

Table 2. Source Overpressures and Transition Heights Between Regimes Estimated for Hawaii and the MacKenzie Dyke Swarm

Parameter	Hawaii	MacKenzie
Dyke cross section (m^2)	10^3-10^4	$3 \times 10^6-3 \times 10^7$
Source overpressure (bar)	40–80	600–1200
Transition height (km)	1–3	20–40

The source overpressures and transition heights have been estimated using equations (24) and (16), respectively.

However, fracture toughness estimated from field measurements are 10^2-10^3 greater than those measured in laboratory on rock samples [*Delaney and Pollard*, 1981; *Atkinson*, 1984; *Reches and Fink*, 1988] and it has been argued that the fracture energy required to propagate a dyke, or measured for earthquakes, is many orders of magnitude larger than laboratory-scale measurements [*Rudnicki*, 1980; *Delaney et al.*, 1986]. Both field and laboratory observations can only really be consistent if fracture toughness is scale dependent. Indeed, it has been argued that rock fracture toughness does scale with the size of the fracture because the volume of rock affected, and hence undergoing damage, is greater [*King*, 1983; *Scholtz et al.*, 1993]. Increase in the resistance to propagation of a fault with the length of the fault can explain why small earthquakes occur; if this were not the case, earthquakes would always propagate unstably and therefore become "megaearthquakes." In short, damage and fracture at one scale lead not to catastrophic failure of the rock (as happens in small-scale experiments on rock samples) but to damage and fracture at larger scales in a process of evolving damage [*King and Sammis*, 1992]. It therefore seems that the fracture dominated regime, which we observed in our experiments and in which a dissipative, scale-dependent process resists fissure propagation, is likely to exist under geological conditions.

5. Conclusion

[40] Fissure propagation from a reservoir with constant overpressure is characterized by two regimes. Initially, the propagation is controlled by a balance between the source pressure and the fracture pressure. In this transient regime both the injection rate and the fissure velocity depend on the initial conditions. Once the buoyancy pressure overcomes the source pressure, a steady state is achieved. The fissure develops a bulbous head, in which buoyancy pressure balances the fracture pressure that resists the propagation, fed by a thinner tail, the thickness of which is determined by a balance between buoyancy and viscous pressure gradient. Fissure velocity and injection rate become constant at the transition between regimes. Even in the steady state regime, the velocity and the injection rate reflect the source conditions because the fissure latches onto a steady state regime that is consistent with the source characteristics. Likewise, the strain energy release rate during the steady propagation is determined by the initial source conditions.

[41] Although our model cannot, at this preliminary stage, predict the propagation velocity of a liquid-filled fissure, it does nevertheless provide constraints on the failure mechanism: the steady propagation velocity appears to be proportional to the square of the height of the buoyant fissure head. Moreover, the fissure can propagate steadily even though the stress intensity factor at its tip is greater than the fracture toughness of the host solid.

[42] Our model suggests that the cross-sectional area of dykes provides two quantitative pieces of information. It first gives the nature of the propagation regime of the dykes, whether it is steady or not. Second, it gives an estimation of the overpressure present in the source at the time of their emplacement. These overpressures appear to depend on the dimensions of the dykes, suggesting a length scale dependence of time-dependent failure of rocks. Hence, like fault propagation, dyke propagation seems very likely to be controlled by the fracture resistance of rocks.

[43] **Acknowledgments.** We thank Claude Jaupart, Geoffrey King, and Allan Rubin for fruitful discussions. Reviews by Amotz Agnon and John Lister have greatly improved the manuscript. We also thank Gérard Bienfait for help with experiments.

References

Atkinson, B. K., Subcritical crack growth in geological materials, *J. Geophys. Res.*, *89*, 4077–4114, 1984.

Barenblatt, G. I., The mathematical theory of equilibrium cracks in brittle fracture, *Adv. Appl. Mech.*, *7*, 55–129, 1962.

Brandsdóttir, B., and P. Einarsson, Seismic activity associated with the September 1977 deflation of the Krafla central volcano in northeastern Iceland, *J. Volcanol. Geotherm. Res.*, *6*, 197–212, 1979.

Delaney, P. T., and D. D. Pollard, Deformation of host rocks and flow of magma during growth of Minette dikes and breccia-bearing intrusions near Ship Rock, New Mexico, *U. S. Geol. Surv. Prof. Pap.*, *1202*, 61 pp., 1981.

Delaney, P. T., D. D. Pollard, J. L. Ziony, and E. H. McKee, Field relations between dikes and joints: Emplacement processes and paleostress analysis, *J. Geophys. Res.*, *91*, 4920–4938, 1986.

Einarsson, P., and B. Brandsdóttir, Seismological evidence for lateral magma intrusion during the July 1978 deflation of the Krafla volcano in NE-Iceland, *J. Geophys.*, *47*, 160–165, 1980.

Emerman, S. H., D. L. Turcotte, and D. A. Spence, Transport of magma and hydrothermal solutions by laminar and turbulent fluid fracture, *Phys. Earth Planet. Inter.*, *41*, 249–259, 1986.

Ernst, R. E., and W. B. A. Baragar, Evidence from magnetic fabric for the flow pattern of magma in the MacKenzie giant radiating dyke swarm, *Nature*, *356*, 511–513, 1992.

Fahrig, W. F., The tectonic settings of continental mafic dyke swarms: Failed arm and early passive margin, in *Mafic Dyke Swarms*, edited by H. C. Halls and W. F. Fahrig, pp. 331–348, Geol. Assoc. of Can., St. Johns, Newfoundland, 1987.

Fiske, R. S., and E. D. Jackson, Orientation and growth of Hawaiian volcanic rifts: The effect of regional structure and gravitational stresses, *Proc. R. Soc. London*, *329*, 299–326, 1972.

Griffith, A. A., The phenomena of rupture and flow in solids, *Philos. Trans. R. Soc. London, Ser. A*, *221*, 163–198, 1920.

Heimpel, M., and P. Olson, Buoyancy-driven fracture and magma transport through the lithosphere: Models and experiments, in *Magmatic Systems*, edited by M. P. Ryan, pp. 223–240, Academic, San Diego, Calif., 1994.

Hyndman, D. W., and D. Alt, Radial dikes, laccoliths and gelatin models, *J. Geol.*, *95*, 763–774, 1987.

Irwin, G. R., Analysis of stresses and strains near the end of a crack traversing a plate, *J. Appl. Mech.*, *24*, 361–364, 1957.

King, G. C. P., The accommodation of large strains in the upper lithosphere of the Earth and other solids by self-similar faults systems: The geometrical origin of b-value, *Pure Appl. Geophys.*, *121*, 761–815, 1983.

King, G. C. P., and C. Sammis, The mechanisms of finite brittle strain, *Pure Appl. Geophys.*, *138*, 611–640, 1992.

Lawn, B., *Fracture of Brittle Solids* (*Second Edition*), 398 pp., Cambridge Univ. Press, New York, 1993.

LeCheminant, A. N., and L. M. Heaman, Mackenzie igneous events, Canada: Middle Proterozoic hotspot magmatism associated with ocean spreading, *Earth Planet. Sci. Lett.*, *96*, 38–48, 1989.

Lister, J. R., Buoyancy-driven fluid fracture: The effects of material toughness and of low-viscosity precursors, *J. Fluid Mech.*, *210*, 263–280, 1990a.

Lister, J. R., Buoyancy-driven fluid fracture: Similarity solutions for the horizontal and vertical propagation of fluid-filled cracks, *J. Fluid Mech.*, *217*, 213–239, 1990b.

Lister, J. R., and R. C. Kerr, Fluid-mechanical models of crack propagation and their application to magma transport in dykes, *J. Geophys. Res.*, *96*, 10,049–10,077, 1991.

Maaløe, S., The generation and shape of feeder dykes from mantle sources, *Contrib. Mineral. Petrol.*, *96*, 47–55, 1987.

McGuire, W. J., and A. D. Pullen, Location and orientation of eruptive fissures and feeder-dykes at Mount Etna: Influence of gravitational and regional tectonic stress regimes, *J. Volcanol. Geotherm. Res.*, *38*, 325–344, 1989.

Menand, T., and S. R. Tait, A phenomenological model for precursor volcanic eruptions, *Nature*, *411*, 678–680, 2001.

Mériaux, C., and C. Jaupart, Dike propagation through an elastic plate, *J. Geophys. Res.*, *103*, 18,295–18,314, 1998.

Mériaux, C., J. R. Lister, V. Lyakhovsky, and A. Agnon, Dyke propagation with distributed damage of the host rock, *Earth Planet. Sci. Lett.*, *165*, 177–185, 1999.

Pollard, D. D., Derivation and evaluation of a mechanical model for sheet intrusion, *Tectonophysics*, *19*, 233–269, 1973.

Pollard, D. D., Elementary fracture mechanics applied to the structural interpretation of dykes, in *Mafic Dyke Swarms*, edited by H. C. Halls and W. F. Fahrig, pp. 5–24, Geol. Assoc. of Can., St. Johns, Newfoundland, 1987.

Pollard, D. D., and A. M. Johnson, Mechanics of growth of some laccolithic intrusions in the Henry Mountains, Utah, II, Bending and failure of overburden layers and sills formation, *Tectonophysics*, *18*, 311–354, 1973.

Reches, Z., and J. Fink, The mechanism of intrusion of the Inyo Dike, Long Valley Caldera, California, *J. Geophys. Res.*, *93*, 4321–4334, 1988.

Rubin, A. M., Tensile fracture of rocks at high confining pressure: Implications for dyke propagation, *J. Geophys. Res.*, *98*, 15,919–15,935, 1993a.

Rubin, A. M., Dikes vs. diapirs in viscoelastic rock, *Earth Planet. Sci. Lett.*, *119*, 641–659, 1993b.

Rubin, A. M., Getting granite dikes out of the source region, *J. Geophys. Res.*, *100*, 5911–5929, 1995a.

Rubin, A. M., Propagation of magma-filled cracks, *Annu. Rev. Earth Planet. Sci.*, *23*, 287–336, 1995b.

Rubin, A. M., and D. D. Pollard, Origin of blade-like dikes in volcanic rift zones, *U. S. Geol. Surv. Prof. Pap.*, *1350*, 1449–1470, 1987.

Rudnicki, J. W., Fracture mechanics applied to the Earth's crust, *Annu. Rev. Earth Planet. Sci.*, *8*, 489–525, 1980.

Ryan, M. P., R. Y. Koyanagi, and R. S. Fiske, Modeling the three-dimensional structure of macroscopic magma transport systems: Application to Kilauea volcano, Hawaii, *J. Geophys. Res.*, *86*, 7111–7129, 1981.

Scholtz, C. H., N. H. Dawers, J.-Z. Yu, M. H. Anders, and P. A. Cowie, Fault growth and fault scaling laws: Preliminary results, *J. Geophys. Res.*, *98*, 21,951–21,961, 1993.

Sneddon, I. N., The distribution of stress in the neighborhood of a crack in an elastic solid, *Proc. R. Soc. London*, *187*, 229–260, 1946.

Sneddon, I. N., and S. C. Das, The stress intensity factor at the tip of an edge crack in an elastic half-plane, *Int. J. Eng. Sci.*, *9*, 25–36, 1971.

Spence, D. A., and P. Sharp, Self-similar solutions for elastohydrodynamic cavity flow, *Proc. R. Soc. London, Ser. A*, *400*, 289–313, 1985.

Spence, D. A., and D. L. Turcotte, Magma-driven propagation of cracks, *J. Geophys. Res.*, *90*, 575–580, 1985.

Spence, D. A., and D. L. Turcotte, Buoyancy-driven magma fracture: A mechanism for ascent through the lithosphere and the emplacement of diamonds, *J. Geophys. Res.*, *95*, 5133–5139, 1990.

Spence, D. A., P. W. Sharp, and D. L. Turcotte, Buoyancy-driven crack propagation: A mechanism for magma migration, *J. Fluid Mech.*, *174*, 135–153, 1987.

Takada, A., Experiments study on propagation of liquid-filled crack in gelatin: Shape and velocity in hydrostatic stress condition, *J. Geophys. Res.*, *95*, 8471–8481, 1990.

Timoshenko, S. P., and J. N. Goodier, *Theory of Elasticity* (*Third Edition*), 567 pp., McGraw-Hill, New York, 1970.

Weertman, J., Theory of water-filled crevasses in glaciers applied to vertical magma transport beneath oceanic ridges, *J. Geophys. Res.*, *76*, 1171–1183, 1971a.

Weertman, J., Velocity at which liquid-filled cracks move in the Earth's crust or in glaciers, *J. Geophys. Res.*, *76*, 8544–8553, 1971b.

White, F. M., *Viscous Fluid Flow*, 725 pp., McGraw-Hill, New York, 1974.

T. Menand, BP Institute for Multiphase Flow, University of Cambridge, Madingley Rise, Madingley Road, Cambridge CB3 0EZ, UK. (thierry@bpi.cam.ac.uk)

S. R. Tait, Department of Earth Sciences and Engineering, Imperial College of Science, Technology and Medicine, RSM Building, Prince Consort Road, London SW7 2BP, UK. (steve.tait@ic.ac.uk)

Available online at www.sciencedirect.com
SCIENCE DIRECT®

Earth and Planetary Science Letters 245 (2006) 799 – 813

EPSL

www.elsevier.com/locate/epsl

An experimental investigation of sill formation and propagation in layered elastic media

Janine L. Kavanagh *, Thierry Menand, R. Stephen J. Sparks

Department of Earth Sciences, University of Bristol, Bristol BS8 1RJ, UK

Received 30 September 2005; received in revised form 6 February 2006; accepted 17 March 2006
Available online 2 May 2006
Editor: V. Courtillot

Abstract

A series of experiments are described where dyed water (a magma analogue) was intruded into solid gelatine (a crustal analogue) to investigate the formation of sills. We considered a layered gelatine system with contrasting adjacent layers. By varying the density and rigidity of the gelatine we found that experimental sills form when the upper layer is more rigid than the lower layer, with intrusion occurring in a plane directly below the interface. Experimental dykes were observed to propagate to the surface when the Young's Modulus ratio of upper to lower gelatine layers was less than one. Experimental dyke arrest occurred when the upper layer was more rigid and the interface was strong. Two varieties of experimental sill formed when the upper layer was more rigid than the lower layer and the interface was sufficiently weak. The form of the intrusion depends on the balance of driving pressures and the Young's Modulus ratio of contrasting adjacent layers. When the rigidity ratio is high and there is a large driving pressure the experimental feeder dyke completely converts to propagate as a sill. However, when the rigidity ratio and driving pressure are both close to one a dyke–sill hybrid forms. Under these conditions the experimental sill formation is accompanied by contemporaneous dyke intrusion into the overlying more rigid layer. During sill propagation deformation structures such as faults and *en echelon* fractures are formed into the lower layer. Experimental sill propagation dynamics are controlled by viscous dissipation along the length of the sill; causing acceleration with increasing length. Our study suggests that rigidity contrasts may play a major role in the location of sills and development of igneous complexes. In ancient cratonic areas the Moho is a suitable site for the preferential formation of sills with higher rigidity continental crust overlying weaker mantle. Mantle plumes impacting ancient continents provide a situation in which large sills can form to fractionate prior to eruption of flood basalts. The boundary between the upper and lower crust (Conrad discontinuity) may provide a preferential focus for the emplacement of sheets of silicic magma at continental arcs where the lower crust is weakened by prolonged heating and possible hydration.

Keywords: sills; fractures; layered crust; intrusions

1. Introduction

Sill intrusion is a major mechanism of constructing continental crust. Repeated sill intrusion with evolution to laccolithic bodies [1] is a favoured mechanism for forming crustal magma chambers and granite plutons

---

* Corresponding author. Tel.: +44 117 954 5400; fax: +44 117 925 3385.
E-mail address: janine.kavanagh@bristol.ac.uk (J.L. Kavanagh).

0012-821X/$ - see front matter © 2006 Elsevier B.V. All rights reserved.
doi:10.1016/j.epsl.2006.03.025

[2–4]. Igneous differentiation also occurs in sills [5]. A common explanation of seismic layering in the lower crust is the formation of sill complexes [6]. However, the dynamics and mechanics of sill emplacement are poorly constrained. There is economic incentive to understand sill emplacement as these intrusions improve the petroleum prospectivity of sedimentary basins [7] and form part of diamond-bearing kimberlite complexes [8].

Sills have been relatively unstudied compared to dykes and there are different concepts regarding their mechanism of emplacement and propagation dynamics. Previous work has focused on the growth of an established sill [7] and has considered the transformation of sills into laccolith [1,9]. The conditions under which vertical magma intrusions convert to propagate as a sill have been studied theoretically [10–13] but these hypotheses are conflicting. Experimental studies of dyke formation [14] and propagation [15–21] are numerous and have proved successful. In comparison, studies of the dyke to sill transition are sparse [22,23].

In this study the controls on sill emplacement have been investigated experimentally by intruding dyed water (a magma analogue) into solidified gelatine (a crustal analogue). The aims are to identify potential controls on sill emplacement and then to characterise sill propagation dynamics. Background information is first provided regarding the characteristics and geological settings of sills, and then a theoretical framework is presented that can be used to characterise them. Using this theoretical framework a series of experiments are described in which dynamical data are collected, and the conditions suitable for sill formation are determined by varying the host material's of density and rigidity. Finally we apply the results to interpretation of preferred levels of intrusion in the continental lithosphere in different tectonic settings.

2. Geological settings, sill morphology and formation hypotheses

Sills commonly intrude parallel to bedding planes [24], though are also found intruded into basement rocks [25], pre-existing lavas, and steeply dipping rocks where the intrusion is discordant to bedding or metamorphic layering (for example the Traigh Bhan na Sgurra Sill, Isle of Mull, Scotland). Sills can extend over thousands of square kilometres and can be hundreds of metres thick [24,26,27]. Sills can be formed in all tectonic contexts though the largest sills tend to be doleritic and are associated with crustal thinning, continental break-up and sedimentary basin formation [24]. Smaller sills (extending over only a few square kilometres) are generally found in association with volcanic centres [28]. Underplating can also produce horizontal planar magma bodies at the crust–mantle interface [29,30]. Here for simplicity we define sills as horizontal magma sheet intrusions, compared to dykes that are defined as vertical sheet intrusions.

Three forms of sill have been identified: radial symmetrical sills, bilaterally symmetrical sills and a hybrid variety that forms due to their interaction. Radial symmetrical sills are commonly thickest at their centre [24,31], though examples where the edge of the sill is thickest have also been described [12]. Dykes feed sills and are either centrally located [31] or offset [12,24,32].

Field studies show that when sills intrude sedimentary sequences they commonly abut rock layers that could have acted as a barrier to vertical propagation and encouraged horizontal propagation. Examples include high rigidity sandstones [33], shales [34], ancient lava flows [25] or a previously formed sill (e.g. Kimberlite sills abut dolerite sills in the Wesselton mine, Kimberley, South Africa [35]). The load of volcanic edifices can trap magma within the crust [36] to form horizontally propagating dykes [37] and potentially horizontal sills.

There are two conflicting hypotheses of sill formation with their emplacement controlled either by buoyancy forces or by the tectonic stress system. Intruding magma is commonly of intermediate density to basement rocks and sedimentary sequences. The hypothesis that sills are emplaced at the magma's level of neutral buoyancy [11] is not consistent with field observations that show basalt sills emplacement both within lower density sedimentary sequences [24] and higher density basement sequences [38]. Roberts' [10] tectonics hypothesis states that sills are emplaced during conditions of horizontal compression. The transition from dyke to sill is attributed to a change in ambient stress from horizontal tension ($\sigma_x < \sigma_z$) that favours dyke propagation at depth, to horizontal compression ($\sigma_x > \sigma_z$), which promotes sill propagation at shallow crustal levels (see Table 1 for parameter definitions). Roberts' [10] and Bradley's [11] hypotheses of sill formation predict a morphology that is either parallel to or mirrors the overlying contemporaneous surface topography, respectively [31]. 3-D seismic reflection data from the North Rockall Trough have shown that neither of these sill morphologies is observed, and consequently there is no current model that adequately describes the mechanism of sill formation. The

Table 1
Notation and parameters

$\bar{U}$	Average flow velocity	m/s
P_b	Buoyancy pressure	Pa
X_G	Composition: gelatine	wt.%
X_{LG}	Composition: gelatine lower layer	wt.%
X_{UG}	Composition: gelatine upper layer	wt.%
X_{LS}	Composition: NaCl lower layer	wt.%
x	Deflection	m
ρ_G	Density: gelatine	kg/m^3
ρ_{liq}	Density: injected liquid	kg/m^3
ρ_L	Density: lower layer gelatine	kg/m^3
ρ_U	Density: upper layer gelatine	kg/m^3
a	Diameter	m
P_e	Elastic pressure	Pa
P_{eL}	Elastic pressure: lower layer	Pa
P_{eU}	Elastic pressure: upper layer	Pa
M	Elastic stiffness	Pa
ρ	Fluid density	kg/m^3
P	Fluid Pressure	Pa
η	Fluid viscosity	Pa s
P_f	Fracture pressure	Pa
P_{fL}	Fracture pressure: lower layer	Pa
P_{fU}	Fracture pressure: upper layer	Pa
K_c	Fracture toughness	Pa m$^{0.5}$
K_{cL}	Fracture toughness: lower layer	Pa m$^{0.5}$
K_{cU}	Fracture toughness: upper layer	Pa m$^{0.5}$
g	Gravity	m/s^2
w	Half-thickness	m
H	Head pressure height	m
h	Height of crack	m
h_L	Height: lower layer thickness	m
h_c	Height: crack thickness	m
l	Length of crack	m
m	Mass	kg
P_0	Overpressure	Pa
v	Poisson's ratio	N/A
P_L	Pressure: load	Pa
U	Propagation velocity	m/s
Re	Reynolds number	N/A
y	Second longest crack dimension	m
μ	Shear modulus	Pa
ε_x	Strain in x-direction	N/A
ε_y	Strain in y-direction	N/A
σ_x	Stress in x-direction	Pa
σ_y	Stress in y-direction	Pa
σ_z	Stress in z-direction	Pa
K	Stress intensity factor	Pa m$^{1/2}$
S	Surface area	m^2
γ_s	Surface energy of gelatine	J m^{-2}
t	Time	s
U	Velocity	m/s
P_v	Viscous pressure	Pa
V	Volume	m^3
E	Young's Modulus	Pa
E_L	Young's Modulus: lower layer	Pa
E_U	Young's Modulus: upper layer	Pa

observation that sills often abut a particularly rigid horizontal layer (such as a previously emplaced sill [35] or a particularly rigid sandstone layer [33]) provides an alternative hypothesis of sill intrusion controlled by rock rigidity.

3. Theoretical background

Dyke and sill intrusion are likely to be mechanically different as dykes are typically discordant whereas sills often intrude horizontal planes of weakness such as bedding planes or unconformities. Dyke propagation has previously been studied using the principles of linear elastic fracture mechanics (LEFM) where the intrusion is idealised as a crack intruding a brittle, elastic material and its propagation is governed by both fluid and fracture mechanics [15–21]. This physical framework is independent of the orientation of the intrusion, and we assume the same principles can be applied to study sill formation and propagation. The intrusion of magma into a propagating crack involves driving and resistive pressure forces, characterising the elastic deformation of the host solid, the resistance to fracture, the buoyancy of the fluid and its viscous resistance to the flow. These pressures are now introduced.

Sills have a thickness over length aspect ratio of $\sim 10^{-3}$ [26], which enables us to consider them as planar sheet intrusions [22]. The crust responds elastically to sill intrusion which exerts a relatively small amount of strain on the host material and has a short timescale of deformation [20]. A magma-filled crack can be divided into three regions: the intact host material, the process zone and the crack itself [39] (see Fig. 1). Between the magma front and crack tip there is a cavity that may be filled by exsolved volatiles from the magma.

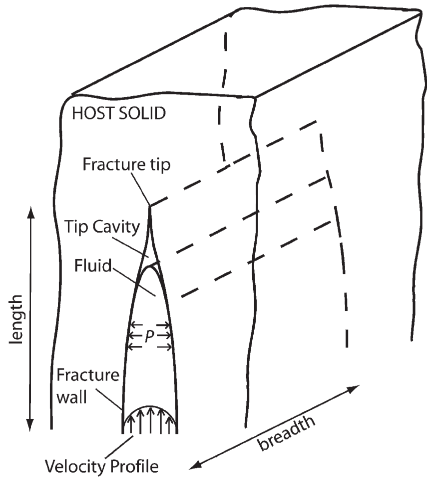

Fig. 1. Schematic diagram of a pressure driven fluid-filled crack propagating in an elastic solid (based on [39]).

In order for magma to intrude its host material the magma pressure P needs to overcome the elastic pressure P_e to deform the host material elastically [20]:

$$P_e = \frac{E}{2(1-v^2)}\frac{w}{y}, \tag{1}$$

where E is Young's Modulus, v is Poisson's ratio, w is the typical half-thickness of the crack and y is half the crack's second smallest dimension. P_e expresses the elastic properties of the host rock and is reflected in the dimensions of the resulting crack. It follows that a higher magma pressure is required to elastically deform a very rigid material with high E.

In order for a fracture to propagate, the pressure at the crack tip has to exceed the strength of the host rock. Stresses are concentrated at the crack tip and are characterised by a stress intensity factor K. This is controlled by the overpressure P_0 (defined as the magma pressure in excess of the ambient stress) and the length of the crack l [39]. Fracture can occur when K exceeds the fracture toughness K_c (which characterises the strength of the host rock) [39]. Therefore, the excess magma pressure, P_0, needs to surpass the fracture pressure, P_f, of the rock in order to initiate crack propagation [20] and can be expressed as follows:

$$P_0 > P_f = \frac{K_c}{\sqrt{l\pi}}. \tag{2}$$

This is the overpressure required to create a stress at the crack tip which is capable of fracturing the host material [16]. It is easier to propagate a crack in a host material that has a low fracture toughness K_c; additionally, the longer the crack the easier it is to propagate.

The density difference ($\Delta\rho$) between that of the intruded host material and the magma results in a buoyancy pressure P_b, [39]:

$$P_b = \Delta\rho g h. \tag{3}$$

The buoyancy pressure thus depends on gravity, g, and the height of the magma, h.

The Reynold's number (Re) determines magma flow dynamics and velocity profile along the thickness of the crack:

$$Re \equiv \frac{\rho_{liq}\bar{U}w}{\eta}, \tag{4}$$

where $\bar{U}$ is the average velocity, w is the half-thickness of the flow, ρ_{liq} is the liquid density and η is its viscosity. A laminar flow regime occurs at low Reynold's number and turbulent flow at a high Reynold's number. The transition from laminar to turbulent flow behaviour occurs between 10 and 1000 depending on the flow geometry [20]. The Reynold's number is typically low for dyke intrusion [40], corresponding to laminar flow behaviour. However, sills can show evidence of turbulent flow [25]. For example, a basaltic dyke propagating at an average velocity of 1 m/s, with a typical half-thickness of 1 m, a density of ~2800 kg/m^3, and viscosity of 100 Pa s would have $Re=28$. This is in the transitional regime between laminar and turbulent flow, though the behaviour will be predominantly laminar. However, as sills are typically thicker than dykes, magma with the same velocity and viscosity in a 10 m thick intrusion would have $Re=280$, and thus may develop local or intermittent turbulence. A 100 m thick intrusion should develop fully turbulent flow. The Reynold's number is used to scale small laboratory experiments to these large natural phenomena.

The velocity profile across the crack thickness depends on the flow regime. Magma is a viscous fluid and, in both laminar and turbulent flows, viscous dissipation P_v along the length of the crack occurs. In laminar flow this viscous pressure drop, P_v, is estimated from the equation [20]:

$$P_v \approx \frac{\eta l^2}{w^2 t}, \tag{5}$$

where t is time. By considering the balance of resistive pressures (P_v and P_f) [20] it can be determined whether sill propagation is controlled predominantly by the viscosity of the intruding fluid or fracture of the host solid. Viscosity is important when $P_v > P_f$ and fracture is dominant when $P_v < P_f$ [20]. Sills are commonly observed to intrude parallel to bedding planes and one can assume that fracturing between two adjacent beds requires less energy than fracturing through coherent, more competent rocks. Therefore, sills are more likely to be controlled by viscous dissipation than dykes. The buoyancy pressure acting over the thickness of a sill can be considered negligible when compared to the elastic pressure as the maximum thickness of sill extends to a few hundred metres; over this distance elastic pressure would dominate [20]. Based on the assumption of negligible buoyancy and fracture pressure, sill propagation would be controlled by a balance between viscous dissipation, P_v, and overpressure, P_0. Consequently, the velocity U along the length of the sill can be calculated [39]:

$$U = \frac{1}{3\eta}\frac{P_0^3}{M^2}l, \tag{6}$$

where M is the elastic stiffness of the host material and is the balance of its shear modulus, μ, and Poisson's ratio, v [39]:

$$M=\frac{\mu}{(1-v)}=\frac{E}{2(1-v^2)}. \tag{7}$$

4. Experimental methods

The mechanics of forming sills are now investigated using layers of gelatine injected by water-filled cracks. The experiments involve varying the pressure driving crack propagation, and the rigidity and density of the gelatine layers.

Three sets of experiments are described. Firstly, fluid was intruded into homogeneous gelatine solid in the presence of a load. Secondly, fluid was intruded into a two-layered system with the upper layer less dense and less rigid than the lower layer. Thirdly, the fluid intruded a two-layered system with layers of approximately equal density but with an upper more rigid layer. From this point onwards vertical to sub-vertical fluid-filled cracks shall be referred to as "experimental dykes" and cracks that propagate in a horizontal plane shall be referred to as "experimental sills". The propagation of each fluid-filled crack was photographed and videoed from the side and above to monitor the propagation and evolution of the intrusion with time. Distances were measured with an accuracy of ±0.5 cm, with errors attributed predominantly to distortion of the viewing perspective by the experimental tank walls. Data collection commenced once the valve on the injector pipe was opened and propagation of the crack had begun.

Gelatine is an elastic material that has brittle behaviour and is thus a good analogue for geological systems [16,41]. It is easily prepared and is transparent when solid, making viewing and measuring an intrusion and its propagation straightforward. We can measure the properties of the host material and injected fluid, the pressures driving and resisting crack propagation, and the propagation velocity. This allows the characterisation of conditions suitable for sill formation to be determined, and the geometry of these bodies to be observed, enabling their propagation dynamics to be analysed.

When magma intrudes crustal material the ambient stress field is likely to differ from hydrostatic. Our experiments are conducted under initially hydrostatic conditions, however the physical principles of sill emplacement identified in our experiments are still valid.

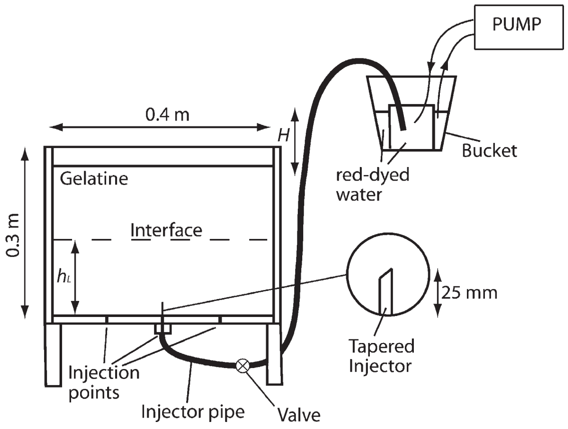

Fig. 2. Apparatus and set-up used during the experimental series.

4.1. Preparation of experiments

The experiments were conducted in a square based 0.4 m∗0.4 m∗0.3 m perspex container with nine equally spaced injection points in its base (see Fig. 2). A forty-litre gelatine solution is poured into the experimental tank to cool and solidify overnight. To accelerate the solidification process all experiments were prepared in a cold room kept at 7 °C. A thin layer of oil poured on top of the solution inhibits water evaporation during the cooling process [14,16]. A two-layered system comprises equal volumes of gelatine with contrasting properties. The properties of the gelatine are altered by varying the wt.% of gelatine, enabling a range of rigidities to be obtained. Adding salt increased the density of the gelatine and injecting fluid.

4.2. Material properties

The material properties of the gelatine solid and injecting fluid were measured prior to an experiment. Density measurements were made using a density bottle of known volume, with a mean average error of ±0.55%. The gelatine rigidity is quantified by the Young's Modulus, E, and is calculated from the deflection, x, caused by a cylindrical load of known mass, m, and radius, a, placed on the free surface. Provided the diameter of the load is small compared to the dimensions of the experimental tank the gelatine solid can be considered a semi-infinite medium [42]. The Young's Modulus, E, is then obtained by the equation:

$$E=\frac{mg(1-v^2)}{2\alpha x}. \tag{8}$$

Gelatine has a Poisson's ratio v of 0.5, and gravity is taken as $g=9.814$ m/s^2. The deflection, x, is measured to a high accuracy using a digital micrometer; the mean average error on the Young's Modulus is ±6%. Young's Modulus of gelatine evolves with time though can be considered to be constant over the duration of an experiment, which typically lasts less than 20 min.

In a two-layered system the Young's Modulus of the lower layer cannot be directly measured. Equal volume samples of each gelatine layer were prepared, left to solidify alongside the filled experimental tank and the Young's Modulus of each sample was measured. The Young's Modulus ratio was assumed to equal that of the layers in the experimental tank, allowing Young's Modulus of the lower layer to be estimated.

Young's Modulus is used to calculate the fracture toughness of each gelatine layer, with an accuracy of ±4%:

$$K_c = \sqrt{2\gamma_s E}, \tag{9}$$

where γ_s is the surface energy. Gelatine has a surface energy of 1 J m^{-2} [16]. Subsequently, the fracture pressure P_f required for crack propagation in each gelatine layer is calculated (see Eq. (2)), with a mean average error of ±6.5%.

Once the gelatine is prepared and all material properties have been determined the fluid-injecting system is attached to the experimental tank (see Fig. 2). An injector pipe is inserted into the base of the tank piercing the gelatine solid. The valve on the pipe is opened and fluid from an external reservoir is forced into the gelatine solid under a constant overpressure, P_0. The orientation of the resulting fluid-filled crack is controlled by the tapered injector [15].

4.3. Pressure measurements

The fracture pressure (see Eq. (2)) of the lower layer, P_{fL}, was evaluated at the start of each experiment when the crack length, created by the insertion of the injector, was approximately 1 cm. In a two-layered system the fracture pressure of the upper layer, P_{fU}, was calculated when the experimental crack had propagated to the interface and the crack length was approximately 12.5 cm (see Table 3). During crack propagation the overpressure, P_0, exceeds the fracture pressure both in the lower layer, P_{fL}, and at the interface P_{fU}. The overpressure was calculated via the following equation:

$$P_0 = \rho_{liq} g H, \tag{10}$$

where H is the distance between the gelatine free-surface and the height of the water in the external reservoir (see Fig. 2). P_0 was varied between experiments by increasing or decreasing H (see Table 3). A small pressure loss at the injector tip resulted in P_0 being measured with ±18% accuracy. By using a pump the external reservoir was kept full ensuring a constant head H, and hence overpressure, throughout each experiment.

During crack propagation the elastic response of the gelatine solid was estimated from the dimensions of the fluid-filled crack. The elastic pressure, P_e, was then calculated (see Eq. (1)) with a mean average error of ±43%; the uncertainty is due to the difficulties in estimating crack thickness accurately as the viewing perspective distorts it.

The buoyancy pressure of the experimental crack was calculated when it had propagated 12.5 cm in vertical height, h_L (see Table 3). This corresponded to the layer half-depth in a single-layered gelatine system and the position of the interface in a two-layered system (see Fig. 2). In the event of crack propagation along the interface the buoyancy contribution across the thickness of the crack, h_c, was added:

$$P_b = (\rho_L - \rho_{liq}) g h_L + (\rho_U - \rho_{liq}) g h_c. \tag{11}$$

Initial stress conditions are hydrostatic due to the undeformable walls of the experimental tank [15]. When crack propagation is initiated the stress field is altered. A load added to the free surface will add to this effect, and it can be calculated with a mean average error of ±1.2%:

$$P_L = \frac{mg}{S}, \tag{12}$$

where P_L is the pressure exerted by the load, m is the mass of the load, g is gravity, and S is the surface area of the load.

5. Experimental observations

5.1. Single-layered system

The aim of these experiments was to determine whether experimental sill intrusion is possible in a homogeneous solid, and to assess the effect of an edifice load on the crack propagation.

A homogeneous gelatine solid was prepared and the injection system set up in the manner described above. Once the initial crack had formed its "penny-shaped" geometry quickly converted to an arc-shaped elliptical disc with greater length than breadth. When a load was placed above the propagating crack it acted as an attractor and it was possible to stop vertical propagation

Fig. 3. Photograph of experimental dyke formation propagated with an overlying load (side view, at 909 s, Experiment 12). The load acts as an attractor to dyke propagation.

directly below the load. Propagation continued laterally along the crack breadth. Vertical propagation was reinitiated when the breadth reached a magnitude where the effect of the load was reduced, and the crack erupted at the surface next to the load (see Fig. 3). When the load was instead placed offset relative to the propagating crack it again acted as an attractor. The propagation front was deflected from vertical to an inclined path towards the load. Horizontal propagation in a plane parallel to the free surface did not occur; under these conditions experimental sill formation is not observed.

5.2. Two-layered system with low rigidity ratio (E_U/E_L)

A two-layered system was then prepared to consider the effect of a density interface that could potentially be intruded to form a sill. A less dense, less rigid upper layer was considered and a fluid with a density intermediate between the densities of the two layers intruded the system (see Table 2). The overpressure of crack propagation was greater than the buoyancy pressure (see Table 3). Initially a "penny-shaped" crack formed, as this propagated vertically it developed into an elliptical form with length greater than breadth. The experimental dyke narrowed in breadth as it reached the horizontal interface between upper and lower layers, and it then propagated through the interface (see Fig. 4). The breadth and thickness of the crack increased as it propagated into the upper layer. Its breadth tapered as it approached and then broke through the free surface and it was observed that the intrusion accelerated towards the free surface. The crack did not stall at the

Table 2
Material properties of each experiment

No.	X_{LG}	X_{LS}	ρ_L	E_L	X_{UG}	ρ_U	E_U	E_U/E_L	ρ_{liq}	Comments
Homogeneous solid										
1	6		1014	4000				1	1000	Dyke
2	5		1010	1200				1	997	Dyke
12	2		1003	1941				1	1000	Dyke
13	2		1003	1941				1	1000	Dyke
Two-layer system										
3	10	3.0	1048.6	14,651	5	1006	2834	0.19	1026	Dyke
4	5	15.0	1125	615	10	1027	24,614	40.02	1002	Sill
5	5	15.0	1125	615	10	1027	24,614	40.02	1002	Sill
6	5	1.0	1018	11,515	6	1014	9979	0.87	1003	Dyke
7	5	1.0	1018	11,515	6	1014	9979	0.87	1003	Dyke
8	5	1.5	1019	22,791	8	1019	44,117	1.94	999	Dyke–sill hybrid
9	5	1.0	1023	22,205	8	1019	28,423	1.28	1001	Sill
10	1	0.5	1003	657	5	1007	7524	11.45	999	Sill
11	4	0.5	1011	16,244	5	1007	17,806	1.10	1000	Dyke–sill hybrid
14	2	1	1008	1429	10	1027	17,945	12.56	1000	Sill
15	2	2	1011	3900	8	1019	25,739	6.60	1002	Sill
16	2	3	1018	2900	10	1027	43,340	14.95	1001	Arrested dyke
17	2	3	1018	2900	10	1027	43,340	14.95	1001	Arrested dyke

Table 3
Pressure scales calculated during experiments

No.	K_{cL}	K_{cU}	P_{fL} [a]	P_{fU} [b]	P_{eL}	P_{eU}	P_L	P_0	P_b [c]	Comments
Homogeneous solid										
1	95		535		27		400	687		Dyke
2	52		293		13		670	192	16	Dyke
12	66		373		28		739	638	3.5	Dyke
13	66		373		33		739	491	3.5	Dyke
Two-layered system										
3	182	79	1024	127	54	13		196	28	Dyke
4	38	235	210	376	18			392	154	Sill
5	38	235	210	376	14			1128	154	Sill
6	161	150	908	239	349	151		932	18.3	Dyke
7	161	150	908	239	349	238		638	18.3	Dyke
8	226	315	1278	503	380			2158	25	Dyke–sill hybrid
9	224	253	1261	404	888			3110	30	Sill
10	38	130	217	208	18			285	5.5	Sill
11	191	200	1079	319	667			1472	14.5	Dyke–sill hybrid
14	57	201	320	321	19			1373	11	Sill
15	94	241	529	384	104			2158	13	Sill
16	81	312	456	498	97			1177	21	Arrested dyke
17	81	312	456	498	77			2354		Arrested dyke

[a] P_{fL} is evaluated at the start of each experiment when the crack length, created by the insertion of the injector, is approximately 1 cm.

[b] P_{fU} is evaluated when the experimental crack has propagated to the interface and the crack length is approximately 12.5 cm.

[c] The buoyancy pressure is calculated when the crack length is 12.5 cm. When an experimental sill forms at the interface the buoyancy pressure contribution over its thickness is included (see Eq. (11)).

interface separating the layers. The presence of an interface between contrasting layers was insufficient to induce experimental sill formation.

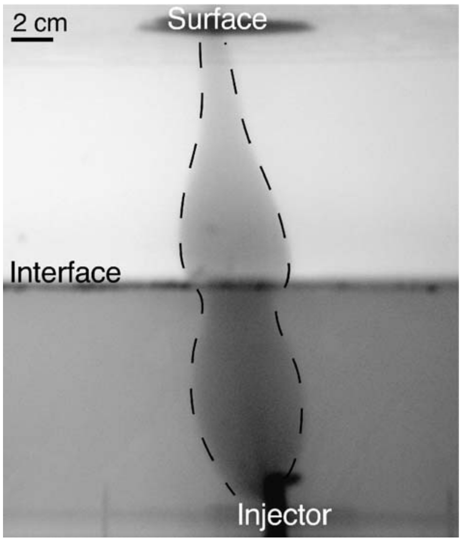

Fig. 4. Photograph of experimental dyke formation in a two-layered system with a less dense and less rigid upper layer (Experiment 3). The dyke (with dashed outline) has propagated through both layers to the surface, with no horizontal propagation parallel to their interface occurring. Note the dyke narrows at the interface and tapers towards the surface. The camera angle is not parallel to crack axis.

5.3. Two-layered system with high rigidity ratio (E_U/E_L)

A two-layered system was then prepared with an upper more rigid layer of approximately equal density to the lower layer. Intrusion was by a lower density fluid (see Table 2). The overpressure of intruding fluid was larger than the fracture pressure of both layers (see Table 3); consequently the crack had the potential to propagate to the free surface.

Initial experimental dyke formation was as a "penny-shaped" disc (see Fig. 5: stage 1). The crack propagated to the horizontal interface between upper and lower layer, developing an elliptical form. The vertical propagation then stalled upon reaching the interface and continued just along its breadth (see Fig. 5: stage 2). During some experiments an arrested experimental dyke formed with no propagation either into the upper layer or into the interface, crack propagation continued purely along the breadth of the crack. In other experiments the experimental dyke propagated along the interface and at the same time propagated into the overlying layer, forming an experimental dyke–sill hybrid (see Fig. 5: stage 3 and Fig. 6b). However, during most experiments the experimental dyke completely turned horizontally at the interface and continued its propagation as an experimental sill (see Fig. 6a). The experimental sill

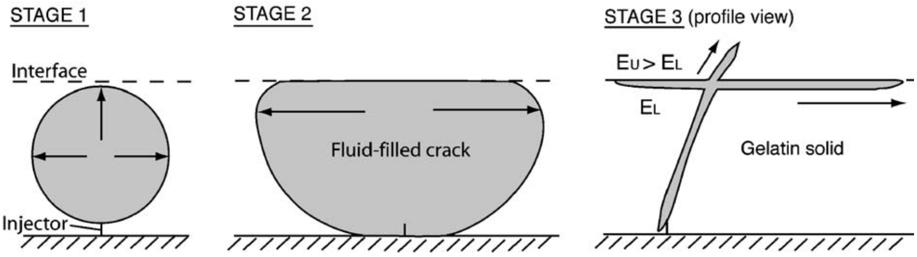

Fig. 5. A schematic sketch of the three stages of sill formation under initially hydrostatic conditions and with an upper more rigid gelatine layer. Stage 1: front view, the initial dyke formation is a circular to elliptical disc. Stage 2: front view, the vertical dyke propagation has stalled at the interface between the contrasting solid layers. The propagation is now lateral along the crack breadth and is perpendicular to the interface. Stage 3: side view, the dyke has fractured parallel to the interface separating upper rigid layer from lower layer forming a sill with contemporary dyke protrusion into the upper more rigid layer.

propagation front was lobed as the fluid-filled crack intruded the interface. During the propagation deformation structures, such as inclined *en echelon* tension structures and faults, formed within the lower less rigid layer (see Fig. 6c and d). Additionally, once the lateral extent of the experimental sill reached greater than ~30 cm diameter upwards doming of the gelatine free surface was observed, forming an experimental laccolith.

6. Experimental data

Plotting the dimensionless driving and resistive pressures, (P_0/P_{fU}), against the rigidity ratio of upper

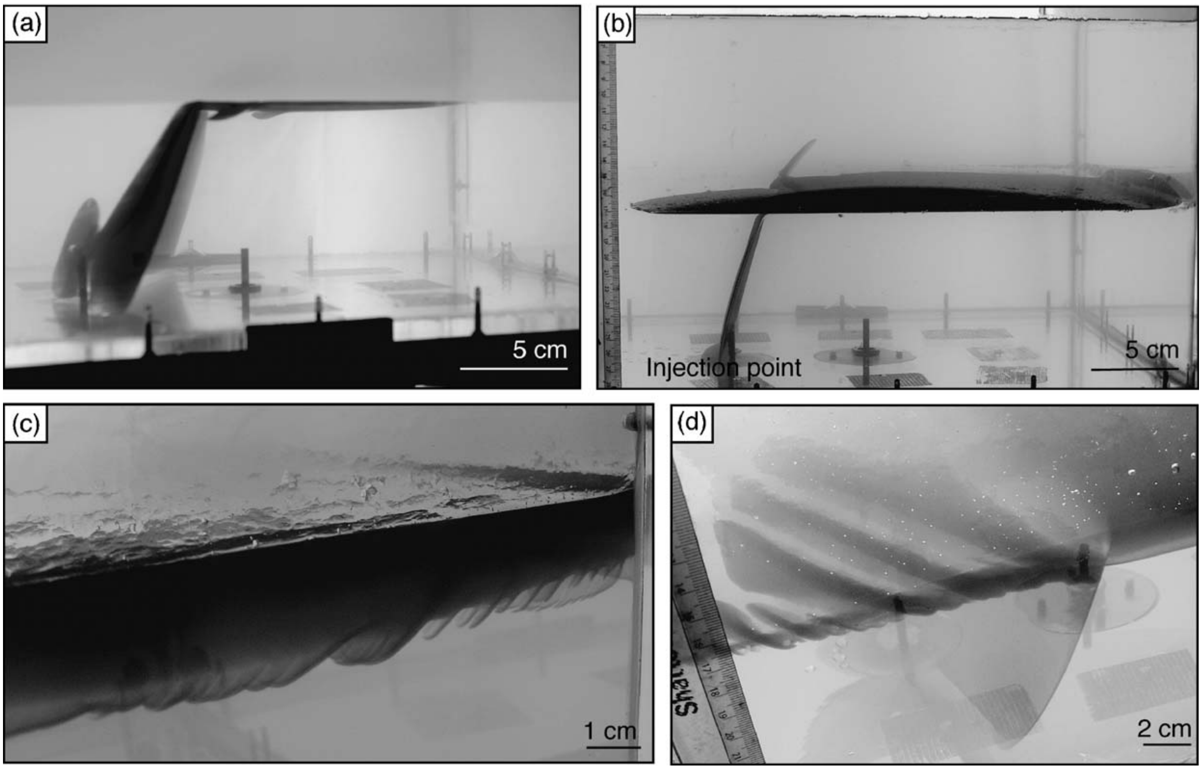

Fig. 6. A series of photographs from the experiments. (a) A vertically propagating dyke has turned to intrude as a sill along the interface separating upper rigid layer from lower layer (Experiment 15, $E_U/E_L=6.6$). Note the protrusions from the sill periphery into the lower less rigid layer. (b) Formation of a dyke–sill hybrid (Experiment 11). The rigidity ratio of upper to lower layer is 1.096. Side view, $T=187$ s. The dyke has reached the interface and has intruded horizontally as a sill and into the upper rigid layer. The camera is not perpendicular to crack axis. (c) Deformation structures that formed during sill emplacement. Side view, *en echelon* fractures formed in the lower less rigid layer during sill emplacement (Experiment 10, $E_U/E_L=11.45$). (d) Plan view, inclined fractures formed into the lower less rigid layer during the sill-to-laccolith transition phase.

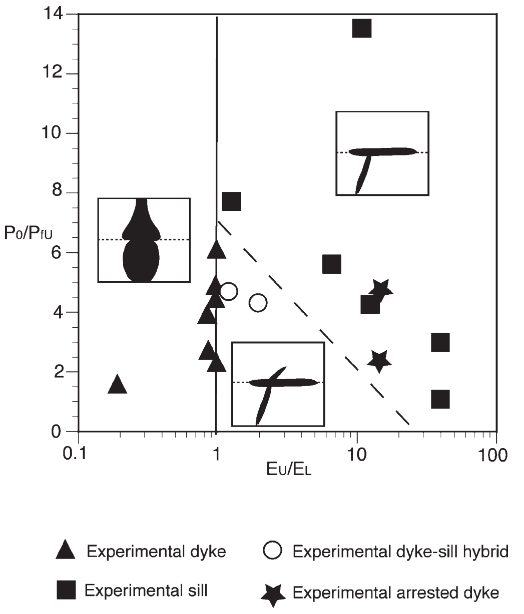

Fig. 7. Dimensionless ratio of driving and resistive pressure scales P_0/P_{fU} (±16%) as a function of a dimensionless rigidity ratio E_U/E_L (±6.7%), showing different styles of intrusive behaviour. The solid line represents the boundary between experimental dyke formation and sill formation. The dashed line represents the approximate boundary between experimental sill formation and dyke–sill hybrid formation.

to lower layer, (E_U/E_L), we show that under initially hydrostatic conditions experimental sills were observed to form only in the presence of a more rigid upper layer (see Fig. 7). Additionally, when the driving pressure was greatly in excess of that required to propagate a crack into the upper layer the experimental feeder dyke turned to propagate horizontally into the interface as an experimental sill. However, when the driving pressure just exceeded the overpressure an experimental dyke–sill hybrid formed with contemporary propagation of an experimental sill along the interface and of an experimental dyke into the upper layer.

The velocity data collected from each experiment show experimental sill propagation dynamics are different to experimental dyke propagation dynamics. After an initial acceleration due to the injection of fluid, experimental dyke propagation maintains an approximately constant velocity with length; however experimental sills accelerate as their length increases (see Fig. 8b). The propagation data show experimental sill formation can be divided into four stages (see Fig. 8). Stage one describes a vertically propagating experimental dyke that propagates towards a horizontal interface between an upper rigid layer and a lower less rigid layer (see Fig. 5). The experimental dyke decelerates as it approaches the interface, though the propagation velocity along the crack breadth is unaffected (see Fig. 8). Stage two of experimental sill formation is characterised by pure lateral propagation along the breadth of the crack (see Fig. 5). Experimental sill nucleation is initiated at the start of stage three,

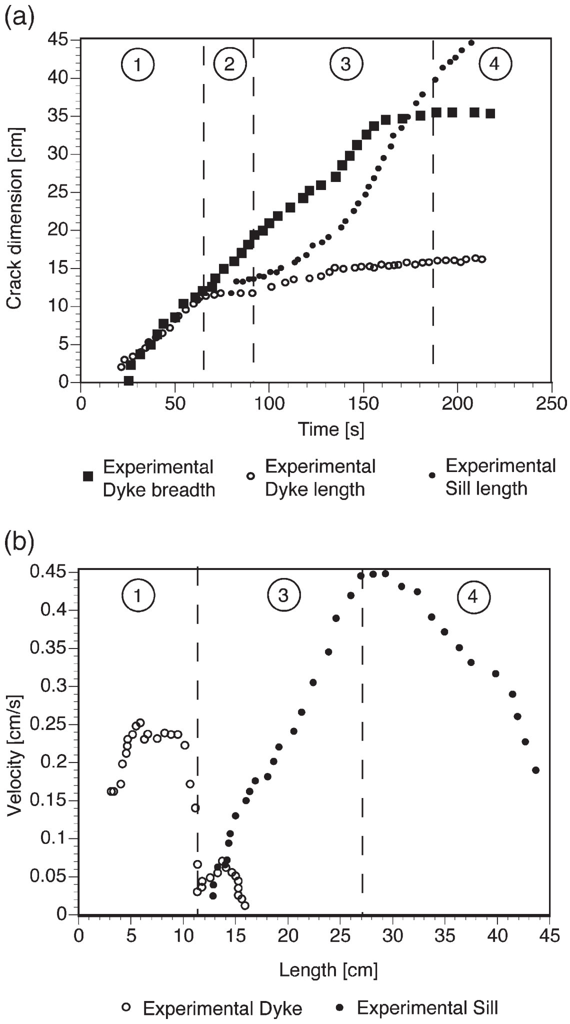

Fig. 8. Example plots of data collected during the experiments showing the four stages of crack propagation where a vertical propagating crack turned to propagate horizontally into the interface. Stage 1: a vertically propagating crack with constant velocity begins to decelerate as it approaches a more rigid horizontal layer. Stage 2: vertical propagation of the crack is inhibited, the propagation continues along the breadth of the crack. Stage 3: horizontal crack propagation into the interface is initiated, sometimes with contemporary inclined propagation into the upper more rigid layer (characterised by an initial acceleration and then rapid deceleration). The crack propagation accelerates as it intrudes the interface. Stage 4: The propagation of the crack into the interface rapidly decelerates when the horizontal crack dimension becomes comparable to the size of the experimental tank. (a) Distance versus time plot of experimental sill formation in a hydrostatic two-layered system, with $E_U/E_L = 1.10$ (Experiment 11). (b) Plot of length velocity versus length of intrusion during experimental sill propagation.

accompanied by contemporary experimental dyke intrusion into the upper rigid layer in some cases. Experimental sill formation only occurred when the interface was comparatively weak. The thickness of the feeder dyke approximately halves in response to sill formation. The continued experimental dyke intrusion into the upper layer is short-lived with an initial acceleration and then rapid deceleration (see Fig. 8). In contrast, the experimental sill maintains almost constant acceleration. The experimental sill propagation then decelerates in stage four, a feature attributed to the influence of the experimental tank walls because the dimensions of the sill are then comparable to those of the tank.

As an example, the average velocity of crack propagation in Experiment 11 was 2.4×10^{-3} m/s as an experimental dyke in the lower layer and 4.5×10^{-3} m/s when propagating as an experimental sill (see Fig. 8). The Reynold's number is calculated as ∼18 during experimental dyke propagation and ∼34 during experimental sill propagation (see Eq. (4)). This corresponds to a predominantly laminar flow regime with local or intermittent turbulence and implies the velocity profile along the thickness of the intrusion is parabolic. Rubin's [39] propagation velocity (Eq. (6)) is applied to assess the controlling dynamics of crack propagation firstly of the experimental dyke propagating in the homogeneous lower layer and then of the experimental sill intruding the interface. Rearranging Eq. (6) for overpressure, P_0, and recalling that this equation assumes a balance where $P_0 \sim P_v$, the viscous dissipation is calculated:

$$P_v = \sqrt[3]{\frac{3U\eta M^2}{l}}. \tag{13}$$

During Experiment 11 the parameter values for the experimental dyke propagating in the homogeneous lower layer were $U=2.4\times10^{-3}$ m/s, $\eta=1\times10^{-3}$ Pa s, $M=10{,}830$ Pa (evaluated using Eq. (7) and E_L) and $l=0.08$ m (see Tables 2 and 3 and Fig. 8b). Substituting these into Eq. (13) gives $P_v \sim 30$ Pa. The overpressure, P_0, of this experiment was 1472 ± 300 Pa and thus the viscous contribution to experimental dyke propagation is minor. Fracture mechanics is therefore the dominant control on experimental dyke propagation dynamics. In contrast, when evaluating the propagation of the experimental sill of Experiment 11, which had parameter values of $U=4.5\times10^{-3}$ m/s, $\eta=1\times10^{-3}$ Pa s, $M=10{,}830$ Pa and $l=0.27$ m (see Tables 2 and 3 and Fig. 8b), Eq. (13) gives $P_v \sim 1800$ Pa and is comparable to the overpressure of the experiment. Therefore the dominant control on the propagation dynamics of a crack intruding an interface as an experimental sill is viscous dissipation.

7. Discussion

7.1. Sill formation

The experiments have shown that under initially hydrostatic and isotropic stress conditions experimental sills are unlikely to form in a homogeneous material. The continued propagation of an experimental dyke will result in either its arrest within the host material or, given sufficient driving pressure, extrusion. Upon extrusion the experimental dyke thickness approximately halves due to a drop in confining pressure [33], as has been documented at Kilauea, Hawaii [43]. Additionally, the experiments imply that the surface expression of dyke breadth during an eruption largely under-represents the breadth of the dyke within the host rock. Our experiments have shown that to form sills in a homogeneous solid a deviatoric stress is likely required, and therefore under these conditions Roberts' [10] hypothesis could be valid, but was not tested in these experiments.

We found that the presence of an interface is a necessary but not sufficient condition to induce experimental sill emplacement. Experimental dyke formation occurred when intruding an intermediate density fluid into a layered system with upper less dense and less rigid layer. However, "pinching" of both the experimental dyke's breadth and thickness occurred at the interface, with these dimensions increasing upon entering the upper less rigid material (see Fig. 4). This change in geometry reflects the upper less rigid layer's greater susceptibility to deformation by the intrusion. To form experimental sills under initial hydrostatic conditions a layered system is required, with an upper more rigid layer that inhibits vertical crack propagation. Many sills have been observed in field studies to lie directly below a more rigid layer [25,33,35,44]. Experimental sill intrusion occurs along the weak interface in a plane underlying the more rigid layer. It was observed that when experimental sills formed they were always preceded by a stage of vertical crack arrest with propagation continuing just along the breadth of the crack (Stage 2). We infer that fluid pressure at the interface increases during this stage and experimental sill initiation then occurs when the fluid pressure overcomes the tensile strength of the interface (Stage 3).

The sills that we obtained in our experiments present several features that have been recognised in various field studies. The propagation of our experimental sills occurred in lobes; the Trachyte Mesa Intrusion of the Henry Mountains, southern Utah, U.S.A. is thought to have formed via the propagation of a series of lobes [44]. Deformation structures were observed in the experiments to form in the less rigid host material, reflecting its relative ease of deformation. Such features were observed in field studies of sills formed within sedimentary sequences. For example, sediments in direct contact with the periphery of the Shonkin Sag laccolith, Montana, U.S.A., show a variety of deformation structures such as cataclastic shear planes in sandstone beds and kink-bands in shale layers [45]. Our experimentally formed *en echelon* fractures may have formed due to stress reorientation [22] (see Fig. 6a, c and d), whereas those that formed during experimental laccolith formation are likely tension fractures formed when the bonded interface was separated as the overlying layer was bent upwards (see Fig. 6d). These deformation features occur in the lower, less rigid layer and therefore highlight the role of the upper, more rigid layer as a barrier to upward intrusion that promotes sill formation.

Our results are consistent with the modelling of Pollard and Johnson [1] which predicted the sill to laccolith transition when the sill has spread horizontally approximately three times the overburden thickness. The overburden thickness of our experimentally formed sills was 12–12.5 cm, and the upward deflection of this layer occurred once the aerial extent of the sill reached approximately 30 cm.

During the experiments some sills occurred with simultaneous experimental dyke intrusion into the upper layer. When this occurred the experimental dyke quickly arrested leading to just propagation of the experimental sill. This outcome is despite all experimental intrusions having sufficient driving pressure to theoretically propagate to the surface. The cessation of experimental dyke propagation occurs when its driving pressure falls below the fracture pressure of the intruded material. The experimental sill intrusion would quickly have a greater length than that of the dyke protrusion, and would therefore have a lower fracture pressure (see Eq. (2)) [20]. Perhaps it is the competition between the energy efficiency of different intrusions that leads to the arrest of the upper layer experimental dyke protrusions, with the preferential propagation of the experimental sill, which has a lower energy consumption. Such dyke protrusions have also been described in field studies. Johnson and Pollard [44] describe a series of dykes protruding from the upper surface of the Trachyte Mesa that could be aborted attempts to propagate dykes from the upper surface of the sill into the overlying sandstone unit. Our experimental results imply that under initially hydrostatic conditions these protrusions would have formed when the rigidity contrast between the overlying sandstone unit and underlying unit was a little greater than one and when the driving pressure was marginally in excess of that required to intrude the more rigid upper layer (see Fig. 7).

7.2. Sill propagation dynamics

During each experiment the overpressure was kept constant. Despite this, experimentally formed sills had contrasted propagation dynamics to those of their feeder dykes. Our data show that experimental dyke propagation occurs at approximately constant or slightly decreasing velocity and fracture mechanics is the dominant control on the propagation dynamics. This supports previous work investigating dyke propagation in a homogeneous solid [16].

In contrast to experimental dykes, experimental sill propagation accelerated with increasing length of the intrusion (see Fig. 8b). Resistance to fracture propagation is much reduced at the interface compared to that of a homogeneous material and as a result the fracture pressure is not the resistive pressure that opposes and controls experimental sill propagation. Instead a viscous drop along the length of the experimental sill exerts the main control on its propagation.

7.3. Geological implications

The experiments suggest that rigidity contrasts might provide important sites of preferential sill emplacement and development of igneous complexes. We consider two contrasted situations. First we consider magmatism during continental break-up and flood basalt volcanism where initially the Mohorovičić discontinuity (Moho) is a site of large rigidity contrast between the cold seismogenic crust above relatively weak mantle. Second we consider magmatism in continental arcs where prolonged heating and possible hydration have weakened the lower crust so that the boundary between the upper and lower crust (Conrad discontinuity) may provide a preferential focus for emplacement of granite and sheets.

Dykes propagating through the upper mantle beneath Shields should be arrested at the Moho, with sill formation below the strong rigid lower crust. Traditional models of the rheological structure of the continental lithosphere describe a relatively weak lower crust “sandwiched” between a strong and rigid upper mantle and upper crust [3,46,47]. However, reanalysis of seismic data has found the seismic thickness of the lithosphere (T_S) varies from 10 to 40 km and the continental mantle is almost completely aseismic [48]. Water can be preferentially removed from the lower crust as the solidus temperature of hydrous basic rock is lower than that of a hydrous peridotite; this produces a strong dry metastable granulite lower crust [49]. This metastability keeps the lower crust both rigid and strong enabling it to support mountain belts. The intrusion and ponding of hot magma at the Moho at regions of thickened crust would reduce the viscosity of the lower crust and provide a mechanism of lower crustal flow [6,50]. Geodynamic situations where sill formation at the Moho is anticipated are in rifting of large continents associated with disruption by mantle plumes and development of flood basalt volcanism. The Iceland plume has been inferred to have formed due to the impingement of hot, subvertical, convective sheets at the base of the lithosphere, which later developed a plume head structure [30]. In the case of the Deccan Traps, India, very large volumes of fractionated basalt are discharged and require very large magma bodies for fractionation to occur. Formation of very large sills at the Moho provides the situation to allow extensive fractionation before eruption.

In the case of continental arcs prolonged magmatism and tectonism provides a hot lower crust below a cold upper crust, so that the boundary between the two is both one of density and rigidity contrast and so a potential preferred site of sill emplacement. Silicic magmas generated by partial melting in the deep crust or residual melts from basalt crystallisation rise to form sills and sheet-like silicic intrusions in the middle crust [4,50]. For example, the Lauterbrunnen migmatites of the central Swiss Alps are believed to have acted as a reaction site in which crystallisation and partial melting of the country rock modified the magma composition feeding the overlying Gastern granite [51]. Magmas in the Taupo Volcanic Zone, New Zealand, form large volume sheet-like intrusions in the middle crust at an estimated 15 km depth [51]. Sills may develop into sheet-like magma bodies or plutons due to the successive accretion and amalgamation of sills [4,52,53] or by having undergone crystallisation and differentiation within a convecting magma body [5]. These magma bodies may founder due to density differences, with an estimated sinking rate of several kilometres per million years [54], and evolve into a pluton [55].

8. Conclusions

Rigidity contrasts provide preferred sites to intrude magma sills and for the development and evolution of major igneous complexes. Sills intrude in a plane underlying the more rigid material. The form of the intrusion depends on the rigidity ratio of adjacent layers, the strength of the interface and the magnitude of the driving pressure. Geological settings where magma could potentially stall and form sills due to rigidity contrasts include beneath ancient cratonic bodies at the Moho beneath the more rigid lower crust, and at continental arcs where the upper crust can be more rigid than the lower crust due to prolonged heating and possible hydration. The viscosity of the intruding magma is likely to play a dominant role controlling the sill propagation dynamics. The evolution of this stored magma as it crystallises and differentiates can proceed to feed higher-level intrusions of increasingly silicic composition. The continued input of magma to these intrusions leads to their transition into laccolithic and plutonic complexes.

Acknowledgements

This research was funded by a Royal Society Wolfson Merit Award to RSJS, DeBeers/Diamond Trading Company and a NERC studentship. We acknowledge R.C. Kerr and M. Saint-Blanchat whose comments helped to improve an earlier version of this manuscript.

References

[1] D.D. Pollard, A.M. Johnson, Mechanics of growth of some laccolithic intrusions in the Henry Mountains, Utah: II. Bending and failure of overburden layers and sill formation, Tectonophysics 18 (1973) 311–354.
[2] D.H.W. Hutton, Granite sheeted complexes: evidence for the dyking ascent mechanism, Trans. R. Soc. Edinb. Earth Sci. 83 (1992) 377–382.
[3] T. Parsons, N.H. Sleep, G.A. Thompson, Host rock rheology controls on the emplacement of tabular intrusions: implications for underplating of extending crust, Tectonics 11 (1992) 1348–1356.
[4] B.E. John, Structural reconstruction and zonation of a tilted mid-crustal magma chamber: the felsic Chemehuevi Mountains plutonic suite, Geology 16 (1988) 613–617.
[5] M.G. Worster, H.E. Huppert, R.S.J. Sparks, Convection and crystallization in magma cooled from above, Earth Planet. Sci. Lett. 101 (1990) 78–89.
[6] D. McKenzie, E.D. Jackson, Conditions for flow in the continental crust, Tectonics 21 (2002) 1055–1061.
[7] A. Malthe-Sorenssen, S. Planke, H. Svensen, B. Jamtveit, Formation of saucer-shaped sills, in: C. Breitkreuz, N. Petford

(Eds.), Physical Geology of High-Level Magmatic Systems, Geological Society, London, Special Publications, vol. 234. The Geological Society of London, London, 2004, pp. 215–227.

[8] R.H. Mitchell, Kimberlites: Mineralogy, Geochemistry and Petrology, Plenum Press, New York, 1986, 442 pp.

[9] A.D. Kerr, D.D. Pollard, Toward more realistic formulations for the analysis of laccoliths, J. Struct. Geol. 20 (1998) 1783–1793.

[10] J.L. Roberts, The intrusion of magma into brittle rocks, in: G. Newall, N. Rast (Eds.), Mechanism of Igneous Intrusion, Journal of Geology Special Issue, vol. 2. Liverpool Letterpress Limited, Liverpool, 1970, p. 380.

[11] J. Bradley, Intrusion of major dolerite sills, Trans. R. Soc. N.Z. 3 (1965) 27–55.

[12] L. Chevalier, A. Woodford, Morph-tectonics and mechanism of emplacement of the dolerite rings and sills of the western Karoo, South Africa, S. Afr. J. Geol. 102 (1999) 43–54.

[13] D.A. Spence, D.L. Turcotte, Magma-driven propagation of cracks, J. Geophys. Res. 90 (1985) 575–580.

[14] P. McLeod, S. Tait, The growth of dykes from magma chambers, J. Volcanol. Geotherm. Res. 92 (1999).

[15] A. Takada, Experimental study on propagation of liquid-filled crack in gelatin: shape and velocity in hydrostatic stress condition, J. Geophys. Res. 95 (1990) 8471–8481.

[16] T. Menand, S. Tait, The propagation of a buoyant liquid-filled fissure from a source under constant pressure: an experimental approach, J. Geophys. Res. 107 (2002) 2306.

[17] T. Wanatanbe, T. Masuyama, K. Nagaoka, T. Tahara, Analog experiments on magma-filled cracks: competition between external stresses and internal pressure, Earth Planets Space 54 (2002) 1247–1261.

[18] J.R. Muller, G. Ito, S.J. Martel, Effects of volcano loading on dike propagation in an elastic half-space, J. Geophys. Res. 106 (2001) 11101–11113.

[19] T. Menand, S. Tait, A phenomenological model for precursor volcanic eruptions, Nature 411 (2001) 678–680.

[20] J.R. Lister, R.C. Kerr, Fluid-mechanical models of crack propagation and their application to magma transport in dykes, J. Geophys. Res. 96 (1991) 10049–10077.

[21] W.J. McGuire, A.D. Pullen, Location and orientation of eruptive fissures and feeder dykes at Mount Etna; influence of gravitational and regional tectonic stress regimes, J. Volcanol. Geotherm. Res. 38 (1989) 325–344.

[22] D.D. Pollard, Derivation and evaluation of mechanical model for sheet intrusions, Tectonophysics 19 (1973) 233–269.

[23] E. Rivalta, M. Bottinger, T. Dahm, Buoyancy-driven fracture ascent: experiments in layered gelatine, J. Volcanol. Geotherm. Res. 144 (2005) 273–285.

[24] E.H. Francis, Magma and sediment: 1. Emplacement mechanism of late Carboniferous tholeiite sills in northern Britain, Geol. Soc. Lond. 139 (1982) 1–20.

[25] M.B. Holness, M.C.S. Humphreys, The Traigh Bhan na Sgurra Sill, Isle of Mull: flow localization in a major magma conduit, J. Petrol. 44 (2003) 1961–1976.

[26] D.N. Shirley, Differentiation and compaction in the Palisades sill, New Jersey, J. Petrol. 28 (1987).

[27] J.C. Jaeger, G. Joplin, Rock magnetism and the differentiation of a dolerite sill, J. Geol. Soc. Aust. 2 (1955) 1–9.

[28] E. Auger, P. Gasparini, J. Virieux, A. Zollo, Seismic evidence of an extended magmatic sill under Mt. Vesuvius, Science 294 (2001) 1510–1512.

[29] M.G. Best, E.H. Christiansen, Igneous Petrology, Blackwell Science, Inc., 2001, 458 pp.

[30] S. Al-Kindi, N. White, M. Sinha, R. England, R. Tiley, Crustal trace of a hot convective sheet, Geol. Soc. Amer. 31 (2003) 207–210.

[31] K. Thomson, D. Hutton, Geometry and growth of sill complexes: insights using 3D seismic from the North Rockall Trough, Bull. Volcanol. 66 (2004) 364–375.

[32] E.H. Francis, B.H. Walker, Emplacement of alkali-dolerite sills relative to extrusive volcanism and sedimentary basins in the Carboniferous of Fife, Scotland, Trans. R. Soc. Edinb. Earth Sci. 77 (1986) 309–323.

[33] D.W. Hyndman, D. Alt, Radial dikes, laccoliths, and gelatin models, J. Geol. 95 (1987) 763–774.

[34] M.R. Mudge, Depth control of some concordant intrusions, Geol. Soc. Amer. Bull. 79 (1968) 315–332.

[35] J.L. White, D.K. Bailey, W.P. Barnett, M. Field, R.S.J. Sparks. Emplacement and petrogenesis of precursor kimberlite sills and dykes, associated with the Wesselton Kimberlite Pipe, Kimberley, South Africa, Journal of the Geological Society, in review.

[36] V. Pinel, C. Jaupart, The effect of edifice load on magma ascent beneath a volcano, Philos. Trans. R. Soc. Lond. 358 (2000) 1515–1532.

[37] V. Pinel, C. Jaupart, Magma storage and horizontal dyke injection beneath a volcanic edifice, Earth Planet. Sci. Lett. 221 (2004) 245–262.

[38] B.M. Gunn, Differentiation in ferrar dolerites, Antarctica, Am. Mineral. 47 (1962) 191.

[39] A.M. Rubin, Propagation of magma-filled cracks, Annu. Rev. Earth Planet. Sci. 23 (1995) 287–336.

[40] P.T. Delaney, D.D. Pollard, Solidification of basaltic magma during flow in a dyke, Am. J. Sci. 282 (1982) 856–885.

[41] R.S. Fiske, E.D. Jackson, Orientation and growth of Hawaiian volcanic rifts: the effect of regional structure and gravitational stresses, Proc. R. Soc. Lond., A Math. Phys. Sci. 329 (1972) 299–326.

[42] S.P. Timoshenko, J.N. Goodier, Theory of Elasticity, McGraw-Hill, New York, 1970, 567 pp.

[43] T.L. Wright, R.S. Fiske, Origin of differentiated and hybrid lavas of Kilauea Volcano, Hawaii, J. Petrol. 12 (1971) 1–66.

[44] A.M. Johnson, D.D. Pollard, Mechanics of growth of some laccolithic intrusions in the Henry Mountains, Utah: 1. Field Observations, Gilbert's Model, Physical Properties and Flow of the Magma, Tectonophysics 18 (1973) 261–309.

[45] D.D. Pollard, O.H. Muller, D.R. Dockstader, The form and growth of fingered sheet intrusions, Geol. Soc. Amer. Bull. 86 (1975) 351–363.

[46] W. Chen, P. Molnar, Focal depths of intracontinental and intraplate earthquakes and their implications for the thermal and mechanical properties of the lithosphere, J. Geophys. Res. 88 (1983) 4183–4214.

[47] P.B. Gans, An open-system, two-layer crustal stretching model for the Eastern Great Basin, Tectonics 6 (1987) 1–12.

[48] A. Maggi, J.A. Jackson, K. Priestley, C. Baker, A re-assessment of focal depth distributions in southern Iran, the Tien Shan and northern India: do earthquakes really occur in the continental mantle? Geophys. J. Int. 143 (2000) 629–661.

[49] J.A. Jackson, H. Austrheim, D. McKenzie, K. Priestley, Metastability, mechanical strength, and the support of mountain belts, Geol. Soc. Amer. 32 (2004) 625–628.

[50] D. McKenzie, F. Nimmo, J.A. Jackson, P.B. Gans, E.L. Miller, Characteristics and consequences of flow in the lower crust, J. Geophys. Res. 105 (2000) 11029–11046.

[51] S.N. Olsen, B.D. Marsh, L.P. Baumgartner, Modelling mid-crustal migmatite terrains as feeder zones for granite plutons: the competing dynamics of melt transfer by bulk versus porous flow, Trans. R. Soc. Edinb. Earth Sci. 95 (2004) 49–58.

[52] F.G.F. Gibb, C.M.B. Henderson, Discontinuities between picritic and crinanitic units in the Shiant Isles sill: evidence of multiple intrusion, Geol. Mag. 126 (1989) 127–137.

[53] D.S. Coleman, W. Gray, A.F. Glazner, Rethinking the emplacement and evolution of zoned plutons: geochronologic evidence for incremental assembly of the Tuolumne intrusive suite, California, Geol. Soc. Amer. 32 (2004) 433–436.

[54] A.F. Glazner, Foundering of mafic plutons and density stratification of continental crust, Geology 22 (1994) 435–438.

[55] A.F. Glazner, D.M. Miller, Late-stage sinking of plutons, Geology 25 (1997) 1099–1102.

Available online at www.sciencedirect.com
ScienceDirect
Earth and Planetary Science Letters 267 (2008) 93 – 99
EPSL
www.elsevier.com/locate/epsl

The mechanics and dynamics of sills in layered elastic rocks and their implications for the growth of laccoliths and other igneous complexes

Thierry Menand

Department of Earth Sciences, Centre for Environmental and Geophysical Flows, University of Bristol,
Wills Memorial Building, Queen's Road, Bristol BS8 1RJ, UK

Received 1 November 2006; received in revised form 4 June 2007; accepted 17 November 2007
Available online 8 December 2007
Editor: C.P. Jaupart

Abstract

The recent experimental work by Kavanagh et al. [Kavanagh, J.L., Menand, T. and Sparks, R.S.J. (2006). An experimental investigation of sill formation and propagation in layered elastic media. Earth Planet. Sci. Lett. 245, 799–813.] shows that lithological discontinuities and rigidity contrasts can control the formation and dynamics of sills at interfaces separating upper, rigid strata from lower, weaker strata. The present paper extends this work and focuses on its implications in terms of the length- and time-scales associated with the development of laccoliths and other igneous complexes. Sill formation controlled by rigidity contrasts is shown to provide a growth mechanism for laccoliths. The formation of a sill provides favourable rigidity anisotropy for the emplacement of subsequent sills so that laccoliths grow by over-accretion, under-accretion or even mid-accretion of successive sills. In accord with field data, this model predicts that laccoliths grow mainly by vertical expansion, representing the cumulative thickness of their internal sills, while maintaining a comparatively constant lateral extend. The model also predicts that the time-scale over which laccoliths form is essentially determined by the cumulative time between successive sill intrusions. Also, sill dynamics are controlled by viscous dissipation of the fluid along their length, which have consequences for the size and shape of sills. Viscously-controlled dynamics would enable sills to propagate further and thus to grow thicker than dykes of similar magmas. These dynamics would also enable sills to propagate faster and thus to induce non-elastic deformations in surrounding rocks that could deviate them from the interface they originally follow. This would allow them to feed new sills along other interfaces and could assist in the formation of the step structures and saucer-shapes that are commonly observed in sill complexes.

Keywords: sills; laccoliths; plutons; emplacement; igneous complexes

1. Introduction

Igneous intrusions represent a major mechanism for the construction and evolution of the Earth's crust. Much of the research on magmatic intrusions has focused on the mechanics and dynamics of dykes, which are the main agent for the vertical transport of magma through the crust (e.g. Lister and Kerr, 1991; Rubin, 1995; Menand and Tait, 2002). In comparison, most of the research on sills (sensu lato) has focused mainly on the mechanical and dynamical aspects of the propagation of sills that have already formed, and on the deformation induced by sill intrusions (Pollard, 1973; Pollard and Holzhausen, 1979; Fialko et al., 2001; Malthe-Sørenssen et al., 2004) but the questions of how and why sills form in the first place and where they are observed have not been studied to the same extent. Yet, geological evidence, conceptual reasoning and numerical models suggest that sills, laccoliths and plutons represent a more fundamental mode of emplacement, and that they are an important mechanism by which chemical differentiation of magma occurs within the crust (Blundy and Gardner, 1997; Annen and Sparks, 2002; Annen et al., 2006).

The crust is layered in density, composition, physical properties and strength (Fountain et al., 1992; Orcutt et al., 1976), with a vertical stratification from a mainly mafic lower crust to a

---

E-mail address: T.Menand@bristol.ac.uk.

0012-821X/$ - see front matter © 2007 Elsevier B.V. All rights reserved.
doi:10.1016/j.epsl.2007.11.043

more granitic upper crust (Rudnicki and Fountain, 1995). This cannot have developed by vertical intrusions. Instead, horizontal seismic layering of the lower crust is consistent with the development of sill complexes (Fountain et al., 1992; Chmielowski et al., 1981; Al-Kindi et al., 2003; Nedimović et al., 2005). There is also a growing body of evidence that magma chambers and plutons develop and grow by amalgamation of numerous but distinct episodes of sill intrusion (Coleman et al., 2004; Glazner et al., 2004). Also, sills increase the petroleum prospectivity of sedimentary basins (Schutter, 2003a,b), are associated with ore deposits (Ramirez et al., 2006) and geothermal systems (Wohletz and Heiken, 1986), and are part of diamond-bearing Kimberlite complexes (Mitchell, 1986; Sparks et al., 2006). Yet, despite their importance and the wealth of available field data, the mechanics and dynamics of sill formation are still poorly understood.

Extensive geological and geophysical data constrain the size of sills and their rate of emplacement. Field measurements of the geometry and dimensions of sills, laccoliths and plutons show that a generic, continuous link exists between the thickness and length of these intrusions. But, as shown by Cruden and McCaffrey (2002) and McCaffrey and Cruden (2002) (see also Breitkreuz and Petford, 2004), this scaling relationship does not follow a single power law. Sills grow mainly by lateral propagation whereas laccoliths seem to grow by vertical thickening before extending laterally again as plutons and batholiths (Fig. 1). This suggests the existence of different growth processes that are related to the length-scale of the intrusions.

Many field and geochronological data indicate that laccoliths, plutons and magma chambers develop and grow by amalgamation of numerous sill intrusions. For instance, ages from U–Pb data from the Tuolumne Intrusive Suite in California show that it was emplaced within 10 Myrs. However this is in contradiction with simple thermal considerations. For instance, a pluton the size of the Half Dome Granodiorite, which is part of the Tuolumne Intrusive Suite, should cool down and solidify in less than 1 Myr if one assumes it represents a single discrete igneous event. Geochronological data, however, reveal that the Half Dome Granodiorite was emplaced in at least 4 Myrs. This result implies that its formation involved multiple igneous events, which is in accord with field observations of the pluton being composed of numerous dykes and sills (Coleman et al., 2004; Glazner et al., 2004). Field studies of smaller plutons suggest even shorter emplacement time-scales, perhaps less than 100 years in the case of the Black Mesa bysmalith in the Henry Mountains in Utah (Habert and de Saint-Blanquat, 2004; de Saint-Blanquat et al., 2006). Therefore, as well as their length-scale, the time-scale for the growth of laccoliths and plutons seems to be dependent on the size of the intrusion considered.

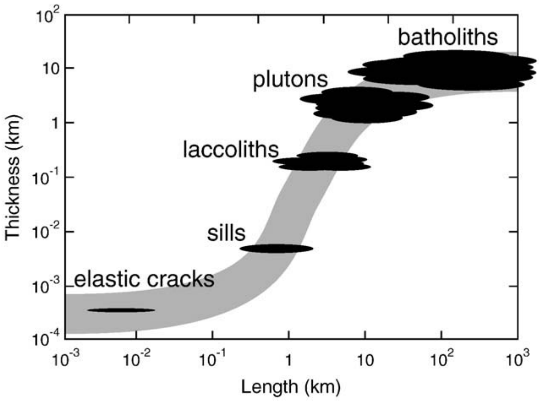

Fig. 1. Schematic diagram showing the scaling relationship between sills, laccoliths, plutons and batholiths based on Cruden and McCaffrey (2002) and McCaffrey and Cruden (2002). Each type of intrusion appears to be linked to the others following an S-shaped growth law over several orders of magnitude.

The main hypotheses for sill formation invoke either a buoyancy (Corry, 1988) or a tectonic stress orientation (Roberts, 1970) control. However, the concept of sill emplacement at the level of neutral buoyancy seems in contradiction with field observations and 3D seismic data of individual sills intruding successively different stratigraphic levels and yet feeding one another (Thomson and Hutton, 2004; Cartwright and Hansen, 2006; Thomson, 2007); if one of these stratigraphic levels represents a level of neutral buoyancy then the intrusion of other stratigraphic levels by the same sills must be controlled by other mechanisms. Alternatively, magmatic intrusions tend to orient themselves parallel to the minimum compressive stress (Anderson, 1951). Therefore a transition from dyke to sill would be expected when the minimum compressive stress changes from horizontal to vertical. This could occur either because of the presence of stress anisotropy or due to stress rotation induced by magmatic intrusions, as shown by Roman et al. (2004, 2006). In the latter case, dyke injection could potentially induce the subsequent formation of a sill by switching stresses such that σ_3 becomes σ_1 due to magma pressure and σ_2 (vertical) becomes σ_3.

Field investigations have led to the view that sills form mostly in more compliant strata such as shales, mudstones or hyaloclastites (e.g. Mudge, 1968; Fridleifsson, 1977; Antonellini and Cambray, 1992). The opposite situation has also been observed, however, with dykes being arrested and sills forming at the interface between a lower more compliant and an upper more rigid strata such as sandstones, limestones or lavas (Fridleifsson, 1977; Hyndman and Alt, 1987; Gudmundsson and Brenner, 2001; Holness and Humphreys, 2003). The soft shales and hyaloclastites that cap some sills may have been ductile at the time of sill emplacement (Mudge, 1968), in which case the rheology contrast with a lower brittle strata would have helped stop the feeder dykes (Parsons et al., 1992). It has also been suggested that stress redistribution in layered elastic media would strengthen some strata relative to others; when a multilayer is subjected to horizontal compression, stiffer layers take up most of the compressive stress, whereas when the same multilayer is subjected to a horizontal extension, softer layers will experience a lower reduction in compressive stress and thus appear, comparatively, to be more horizontally compressive (Gudmundsson, 1986; Gudmundsson and Brenner, 2001). Recently, Kavanagh et al. (2006) showed that in the absence of tectonic stresses sills can form only at the interface between lower more compliant and upper more rigid elastic strata. Thus these studies suggest that, assuming elastic rock behaviour, favourable interfaces for sill formation are those with an upper strata which appears more rigid, either because of stress redistribution or because of their mechanical properties.

The present paper extends this finding and focuses on its implications in terms of the length- and time-scales associated with the development of laccoliths and other igneous complexes. Here, laccoliths are defined in a generic sense as large igneous bodies that have formed by forced, and possibly repeated, intrusion of magma between adjacent strata that could deform and lift upper rock layers. (No distinction is made between laccoliths and lopoliths given the lack of a clear distinction between the two terms and the possibility that with time one could evolve into the other (Corry, 1988)).

2. Sill formation controlled by rock rigidity contrasts

Kavanagh et al. (2006) tested different hypotheses for sill emplacement using analogue experiments involving the injection of fluid into a solid of gelatine, and found that under hydrostatic conditions, the formation of sills requires the presence of layers of different rigidity. Sills were observed to form only when their feeder dyke intersected the interface between an upper more rigid, stronger layer and a lower less rigid, weaker layer. In these experiments, a feeder dyke would rise vertically from the injection point up to the interface where it would stop its vertical propagation. There it generated deformations which, once large enough, allowed the fluid to intrude the interface and thus to form a sill between the two layers (Fig. 2). Sometimes, the sill was accompanied by a small dyke protruding into the upper more rigid layer (Fig. 2). However this dykelet would always be short lived and stopped while the sill continued its propagation.

The conditions for the formation of sills and their resulting morphology are summarized in Fig. 3. Sills cannot form if the ratio of the rigidity of the upper layer to that of the lower layer is less than unity, that is if the upper layer is weaker than the lower layer. Sills only form if the rigidity ratio is greater than one. In most cases, the feeder dyke turns completely into a single sill. However, for certain conditions of pressure and rigidity ratios greater than but close to one, a dyke-sill hybrid would form (whose geometry is illustrated in Fig. 2) with a dykelet protruding over a short distance into the upper rigid layer during the sill propagation. Interestingly, these conditions could be the most commonly present in the crust because rock rigidities differ marginally from one another, usually by less than an order of magnitude (Birch, 1966; Turcotte and Schubert, 1982). Likewise, the fluid pressure driving a dyke is mainly determined by the amount of stress rocks can sustain before breaking and in which case it will be marginally larger than the strength of rocks. These experiments thus suggest that hybrids composed of interconnected dykes and sills could be more common than simpler sills connected to their underlying feeder.

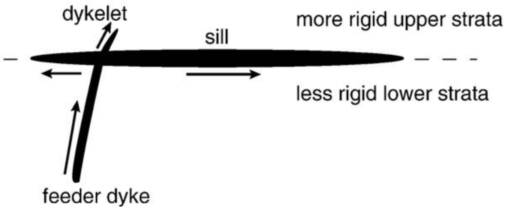

Fig. 2. Diagram illustrating the experimental observations of Kavanagh et al. (2006) for the formation of sills in layered elastic solids under lithostatic stress conditions. Sills were observed to form only when their feeder dyke intersected an interface separating a lower, less rigid layer from an upper, more rigid one. In some cases, a dykelet would protrude into the upper rigid layer, yet would always quickly strop propagating while the sill pursues its propagation. Arrows show the directions of propagation.

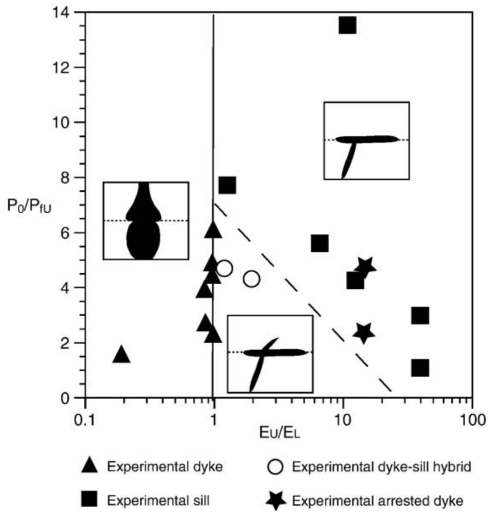

Fig. 3. The conditions for sill formation and the resulting morphologies as a function of the ratio of driving and resistive pressure scales $P_0/P_{f\mathrm{U}}$ and the ratio of upper and lower rigidities $E_\mathrm{U}/E_\mathrm{L}$. The solid line represents the boundary between the formation of dykes and that of sills. The dashed line represents the approximate boundary between the formation of simple sills and that of dyke-sill hybrids. Reprinted from Kavanagh et al. (2006) with permission from Elsevier.

3. Formation of laccoliths by sill accumulation

Fig. 3 shows how rigidity contrasts control sill formation, and this has implications for the length-scale and the time-scale associated with the growth of laccoliths (sensu lato).

As a sill forms and solidifies, it generates a rigidity contrast with the rocks both above and below it. One possibility is that the solidified sill becomes more rigid than the rocks below it. Alternatively, it can become less rigid than these rocks but in this case it will also become less rigid than the rocks above it. Either way, the solidified sill will provide a favourable site for the emplacement of subsequent sills, either underneath or above itself. This will be the case irrespective of the exact mechanism for the emplacement of the sill. The key point here is that once a sill has solidified it will provide a favourable rigidity anisotropy for the emplacement of other sills. Therefore, this gives a mechanism for the formation and growth of laccoliths by the vertical stacking of successive sills (Fig. 4).

This concept is in accord with field observations of sheeted granite plutons (Hutton, 1992) and of laccoliths, such as the

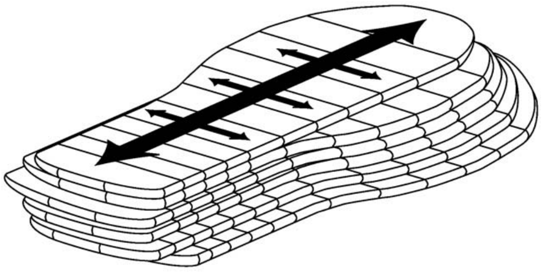

Fig. 4. Schematic illustration of the growth of the Trachyte Mesa laccolith by vertical stacking of individual and separate sills (Morgan et al., 2005). The model of rigidity-controlled sill emplacement predicts that once solidified a sill will induce a strength anisotropy that will enable subsequent sills to emplace either underneath it (under-accretion) or above it (over-accretion). Subsequently, mid-accretion can also occur whereby a new sill intrudes in between previously emplaced sills. In the case of the Trachyte Mesa laccolith, growth occurred mainly by under-accretion with some observations of mid-accretion (Morgan et al., 2005). Arrows show the directions of magma flow as a sill formed.

Maiden Creek sill and the Trachyte Mesa laccolith, both in the Henry Mountains in Utah. These intrusions in the Henry Mountains have been studied in detail and appear to be composed of two separate igneous sheets in the case of the small Maiden Creek sill, and of dozens of separate sills in the case of the Trachyte Mesa laccolith (Horsman et al., 2005, 2006; Morgan et al., 2005). There is no definitive evidence whether the Maiden Creek intrusion formed through successive emplacement of new sheets atop old sheets or vice versa, referred to as over-accretion and under-accretion, respectively. Emplacement of the Trachyte Mesa intrusion, in contrast, clearly involves at least some under-accretion, although there is also evidence that some sheets intruded in between older ones (Morgan et al., 2005), which could be defined as a case of mid-accretion.

According to this growth mechanism, the length of a laccolith would be essentially comparable to the length of the sills that composes it whereas its thickness would represent the cumulative thickness of all these sills, in accord with field observations (Horsman et al., 2005, 2006; Morgan et al., 2005). This growth mechanism is therefore able to explain the trend displayed by field measurements of the dimensions of igneous intrusions, where laccoliths appear to grow mainly by vertical expansion and thus depart from the trend of sills, which instead grow mainly by lateral propagation (Cruden and McCaffrey, 2002; McCaffrey and Cruden, 2002).

Another implication is that the time-scale for the growth of laccoliths is mainly determined by the time that separates successive sill intrusions since, comparatively, the time for the emplacement of a single injection can be seen as instantaneous. Therefore, this model predicts that larger laccoliths and plutons would develop over much longer periods of time than smaller plutons, as suggested by field and geochronological data.

Previous theoretical and experimental works have established that a transition from sill to laccolith occurs when the characteristic size of a sill becomes comparable to its depth, at which point the sill is able to lift the overlying strata upwards (Pollard and Johnson, 1973; Pollard and Holzhausen, 1979; Fialko et al., 2001; Kavanagh et al., 2006). The growth mechanism presented here is complementary and indicates that sill-laccolith transitions may not necessarily involve single episodes or pulses of magma injection but could instead involve multiple pulses. This could explain the observed lack of correlation between the depth of intrusion and the size of multilevel laccoliths, such as Christmas-tree laccoliths (Corry, 1988). Also, deeper sill-laccolith transitions would require larger magma volumes which would be more easily achieved by multiple injection episodes, although over longer periods of time.

4. Dynamical implications for the geometry of igneous intrusions and complexes

Kavanagh et al. (2006) found that the dynamics of their experimental sills differ markedly from those of the feeder dykes. They measured the evolution with time of the intrusions which allowed them to calculate their propagation velocity. Their results show that the velocity of the feeder dykes remained approximately constant, until the dykes reached the interface where they stopped before turning into sills. Sills on the contrary propagated in accelerating continuously with a velocity proportional to their length. This accelerating behaviour indicates that the dynamics of the sills were controlled by the viscous dissipation of the fluid along their length, presumably because of a low cohesion between the gelatine layers at the horizontal interface. This contrasts with the dynamics of the feeder dykes, which were controlled instead by the time-dependent failure of the gelatine solid at their tip and which, as a result, propagated at approximately constant velocity (Menand and Tait, 2002).

It has been argued, however, that gelatine experiments are not in the same regime as magma-filled dykes propagating through rocks based on scaling analyses and laboratory measurements of rock strength, and that in fact dyke dynamics are controlled instead by a balance between the fluid pressure and the viscous dissipation induced by the magma flow within dykes (Lister and Kerr, 1991). But it has also been suggested that the effective fracture toughness of rocks could be two to three orders of magnitude greater than that inferred from laboratory measurements on rock cores due to extensive inelastic deformation around and ahead of the crack tip as revealed by field observations (Delaney et al., 1986; Fialko and Rubin, 1997). This would support the argument that dyke dynamics are controlled by the time-dependent failure of rocks at their tip (Menand and Tait, 2002). It is probable that the true dynamics of dykes will be somewhere between these two alternative models, considering that dykes propagate both by fracturing their own way through rocks and by intruding pre-existing fractures and joins (Delaney et al., 1986). However, the two models have different implications for the relative size of sills and dykes.

Both models predict that the dynamics of sills are viscously-controlled. As a sill propagates and extends its length it becomes also thicker owing to the elastic deformation of the surrounding rocks. But because the sill becomes thicker, the viscous dissipation decreases. Unless the source pressure decreases at the same rate, the only way for the sill to restore the balance with the source pressure is to accelerate. If the velocity of dykes is also controlled by viscous dissipation, then dykes would propagate faster than sills owing to their higher buoyancy and hence higher driving pressure gradient. A higher buoyancy would also imply that, everything else being equal, dykes have a greater magma pressure and thus would tend to be thicker than sills. If dyke dynamics are instead controlled by time-dependent failure of rocks, they would then propagate at approximately constant velocity even if the source pressure remains constant (Menand and Tait, 2002), and thus for identical source pressure conditions sills would propagate faster and be thicker than dykes. In this case, sills could thus propagate further and their propagation could be sustained over a much longer period of time than dykes.

The latter finding seems to be supported by several field observations. For instance, sills are commonly observed to be much thicker than dykes of similar magmas. An explanation could be that magma pressures are larger within sills than in dykes or that shallower sills deform more easily the nearby free surface. However, magma pressure is essentially determined by the strength of surrounding rocks and magma buoyancy. Given that rock strength should be the same whether rocks are intruded by dykes or sills, one would thus expect greater magma pressures in dykes owing to their higher buoyancy hence dykes to be thicker than sills. On the other hand, assuming that deformations around intrusions are elastic, a larger or longer intrusion will be thicker than a smaller intrusion for identical pressure conditions. Therefore faster propagating viscously-controlled sills would be expected to grow larger than fracturing-controlled dykes and thus to be thicker as well.

Also, some sills display evidences of prolonged flow such as the Traigh Bhàn na Sgùrra sill that is part of the Loch Scridain Sill Complex on the Isle of Mull, Scotland. The Traigh Bhàn na Sgùrra sill ranges in thickness from 2.5 m to more than 10 m, and other sills from the Loch Scridain Complex are as 14 m thick (Holness and Humphreys, 2003). One particular feature of the Traigh Bhàn na Sgùrra is that surrounding rocks display substantial thermal aureoles around the thickest parts of that sill. By measuring the size distribution of crystals within the sill, Holness and Humphreys (2003) were able to relate the thickest parts of the sill with a localization of magma flow. They then determined flow duration from the width of the metamorphic aureole and found that where flow had been localized it had been sustained for up to 5 months. As shown by Holness and Humphreys (2003) this analysis is fully consistent with independent theoretical models of viscously-controlled magma flow, in which magma cools the fastest in the thinnest parts of intrusions thus leading to flow localization where intrusions are the widest. Although flow localization could conceivably happen in non-viscously-controlled flows, flow localization would occur more strongly in viscously-controlled flows because of the positive feedback that exists between the increase in magma viscosity in the thinnest parts of an intrusion, as a result of a fastest cooling, and the localized flow in the widest parts of the intrusion which channels more heat. Therefore the findings of long flow duration in the Traigh Bhàn na Sgùrra could provide indications of viscously-controlled dynamics for that sill.

A second implication is that viscously-dominated dynamics could also affect the shape of sills and the subsequent development of igneous complexes. Kavanagh et al. (2006) observed that sill propagation can induce deformation structures such as en echelon fractures for instance. These fractures can occur either because the sill intrusion induces a rotation of the local stress field at its tip, or because the sill induces deformations that are too large for the ambient solid to sustain without breaking. A viscously-dominated sill that accelerates will get thicker and thus deforms the surrounding rocks at an accelerating rate, and so ultimately fracture of the surrounding strata is bound to happen. This could happen in the softer rock layer underneath the sill or in the rock layer above the sill where the overburden is lower and which has potentially a nearby free surface. In this case, the sill would pursue its course through stiffer rocks and two different outcomes could then arise. The stiffer rocks of the upper strata could arrest the propagation of the sill, or alternatively the sill might be able to reach another favourable interface and then feed another horizontal sill at this new interface before being arrested (Fig. 5). In both cases, the main point is that the sill will deviate from the interface it initially intruded and adopt an out-of-plane, transgressive propagation.

Previous studies have shown that an upward, transgressive propagation is expected as a consequence of lateral expansion and interaction of a sill with the free surface (Fialko, 2001; Malthe-Sørenssen et al., 2004). This interaction with the free surface could explain the saucer-shaped geometry that is commonly exhibited by many sills and their feeders, particularly within sedimentary basins (Malthe-Sørenssen et al., 2004; Thomson and Hutton, 2004; Thomson, 2007). Interaction with the free surface is expected to occur when the characteristic horizontal size of sills exceeds their emplacement depth (Fialko, 2001; Malthe-Sørenssen et al., 2004), so this would imply that

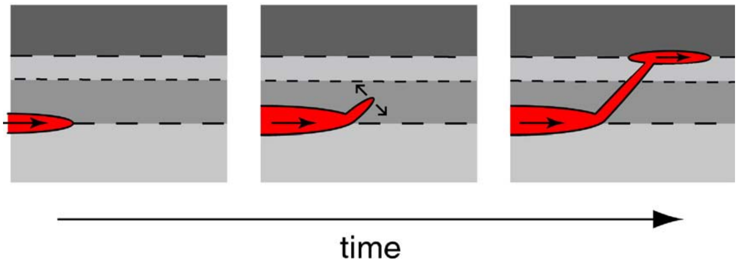

Fig. 5. A viscously-controlled sill is likely to fracture surrounding strata and thus to branch off from the interface it initially follows. It could then be able to reach another favourable interface and feed another sill at this new interface.

the horizontal part of deeper saucer-shaped sills is larger than that of shallower sills.

Here I propose that viscously-controlled dynamics could facilitate the out-of-plane propagation of sills. This mechanism would presumably be independent of the emplacement depth. However, it would certainly depend on the deformation rate, with higher deformation rates increasing the sill tendency for transgressive propagation. Following Rubin (1995), the length of a viscously-controlled intrusion increases exponentially with time as

$$l(t) \simeq l_0 \ \exp\left(\frac{P^3 t}{3\eta m^2}\right), \tag{1}$$

where l_0 is the intrusion length at time $t=0$, P is the magma pressure in excess of the stress acting normal to the intrusion, η is magma viscosity and the rock elastic stiffness m depends on rock elastic shear modulus μ and Poisson's ratio v as $m=\mu/(1-v)$. As the intrusion increases in length, its deformation ϵ increases as $(l-l_0)/l_0$ so that the deformation rate is $\dot{\epsilon} \simeq u/l_0$. The intrusion velocity u is readily obtained by deriving Eq. (1) with respect to time, which gives a deformation rate

$$\dot{\epsilon} \simeq \frac{P^3}{3\eta m^2 l_0}. \tag{2}$$

Eq. (2) suggests higher deformation rates in softer, less rigid layers (lower stiffness m). It is therefore unlikely that saucer-shaped sills, with upward transgressive propagation, could form solely by viscously-controlled dynamics. However, Eq. (2) also suggests that if two sills were to propagate under identical conditions, the only difference being the magma viscosity, one would expect the sill with the lowest magma viscosity to induce higher deformation rate and thus to have a greater tendency to propagate out-of-plane and help produce a saucer-shaped geometry. In this sense, viscously-dominated sill dynamics could affect the shape of sills with low viscosity magmas in promoting or facilitating their saucer-shaped geometry. This could be tested by looking at the distribution of saucer-shaped sills as a function of magma viscosity.

5. Conclusions

Recently Kavanagh et al. (2006) have shown that under hydrostatic conditions, sill formation requires the presence of layers of different rigidity, and that sills can only form at the interface between upper, rigid layers overlaying lower, weaker layers.

It is shown here that this control of sill formation by rigidity contrasts provides a mechanism for the growth of laccoliths whereby a sill provides favourable rigidity anisotropy for the emplacement of successive sills. Thus laccoliths can grow by vertical stacking of successive sills, either by over-accretion, under-accretion or even mid-accretion. In accord with field data, this mechanism for the growth of laccoliths predicts that laccoliths grow mainly by vertical expansion, representing the cumulative thickness of their internal sills, while maintaining a comparatively constant lateral extend. The model also predicts that the time-scale over which laccoliths form is essentially determined by the cumulative time between successive sill intrusions.

From a dynamical perspective, sill dynamics are controlled by viscous dissipation of the fluid along their length. This could have consequences for the size and shape of sills. Viscously-dominated dynamics would enable sills to propagate faster and further than dykes whose dynamics are controlled by the fracture of rocks at their tip. In turn, this would enable sills to become thicker than dykes of similar magmas.

Furthermore, faster sills induce non-elastic deformations in surrounding rocks that could deviate them from the interface they originally follow and would potentially allow them to feed new sills along other interfaces. This mechanism could assist in the formation of the intricate geometry displayed by sills and their feeders in igneous complexes, such as step structures and saucer-like shapes, particularly when involving low viscosity magmas.

Acknowledgements

I thank Eric Horsman for the many discussions we have had about the geology and the emplacement of the Henry Mountains intrusions, and for kindly providing Fig. 4 of the present paper. I thank an anonymous reviewer, whose review and comments have substantially improved the manuscript. Elsevier is acknowledged for providing permission to reprint Fig. 3 from Earth and Planetary Science Letters, Vol 245, Kavanagh, Menand and Sparks, An experimental investigation of sill formation and propagation in layered elastic media, pages 799–813, Copyright (2006). This research was supported by a Leverhulme Trust research grant.

References

Al-Kindi, S., White, N., Sinha, M., England, R., Tiley, R., 2003. Crustal trace of a hot convective sheet. Geology 31, 207–210.

Anderson, E.M., 1951. The Dynamics of Faulting and Dyke Formation with Applications to Britain, Second Edition. Oliver and Boyd Ltd., Edinburgh.

Annen, C., Blundy, J.D., Sparks, R.S.J., 2006. The genesis of intermediate and silicic magmas in deep crustal hot zones. J. Petr 47, 505–539.

Annen, C., Sparks, R.S.J., 2002. Effects of repetitive emplacement of basaltic intrusions on thermal evolution and melt generation in the crust. Earth Planet. Sci. Lett 203, 937–955.

Antonellini, M.A., Cambray, F.W., 1992. Relations between sill intrusions and bedding-parallel extensional shear zones in the mid-continent rift system of the Lake Superior region. Tectonophysics 202, 331–349.

Birch, F., 1966. Compressibility; elastic constants. In: Clark Jr., S.P. (Ed.), Handbook of Physical Constants, Volume 97 of Mem. Geol. Soc. Am., pp. 97–173.

Blundy, J., Gardner, J., 1997. Origin of Mount St. Helens dacites by partial melting of underplated cascades basalts. J. Conf. Abstr 2 (1), 16.

Breitkreuz, C., Petford, N., 2004. Physical geology of high-level magmatic systems: introduction. In: Breitkreuz, C., Petford, N. (Eds.), Physical Geology of High-level Magmatic Systems, Volume 234 of Geol. Soc. London Spec. Publ., pp. 1–4.

Cartwright, J., Hansen, D.M., 2006. Magma transport through the crust via interconnected sill complexes. Geology 34, 929–932.

Chmielowski, J., Zandt, G., Haberland, C., 1981. The central Andean Altiplano-Puna magma body. Geophys. Res. Lett 26, 783–786.

Coleman, D.S., Gray, W., Glazner, A.F., 2004. Rethinking the emplacement and evolution of zoned plutons: geochronologic evidence for incremental assembly of the Tuolumne Intrusive Suite, California. Geology 32, 433–436.

Corry, C.E., 1988. Laccoliths: mechanics of emplacement and growth. Geol. Soc. Am. Spec. Pap. 220.

Cruden, A.R., McCaffrey, K.J.W., 2002. Different scaling laws for sills, laccoliths and plutons: mechanical thresholds on roof lifting and floor depression. In: Breitkreuz, C., Mock, A., Petford, N. (Eds.), First International Workshop: Physical Geology of Subvolcanic Systems—Laccoliths, Sills, and Dykes (LASI), Volume 20 of Wissenschaftliche Mitteilungen des Institutes für Geologie der TU Bergakademie Freiberg, pp. 15–17.

de Saint-Blanquat, M., Habert, G., Horsman, E., Morgan, S.S., Tikoff, B., Launeau, P., Gleizes, G., 2006. Mechanisms and duration of non-tectonically assisted magma emplacement in the upper crust: the Black Mesa pluton, Henry Mountains, Utah. Tectonophysics 428, 1–31.

Delaney, P.T., Pollard, D.D., Ziony, J.L., McKee, E.H., 1986. Field relations between dikes and joints: emplacement processes and paleostress analysis. J. Geophys. Res 91, 4920–4938.

Fialko, Y.A., 2001. On origin of near-axis volcanism and faulting at fast spreading mid-ocean ridges. Earth Planet. Sci. Lett 190, 31–39.

Fialko, Y.A., Khazan, Y., Simons, M., 2001. Deformation due to a pressurized horizontal circular crack in an elastic half-space, with application to volcano geodesy. Geophys. Int. J 146, 181–190.

Fialko, Y.A., Rubin, A.M., 1997. Numerical simulation of high-pressure rock tensile fracture experiments: evidence of an increase in fracture energy with pressure? J. Geophys. Res 102, 5231–5242.

Fountain, D.M., Arculus, R.J., Kay, R.W., 1992. Continental Lower Crust, Volume 23 of Development in Geotectonics. Elsevier.

Fridleifsson, I.B., 1977. Distribution of large basaltic intrusions in the Icelandic crust and the nature of the layer 2–layer 3 boundary. Geol. Soc. Am. Bull 88, 1689–1693.

Glazner, A.F., Bartley, J.M., Coleman, D.S., Gray, W., Taylor, R.Z., 2004. Are plutons assembled over millions of years by amalgamation from small magma chambers? GSA Today 14, 4–11.

Gudmundsson, A., 1986. Formation of crustal magma chambers in Iceland. Geology 14, 164–166.

Gudmundsson, A., Brenner, S.L., 2001. How hydrofractures become arrested. Terra Nova 13, 456–462.

Habert, G., de Saint-Blanquat, M., 2004. Rate of construction of the Black Mesa bysmalith, Henry Mountains, Utah. In: Breitkreuz, C., Petford, N. (Eds.), Physical Geology of High-level Magmatic Systems, Volume 234 of Geol. Soc. London Spec. Publ., pp. 163–173.

Holness, M.B., Humphreys, M.C.S., 2003. The Traigh Bhàn na Sgùrra sill, Isle of Mull: flow localization in a major magma conduit. J. Petrol 44, 1961–1976.

Horsman, E., de Saint-Blanquat, M., Habert, G., Morgan, S., Tikoff, B., 2006. Examining relationships between geometric evolution and fabric development during incremental emplacement of sheeted igneous intrusions, Henry Mountains, southern Utah, U.S.A. Visual Geosciences.

Horsman, E., Tikoff, B., Morgan, S., 2005. Emplacement-related fabric and multiple sheets in the Maiden Creek sill, Henry Mountains, Utah, USA. J. Struc. Geol 27, 1426–1444.

Hutton, D.H.W., 1992. Granite sheeted complexes: evidence for the dyking ascent mechanism. Trans. R. Soc. Edinburgh: Earth Sci 83, 377–382.

Hyndman, D.W., Alt, D., 1987. Radial dikes, laccoliths and gelatin models. J. Geol 95, 763–774.

Kavanagh, J.L., Menand, T., Sparks, R.S.J., 2006. An experimental investigation of sill formation and propagation in layered elastic media. Earth Planet. Sci. Lett 245, 799–813.

Lister, J.R., Kerr, R.C., 1991. Fluid-mechanical models of crack propagation and their application to magma transport in dykes. J. Geophys. Res 96, 10049–10077.

Malthe-Sørenssen, A., Planke, S., Svensen, H., Jamveit, B., 2004. Formation of saucer-shaped sills. In: Breitkreuz, C., Petford, N. (Eds.), Physical Geology of High-level Magmatic Systems, Volume 234 of Geol. Soc. London Spec. Publ., pp. 215–277.

McCaffrey, K.J.W., Cruden, A.R., 2002. Dimensional data and growth models for intrusions. In: Breitkreuz, C., Mock, A., Petford, N. (Eds.), First International Workshop: Physical Geology of Subvolcanic Systems—Laccoliths, Sills, and Dykes (LASI), Volume 20 of Wissenschaftliche Mitteilungen des Institutes für Geologie der TU Bergakademie Freiberg, pp. 37–39.

Menand, T., Tait, S.R., 2002. The propagation of a buoyant liquid-filled fissure from a source under constant pressure: an experimental approach. J. Geophys. Res. 107 (B11). doi:10.1029/2001JB000589 (2306).

Mitchell, R.H., 1986. Kimberlites: Mineralogy, Geochemistry and Petrology. Plenum Press, New York.

Morgan, S.S., Horsman, E., Tokoff, B., de Saint-Blanquat, M., Habert, G., 2005. Sheet-like emplacement of satellite laccoliths, sills and bysmaliths of the Henry Mountains, Southern Utah. In: Pederson, J., Dehler, C.M. (Eds.), Interior Western United Sates, Volume 6 of Geological Society of America Field Guide. doi:10.1130/2005.fld006(14).

Mudge, M.R., 1968. Depth control of some concordant intrusions. Geol. Soc. Am. Bull 79, 315–332.

Nedimović, M.R., Carbotte, S.M., Harding, A.J., Detrick, R.S., Canales, J.P., Diebold, J.B., Kent, G.M., Tischer, M., Babcock, J.M., 2005. Frozen magma lenses below the oceanic crust. Nature 436, 1149–1152.

Orcutt, J.A., Kennett, B.L., Dorman, L.M., 1976. Structure of the East Pacific Rise from an ocean bottom seismometer survey. Geophys. J. Roy. Astron. Soc 45, 305–320.

Parsons, T., Sleep, N.H., Thompson, G.A., 1992. Host rock rheology controls on the emplacement of tabular intrusions: implications for under-plating of extending crust. Tectonics 11, 1348–1356.

Pollard, D.D., 1973. Derivation and evaluation of a mechanical model for sheet intrusion. Tectonophysics 19, 233–269.

Pollard, D.D., Holzhausen, G., 1979. On the mechanical interaction between a fluid-filled fracture and the Earth's surface. Tectonophysics 53, 27–57.

Pollard, D.D., Johnson, A.M., 1973. Mechanics of growth of some laccolithic intrusions in the Henry Mountains, Utah, II. Bending and failure of overburden layers and sills formation. Tectonophysics 18, 311–354.

Ramirez, L.E., Palacios, C., Townley, B., Parada, M.A., Sial, A.N., Fernandez-Turiel, J.L., Gimeno, D., Garcia-Valles, M., Lehmann, B., 2006. The Mantos Blancos copper deposit: an upper Jurassic breccia-style hydrothermal system in the coastal range of Northern Chile. Miner. Depos 41, 246–258.

Roberts, J.L., 1970. The intrusion of magma into brittle rocks. In: Newhall, G., Rast, N. (Eds.), Mechanism of Igneous Intrusion, Volume 2 of Journal of Geology Special Issue, pp. 287–338.

Roman, D.C., Moran, S.C., Power, J.A., Cashman, K.V., 2004. Temporal and spatial variation of local stress fields before and after the 1992 eruptions of Crater Peak Vent, Mount Spurr volcano, Alaska. Bull. Seismol. Soc. Am 94, 2366–2379.

Roman, D.C., Neuberg, J., Luckett, R.R., 2006. Assessing the likelihood of volcanic eruption through analysis of volcanotectonic earthquake faultplane solutions. Earth Planet. Sci. Lett 248, 244–252.

Rubin, A.M., 1995. Propagation of magma-filled cracks. Ann. Rev. Earth Planet. Sci 23, 287–336.

Rudnicki, R.L., Fountain, D.M., 1995. Nature and composition of the continental crust: a lower continental perspective. Rev. Geophys 33, 267–309.

Schutter, S.R., 2003a. Hydrocarbon occurrence and exploration in and around igneous rocks. In: Petford, N., McCaffrey, K.J.W. (Eds.), Hydrocarbons in Crystalline Rocks, Volume 214 of Geol. Soc. London Spec. Publ., pp. 7–33.

Schutter, S.R., 2003b. Occurrences of hydrocarbons in and around igneous rocks. In: Petford, N., McCaffrey, K.J.W. (Eds.), Hydrocarbons in Crystalline Rocks, Volume 214 of Geol. Soc. London Spec. Publ., pp. 35–68.

Sparks, R.S.J., Baker, L., Brown, R.J., Field, M., Schumacher, J., Stripp, G., Walters, A., 2006. Dynamical constraints on kimberlite volcanism. J. Volcanol. Geotherm. Res 155, 18–48.

Thomson, K., 2007. Determining magma flow in sills, dykes and laccoliths and their implications for sill emplacement mechanisms. Bull. Volcanol 70, 183–201.

Thomson, K., Hutton, D., 2004. Geometry and growth of sill complexes: insights using 3d seismic from the North Rockall Trough. Bull. Volcanol 66, 364–375.

Turcotte, D.L., Schubert, G., 1982. Geodynamics. Applications of continuum physics to geological problems. John Wiley & Sons, New York.

Wohletz, K., Heiken, G., 1986. Volcanology and Geothermal Energy. University of California Press.

JOURNAL OF GEOPHYSICAL RESEARCH, VOL. 115, B08201, doi:10.1029/2009JB006791, 2010

Dyke propagation and sill formation in a compressive tectonic environment

T. Menand,[1] K. A. Daniels,[1] and P. Benghiat[1,2]

Received 16 July 2009; revised 19 March 2010; accepted 25 March 2010; published 6 August 2010.

[1] Sills could potentially form as a result of dykes modifying their trajectory in response to remote tectonic compression. Here, we use analogue experiments to investigate how a buoyant vertical dyke adjusts its trajectory to a compressive remote stress to form a sill, and over which vertical distance this sill formation does occur. Our investigation is restricted to an intrusion propagating through a homogeneous solid, which enables us to identify the characteristic length-scale over which a dyke responds to remote stress compression, independently of the presence of crustal layers. The experiments involve the injection of air in a gelatine solid that experiences lateral deviatoric compression. The response of the buoyant air crack to the compressive stress in not instantaneous but operates over some distance. An important observation is that some cracks reach the surface despite the compressive environment. Dyke-to-sill rotation occurs only for large compressive stress or small effective buoyancy. Dimensional analysis shows that the length-scale over which this rotation takes place increases exponentially with the ratio of crack effective buoyancy to horizontal compressive stress. Up-scaled to geological conditions, our analysis indicates that a dyke-to-sill transition in response to tectonic compression in homogeneous rocks cannot occur over less than two hundred meters and would need several kilometers in most cases. This is typically greater than the average thickness of lithological units, which supports the idea that crustal heterogeneities play an important role in determining the fate of dykes and in controlling where sills could form.

Citation: Menand, T., K. A. Daniels, and P. Benghiat (2010), Dyke propagation and sill formation in a compressive tectonic environment, *J. Geophys. Res.*, *115*, B08201, doi:10.1029/2009JB006791.

1. Introduction

[2] The transport of magma from its source regions up to the Earth's surface occurs essentially via vertical or sub-vertical dykes, which ultimately feed volcanoes. However, not all dykes lead to eruptions. In fact, the vast majority of dykes stall en route and remain trapped in the crust. Ratios of intrusive to extrusive magma volumes have been estimated to be of the order of 10: 1 [*Crisp*, 1984; *Shaw*, 1985] whilst *Gudmundsson et al.* [1999] have calculated that the actual proportion of dykes reaching the surface in Iceland and Tenerife, Canary Islands, is only a few %. In many cases, those dykes which did not make it to the surface are associated with the formation or feeding of sub-horizontal sills [e.g., *Gudmundsson et al.*, 1999; *Burchardt*, 2008]. Sills could therefore be envisaged as either arresting the advance of dykes or, conversely, forming as a result of dykes being prevented from propagating further.

[3] There is a renewed interest in the formation of sills because they are increasingly recognized as being the building blocks of larger magma chambers and their frozen equivalent that are laccoliths, plutons and other larger batholiths [*Gudmundsson*, 1990; *Menand*, 2008]. Indeed, there is mounting geological, geophysical and geochronological evidence that plutons grow by the amalgamation of individual intrusive igneous sheets [*Bedard et al.*, 1988; *John*, 1988; *Hutton*, 1992; *John and Blundy*, 1993; *Vigneresse and Bouchez*, 1997; *Wiebe and Collins*, 1998; *Coleman et al.*, 2004; *Glazner et al.*, 2004; *Horsman et al.*, 2005, 2008; *Morgan et al.*, 2005, 2008; *Belcher and Kisters*, 2006; *de Saint-Blanquat et al.*, 2006; *Pasquarè and Tibaldi*, 2007]. Consequently, sills are also being recognized as potential sites of magma differentiation [*Annen and Sparks*, 2002; *Annen et al.*, 2006; *Michaut and Jaupart*, 2006].

[4] Sills form when their feeder dyke stops propagating mainly vertically and instead intrude concordantly along a lithological plane of weakness. However, the vast majority of magmatic intrusions are discordant, and so the mere presence of lithological discontinuities or planes of weakness is not a sufficient condition for the formation of sills. This observation is also corroborated by analogue experiments [*Kavanagh et al.*, 2006].

---

[1] Centre for Environmental and Geophysical Flows, Department of Earth Sciences, University of Bristol, Bristol, UK.

[2] Now at Atlas Iron Limited, West Perth, Western Australia, Australia.

0148-0227/10/2009JB006791

[5] One of the early model for sill formation proposed that sills tend to form when dykes become neutrally buoyant and lose their vertical driving force. Sills were therefore thought to form preferentially at levels of neutral buoyancy [*Gilbert*, 1877; *Corry*, 1988], that is at stratigraphic horizons where magma density equals that of the host rocks. However, this is contradicted by field and seismic data, which show many sills intruding successively different stratigraphic levels, likely characterized by different density [*Johnson and Pollard*, 1973; *Cartwright and Hansen*, 2006; *Thomson*, 2007]. This suggests that levels of neutral buoyancy do not provide a complete explanation for the mechanism and level of sill emplacement. In fact, as illustrated by the laboratory experiments of *Lister and Kerr* [1991], magma accumulation at levels of neutral buoyancy is more likely to involve lateral dyke propagation rather than sill formation because the latter case requires an additional rotation of the intrusion or the presence of a lithological plane of weakness that could be intruded. If a plane of weakness is present, levels of neutral buoyancy could assist sill formation, but *Taisne and Jaupart* [2009] showed that sill intrusion would still require very specific conditions with low-density stratigraphic layers that are at least 700-meter thick, and 2-kilometer thick on average. Other mechanisms that have been proposed for the formation of sills include the presence of layered rocks with rigidity contrast [*Fridleifsson*, 1977; *Hyndman and Alt*, 1987; *Gudmundsson and Brenner*, 2001; *Holness and Humphreys*, 2003; *Rivalta et al.*, 2005; *Kavanagh et al.*, 2006; *Burchardt*, 2008], rheology contrast between adjacent layers of elastic and ductile rocks [*Mudge*, 1968; *Fridleifsson*, 1977; *Antonellini and Cambray*, 1992; *Watanabe et al.*, 1999], as well as the presence of weak layer contacts [e.g., *Gudmundsson*, 2003].

[6] Additionally, it has been observed that magmatic intrusions tend to orient themselves perpendicular to the least compressive stress. As a result they modify their propagation trajectories in response to spatial changes in, or rotation of, the surrounding stresses [*Odé*, 1957; *Muller and Pollard*, 1977; *Dahm*, 2000; *Mériaux and Lister*, 2002]. Therefore, an initially vertical dyke would be expected to turn into a horizontal sill if it were to become subjected to a horizontal compressive stress field where the least compressive stress is vertical [e.g., *Gretener*, 1969; *Gudmundsson and Phillip*, 2006]. However, theoretical studies have shown that the dynamics and direction of propagation of dykes depend on their buoyancy as well as the external deviatoric stress field including the stresses induced by the dykes themselves at their tip [e.g., *Lister and Kerr*, 1991; *Dahm*, 2000; *Mériaux and Lister*, 2002]. Also, the difference in density between rocks and magma is not the only source of buoyancy for dykes; vertical gradients of the normal external deviatoric stress contribute also to the effective buoyancy of the intrusions [*Takada*, 1989]. Therefore, whether propagating buoyant dykes could reach the Earth's surface or instead stall in the crust and lead to magma accumulation depends on the relative importance of their effective buoyancy and the ambient deviatoric stress [*Watanabe et al.*, 1999; *Dahm*, 2000; *Pinel and Jaupart*, 2000, 2004]. The numerical work of *Dahm* [2000] and analogue experiments of *Watanabe et al.* [2002], for instance, show that dykes can stop their propagation and form sills, despite being buoyant, if they experience relatively large stress gradients. Conversely, dykes could reach the surface even when experiencing a compressive stress field provided their effective buoyancy is large enough. As an example, *Kühn and Dahm* [2004, 2008] adapted and applied the model of *Dahm* [2000] to dyke propagation at mid-ocean ridges and showed how the relative strength of magma pressure and gradient of deviatoric stress could focus dykes as sheeted-dyke complex or instead lead to the formation of sill-like magma chambers.

[7] One key question that remains unanswered, however, is the length-scale over which a dyke-to-sill rotation occurs since this will determine whether a dyke can reach the surface or stalls as a sill instead. Both crustal heterogenities and adequate stress field can lead to sill formation, but they involve separate length-scales.

[8] Gradients in or rotation of a stress field could be induced by various mechanisms and could thus occur over different length-scales. These mechanisms can, however, be sorted into two broad categories. A modification in stress field could occur because of remote, i.e. non localized, change or rotation. Magma initially originates from the mantle and propagates toward the surface through dykes, so the minimum compressive stress is likely to be horizontal in the lower crust. Yet crustal compressive and horizontal stress fields with a vertical minimum compressive stress, which would thus favor sill formation, do also exist. Stress rotation can also operate at the length-scale of a volcanic edifice, either in response to magma intrusion within the edifice[*Roman et al.*, 2004, 2006] or as an effect of the load of the edifice itself [*Watanabe et al.*, 2002; *Pinel and Jaupart*, 2004].

[9] The second type of mechanism that could induce stress rotation is more localized, and involves the presence of heterogeneous rock layers. For instance, a rheology contrast between a ductile rock layer and an adjacent elastic and brittle strata underneath might stop feeder dykes and promote sill formation into the ductile layer because the ductile zone would, at least partially, relax the pre-existing deviatoric stress favorable to dyke injection in the elastic layer [*Parsons et al.*, 1992; *Watanabe et al.*, 1999]. Alternatively, stress redistribution could also occur in layered elastic rocks with different mechanical properties. Adequate contrasts in Young's modulus and toughness between adjacent layers would lead to heterogeneous stress distribution with some layers concentrating horizontally compressive stress more than others [*Gretener*, 1969; *Gudmundsson*, 1986; *Gudmundsson and Phillip*, 2006]. Previously emplaced intrusions would also modify the ambient stress field. Such intrusion-induced stress anistropy would affect the crust over distances proportional to the intrusion thickness [*Westergaard*, 1939], until it is relaxed by the crust.

[10] The key difference between these two broadly defined mechanisms for stress rotation is the presence, or absence, of crustal heterogeneous layered rocks; in one case stress anisotropy is induced by the presence of crustal heterogeneities (strata of different properties or previous intrusions), whereas in the other case stress rotation occurs remotely and whether heterogeneous rock strata are present or not. Here, we investigate (1) how a buoyant vertical dyke responds and adjusts its trajectory to a compressive remote stress to form a sill, and (2) over which vertical distance this sill

formation occurs. We restrict our investigation to the case of an intrusion propagating through a homogeneous elastic solid. This does not mean that crustal heterogeneities are considered unimportant for the growth and orientation of intrusions, or that our analysis only applies to homogeneous crustal regions. Rather, considering the case of a homogeneous crust enables us to identify the characteristic length-scale over which a dyke would respond to a remote stress rotation, independently of the potential presence of crustal layers and their properties. This will in turn enable us to quantify if and under which conditions crustal heterogeneities need to be taken into account when dealing with dyke propagation under anisotropic stress conditions. For the same reason, we limit ourselves to the case of a single intrusion, and do not investigate the effect previously formed sills could have on the propagation of subsequent intrusions. Although the state of stress in the Earth's crust can be complex, we also simplified our analysis to a uniform compressive deviatoric stress. Indeed, tectonic stresses have been shown to play an important role on the propagation of dykes only when their variations occur over the length scale of the dykes [*Lister and Kerr*, 1991; *Dahm*, 2000], and vertical stress gradients can be incorporated into the effective buoyancy force that drives the intrusion [*Takada*, 1989; *Lister and Kerr*, 1991]. Finally, we neglect any potential interaction between the intrusion and the free surface, which is a reasonable assumption provided the intrusion depth is greater than half the height of the intrusion [*Rivalta and Dahm*, 2006]. In section 2 we describe laboratory analogue experiments investigating the propagation of a buoyant crack in a compressive environment, and in section 3 we analyze our experimental data using dimensional analysis. In section 4 we apply our results to geological conditions, discuss their implications and the limitations of our work, before concluding in section 5.

2. Experimental Method

[11] The behavior of a buoyant dyke in a compressive stress field was investigated by injecting air into a solid of gelatine that was compressed laterally. The solid gelatine was used as an analogue for elastic crustal rocks, and air acted as an analogue for buoyant magma. (Since we are interested in the mechanics and not the dynamics of dyke propagation and sill formation, inviscid air could be used as a magma analogue.) These materials enable us to scale down and investigate at the laboratory scale the elastic and brittle response of magmatic intrusions and elastic rocks to buoyancy and tectonic forces at the geological scale [*Menand and Tait*, 2002].

[12] The experiments involved varying the amount of injected air, which determined the buoyancy of the crack at the start of its propagation, and the amplitude of the compressive stress applied to the gelatine solid. The experiments were initially carried out in a square-based 40 cm × 40 cm × 30 cm acrylic tank, with equally spaced injection points in its base that allowed several successive experiments to be carried out with a single gelatine solid. Additional experiments were later on carried out with higher buoyancy and lower compressive stress in a taller (30 cm × 30 cm × 50 cm) acrylic reservoir so that dyke-sill transition could be investigated over larger vertical distances.

2.1. Preparation of the Gelatine Solid

[13] High-clarity, 260 bloom, acid, pigskin-derived gelatine in granular form was supplied by Gelita UK Ltd. The gelatine was prepared by dissolving the powder in distilled water. Once complete dissolution of the powder was achieved, the solution was poured into the experimental tank, and left to cool and solidify overnight. To accelerate the solidification process, all experiments were prepared and then performed in a cold room kept at 7°C. A thin layer of oil poured on top of the gelatine solution inhibited water evaporation during the cooling process [*Menand and Tait*, 2002]. The rigidity of the gelatine was controlled by varying the mass concentration of gelatine (between 2 wt% and 4 wt% in our experiments), and characterized by measuring the gelatine Young's modulus E following the method of *Menand and Tait* [2002]. (Knowledge of the gelatine Young's modulus enables also to calculate its fracture toughness K_c via the relationship $K_c = \sqrt{2\gamma_s E}$, where the surface energy of the gelatine $\gamma_s \simeq 1$ J m^{-2} [*Menand and Tait*, 2002].)

2.2. Lateral Compressive Stress

[14] After solidification, the gelatine solid was in a hydrostatic state of stress (section A1) [see also *Takada*, 1990]. A lateral deviatoric compressive stress was applied to the gelatine solid by inserting plastic sheets between the solid gelatine and the lateral walls of the tank. These plastic sheets had the same dimensions as the tank walls and covered them entirely to ensure a uniform and homogeneous lateral compressive stress. To facilitate the insertion of these sheets without tearing the gelatine, copper plates were inserted in the tank, against opposite walls, before the gelatine was let to solidify. Once the gelatine was set, hot water was circulated through the copper plates to initiate a slight melting of the gelatine so that it no longer adhered to the copper plates. Plastic sheets could then be easily inserted between the gelatine solid and the copper plates. Several plastic sheets could be successively inserted, thus inducing higher compressive stress.

[15] The insertion of the plastic sheets in the plane yOz compressed the gelatine solid in the x direction by an amount equal to the total thickness of the plastic sheets u. This compression also induced a vertical uplift of the upper free surface of the gelatine solid because the tank walls prevented the gelatine to deform in the y direction. With a knowledge of the gelatine Young's modulus E and Poisson's ratio ν (0.5 for gelatine [*Crisp*, 1952; *Richards and Mark*, 1966]), the compressive stress field generated by the insertion of the plastic sheets can be calculated (see Appendix A)

$$\sigma_x = \frac{4Eu}{3L}, \quad \sigma_y = \frac{2Eu}{3L}, \quad \sigma_z = 0, \tag{1}$$

where L is the initial lateral extent of the gelatine solid. The compressive stress field is therefore uniform with the maximum compressive stress $\sigma_1 = \sigma_x$, the intermediate principal stress $\sigma_2 = \sigma_y$, and the least compressive stress $\sigma_3 = \sigma_z$,

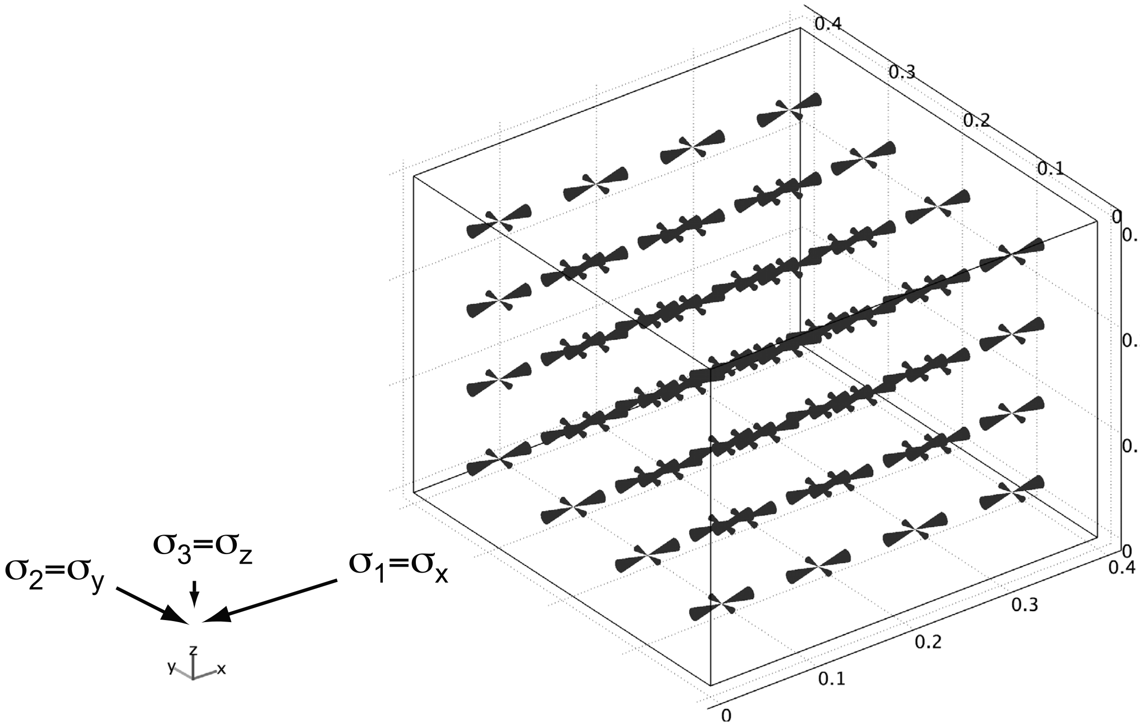

Figure 1. Numerical computation of the compressive stress field within the prism of gelatine solid using the finite element software COMSOL Multiphysics (see sections A2 and A3). The compressive stress field appears uniform with principal stresses $\sigma_1 = \sigma_x = 0.998\frac{4Eu}{3L}$, $\sigma_2 = \sigma_y = 0.498\frac{4Eu}{3L}$, and $\sigma_3 = \sigma_z = 310^{-11}$–$410^{-11}$. This compressive stress field is independent of the size of the gelatine solid.

which is thus always vertical (Figure 1). Experimental dykes were therefore expected to rotate about a horizontal axis and to ultimately form horizontal sills. The Young's modulus of the gelatine solid was measured just prior to carrying out an experiment following the method of *Menand and Tait* [2002].

2.3. Experiments and Data Measurements

[16] For each experiment, once the gelatine solid was set and its Young's modulus measured, a small amount of air was injected with a syringe at the base of the gelatine to initiate a crack parallel to the walls of the tank on which the compression is applied. Air was then withdrawn from that tiny crack, and plastic sheets were inserted to apply the desired compressive stress. The experiment was then carried out by injecting into the pre-existing crack a volume of air, the amount of which was chosen before the start of the experiment. The progression of the air-filled crack was then recorded on video. From the video record (see Movies S1–S3 in auxiliary material), the height of the crack when it started propagating was measured to calculate its buoyancy (referred to as initial height and initial buoyancy, respectively) as well as the vertical distance the crack propagated before turning into a sill in response to the lateral compressive stress. We note that since the applied compressive stress field is uniform, the effective buoyancy of the crack at the start of each experiment is simply its initial buoyancy.[1]

3. Experimental Results

3.1. Observations

[17] In all experiments, it was observed that as air was being injected, the crack propagated radially with a penny-shaped geometry in a vertical to sub-vertical plane, including downward movement towards the base of the tank. This condition lasted only a few seconds before the crack stretched out vertically upward. This transition occurred once all of the air had been injected and buoyancy had taken over as the driving force from the pressure induced by injection. From this point, the crack propagated smoothly vertically upward, and with no further influx of air the crack extended and detached from the needle point source, propagating upwards whilst closing fully at its lower tip.

[18] An important observation was that sill did not always formed despite the presence of a horizontal compressive stress field. When a small compressive stress was applied, or when a large amount of air was injected into the gelatine solid, the air crack propagated up to the upper free surface of the gelatine with its trajectory barely deviating from the vertical (Movie S1 in auxiliary material).

---

[1] Auxiliary materials are available in the HTML. doi:10.1029/2009JB006791.

Table 1. Experimental Data Associated With Sill Formation[a]

Experiment	h_0 (cm)	d (cm)	E (Pa)	σ_x (Pa)	Π_1	Π_2	Observations
4	4.4	9.4	1713	95.6	2.1 ± 0.3	4.6 ± 0.7	–
6	5.1	12.5	1713	95.6	2.5 ± 0.3	5.2 ± 0.7	–
7	4.1	7.0	4736	268.8	1.7 ± 0.2	1.5 ± 0.2	–
8	5.4	10.0	4736	268.8	1.8 ± 0.2	2.0 ± 0.3	–
12	4.6	15.4	3877	55.6	3.3 ± 0.4	8.2 ± 1.2	–
13	3.7	5.8	3877	389.0	1.6 ± 0.3	0.9 ± 0.2	–
17	2.8	5.3	3734	56.9	1.9 ± 0.4	4.8 ± 1.0	–
18	5.2	7.4	3734	56.9	1.4 ± 0.2	8.9 ± 1.5	–
23	5.5	43.1	3100	29.0	7.8 ± 1.5	18.7 ± 3.3	rotation, wall hit
24	4.1	22.6	3100	29.0	5.6 ± 2.0	13.7 ± 2.7	rotation
34	4.4	42.6	2645	24.6	9.6 ± 2.0	17.6 ± 3.3	rotation, wall hit
35	4.0	35.2	2306	21.6	8.9 ± 2.2	18.1 ± 3.6	rotation, wall hit
36	4.4	43.8	2306	21.6	10.0 ± 2.1	19.9 ± 3.8	rotation, wall hit
44	3.0	50	1564	14.6	16.9 ± 3.8	19.9 ± 4.5	Rotation, surface hit
45	2.7	26.6	1564	14.6	9.9 ± 3.3	18.2 ± 4.4	wall hit

[a] Π_1 is normalized traveled distance d/h_0, and Π_2 is stress ratio $(\Delta\rho g h_0)/\sigma_x$. Observations: rotation indicates rotation around a vertical axis; wall or surface hit occurred before the crack could form a horizontal sill. The uncertainty on the dimensionless ratios Π_1 and Π_2 takes each observation into account (see text).

[19] Only when a large compressive stress was applied or when the crack had a small volume, did the crack rotate toward the horizontal to form a sill (Movie S2 in auxiliary material). Experiments which lead to sill formation are summarized in Table 1. Sill formation always followed the same pattern. Initially, the crack started to propagate vertically driven by the air buoyancy (Figure 2a). The crack then experienced the horizontal compressive stress that was applied to the gelatine solid, and the crack changed its direction of propagation (Figure 2b). In those experiments where the compressive stress was relatively large, the crack ultimately formed a sill, having turned 90° and stopped its propagation (Figure 2c).

[20] In experiments involving intermediate compressive stress and air amount, the crack deviated and rotated its trajectory towards one of the walls, but the compressive stress was not large enough for a sill to form. Instead the crack was observed to propagate to either the free surface of the gelatine or the wall of the tank at an angle before it could really form a sill (Movie S3 in auxiliary material).

[21] These experimental observations are in accord with the results of previous numerical and analogue studies [e.g., *Dahm*, 2000; *Watanabe et al.*, 2002], and show that the response of buoyant crack propagating in a horizontal compressive environment is not instantaneous but instead occurs over some distance. If this distance is greater than the vertical extend of the solid the buoyant crack is intruding then the crack will reach the solid surface even though it is in a compressive environment.

3.2. Data Analysis

[22] The distance traveled by the crack before it fully formed a sill was found to be determined by a balance between its initial buoyancy, which drove the crack upwards, and the applied horizontal compressive stress that opposed this buoyancy and promoted the formation of the sill: relatively higher buoyancies were observed to favor further propagation distances whereas relatively stronger lateral compressive stress promoted faster crack rotation into sills. In order to quantify this better, experiments were repeated with different amounts of air injected in the gelatine and different compressive stresses applied. In each experiment, the initial height h_0 of the crack and the vertical distance d traveled by the crack before its arrest as a sill were measured. Based on our observations, we defined and measured h_0 as the height the crack had when it detached from the needle, which also corresponded to its maximum vertical extension. Experimental data are summarized in Table 1.

[23] Dimensional analysis was used to relate the vertical distance traveled by the crack before it formed a sill to the other parameters. The initial buoyancy of the crack drives it vertically and opposes the effect of the applied horizontal compressive stress. The problem only depends on four parameters characterized by two independent dimensions: the initial height of the crack h_0, the vertical distance d traveled by the crack, the initial buoyancy of the crack $\Delta\rho g h_0$ (g is the gravitational acceleration, and $\Delta\rho$ is the density difference between the gelatine and the air), and the applied compressive deviatoric stress σ_x. Dimensional analysis yields the two dimensionless groups

$$\Pi_1 = \frac{d}{h_0}, \quad \Pi_2 = \frac{\Delta\rho g h_0}{\sigma_x}, \tag{2}$$

such that $\Pi_1 = f(\Pi_2)$ where f is an unknown function that needs to be determined [*Barenblatt*, 1996].

[24] When plotting, for all experiments that produced a sill, the final distance traveled by the crack normalized by its initial height Π_1 as a function of the stress ratio Π_2, all the experimental data indeed follow a single curve (Figure 3). Careful analysis of the data suggests a linear relationship between $Ln(\Pi_1)$ and Π_2 (Figure 4). Using the method of least squares [*Bevington and Robinson*, 2003], we find the linear fit

$$Ln(\Pi_1) = (0.36 \pm 0.07) + (0.10 \pm 0.01)\Pi_2, \tag{3}$$

with a correlation coefficient $R^2 = 0.8964$. This equation can be re-expressed as the following exponential relationship between the vertical travel distance d and the other parameters:

$$d = (1.4 \pm 0.1) h_0 \exp\left[(0.10 \pm 0.01)\frac{\Delta\rho g h_0}{\sigma_x}\right]. \tag{4}$$

As expected, when the stress ratio tends to zero (corresponding to negligible initial buoyancy or extremely high remote compressive stress) the crack rotates and turns into a sill over a distance comparable to its initial height. Conversely, when the stress ratio tends to infinity (thus corresponding to negligible remote compressive stress or extremely high initial buoyancy) the crack needs to propagate over an infinite distance in order to rotate and form a sill; in effect, sill formation is prevented by the buoyancy of the crack.

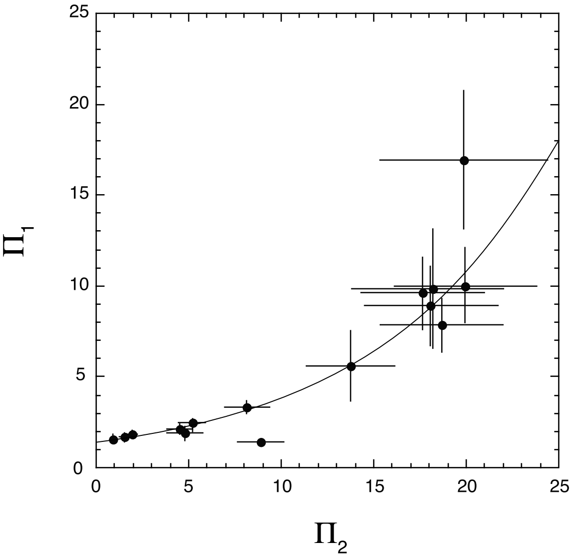

Figure 3. Experimental results. The final distance d traveled by the crack normalized by its initial height h_0 is plotted as a function of the stress ratio $(\Delta\rho g h_0)/\sigma_x$. As predicted by dimensional analysis, all data follow a single curve (the solid curve is equation (4)). Each point corresponds to one experiment.

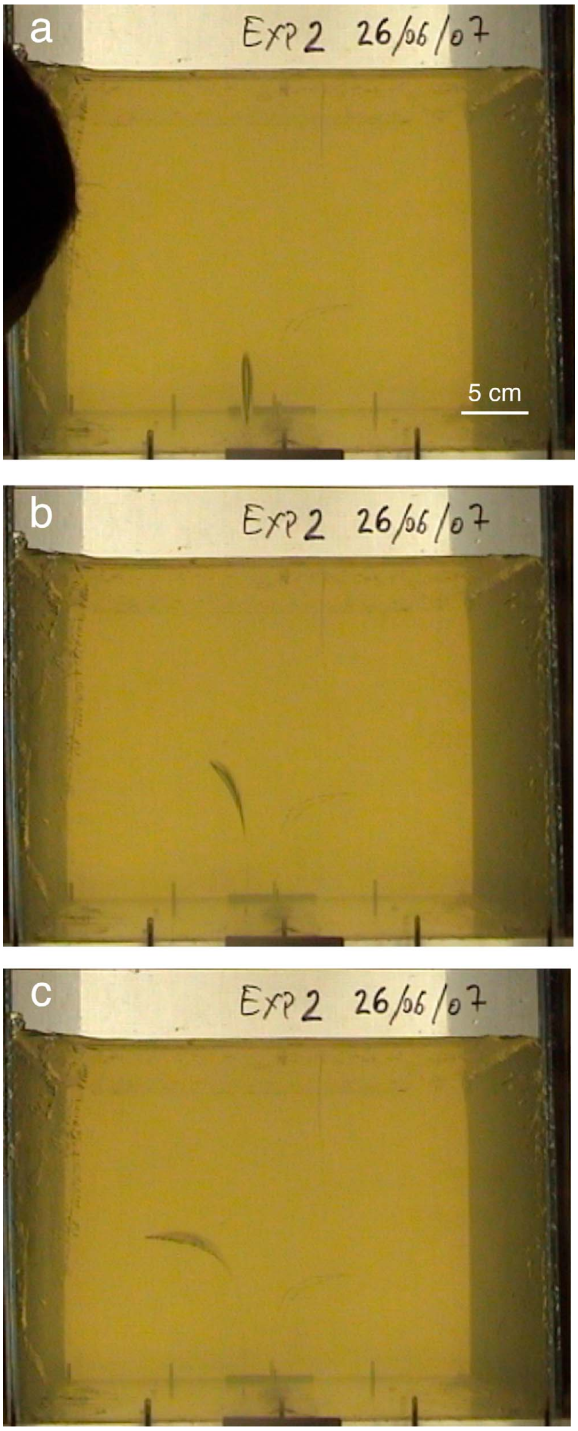

Figure 2. Three successive photographs of an experiment that lead to the formation of a sill. (a) When all the air has been injected into the gelatine solid, the crack stretched vertically and started to detach itself from the needle point source, propagating at a speed of typically a few mm/s. (b) As the crack propagated vertically, driven by the air buoyancy, it felt the applied compressive deviatoric stress and as a consequence started to adjust its trajectory by rotating to the left. (c) Ultimately, the crack rotated to the horizontal and came to a halt as an experimental sill.

3.3. Evaluation of the Quality of the Data

[25] Some experimental limitations mean that some of our data have rather large uncertainties. This only affected those experiments carried out in the taller tank (normalized distance $\Pi_1 > 5$ and stress ratio $\Pi_2 > 20$). We evaluate the possible causes and discuss the implications this would have on the relationship that has just been determined (equation (4)).

[26] As noted previously, in some experiments, the crack propagated towards a tank wall or the free surface of the gelatine before it could form a sill. However, when the crack hit the wall or the surface at a small angle, typically less than ~ 30° relative to the horizontal, the vertical distance traveled by the crack before it hit the wall or the surface was measured and included to the data set in Table 1. These data, therefore, correspond to under-estimations of the vertical distance the crack would have traveled had the tank been

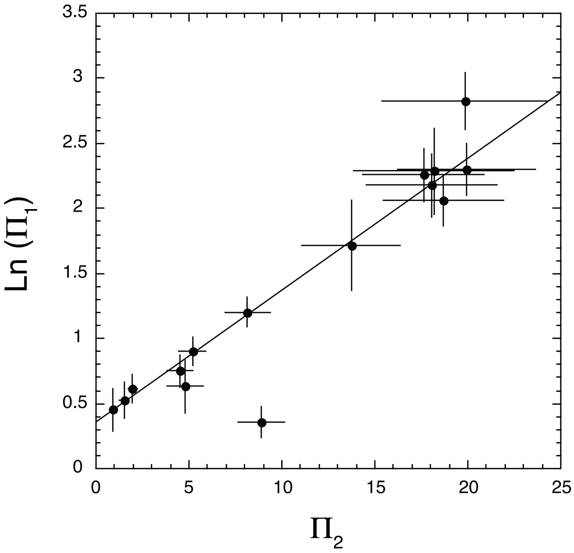

Figure 4. Plotting the natural logarithm of the vertical traveled distance as a function of the stress ratio reveals a linear relationship: $Ln(\Pi_1) = (0.36 \pm 0.07) + (0.10 \pm 0.01)\Pi_2$ (equation (3)). Correlation coefficient of the fit R^2 = 0.8964. Each point corresponds to one experiment.

much larger. These under-estimated distances were nevertheless included into the overall data set because they corresponded to some of the highest values of both normalized distance Π_1 and stress ratio Π_2 of the whole set. From our observations of crack trajectories in experiments where the crack truly stopped and formed a sill, we estimate the under-estimations to be less than 5–10 cm, and these latter values were incorporated into the data uncertainties. We note that our data set is therefore likely to be skewed toward these higher values, but also that data uncertainties, at least partly, take this skewness into account.

[27] Other experiments showed some rotation of the crack around a vertical axis towards or away from the observer. This could reflect the stress field being non-uniform as a result of the gelatine adhering to the tank walls where no deformation was imposed on the gelatine solid (the walls closest and furthest away from the observer). Potentially restricted movement along both these walls would have induced a non-slip boundary condition, which would thus have affected the stress field, causing some rotation of the cracks around a vertical axis. In this case, our stress calculations would therefore overestimate compressive stress and thus skew data towards lower stress ratio Π_2. This potential effect of non-uniform stress field is difficult to quantify, but by comparing the degree of crack rotation around a vertical axis relative to crack rotation around the horizontal axis *Oy* towards plastic sheets, we estimated a maximum additional uncertainty on our stress calculations to be of the order of 10 %.

[28] It is difficult to assess the implication of these potential under-estimations of normalized distance Π_1 and over-estimations of stress ratio Π_2 on the experimental relationships (3) and (4). We note, however, that the potential increase or decrease in the experimental constants is partly accounted for by the data uncertainties.

4. Geological Implications and Limitations

4.1. Upscaling to Magmatic Conditions

[29] Dimensional analysis was used to analyze our experimental results, as detailed in section 3. Considering reasonable ranges of natural parameters result in values of the dimensionless ratios falling in the same range as the one investigated in our experiments (Table 2). Thus, our analysis also enables us to upscale our experimental results to magmatic conditions since the experimental constants in equation (4) are dimensionless.

[30] As a dyke propagates away from its source under lithostatic conditions, the effective buoyancy of that dyke increases. *Menand and Tait* [2002] have shown that once the effective buoyancy of the dyke becomes comparable to the source overpressure, it becomes the main driving force and the dyke then propagates steadily. The height of the buoyant dyke at that point, which we defined as its initial height h_0 in our experiments, is not really well constrained but can be estimated, however, from the dyke overpressure, which depends on the initial stress conditions in the source region.

[31] Here, we assume that a buoyant dyke rises from a source under lithostatic conditions and then, some distance from the source, enters a region of the crust subjected to a horizontal compressive deviatoric stress. We assume that initially, as the dyke leaves its source, buoyancy is negligible and that the magma overpressure, ΔP, in the source drives the dyke away from the source region.

[32] It can be constrained by the tensile strength of surrounding rocks, T_s, so that

$$\Delta P \simeq T_s. \tag{5}$$

The effective buoyancy becomes the main driving force of the dyke when it becomes comparable to the source overpressure so that

$$\Delta P = \Delta\rho g h_0. \tag{6}$$

At this point, the buoyant dyke has reached it initial buoyant height h_0 and subsequently propagates in a steady-state

Table 2. Parameters and Dimensionless Ratios in Nature and Experiments[a]

	h_0 (m)	d (m)	$\Delta\rho$ (kg/m^3)	σ_x (Pa)	T_s (Pa)	Π_1	Π_2
Experiment	0.02–0.06	0.05–0.5	1000	15–390	–	1–17	1–20
Nature	200–10^4	100–10^4	100–500	10^5–10^8	10^6–10^7	0.01–50	0.01–100

[a] The experimental value for $\Delta\rho$ neglects the density of air and thus corresponds to that of gelatine [*Di Giuseppe et al.*, 2009]. Other experimental values are taken from Table 1. Natural values for h_0 are estimated from equation (7). Other ranges of natural values are taken as representative of geological conditions.

[*Menand and Tait*, 2002] until it enters a region of the crust that is subject to some deviatoric stress field. These two different expressions for magma overpressure can be combined to express the initial height of the dyke as a function of the rock tensile strength and the density difference between magma and rocks

$$h_0 \simeq \frac{T_s}{\Delta\rho g}. \tag{7}$$

[33] Alternatively, we can define the magma overpressure needed to initiate dyke propagation as that for which the resistance to fracture, or fracture toughness K_c, of the source rocks is exceeded (which depends on the dyke height h, and thus corresponds to a length-scale dependent tensile strength)

$$\Delta P \simeq \frac{K_c}{\sqrt{h}}, \tag{8}$$

in which case the dyke becomes buoyancy-driven when its initial height

$$h_0 \simeq \left(\frac{K_c}{\Delta\rho g}\right)^{2/3}. \tag{9}$$

[34] We assume that the dyke propagates some distance and becomes fully driven by buoyancy before entering a region where a compressive deviatoric stress acts horizontally. For the sake of simplicity, we also assume that this deviatoric stress is uniform with value σ_x. Combining equation (7) with our experimental expression (4) gives the vertical distance the buoyant dyke would have to propagate within the region under compression before turning into a sill in response to the deviatoric stress a_x

$$d \simeq \frac{T_s}{\Delta\rho g}\exp\left[(0.10 \pm 0.01)\left(\frac{T_s}{\sigma_x}\right)\right]. \tag{10}$$

Using equation (9) instead yields

$$d \simeq \left(\frac{K_c}{\Delta\rho g}\right)^{2/3}\exp\left[(0.10 \pm 0.01)\frac{\left(\Delta\rho g K_c^2\right)^{\frac{1}{3}}}{\sigma_x}\right]. \tag{11}$$

[35] Equations (10) and (11) are represented in Figure 5 as a function of the compressive stress for a range of density differences, 100–500 kg/m^3, two different tensile strengths, 1 and 10 MPa, and a corresponding range of fracture toughness 10–1000 Pa m$^{1/2}$ (see equations (7) and (9)). Figure 5 shows that the dyke-to-sill transition takes place over some non-negligible distance. Over the range of geological parameters considered here, Figure 5 shows that a dyke propagating in homogeneous, elastic rocks would require a minimum distance of two hundred meters, and in most cases of the order of one to ten kilometers, to fully adjust to a horizontal compressive stress field and turn into a sill.

[36] As expected, Figure 5 shows that dykes entering regions that are subjected to higher compressive deviatoric stresses would adjust more rapidly to those stresses and thus form sills over shorter vertical distances. However, even for very high compressive stress, the dyke-to-sill transition does not happen instantaneously but instead occurs over a minimum distance of the order of the initial buoyant height of the dyke (see equation (4)).

[37] Figure 5 also shows that a dyke propagating through stiffer rocks would need to propagate over a greater distance before forming a sill. This can be understood by recalling that a dyke originating from a stiffer rock region would need a higher source overpressure in order to overcome that relatively higher rock resistance to fracture which in turn would result in a higher subsequent driving effective buoyancy. This higher effective buoyancy would then be able to drive the dyke over a greater distance before it fully rotates into a sill.

4.2. Implications for the Formation of Sills

[38] Equations (10) and (11) represent the distance over which a buoyant dyke would transform into a sill owing to remote compressive deviatoric stress in homogeneous elastic rocks. In the absence of crustal heterogeneities, a stress-controlled dyke-to-sill transition would occur over a minimum distance of two hundred meters, and presumably of several kilometers in most cases (Figure 5).

[39] This contrasts with the fact that the crust involves a large number of strata with different mechanical properties that alternate rapidly. For instance, the Michigan basin sedimentary strata exhibit vertical density variations over distances ranging from few tens to several hundred of meters [*Hinze et al.*, 1978]. Likewise, composite volcanoes and rift zones in Iceland are composed of layers with contrasting mechanical properties, mostly pyroclastic rocks, lava flows and other igneous sheets, many of which are only a few meters thick although some unit thicknesses can reach up to 100 m [*Gudmundsson*, 2003; *Gudmundsson and Phillip*, 2006].

[40] Our study shows that the characteristic length-scale for stress-controlled sill formation is typically greater (and in many instances much greater) than the average thickness of lithological units. In accord with previous studies [e.g., *Dahm*, 2000; *Watanabe et al.*, 2002], our experiments show also that dykes would reach the surface even in a compressive tectonic environment if the characteristic length-scale for a dyke-to-sill transition is greater than the distance that separates them from the surface. This contrasts with the field observations that only a few percentage of dykes reach the surface, and that not all the dykes that do not reach the surface turns into sills [*Gudmundsson et al.*, 1999].

[41] These findings reinforces the point made by previous studies that crustal heterogeneities play an important role in determining where in the crust sills form, even when dykes are subject to horizontal compressive deviatoric stress. Contrasts in mechanical and rheological properties can indeed arrest the advance of dykes and lead to sill emplacement [*Mudge*, 1968; *Gudmundsson and Brenner*, 2001; *Gudmundsson*, 2003; *Kavanagh et al.*, 2006; *Taisne and Jaupart*, 2009]. Moreover, the finding that stress-controlled sill formation operates over distances that likely encompass numerous crustal strata would also imply that a stress control on sill formation involves almost certainly some stress interactions with these rock strata [*Gretener*, 1969; *Gudmundsson*, 1986; *Gudmundsson and Phillip*,

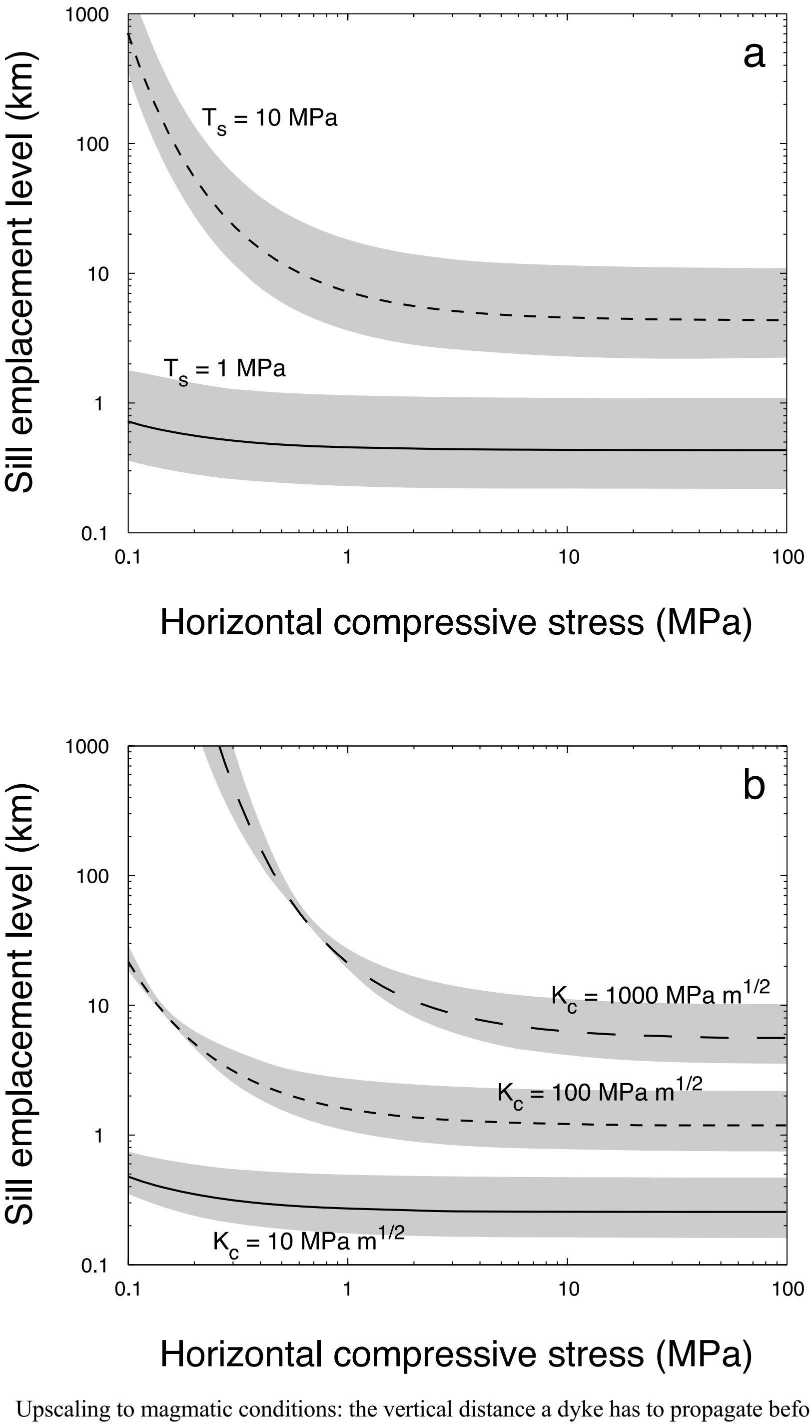

Figure 5. Upscaling to magmatic conditions: the vertical distance a dyke has to propagate before turning into a sill is represented as a function of the ambient horizontal compressive stress (equations (10) and (11)). (a) The two curves correspond to two different rock tensile strengths, T_s = 1 MPa (solid curve) and T_s = 10 MPa (dashed curve), and the grey areas represent a range of density differences between 100 and 500 kg/m^3. (b) The three curves correspond to three different fracture toughnesses, K_c = 10 MPa $m^{1/2}$ (solid curve), K_c = 100 MPa $m^{1/2}$ (short-dashed curve) and K_c = 1000 MPa $m^{1/2}$ (long-dashed curve), and the grey areas represent a range of density differences between 100 and 500 kg/m^3.

2006]. These stress interactions must therefore be taken into account when considering potential stress control on the emplacement of sills and indeed on the mechanical behavior of igneous sheets.

4.3. Limitation of Our Analysis

[42] Our experiments and analysis have only considered the case of buoyancy-driven cracks, when dykes could also be driven by their source overpressure. Indeed, a dyke overpressure is really the sum of that from its source and of the dyke effective buoyancy, minus the loss due to viscous pressure drop.

[43] Once the effective buoyancy is large enough and becomes comparable to the source overpressure, it becomes the main driving force of a steady-state propagation [*Menand and Tait*, 2002]. We note, however, that as a buoyant dyke modifies its trajectory in response to a horizontal compressive stress, it would also experience a decrease in effective buoyancy owing to a reduction in its vertical extent. Indeed, propagation of buoyant dykes is controlled by the local effective buoyancy balance that takes place at the dyke nose region [*Lister and Kerr*, 1991]. In our experiments, the air-filled cracks represent the dyke nose region. (The elastic gelatine solid closes shut behind these cracks because of the inviscid air, whereas if the cracks were filled by a viscous fluid, as magma-filled dykes are, then the dykes would develop a tail behind their nose region. Yet, in this latter case the material left within the tail would not contribute to the force budget that drives crack propagation; buoyancy crack propagation is entirely and only controlled by local effective buoyancy considerations [*Lister and Kerr*, 1991].) Therefore, as a buoyant dyke starts adjusting its trajectory to a horizontal compressive stress field and starts turning into a sill, the vertical extent over which the effective buoyancy balance operates decreases. Ultimately this vertical dimension is the thickness of the new sill formed by the complete rotation of the dyke.

[44] The case we have not dealt with is that of dykes entering compressive regions before they are fully driven by buoyancy. In this case, source overpressure and potential viscous pressure drop should be taken into account. If one assumes that a dyke overpressure remains essentially constant then, by definition, this dyke would continually experience the same constant internal driving pressure, and thus would be expected, perhaps paradoxically, to be able to rise vertically further than a buoyancy-driven dyke (which would instead experience a continuous reduction in effective buoyancy). One would therefore expect, everything else being equal, constant-pressure-driven dykes to adjust their course to a horizontal compressive stress over greater vertical distances when compared to buoyant dykes.

[45] However, dyke overpressure is likely not to remain constant because magma withdrawal from the source into the dyke and viscous pressure drop would continuously reduce it whilst the effective buoyancy would continuously increase it (before the dyke enters the compressive region). The response of such a vertically-propagating pressure-driven dyke to horizontal compressive stress cannot be deduced from our buoyant experiments, and would require addressing the dynamics of such a pressure-driven dyke. Nevertheless, what our work suggests, in conjunction with the observation that most dykes get arrested by crustal heterogeneities, is that these heterogeneities are likely to be very important in affecting the trajectories of dykes and in controlling where sills form.

5. Conclusions

[46] Using analogue experiments, the behavior of a buoyant crack rising through a horizontal compressive deviatoric stress field in a homogeneous elastic solid has been investigated and quantified. These experiments show that the horizontal compressive stress opposes the vertical advance of the buoyant crack, and forces the crack to modify its trajectory into the horizontal plane.

[47] The experimental data show how the balance between the driving effective buoyancy and the deviatoric horizontal compressive stress determines the vertical distance over which the crack rotation takes place. Using dimensional analysis, the characteristic length-scale for this dyke-to-sill rotation is shown to increase exponentially with the ratio of the initial crack effective buoyancy to horizontal compressive stress. If this length-scale is larger than the distance that separates the crack from the surface then the crack reaches the surface even though it is subject to a horizontal compressive deviatoric stress. Conversely, if this length-scale is smaller then the crack stops its propagation as a sill despite being buoyant.

[48] When upscaled to magmatic conditions and over a range of typical values for tensile strength, fracture toughness, density difference and deviatoric compressive stress, our results suggest that a dyke propagating through homogeneous elastic rocks would need to propagate vertically over a minimum distance of two hundred meters and more likely of several kilometers in most cases before it could form a sill in response to the horizontal compressive deviatoric stress.

[49] The characteristic length-scale for stress-controlled sill formation is typically greater than the average thickness of lithological units, which thus supports the idea that crustal heterogeneities play an important role in determining the fate of dykes and in controlling where sills form, and that a stress control on igneous sheets propagation and sill formation most likely involves stress interactions with and redistribution within rock strata.

Appendix A: State of Stress of the Gelatin Solid

[50] Stresses $\boldsymbol{\sigma}$ and strains $\boldsymbol{\epsilon}$ in an elastic solid can be linearly related according to Hooke's law, which in Cartesian coordinates is expressed as

$$\begin{aligned}\epsilon_x &= \frac{1}{E}\left[\sigma_x - \nu(\sigma_y + \sigma_z)\right],\\ \epsilon_y &= \frac{1}{E}\left[\sigma_y - \nu(\sigma_x + \sigma_z)\right],\\ \epsilon_z &= \frac{1}{E}\left[\sigma_z - \nu(\sigma_x + \sigma_y)\right],\end{aligned} \tag{A1}$$

where E and ν are the Young's modulus and Poisson's ratio of the elastic solid, respectively [*Timoshenko and Goodier*, 1970].

A1. Initial State of Stress

[51] Initially, the gelatine solid adheres to the tank walls and so there is no horizontal strain, $\epsilon_x = \epsilon_y = 0$. Using Hooke's law (A1), we obtain the following relationship between the three stress components:

$$\sigma_x = \sigma_y = \frac{\nu}{(1-\nu)}\sigma_z. \tag{A2}$$

Given that gelatine has a Poisson's ratio $\nu = 0.5$ [*Crisp*, 1952; *Richards and Mark*, 1966], $\sigma_x = \sigma_y = \sigma_z$ and the initial stress field is hydrostatic.

A2. Compressive Stress Field

[52] Gelatine is compressed by imposing a horizontal displacement u in the x direction, whilst the tank walls prevent any deformation in the horizontal y direction. This induces a horizontal deformation $\epsilon_x = \frac{u}{L}$ (L is the initial lateral extend of the gelatine solid) and $\epsilon_y = 0$. This reduces Hooke's law (A1) to

$$\begin{aligned} E\epsilon_x &= \sigma_x - \nu\sigma_y - \nu\sigma_z, \\ \sigma_y &= \nu\sigma_x + \nu\sigma_z, \\ E\epsilon_z &= \sigma_z - \nu\sigma_x - \nu\sigma_y, \end{aligned} \tag{A3}$$

from which we obtain

$$E\epsilon_x = \frac{(1+\nu)(1-2\nu)}{(1-\nu)}\sigma_x - \frac{\nu}{(1-\nu)}E\epsilon_z. \tag{A4}$$

Gelatine Poisson's ratio $\nu = 0.5$, and it follows that

$$\epsilon_x = -\epsilon_z. \tag{A5}$$

Combining this expression with the modified Hooke's law (A3) for a Poisson's ratio of 0.5, we obtain

$$\sigma_x = \frac{4}{3}E\epsilon_x + \sigma_z, \quad \sigma_y = \frac{2}{3}E\epsilon_x + \sigma_z. \tag{A6}$$

The vertical stress σ_z cannot be calculated analytically because the modified Hooke's law (A3) reduces to a system of two equations with three unknowns in the limit of a Poisson's ratio $\nu = 0.5$. Finite element computations were therefore carried out to evaluate σ_z (section A3). These numerical calculations indicate that the vertical stress is nil, and therefore, recalling that $\epsilon_x = \frac{u}{L}$, that the compressive stress field within the prism of solid gelatine is

$$\sigma_x = \frac{4Eu}{3L}, \quad \sigma_y = \frac{2Eu}{3L}, \quad \sigma_z = 0. \tag{A7}$$

The compressive stress field is thus uniform with σ_x as the maximum compressive stress, σ_y the intermediate principal stress, and σ_z the least compressive stress which is thus always vertical.

A3. Numerical Validation

[53] The finite element software COMSOL Multiphysics was used to evaluate the three-dimensional stress field within the elastic gelatin solid, and to test the validity of the expressions for the compressive stresses (A6). The geometry was that of the gelatine prism, and the boundary conditions were identical to those in the experiments: imposed displacement u in the x direction, no displacement in the y direction, no displacement at the base of the prism and a free upper surface. A displacement $u = 8$ mm and a Young's modulus $E = 2000$ Pa were chosen as representative of the experimental values, whereas the Poisson's ratio ν had value 0.499 since a value of 0.5 could not be handled numerically.

[54] Figure 1 shows that the compressive stress field is uniform, with the maximum compressive stress being σ_x and the least compressive stress being σ_z. To test the validity of the analytical expressions of the compressive stresses (A6), the computed principal stress values have been normalized by σ_x theoretical value $\frac{4Eu}{3L}$. Computed normalized values gives $\sigma_x = 0.998$, $\sigma_y = 0.498$, and σ_z in the range 310^{-11}–410^{-11}.

[55] **Acknowledgments.** Agust Gudmundsson and Olivier Merle are thanked for their constructive comments on an earlier version of the manuscript. We also thank the Associate Editor and three anonymous reviewers for their constructive reviews and comments which lead to substantial improvement of the manuscript. This research was supported by a Leverhulme Trust research grant.

References

Annen, C., and R. S. J. Sparks (2002), Effects of repetitive emplacement of basaltic intrusions on thermal evolution and melt generation in the crust, *Earth Planet. Sci. Lett.*, *203*, 937–955.

Annen, C., J. D. Blundy, and R. S. J. Sparks (2006), The sources of granitic melt in deep hot zones, *Trans. R. Soc. Edinburgh Earth Sci.*, *97*, 297–309.

Antonellini, M. A., and F. W. Cambray (1992), Relations between sill intrusions and bedding-parallel extensional shear zones in the Mid-continent Rift System of the Lake Superior region, *Tectonophysics*, *202*, 331–349.

Barenblatt, G. I. (1996), *Scaling, Self-Similarity, and Intermediate Asymptotics*, Cambridge Univ. Press, Cambridge, U. K.

Bedard, J. H., R. S. J. Sparks, M. Renner, M. J. Cheadle, and M. A. Hallworth (1988), Peridotite sills and metasomatic gabbros in the Eastern Layered Series of the Rhum complex, *J. Geol.*,*145*, 207–224.

Belcher, R. W., and A. F. M. Kisters (2006), Progressive adjustments of ascent and emplacement controls during incremental construction of the 3.1 Ga Heerenveen batholith, South Africa, *J. Struc. Geol.*, *28*, 1406–1421.

Bevington, P. R., and D. K. Robinson (2003), *Data Reduction and Error Analysis for the Physical Sciences*, McGraw-Hill, Boston.

Burchardt, S. (2008), New insights into the mechanics of sill emplacement provided by field observations of the Njardvik Sill, northeast Iceland, *J. Volcanol. Geotherm. Res.*, *173*, 280–288.

Cartwright, J., and D. M. Hansen (2006), Magma transport through the crust via interconnected sill complexes, *Geology*, *34*, 929–932.

Coleman, D. S., W. Gray, and A. F. Glazner (2004), Rethinking the emplacement and evolution of zoned plutons: Geochronologic evidence for incremental assembly of the Tuolumne Intrusive Suite, California, *Geology*, *32*, 433–436.

Corry, C. E. (1988), *Laccoliths: Mechanics of Emplacement and Growth*, *Geol. Soc. Am. Spec. Pap. Ser.*, vol. 220, Geol. Soc. of Am., Boulder, Colo.

Crisp, J. A. (1984), Rates of magma emplacements and volcanic output, *J. Volcanol. Geotherm. Res.*, *20*, 177–211.

Crisp, J. D. C. (1952), The use of gelatin models in structural analysis, *Proc. Inst. Mech. Eng. Part B*, *1B*(12), 580–604.

Dahm, T. (2000), Numerical simulations of the propagation path and the arrest of fluid-filled fractures in the Earth, *Geophys. J. Int.*, *141*, 623–638.

de Saint-Blanquat, M., G. Habert, E. Horsman, S. S. Morgan, B. Tikoff, P. Launeau, and G. Gleizes (2006), Mechanisms and duration of non-tectonically assisted magma emplacement in the upper crust: The Black Mesa pluton, Henry Mountains, Utah, *Tectonophysics*, *48*, 1–31.

Di Giuseppe, E., F. Funiciello, F. Corbi, G. Ranalli, and G. Mojoli (2009), Gelatins as rock analogs: A systematic study of their rheological and physical properties, *Tectonophysics*, *473*, 391–403.

Fridleifsson, I. B. (1977), Distribution of large basaltic intrusions in the Icelandic crust and the nature of the layer 2–layer 3 boundary, *Geol. Soc. Am. Bull.*, *88*, 1689–1693.

Gilbert, G. K. (1877), Geology of the Henry Mountains, Utah, in *U.S. Geographical and Geological Survey of the Rocky Mountain Region*, report, pp. 1–160, Gov. Print. Off., Washington, D. C.

Glazner, A. F., J. M. Bartley, D. S. Coleman, W. Gray, and R. Z. Taylor (2004), Are plutons assembled over millions of years by amalgamation from small magma chambers?, *GSA Today*, *14*, 4–11.

Gretener, P. E. (1969), On the mechanics of the intrusion of sills, *Can. J. Earth Sci.*, *6*, 1415–1419.

Gudmundsson, A. (1986), Formation of crustal magma chambers in Iceland, *Geology*, *14*, 164–166.

Gudmundsson, A. (1990), Emplacement of dikes, sills and crustal magma chambers at divergent plate boundaries, *Tectonophysics*, *176*, 257–275.

Gudmundsson, A. (2003), Surface stresses associated with arrested dykes in rift zones, *Bull. Volcanol.*, *65*, 606–619.

Gudmundsson, A., and S. L. Brenner (2001), How hydrofractures become arrested, *Terra Nova*, *13*, 456–462.

Gudmundsson, A., and S. L. Phillip (2006), How local stress fields prevent volcanic eruptions, *J. Volcanol. Geotherm. Res.*, *158*, 257–268.

Gudmundsson, A., L. B. Marinoni, and J. Marti (1999), Injection and arrest of dykes: Implications for volcanic hazards, *J. Volcanol. Geotherm. Res.*, *88*, 1–13.

Hinze, W. J., J. W. Bradley, and A. R. Brown (1978), Gravimeter survey in the Michigan Basin deep borehole, *J. Geophys. Res.*, *83*, 5864–5868.

Holness, M. B., and M. C. S. Humphreys (2003), The Traigh Bhàn na Sgùrra sill, Isle of Mull: Flow localization in a major magma conduit, *J. Petrol.*, *44*, 1961–1976.

Horsman, E., B. Tikoff, and S. Morgan (2005), Emplacement-related fabric and multiple sheets in the Maiden Creek sill, Henry Mountains, Utah, USA, *J. Struc. Geol.*, *27*, 1426–1444.

Horsman, E., S. Morgan, M. de Saint-Blanquat, G. Habert, R. Hunter, A. Nugent, and B. Tikoff (2008), Emplacement and assembly of shallow intrusions from multiple magma pulses, Henry Mountains, Utah, in *Sixth Hutton Symposium on the Origin of Granite and Related Rocks*, edited by A. F. E. A. Kisters, R. Soc. of Edinburgh, Edinburgh, in press.

Hutton, D. H. W. (1992), Granite sheeted complexes: Evidence for the dyking ascent mechanism, *Trans. R. Soc. Edinburgh Earth Sci.*, *83*, 377–382.

Hyndman, D. W., and D. Alt (1987), Radial dikes, laccoliths and gelatin models, *J. Geol.*, *95*, 763–774.

John, B. E. (1988), Structural reconstruction and zonation of a tilted mid-crustal magma chamber: The felsic Chemehuevi Mountains plutonic suite, *Geology*, *16*, 613–617.

John, B. E., and J. D. Blundy (1993), Emplacement-related deformation of granitoid magmas, southern Adamello Massif, Italy, *Geol. Soc. Am. Bull.*, *105*, 1517–1541.

Johnson, A. M., and D. D. Pollard (1973), Mechanics of growth of some laccolithic intrusions in the Henry Mountains, Utah, part I. Field observations, Gilbert's model, physical properties and flow of the magma, *Tectonophysics*, *18*, 261–309.

Kavanagh, J. L., T. Menand, and R. S. J. Sparks (2006), An experimental investigation of sill formation and propagation in layered elastic media, *Earth Planet. Sci. Lett.*, *245*, 799–813.

Kühn, D., and T. Dahm (2004), Simulation of magma ascent by dykes in the mantle beneath mid-ocean ridges, *J. Geodyn.*, *38*, 147–159.

Kühn, D., and T. Dahm (2008), Numerical modelling of dyke interaction and its influence on oceanic crust formation, *Tectonophysics*, *447*, 53–65.

Lister, J. R., and R. C. Kerr (1991), Fluid-mechanical models of crack propagation and their application to magma transport in dykes, *J. Geophys. Res.*, *96*, 10,049–10,077.

Menand, T. (2008), The mechanics and dynamics of sills in elastic layered media and their implications for the growth of laccoliths, *Earth Planet Sci. Lett.*, *267*, 93–99.

Menand, T., and S. R. Tait (2002), The propagation of a buoyant liquid-filled fissure from a source under constant pressure: An experimental approach, *J. Geophys. Res.*, *107*(B11), 2306, doi:10.1029/2001JB000589.

Mériaux, C., and J. R. Lister (2002), Calculation of dike trajectories from volcanic centers, *J. Geophys. Res.*, *107*(B4), 2077, doi:10.1029/2001JB000436.

Michaut, C., and C. Jaupart (2006), Ultra-rapid formation of large volumes of evolved magma, *Earth Planet. Sci. Lett.*, *250*, 38–52.

Morgan, S. S., E. Horsman, B. Tikoff, M. de Saint-Blanquat, and G. Habert (2005), Sheet-like emplacement of satellite laccoliths, sills and bysmaliths of the Henry Mountains, southern Utah, in *Interior Western United Sates*, *Geol. Soc. Am.Field Guide Ser.*, vol. 6, edited by J. Pederson and C. M. Dehler, pp. 283–309, doi:10.1130/2005.fld006(14), Geol. Soc. of Am., Boulder, Colo.

Morgan, S. S., A. Stanik, E. Horsman, B. Tikoff, M. de Saint-Blanquat, and G. Habert (2008), Emplacement of multiple magma sheets and wall rock deformation: Trachyte Mesa intrusion, Henry Mountains, Utah, *J. Struc. Geol.*, *30*, 491–512.

Mudge, M. R. (1968), Depth control of some concordant intrusions, *Geol. Soc. Am. Bull.*, *79*, 315–332.

Muller, O. H., and D. D. Pollard (1977), The stress state near Spanish Peaks, Colorado determined from a dike pattern, *Pure Appl. Geophys.*, *115*, 69–86.

Odé, H. (1957), Mechanical analysis of the dike pattern of the Spanish Peaks area, Colorado, *Geol. Soc. Am. Bull.*, *68*, 567–576.

Parsons, T., N. H. Sleep, and G. A. Thompson (1992), Host rock rheology controls on the emplacement of tabular intrusions: Implications for underplating of extending crust, *Tectonics*, *11*, 1348–1356.

Pasquarè, F., and A. Tibaldi (2007), Structure of a sheet-laccolith system revealing the interplay between tectonic and magma stresses at Stardalur Volcano, Iceland, *J. Volcanol. Geotherm. Res.*, *161*, 131–150.

Pinel, V., and C. Jaupart (2000), The effect of edifice load on magma ascent beneath a volcano, *Philos. Trans. R. Soc. London A*, *358*, 1515–1532.

Pinel, V., and C. Jaupart (2004), Magma storage and horizontal dyke injection beneath a volcanic edifice, *Earth Planet. Sci. Lett.*, *221*, 245–262.

Richards, R., Jr., and R. Mark (1966), Gelatin models for photoelastic analysis of gravity structures, *Exp. Mech.*, *6*, 30–38.

Rivalta, E., and T. Dahm (2006), Acceleration of buoyancy-driven fractures and magmatic dikes beneath the free surface, *Geophys. J. Int.*, *166*, 1424–1439.

Rivalta, E., M. Böttinger, and T. Dahm (2005), Buoyancy-driven fracture ascent: Experiments in layered gelatine, *J. Volcanol. Geotherm. Res.*, *144*, 273–285.

Roman, D. C., S. C. Moran, J. A. Power, and K. V. Cashman (2004), Temporal and spatial variation of local stress fields before and after the 1992 eruptions of Crater Peak Vent, Mount Spurr volcano, Alaska, *Bull. Seismol. Soc. Am.*, *94*, 2366–2379.

Roman, D. C., J. Neuberg, and R. R. Luckett (2006), Assessing the likelihood of volcanic eruption through analysis of volcanotectonic earthquake fault plane solutions, *Earth Planet. Sci. Lett.*, *248*, 244–252.

Shaw, H. R. (1985), Links between magma-tectonic rate balances, plutonism, and volcanism, *J. Geophys. Res.*, *90*, 11,275–11,288.

Takada, A. (1989), Magma transport and reservoir formation by a system of propagating cracks, *Bull. Volcanol.*, *52*, 118–126.

Taisne, B., and C. Jaupart (2009), Dike propagation through layered rocks, *J. Geophys. Res.*, *114*, B09203, doi:10.1029/2008JB006228.

Takada, A. (1990), Experimental study on propagation of liquid-filled crack in gelatin: Shape and velocity in hydrostatic stress condition, *J. Geophys. Res.*, *95*, 8471–8481.

Thomson, K. (2007), Determining magma flow in sills, dykes and laccoliths and their implications for sill emplacement mechanisms, *Bull. Volcanol.*, *70*, 183–201.

Timoshenko, S. P., and J. N. Goodier (1970), *Theory of Elasticity*, 3rd ed., McGraw-Hill, Singapore.

Vigneresse, J. L., and J. L. Bouchez (1997), Successive granitic magma batches during pluton emplacement: The case of Cabeza de Araya (Spain), *J. Petrol.*, *38*, 1767–1776.

Watanabe, T., T. Koyaguchi, and T. Seno (1999), Tectonic stress controls on ascent and emplacement of magmas, *J. Vocanol. Geotherm. Res.*, *91*, 65–78.

Watanabe, T., T. Masuyama, K. Nagaoka, and T. Tahara (2002), Analog experiments on magma-filled cracks: Competition between external stresses and internal pressure, *Earth Planets Space*, *54*, 1247–1261.

Westergaard, H. M. (1939), Bearing pressures and cracks, *Trans. Am. Soc. Mech. Eng.*, *61*, A49–A53.

Wiebe, R. A., and W. J. Collins (1998), Depositional features and stratigraphic sections in granitic plutons: Implications for the emplacement and crystallization of granitic magma, *J. Struc. Geol.*, *20*, 1273–1289.

P. Benghiat, Atlas Iron Limited, PO Box 223, West Perth, WA 6872, Australia. (philipb@atlasiron.com.au)

K. A. Daniels and T. Menand, Centre for Environmental and Geophysical Flows, Department of Earth Sciences, University of Bristol, Wills Memorial Building, Queen's Road, Bristol BS8 1RJ, UK. (k.a.daniels@bristol.ac.uk; t.menand@bristol.ac.uk)

Tectonophysics 500 (2011) iv

Contents lists available at ScienceDirect

Tectonophysics

journal homepage: www.elsevier.com/locate/tecto

Special Issue

Emplacement of magma pulses and growth of magma bodies

Thierry Menand
University of Bristol, United Kingdom
(Now at Clermont Université, France)

Michel de Saint-Blanquat
CNRS - Universite de Toulouse, France

Catherine Annen
University of Bristol, United Kingdom

CONTENTS

Editorial

Research Papers

doi:10.1016/S0040-1951(11)00054-0

Tectonophysics 500 (2011) 1–2

Contents lists available at ScienceDirect

Tectonophysics

journal homepage: www.elsevier.com/locate/tecto

Preface

Emplacement of magma pulses and growth of magma bodies

Keywords:
Plutons
Sills
Granite
Incremental emplacement

1. Introduction

Magmatism is responsible for the formation of continental and oceanic crusts. It is the main agent of mass and heat transfers from the mantle towards the crust, the hydrosphere (oceanic and continental hydrothermalism) and the atmosphere (emissions of volcanic gas and ashes). Its expressions are the crystallization of intrusive rocks and the eruption of volcanic products. However, with a ratio between the volumes of extrusive and intrusive magmatic rocks estimated to be of the order of 1:5 for most magmatic systems (White et al., 2006), one of the main characteristics of magmatism is that magmas rarely reach the Earth's surface. This suggests that the prevailing conditions in the crust are not favourable to the arrival of magma on the Earth's surface, but instead lean heavily towards the formation of intrusive bodies in the crust. These intrusive bodies, referred to here as plutons, constitute the elementary building brick of the continental crust. An increasing number of geophyscial and geochronological data as well as geological observations is currently modifying our understanding of pluton construction. When plutons were initially envisaged as quasi-spherical bodies growing slowly and essentially by an overall inflation, they are now recognized as growing incrementally by the accretion of successive and relatively small magma pulses, over variable periods of time, from hundred to millions of years, depending on geodynamic setting and source fertility. This brings new challenges and has far-reaching implications. According to this new model of plutonism, the evolution of magma bodies is related to the processes that control the timescale and the spatial distribution of the successive pulses. Depending on their emplacement rate and on their ability to amalgamate, repeated magma pulses can either rapidly solidify or ultimately build up an active magma chamber. Thus understanding how magma bodies grow has fundamental implications for the link between volcanism and plutonism as well as for magma differentiation and ultimately for our understanding of the growth and evolution of the Earth crusts. The concept of pluton incremental growth challenges our understanding as well as our field interpretations of the processes involved during pluton construction. Indeed, these processes and how they operate in governing the emplacement and growth of plutons, both in space and time, are still debated.

A state-of-the-art session on these very issues was held at the 2008 General Assembly of the European Geosciences Union. As a follow-up of this session, this special volume *Emplacement of magma pulses and growth of magma bodies* brings together both theoretical models and field studies that cover most aspects of the emplacement and growth of plutons.

2. This volume

The volume starts with three reviews of the thermal, mechanical and structural aspects of the emplacement and construction of crustal magma bodies. Annen (this issue) reviews the thermal evolution of magma bodies growing by slow amalgamation of discrete pulses, and suggests that incremental growth could explain the bi-modal character of magmatic provinces with intermediate magmas resulting from the open nature of the systems through the mixing of both mafic and silicic end-members. This review also supports a model of magma bodies construction as a multi-time-scale process with the development of large magma chambers corresponding to the highest magma fluxes, several orders of magnitude higher than the average pluton emplacement rate. Menand (this issue) then reviews the different mechanisms controlling the formation and emplacement depths of sills, and how these can amalgamate to form larger igneous bodies. The main conclusion of this review is that the dominant control on sill emplacement is exerted by crustal heterogeneities via their rigidity and rheological anisotropy, and their interaction with the local and tectonic stress fields. In turn, this determines whether and how successive sills can amalgamate to form larger magma bodies. Finally, Saint Blanquat et al. (this issue) review the mechanisms and duration of pluton construction in continental magmatic arcs. Field studies on plutons of various sizes (from 1 to more than 1000 km^3) show that each pluton size is related to a pulsed magmatic activity with a characteristic time scale, and that each of these coupled time-space scales is related to a specific process. High magma fluxes relative to crustal tectonic strain rates ensure that magmatic processes control the system from below. One of the main consequences is that for high fluxes or over short time scales the dynamics of the pulsed magmatism observed in continental arc plutonic systems are a direct proxy for deep lithospheric and magmatic processes.

These reviews are complemented by two thermal and mechanical studies. First, Michaut and Jaupart (this issue) discuss two thermal models for the formation of magma reservoirs by small increments. The authors show that if a magma body grows by amalgamation of relatively thick individual igneous sheets, crystallization in that body proceeds at equilibrium as described by Annen (this issue). If the body grows instead by amalgamation of relatively thin sheets, the thermal evolution of the body is kinetically controlled such that the initial sheets do not crystallize completely but instead preserve a glassy residue. As the temperature of the system subsequently increases, devitrification of this glass occurs which leads crystallization to proceeds catastrophically in a positive feedback loop involving latent heat release and temperature rise. These two thermal models have different implications for the formation of magma chambers as well as

doi:10.1016/j.tecto.2010.05.014

the amount of melt generated. Then, Gudmundsson (this issue) discusses the mechanisms for the arrest of dykes and their deflection into sills at discontinuities in the upper crust in relation to the formation of shallow plutons and magma chambers. The emphasis is put on the role of host-rock layering and three associated mechanisms for the arrest of dykes and their deflection into sills. The Cook–Gordon mechanism corresponds to a weak contact that opens up as a result of tensile stresses induced by a nearby dyke, a mechanism that is likely to operate primarily at shallow crustal depths. A second mechanism is the development of stress barriers, which occurs within rock layers where the minimum compressive stress becomes vertical and thus opposes the advance of dykes and favours sill emplacement. In the third mechanism, adjacent layers with different elastic properties can lead to material-toughness ratios that are favourable to sill formation. This situation is most likely to arise when a rock layer is stiffer than the one underneath, such as in the case of a relatively stiff lava flow overlying a comparatively softer pyroclastic layer; a propagating dyke would then have a greater tendency to be deflected into the contact between the adjacent rock layers.

The volume closes with three field-based studies that cover a range of pluton emplacement settings, sizes and localities. They also illustrate the challenges faced when interpreting field observations in the light of our improved understanding of pluton emplacement and growth.

Numerous evidence suggest and support an incremental growth of plutons. Yet well-defined contacts within plutons remain commonly elusive. Miller et al. (this issue) compare and contrast the structural and zircon features of the Spirit Mountain batholith and the smaller Aztec Wash pluton in southern Nevada, USA, to explain this discrepancy. Both are proposed to have grown by magma replenishments and sheet-stacking into low-strength mush zones, but the contacts between successive sheets would have disappeared gradually owing to the continuous increase in magma content and heat during their growth. According to Miller et al. (this issue), the smaller Aztec Wash pluton retained a more diverse composition and texture because of its smaller volume and history, whereas a much more protracted history lead to a much larger and more homogenized Spirit Mountain batholith except for the latest stage of its construction. This interpretation explains not only the apparent contradiction between incremental and protracted pluton growth and a seeming absence of intrusive contacts, but is also consistent with the recent thermal models exposed in this special volume on the thermal evolution of plutons growing by amalgamation of sills and the conditions for the existence of long-lived shallow crustal magma chambers (Annen, this issue; Michaut and Jaupart, this issue). Allibon et al. (this issue) document a rare example of a pluton located in the oceanic crust which could be interpreted as a feeder of the Fuerteventura volcano, in Canary Islands. It is a vertically layered mafic dyke-like pluton constructed in a transtensive tectonic environment. The structural features of the pluton attest of an incremental growth by periodic injections and amalgamations of dykes similar to a sheeted-dyke complex, and the authors interpret this emplacement geometry as controlled by the extensional regional tectonic setting that prevailed during the Miocene pluton growth. The authors attribute also the observed sequence of internal differentiation of individual dykes, their subsequent compaction and the migration of interstitial melt that followed, as reflecting the interplay between the regional tectonic setting and the rate and volume of the successive dyke injections that were controlled instead by source-related processes. Finally, Marko and Yoshinobu (this issue) document the structural and thermal aureoles of the White Horse Pluton in eastern Nevada, USA. The authors use the structures of the contact aureole to show both spatial and temporal variations in the rheology of the host rocks associated with the repeated injections of magma that lead to the formation of the pluton, and thus to constrain the temporal and spatial construction of this pluton. The authors show evidence of both ductile and brittle deformation within the contact aureole, and that brittle deformation occurred in the late stage of the pluton construction following previous episode of ductile deformation. Additionally, the authors place geometric constraints on the shape and growth of the White Horse Pluton, and their estimates of the strain associated with the pluton growth suggest that shortening of the contact aureole could accounts for half the space created during the pluton formation. Other deformation mechanisms are thus required to account for the remaining space created during pluton emplacement.

Our understanding of pluton construction is sharpening, and we hope this special volume *Emplacement of magma pulses and growth of magma bodies* provides a balanced and critical overview of our current knowledge of the incremental growth of plutons. With a set of both theoretical models and field studies that, we think, covers most aspects of the emplacement and growth of plutons, we also hope that this volume will be of interest for both the volcanic and plutonic communities, including theoreticians, field geologists and petrologists.

Acknowledgments

We would like to acknowledge the effort and expertise of all the reviewers who helped us with this volume: Pierre Barbey, Keith Benn, George Bergantz, Barrie Clarke, Sandy Cruden, Jo Dufek, Adelina Geyer, Agust Gudmundsson, Olivier Merle, Calvin F Miller, Philippe Olivier, Alessandro Tibaldi, Jean-Louis Vigneresse, Roberto Weinberg and Robert Wiebe.

Furthermore, we would like to thank the editorial support from Mike Sandiford, Mian Liu, Andrés Villavicencio, Tim Horscroft, Frank Wang, Sheilagh Douma and Yvonne Philippo.

Reference

White, S.M., Crisp, J.A., Spera, F.J., 2006. Long-term volumetric eruption rates and magma budgets. Geochemistry, Geophysics, Geosystems 7, Q03010. doi:10.1029/2005GC001002.

Thierry Menand
University of Bristol, United Kingdom
Corresponding author.
E-mail address: t.menand@bristol.ac.uk.

Michel de Saint-Blanquat
CNRS - Université de Toulouse, France
E-mail address: michel@lmtg.obs-mip.fr.

Catherine Annen
University of Bristol, United Kingdom

10 May 2010

Tectonophysics 500 (2011) 11–19

Contents lists available at ScienceDirect

Tectonophysics

journal homepage: www.elsevier.com/locate/tecto

Review Article

Physical controls and depth of emplacement of igneous bodies: A review

Thierry Menand

Department of Earth Sciences, Centre for Environmental and Geophysical Flows, University of Bristol, Wills Memorial Building, Queen's Road, Bristol BS8 1RJ, UK

ARTICLE INFO

Article history:
Received 5 November 2008
Received in revised form 9 October 2009
Accepted 19 October 2009
Available online 5 November 2009

Keywords:
Sills
Laccoliths
Plutons
Emplacement
Magma pulses

ABSTRACT

The formation and growth of magma bodies are now recognised as involving the amalgamation of successive, discrete pulses such as sills. Sills would thus represent the building blocks of larger plutons (*sensu lato*). Mechanical and thermal considerations on the incremental development of these plutons raise the issue of the crustal levels at which magma can stall and accumulate as sills. Reviewing the mechanisms that could *a priori* explain sill formation, it is shown that principal physical controls include: rigidity contrast, where sills form at the interface between soft strata overlaid by comparatively stiffer strata; rheology anisotropy, where sills form within the weakest ductile zones; and rotation of deviatoric stress, where sills form when the minimum compressive stress becomes vertical. Comparatively, the concept of neutral buoyancy is unlikely to play a leading control in the emplacement of sills, although it could assist their formation. These different controls on sill formation, however, do not necessarily operate on the same length scale. The length scale associated with the presence of interfaces separating upper stiffer layers from lower softer ones determines the depth at which rigidity-controlled sills will form. On another hand, the emplacement depths for rheology-controlled sills are likely to be determined by the distribution of the weakest ductile zones. Whereas the emplacement depth of stress-controlled sills is determined by a balance between the horizontal maximum compressive stress, which favours sill formation, and the buoyancy of their feeder dykes, which drives magma vertically. Ultimately, the depth at which a sill forms depends on whether crustal anisotropy or stress rotation is the dominant control, i.e. which of these processes operates at the smallest length scale. Using dimensional analysis, it is shown that sill formation controlled by remote stress rotation would occur on length scales of hundreds of meters or greater. This therefore suggests that crustal heterogeneities and their associated anisotropy are likely to play a larger role than remote stress rotation in controlling sill emplacement, unless these heterogeneities are several hundred meters or more apart. This also reinforces the role of local stress barriers, owing to interactions between deviatoric stress and crustal heterogeneities, in the formation of sills.

Contents

E-mail address: T.Menand@bristol.ac.uk.

0040-1951/$ – see front matter © 2009 Elsevier B.V. All rights reserved.
doi:10.1016/j.tecto.2009.10.016

1. The formation of plutons

The formation and growth of igneous bodies (plutons *sensu lato*) have long been recognised as important processes that have shaped much of the Earth's crust. Over the years, a growing body of geological evidence, conceptual reasoning and theoretical models has lead to a better understanding of pluton construction. When plutons, especially those of granitic nature, were before envisaged as growing by an overall inflation, their construction is now recognised as involving the accretion of repeated, discrete magma injections or pulses. Yet, these processes and how they operate in governing the emplacement and growth of plutons, both in space and time, are still debated.

1.1. Mechanical challenge or “the space problem”

The formation of plutons is first a mechanical challenge. Plutons are large igneous bodies up to several kilometres to tens of kilometres in thickness. Their formation and the associated deformation of the host rocks must be mechanically compatible on the long term with the average lithospheric strain rate (Petford et al., 2000), and the depth of emplacement of these bodies does certainly play a significant role. Indeed, the emplacement of a pluton in the shallow upper crust will be facilitated by the presence of the near free surface, whereas the deformation induced by the emplacement of deeper plutons in the lowermost parts of the crust will benefit from ductile flow, either from the mantle or the ductile crust or even both (Petraske et al., 1978; Cruden, 1998; Cruden and McCaffrey, 2001). However, the development of igneous bodies may not follow a single growth process. Extensive field measurements of the geometry and dimensions of many intrusions, from the smaller sills to the larger batholiths, seem to indicate that a generic, continuous link exists between the thickness and the average horizontal dimension of these intrusions, but also that this scaling relationship does not seem to follow a single power law (McCaffrey and Cruden, 2002; Cruden and McCaffrey, 2006). Instead, sills seem to grow mainly by lateral propagation whereas laccoliths seem to grow by vertical thickening before extending laterally again as plutons and batholiths, hence suggesting different growth mechanisms depending on the size of the intrusive body that is considered (Pollard and Johnson, 1973; Cruden and McCaffrey, 2002).

1.2. Thermal considerations

The construction and development of an active magma chamber is also a thermal problem. For a magma chamber to remain active or for an igneous body to be able to convect, heat must be accumulated in that body at rates that are higher than that at which heat is conducted away from the body. Recent studies have shown that the thermal evolution of an igneous body depends critically on several parameters including the supply rate of magma that feeds that body as well as the position of this igneous body along the ambient geotherm. Indeed, the depth at which magma is accumulated, or stored, in the crust is important because this determines the initial temperature of the igneous body and thus its subsequent thermal evolution (Annen et al., 2006; Michaut and Jaupart, 2006; Annen, 2009).

The mechanical and thermal aspects of pluton formation and growth are also intimately intertwined. The mechanics and associated styles of pluton formation directly affect the geometry of a pluton, which in turn controls its thermal evolution. This has strong implications for magma differentiation and anatexis. Plutons can grow through different emplacement sequences. Repeated amalgamation of magma of younger age underneath older igneous material would lead to grow by under-accretion (Harrison et al., 1999; de Saint-Blanquat et al., 2001; Michel et al., 2008). The opposite growth sequence, referred to as over-accretion, occurs when younger igneous units accumulate on top of older ones (Wiebe and Collins, 1998; Benn et al., 1999; Galerne et al., 2008). Finally, pluton formation can also involved scattered injections of magma, with septa of host rocks trapped in between individual intrusions (Quick et al., 1994; Westerman et al., 2004). These different growth sequences will lead to radically different thermal evolutions, and thus to extremely different relative amounts of residual melt from incomplete crystallization of the pulses and of partial crustal melt (Annen et al., 2008; Annen, 2011-this issue).

1.3. Evidences for sills as pluton-building blocks

There is a vast body of evidence from geological, geophysical and geochronological data (Cargill et al., 1928; Hawkes and Hawkes, 1933; Gretener, 1969; Bedard et al., 1988; John, 1988; Gudmundsson, 1990; Hutton, 1992; John and Blundy, 1993; Rutter et al., 1993; Vigneresse and Bouchez, 1997; Wiebe and Collins, 1998; Benn et al., 1999; Coleman et al., 2004; Glazner et al., 2004; Horsman et al., 2005; Morgan et al., 2005; Belcher and Kisters, 2006; de Saint-Blanquat et al., 2006; Pasquarè and Tibaldi, 2007; Horsman et al., in press; Morgan et al., 2008; Miller et al., this issue) as well as theoretical models (Gudmundsson, 1990; Annen and Sparks, 2002; Michaud and Jaupart, 2006; Menand, 2008) that plutons (*sensu lato*) throughout the crust grow by the amalgamation of individual intrusive igneous sheets. Although rare instances of plutons that grew by amalgamation of vertical dykes have been identified (Allibon et al., 2011-this issue), the individual sheets making up most plutons can be described as sills. Sills could therefore be envisaged as representing the building blocks of larger bodies (Horsman et al., 2005; Morgan et al., 2005; de Saint-Blanquat et al., 2006; Menand, 2008; Horsman et al., in press; Morgan et al., 2008; Miller et al., this issue). This in turn raises the questions of the formation of sills, their emplacement depth, and how this depth is determined.

2. Existing models of sill formation

A sill forms when a dyke stops it vertical propagation and then intrudes along an existing discontinuity (Fig. 1). Several models have been proposed for the arrest of dykes and associated sill formations.

2.1. Buoyancy control

Neutral buoyancy has long been proposed as a mechanism to form sills, with sills emplacing at crustal levels where their magma becomes

Fig. 1. Photograph of a rotated sill with its feeder dike on the south side of Gold Creek, east Mount Hillers, Henry Mountains, Utah, USA. The sill is about 10 m thick. The view is from the east. The sill, its feeder and the intruded sandstone have all been rotated almost 90° by the later formation of Mount Hillers' intrusive centre (situated further north, to the right of the photograph). Photo courtesy of Michel de Saint-Blanquat.

neutrally buoyant (Gilbert, 1877; Corry, 1988). However, this model contradicts field observations (e.g. the Buckhorn Ridge intrusion in Utah, USA, Johnson and Pollard, 1973) and 3D seismic data (Thomson and Hutton, 2004; Cartwright and Hansen, 2006; Thomson, 2007) of sills intruding different rock strata, and thus characterised by different density, and of transgressive sills intruding successively different stratigraphic levels; if one of those levels represents a level of neutral buoyancy the others clearly cannot. Likewise, if neutral buoyancy were to control the formation of sills and therefore the arrest of dykes then it would almost invariably prevent basaltic lava flows to occur on the Earth's surface owing to their larger density.

Thus, alone, a level of neutral buoyancy is unlikely to be sufficient for promoting sill formation. Although in some cases it could indeed arrest the vertical propagation of a dyke (Pinel and Jaupart, 2004), further magma flow would most likely result in lateral dyke propagation, as illustrated by the laboratory experiments of Lister and Kerr (1991), rather than sill formation because this would also requires a rotation of the intrusion so that it propagates in a horizontal plane. However, Taisne and Jaupart (2009) have recently shown that buoyancy effect may lead to sill formation in specific conditions. Buoyancy-driven dyke propagation is determined by a local buoyancy balance in the inflated nose region of the dike, independently of the total buoyancy of the magma column between source and tip (Lister and Kerr, 1991; Taisne and Jaupart, 2009). Therefore, a dyke intruding low-density layers would develop an internal overpressure that may be large enough to generate a horizontally propagating sill at or near the base of the low-density layers. However, the development of such a large overpressure requires the thickness of these low-density layers to be at least 700 m and 2 km on average. This is typically larger than the thickness of sedimentary strata (e.g. Hinze et al., 1978), and therefore suggests that the concept of neutral buoyancy does not provide a complete explanation for the mechanism and level of sill emplacement, although they could assist their formation. Additional mechanisms are thus required.

2.2. Rheology control

The observations of sills intruding soft layers such as shales, mudstones or hyaloclastites (Mudge, 1968; Fridleifsson, 1977; Antonellini and Cambray, 1992), which might have deformed ductily at the time of sill formation, suggest that rheology contrasts between adjacent crustal layers can play an important role in controlling sill formation.

Parsons et al. (1992) suggest that the rheology contrast between ductile rock layers and adjacent elastic, brittle strata would help stop feeder dykes and promote sill formation. Their reasoning is that a vertical dike increases locally the horizontal least principal stress of the host rocks it intrudes. This effect would be magnified in rheologically ductile zones owing to partial relaxation of pre-existing deviatoric stress. Therefore, a dyke or a series of dyking events within ductile rocks could modify the stress conditions to the extent that the local least principal stress becomes vertical, which would thus force subsequent magma intrusions within this ductile region to form sills.

Ductile behaviour is also expected from partially solidified, or heated, successive magma pulses, as they accumulate in the same region. In this case, the emplacement of sills could be controlled by the presence of horizons separating crystal-poor from crystal-rich material with sills forming within the weakest ductile zones (Wiebe and Collins, 1998; Miller et al., this issue).

2.3. Rigidity anisotropy

However, in many and perhaps most cases, sills form within rocks that deform elastically instead of ductily. One possibility is that sills form because of a favourable crustal rigidity anisotropy. Many field studies show that when sills intrude sedimentary sequences they commonly abut stiff rock layers, thus suggesting that these rigid layers could have arrested the vertical propagation of the feeder dyke and encouraged sill formation. Examples include high rigidity sandstones, limestones, ancient lava flows and solid mushes of high-crystal content (Fridleifsson, 1977; Hyndman and Alt, 1987; Gudmundsson and Brenner, 2001; Holness and Humphreys, 2003; Miller et al., this issue).

Using analogue experiments with gelatine solids, Kavanagh et al. (2006) have tested this hypothesis. Their experiments show that under lithostatic conditions the formation of sills requires the presence of interfaces. However, the presence of an interface is not sufficient. The experiments show that sills could only form when their feeder encountered an interface that separates a rigid layer that overlies a less rigid, lower layer (Fig. 2). In the opposite case, where a less rigid layer lies on top of a more rigid one, feeders would not intrude the interface between the two layers but would instead cross-cut that interface and carry on their propagation as vertical dykes (Kavanagh et al., 2006).

Additionally, the properties of the interface itself can also have an important effect on whether a dyke would be deflected and intrude the interface. Theoretical analysis shows that whether an interface is intruded or crossed over depends on the elastic properties of the adjacent layers as well as the interface toughness relative to that of the upper layer, with stiffer upper layers favouring intrusion of the interface (He and Hutchinson, 1989; Gudmundsson, this issue). This analysis is supported by the analogue experiments of Kavanagh et al. (2006), who report instances where a dyke was expected to form a sill, because a rigid layer was overlying a less rigid layer, but instead was arrested by the interface without intruding the interface nor penetrating the upper layer; the interface was inferred to be too strong to be intruded by the dyke. Also, in the case of weak and shallow contacts, sill intrusion of these contacts could also occur by debounding whereby as a dyke approaches a weak contact, the tensile stress generated at the dyke tip is large enough to open up this contact and intrude it as a sill (the Cook–Gordon mechanism referred to by Gudmundsson (this issue).

2.4. Stress control

Sill formation can also result from adequate stress conditions. Igneous intrusions tend to propagate perpendicular to the least compressive stress (Anderson, 1951). Therefore, dykes are expected to form when the least compressive stress is horizontal, whereas sills should form when the least compressive stress is vertical. A corollary is that a transition from dyke to sill is expected when the minimum compressive stress rotates from being horizontal, such as in extension tectonic environment, to being vertical, which would be the case in a horizontally compressive stress field.

However, the orientation of an intrusion does not solely depend on the principal stress directions. It depends also on the magma overpressure, in that intrusions with higher overpressure need to propagate over greater distance before they can fully adjust their propagation to the principal directions (Mériaux and Lister, 2002). This is confirmed by recent analogue experiments which investigated the transition from dyke to sill as a result of a rotation of the deviatoric stresses (Menand et al., 2009). In these experiments, air was injected into a solid of gelatine that was then compressed laterally so that the minimum deviatoric compressive stress became vertical. Air acted as an analogue for buoyant magma, and the solid gelatine was used as an analogue for elastic crustal rocks. Air-filled cracks initially driven vertically by their buoyancy change their direction of propagation and ultimately form sills in response to the minimum compressive stress being vertical (Fig. 3). But this trajectory re-adjustment is not instantaneous. Cracks of higher buoyancy require greater distances to re-orient themselves fully, and they could reach the surface in spite of the vertical minimum compressive stress, and therefore not form sills, if these distances happen to be larger than that separating the intrusions from the surface (Menand et al., 2009).

Stress conditions favourable to sill formation can also result from the presence of layered elastic rocks. A multilayer subjected to horizontal compression, for instance, would result in the stiffest layers taking up most of the compressive stress, whereas if this multilayer

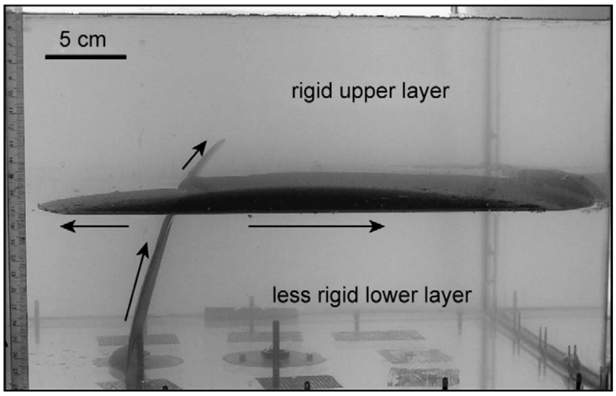

Fig. 2. A photograph of a rigidity-controlled sill formation (Kavanagh et al., 2006). The rigidity modulus of the upper layer was 10% larger than that of the lower layer. The feeder dyke propagated from the injection point toward the interface, reached it and then intruded the interface as a sill in both opposite directions from the point where the dyke intersected the interface. Note the protruding dykelet that extended beyond the interface and into the more rigid upper layer; this dykelet was short-lived and stalled whilst the sill continued propagating. The arrows indicate flow directions.

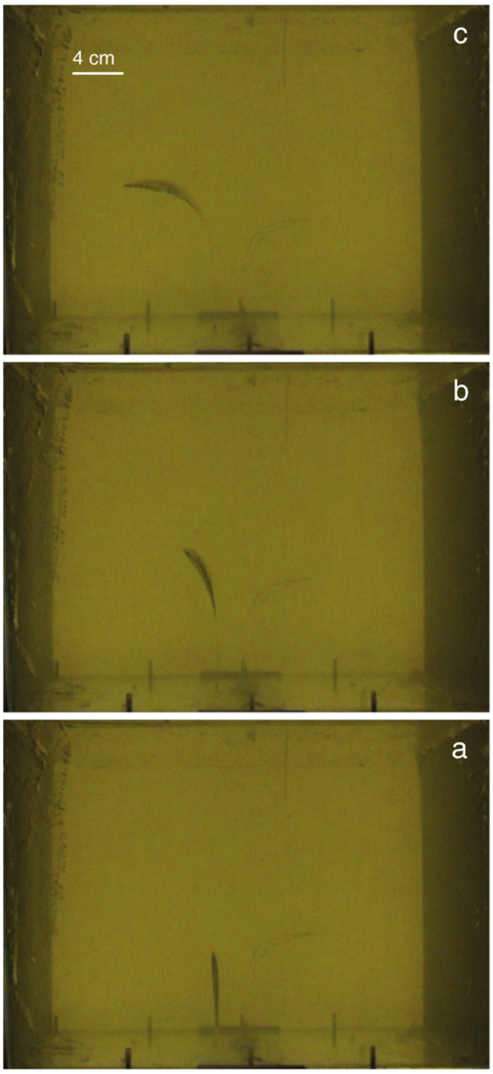

Fig. 3. A series of photographs of a stress-controlled sill formation (Menand et al., 2009). The ratio of initial crack buoyancy to horizontal compressive stress was 2.1. (a) The injection of air in the gelatine solid created a crack that was initially driven vertically by the air buoyancy. (b) The gelatine solid was compressed laterally, and so the crack experienced an additional horizontal compressive stress to which it reacted by changing its direction of propagation. (c) Ultimately, the crack rotated by 90° and formed a sill before coming to a stop.

were in horizontal extension, the softest layers would experience lower reduction in compressive stress and thus appear comparatively more compressive (Gudmundsson, 1986, 1990). Those layers where the minimum compressive stress becomes vertical would thus represent favourable horizons for sill intrusions.

3. Depth of emplacement: what are the controls?

Sills are expected to form in the crust owing to either favourable contrasts in mechanical or rheological properties, or favourable stress conditions. These different controls on sill formation, however, do not necessarily operate on the same length scale. In fact, the depth at which a sill forms will depend on which process is dominant, i.e. which process operates on the smallest length scale.

3.1. Rheology-contrast control

Field observations suggest that the formation of sills controlled by rheology contrasts and, by extension, the depth at which these sills are emplaced are likely to be determined by the distribution of the weakest ductile zones (Wiebe and Collins, 1998; Miller et al., this issue).

3.2. Rigidity-contrast control

The formation of sills through a rigidity-contrast control requires not only the presence of layers with different mechanical properties but also necessitates the presence of interfaces that separate more competent layers overlaying less rigid ones (Kavanagh et al., 2006; Gudmundsson, this issue). Therefore, the length scale associated with the presence of these specific interfaces is what determines the depth at which rigidity-controlled sills would form.

3.3. Stress control

In contrast, stress rotation can occur in homogeneous as well as heterogeneous solids. Stress rotation could occur in response to magma intrusion within an edifice (Roman et al., 2004, 2006) or owing to the load of an edifice itself (Pinel and Jaupart, 2004), for instance. Although the Earth's crust is highly heterogeneous, considering the homogeneous case is instructive because it reveals the length scale over which the effect of the stress-control alone operates. Considering the crust as homogeneous, sills would be expected to form within the crustal regions where the minimum compressive stress has been rotated vertically. In these specific regions, Menand et al. (2009) have shown that the depth at which sills form is determined by a balance between the horizontal maximum deviatoric compressive stress, which favours the formation of sills, and magma buoyancy, which drives magma vertically and thus opposes sill formation. This competition between maximum deviatoric compressive stress and buoyancy determines the length scale over which stress-controlled sill formation occurs.

Menand et al. (2009) applied dimensional analysis to their experimental data, which enabled them to relate the vertical distance, *d*, the buoyant crack needed to propagate before turning into a sill to the buoyancy of the crack and the horizontal maximum deviatoric compressive stress, σ_x. Upscaled to magmatic conditions over a range of reasonable geological values — tensile strength of homogeneous host rock $T_s = 1 - 10$ MPa, density difference between dyke and host rock $\Delta\rho = 100 - 500$ kg/m^3, and $\sigma_x = 0.1 - 100$ MPa — Menand et al. (2009) expressed the vertical distance, *d*, as

$$d \simeq \frac{T_s}{\Delta\rho g} \exp\left[(0.10 \pm 0.01)\frac{T_s}{\sigma_x}\right], \qquad (1)$$

where the dimensionless constant was determined by their dimensional analysis. (The reader is referred to Menand et al. (2009) for a more detailed account of how this equation was determined.) Their results show that in a homogeneous and elastic crust, and over this range of geological conditions, a dyke would have to travel a distance of the order of at least 200 m and in most cases of the order of 1 to 10 km to adjust to a vertical minimum compressive stress and turn into a sill (Menand et al., 2009).

This distance is typically greater than the average thickness of lithological units, and therefore suggests that in most cases crustal heterogeneities and the distance between interfaces that are favourable to sill intrusions will play a larger role than remote tectonic stress rotation in determining where in the crust sills form, unless these favourable interfaces are several hundred meters or more apart.

3.4. Level of neutral buoyancy

As discussed previously, neutral buoyancy alone is not expected to control sill formation, although it could arrest the vertical propagation of a rising buoyant dyke (Lister and Kerr, 1991; Pinel and Jaupart, 2004). However, overpressures large enough for sill intrusion could potentially develop provided high-density dykes manage to propagate far enough into low-density rocks (Taisne and Jaupart, 2009). Also, because a level of neutral buoyancy corresponds to the crustal level where a dyke is no longer buoyant and thus does not have any more internal vertical driving force, a dyke would become even more sensitive to horizontal compressive stress near its level of neutral buoyancy. So in principle, levels of magma neutral buoyancy could assist the formation of stress-controlled sills because, provided adequate stress conditions, levels of neutral buoyancy would represent advantageous horizons for sill emplacement.

3.5. Implications

In reviewing the processes that control the emplacement of sills and the length scales over which these processes operate, it appears that crustal heterogeneities are likely to play a dominant role. Heterogeneities can directly induce sill formation through rigidity or rheology anisotropy, but they can also interact with tectonic stresses and lead to sill-favourable conditions. The presence of a level of neutral buoyancy in a horizontal compressive stress field is one example. Interplay between stress field and heterogeneous crustal layers is another. Indeed, layered elastic rocks can lead to strong stress anisotropy, even in the case of isotropic remote stress, which would thus strengthen some strata relative to others (Gudmundsson, 1986; Gudmundsson and Brenner, 2001; Menand, 2008).

Better constraints on the geometry of crustal heterogeneities, their physical and rheological properties as well as the tectonic stresses that they experience are therefore crucial in order to improve our understanding of how and where sills form in the crust.

4. Sill amalgamation and the formation of plutons

4.1. Field evidences

Field evidences for pluton formation by sill amalgamation at mid-crustal levels or in the upper crust are numerous (e.g. John and Blundy, 1993; Horsman et al., 2005; Morgan et al., 2005; Belcher and Kisters, 2006; de Saint-Blanquat et al., 2006; Pasquarè and Tibaldi, 2007; Horsman et al., in press; Morgan et al., 2008). Although more scarce, field evidences of sills or magma pulses amalgamating to form plutons in the lower crust do also exist (Rutter et al., 1993; Quick et al., 1994). Additional, indirect evidences come from seismic studies of magma underplating that reveal an internal layering, suggestive of sills or sill-like igneous intrusions (Al-Kindi et al., 2003). It has also been proposed that underplating involving successive episodes of repeated sill injections and their subsequent cooling could generate episodes of surface uplift and subsidence, and thus explain the occurrence of rapid sea-level rises observed on very short time-scales (Maclennan and Lovell, 2002).

4.2. A mechanical model

Recently, Menand (2008) proposed a model for the growth of igneous bodies by vertical stacking of successive sills. This generic model is applicable to bodies of moderate to intermediate size, from sills to plutons (*sensu lato*) and including laccoliths. It would not be appropriate to larger bodies such as batholiths, however, as they seem to develop essentially by lateral growth, which would thus require another mechanism (Cruden and McCaffrey, 2006). This model is based on the experiments of Kavanagh et al. (2006), which show that in the absence of external stresses sills form at the interfaces between upper, rigid layers overlaying lower, weaker layers. From these experimental observations, it follows that if a sill forms owing to a favourable rigidity contrast then once this sill has solidified it will necessarily provide another interface with favourable rigidity contrast for the emplacement of a subsequent sill. Indeed, once solidified this sill will either become more rigid than the rocks beneath itself or, alternatively, less rigid than these rocks and thus less rigid than the rocks above itself. In either case, this solidified sill will provide a favourable site for the emplacement of another sill either beneath or above itself, respectively. Therefore, this model provides a mechanism for the vertical stacking of successive sills, and thus the formation and growth of laccoliths, by under- or over-accretion, or even by mid-accretion if favourable rigidity interfaces develop between adjacent sills.

The suggestion that laccoliths can develop and grow by the vertical stacking of individual and successive sills is in agreement with unequivocal field observations made in the Henry Mountains, Utah, and in Iceland (Hawkes and Hawkes, 1933; Horsman et al., 2005; Morgan et al., 2005; de Saint-Blanquat et al., 2006; Pasquarè and Tibaldi, 2007; Horsman et al., in press; Morgan et al., 2008; Tibaldi and Pasquarè, 2008). Moreover, it has also been proposed that laccoliths of different sizes could represent the various stages of pluton formation as one moves in time from sills to laccolith to larger pluton (Morgan et al., 2005; Horsman et al., in press), as illustrated in Fig. 4.

4.3. Implications

This mechanical model implies that laccolith formation does not necessarily requires a single episode of magma injection, with laccolith only forming by inflation of a single sill when it is able to lift up the overlying strata (Pollard and Johnson, 1973; Pollard and Holzhausen, 1979; Fialko et al., 2001). The complementary view is that laccoliths can also develop out of multiple, vertically-stacked pulses (Horsman et al., in press). The model could thus explain the formation of internally-layered laccoliths (Tibaldi and Pasquarè, 2008) and plutons (Benn et al., 1999; Miller et al., this issue), as well as Christmas-tree laccoliths (Westerman et al., 2004).

This model has also implications for the length scale of large igneous bodies. The lateral size of plutons growing by amalgamation of successive pulses or sills would essentially be of the same order of the length of the pulses that compose them. The pluton thickness, on the contrary, would be the cumulative thickness of all these pulses. This is in accord with field observations (Horsman et al., 2005; de Saint-Blanquat et al., 2006; Horsman et al., in press; Morgan et al., 2008), and would also explain why and how laccoliths, and to a lesser extend larger plutons (~10–100 km of lateral extend), tend to grow mainly by vertical expansion with comparatively little lateral propagation (Cruden and McCaffrey, 2006).

Another inference is that the time scale for the growth of laccoliths and larger plutons is much larger than the time scale associated with the successive magma injections. In fact, the time scale of pluton growth would mainly be the cumulative time that separates the individual pulses since, comparatively, the time for their emplacement is instantaneous (Cruden and McCaffrey, 2001). Therefore, in accord with field and geochronological data, larger plutons develop over much longer periods of time than smaller laccoliths and sills (de Saint-Blanquat et al., this issue). That the average rate of pluton construction is much smaller than the flux of individual magma injections is an important consideration for the thermal evolution of plutons (Annen, 2011-this issue).

5. Discussion and challenges

Our understanding of pluton construction has improved, leading to a better perception of how igneous bodies intrude into the crust. Pluton formation is now recognised as being an incremental, discontinuous process. This leads to new challenges for the interpretation of field observations, as well as fundamental questions about the mechanics of pluton emplacement and assembly that need to be fully addressed.

5.1. Geometry and structure of plutons

Incremental growth of plutons by amalgamation of repeated small magma pulses is mechanically more viable than plutons growing by

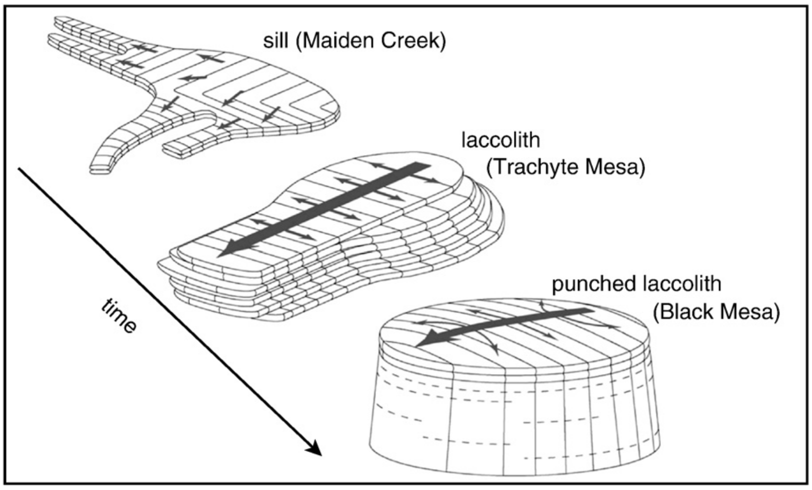

Fig. 4. Illustration of the evolution through time of an idealized upper crustal pluton, based on field observations in the Henry Mountains, Utah by Morgan et al. (2005) and Horsman et al. (in press). These intrusions would initiate as sills, then evolve into laccoliths, before becoming punched-laccoliths.

emplacement of larger magma volumes, and thus alleviates the space problem associated with pluton growth by overall inflation (e.g. Petford et al., 2000). Also, the growth of laccoliths by incremental stacking of igneous sheets enables to explain why and how their geometry depart from that of individual sills (Cruden and McCaffrey, 2006).

However, this also leads to new challenges when interpreting field observations and relating them to the processes involved during pluton construction. The relationship between tectonics and pluton emplacement, and their possible interactions, remain to be clarified (see for instance Allibon et al., this issue; de Saint-Blanquat et al., this issue). Another illustration is the recent and controversial view that stoping might not be a volumetrically significant process during pluton emplacement (Clarke and Erdmann, 2008; Glazner and Bartley, 2008a,b; Paterson et al., 2008; Yoshinobu and Barnes, 2008). New challenges arise when interpreting field observations because plutons growth is a discontinuous process. It involves a succession of processes, both in space and time, that do not necessarily operate at the same length- and time-scales. With time, and depending on the amount of magma that is emplaced and on the manner in which the host rocks accommodate this emplacement, these processes tend to overprint each other and become increasingly more cryptic as pluton volume increases (Glazner et al., 2004; Horsman et al., in press; Miller et al., this issue).

5.2. Rate of growth and igneous petrogenesis

Incrementally growing plutons reconcile the apparent contradicting requisites of rapid magma emplacement, to prevent its freezing on its way from source region to emplacement level, and overall formation over large periods of time (Petford et al., 2000; Glazner et al., 2004). This has also implications for the thermal evolution and differentiation of magmas. Indeed, the incremental injection of magma in a crustal region leads to a thermal evolution of that system that is fundamentally different from that associated with the emplacement of a single larger volume of magma, not only because magma, hence heat, is injected incrementally through time but also because of the way the pluton will evolve and grow, e.g. under- versus over-accretion (Annen et al., 2008; Annen, 2011-this issue), and also because of potential kinetics effects that could take place in the thinnest increments (Michaut and Jaupart, 2006, this issue).

There are also important implications for the relationship between plutonism and volcanism. Developing and maintaining a magma chamber active requires a delicate balance between the rate at which heat is accumulated within a region of the crust and that at which it is conducted away, so that a significant portion of the magmatic body could be eruptible (Gudmundsson, 1990). In fact, recent numerical simulations show that active magma chambers can only develop over a rather limited range of emplacement rates (Annen, 2009); lower rates would prevent magma chambers to develop whereas higher rates would lead to eruption and drainage of the magma chamber, which would then accelerate its cooling and solidification. This would be especially true for developing the large magma chambers needed to feed super-eruptions. Moreover, these results suggest that the growth of plutons would be a multi-timescale process with large magma chambers developing during episodes of highest magma flux, and that these transient magma chambers would only represent small portions of the pluton final volume (Annen, 2009). This in turn raises the issue of the magma fluxes associated with the construction of plutons (de Saint-Blanquat et al., this issue), and more specifically how these fluxes can be determined with enough accuracy over the various time-scales of pluton growth.

5.3. What is the impact on the local stress field?

One consequence of incremental pluton growth is that the local stress field is likely to change over time as subsequent pulses are assembled together. Although not yet fully quantified, this is likely to have an impact on the emplacement of subsequent pulses, with potentially the exchange of principal stresses and thus on the overall geometry of the pluton as it grows. Therefore, further studies need to concentrate on how the local stress field evolves during pluton growth and how this impacts on pluton development.

5.4. How does pluton growth affect the rheology of both host rocks and magmas?

Another and related issue that further studies need to address is that of the rheology of both the host rocks and the magma. As plutons form, heat accumulates within an increasingly larger crustal zone. How heat accumulates over time dictates the thermal evolution of magmas (Michaut and Jaupart, 2006; Annen et al., 2008). Therefore, this will also affect their rheology, how much magma solidifies and remains solid within a pluton or instead becomes fluid or forms a mush. This has strong implications on the manner with which successive pulses will amalgamate and thus on potential magma mixing or mingling (Miller et al., this issue).

As magma and heat are stored in a crustal region, the rheological properties of the host rock will also evolve. These rheological properties control how host rocks accommodate the deformation induced by pluton growth, and this response is coupled with the temperature of the rocks; cold rocks cannot sustain high emplacement rates without fracturing and thus promoting eruptions, whereas hotter rocks would instead behave in a more viscous manner and thus accommodate the associated deformation (Jellinek and DePaolo, 2003). Furthermore, the response of rocks will depend on the volume of the pluton, or the magma chamber, and therefore on how it grows over time because a given magma emplacement rate will induce comparatively lower deformation for a larger pluton (Jellinek and DePaolo, 2003). What remains difficult to assess, however, is how the rheological behaviour of the host rocks evolves during pluton growth, from initially being essentially elastic to gradually becoming more viscous, and how this affects the subsequent amalgamation of magma pulses (Marko and Yoshinobu, this issue).

Acknowledgements

I thank Michel de Saint-Blanquat and Eric Horsman for discussing at length the geology and formation of the Henry Mountains intrusions. I also acknowledge Michel de Saint-Blanquat for kindly providing Fig. 1 and Eric Horsman for providing the graphic material used in Fig. 4 of the present paper. This paper was greatly improved thanks to the constructive reviews of Michel de Saint-Blanquat, Agust Gudmundsson and Olivier Merle. This research was supported by a Leverhulme Trust research grant. Additional funding from the CNRS-INSU-3F PULSE 2008 grant is also acknowledged.

References

Al-Kindi, S., White, N., Sinha, M., England, R., Tiley, R., 2003. Crustal trace of a hot convective sheet. Geology 31, 207–210.

Allibon, J., Bussy, F., Léwin, E., Darbellay, B., 2011. The tectonically controlled emplacement of a vertically sheeted gabbro-pyroxenite intrusion: feeder-zone of an ocean-island volcano (Fuerteventura, Canary Islands). Tectonophysics 500, 78–97 (this issue).

Anderson, E.M., 1951. The Dynamics of Faulting and Dyke Formation with Applications to Britain (Second ed.). Oliver and Boyd Ltd., Edinburgh and London.

Annen, C., 2011. Implications of incremental emplacement of magma bodies for magma differentiation, thermal aureole dimensions and plutonism–volcanism relationships. Tectonophysics 500, 3–8 (this issue).

Annen, C., 2009. From plutons to magma chambers: thermal constraints on the accumulation of eruptible silicic magma in the upper crust. Earth Planet. Sci. Lett. 284 (3–4), 409–416.

Annen, C., Sparks, R.S.J., 2002. Effects of repetitive emplacement of basaltic intrusions on thermal evolution and melt generation in the crust. Earth Planet. Sci. Lett. 203, 937–955.

Annen, C., Blundy, J.D., Sparks, R.S.J., 2006. The genesis of intermediate and silicic magmas in deep crustal hot zones. J. Petrol. 47, 505–539.

Annen, C., Blundy, J.D., Sparks, R.S.J., 2008. The sources of granitic melt in deep hot zones. Trans. R. Soc. Edinburgh: Earth Sci. 97, 297–309.

Antonellini, M.A., Cambray, F.W., 1992. Relations between sill intrusions and bedding-parallel extensional shear zones in the Mid-continent Rift System of the Lake Superior region. Tectonophysics 202, 331–349.

Bedard, J.H., Sparks, R.S.J., Renner, M., Cheadle, M.J., Hallworth, M.A., 1988. Peridotite sills and metasomatic gabbros in the Eastern Layered Series of the Rhum complex. J. Geol. 145, 207–224.

Belcher, R.W., Kisters, A.F.M., 2006. Progressive adjustments of ascent and emplacement controls during incremental construction of the 3.1 Ga Heerenveen batholith, South Africa. J. Struct. Geol. 28, 1406–1421.

Benn, K., Roest, W., Rochette, P., Evans, N., Pignotta, G., 1999. Geophysical and structural signatures of syntectonic batholith construction: the South Mountain Batholith, Meguma Terrane, Nova Scotia. Geophys. J. Int. 136 (1), 144–158.

Cargill, H., Hawkes, L., Ledeboer, J., 1928. The major intrusions of south-eastern Iceland. Q. J. Geol. Soc. 84 (1–4), 505–539.

Cartwright, J., Hansen, D.M., 2006. Magma transport through the crust via interconnected sill complexes. Geology 34, 929–932.

Clarke, D.B., Erdmann, S., 2008. Is stoping a volumetrically significant pluton emplacement process? Comment. Geol. Soc. Amer. Bull. 120, 1072–1074.

Coleman, D.S., Gray, W., Glazner, A.F., 2004. Rethinking the emplacement and evolution of zoned plutons: geochronologic evidence for incremental assembly of the Tuolumne Intrusive Suite, California. Geology 32, 433–436.

Corry, C.E., 1988. Laccoliths: mechanics of emplacement and growth. Geol. Soc. Am. Spec. Pap. 220.

Cruden, A.R., 1998. On the emplacement of tabular granites. J. Geol. Soc. London 155, 853–862.

Cruden, A.R., McCaffrey, K.J.W., 2001. Growth of plutons by floor subsidence: implications for rates of emplacement, intrusion spacing and melt-extraction mechanisms. Phys. Chem. Earth (A) 26, 303–315.

Cruden, A.R., McCaffrey, K.J.W., 2002. Different scaling laws for sills, laccoliths and plutons: mechanical thresholds on roof lifting and floor depression. In: Breitkreuz, C., Mock, A., Petford, N. (Eds.), First International Workshop: Physical Geology of Subvolcanic Systems — Laccoliths, Sills, and Dykes (LASI), Volume 20 of Wissenschaftliche Mitteilungen des Institutes für Geologie der TU Bergakademie Freiberg, pp. 15–17.

Cruden, A.R., McCaffrey, K.J.W., 2006. Dimensional scaling relationships of tabular igneous intrusions and their implications for a size, depth and compositionally dependent spectrum of emplacement processes in the crust. EOS Trans. AGU 87 (52) Fall Meet. Suppl., Abstract V12B-06.

de Saint-Blanquat, M., Law, R., Bouchez, J., Morgan, S., 2001. Internal structure and emplacement of the Papoose Flat pluton: an integrated structural, petrographic, and magnetic susceptibility study. Bull. Geol. Soc. Am. 113 (8), 976–995.

de Saint-Blanquat, M., Habert, G., Horsman, E., Morgan, S.S., Tikoff, B., Launeau, P., Gleizes, G., 2006. Mechanisms and duration of non-tectonically assisted magma emplacement in the upper crust: the Black Mesa pluton, Henry Mountains, Utah. Tectonophysics 48, 1–31.

de Saint-Blanquat, M., Habert, G., Horsman, E., Law, R.D., Vanderaeghe, O., Morgan, S., Tikoff, B., this issue. Multiscale magmatic cyclicity, duration of pluton construction, and the paradoxical relationship between tectonism and plutonism in continental arcs. Tectonophysics.

Fialko, Y.A., Khazan, Y., Simons, M., 2001. Deformation due to a pressurized horizontal circular crack in an elastic half-space, with application to volcano geodesy. Geophys. Int. J. 146, 181–190.

Fridleifsson, I.B., 1977. Distribution of large basaltic intrusions in the Icelandic crust and the nature of the layer 2–layer 3 boundary. Geol. Soc. Amer. Bull. 88, 1689–1693.

Galerne, C.Y., Neumann, E.-R., Planke, S., 2008. Emplacement mechanisms of sill complexes: information from the geochemical architecture of the Golden Valley sill complex, South Africa. J. Volcanol. Geotherm. Res. 177 (2), 425–440.

Gilbert, G.K., 1877. Geology of the Henry Mountains, Utah. U.S. Geographical and Geological Survey of the Rocky Mountain Region.

Glazner, A.F., Bartley, J.M., 2008a. Is stoping a volumetrically significant pluton emplacement process? Geol. Soc. Amer. Bull. 118, 1185–1195.

Glazner, A.F., Bartley, J.M., 2008b. Reply to comments on “Is stoping a volumetrically significant pluton emplacement process?”. Geol. Soc. Amer. Bull. 120, 1082–1087.

Glazner, A.F., Bartley, J.M., Coleman, D.S., Gray, W., Taylor, R.Z., 2004. Are plutons assembled over millions of years by amalgamation from small magma chambers? GSA Today 14, 4–11.

Gretener, P.E., 1969. On the mechanics of the intrusion of sills. Can. J. Earth Sci. 6, 1415–1419.

Gudmundsson, A., this issue. Deflection of dykes into sills at discontinuities and magma-chamber formation. Tectonophysics. doi:10.1016/j.tecto.2009.10.015.

Gudmundsson, A., 1986. Formation of crustal magma chambers in Iceland. Geology 14, 164–166.

Gudmundsson, A., 1990. Emplacement of dikes, sills and crustal magma chambers at divergent plate boundaries. Tectonophysics 176, 257–275.

Gudmundsson, A., Brenner, S.L., 2001. How hydrofractures become arrested. Terra Nova 13, 456–462.

Harrison, M., Grove, M., Mckeegan, K., Coath, C., Lovera, O., Fort, P., 1999. Origin and episodic emplacement of the Manaslu intrusive complex, central Himalaya. J. Petrol. 40 (1), 3–19.

Hawkes, L., Hawkes, H.K., 1933. The Sandfell laccolith and “dome of elevation”. Q. J. Geol. Soc. London 89, 379–400.

He, M.Y., Hutchinson, J.W., 1989. Crack deflection at an interface between dissimilar elastic materials. Int. J. Solids Struct. 25 (9), 1053–1067.

Hinze, W., Bradley, J., Brown, A., 1978. Gravimeter survey in the Michigan basin deep borehole. J. Geophys. Res. 83 (B12), 5864–5868.

Holness, M.B., Humphreys, M.C.S., 2003. The Traigh Bhàn na Sgùrra sill, Isle of Mull: flow localization in a major magma conduit. J. Petrol. 44, 1961–1976.

Horsman, E., Tikoff, B., Morgan, S., 2005. Emplacement-related fabric and multiple sheets in the Maiden Creek sill, Henry Mountains, Utah, USA. J. Struct. Geol. 27, 1426–1444.

Horsman, E., Morgan, S., Saint-Blanquat (de), M., Habert, G., Nugent, A., Hunter, R.A., Tikoff, B., in press. Emplacement and assembly of shallow intrusions from multiple magma pulses, Henry Mountains, Utah. Earth and Environmental Science Transactions of the Royal Society of Edinburgh 100, 1–16. doi:10.1017/S175569100901608X.

Hutton, D.H.W., 1992. Granite sheeted complexes: evidence for the dyking ascent mechanism. Trans. R. Soc. Edinburgh: Earth Sci. 83, 377–382.

Hyndman, D.W., Alt, D., 1987. Radial dikes, laccoliths and gelatin models. J. Geol. 95, 763–774.

Jellinek, A.M., DePaolo, D.J., 2003. A model for the origin of large silicic magma chambers: precursors of caldera-forming eruptions. Bull. Volcanol. 65, 363–381.

John, B.E., 1988. Structural reconstruction and zonation of a tilted mid-crustal magma chamber: the felsic Chemehuevi Mountains plutonic suite. Geology 16, 613–617.

John, B.E., Blundy, J.D., 1993. Emplacement-related deformation of granitoid magmas, southern Adamello Massif, Italy. Geol. Soc. Amer. Bull. 105, 1517–1541.

Johnson, A.M., Pollard, D.D., 1973. Mechanics of growth of some laccolithic intrusions in the Henry Mountains, Utah, I. Field observations, Gilbert's model, physical properties and flow of the magma. Tectonophysics 18, 261–309.

Kavanagh, J.L., Menand, T., Sparks, R.S.J., 2006. An experimental investigation of sill formation and propagation in layered elastic media. Earth Planet. Sci. Lett. 245, 799–813.

Lister, J.R., Kerr, R.C., 1991. Fluid-mechanical models of crack propagation and their application to magma transport in dykes. J. Geophys. Res. 96, 10,049–10,077.

Maclennan, J., Lovell, B., 2002. Control of regional sea level by surface uplift and subsidence caused by magmatic underplating of Earth's crust. Geology 30, 675–678.

Marko, W.T., Yoshinobu, A.S., this issue. Using restored cross sections to disassemble a magma chamber: Construction of the White Horse pluton, eastern Nevada, USA. Tectonophysics.

McCaffrey, K.J.W., Cruden, A.R., 2002. Dimensional data and growth models for intrusions. In: Breitkreuz, C., Mock, A., Petford, N. (Eds.), *First International Workshop: Physical Geology of Subvolcanic Systems — Laccoliths, Sills, and Dykes (LASI)*, Volume 20 of *Wissenschaftliche Mitteilungen des Institutes für Geologie der TU Bergakademie Freiberg*, pp. 37–39.

Menand, T., 2008. The mechanics and dynamics of sills in elastic layered media and their implications for the growth of laccoliths. Earth Planet Sci. Lett. 267, 93–99.

Menand, T., Daniels, K., Benghiat, P., (2009). Dyke propagation and sill formation in a compressive tectonic environment. J. Geophys. Res. sub judice.

Mériaux, C., Lister, J.R., 2002. Calculation of dike trajectories from volcanic centers. J. Geophys. Res. 107 (B4). doi:10.1029/2001JB000436 2077.

Michaut, C., Jaupart, C., 2006. Ultra-rapid formation of large volumes of evolved magma. Earth Planet. Sci. Lett. 250, 38–52.

Michaut, C., Jaupart, C., this issue. Two models for the formation of magma reservoirs by small increments. Tectonophysics, 1–16. doi:10.1016/j.tecto.2009.08.019.

Michel, J., Baumgartner, L., Putlitz, B., Schaltegger, U., Ovtcharova, M., 2008. Incremental growth of the Patagonian Torres del Paine laccolith over 90 ky. Geology 36 (6), 459–462.

Miller, C.F., Furbish, D.J., Walker, B.A., Claiborne, L.L., Koteas, G.C., Bleick, H.A., Miller, J.S., this issue. Growth of plutons by incremental emplacement of sheets in crystal-rich host: evidence from Miocene intrusions of the Colorado River region, Nevada, USA. Tectonophysics, 1–13. doi:10.1016/j.tecto.2009.07.011.

Morgan, S.S., E. Horsman, B. Tikoff, M. de Saint-Blanquat, and G. Habert (2005). Sheet-like emplacement of satellite laccoliths, sills and bysmaliths of the Henry Mountains, Southern Utah. In J. Pederson and C. M. Dehler (Eds.), *Interior Western United Sates*, Volume 6 of *Geological Society of America Field Guide*. doi:10.1130/2005.fld006(14).

Morgan, S.S., Stanik, A., Horsman, E., Tikoff, B., de Saint-Blanquat, M., Habert, G., 2008. Emplacement of multiple magma sheets and wall rock deformation: Trachyte Mesa intrusion, Henry Mountains, Utah. J. Struct. Geol. 30, 491–512.

Mudge, M.R., 1968. Depth control of some concordant intrusions. Geol. Soc. Amer. Bull. 79, 315–332.

Parsons, T., Sleep, N.H., Thompson, G.A., 1992. Host rock rheology controls on the emplacement of tabular intrusions: implications for underplating of extending crust. Tectonics 11, 1348–1356.

Pasquarè, F., Tibaldi, A., 2007. Structure of a sheet-laccolith system revealing the interplay between tectonic and magma stresses at Stardalur Volcano, Iceland. J. Volcanol. Geotherm. Res. 161, 131–150.

Paterson, S.R., Pignotta, G.S., Farris, D., Memeti, V., Miller, R.B., Vernon, R.H., Žák, J., 2008. Is stoping a volumetrically significant pluton emplacement process? Discussion. Geol. Soc. Amer. Bull. 120, 1075–1079.

Petford, N., Cruden, A.R., McCaffrey, K.J.W., Vigneresse, J.L., 2000. Granite magma formation, transport and emplacement in the Earth's crust. Nature 408, 669–673.

Petraske, A., Hodge, D., Shaw, R., 1978. Mechanics of emplacement of basic intrusions. Tectonophysics 46 (1–2), 41–63.

Pinel, V., Jaupart, C., 2004. Magma storage and horizontal dyke injection beneath a volcanic edifice. Earth Planet. Sci. Lett. 221, 245–262.

Pollard, D.D., Holzhausen, G., 1979. On the mechanical interaction between a fluid-filled fracture and the Earth's surface. Tectonophysics 53, 27–57.

Pollard, D.D., Johnson, A.M., 1973. Mechanics of growth of some laccolithic intrusions in the Henry Mountains, Utah, II. Bending and failure of overburden layers and sills formation. Tectonophysics 18, 311–354.

Quick, J.E., Sinigoi, S., Mayer, A., 1994. Emplacement dynamics of a large mafic intrusion in the lower crust, Ivrea–Verbano Zone, northern Italy. J. Geophys. Res. 99, 21,559–21,573.
Roman, D.C., Moran, S.C., Power, J.A., Cashman, K.V., 2004. Temporal and spatial variation of local stress fields before and after the 1992 eruptions of Crater Peak Vent, Mount Spurr volcano, Alaska. Bull. Seismol. Soc. Am. 94, 2366–2379.
Roman, D.C., Neuberg, J., Luckett, R.R., 2006. Assessing the likelihood of volcanic eruption through analysis of volcano tectonic earthquake fault plane solutions. Earth Planet. Sci. Lett. 248, 244–252.
Rutter, E.H., Brodie, K.H., Evans, P.J., 1993. Structural geometry, lower crustal magmatic underplating and lithospheric stretching in the Ivrea–Verbano zone, northern Italy. J. Struct. Geol. 15, 647–662.
Taisne, B., Jaupart, C., 2009. Dike propagation through layered rocks. J. Geophys. Res. 114 (B9), B09203.
Thomson, K., 2007. Determining magma flow in sills, dykes and laccoliths and their implications for sill emplacement mechanisms. Bull. Volcanol. 70, 183–201.
Thomson, K., Hutton, D., 2004. Geometry and growth of sill complexes: insights using 3D seismic from the North Rockall Trough. Bull. Volcanol. 66, 364–375.
Tibaldi, A., Pasquarè, F.A., 2008. A new mode of inner volcano growth: the "flower intrusive structure". Earth Planet. Sci. Lett. 271, 202–208.
Vigneresse, J.L., Bouchez, J.L., 1997. Successive granitic magma batches during pluton emplacement: the case of Cabeza de Araya (Spain). J. Petrol. 38, 1767–1776.
Westerman, D., Dini, A., Innocenti, F., Rocchi, S., 2004. Rise and fall of a nested Christmas-tree laccolith complex, Elba Island, Italy. In: Breitkreuz, C., Petford, N. (Eds.), Physical Geology of High-Level Magmatic Systems, Geol. Soc., Lond., Spec. Publ. 234, 195–213.
Wiebe, R.A., Collins, W.J., 1998. Depositional features and stratigraphic sections in granitic plutons: implications for the emplacement and crystallization of granitic magma. J. Struct. Geol. 20, 1273–1289.
Yoshinobu, A.S., Barnes, C.G., 2008. Is stoping a volumetrically significant pluton emplacement process? Discussion. Geol. Soc. Amer. Bull. 120, 1080–1081.

The shapes of dikes: Evidence for the influence of cooling and inelastic deformation

Katherine A. Daniels[1,†], Janine L. Kavanagh[2], Thierry Menand[3,4,5], and R. Stephen J. Sparks[1]
[1]*School of Earth Sciences, University of Bristol, Wills Memorial Building, Queen's Road, Bristol BS8 1RJ, UK*
[2]*School of Geosciences, Monash University, Clayton Campus, Wellington Road, Clayton, Victoria 3800, Australia*
[3]*Clermont Université, Laboratoire Magmas et Volcans, Université Blaise Pascal, BP 10448, F-63000 Clermont-Ferrand, France*
[4]*Centre National de la Recherche Scientifique, UMR 6524, Laboratoire Magmas et Volcans, F-63038 Clermont-Ferrand, France*
[5]*Institut de Recherche pour le Développement, R 163, Laboratoire Magmas et Volcans, F-63038 Clermont-Ferrand, France*

ABSTRACT

We provide detailed observations on the shape of dikes from well-exposed field locations in the Isle of Rum, Scotland, and Helam Mine, South Africa. The basaltic Rum dikes crop out on a smaller scale than the Helam kimberlite dikes and have a smaller length to thickness ratio (~100:1 Isle of Rum, ~1000:1 Helam Mine). We compare the dike thickness field measurements with the geometry predicted by elastic theory, finding best-fit models to estimate magma overpressure and regional stress gradients at the time of dike emplacement. Most of the dike shapes fit poorly with elastic theory, being too thick at the dike ends and too narrow in the middle. Even for dikes where the model fit is acceptable, the calculated overpressures and stress gradients are very large and much larger than independent estimates based on rock strength, particularly for the small-scale basaltic dikes on Rum, where calculated overpressures average 687 MPa, and calculated stress gradients average 622 MPa m^{-1}. The Swartruggens dikes have calculated overpressures of between 4 and 40 MPa and calculated stress gradients in the range of 15–87 kPa m^{-1}. Dike shape can be explained by a combination of host-rock inelastic deformation prior to and coeval with magma emplacement, and by magma chilling at the dike's tapering edges, which prevented its closure as magma pressure declined during emplacement; this sequence provides the most complete explanation for the mismatches between the data and the model. The permanent wedging of the dike edges due to chilling has implications for crustal magma transport and strain response in the crust due to dike emplacement.

INTRODUCTION

Dikes are the end result of the flow of pressurized magma through fractures, recording a fundamental mechanism of magma transport through the crust. Dike shapes reflect the integration of complex emplacement and eruption processes, where host-rock deformation, magma viscosity, magma pressure variations, stress distribution, and heat transfer all play a role. Many theoretical and experimental studies of dike emplacement have emphasized elastic deformation by pressurized magma-filled fractures (e.g., Gudmundsson, 1983; Lister and Kerr, 1991; Kerr and Lister, 1995; Rubin, 1995; Menand and Tait, 2001, 2002; Ray et al., 2007; Menand et al., 2010).

The shape of a preserved solidified dike can be used to calculate the pressure in the crack at the time of solidification, assuming that the shape reflects a simple elastic deformation control with fixed overpressure. Previous studies of dike shape have involved the measurement of dike thicknesses in the field, and the observed dike cross-sectional profiles have been compared with elastic models in order to estimate the driving pressures and stress gradients at the time of emplacement (Pollard and Muller, 1976; Delaney and Pollard, 1981; Rubin and Pollard, 1987; Poland et al., 2008; Geshi et al., 2010; Kavanagh and Sparks, 2011). Others have used theoretical numerical models to interpret the evolution of dike thickness. Buck et al. (2006) found that the stopping pressure of a dike (the point where the difference between the magma pressure and the tectonic stress [the driving pressure] at the dike tip becomes too small to propagate the dike) is proportional to its thickness. They also found that the propagation distance is dependent on the initial distribution of tectonic stress and that dike intrusions affect the tectonic stress distribution, therefore affecting the propagation of subsequent dikes. Gudmundsson (2011) suggested that dike arrest is dependent on a number of factors, including the size of the process zone (a region of highly fractured host rock formed ahead of the propagating intrusion; see, for example, White et al., 2011) and the fracture toughness of both the host rock itself and the interfaces between rock units. As a consequence, two dikes with the same overpressure could have quite different thicknesses.

We document the shapes of well-exposed examples of basaltic dikes from the Isle of Rum, Scotland, and kimberlite dikes from Helam Mine, South Africa. First, we describe the geological settings of the dikes and present detailed dike thickness data sets. We then summarize the theoretical framework used to assess the extent to which elastic deformation can describe dike shape. We find that the shapes of most of the dikes have a poor fit with that expected from elastic theory and propose that the shapes can be explained by including the complicating effects of magma chilling at the dike's tapering edges and host-rock inelastic deformation.

Our observations have implications for understanding the development of dikes as conduits and for the effects of dikes on transient stresses and crustal strain. Through the permanent wedging open of the crust by chilled dike edges, a dike can act as a potential conduit for longer, increasing the longevity of eruptions. In addition, the crustal strains implicit in dike emplacement reflect not only responses to tectonic stress but also magma overpressures preserved at the dike edges by chilling.

GEOLOGICAL SETTINGS

Basaltic Dikes from the Isle of Rum

Situated off the west coast of Scotland, the Isle of Rum represents the eroded remnants of a shallow-level igneous complex emplaced into Torridonian Precambrian sandstone at ~2–3 km depth (e.g., Emeleus, 1997; Nicoll et al., 2009).

[†]E-mail: k.a.daniels@bristol.ac.uk

GSA Bulletin; July/August 2012; v. 124; no. 7/8; p. 1102–1112; doi: 10.1130/B30537.1; 9 figures; 1 table.

Rum's igneous rocks include layered basic and ultrabasic intrusions, granophyres, volcanic rocks ranging from rhyolite to picrite, and hypabyssal intrusions (Emeleus, 1997). The focus of this study is a late stage NW- to NNW-striking basaltic dike swarm (Emeleus, 1997) dated to 60.53 ± 0.08 Ma (Hamilton et al., 1998). The Isle of Rum and the dike measurement locations are shown in Figures 1A and 1B.

A dike length and thickness data set was compiled. The length of each of the dikes selected was measured using a tape measure; only dikes with crack tips exposed at both ends were selected for measurement. The thickness of the dike was then measured at regular intervals. For the majority of the dikes, this was done by hand in the field. For a few of the largest dikes measured, this was done using scaled photographs. All measured thicknesses were then corrected for the dip angle of the dike to give the true thickness. In total, 1068 thickness measurements along the length of 41 dikes are presented; some of these are thought to be en echelon segments of a single dike; for simplicity, we treat each segment individually as if they were separate dikes, referring to them as dikes rather than dike segments. We will address this simplification later on in the Discussion section. The Isle of Rum dikes have a thickness:length ratio ranging from 1:11 to 1:449, with an average of 1:56. The measured lengths range between 0.08 and 47.6 m; the measured thicknesses range between 0.007 m and 0.62 m, with an average maximum thickness of 0.052 m. For most dikes, the thickness measurements are accurate to ~2 mm. The largest dikes have thicknesses that are accurate to within 5 mm, and lengths that are accurate to the nearest 0.05 m. The smallest dikes are likely to be part of a segmented dike, or offshoots from a larger dike, and are not expected to have traveled far. The dikes intruded contact metamorphosed Torridonian sandstone. Most dikes show pronounced chilled margins of at least a few millimeters perpendicular to the surface of the contact (Fig. 2A), and many show internal cooling fractures (Fig. 2B). Many Rum dikes exhibit crack tips infilling with sediment (Fig. 2A), and some show branching. Most dikes crosscut preexisting bedding and joints, or are themselves affected by postemplacement jointing (Fig. 2B). Few dikes have joint-controlled orientations (Fig. 2C), and those affected by a previous joint set were not included in the analysis. Occasional host-rock inclusions are seen (Fig. 2B).

Swartruggens Kimberlite Dike Swarm

The Swartruggens kimberlite dike swarm, Helam Mine, South Africa, consists of three dikes, two kimberlites (Main and Changehouse dikes) and a lamprophyre (Muil dike). The dikes were intruded at the end of the Jurassic (Allsopp and Barrett, 1975; Phillips, 1991; Gurney and Kirkley, 1996) and cut a stratigraphy composed of dolerite, quartzite, shale, and andesite lava from the Proterozoic Pretoria Group, central Kaapvaal craton. The estimated magma emplacement depth is 2–3 km (Brown et al., 2007). Mine excavations extend to 750 m deep and give a three-dimensional view of the structure of the kimberlite dikes. We present a unique data set of 683 dike thickness measurements from levels 16–21 of John's dike segment and 704 dike thickness measurements from levels 19–22 of Edward's dike segment. The measurements were made by hand using a tape measure by a number of geologists systematically since the mine has been active. A simplified diagram of the field relationships of these dike segments is shown in Figures 3A and 3B.

The Main dike consists of a series of anastomosing en echelon segments extending 7 km (Basson and Viola, 2003). The dike segments trend approximately east-west with a thickness:length ratio of ~1:1000; each segment strikes ~1 km in length and has a mean thickness of 0.64 m (Kavanagh, 2010; Kavanagh and Sparks, 2011). The measurements made of dike thickness are accurate to the nearest 0.05 m. The lateral extent of the mined excavation is used as a proxy for the breadth of the dike, as this closely follows the dike geometry; the errors associated with this measurement are estimated at less than 10 m. Breccia zones up to several tens of meters wide occur in the regions between dike segments, where centimeter-sized angular country rock fragments have formed (Brown et al., 2007). These fragments occur as inclusions within the kimberlite. Spheroidally weathered dolerite is associated with breccia zones and centimeter-thick dike-parallel fracture zones that occur in the host rock at the dike margins (Brown et al., 2007). The country rock away from the dike is unbrecciated, lacking closely spaced fracturing and spheroidal weathering.

The Swartruggens dikes are not thought to be controlled by preexisting fractures, having instead created and intruded their own fractures during ascent. The host rock is jointed, shows no dominant orientation, and is brecciated, especially near the fracture tips, and there is evidence for stoping (Brown et al., 2007). Chilled margins were not recognized in the Swartruggens dikes; they likely exist but are obscured by postemplacement serpentinization. Closely spaced host-rock fracturing, predominantly subparallel to the dike contact, is pervasive in the vicinity (0.1–1 m) of the Swartruggens dike margins.

THEORETICAL FRAMEWORK AND COMPARISON WITH FIELD DATA

Elasticity theory (e.g., Timoshenko and Goodier, 1970; Landau and Lifshitz, 1986) describes the two-dimensional shape of a fluid-filled fracture subjected to a stress field in a homogeneous and isotropic material (Sneddon, 1946; Pollard and Muller, 1976):

$$\begin{aligned} u_y &= \frac{l\sin\theta}{2G}\left[\left(P_0 - S_{y0}\right)(1-\nu)\right] \\ &= \frac{l\sin\theta}{2G}\left[(\Delta P)(1-\nu)\right] \equiv \mathrm{A}\sin\theta, \end{aligned} \tag{1}$$

$$\begin{aligned} u_y &= \frac{l^2\sin 2\theta}{16G}\left[\left(\nabla P - \nabla S_y\right)(1-\nu)\right] \\ &\equiv \mathrm{B}\sin 2\theta, \end{aligned} \tag{2}$$

where l and u_y are the crack length and displacement, θ is the angular position along the slit from the crack center, G is the elastic shear modulus, P_0 and S_{y0} are the magma pressure and regional stress normal to the crack, ΔP is the excess magma pressure $P_0 - S_{y0}$, ν is the host rock's Poisson's ratio, ∇P is the magma pressure gradient along the crack, ∇S_y is the regional normal stress gradient along the crack, and A and B are constants. Model parameter values are given in the caption to Figure 4.

The overall displacement of the margins of the fluid-filled crack is the result of a summation of both Equations 1 and 2. Equation 1 gives the displacement due to the application of a uniform internal pressure with no gradient in regional stress, while Equation 2 gives the displacement as a result of a linear gradient along the dike length as the difference between the regional stress and magma pressure. Models including a constant driving pressure plus a gradient in driving pressure or regional stress along the dike length will create a dike profile with a teardrop shape (Pollard, 1987). Asymmetrical dike profiles have been attributed to gradients in magma pressure or regional stress, with the magnitude of asymmetry being controlled by the length of fracture, overpressure, and effective stress gradient (Pollard and Muller, 1976).

We analyzed dike thickness measurements from the two data sets using the method of Pollard and Muller (1976). Equations 1 and 2 were iterated through 10,000 permutations of A and B to estimate the best parameter values that minimize the least-squares misfit between the model and the observations. Overpressures and linear stress gradients were estimated from the best-fit models. The estimated values of overpressure and linear stress gradient were then used as a reference for comparison with the field data.

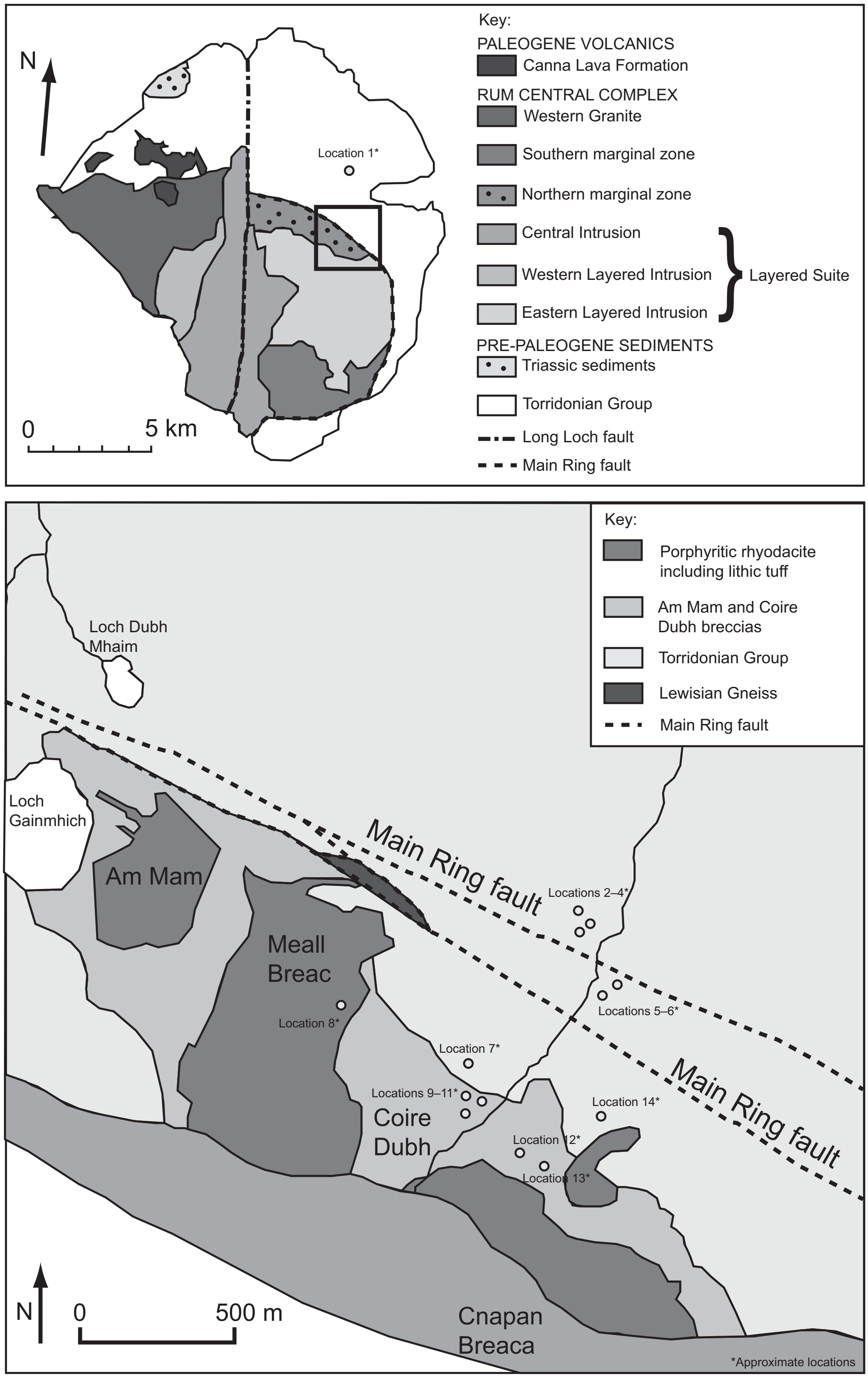

Figure 1. Generalized geological maps of the isle of Rum with each of the dike measurement localities highlighted.

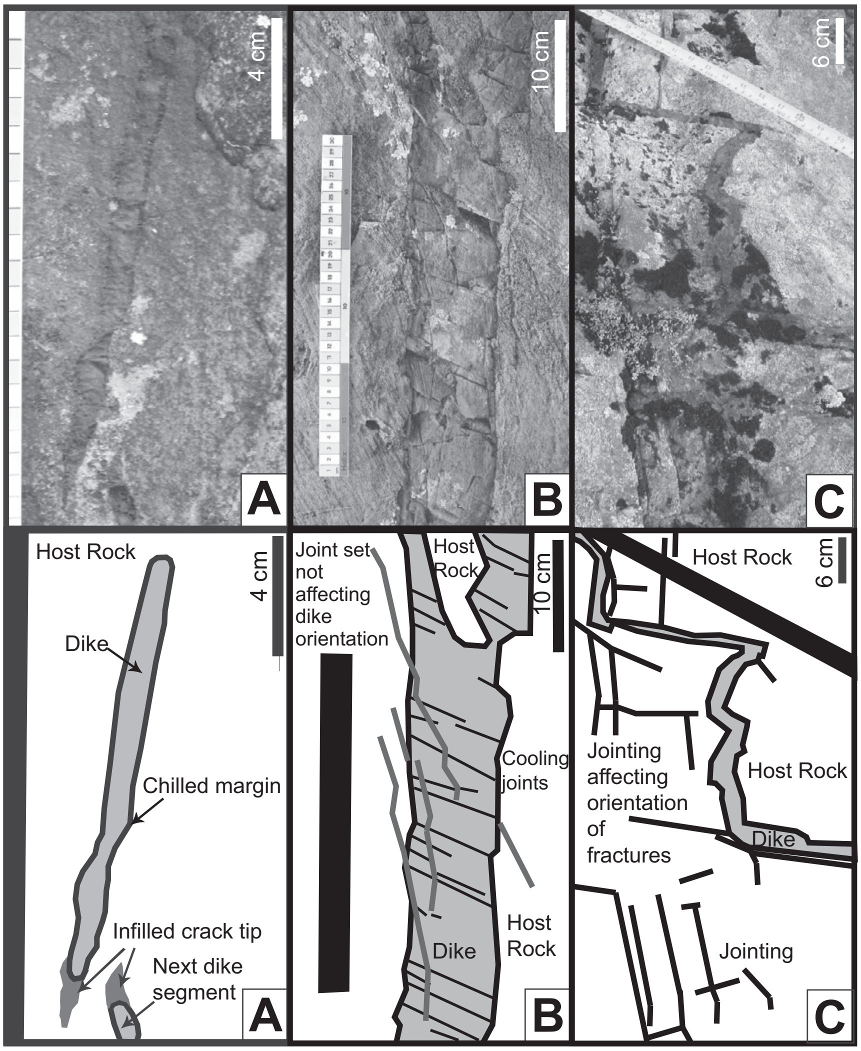

Figure 2. Photographs and sketches of Rum dikes. (A) Plan view of dike with crack tips showing pronounced chilled margins. One crack tip shows infilling with sediment. There is overlap between dike segments; one segment shows an apparent skew. (B) Dike orientation unaffected by secondary jointing. (C) Joint affected dike orientation.

These equations were then used to generate a model to fit the shape of an observed solidified magma-filled crack. By interpreting the static shape, the assumption has been made that the fluid-filled crack had reached a static equilibrium and that flow effects as solidification occurred can be neglected.

SHAPES AND THICKNESSES OF THE DIKES

Figure 4 shows examples of representative dike profiles for Rum and Swartruggens as horizontal cross-sectional slices. It is assumed that the cross-sectional profile of the dikes at each field locality is approximately horizontal. The best-fitting elastic model is shown as the solid black line. Overpressures estimated from the models range from 37 to 1990 MPa, averaging 678 MPa (R^2 = 0.389–0.997, average = 0.921) for Rum, and from 4 to 40 MPa (R^2 = 0.50–0.72) for Swartruggens (Table 1). Estimated regional stress gradients for the Rum dikes estimated from the theory are up to 3 GPa m^{-1}, averaging 622 MPa m^{-1}, and range from 15 to 87 kPa m^{-1} for Swartruggens (Table 1). A comparison of the values of overpressure and stress gradient estimated for the Rum and Swartruggens dikes with values obtained by previous studies is also given in Table 1.

The range of R^2 values for the best-fit models indicates that many of the dike segments do not fit the elastic model well. In Figure 4, the data have been normalized (L*) to the overall length of each dike, giving the tips at –0.5 and +0.5. This normalization procedure allows us to compare the dikes of different length scales, and to compare all the data with the elastic model in one diagram.

In Figures 5A to 5D, all thickness measurements have been referenced to the model fit, which is plotted as a horizontal line in the normalized coordinates to show departures in dike thickness from the model. Figures 5C and 5D show the same graphs as Figures 5A and 5B but with a larger scale on the *y*-axis. Negative *y*-axis values indicate a dike that is thicker than predicted by the model, while positive values show a dike that is thinner than predicted. Frequency histograms of the difference between the modeled thickness and the measured thickness for the Rum and Swartruggens dikes are shown in Figures 5E and 5F, respectively. For both localities, the distribution of the data from the central portions of the dikes (L* = –0.3–0.3; gray bars) is positively offset from 0 on the *x*-axis, while the distribution of the data from the edge portions of the dikes (L* < –0.3 and > 0.3; black bars) is negatively offset from 0 on the *x*-axis. The mean average difference between the model and the measured data in the central portion is 0.11 for the Rum data and 0.02 for the Swartruggens data, while for the edges, the difference is –0.10 for the Rum data and –0.29 for the Swartruggens data. The Rum and Swartruggens dikes both show, irrespective of goodness of fit, that dikes strongly tend to be thicker than expected by the model at their edges and thinner than expected in their centers.

Our data show that dike segments are commonly asymmetrical about their length midpoint. In plan view, the Swartruggens dikes and many Rum dikes are skewed, so the point of maximum thickness is not at the dike center (e.g., Fig. 4B). We quantified dike asymmetry (δ) by comparing the best-fit model center with the dike's normalized length midpoint: a δ of 0 is symmetrical, and 0.5 is maximum possible asymmetry. For the Rum dikes, δ ranges from 0 to 0.47 (average 0.142, standard deviation [s.d.] 0.110); for the Swartruggens dike, δ ranges from 0.087 to 0.203 for John's segment (average 0.154, s.d. 0.054), and from 0.179 to 0.242 (average 0.205, s.d. 0.031) for Edward's segment. The Rum dikes have a broader range of δ values; some dikes show extreme asymmetry. The Swartruggens dikes are more skewed than the Rum dikes with less variation in δ. We found no

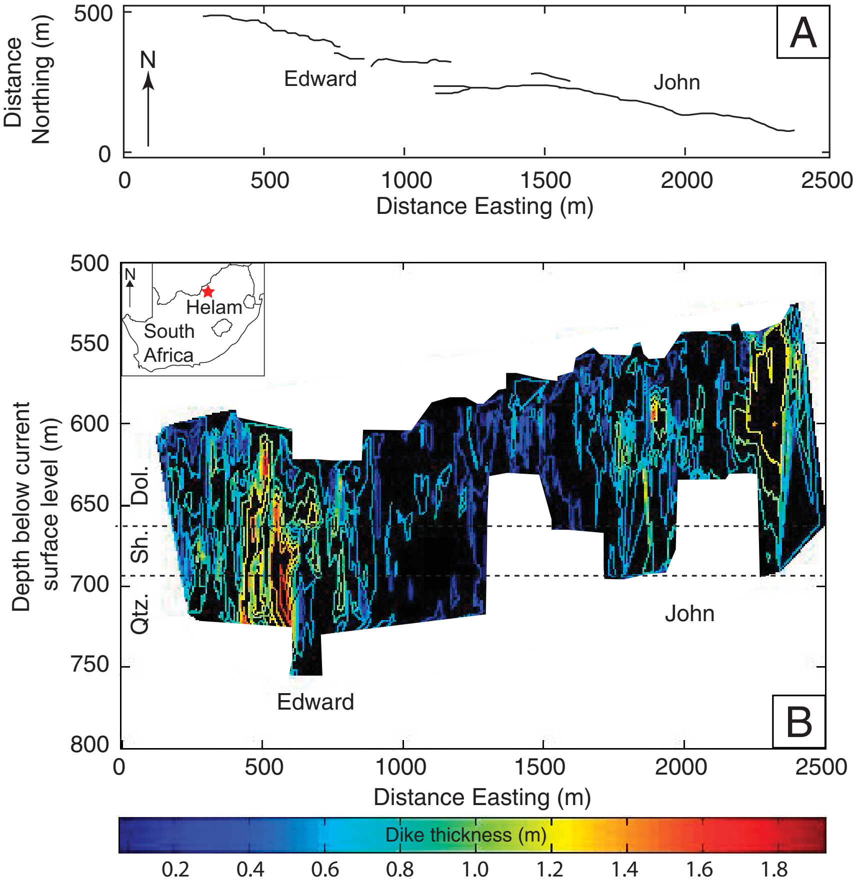

Figure 3. (A) Surface outcrop map of the John and Edward kimberlite dike segments, Helam Mine, South Africa. (B) Contour plot of dike thickness for the John and Edward dike segments plotted against depth below the current surface and distance easting. The shaded area indicates locations where data were collected. The approximate stratigraphy and unit contacts (dashed line) are shown: quartzite (Qtz), shale (Sh), and dolerite (Dol). The map inset indicates the location of Helam Mine in southern Africa (25.594°S, 26.659°E).

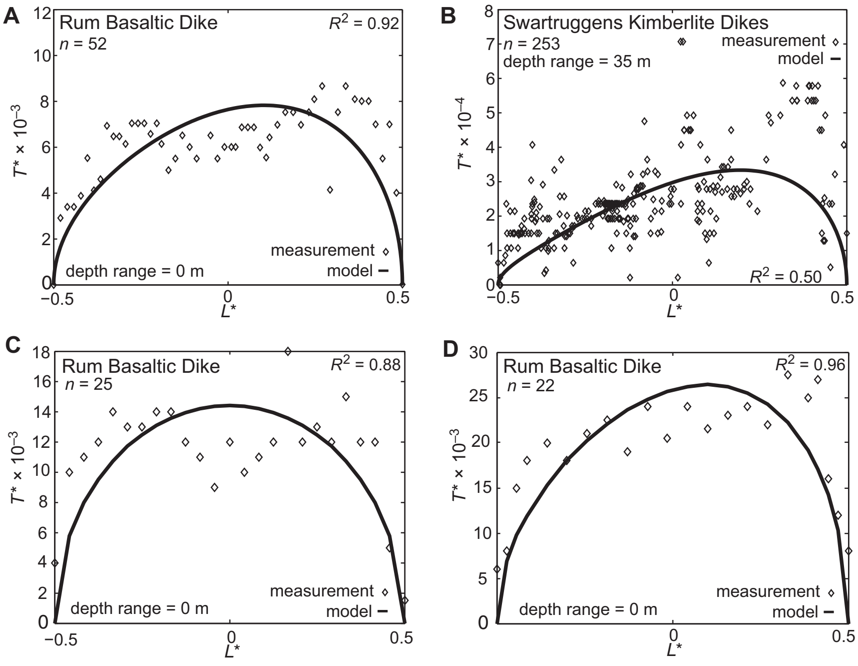

Figure 4. Thickness versus length profile of Rum (Figs. 3A, 3C, and 3D) and Swartruggens (John's dike segment, 18th level) (Fig. 3B) dikes. A best-fit model (line) is plotted through the data (diamonds). Both data sets show asymmetrical dike thicknesses, with fatter edges and thinner middles compared to the elastic model. Best-fit model parameter values are: (A), (C), and (D) G = 15.4 GPa (Khazanehdari and Sothcott, 2003), ν = 0.215 (Domenico, 1983), Δ*P* = 367 MPa, and ∇*P* = 48 MPa m^{-1}; (B) G = 40 GPa, Δ*P* = 34 MPa, and ∇*P* = 65 kPa m^{-1}. *L is the along-dike distance normalized by the dike length, and *T** is the half-thickness normalized by the dike length.**

TABLE 1. ESTIMATED VALUES FOR DRIVING PRESSURE ($P_0 - S_{y0}$) AND STRESS GRADIENT ($\nabla P - \nabla S_y$) FOR RUM AND SWARTRUGGENS DIKES (THIS STUDY), NONFEEDER DIKES AT MIYAKEJIMA VOLCANO (GESHI ET AL., 2010), SILICIC DIKES AT SUMMER COON VOLCANO (POLAND ET AL., 2008), AND WALSEN DIKE AND THEATRE CANYON SILL (POLLARD AND MULLER, 1976)

Intrusive body	Number of observations	$P_0 - S_{y0}$ (MPa)	$\nabla P - \nabla S_y$ (kPa m^{-1})
Rum dikes	784	37–1990	0–3 × 10^6
Swartruggens dikes	1387	4–40	15–87
Miyakejima volcano	>88	7–12	–
Summer Coon volcano	238	4.6–148.3	0.003–0.133
Walsen dike	256	0.35–4.8	–0.052 to –0.71
Theatre Canyon Sill	44	3.6–50	–8.4 to –12

correlation between asymmetry and dike size. Neighboring segments commonly show asymmetry in alternating directions, which may be the result of compression as one dike segment influences the next one (e.g., Pollard et al., 1982; Roman and Cashman, 2006).

DISCUSSION

We first discuss dike segmentation and our simplified analysis before discussing the two kinds of mismatch we found between the elastic theory and the observations: estimated overpressure and stress gradient values are implausibly high, and dikes are systematically thicker at the edges and thinner in the middle.

Segmented Dikes

Some of the dikes measured on Rum are individual dikes (4) (Fig. 6A), while others are segments of a larger dike (37) (Fig. 6B). The Swartruggens dikes are segments of a larger regional intrusion. Previous workers have treated segmented dikes as individual intrusions, and they have modeled the segments together as one intrusion (e.g., Pollard and Muller, 1976; Delaney and Pollard, 1981; Baer, 1991; Poland et al., 2008). Dike segmentation commonly

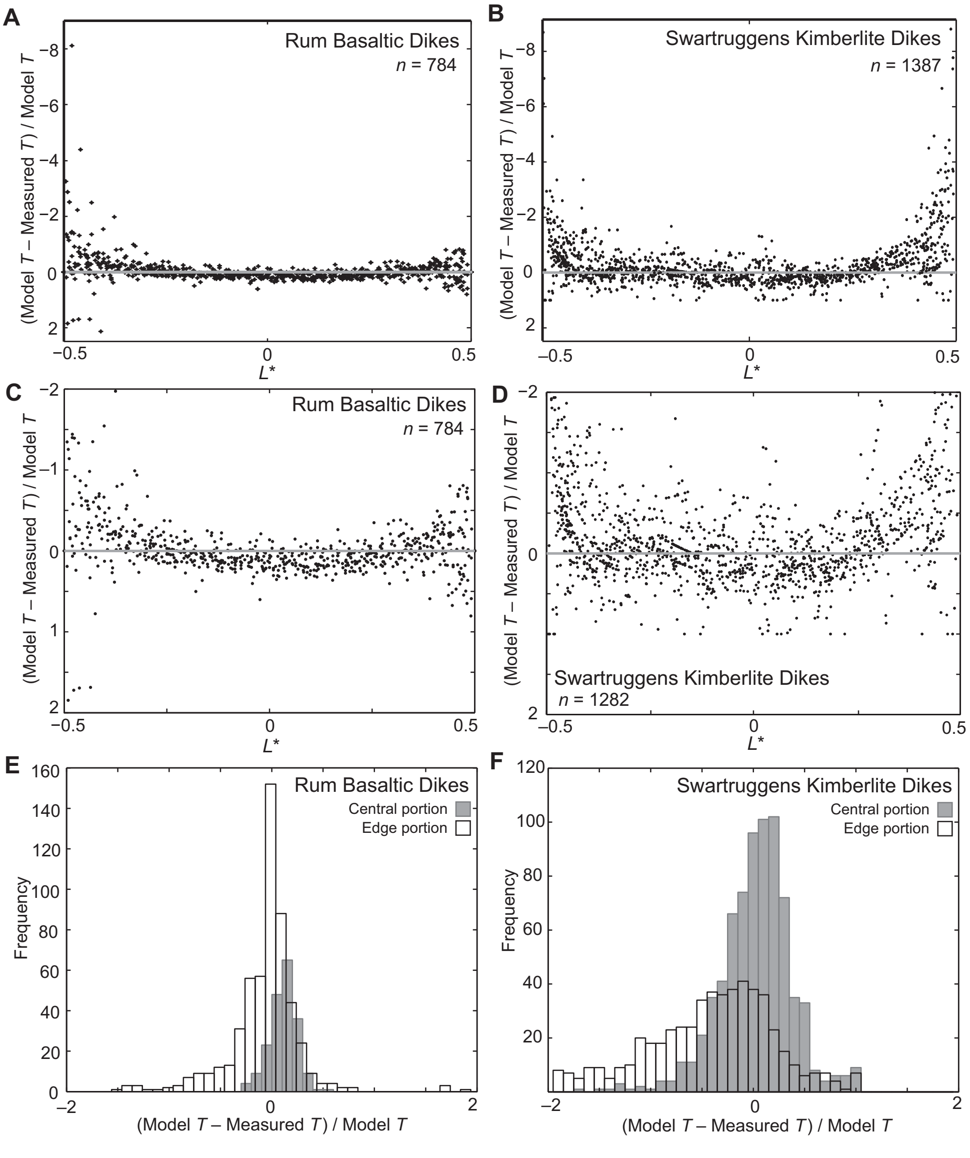

Figure 5. (A–D) T is dike thickness. The line at $y = 0$ is a perfect model fit to the data. Negative y-axis values indicate a dike that is fatter than the model; positive y-axis values show a thinner dike than the model. Positive values are in the downwards direction. Both the Rum dikes (A and C) and the Swartruggens dikes (John segment, levels 16–21, and Edward segment, levels 19–22) (B and D) have fatter edges and thinner centers than is expected from the model fit. C and D are the same as A and B, but with the vertical axis changed to show the range of –2 to 2 in order to more clearly see the distribution of the points above and below the perfect model fit (gray) line. Note: for both field localities, the majority of the points in the central region (L^* = –0.3 to 0.3) show thicknesses that are narrower than expected, and at the edges (L^* <–0.3 and >0.3), the thicknesses are larger than expected. (E–F) Frequency histograms of the difference between the modeled T and the measured T for (E) the Rum and (F) Swartruggens dikes showing the distribution of data relative to 0 (the perfect model fit) for the central region of each dike (gray) and the edges of each dike (black).

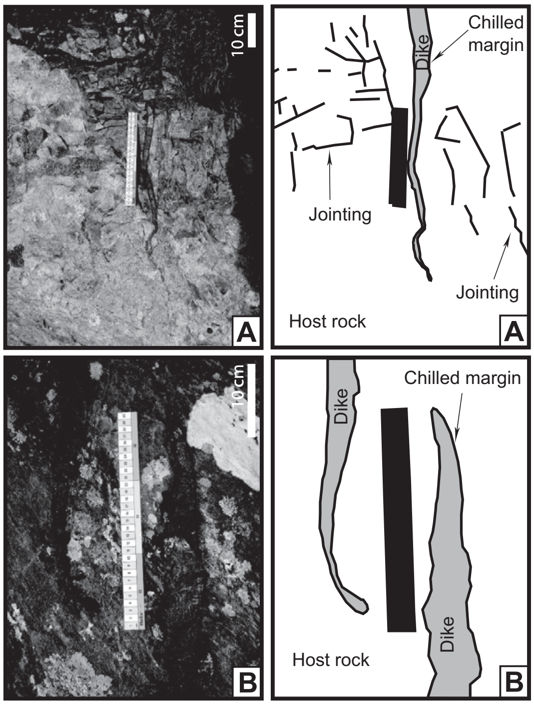

Figure 6. (A–B) The relationship between dike tips of segmented and nonsegmented dikes. (A) The tip of a dike with no neighboring dikes or dike segments (Rum). (B) The overlapping dike tips of two segmented dikes observed at locality 5 on Rum. The dike tips are separated at this locality by ~10 cm.

occurs in response to stress field rotation or propagation at an angle to the principal stress directions, giving a series of en echelon dike fingers, or segments, with systematic step-overs between segments owing to tangential stress on the dike walls (Pollard, 1987). Segmentation may also reflect dike propagation through heterogeneous geological media with local deviations of the stress field. The Swartruggens dikes and most of the Rum dikes are better interpreted with the latter explanation because the segments' step direction is nonsystematic. Segmentation implies a more complicated local stress regime than a static elastic theory based on a fluid-filled crack, and these complications are not easily quantified. Indeed, the correct mathematical treatment of this complex problem requires knowledge of the principal directions, principal stresses, and magma overpressure distribution along the fluid-filled crack (Mériaux and Lister, 2002); a priori estimates based solely on dike orientations can lead to significant errors in the principal stress values (Mériaux and Lister, 2002) and thus the quantification of dike segmentation.

Additionally, we note some difficulties in treating a dike with several segments as a single dike. Although in some cases, this can provide a better fit to the thickness data (e.g., Delaney and Pollard, 1981; Poland et al., 2008), especially if the thickness close to the tips is not measured, the quality of the fit inherently depends on the amount of data and their position along each segment. Our dike thickness measurements have a high frequency, including measurements made at the segment tips. As the thickness decreases to zero at the tips, this cannot be properly fit by a single opening curve for a set of segments. In addition, the true lateral extent of a segmented dike is rarely known for certain. Yet, this information is crucial because it constrains the overpressure estimate: all else being equal, a larger dike length will provide a lower overpressure estimate to explain the observed dike thickness.

A simplified static analysis whereby a segmented dike is represented by a series of collinear, identical, and equally spaced segments with the same overpressure ΔP allows the opening u_s of the segments along their length $2a$ to be calculated analytically as a function of their overpressure, length, and spacing (Tada et al., 2000; Gudmundsson, 2011):

$$u_{\mathrm{s}} = \frac{2\Delta P(1-\nu)}{\pi G} a(1+s)\left\{ \ln\left[\cos\left(\frac{\pi x}{2(1+s)} \right) + \sqrt{\cos^2\left(\frac{\pi x}{2(1+s)} \right) - \cos^2\left(\frac{\pi}{2(1+s)} \right)} \right] - \ln\left[\cos\left(\frac{\pi}{2(1+s)} \right) \right] \right\}, \quad (3)$$

where ν is the host-rock Poisson's ratio, G is its shear modulus, and the tip-to-tip distance d between adjacent dike segments is normalized to the segment length: $s = d/2a$. Figure 7 shows the extent to which the opening of multiple segments differs from that of a single one with the same overpressure. Closer dike segments have greater openings, but even for dike segments separated by 1/1000 of their length, this opening is increased only by a factor of less than five (Fig. 7B). The segment openings are proportional to their overpressure, and consequently this simplified analysis suggests that, by considering each segment separately, the overpressure is overestimated by a factor of about five. A more robust analysis would consider the relative positions of observed segments, but this would require a numerical treatment. However, the contribution of segments with larger spacing would be lower and could offset some of the closest segments.

To investigate further the effect of analyzing dike segments collectively rather than separately, we compared this analysis with the profile of six en echelon dikes from one locality on the Isle of Rum. The dikes at this particular locality are thought to be a completely exposed segmented dike; at all other localities where the dikes were segmented, the complete extent of the dike is less certain. These six dike segments are not truly collinear, however. There is always some separation, as measured normal to one segment, and they also tend to overlap, with both separation and overlap distances varying significantly from a pair of segments to one another. We thus used the collinear, segmented dike analysis with a range of tip-to-tip spacing between segments, from 1 m down to 0.1 mm. As for the previous analysis, Equation 3 was iterated through 1000 permutations of ΔP to estimate the best overpressure value that minimizes the least-squares misfit between Equation 3 and the measured opening for each segment. The best overpressure estimates range from 73 MPa to 1906 MPa, with an averaged estimate of 430 MPa. The highest estimate, found for only one of the six segments, is an order of magnitude higher than the other five estimates; adjacent segments belonging to the same dike should have similar overpressures. Neglecting this highest value gives an average overpressure estimate of 135 MPa. Although these values are lower than those estimated with Pollard and Muller's analysis, the best overpressure estimates predicted by the segment analysis are still much higher than values documented in previous studies (Table 1). Figure 8 shows the best-fit profiles for both single dike and segmented dike analyses for two of the selected segments. Both analyses fail to explain the thick edges displayed

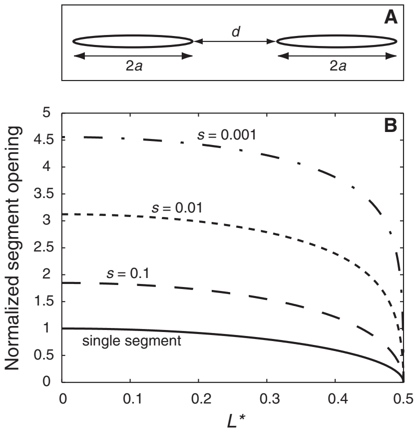

Figure 7. (A) Schematic diagram of a segmented dike. All the segments are identical, collinear, equally spaced, and loaded with the same overpressure. Two segments are represented here, but the analysis considers an infinite number of segments. (B) Along-strike opening of the dike segments. The along-strike position *x*, measured from the segment center, is normalized to the segment half-length *a*, and the segment opening u_s is normalized to the maximum opening, $\Delta P(1 - \nu)a/G$, of a single dike with the same half-length and overpressure ΔP. The tip-to-tip distance *d* between adjacent dike segments is normalized to the length of the segments: $s = d/2a$. Only half of the segment length is shown ($0 < L^* < 0.5$). The continuous curve corresponds to the case of a single dike, and the dashed curves correspond to different normalized spacings *s*.

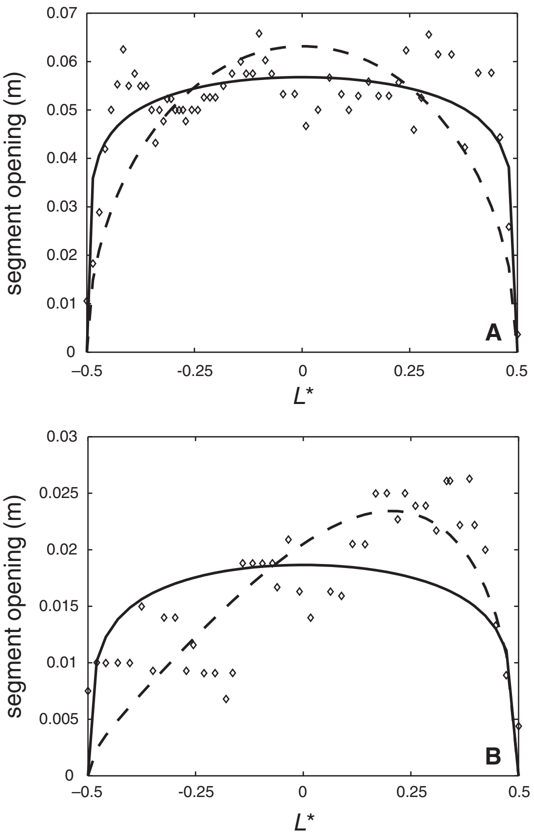

Figure 8. Opening profiles of two segments belonging to the same dike from the Isle of Rum (diamonds) compared with the segmented analysis (Eq. 3; black curve) and the analysis of Pollard and Muller (1976; dashed curve). (A) Best overpressure estimates: 110 MPa (black curve) and 332 MPa (dashed curve). There is no stress gradient. (B) Best overpressure estimates: 73 MPa (black curve) and 150 MPa (dashed curve). The segmented analysis cannot explain the teardrop shape of this segment. Best stress gradient estimated from Pollard and Muller's analysis (dashed curve): 136 MPa/m.

by the segments (Fig. 8A). Additionally, the segment analysis only deals with constant stress, and so cannot say anything about regional stress gradients nor explain the asymmetrical, teardrop shape displayed by most segments (Fig. 8B).

Finally, several of the Rum segments overlap. We are not aware of any analytical solution for estimating overpressures, stress gradients, or shape for overlapping segments; this would require numerical computations. Considering a constant overpressure, Pollard et al. (1982) showed that overlapping segmented dikes would be fatter than a single one. So by considering each segment as an individual dike, one would overestimate its overpressure. This overestimation will increase with the number of segments that constitute a whole dike, but it will decrease for increasingly overlapping segments and higher rotation angle between the segment direction and that of the main dike (Pollard et al., 1982). Overlapping segments will also tend to induce segment asymmetry as well as pinching or thinning of the edges (Pollard et al., 1982). This could potentially explain the extremely high stress gradients derived from Pollard and Muller's analysis as well as some of the pinched segment profiles. However, this cannot explain the overall, general shape pattern displayed by both the Rum and Swartruggens dikes: All these dikes appear fatter at their edges than predicted by both Pollard and Muller's and the segmented analyses, and they would appear even fatter for overlapping, pinching segments.

Considering all these limitations and effects together, it seems our single dike analysis would overestimate overpressures by at most a factor of 10, and it appears to be the best analytical method for fitting the measured profiles. Therefore, treating each segment as an individual dike provides a fairer assessment of their overpressure, stress gradient, and shape.

Overpressure and Stress Gradients

The elastic model of Pollard and Muller (1976) fits the data poorly for most of our studied dikes. The first mismatch between the data and the elastic model is the calculated values of overpressure and stress gradient, which are very large. This is evident from the comparison with the values estimated in previous studies (Table 1; Geshi et al., 2010; Poland et al., 2008; Pollard and Muller, 1976). The overpressures are especially large and likely unphysical for the Rum dikes, while the Swartruggens dike values are large but more plausible. The stress and overpressure gradients calculated are mostly implausible for both examples. If the Rum dikes with lengths <1 m are neglected, the range of estimated overpressure values is unchanged (37–1990 MPa), although the average is slightly reduced to 398 MPa. If the Rum dikes with thicknesses <0.05 m are neglected, the estimated values of overpressure are 70–1990 MPa, averaging 710 MPa. There appears, therefore, to be no dependence of these results on dike size. We could reduce these overpressure and stress gradient estimates by up to an order of magnitude if we consider each dike individually and not as segments from a larger dike (see previous section), yet the majority of these estimates remain much higher than values reported in previous studies (Table 1).

Very high values of overpressures and stress gradients cannot be explained using an elastic model. A rock's tensile and compressive strengths are typically of the order 10 MPa and 50 MPa, respectively, while magma overpressures have been estimated at <20 MPa (Stasiuk et al., 1993; Gudmundsson, 1999). For a 20 MPa magma source overpressure (the magma pressure in excess of the regional, compressive tectonic stress), a dike propagating 1 km from its source would experience a regional stress gradient of ≤20 kPa m^{-1} (Jaupart and Allègre, 1991), and this stress gradient estimate would decrease as the dike propagates further from its source. A dike driven by buoyancy would have a driving stress gradient of $\Delta\rho g$, where $\Delta\rho$ is the density difference between the magma and the host rocks, and g is the gravitational acceleration. A magma-host density difference of 100 kg m^{-3} gives a stress gradient of only 1 kPa m^{-1}. Stress gradients as high as those estimated for the Rum and Swartruggens dikes would therefore necessitate magma buoyancies greatly in excess of natural values governed by density differences between magmas and host rocks.

The fracture toughness of a rock is important in terms of the dike opening. According to linear elastic fracture mechanics, the intrusion of magma into a rock requires the concentration of stress at the intrusion tip to exceed the fracture toughness (K_c) of that rock (Pollard, 1987). This is equivalent to having an overpressure greater than ~$K_c/(L)^{1/2}$, where L is the length of the magma-filled crack. Rocks with higher fracture toughness both require higher magma overpressure for the dikes to propagate, and they induce greater blunting of the dikes at their tip. Laboratory measurements of fracture toughness give values on the order of 1–10 MPa $m^{1/2}$, and so kilometer-long dikes would be expected to propagate with overpressures of 1 MPa. Larger dikes would require even lower overpressures. Conversely, our estimated overpressures would suggest rock fracture toughness of the order 10–10^4 MPa $m^{1/2}$ and 10^2–10^3 MPa $m^{1/2}$ for the Rum and Swartruggens dikes, respectively. These are much higher values than those measured in the laboratory (e.g., Schmidt and Huddle, 1977), but they are similar to other field-based fracture toughness estimates (Delaney and Pollard, 1981; Delaney et al., 1986; Reches and Fink, 1988; Gudmundsson, 2009). Such high values are either explained by large confining pressures at the time of dike intrusions or extensive inelastic deformation ahead and around the dike tip (Delaney et al., 1986; Rubin, 1993; Fialko and Rubin, 1997). The former explanation would necessitate depths of intrusion greater than that of the Rum and Swartruggens dikes, while the latter explanation is plausible but requires extensive inelastic deformation.

Various nonelastic explanations could be invoked to explain the high estimated overpressure and stress gradient values. If the elastic parameter values used in the model were too large, the overpressures and stress gradients would be overestimated. Dikes may form through the dilation of preexisting fractures that are suitably orientated with regard to principal stress directions (e.g., Gudmundsson, 1984; Delaney et al., 1986; Valentine and Krogh, 2006), reducing the stress required to fracture the host rock. Once a fracture is resealed, the probability of a fracture reinitiating in the same location is greater (the host rock's compliance), and the shear modulus of the rock can be reduced by a factor of 2 or 3 (Worthington and Lubbe, 2007; Kavanagh, 2010), effectively making the crust less rigid. For the Rum dikes showing evidence of intruding host rocks with many preexisting joints, the compliance may have been significant. The opening of a dike is linearly proportional to its overpressure and inversely proportional to the shear modulus of the host rocks (e.g., Pollard, 1987). Therefore, accounting for the compliance can only partly explain the large overpressures estimated for the Rum dikes; typical changes in elastic properties due to compliance would only alter the calculated values by about a factor of 3 in the Rum and Swartruggens cases.

Magma extrusion from a greatly pressurized chamber into surrounding rock also provides an explanation for high calculated overpressures, particularly on Rum. Magma chamber overpressure increases during edifice growth until edifice destruction occurs (Pinel and Jaupart, 2000, 2003, 2004). The Rum dikes may represent magma extrusion from a chamber during the high-overpressure edifice-building stage. Typical stratovolcanic cones exert a load of ~50 MPa, significantly affecting the rock stresses beneath the volcanic edifice (Pinel and Jaupart, 2003). Edifice size strongly affects the critical magma overpressure required for eruption, which may be much larger than the host-rock tensile strength (Pinel and Jaupart, 2003). This is a more plausible model for explaining some of the overpressures calculated for the Rum dikes as a volcanic edifice was present at the time of diking.

High overpressures may also be partly attributed to shear failure. Assuming a shear component is present while diking occurs, dikes may tend to be wider than otherwise expected, leading to higher calculated overpressures. A shear component could be caused along the dike length if intrusion occurs in an orientation divergent from σ_1, as would be likely when intruding preexisting joints. This is consistent with the offset and overlapping dike segment pattern commonly seen on Rum, suggesting propagation along nonprincipal stress directions.

Both Rum and Swartruggens dikes give very high calculated stress gradient values, much larger than the values estimated from previous studies (Table 1). Assuming constant elastic properties and local horizontal magma pressure, the calculated stress gradients represent mainly horizontal gradients in crustal stress. Taking a calculated stress gradient value of 65 kPa m^{-1} for a Swartruggens dike, the crustal stress normal to the dike would change by 65 MPa over a 1 km region, which is an implausibly large horizontal value in the upper crust. This stress gradient would require a surface topography change of ~3 km, which is unlikely in this region of southern Africa. The Rum dikes give calculated stress gradients that are two orders of magnitude larger; even with very strong lateral stress gradients, these values are extremely large.

A lateral variation in host-rock properties has also been invoked in order to explain stress gradient values (e.g., Pollard and Muller, 1976; Kavanagh and Sparks, 2011), as well as variations in dike thickness (e.g., Baer, 1991; Geshi et al., 2010). This is unlikely to be the cause of the high stress gradients estimated for the Rum dikes because these were intruded within one rock unit; variations in burial depth along their strike would also be too small to have a significant effect. Heterogeneities in the sandstone layers may add to the variations in dike thickness of the Rum dikes. However, the majority have a small enough scale that even the properties of the single rock unit are unlikely to have changed significantly. Variable host-rock properties are thus unlikely to have caused the thickness variations or the stress gradient values measured on Rum.

The cause of the dike asymmetry is most likely due to host-rock inelasticity, small-scale lateral host-rock property variations, and, most importantly, the interference of dike edges and overlapping segments. Successive emplacement of neighboring dikes and dike segments will alter the stress distribution in the host rock (e.g., Rubin and Pollard, 1987). Overlapping segments with solidified magma pinning the dike edges in position are the likely cause of the observed asymmetry.

Dike Shape

Changes in the elastic parameters in the model do not improve the overall fit because of the mismatch between the predicted and observed dike shape. The modeled dike thickness is overestimated at the center and mostly underestimated at the edges (Fig. 5). Most of the dikes measured had a flatter central section than predicted. An active dike's width is determined by the overpressure, which usually declines with time as the chamber pressure decreases, as evidenced by waning flow rate in many lava eruptions

(Stasiuk et al., 1993), although the thickness can also be determined by the dike length for a fixed overpressure. If a dike erupts, this dike and the overall, not-yet-solidified, intrusive system will experience a reduction in overpressure. However, the majority of dikes are not thought to erupt (e.g., Gudmundsson, 1984; Gudmundsson et al., 1999). Arrested dikes can still, however, experience a reduction in overpressure during intrusion. We were not able to find unequivocal field evidence of the magma transport direction at either of the studied field localities; these may therefore have propagated vertically or laterally. For a constant magma volume, provided that the crack is not buoyancy driven, the overpressure in an intruding crack will decrease as the length of the crack increases (McLeod and Tait, 1999). Moreover, however the intrusion is driven, its overpressure will decrease because of the viscous pressure drop it will experience during propagation (Lister and Kerr, 1991). We do not see direct evidence that the dikes from either locality are connected to their paleosurface, and therefore we must rely on indirect evidence to assess whether or not these dikes were feeders. If it can be assumed that at tens of meters depth, a dike with a maximum thickness greater than 1 m has the potential to act as a feeder dike (Geshi et al., 2010), the Swartruggens dike segments (which have a maximum thickness of 1.95 m; Kavanagh and Sparks, 2011) could potentially have acted as feeder dikes. Since the mean thickness of the dikes measured at both field locations is less than 1 m, it is assumed that our analysis can only be applied to dikes fulfilling this criterion, and the application of our results to thicker dikes will require further investigation.

As magma flows through a fracture (Fig. 9A), chilling of the magma at the dike margins prevents it from closing at the tips (Fig. 9B). Viscosity increase by preferential cooling at the dike edges adds to this effect. As the overpressure wanes, if the position of the edges becomes fixed, and the dike is no longer propagating in the direction of the tip, the preserved thickness is then determined by the initial overpressure (Fig. 9C). However, the nonsolid and less viscous central parts of the dike can close as the overpressure declines; the initial dike injection shape is not the shape that is ultimately preserved as the solidified dike. We suggest therefore that the shape mismatch is principally a result of chilling and solidification during dike emplacement.

Inelasticity can also account for some of the dike thickness variation. There is strong evidence for inelastic deformation in the zones between the Swartruggens dike segments, which may have reduced the host-rock rigidity and shear strength. Mechanical processes such as brecciation, stoping, and weathering (preferentially focused at dike termination points, overlaps, and relay zones) can weaken the rocks prior to magma emplacement and produce an inelastic host-rock response during emplacement (Brown et al., 2007; Kavanagh, 2010; Kavanagh and Sparks, 2011). Similar inelastic deformation between adjacent segments has been observed by Schofield et al. (2010) at the Golden Valley Sill, South Africa. Additionally, small segments such as those observed on Rum are likely to correspond to segments lying close to the very tip of their main dike, and so be embedded within the inelastic, damaged region that surrounds that main dike tip. Indeed, the size of this damage region tends to scale with that of the dike that created it (Faulkner et al., 2011), and it could reach several meters or tens of meters (e.g., Delaney et al., 1986). Inelastic deformation within the damage zone would contribute to blunting of the edges of the segments embedded there. Thus, inelastic deformation could explain both the apparent high values of rock fracture toughness, suggested by our high overpressure estimates, and the observations of dike tips that are thicker than expected from elastic theory. Inelastic deformation in the steps between segments also provides an explanation for those dikes that are markedly asymmetric. Much more inelastic deformation at one end of the dike than the other will mean a distortion of the shape that results in asymmetry. The observation of alternations in the sense of asymmetry of segments indicates too that complex inelastic deformation in the step-over regions has occurred.

Implications for Eruption Longevity and Crustal Strain

The tendency toward thick dike tips and narrow centers has broader implications. The wedging of the dike edges formed at high magma overpressures is made permanent by chilling. Thus, as the pressure reduces and the eruption wanes, the fracture will be prevented from closing fully, and the dike can continue to act as an open conduit for longer than it otherwise would have been able to. Dike emplacement can be regarded as the accommodation of crustal strain as a response to tectonic stresses. However, the dimensions of an active dike with magma pressures exceeding tectonic stresses indicate that the transient strain can exceed the tectonic strain expected. Since the now-chilled edges have previously been pushed apart under a high magma overpressure, the additional strain can be permanently preserved due to the chilled and wedged dike edges. For large dikes with prolonged flow at overpressures exceeding tectonic stresses and with substantial solidification along the dike edges, the excess strain could be substantial.

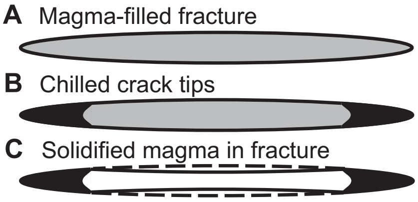

Figure 9. Schematic illustration of the impact of cooling on preserved dike geometry, presented as three time steps in the evolution of a horizontal section through the dike. (A) Magma intrudes a fracture, and (B) cooling ensues at the dike margins. (C) Chilled fracture tip magma props the fracture open as the overpressure reduces, preventing crack closure and creating the observed dike profile (solid line) with a thinner center and thicker tips. The dashed line in C indicates the expected profile of a pressurized magma-filled fracture in an elastic media.

CONCLUSIONS

Many of the dikes measured on Rum and at Helam Mine are poorly fit by the classical elastic model of Pollard and Muller (1976). There are two distinct mismatches between the presented data and the elastic model. First, many dike shapes are too thin in the middle and too thick at the edges to be fit by an elastic profile; the calculated R^2 values range from 0.389 to 0.997, and the misfits are larger than measurement uncertainties. Second, even for dikes where the model fit is acceptable, the calculated magma driving pressures and linear stress gradients are very large, particularly for the small-scale basaltic dikes on Rum. Many explanations have been provided to account for the differences. Of these, cooling of the dike edges, wedging the fracture open, and host-rock inelastic deformation prior to and during magma emplacement provide the most complete explanation for the mismatches between the data and the model. Care should be taken when extrapolating the observations from the dikes measured from the Swartruggens swarm and on Rum. Because the mean observed dike thickness was less than 1 m, it should not automatically be assumed that the analysis will apply to larger dikes; the application of these results to thicker dikes will require further investigation.

ACKNOWLEDGMENTS

Daniels would like to thank R.C. Ogilvie-Harris for assistance with the Rum data collection. A. Gudmundsson, A.E.L. Ferrari, and an anonymous reviewer are gratefully acknowledged for providing valuable comments to improve the manuscript. M. Poland and two anonymous reviewers are thanked for helpful comments on an earlier, shorter form of the manuscript. J. Davidson and A. Rogers are thanked for permission to publish the data set from Helam Mine. Sparks, Kavanagh, and Menand were supported by a grant from the Leverhulme Trust. Sparks is co-supported by an advanced grant from the European Research Council. Daniels was supported by a Natural Environment Research Council (NERC) Consortium Grant. This is Laboratory of excellence *ClerVolc* contribution number 6.

REFERENCES CITED

Allsopp, H.L., and Barrett, D.R., 1975, Rb-Sr age determinations on South African kimberlite pipes: Physics and Chemistry of the Earth, v. 9, p. 605–617.

Baer, G., 1991, Mechanisms of dike propagation in layered rocks and in massive, porous sedimentary rocks: Journal of Geophysical Research, v. 96, p. 11,911–11,929, doi:10.1029/91JB00844.

Basson, I.J., and Viola, G., 2003, Structural overview of selected group II kimberlite dyke arrays in South Africa: Implications for kimberlite emplacement mechanisms: South African Journal of Geology, v. 106, p. 375–394, doi:10.2113/106.4.375.

Brown, R.J., Kavanagh, J.L., Sparks, R.S.J., Tait, M., and Field, M., 2007, Mechanically disrupted and chemically weakened zones in segmented dike systems cause vent localization: Evidence from kimberlite volcanic systems: Geology, v. 35, p. 815–818, doi:10.1130/G23670A.1.

Buck, W.R., Einarsson, P., and Brandsdottir, B., 2006, Tectonic stress and magma chamber size as controls on dike propagation: Constraints from the 1975–1984 Krafla rifting episode: Journal of Geophysical Research, v. 111, doi:10.1029/2005JB003879.

Delaney, P.T., and Pollard, D.D., 1981, Deformation of Host Rocks and Flow of Magma during Growth of Minette Dikes and Breccias-Bearing Intrusions near Ship Rock, New Mexico: U.S. Geological Survey Professional Paper 1202, 61 p.

Delaney, P.T., Pollard, D.D., Ziony, J.I., and McKee, E.H., 1986, Field relations between dykes and joints' emplacement processes and paleostress analysis: Journal of Geophysical Research, v. 91, p. 4920–4938, doi:10.1029/JB091iB05p04920.

Domenico, S.N., 1983, Sandstone and limestone porosity determination from shear and compressional wave velocity: Bulletin of the Australian Society of Exploration Geophysicists, v. 14, p. 81–90, doi:10.1071/EG983081.

Emeleus, C.H., 1997, Geology of Rum and the Adjacent Islands: British Geological Survey Memoir for Geological Sheet 60, scale 1:50,000.

Faulkner, D.R., Mitchell, T.M., Jensen, E., and Cembrano, J., 2011, Scaling of fault damage zones with displacement and the implications for fault growth processes: Journal of Geophysical Research, v. 116, p. B05403, doi:10.1029/2010JB007788.

Fialko, Y.A., and Rubin, A.M., 1997, Numerical simulation of high-pressure rock tensile fracture experiments: Evidence of an increase in fracture energy with pressure?: Journal of Geophysical Research, v. 102, p. 5231–5242, doi:10.1029/96JB03859.

Geshi, N., Kusumoto, S., and Gudmundsson, A., 2010, Geometric difference between non-feeder and feeder dikes: Geology, v. 38, p. 195–198, doi:10.1130/G30350.1.

Gudmundsson, A., 1983, Form and dimensions of dykes in eastern Iceland: Tectonophysics, v. 95, p. 295–307, doi:10.1016/0040-1951(83)90074-4.

Gudmundsson, A., 1984, Formation of dykes, feeder-dykes, and the intrusion of dykes from magma chambers: Bulletin of Volcanology, v. 47, p. 537–550, doi:10.1007/BF01961225.

Gudmundsson, A., 1999, Fluid overpressure and stress drop in fault zones: Geophysical Research Letters, v. 26, p. 115–118, doi:10.1029/1998GL900228.

Gudmundsson, A., 2009, Toughness and failure of volcanic edifices: Tectonophysics, v. 471, p. 27–35, doi:10.1016/j.tecto.2009.03.001.

Gudmundsson, A., 2011, Rock Fractures in Geological Processes: Cambridge, UK, Cambridge University Press, 592 p.

Gudmundsson, A., Marinoni, L.B., and Marti, J., 1999, Injection and arrest if dykes: Implications for volcanic hazards: Journal of Volcanology and Geothermal Research, v. 88, p. 1–13, doi:10.1016/S0377-0273(98)00107-3.

Gurney, J.J., and Kirkley, M.B., 1996, Kimberlite dyke mining in South Africa: Africa Geoscience Review, v. 3, p. 191–201.

Hamilton, M.A., Pearson, D.G., Thompson, R.N., Kelley, S.P., and Emeleus, C.H., 1998, Rapid eruption of Skye lavas inferred from precise U-Pb and Ar-Ar dating of the Rum and Cuillin plutonic complexes: Nature, v. 394, p. 260–263, doi:10.1038/28361.

Jaupart, C., and Allègre, C.J., 1991, Gas content, eruption rate and instabilities of eruption regime in silicic volcanoes: Earth and Planetary Science Letters, v. 102, p. 413–429, doi:10.1016/0012-821X(91)90032-D.

Kavanagh, J., 2010, Ascent and Emplacement of Kimberlite Magmas [Ph.D. thesis]: Bristol, UK, University of Bristol, 356 p.

Kavanagh, J., and Sparks, R.S.J., 2011, Insights of dyke emplacement mechanics from detailed 3D dyke thickness datasets: Journal of the Geological Society of London, v. 168, p. 965–978, doi:10.1144/0016-76492010-137.

Kerr, R.C., and Lister, J.R., 1995, The lateral intrusion of silicic magmas into unconsolidated sediments: The Tennant Creek porphyry revisited: Australian Journal of Earth Sciences, v. 42, p. 223–224, doi:10.1080/08120099508728193.

Khazanehdari, J., and Sothcott, J., 2003, Variation in dynamic elastic shear modulus of sandstone upon fluid saturation and substitution: Geophysics, v. 68, p. 472–481, doi:10.1190/1.1567215.

Landau, L.D., and Lifshitz, E.M., 1986, Theory of Elasticity (3rd ed.): Oxford, UK, Butterworth Heinemann, 187 p.

Lister, J.R., and Kerr, R.C., 1991, Steady solutions for feeder dykes in a density-stratified lithosphere: Journal of Geophysical Research, v. 96, p. 10,049–10,077, doi:10.1029/91JB00600.

McLeod, P., and Tait, S., 1999, The growth of dykes from magma chambers: Journal of Volcanology and Geothermal Research, v. 92, p. 231–245, doi:10.1016/S0377-0273(99)00053-0.

Menand, T., and Tait, S.R., 2001, A phenomenological model for precursor volcanic eruptions: Nature, v. 411, p. 678–680, doi:10.1038/35079552.

Menand, T., and Tait, S.R., 2002, The propagation of a buoyant liquid-filled fissure from a source under constant pressure: An experimental approach: Journal of Geophysical Research, v. 107, p. 2306, doi:10.1029/2001JB000589.

Menand, T., Daniels, K.A., and Benghiat, P., 2010, Dyke propagation and sill formation in a compressive tectonic environment: Journal of Geophysical Research, v. 115, p. B08201, doi:10.1029/2009JB006791.

Mériaux, C., and Lister, J.R., 2002, Calculation of dike trajectories from volcanic centres: Journal of Geophysical Research, v. 107, p. 2077, doi:10.1029/2001JB000436.

Nicoll, G.R., Holness, M.B., Troll, V.R., Donaldson, C.H., Holohan, E.P., Emeleus, C.H., and Chew, D., 2009, Early mafic magmatism and crustal anatexis on the Isle of Rum: Evidence from the Am Mam intrusion breccia: Geological Magazine, v. 146, p. 368–381, doi:10.1017/S0016756808005864.

Phillips, D., 1991, Argon isotope and halogen chemistry of phlogopite from South African kimberlites: A combined step-heating, laser probe, electron microprobe and TEM study: Chemical Geology–Isotope Geoscience Section, v. 87, p. 71–98, doi:10.1016/0168-9622(91)90043-V.

Pinel, V., and Jaupart, C., 2000, The effect of edifice load on magma ascent beneath a volcano: Philosophical Transactions of the Royal Society of London, ser. A, Mathematical and Physical Sciences, v. 358, p. 1515–1532, doi:10.1098/rsta.2000.0601.

Pinel, V., and Jaupart, C., 2003, Magma chamber behaviour beneath a volcanic edifice: Journal of Geophysical Research, v. 108, p. 2072, doi:10.1029/2002JB001751.

Pinel, V., and Jaupart, C., 2004, Magma storage and horizontal dyke injection beneath a volcanic edifice: Earth and Planetary Science Letters, v. 221, p. 245–262, doi:10.1016/S0012-821X(04)00076-7.

Poland, M., Moats, W.P., and Fink, J.H., 2008, A model for radial dike emplacement in composite cones based on observations from Summer Coon volcano, Colorado, USA: Bulletin of Volcanology, v. 70, p. 861–875, doi:10.1007/s00445-007-0175-9.

Pollard, D.D., 1987, Elementary fracture mechanics applied to the structural interpretation of dykes, *in* Halls, H.C., and Fahrig, W.F., eds., Mafic Dyke Swarms: Geological Association of Canada Special Paper 34, p. 5–24.

Pollard, D.D., and Muller, O.H., 1976, The effect of gradients in regional stress and magma pressure on the form of sheet intrusions in cross section: Journal of Geophysical Research, v. 81, p. 975–984, doi:10.1029/JB081i005p00975.

Pollard, D.D., Segall, P., and Delaney, P.T., 1982, Formation and interpretation of dilatant echelon cracks: Geological Society of America Bulletin, v. 93, p. 1291–1303, doi:10.1130/0016-7606(1982)93<1291:FAIODE>2.0.CO;2.

Ray, R., Hetu, C.S., and Jyotirmoy, M., 2007, Structure and emplacement of the Nandurbar–Dhule mafic dyke swarm, Deccan Traps, and the tectonomagmatic evolution of flood basalts: Bulletin of Volcanology, v. 69, p. 537–551, doi:10.1007/s00445-006-0089-y.

Reches, Z., and Fink, J., 1988, The mechanism of intrusion of the Inyo dike, Long Valley caldera, California: Journal of Geophysical Research, v. 93, p. 4321–4334, doi:10.1029/JB093iB05p04321.

Roman, D.C., and Cashman, K.V., 2006, The origin of volcano-tectonic earthquake swarms: Geology, v. 34, p. 457–460, doi:10.1130/G22269.1.

Rubin, A.M., 1993, Tensile fracture of rocks at high confining pressure: Implications for dike propagation: Journal of Geophysical Research, v. 98, p. 15,919–15,935, doi:10.1029/93JB01391.

Rubin, A.M., 1995, Propagation of magma-filled cracks: Annual Review of Earth and Planetary Sciences, v. 23, p. 287–336, doi:10.1146/annurev.ea.23.050195.001443.

Rubin, A.M., and Pollard, D.D., 1987, Origins of blade-like dikes in volcanic rift zones, *in* Decker, R.W., Wright, T.L., and Stauffer, P.H., eds., Volcanism in Hawaii: U.S. Geological Survey Professional Paper 1350, p. 1449–1470.

Schmidt, R.A., and Huddle, C.W., 1977, Effect of confining pressure on fracture toughness of Indiana limestone: International Journal of Rock Mechanics and Mining Sciences & Geomechanics Abstracts, v. 14, p. 289–293, doi:10.1016/0148-9062(77)90740-9.

Schofield, N., Stevenson, C., and Reston, T., 2010, Magma fingers and host rock fluidization in the emplacement of sills: Geology, v. 38, p. 63–66, doi:10.1130/G30142.1.

Sneddon, I.N., 1946, The distribution of stress in the neighborhood of a crack in an elastic solid: Proceedings of the Royal Society of London, ser. A, v. 187, p. 229–260, doi:10.1098/rspa.1946.0077.

Stasiuk, M.V., Jaupart, C., and Sparks, R.S.J., 1993, Influence of cooling on lava-flow dynamics: Geology, v. 21, p. 335–338, doi:10.1130/0091-7613(1993)021<0335:IOCOLF>2.3.CO;2.

Tada, H., Paris, P.C., and Irwin, G.R., 2000, The Stress Analysis of Cracks Handbook (3rd ed.): New York, ASME Press, 698 p.

Timoshenko, S.P., and Goodier, J.N., 1970, Theory of Elasticity (3rd ed.) International Edition: McGraw-Hill, 567 p.

Valentine, G.A., and Krogh, K.E.C., 2006, Emplacement of shallow dikes and sills beneath a small basaltic volcanic center: The role of pre-existing structure (Paiute Ridge, southern Nevada, USA): Earth and Planetary Science Letters, v. 246, p. 217–230, doi:10.1016/j.epsl.2006.04.031.

White, R.S., Drew, J., Martens, H.R., Key, J., Soosalu, H., and Jakobsdóttir, S.S., 2011, Dynamics of dyke intrusion in the mid-crust of Iceland: Earth and Planetary Science Letters, v. 304, p. 300–312, doi:10.1016/j.epsl.2011.02.038.

Worthington, M.H., and Lubbe, R., 2007, The scaling of fracture compliance, *in* Fractured Reservoirs (edited by L. Lonergan, R.J.H. Jolly, K. Rawnsley and D.H. Sanderson), Geological Society [London] Special Publication 270, p. 73–82.

Science Editor: Nancy Riggs
Associate Editor: Luca Ferrari

Manuscript Received 24 April 2011
Revised Manuscript Received 25 August 2011
Manuscript Accepted 5 October 2011

Printed in the USA

ARTICLE IN PRESS
TECTO-125635; No of Pages 11
Tectonophysics xxx (2012) xxx–xxx

Contents lists available at SciVerse ScienceDirect

Tectonophysics

journal homepage: www.elsevier.com/locate/tecto

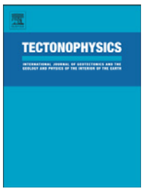

Gelatine as a crustal analogue: Determining elastic properties for modelling magmatic intrusions

J.L. Kavanagh [a,*], T. Menand [b,c,d], K.A. Daniels [e]

[a] School of Geosciences, Monash University, Clayton Campus, Clayton, VIC 3800, Australia
[b] Clermont Université, Université Blaise Pascal, Laboratoire Magmas et Volcans, BP 10448, F-63000 Clermont-Ferrand, France
[c] CNRS, UMR 6524, LMV, F-63038 Clermont-Ferrand, France
[d] IRD, R 163, LMV, F-63038 Clermont-Ferrand, France
[e] School of Earth Sciences, University of Bristol, Bristol, BS8 1RJ, UK

ARTICLE INFO

Article history:
Received 14 February 2012
Received in revised form 17 September 2012
Accepted 28 September 2012
Available online xxxx

Keywords:
Gelatine
Dyke sill
Magma
Analogue scaling

ABSTRACT

Gelatine has often been used as an analogue material to model the propagation of magma-filled fractures in the Earth's brittle and elastic crust. Despite this, there are few studies of the elastic properties of gelatine and how these evolve with time. This important information is required to ensure proper scaling of experiments using gelatine. Gelatine is a viscoelastic material, but at cool temperatures (T_r ~5–10 °C) it is in the solid 'gel' state where the elastic behaviour dominates and the viscous component is negligible over short to moderate timescales. We present results from a series of experiments on up to 30 litres of maximum 30 wt.% pigskin gelatine mixtures that document in detail how the elastic properties evolve with time, as a function of the volume used and gel concentration (C_{gel}). Gelatine's fracture toughness is investigated by measuring the pressure required to propagate a pre-existing crack. In the gel-state, gelatine's Young's modulus can be calculated by measuring the deflection to the free-surface caused by an applied load. The load's geometry can affect the Young's modulus measurement; our results show its diameter needs to be $\lesssim$ 10% of both the container diameter and the gelatine thickness (H_{gel}) for side-wall and base effects to be ignored. Gelatine's Young's modulus increases exponentially with time, reaching a plateau (E_∞) after several hours curing. E_∞ depends linearly on C_{gel}, while T_r, H_{gel} and the gelatine's thermal diffusivity control the time required to reach this value. Gelatine's fracture toughness follows the same relationship as ideal elastic-brittle solids with a calculated surface energy $\gamma_s = 1.0 \pm 0.2$ J m^{-2}. Scaling laws for gelatine as a crustal analogue intruded by magma (dykes or sills) show that mixtures of 2–5 wt.% gelatine cured at ~5–10 °C ensure the experiments are geometrically, kinematically and dynamically scaled.

1. Introduction

Analogue experimentation is an important technique in science and engineering. In practice, it is the selection of appropriate analogue materials that is often the biggest challenge in developing a set of experiments that are geometrically, kinematically and dynamically scaled (*sensu* Hubbert (1937)). Experiments that meet these criteria can be considered a laboratory-scale version of the natural counterpart. In this paper we detail a series of experiments carried out to document the properties of gelatine, a widely used analogue for the Earth's crust.

Gelatine is an ideal analogue for those modelling homogeneous, isotropic and elastic materials, for example it has been used by mechanical engineers (e.g. Crisp (1952), Richards & Mark (1966)) and as a biological tissue analogue in the medical sciences (e.g. Righetti et al. (2004)). The use of gelatine in geological sciences has taken advantage of both its elastic and viscous properties, proving especially fruitful in developing our understanding of magmatic intrusions (dykes and sills) and volcanic feeder systems and providing constraints on their propagation dynamics in the Earth's brittle and elastic crust (e.g. Acocella & Tibaldi (2005), Cañón-Tapia & Merle (2006), Dahm (2000), Fiske & Jackson (1972), Heimpel & Olson (1994), Hyndman & Alt (1987), Ito & Martel (2002), Kavanagh et al. (2006), Kervyn et al. (2009), Maaløe (1987), Maccaferri et al. (2010), Mathieu et al. (2008), McGuire & Pullen (1989), McLeod & Tait (1999), Menand et al. (2010), Menand & Tait (2001, 2002), Muller et al. (2001), Pollard (1973), Pollard & Johnson (1973), Rivalta et al. (2005), Taisne et al. (2011), Taisne & Tait (2011), Takada (1990, 1994, 1999) Walter & Troll, (2003), Watanabe et al. (2002)). The photoelastic properties of gelatine have been of particular use to experimental geologists (e.g. Taisne & Tait (2011)) and civil engineers (e.g. Crisp (1952), Farquharson & Hennes (1940), Richards & Mark (1966), Tan (1947)), where the internal stresses of a deformed gelatine can be visualised with the aid of polarised light. The prolific use of gelatine in the food industry has made a wealth of information available on its rheological properties (e.g. Watase & Nishinari (1980)).

---

[*] Corresponding author. Tel.: +61 3 9902 0062; fax: +61 3 990 54903.
E-mail address: janine.kavanagh@monash.edu (J.L. Kavanagh).

0040-1951/$ – see front matter © 2012 Elsevier B.V. All rights reserved.
http://dx.doi.org/10.1016/j.tecto.2012.09.032

Please cite this article as: Kavanagh, J.L., et al., Gelatine as a crustal analogue: Determining elastic properties for modelling magmatic intrusions, Tectonophysics (2012), http://dx.doi.org/10.1016/j.tecto.2012.09.032

However, relatively few studies have documented the elastic properties of gelatine or how these evolve with time (e.g. Di Giuseppe et al. (2009)).

We present results from a series of experiments that investigate the elastic properties of gelatine over a range of concentrations and volumes. Firstly the material properties of gelatine are detailed, followed by a description of the experimental setup and the theoretical basis for our measurements. The accuracy to which the experimentalist can determine the Young's modulus of the gelatine is evaluated by considering the uncertainties involved in the measurement, the effect of the properties of the applied load used to make the measurements and any apparatus side-wall or floor effects. In particular, our experimental results are focused on how the Young's modulus of the gelatine evolves with time. We also determined the gelatine's fracture toughness, a measure of the material's resistance to the growth of a crack. To aid the application of the results, we present some scaling laws that are appropriate for the use of gelatine as an analogue for the Earth's crust in geological studies focused on the formation controls and propagation dynamics of magma-filled fractures.

2. Material properties

Gelatine is a polypeptide formed from the hydrolytic degradation of collagen (Ross-Murphy, 1992). It is classified as a ‘physical gel’ (e.g. Peyrelasse et al. (1996)), meaning that during gelification Van der Waals forces lead to the development of a complex and continuously connected three-dimensional network (lattice) of macromolecules (Djabourov et al., 1988a). The hydrogen bonds that are formed in this process are reversible and can be broken by changing temperature or pH (Djabourov et al., 1988b). From the onset, those working with gelatine have commented on its "fickle" nature (Richards & Mark, 1966). In order to use this material for quantitative modelling purposes, control needs to be kept on a range of factors including temperature, pH and gelatine concentration.

Gelatine is a viscoelastic material so during deformation it can display both elastic and viscous behaviour. High stresses applied for a short timescale cause the gelatine to behave elastically, whereas small stresses applied over a long time period will produce a viscous response. Viscoelasticity is traditionally modelled with an arrangement of springs and dashpots that can reproduce a measured creep curve (e.g. Richards & Mark (1966)). The proportion of elastic to viscous behaviour can be quantified by a phase shift δ angle, also known as the “loss angle” (Mezger, 2002):

$$\delta = arctan\frac{G''}{G'} \tag{1}$$

where G'' is the energy loss (viscous-related) and G' is the energy stored (elastic-related) for a given strain or strain rate. δ is equal to 0° for an ideal-elastic material and 90° for an ideal-viscous material. The transition from viscously dominated to elastically dominated behaviour (or *vice versa*) occurs at the ‘gel-point’ (Djabourov et al., 1988b), which is the condition where elastic and viscous energies are equal ($G''=G'$ and $\delta=45°$). Gelatine is in the ‘sol-state’ (fluid) when $G''>G'$ and $\delta>45°$, but is in the ‘gel-state’ (solid) when $G'>G''$ and $\delta<45°$ (Mezger, 2002; Nelson & Dealy, 1993; Ross-Murphy, 1992). For gelatine, this marked change in mechanical properties can be brought about by changing the extent of deformation (strain) or temperature; the gel-point itself depends on time, temperature and concentration (Askeland et al., 2010; Di Giuseppe et al., 2009).

The focus of this paper will be on the ideal-elastic behaviour of gelatine. When a 2.5 wt.% gelatine mixture at 10 °C is deformed at low strain it has G' two orders of magnitude higher than G'' and $\delta<1°$ (Di Giuseppe et al., 2009). At these conditions the material is in the ‘gel-state’ and it is possible to assume an almost ideal-elastic behaviour. When this is the case, Hooke's Law is obeyed and deformation is recoverable when high stresses are applied over short timescales: the applied stress (σ) is proportional to strain (γ) and independent of the strain rate ($\dot{\gamma}$).

The elastic properties of a homogeneous and isotropic solid can be described fully by a combination of the Young's modulus E (ratio of tensile stress to tensile strain) and the Poisson's ratio ν (the relative contractive to expansive response of the deformed material). For gelatine, $\nu\simeq0.5$ (e.g. Crisp (1952), Farquharson & Hennes (1940), Righetti et al. (2004), Richards & Mark (1966)) and is theoretically incompressible such that deformation results in no net volume change.

3. Experimental set-up and data processing

3.1. Young's modulus experiments

A series of twenty-six experiments were carried out to investigate the effect of time, gelatine concentration, volume, experimental apparatus dimensions and applied load properties on the calculated Young's modulus of solidified gelatine.

A gelatine solution was prepared by adding a measured quantity of approximately 80 °C deionised water to the required weight of gelatine granules (260 Bloom, 20 Mesh, Pigskin Gelatine supplied by Gelita UK) to achieve the desired concentration (see Table 1). The use of deionised water is required to produce a clear and transparent mixture that hinders bacterial growth, which would otherwise produce a cloudy appearance to the gelatine solid. This hot mixture was then poured into a specified container and any bubbles were removed from the surface using a spoon. To prohibit the formation of a toughened ‘skin’ on the gelatine surface by water evaporation, a thin layer of vegetable oil was poured on top. The container was then placed into a temperature-controlled cold room at 5–10 °C (T_r), and the mixture temperature (T_0) and time were recorded. The gelatine was left in the cold room for several hours until the mixture temperature had equilibrated with its surroundings.

One way of calculating the gelatine's Young's modulus is to measure the deflection imposed by a load applied to the gelatine's surface (Timoshenko & Goodier, 1970):

$$E = \frac{M_L g\left(1-\nu^2\right)}{D_L w}, \tag{2}$$

where D_L is the diameter (m) of the cylindrical load, M_L is its mass (kg), w is the displacement (m) caused, and g is the gravitational acceleration.

Measurement of the Young's modulus commenced once the gelatine was able to support a load placed on its free surface. The container was removed from the cold room to make the measurements and then replaced afterwards. All of the oil was carefully removed from the surface of the gelatine prior to any measurement being taken, using a spoon and then paper towel in order to achieve complete contact between the load and the gelatine. The load was applied by carefully placing a rigid metallic cylinder of known mass and dimensions onto the gelatine surface (see Fig. 1 for a schematic sketch of the experimental setup and Table 2 for experimental load properties). Using a digital micrometer attached to a fixed reference position, the displacement of the free surface was measured (with an estimated error of ±0.1 mm) and recorded by hand. The load was applied just prior to the measurement being made, and the total time in which it was in contact with the gelatine was approximately 30 seconds per measurement. E was calculated systematically for the duration of each experiment; measurements were made using each of the loads when possible, approximately every one to two hours for up to 140 hours after the gelatine was prepared (nearly six days). For each time interval, the gelatine was at ambient room temperature for an interlude of less than ten minutes before being returned to

Please cite this article as: Kavanagh, J.L., et al., Gelatine as a crustal analogue: Determining elastic properties for modelling magmatic intrusions, Tectonophysics (2012), http://dx.doi.org/10.1016/j.tecto.2012.09.032

Table 1
Table of experimental conditions. C_{gel} = gelatine concentration (wt.%), M_{gel} = mass of tested gelatine plus water mixture (kg), V_{gel} = volume of tested gelatine plus water mixture (l), H_{gel} = thickness of gelatine mixture (±0.5 cm), D_C = container diameter (±0.1 cm), T_r = cold room temperature, T_0 = starting temperature of gelatine mixture (±0.5 °C). Experimental containers were circular in cross-section, except those indicated by * which were square (measuring 40 cm × 40 cm) and † which was oblong (measuring 50 cm × 30 cm). H_{gel} was calculated retrospectively from the container surface area and tested volume.

Exp.	C_{gel}	M_{gel}	V_{gel}	H_{gel}	D_C	T_r (°C)	T_0 (°C)
1	2.5	4	4	17.0	17.3	10	34.5
2	2.5	3	3	12.7	17.3	10	35.0
3	2.5	2	2	8.5	17.3	10	35.5
6	2.5	20	20	12.5	40.0*	10	36.0
7	2.5	30	30	18.8	40.0*	10	38.0
8	2.5	0.5	0.5	4.1	12.5	10	35.5
9	2.5	0.5	0.5	6.4	10.0	10	34.5
10	2.5	0.5	0.5	8.7	8.6	10	34.5
11	2.5	20	20	12.5	40.0*	5	34.0
12	2.5	30	30	18.8	40.0*	5	34.5
13	2	2	2	16.4	12.5	5	37.5
14	2	1	1	8.2	12.5	5	37.5
15	2	3	3	12.7	17.3	5	38.0
16	2	4	4	17.0	17.3	5	38.0
17	2	10	10	19.6	25.5	5	37.0
18	2	20	20	27.0	30.7	5	38.5
19	2	30	30	20.0	30.2†	5	44.5
25	2.5	4	4	17.0	17.3	5	40.5
26	3	4	4	17.0	17.3	5	39.5
27	3.5	4	4	17.0	17.3	5	39.0
28	4	4	4	17.0	17.3	5	38.0
29	5	4	4	17.0	17.3	5	35.0
30	5	4	4	17.0	17.3	5	64.0
31	10	4	4	17.0	17.3	5	60.0
32	20	4	4	17.0	17.3	5	65.0
33	30	4	4	17.0	17.3	5	56.0

Table 2
Properties of the experimental loads: β = thickness (±0.1 mm), M_L = mass of load (±0.1 g), D_L = diameter of load (±0.1 mm). In all cases the data are mean averages of three measurements. Loads are cylindrical.

	Material	β (mm)	M_L (g)	D_L (mm)
Load $_1$	Aluminium	27.9	393.8	81.6
Load $_2$	Aluminium	18.0	255.0	81.6
Load $_3$	Brass	12.2	50.6	25.1
Load $_4$	Brass	9.2	37.9	25.1
Load $_5$	Brass	6.2	25.5	25.0
Load $_6$	Brass	11.3	35.9	22.6
Load $_7$	Brass	14.3	37.8	20.0
Load $_8$	Brass	8.9	48.5	30.0
Load $_9$	Steel	23.9	130.2	30.0
Load $_{10}$	Steel	92.8	2279.3	63.5
Load $_{11}$	Steel	62.8	2808.5	85.6

the cold room. No experimental load was applied to the gelatine surface between time steps. The displacement measurement 'w' and the properties of the load were input into Eq. (2) to calculate the Young's modulus of the gelatine solid.

The experimental series considers gelatine concentration C_{gel} (2–30 wt.%), temperature of the cold room T_r (5–10 °C), volume of gelatine V_{gel} (0.5 to 30 litres), diameter of the experimental container D_C (8.6–40.0 cm), thickness of the gelatine H_{gel} (4.1–27.0 cm), and applied load (with mass M_L of 25.5–2808.5 g and diameter D_L 20.0–85.6 mm) (see Tables 1 and 2). These experiments allowed the characterisation of the evolution of the Young's modulus of gelatine over a range of conditions, and for the factors affecting our measurements to be assessed.

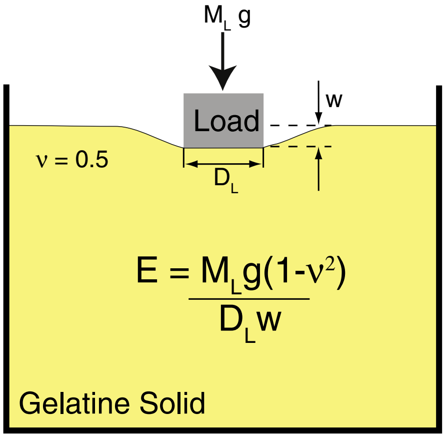

Fig. 1. Schematic illustration of the Young's modulus measurement procedure on a gelatine solid able to support an applied load. The deflection caused by a load placed on the surface of the solidified gelatine is measured, and this information is combined with the properties of the load to calculate the Young's modulus of the material.

3.2. Fracture toughness experiments

The fracture toughness K_c is a measure of a material's resistance to the growth of a crack. The fracture toughness of gelatine solids was determined by experimental means, measuring the pressure required to propagate an existing crack (following the analysis of Sneddon & Das (1971)). This experimental method for calculating the fracture toughness of gelatine solid is briefly described by Menand & Tait (2002). However, the mathematical procedure is not detailed explicitly. Therefore, here we present the experimental procedure again and detail in the Appendix the mathematical method so that other experimentalists can replicate them.

For these fracture-toughness experiments high-clarity pigskin-derived gelatine (acid, 200 bloom) was supplied in granular form by SKW Bio-Systems. The gelatine mixture was prepared by first hydrating 5 to 8 wt.% gelatine powder in distilled water, and then heating the solution to 60 °C until the powder was completely dissolved. Sodium hypochlorite was then added to the solution so that it contained 0.1 wt.% of active chlorine, in order to prevent fungal and bacterial growth. This amount was kept small to minimise its potential effect on the gelatine mechanical properties.

The gelatine solution was poured into a cubic acrylic tank (30 cm wide) and left to solidify for 48 hours at room temperature. A thin layer of silicon oil was poured on the gelatine surface in order to avoid evaporation during solidification and prevent the development of a gradient in gelatine properties. The tank was only filled to two thirds its height, immersing a metallic blade that was elliptical in cross-section and had been inserted 5 cm into the gelatine solution. The blade measured 20 cm in length with a 1 cm thickness at its base. Once the gelatine had solidified, the blade was carefully removed thus creating an empty edge-crack in the gelatine solid. Both the crack and the remaining part of the tank were then filled with water, and the tank was overturned so that in its final position the crack was oriented vertically and at the bottom of the gelatine solid (Fig. 2a). An outlet enabled water to bleed off any excess pressure in the lower part of the tank, and so ensured the water pressure balanced precisely with the weight of the overlying gelatine. Thus there was no excess pressure within the crack. Moreover, the initial state of stress within the gelatine solid was hydrostatic. (The gelatine solid adheres to the tank walls and so there is no horizontal strain, $\varepsilon_x = \varepsilon_y = 0$. Using Hooke's law, the relationship between the three stress components is $\sigma_x = \sigma_y = \frac{\nu}{(1-\nu)}\sigma_z$; and given that gelatine has a Poisson's ratio $\nu = 0.5$, $\sigma_x = \sigma_y = \sigma_z$.)

These fracture toughness experiments were carried out at a room temperature of 19 ± 2 °C. At the beginning of an experiment, the Young's modulus of the gelatine was measured as described in Section 1 (using a load with diameter approximately one tenth of the tank width). The crack excess pressure was then increased by

Please cite this article as: Kavanagh, J.L., et al., Gelatine as a crustal analogue: Determining elastic properties for modelling magmatic intrusions, Tectonophysics (2012), http://dx.doi.org/10.1016/j.tecto.2012.09.032

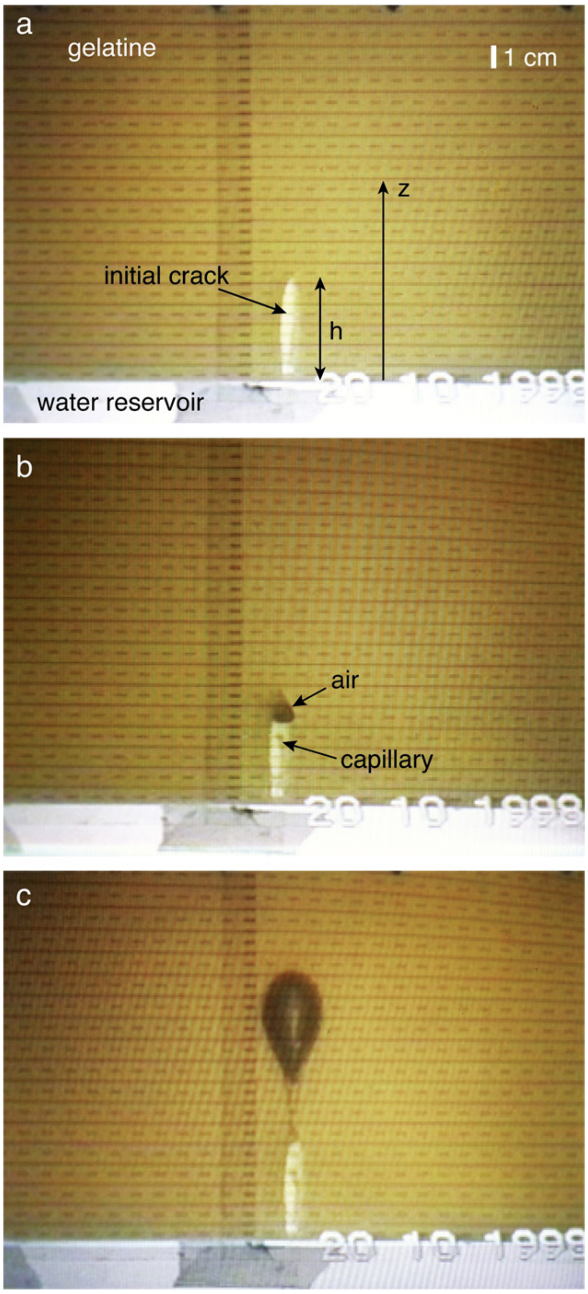

Fig. 2. Three successive photographs taken during a fracture-toughness experiment. (a) An edge-crack is initially created at the base of a gelatine solid, and filled with water. The initial reservoir pressure matches exactly the weight of the overlying gelatine solid. (b) Air is injected through a capillary and within the crack. Any potential reservoir excess pressure is released, so that only the crack buoyancy increases during air injection (see text). (c) When the crack buoyancy is high enough, the air-filled crack fractures the gelatine and propagates vertically.

injecting air using a thin capillary which protruded into the crack (Fig. 2b). During this injection of air, any excess water bled off ensuring that only the crack buoyancy increased; the excess pressure in the other water-filled part of the tank remained nil. As more air entered the crack, its buoyancy increased until it was sufficient to fracture the gelatine at the tip of the crack (Fig. 2c). The process was recorded by video camera, and from this video record the exact amount of air that was present within the crack just prior to the gelatine fracture was measured. The Young's modulus of the gelatine was systematically varied between experiments, by changing the concentration of gelatine used during preparation, and the amount of air needed to propagate the initial crack was recorded, as summarised in Table 3.

The fracturing of the gelatine solid was analysed within the Linear Elastic Fracture Mechanics framework, according to which a crack propagates once the stress intensity factor at its tip K_I exceeds the fracture toughness K_c of the solid host (Griffith, 1921). Measuring the height of air present in the crack enabled us to calculate the pressure distribution within the crack and thus the stress intensity factor at its tip following the method of Sneddon & Das (1971) (see Section 4.2 and Appendix). We thus measured the height of air just prior to the crack propagation, and equated the calculated stress intensity factor with the gelatine fracture toughness.

3.3. Data processing

Data processing was undertaken in order to identify and quantify potential sources of uncertainty in the Young's modulus measurements before analysing the results. To account for experimental uncertainties, both the effect of the dimensions of the applied load relative to the size of the experimental container and also the effect of the propagation of errors in the Young's modulus calculation have been considered. A data weighting procedure has then been carried out before modelling the experimental results.

3.3.1. Effect of applied load and container size

We calculate the Young's modulus of gelatine by measuring by how much its free surface is deformed by an applied load. In doing so, we effectively assume that the gelatine solid is semi-infinite. However, the finite lateral dimensions of the gelatine container and distance to its base may have an important effect by restricting the movement of the deformed gelatine.

Fig. 3 shows the relationship between the calculated Young's modulus and the relative size of the applied load diameter and the experiment container (D_L/D_C). Data from eight experiments at one time interval are shown (22 hours curing at 10 °C). These experiments have equal gelatine concentration (2.5 wt.%), but a range of volumes (0.5–30 litres), measured by Loads 1–8 in ten container sizes (see Table 1). Pearson product–moment correlation coefficients (r) were calculated for each experiment:

$$r = \frac{S_{xy}}{\sqrt{S_{xx}S_{yy}}}, \tag{3}$$

where

$$S_{xx} = \sum(x-\bar{x})^2 \quad S_{yy} = \sum(y-\bar{y})^2 \quad S_{xy} = \sum(x-\bar{x})(y-\bar{y}), \tag{4}$$

Table 3
The values of gelatine fracture toughness K_c determined from eight successful experiments. z_l is the level of the air-water interface within the crack just prior to its propagation; $z_l = 0$ when the crack is full of air. $\overline{\Delta P}$ is the corresponding averaged excess pressure. The gelatine and water densities, ρ_g and ρ_w, were both measured to within 4 kg m^{-3} and 1 kg m^{-3}, respectively, and the air level z_l to within 2.5 mm.
♮ The crack was initially 5.0 ± 0.2 cm high in all experiments, except in experiment 129 where it was 10 cm high.

Exp.	ρ_g (kg m^{-3})	ρ_w (kg m^{-3})	E (Pa)	z_l (cm)	$\overline{\Delta P}$ (Pa)	K_c (Pa $m^{1/2}$)
123	1062.0	1000.0	1449 ± 14	2.25	89 ± 27	59 ± 18
124	1072.3	1000.0	3969 ± 100	1.25	156 ± 26	93 ± 15
125	1079.3	1000.0	7603 ± 125	1.00	176 ± 26	103 ± 15
126	1063.3	1000.0	1877 ± 36	3.10	54 ± 29	40 ± 21
127	1072.7	1001.0	3906 ± 161	3.15	65 ± 29	48 ± 21
128	1079.3	1000.6	7328 ± 116	0.00	270 ± 25	148 ± 14
129♮	1025.5	1000.3	10959 ± 354	4.00	189 ± 27	175 ± 25
131	1015.6	999.4	2254 ± 57	2.20	85 ± 27	57 ± 18

Please cite this article as: Kavanagh, J.L., et al., Gelatine as a crustal analogue: Determining elastic properties for modelling magmatic intrusions, Tectonophysics (2012), http://dx.doi.org/10.1016/j.tecto.2012.09.032

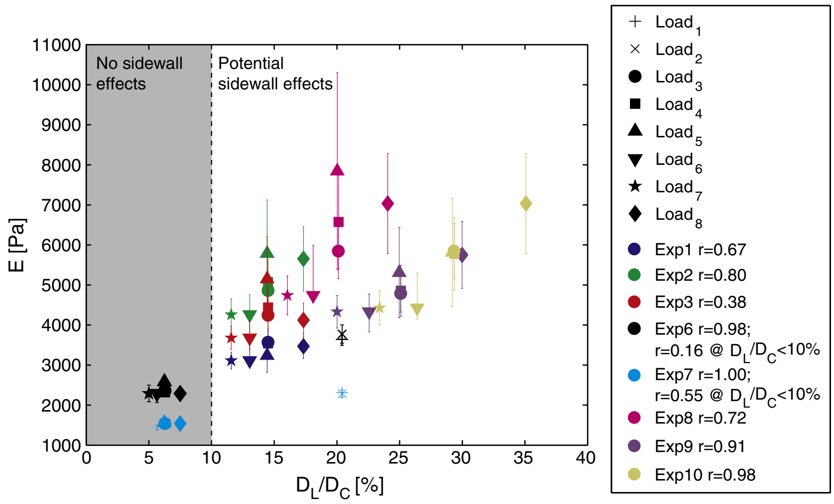

Fig. 3. Young's modulus (E) of 2.5 wt.% gelatine solids, after approximately 22 hours curing at 10 °C, plotted against the diameter of the applied load relative to the diameter of the container (D_L/D_C) for loads 1–8 (Table 2) and five container sizes (Table 1). In the region $D_L/D_C>10\%$ (unshaded) each experiment individually shows a positive correlation between E and D_L/D_C (see legend for Pearson product–moment correlation coefficients), indicating interaction between the load and container could produce artificially high calculated Young's moduli. Where $D_L/D_C \leq 10\%$ (shaded) there appears to be no correlation between E and D_L/D_C, and here sidewall affects can be neglected. When no error bars can be seen, the error is smaller than the symbol size.

and x and y are experimentally determined variables (in this case E and D_L/D_C). The correlation coefficient ranges from -1 to $+1$; $r=+1$ indicates a positive linear correlation, $r=-1$ suggests a negative linear correlation, and $r=0$ when no correlation is found. In the region $D_L/D_C>10\%$ the results show a strong positive correlation ($r\geq 0.65$), implying interaction between the applied load and container walls is producing artificially high Young's modulus calculations (an exception is experiment 3, where $r=0.38$). However, when $D_L/D_C<10\%$ the correlation is poor and in this region the experimentalist can be confident of avoiding sidewall effects. Providing this is the case, Eq. (2) holds and can be used to calculate the Young's modulus of the gelatine. Note that from the experiments shown, only experiments with a larger volume (20–30 litres) with Young's modulus measured with loads 3–8 fall into this category.

The Young's modulus measurements may also be affected by the distance to the base of the experimental container. If we assume the gelatine is semi-infinite and behaves as a purely elastic solid, we can estimate the stresses variation with depth induced by a load applied to the surface. The largest stress component induced by a load σ_0 is the vertical component σ_z, which can expressed as (Timoshenko & Goodier, 1970):

$$\sigma_z = \sigma_0\left[1-\frac{8z^3}{\left(1+4z^2\right)^{3/2}}\right], \tag{5}$$

where z has been normalised by the diameter of the load D_L. Following this expression, the stress induced by the load at a depth ten times its diameter is only 0.4% of that imposed by the load at the surface.

We therefore recommend that both the lateral and vertical dimensions of the container be at least ten times the diameter of the load to avoid both container sidewall and base effects.

3.3.2. Propagation of errors

The uncertainty associated with the Young's modulus (Eq. (2)) was calculated according to the principles of the 'Propagation of Errors' (Bevington & Robinson, 2003), where the relative error is expressed as:

$$\frac{\Delta E}{E} = \sqrt{\left(\frac{\Delta M}{M}\right)^2+\left(\frac{\Delta D_L}{D_L}\right)^2+\left(\frac{\Delta w}{w}\right)^2}, \tag{6}$$

where:

$$w = \beta + X_1 - X_0. \tag{7}$$

β is the thickness of the load, X_0 is the distance to the unloaded surface and X_1 is the distance to the surface of the applied load (both X_1 and X_0 are measured relative to a fixed point of reference). Values of M, D_L, β, X_1 and X_0 used in the calculation are averages of three separate and successive measurements. β, X_1 and X_0 have independent random errors such that calculated values of w have an absolute error (Δw):

$$\Delta w = \sqrt{\Delta\beta^2 + \Delta {X_1}^2 + \Delta {X_0}^2}. \tag{8}$$

Following this, the 'compound uncertainty' associated with each measurement of w is calculated as ± 0.3 mm. As the Young's modulus of the gelatine increases with time, correspondingly the deflection caused by the applied load decreases. Therefore the magnitude of w relative to Δw increases with time, as does the compound uncertainty associated with E ($\Delta E/E$). This is illustrated by the increasing size of the Young's modulus error-bars with time (Fig. 4).

3.3.3. Weighting the data

At each time interval, E was calculated using the deflection caused by each individual load (an average of three successive measurements). So for example, the complete dataset from experiment 25 (4 litres of 2.5 wt.% gelatine; Fig. 5) comprised 14 time intervals at which the Young's modulus was measured by loads 3–8 (where possible). The Young's modulus calculations were thus based on a total of 294 measurements of X_0 and X_1. In order that all the measurements for each experiment could be considered in the analysis, a data weighting process was carried out.

To account for the uncertainties associated with each Young's modulus measurement, the data were weighted (W) taking into account both the precision of the measurement and also the applied load used to take the measurement. Table 4 shows the quantitative weightings (depending on the uncertainty in E: $W_{\Delta E}$) and qualitative weightings (depending on the applied load used: $W_{\Delta\mathrm{Load}}$).

Weighting the Young's modulus data was straightforward, with high precision data ($\Delta E/E<5\%$) being weighted most highly ($W_{\Delta E}=8$). In comparison, weighting the applied loads could only be done qualitatively. Loads 1, 2 and 8–11 had low weightings ($W_{\Delta\mathrm{Load}}=1$ or 2) as

Please cite this article as: Kavanagh, J.L., et al., Gelatine as a crustal analogue: Determining elastic properties for modelling magmatic intrusions, Tectonophysics (2012), http://dx.doi.org/10.1016/j.tecto.2012.09.032

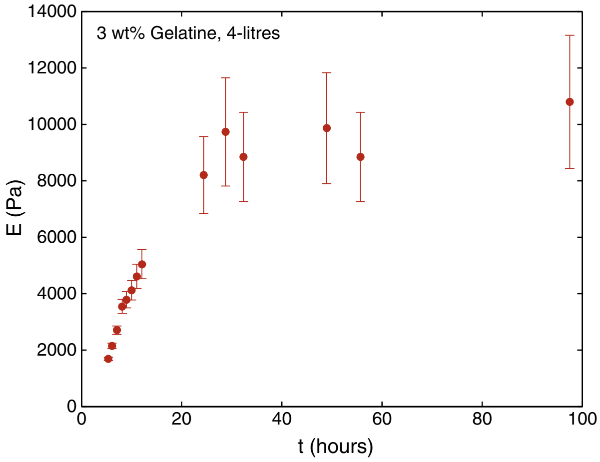

Fig. 4. Young's modulus evolution with time of 4 litres of 3 wt.% gelatine stored at 5 °C (Experiment 26). The Young's modulus was calculated from the deflection caused to the gelatine surface by Load 3 (see Table 2). Error bars show the uncertainty in E increases with time.

these had the highest D_L/D_C values and so their data were most likely to suffer from container sidewall effects (see Fig. 3). Loads 6 and 7 were also weighted poorly ($W_{\Delta Load}=2$ and 4, respectively), as their relatively high thicknesses caused stability issues (see Table 2). Load 5 exerted the lowest pressure and so inflicted only a small deflection to the gelatine surface; this deflection became increasingly small (and so measured with higher uncertainty) as the gelatine's Young's modulus increased during cooling. Therefore, Load 5 was weighted relatively low ($W_{\Delta Load}=4$). Loads 3 and 4 were weighted most highly ($W_{\Delta Load}=8$), deemed to have the most favourable balance between causing a deflection of the gelatine surface that could be measured to high precision, whilst experiencing minimal interaction with the container sidewalls.

The sum of the weights ($W_{\Delta E}+W_{\Delta Load}$) was used to give an overall weighting for each datum. This procedure enabled the 'best' data to have the strongest influence on the modelling results, whilst enabling all the data to be included in the analysis process.

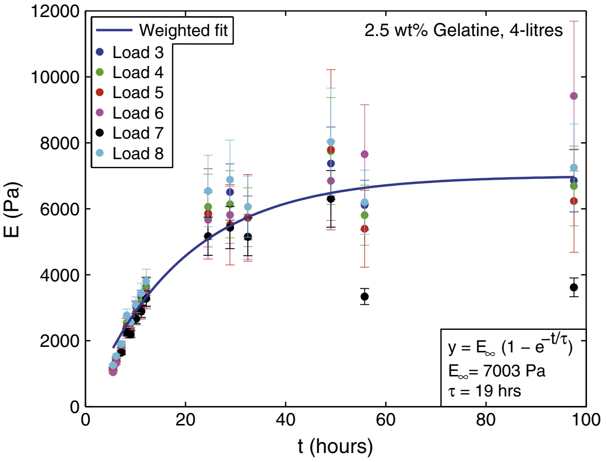

Fig. 5. Young's modulus evolution with time of 4 litres of 2.5 wt.% gelatine stored at 5 °C (Experiment 25). The Young's modulus was calculated from the deflection caused to the gelatine surface by a range of applied loads (loads 3–8; see Table 2). An exponential relationship best fits the data ($E=E_\infty(1-e^{-t/\tau})$), where $E_\infty=7003$ Pa and $\tau=19$ hr). E increases with time to an "effective plateau" ($0.9E_\infty$) of 6300 Pa after 44 hours curing ($t_{0.9E_\infty}$). The best-fit model (solid line) takes into account all measurements weighted according to $\Delta E/E$ and the load used (see Table 4). The outliers at ~55 hours and ~98 hours are from Load 7; these data have low weighting on the fitted trend due to this load having high thickness and small diameter that caused stability issues.

Table 4
Weightings (W) used to quantify the quality of Young's modulus measurement data. Quantitative-based weightings consider the uncertainty in $\Delta E/E$, whereas the effect of the load used to take the measurements could only be weighted qualitatively based on the results from Fig. 2. The combined weightings ($W_{\Delta E}+W_{\Delta Load}$) are then used in the subsequent data analysis.

Quantitative W	$\Delta E/E$ (%)	$W_{\Delta E}$
	<5	8
	5–10	7
	10–15	6
	15–20	5
	20–30	4
	30–50	3
	50–100	2
	>100	1
Qualitative W	Applied load	$W_{\Delta Load}$
	$Load_1$	1
	$Load_2$	1
	$Load_3$	8
	$Load_4$	8
	$Load_5$	4
	$Load_6$	4
	$Load_7$	2
	$Load_8$	2
	$Load_9$	1
	$Load_{10}$	1
	$Load_{11}$	1

4. Results

4.1. Young's modulus of gelatine

By measuring the deflection caused by a load applied to the surface of the solidified gelatine, we have been able to document the evolution of the gelatine's Young's modulus relative to a number of parameters. These will now be considered separately.

4.1.1. Effect of time

Fig. 5 shows the Young's modulus evolution with time of a 4-litre, 2.5 wt.% concentrated gelatine mixture kept at 5 °C (Experiment 25). The results show that, over the range of experimental conditions reported here, the gelatine is not able to support an applied load until it has a Young's modulus of approximately 1000 Pa. The Young's modulus then evolves exponentially with time to reach a plateau maximum value after which, as long as the experimental conditions are unchanged, the Young's modulus can be considered approximately constant with time. This exponential relationship between Young's modulus of the gelatine and time was documented for all the experiments:

$$E=E_\infty\left(1-e^{-\frac{t}{\tau}}\right), \qquad (9)$$

where E_∞ (the Young's modulus plateau; Pa) and τ (hr) are both empirically based constants determined from the exponential fit, and t is time (hr). The values of E_∞ and τ vary depending on V_{gel}, T_r and C_{gel} (see Table 5). As it is not feasible to wait for E_∞ to be reached during the timescale of an experiment, we define $0.9E_\infty$ as an "effective" Young's modulus plateau and $t_{0.9E_\infty}$ as the time taken to reach within 10% of E_∞. These values are provided as a guide for the experimentalist in Table 5. The only effects of decreasing the room temperature from 10 °C to 5 °C were to accelerate the rate of Young's modulus increase with time and so decrease $t_{0.9E_\infty}$.

The values of Young's modulus plateau reported on Table 5 were all measured with loads 3–8, so that in these experiments the height of gelatine was at least 2.7 times as large as the greatest load diameter. Therefore, according to Eq. (5), the stress at the base of the gelatine layer induced by the loads was less than 5% of their value, and the

Please cite this article as: Kavanagh, J.L., et al., Gelatine as a crustal analogue: Determining elastic properties for modelling magmatic intrusions, Tectonophysics (2012), http://dx.doi.org/10.1016/j.tecto.2012.09.032

Table 5
Model results showing E_∞ and τ values (correct to the nearest hour) for an exponential best-fit model $E = E_\infty(1-e^{-\frac{t}{\tau}})$ of calculated gelatine Young's moduli against time for a select group of experiments with the same T_r (5 °C). As E_∞ can not be reached within the timescale of an experiment, we define 0.9 E_∞ as an "effective" Young's modulus plateau. $t_{0.9E_\infty}$ is the time taken (correct to the nearest hour) to reach within 10% of E_∞. See Table 1 for experiment settings.

Experiment	C_{gel}	E_∞ (Pa)	τ (hr)	$0.9E_\infty$ (Pa)	$t_{0.9E_\infty}$ (hr)
13	2	4431 ± 44	14	3988	34
14	2	4475 ± 58	12	4028	28
15	2	4317 ± 82	15	3885	35
16	2	4172 ± 54	17	3755	38
17	2	3972 ± 36	30	3575	70
18	2	3628 ± 49	22	3265	52
19	2	4106 ± 109	33	3695	75
25	2.5	7003 ± 233	19	6303	44
26	3	10165 ± 284	19	9149	44
27	3.5	12775 ± 548	16	11498	37
28	4	15973 ± 441	16	14376	39

potential effect of the base of the tank on these values of Young's modulus plateau was neglected.

It should be noted that both the use of deionised water and storing the gelatine mixtures in a cold room (set at 5–10 °C) led to the inhibition of bacterial growth in the media. Thorough cleaning of the experimental container was also vital. Following these methods, our data shows that once the gelatine mixtures have reached their plateau in Young's modulus they can maintain this up to 140 hours after the initiation of the experiment.

4.1.2. Effect of concentration

For low concentrations (≥2 wt.% and <5 wt.%), the Young's modulus plateau (E_∞) of gelatine is linearly correlated with the concentration of the mixture (with a Coefficient of Determination $R^2 = 0.9992$), as shown in Fig. 6 for equal V_{gel} and H_{gel} (Experiments 16, 25–28). Values of E_∞ were calculated according to models fit to weighted Young's modulus data for a range of applied loads (see Section 1). It is unclear whether or not this linear relationship can be extrapolated to more highly concentrated gelatine mixtures.

Highly concentrated mixtures of gelatine (≥5 wt.%) proved difficult to work with, both in terms of preparing the experiments and then measuring their Young's moduli during the gelification process. During preparation of the mixtures, difficulties were encountered dissolving such highly concentrated mixtures and also removing all bubbles from the highly viscous solution was unachievable so that creating a homogeneous solid was not possible. Once the mixtures were in the 'gel-state' additional problems arose when attempting to measure their Young's moduli. When the loads were applied to these very rigid solids they were insufficient to cause a deflection of the gelatine surface that could be measured precisely; even the heaviest applied loads (Loads 9–11, see Table 2) caused such small deflections that the calculated Young's modulus value would have very large errors.

Due to the problems associated with these experiments we present only average Young's moduli for each experiment (Experiments 29–33); these were averaged from measurements taken from the time when the gelatine was deemed to have reached its Young's modulus plateau, an assumption verified by the lack of correlation between Young's modulus and time (indicated by a low r; see Table 6). The results suggest that more strongly concentrated gelatines have a higher Young's modulus plateau strength, though the associated standard deviations of the data were so large we were unable to evaluate whether this relationship continues the linear trend identified in Fig. 6.

The experimental setup and method described here to measure the Young's modulus of gelatine solids proved unsuitable for highly concentrated mixtures. In order to quantify the Young's modulus of highly concentrated gelatine mixtures (≥5 wt.% gelatine mixtures, where the Young's modulus ≳20,000 Pa), equipment more often associated with measuring the strength of rocks would be required. These tests are however beyond the scope of this study.

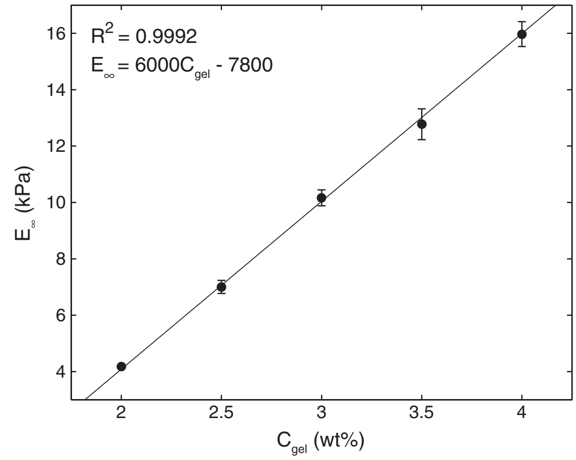

Fig. 6. Modelled plateau Young's modulus (E_∞) of a range of gelatine concentrations C_{gel} (Experiments 16, 25–28). Each test volume was 4 litres and was kept at 5 °C (T_r) in an equivalent container. The best-fit model indicates there is a positive-linear correlation ($R^2 = 0.9992$) between E_∞ and C_{gel}. More concentrated gelatine mixtures reach a higher Young's modulus plateau.

4.1.3. Effect of volume

Volume appears to have no impact on the Young's modulus plateau (E_∞) of the gelatine mixtures, as experiments that used the same concentration gelatine, stored at the same T_r, evolved to give the same value of E_∞(±500 Pa; Fig. 7). The small discrepancy between modelled values of E_∞ is assumed to be related to errors associated with the properties of the applied load and the measuring technique, as described above (Section 3.3.1). There is a broadly positive correlation between the volume of gelatine and the time taken to reach the plateau in Young's modulus (modelled from the weighted data), i.e. larger volumes of gelatine take longer to reach their Young's modulus plateau.

4.1.4. Effect of layer thickness

The time to reach the Young's modulus plateau value appears to correlate well with the time needed for the gelatine to cool down to T_r, and so we can use this correlation to predict the time an experimentalist would have to wait until the gelatine Young's modulus has reached its plateau value. The thermal diffusivity of gelatine is assumed to be that of its solvent, that is water: $\kappa = 1.4 \text{x} 10^6\ \text{m}^2\ \text{s}^{-1}$. The different containers used in the Young's modulus experiments were made of PMP, PP or Perspex (PMMA), and the thermal diffusivity for these thermoplastic polymers is about $10^{-7}\ \text{m}^2\ \text{s}^{-1}$, one order of magnitude lower than that of gelatine. Therefore, to a leading order,

Table 6
Average Young's modulus of highly concentrated (≥5 wt.%) gelatine mixtures. An average of 'n' measurements of the Young's modulus is shown ($\overline{E}$, correct to 2 s.f.), measurements were taken periodically using a range of applied loads for several hours after 16.5 hours curing at 5 °C. Calculated standard deviations (St. Dev.) indicate a high degree of uncertainty. The low Pierson Product–moment Correlation Coefficients (r) suggests no correlation between the Young's modulus measurements and time, supporting the assumption that the measurements were all made when the Young's modulus had plateaued.

Experiment	29	30	31	32	33
wt.%	5	5	10	20	30
$\overline{E}$	2.9×10^4	3.6×10^4	1.5×10^5	7.1×10^5	4.5×10^5
St. Dev.	1.4×10^4	2.0×10^4	1.6×10^4	1.4×10^6	5.6×10^5
r	0.40	0.32	−0.11	0.10	−0.55
n	36	9	12	13	13

Please cite this article as: Kavanagh, J.L., et al., Gelatine as a crustal analogue: Determining elastic properties for modelling magmatic intrusions, Tectonophysics (2012), http://dx.doi.org/10.1016/j.tecto.2012.09.032

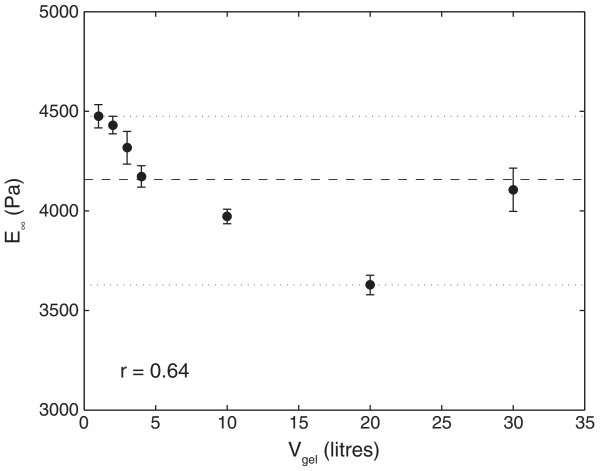

Fig. 7. Relationship between the modelled Young's modulus plateau ($E_\infty \pm \Delta E_\infty$) and gelatine mixture volume V_{gel} for 2 wt.% gelatine mixtures cured at 5 °C (Experiments 13–19). The mean E_∞ (dashed line) is shown and is most closely modelled by the 4-litre experiment (Experiment 16). The Pearson product–moment correlation coefficient ($r = 0.64$) indicates there is little or no correlation between E_∞ and V_{gel}. Gelatine mixtures of the same concentration (C_{gel}) evolve to the same $E_\infty \pm 500$ Pa independent of volume.

a gelatine solid cools down by conducting its heat through its upper surface, and the time t needed for thermal equilibrium is:

$$t = \frac{H_{gel}^2}{\kappa}, \tag{10}$$

where H_{gel} is the height of the gelatine solid in the container. Fig. 8 compares this cooling time with the time $t_{0.9E_\infty}$ taken to reach 90% of the Young's modulus plateau E_∞ for gelatine mixtures of various concentrations (2 wt.% to 5 wt.%), but all cured at the same temperature of 5 °C (Experiments 13–19 and 25–28, Table 1). We find reasonable agreement with a best linear fit:

$$t_{0.9E_\infty} \simeq (29.0 \pm 8.7) + (2.6 \pm 1.2)\frac{H_{gel}^2}{\kappa}. \tag{11}$$

Eq. (11) gives experimentalists a first-order estimate of the time they would need to wait for before a 2 wt.% to 5 wt.% gelatine solid cured at 5 °C reaches its Young's modulus plateau.

4.2. The fracture toughness of solidified gelatine

The stress intensity factor K_I at the tip of a two-dimensional, edge crack of height h can be expressed as:

$$K_I = \alpha\, \overline{\Delta P} \sqrt{\pi h}, \tag{12}$$

where α is a dimensionless factor that accounts for the conditions at the solid boundary (Lawn, 1993; Menand & Tait, 2002; Sneddon & Das, 1971), and $\overline{\Delta P}$ denotes the averaged excess pressure within the crack:

$$\overline{\Delta P} = \frac{1}{h}\int_0^h \Delta P(z)\ \mathrm{d}z, \tag{13}$$

where z is the vertical distance with origin at the reservoir-gelatine interface (Fig. 2a). Determining the value of α is a mixed problem, which simplifies when the edge of the elastic solid is a free boundary (Sneddon & Das, 1971), as was the case in our experiments. We measured the value of the coefficient α using the method of Sneddon & Das (1971), summarised in the Appendix.

Griffith (1921) and Irwin (1957) showed that the fracture toughness K_c of an ideal elastic and brittle solid is related to its Young's modulus E by the following theoretical relationship:

$$K_c = \sqrt{2\gamma_s E}, \tag{14}$$

where γ_s is the surface energy of the solid. This is the energy required to create a unit surface area within that solid, and is thought to depend only on the composition and temperature of the solid (Griffith, 1921).

The calculated values of gelatine fracture toughness are shown in Fig. 9. Despite some scattering, we find that Eq. (14) fits reasonably well these values, and that our best fit is:

$$K_c = (1.4 \pm 0.1)\sqrt{E}. \tag{15}$$

This equation and Fig. 9 show that provided the viscous behaviour of gelatine solids is negligible and deformation is essentially elastic, gelatine solids behave as ideal elastic and brittle solids in that their fracture toughness K_c and their Young's modulus E follow the theoretical relationship (Eq. (14)) expected for such solids.

We find a best estimate for the gelatine surface energy:

$$\gamma_s = 1.0 \pm 0.2\ \mathrm{J\ m^{-2}}. \tag{16}$$

Remarkably, this value is similar to the surface energy of brittle monocrystals such as diamond ($\gamma_s = 6$ J m^{-2}), silicon ($\gamma_s = 1.2$ J m^{-2}), silicon carbide ($\gamma_s = 4$ J m^{-2}), silica ($\gamma_s = 1$ J m^{-2}), sapphire ($\gamma_s = 4$ J m^{-2}), magnesium oxide ($\gamma_s = 1.5$ J m^{-2}), or lithium fluoride ($\gamma_s = 0.3$ J m^{-2}) (Lawn, 1993). We note, however, that in principle γ_s should depend on the composition and temperature of the solid (Griffith, 1921), and so the exact value of γ_s may vary from one type of gelatine to the other. But given the rather small range of values for brittle monocrystals, which are also similar to that for gelatine, we believe $\gamma_s = 1.0 \pm 0.2$ J m^{-2} is a fair estimate for acid, pig-skin derived gelatine with Bloom values between 200 and 260. Experiments carried out at lower temperatures than reported here will either result in higher Young's moduli or will take less time to reach their Young's modulus plateau, but their fracture toughness will scale following Eq. (15).

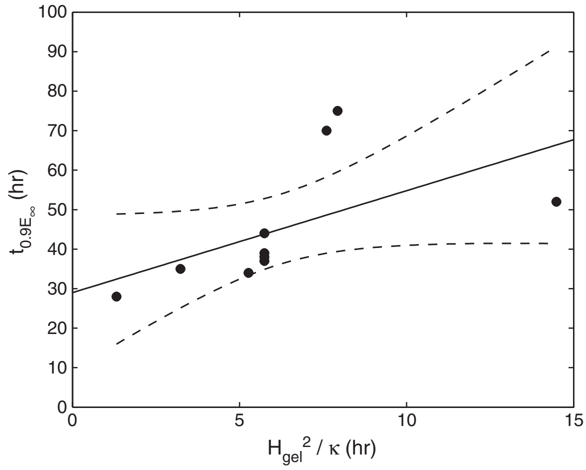

Fig. 8. Comparison of the time $t_{0.9E_\infty}$ needed to reach 90% of the Young's modulus plateau E_∞, with the conductive cooling time H_{gel}^2/κ given by Eq. (10). Data points correspond to experiments 13 to 19 and 25 to 28 (Table 1). These experiments had gelatine concentrations between 2 wt.% and 5 wt.%, and were all cured at 5 °C. The plateau time appears to correlate linearly with the cooling time: the line is the best linear fit, $t_{0.9E_\infty} \simeq (29.0 \pm 8.7) + (2.6 \pm 1.2)\frac{H_{gel}^2}{\kappa}$ (Eq. (11), $\boldsymbol{R^2} = 0.3211$); 95% confidence limits are indicated by dashed lines.

Please cite this article as: Kavanagh, J.L., et al., Gelatine as a crustal analogue: Determining elastic properties for modelling magmatic intrusions, Tectonophysics (2012), http://dx.doi.org/10.1016/j.tecto.2012.09.032

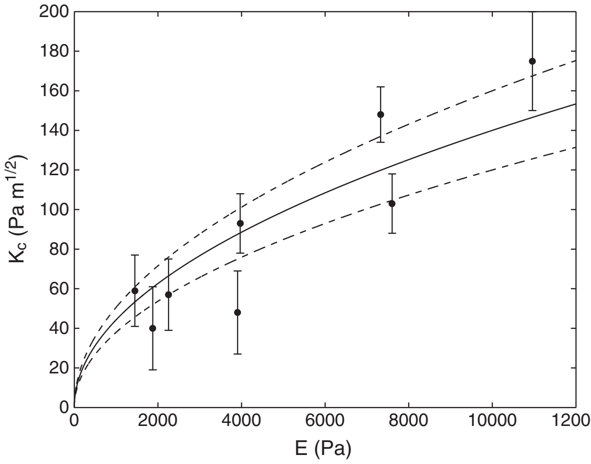

Fig. 9. The fracture toughness K_c of gelatine solids as a function of their Young's modulus E. The curve is the best fit through the data: $K_c = (1.4 \pm 0.1)\sqrt{E}$ (Eq. (18), $\boldsymbol{R^2} = 0.8196$), with the 95% confidence limits (dashed lines).

5. Geological applications

Di Giuseppe et al. (2009) summarise the application of gelatine as an analogue material for studying tectonic scale processes. They concluded low concentration gelatine mixtures (~2.5 wt.%) could be an appropriate analogue for upper crustal deformation experiments. Complementary to this, we now present scaling laws appropriate for studying magmatic intrusion dynamics. The scaling for this case is distinct to that presented by Di Giuseppe et al. (2009) as the stress and strain relations are different, and in particular the strain rates for dyke propagation are many order of magnitude faster than those of tectonic processes.

5.1. Scaling gelatine for experiments on dyke and sill propagation dynamics

An ideal scaled experiment has an analogue material that obeys geometric, kinematic and dynamic similarity with its natural counterpart (Hubbert, 1937); only then can observations and results of the experiment be used to understand the behaviour of the natural system. Other workers have presented simple scalings for the use of gelatine in its elastic-state as a crustal analogue for studying the propagation dynamics of magma-filled fractures (Acocella & Tibaldi, 2005; Cañón-Tapia & Merle, 2006). We now expand on these to present a comprehensive guide for scaling gelatine for this type of geological experiment.

Unlike tectonic processes, which occur on a length scale comparable with the thickness of the crust, dyke propagation is characterised by a much smaller length scale. This characteristic length scale is the buoyancy length L_b, as defined by Taisne & Tait (2009), which is the length over which magma buoyancy driving ascent balances resistance from rock fracture:

$$L = L_\mathrm{b} = \left(\frac{K_\mathrm{c}}{\Delta\rho g}\right)^{\frac{2}{3}}, \tag{17}$$

where L_b is the length of the buoyant head region of the propagating dyke, K_c is the fracture toughness of the intruded medium and $\Delta\rho$ is the density difference between the intruding fluid and its surroundings. Dyke propagation is determined by a local buoyancy balance in the inflated head region of the dyke, independent of the total buoyancy of the magma column between source and tip (Lister & Kerr, 1991; Taisne & Tait, 2009). In this case the reduced gravity (g') is the relevant parameter for scaling the dyke driving force:

$$g' = \frac{\Delta\rho}{\rho_\mathrm{solid}} g. \tag{18}$$

The timescale for the experiments is obtained by combining L_b (Eq. (17)) and g' (Eq. (18)):

$$T = \sqrt{\frac{L_\mathrm{b}}{g'}} = \rho_\mathrm{solid}^{\frac{1}{2}} K_\mathrm{c}^{\frac{1}{3}} (\Delta\rho g)^{-\frac{5}{6}}, \tag{19}$$

and from this the dyke velocity scale follows easily:

$$U = \frac{L_\mathrm{b}}{T} = (\Delta\rho g)^{\frac{1}{6}} K_\mathrm{c}^{\frac{1}{3}} \rho_\mathrm{solid}^{-\frac{1}{2}}. \tag{20}$$

This approach provides the appropriate scales (length, time and velocity) for each experiment, as one parameter or another is varied, and so provides the appropriate scaling factors $L^* = \frac{L_\mathrm{l}}{L_\mathrm{n}}$, $T^* = \frac{T_\mathrm{l}}{T_\mathrm{n}}$ and $U^* = \frac{U_l}{U_n}$:

$$L^* = \left(\frac{K_\mathrm{c}^*}{\Delta\rho^*}\right)^{\frac{2}{3}}, \tag{21}$$

$$T^* = \rho_\mathrm{solid}^{*\frac{1}{2}} K_\mathrm{c}^{*\frac{1}{3}} (\Delta\rho^*)^{-\frac{5}{6}}, \tag{22}$$

$$U^* = (\Delta\rho^*)^{\frac{1}{6}} K_\mathrm{c}^{*\frac{1}{3}} \rho_\mathrm{solid}^{*-\frac{1}{2}}, \tag{23}$$

where * refers to the ratio of the parameter values measured at the laboratory (subscript l) and natural (subscript n) scale.

Finally, the driving buoyancy pressure (P_b) scale for dykes is:

$$P_b = \Delta\rho g L_b, \tag{24}$$

which leads to deformation of the host medium around the head of the dyke. The elastic pressure scale (P_e) associated with this deformation is:

$$P_e = \frac{E}{2(1-\nu^2)} \frac{\psi}{L_b}, \tag{25}$$

where E and ν are the Young's modulus and Poisson's ratio of the elastic host, respectively, and ψ is the thickness (i.e. the opening) of the dyke head. These two stress scales balance each other during dyke propagation (e.g. (Lister & Kerr, 1991)), which gives:

$$E = 2\left(1-\nu^2\right) \Delta\rho g \frac{L_\mathrm{b}^2}{\psi}. \tag{26}$$

The Poisson's ratio for gelatine solids is $\nu \simeq 0.5$, whereas that of rocks lies usually between 0.25 and 0.3. As a result, the factor $2(1-\nu^2)$ varies by 15–20% between nature and laboratory experiments, and the Young's modulus scale factor simplifies as:

$$E^* = \Delta\rho^* L_\mathrm{b}^* \left(\frac{L_\mathrm{b}}{\psi}\right)^*. \tag{27}$$

Strictly speaking, field measurements made on the geometry of solidified dykes inform only on the final static state once solidification has taken place, and not on the geometry of propagating dykes. The discrepancy between the propagating and the final static geometry will certainly be important for those dykes that reached the surface because their thickness will decrease as magma erupts at the surface and elastic deformation of surrounding rocks is released. However, because of mass balance the discrepancy should be marginal for the majority of dykes, which stall in the crust and do not reach the surface; notwithstanding potential volume change due to solidification, the volume of a propagating dyke should be the same as the volume of a static dyke. This caveat aside, we can use the geometrical measurements made on solidified dykes as proxies for their geometry during propagation.

The aspect ratio $\frac{\psi}{L_b}$ of solidified dykes in nature is typically of the order of 10^{-4} to 10^{-3} (e.g. Gudmundsson (2011), Kavanagh &

Please cite this article as: Kavanagh, J.L., et al., Gelatine as a crustal analogue: Determining elastic properties for modelling magmatic intrusions, Tectonophysics (2012), http://dx.doi.org/10.1016/j.tecto.2012.09.032

Sparks (2011)), and on the order of 10^{-2} to 10^{-1} in gelatine experiments. Taking the following values as representative for natural dykes: $K_c = 10^7$ Pa $m^{\frac{1}{2}}$, $\Delta\rho = 100$ kg m^{-3}, $\rho_{solid} = 2800$ kg m^{-3}, and for experimental conditions: $K_c = 100$ Pa $m^{\frac{1}{2}}$, $\Delta\rho = 1000$ kg m^{-3} (air) or $\Delta\rho = 10$ kg m^{-3} (water), $\rho_{solid} = 1000$ kg m^{-3}, one gets:

$$L^* = 10^{-4}(\text{air}) \qquad \text{or} \qquad L^* = 2 \times 10^{-3}(\text{water}), \tag{28}$$

$$T^* = 2 \times 10^{-3}(\text{air}) \qquad \text{or} \qquad T^* = 9 \times 10^{-2}(\text{water}), \tag{29}$$

$$U^* = 5 \times 10^{-2}(\text{air}) \qquad \text{or} \qquad U^* = 2 \times 10^{-2}(\text{water}), \tag{30}$$

$$E^* = 10^{-6} - 10^{-5}(\text{air}) \qquad \text{or} \qquad E^* = 2 \times 10^{-6} - 2 \times 10^{-5}(\text{water}). \tag{31}$$

In the experiments, $L_l \simeq 5$ cm with air or $\simeq 1$ m with water; this corresponds in nature to $L_n \simeq 500$ m, which seems reasonable. Likewise, a velocity of a couple of mm/s (water) or cm/s (air) in the experiments would give dyke velocities on the order of 0.1–0.5 m/s in nature, in good agreement with estimates of dykes velocities (White et al., 2011). As for elastic deformation, the Young's modulus of rocks typically lies in the range $E_n = 10^9 - 10^{10}$ Pa, and so properly scaled experiments should involve gelatine solids with Young's modulus in the range $E_l = 10^3 - 10^5$ Pa when air is used as a magma analogue, or $E_l = 2 \times 10^3 - 2 \times 10^5$ Pa when water is used instead. Both ranges include values that have typically been used in dyke and sill experiments, and the data presented in this paper shows that 2–5 wt.% of gelatine is sufficient to reach this range of Young's modulus plateau (Fig. 6).

These calculations suggest gelatine experiments for magmatic intrusion propagation (dykes or sills) carried out at ~5–10 °C and with gelatine concentrations of 2–5 wt.% are adequately scaled geometrically, kinematically and dynamically.

6. Conclusions

We present results from a series of experiments that quantify the evolution of the elastic properties of gelatine with time. At 5–10 °C gelatine is in the 'gel-state,' over the range of stresses and strain rates presented here, and behaves like a solid, with almost ideal-elastic deformation. The Young's modulus of gelatine evolves with time, modelled best by an exponential relationship, with E evolving to a plateau value that would theoretically be achieved after an infinite amount of time. At low gelatine concentrations (<5 wt.%) the plateau Young's modulus depends linearly on the concentration of gelatine, and different volumes of equally concentrated gelatine evolve to the same plateau value. The method we use to measure the Young's modulus of the gelatine requires that the diameter of the load is ≲10% of both the diameter of the experimental container and thickness of the gelatine solid in order for side-wall and base effects to be avoided; larger dimensions relative to the gelatine solid will affect and lead to artificially high calculated values. Fracture toughness measurements show the K_c of gelatine follows the same relationship as ideal elastic-brittle solids: it is proportional to the square-root of the Young's modulus multiplied by twice its surface energy, which was calculated experimentally as 1.0 ± 0.2 J m^{-2}.

The transparent nature and photoelastic properties of gelatine mean deformations can be easily visualised and monitored, giving the experimental geologist insight into the propagation dynamics of magmatic intrusions. However, caution needs to be taken when using gelatine as an analogue for the Earth's elastic crust. These type of experiments are best carried out at 5–10 °C in order for the viscous component of gelatine's deformation behaviour to be negligible. At these temperatures gelatine is a good analogue for magmatic intrusion propagation in Earth's elastic crust; using gelatine concentrations from 2 to 5 wt.% will ensure gelatine is adequately scaled geometrically, kinematically and dynamically.

Acknowledgements

JK gratefully acknowledges the support of a Monash University Margaret Clayton Women in Research Postdoctoral Fellowship, and a Leverhulme grant awarded to R.S.J. Sparks and J. Blundy at Bristol University's Geophysical Fluid Dynamics Laboratory where the Young's modulus experiments were carried out. The fracture toughness experiments were carried out at Institut de Physique du Globe de Paris in 1998 during TM's PhD, and the valuable help of Steve Tait and Gérard Bienfait is acknowledged. KAD acknowledges a NERC consortium grant. This is Laboratory of Excellence *ClerVolc* contribution no 29. E. Di Giuseppe, M. Diez and N. Le Corvec are thanked for thought-provoking discussions that inspired this work. B. Taisne and an anonymous reviewer are thanked for thoughtful comments which improved the manuscript.

Appendix A

In the fracture toughness experiments, the pressure distribution (ΔP) within the crack just prior to its propagation was:

$$\Delta P(z) = \left(\rho_g - \rho_w\right) gz, \qquad 0 \le z \le z_l, \tag{32}$$

$$\Delta P(z) = \rho_g gz - \rho_w g z_l, \qquad z_l \le z \le h, \tag{33}$$

where z_l is the level of the air-water interface within the crack ($z_l = 0$ when the crack is full of air), ρ_g and ρ_w are the density of the solid gelatine and water, respectively. The density of air ρ_a is assumed to be negligible. Following Sneddon & Das (1971), by expressing this crack excess pressure as $\Delta P(z) = \overline{\Delta P} f(z)$, the value of α in Eq. (12) is then determined by calculating the value $\Lambda(1)$, where Λ is the solution of the following integral:

$$\Lambda(z) - \int_0^1 \Lambda(u) L(z,u)\, du = \frac{2}{\pi} \int_0^z \frac{f(s)\, ds}{\sqrt{z^2 - s^2}}, \qquad 0 \le z \le 1, \tag{34}$$

where z has been normalised with respect to the crack height h, u and s are integration variables, and:

$$L(z,u) = \frac{16zu}{\pi^2} \left[\frac{z^2 + u^2}{\left(z^2 - u^2\right)^3} ln\left(\frac{z}{u}\right) - \frac{1}{\left(z^2 - u^2\right)^2} \right], \qquad \text{if } z \ne u, \tag{35}$$

and:

$$L(z,u) = \frac{4}{3\pi^2 u}, \qquad \text{if } z = u. \tag{36}$$

Eq. (34) was solved using the gaussian quadrature method. This leads to n linear equations:

$$\Lambda(x_i) - \sum_{j=1}^{n} w_j L\left(x_i, x_j\right) \Lambda\left(x_j\right) = \frac{2}{\pi} \int_0^{x_i} \frac{f(s)\, ds}{\sqrt{x_i^2 - s^2}}, \qquad (i = 1, 2, \ldots, n), \tag{37}$$

to be solved in order to determine the values $\Lambda(x_1)$, $\Lambda(x_2)$, …, $\Lambda(x_n)$, using the values x_1, x_2,…, x_n and their respective weights w_1, w_2, …, w_n (as listed in Table 52.8 from Abramowitz & Stegun, (1964)). The value of α is then:

$$\alpha = \Lambda(1) = \frac{2}{\pi} \int_0^1 \frac{f(s)\, ds}{\sqrt{1^2 - s^2}} + \sum_{j=1}^{n} w_j L\left(1, x_j\right) \Lambda\left(x_j\right). \tag{38}$$

The gelatine fracture toughness K_c was then equated with the stress intensity factor (12), using the average excess pressure $\overline{\Delta P}$

Please cite this article as: Kavanagh, J.L., et al., Gelatine as a crustal analogue: Determining elastic properties for modelling magmatic intrusions, Tectonophysics (2012), http://dx.doi.org/10.1016/j.tecto.2012.09.032

measured just prior to the crack propagation and the corresponding value of α (Eq. (38)).

References

Abramowitz, M., Stegun, I., 1964. Handbook of Mathematical Functions. Dover Publications Inc.

Acocella, V., Tibaldi, A., 2005. Dike propagation driven by volcano collapse: a general model tested at stromboli, italy. Geophysical Research Letters 32 (8), L08308.

Askeland, D., Fulay, P., Wright, W., 2010. The Science and Engineering of Materials, 6th Edition. Thomson Engineering.

Bevington, P., Robinson, D., 2003. Data Reduction and Error Analysis for the Physical Sciences, 3rd Edition. Mc Graw-Hill, USA.

Cañón-Tapia, E., Merle, O., 2006. Dyke nucleation and early growth from pressurized magma chambers: insights from analogue models. Journal of Volcanology and Geothermal Research 158 (3–4), 207–220.

Crisp, J., 1952. The Use of Gelatin Models in Structural Analysis. Proceeding IB of the Institute of Mechanical Engineers 12, 580–604.

Dahm, T., 2000. On the shape and velocity of fluid-filled fractures in the earth. Geophysical Journal International 142 (1), 181–192.

Di Giuseppe, E., Funiciello, F., Corbi, F., Ranalli, G., Mojoli, G., 2009. Gelatins as rock analogs: a systematic study of their rheological and physical properties. Tectonophysics 473 (3–4), 391–403.

Djabourov, M., Leblond, J., Papon, P., 1988a. Gelation of aqueous gelatin solutions. I. Structural investigation. Journal de Physique France 49 (2), 319–332.

Djabourov, M., Leblond, J., Papon, P., 1988b. Gelation of aqueous gelatin solutions. II. Rheology of the sol–gel transition. Journal de Physique France 49, 333–343.

Farquharson, F., Hennes, R., 1940. Gelatin models for photoelastic analysis of stress in earth masses. Civil Engineering 10 (4), 211–214.

Fiske, R., Jackson, E., 1972. Orientation and growth of Hawaiian volcanic rifts: the effect of regional structure and gravitational stresses. Proceedings of the Royal Society of London. Series A: Mathematical and Physical Sciences 329, 299–326.

Griffith, A., 1921. The phenomena of rupture and flow in solids. Philosophical transactions of the Royal Society of London. Series A: Mathematical and physical sciences 221, 163–198.

Gudmundsson, A., 2011. Rock Fractures in Geological Processes. Cambridge University Press.

Heimpel, M., Olson, P., 1994. Buoyancy-driven fracture and magma transport through the lithosphere: models and experiments. International Geophysics 57, 223–240.

Hubbert, M., 1937. Theory of scale models as applied to the study of geologic structures. Bulletin of the Geological Society of America 48 (10), 1459–1517.

Hyndman, D., Alt, D., 1987. Radial dikes, laccoliths, and gelatin models. Journal of Geology 95, 763–774.

Irwin, G., 1957. Analysis of stresses and strains near the end of a crack traversing a plate. Journal of Applied Mechanics 24, 361–364.

Ito, G., Martel, S., 2002. Focusing of magma in the upper mantle through dike interaction. Journal of Geophysical Research 107 http://dx.doi.org/10.1029/2001JB000251.

Kavanagh, J., Sparks, R., 2011. Insights of dyke emplacement mechanics from detailed 3D dyke thickness datasets. Journal of the Geological Society 168, 965–978.

Kavanagh, J., Menand, T., Sparks, R., 2006. An experimental investigation of sill formation and propagation in layered elastic media. Earth and Planetary Science Letters 245 (3–4), 799–813.

Kervyn, M., Ernst, G., de Vries, B., Mathieu, L., Jacobs, P., 2009. Volcano load control on dyke propagation and vent distribution: Insights from analogue modeling. Journal of Geophysical Research 114 (B3), B03401.

Lawn, B., 1993. Fracture of Brittle Solids, 2nd Edition. Cambridge University Press, New York.

Lister, J., Kerr, R., 1991. Fluid-mechanical models of crack propagation and their application to magma transport in dykes. Journal of Geophysical Research - Solid Earth 96 (B6), 10049–10077.

Maaløe, S., 1987. The generation and shape of feeder dykes from mantle sources. Contributions to Mineralogy and Petrology 96 (1), 47–55.

Maccaferri, F., Bonafede, M., Rivalta, E., 2010. A numerical model of dyke propagation in layered elastic media. Geophysical Journal International 180 (3), 1107–1123.

Mathieu, L., van Wyk de Vries, B., Holohan, E., Troll, V., 2008. Dykes, cups, saucers and sills: analogue experiments on magma intrusion into brittle rocks. Earth and Planetary Science Letters 271 (1–4), 1–13.

McGuire, W., Pullen, A., 1989. Location and orientation of eruptive fissures and feeder dykes at Mount Etna; influence of gravitational and regional tectonic stress regimes. Journal of Volcanology and Geothermal Research 38 (3–4), 325–344.

McLeod, P., Tait, S., 1999. The growth of dykes from magma chambers. Journal of Volcanology and Geothermal Research 92 (3–4), 231–245.

Menand, T., Tait, S., 2001. A phenomenological model for precursor volcanic eruptions. Nature 411, 678–680.

Menand, T., Tait, S., 2002. The propagation of a buoyant liquid-filled fissure from a source under constant pressure: an experimental approach. Journal of Geophysical Research 107 (2306), 177–185.

Menand, T., Daniels, K., Benghiat, P., 2010. Dyke propagation and sill formation in a compressive tectonic environment. Journal of Geophysical Research 115 (B8), B08201.

Mezger, T., 2002. The Rheology Handbook. Vincentz.

Muller, J., Ito, G., Martel, S., 2001. Effects of volcano loading on dike propagation in an elastic half-space. Journal of Geophysical Research - Solid Earth 106 (B6), 11101–11113.

Nelson, B., Dealy, J., 1993. Dynamic Mechanical Analysis Using Complex Waveforms. Chapman & Hall, Cambridge, Ch.

Peyrelasse, J., Lamarque, M., Habas, J., El-Bounia, N., 1996. Rheology of gelatin solutions in the sol–gel transition. Physical Review E 53 (6), 6126–6133.

Pollard, D., 1973. Derivation and evaluation of a mechanical model for sheet intrusions. Tectonophysics 19 (3), 233–269.

Pollard, D., Johnson, A., 1973. Mechanics of growth of some laccolithic intrusions in the Henry mountains, Utah, II: bending and failure of overburden layers and sill formation. Tectonophysics 18 (3–4), 311–354.

Richards, R., Mark, R., 1966. Gelatin models for photoelastic analysis of gravity structures. Experimental Mechanics 6 (1), 30–38.

Righetti, R., Ophir, J., Srinivasan, S., Krouskop, T., 2004. The feasibility of using elastography for imaging the Poisson's ratio in porous media. Ultrasound in Medicine and Biology 30 (2), 215–228.

Rivalta, E., Böttinger, M., Dahm, T., 2005. Buoyancy-driven fracture ascent: experiments in layered gelatine. Journal of Volcanology and Geothermal Research 144 (1–4), 273–285.

Ross-Murphy, S., 1992. Structure and rheology of gelatin gels: recent progress. Polymer 33 (12), 2622–2627.

Sneddon, I., Das, S., 1971. The stress intensity factor at the tip of an edge crack in an elastic half-plane. International Journal of Engineering Science 9 (1), 25–36.

Taisne, B., Tait, S., 2009. Eruption versus intrusion? Arrest of propagation of constant volume, buoyant, liquid-filled cracks in an elastic, brittle host. Journal of Geophysical Research 114 (B6), B06202.

Taisne, B., Tait, S., 2011. Effect of solidification on a propagating dike. Journal of Geophysical Research 116 (B1), B01206.

Taisne, B., Tait, S., Jaupart, C., 2011. Conditions for the arrest of a vertical propagating dyke. Bulletin of Volcanology 73, 191–204.

Takada, A., 1990. Experimental study on propagation of liquid-filled crack in gelatin: shape and velocity in hydrostatic stress condition. Journal of Geophysical Research 95, 8471–8481.

Takada, A., 1994. Accumulation of magma in space and time by crack interaction. International Geophysics 57, 241–257.

Takada, A., 1999. Variations in magma supply and magma partitioning: the role of tectonic settings. Journal of Volcanology and Geothermal Research 93 (1–2), 93–110.

Tan, E., 1947. Stability of soil slopes. Proceedings of the American Society of Civil Engineers 73, 19–38.

Timoshenko, S., Goodier, J., 1970. Theory of Elasticity. McGraw-Hill Higher Education.

Walter, T., Troll, V., 2003. Experiments on rift zone evolution in unstable volcanic edifices. Journal of Volcanology and Geothermal Research 127 (1–2), 107–120.

Watanabe, T., Masuyama, T., Nagaoka, K., Tahara, T., 2002. Analogue experiments on magma-filled cracks: competition between external stresses and internal pressure. Earth Planets and Space 54, 1247–1261.

Watase, M., Nishinari, K., 1980. Rheological properties of agarose-gelatin gels. Rheologica Acta 19 (2), 220–225.

White, R., Drew, J., Martens, H., Key, J., Soosalu, H., Jakobsdóttir, S., 2011. Dynamics of dyke intrusion in the mid-crust of Iceland. Earth and Planetary Science Letters 304, 300–312.

Please cite this article as: Kavanagh, J.L., et al., Gelatine as a crustal analogue: Determining elastic properties for modelling magmatic intrusions, Tectonophysics (2012), http://dx.doi.org/10.1016/j.tecto.2012.09.032

Chapter 5

Prospective Projects

(Potential funding fo the next couple of years: *AXA*, *ANR*, and *ClerVolc*)

Over the next years, I plan to conduct a series of projects related to the transport, storage and degassing of magma in the Earth's crust. The long-term aim is to improve our understanding of magma chamber formation, our ability to read geodetic surface signals related to magmatic activity, existing models for dyke propagation, and the relationship between magma degassing and magma movement within volcanic plumbing systems.

5.1 Magma storage in the crust

5.1.1 Solidification effects on sills dynamics

Last spring, during two months, Lola Chanceaux, a Master student at the LMV, carried out analogue experiments to investigate the potential effect on solidification of the formation of sills. These preliminary experiments involved the injection of fluid at a constant rate into a two-layer, stratified gelatine solid with an upper, stiffer elastic layer, an *a priori* favourable configuration for sill formation (Kavanagh et al., 2006). The injected fluid was a vegetable oil with a well defined phase transition at 31 °C: it solidifies almost instantaneously below this temperature but is fluid at lower temperature with a viscosity of $\sim 10^{-2}$ Pa s (Galland et al., 2006).

These experiments suggest that contrary to the isothermal case, the range of conditions for sill formation is much reduced and depends on both the temperature contrast between injected fluid and solid host, and the injection rate (Fig. 5.1). Following Taisne and Tait (2011), these can be quantified by a dimensionless temperature $\Theta = (T_s - T_\infty)/(T_i - T_\infty)$, where T_i is the initial temperature of the injected fluid, T_s its solidification temperature, T_∞ the far-field temperature of the solid, and which characterises the strength of the temperature contrast between fluid and solid; and a dimensionless flux Φ_{dyke}, which is the ratio of advected heat by the incoming fluid in the dyke to that conducted away by the solid, and which for a buoyant feeder dyke can be expressed as $\Phi_{dyke} \sim (Q\Delta\rho g)/(E\kappa)$. $\Theta \to 0$ when the fluid is injected at a temperature that is much higher than its solidification temperature, whereas an initial temperature close to the solidification temperature leads to $\Theta \to 1$ and solidification will be expected to affect dyke propagation (Taisne and Tait, 2011) and potentially sill formation. Likewise, solidification effects will be expected for low magma influx ($\Phi_{dyke} \to 0$) and should be negligible for high magma influx ($\Phi_{dyke} \to \infty$).

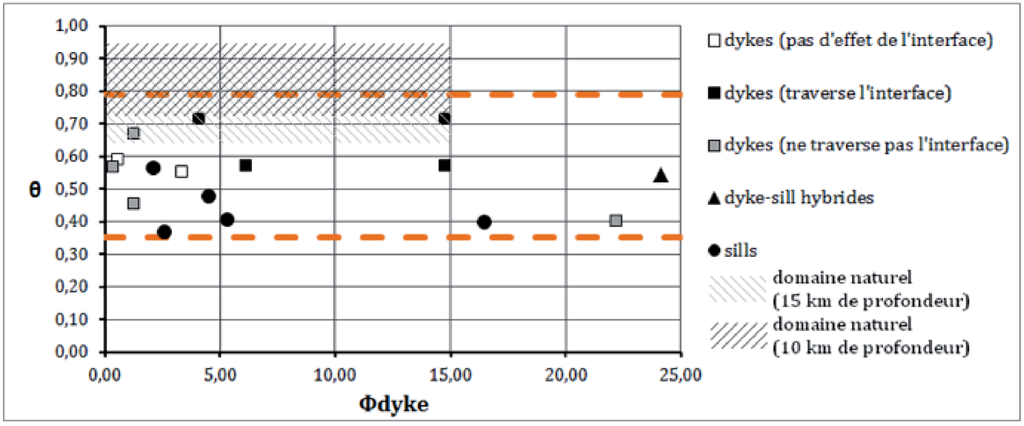

Figure 5.1: Outcomes of preliminary thermal sill experiments as a function of dimensionless injection rate Φ and initial dimensionless temperature Θ. Dashed lines represent the experimental range of Θ values. Hatched areas correspond to expected range of natural conditions: T_i = 1200 °C and T_s = 950 °C were taken as representative of basalts, T_i = 800 °C and T_s = 775 °C as representative of rhyolites, T_∞ = 300 °C and T_∞ = 500 °C at 10 and 15 km depth, respectively, E = 10 GPa, $\kappa = 10^{-6}$ m^2/s, $\Delta\rho$ = 100 kg/m^3 and magma influx in the range 1–100 m^3/s.

The results revealed that too high dimensionless temperatures or too low injection rates lead to feeder dykes stopping at the interface between the upper rigid layer and the lower more compliant layer, but their partial solidification prevented them to intrude the interface and form sills (Fig. 5.1). Thus the range of conditions for the formation of sills appears reduced compare to the isothermal case: sills could only form when the dimensionless injection rate Φ was greater than ~ 2 and when the dimensionless temperature Θ was less than ~ 0.6. Interestingly, compared to geological conditions, these experiments would suggest that sills would be extremely difficult to form owing to unfavourable thermal conditions. This might reflect ill-constrained temperatures as these were only crudely measured in these primarily experiments. Thus these results and comparison with natural conditions need to be clarified.

Additionally, solidification might impede the propagation of sills. Sill dynamics are controlled by a balance between viscous pressure drop and elastic deformation of the surrounding host (section 4.3). Furthermore, a constant magma influx seems a geophysically realist, initial condition for individual intrusion propagation (Traversa et al., 2010). In this case, and assuming an axisymmetric sill geometry for simplicity, one can define a dimensionless flux associated with sill propagation

$$\Phi_{sill} \sim \frac{1}{\kappa}\left(\frac{\mu(1-\nu^2)Q^5}{EL^7}\right)^{1/4}, \tag{5.1}$$

where L is the length of a propagating sill fed by a constant magma influx Q. This dimensionless flux Φ_{sill} decreases as $L^{-7/4}$, and so solidification would be expected to exert a control on sill dynamics and ultimately limit their lateral extent. Equation (5.1) being dimensionless, it can be directly upscaled to natural conditions, and so used to test whether syn-propagation magma solidification can indeed limit the size of sills. As discussed previously, larger igneous bodies such as laccoliths and larger plutons can grow by vertical accretion of sills (Menand, 2008, 2011, section 4.3), thus assessing the validity of equation (5.1) is also of importance to understand what determines the lateral extent of plutons *sensu lato*.

This hypothesis will be tested with well-constrained thermal sill experiments (experimental conditions will be better controlled by means of thermocouples both at the injection point and within the gelatine solids). These will be carried out in 2013, and the conditions for sill formation will be first clarified, before quantifying the sill dynamics and testing them against equation (5.1).

5.1.2 The formation of magma chambers

Until recently, Santorini volcano, Greece, was understood as a volcano whose shallow reservoir is regularly recharged with small volumes of mafic magmas during extremely short duration (Martin et al., 2008). Crystal diffusion chronometry applied to erupted feldspars crystals has challenged this view by revealing that a reactivation of the shallow magma chamber by the injection of silicic magma took place before the Minoan caldera-forming eruption around 1600 BC (Druitt et al., 2012). This reactivation was rapid (< 100 years) and at a rate more than 50 times faster than the long-term average influx of magma that feeds the volcano (> 0.05 km^3/yr instead of 10^{-3} km^3/yr on average). Furthermore, this recharge would have represented a sizable proportion (at least 15 vol.% of the erupted material) of the shallow magma chamber. This view of the inner workings of Santorini volcano is supported by recent InSAR and GPS measurements of surface deformation (Parks et al., 2012) which show that since January 2011 the shallow reservoir of Nea Kameni volcano has been recharged with a similarly large influx of magma,

~ 0.01 km^3/yr, and that the volume of this recharge would represent 10-50 % of the volumes of recorded dome-building eruptions that have occurred since AD 1570. Furthermore, that the shallow magma chamber could be recharged by large volumes of magma and then erupt dome-forming dacitic material with only a minor volumetric proportion of mafic enclaves strongly suggests a deep origin of the dacitic recharge. The emerging view of Santorini is thus that of a volcano, whose shallow reservoir is regularly replenished from deep with high-flux batches of already differentiated magma, the duration of which is much shorter than that of intervening repose periods (Druitt et al., 2012; Parks et al., 2012). This fits perfectly with the developing consensus on the generation of evolved magmas in deep crustal hot zones (Annen et al., 2006) and the incremental emplacement and growth of igneous bodies in the upper crust (Menand et al., 2011). This points to an intimate relationship between the recharge of volcanoes and their shallow magma chambers and the growth of now solidified plutons.

In the deep hot zone model (Annen et al., 2006), mafic sills are repeatedly injected at the base of the lower crust. The first sills solidify completely and transfer heat to the crust. Over time, as more sills are emplaced, the temperature of the intruded region rises and ultimately reaches the solidus of the mafic material. Subsequent intrusions do not completely solidify, which leads to the progressive accumulation of residual melts, the remelting of previously intruded mafic material, and the partial melting of the surrounding crust. Accordingly, the chemical diversity of arc magmas and granites is generated in these deep hot crustal zones owing to the coexistence and mixing of both crustal and mantle melts in proportions dictated by the fertility of the intruded crust as well as the geometric distribution and rate of emplacement of the mafic sills. Comparatively, textural diversity is related to shallow-level crystallisation in upper parts of the crust. As magmas leave their hot zones in the form of dykes, the vast majority of them stalls before reaching the surface, many of them as sills. Numerous geological, geophysical and geochronological evidence indicate that many sills amalgamate together to form larger igneous bodies (Menand, 2011). Numerical modelling of pluton growth by this mechanism suggests that the emplacement of magma bodies is a multi-timescale process, and that magma chambers are ephemeral. Their development would correspond to the highest magma fluxes as growing a sizable amount of eruptible magma requires minimum magma fluxes from deeper source of 10^{-3} to 10^{-2} km^3/yr, i.e. several orders of magnitude larger than the long-term-averaged rates estimated form field studies (Annen, 2009). An incremental growth for plutons is widely accepted, and the issue is now to identify the processes and quantify the mechanisms what control the size and frequency of these increments. The latest developments in analytical U-Pb dating on zircons allow age measurements with a precision down to less than $\pm$ 50 kyrs, which in turn enable us to recognise the incremental growth of large plutons with unprecedented details. Spectacular examples include the southern part of the Adamello batholith, northern Italy (Schaltegger et al., 2009) and the Torres del Paine laccolith in Chile (Michel et al., 2008; Leuthold et al., 2012). U-Pb dating extends to large scales the detailed field observations made on smaller plutons in Utah and Nevada, USA (Horsman et al., 2010; Miller et al., 2011), and thus gives additional arguments for a plutons growth by accumulation and amalgamation of successive magmatic sheets.

Simple thermal considerations provide additional support to the conclusions that the vast majority of plutons could not have developed from a single episode of continuous magma injection. Dykes need to propagate fast enough through the crust to avoid death by solidification. Indeed, flowing magma advects heat along a propagating dyke whilst heat is conducted away by the colder host rocks. If advection occurs at a lower rate than conduction then magma will ultimately solidify completely and dyke propagation will cease. That much is well known, and it has been shown that a dyke must be wider than a critical minimum width w_c so that magma may ascend through the crust over a distance H without freezing:

$$w_c = 1.5\left(\frac{S_m}{S_\infty^2}\right)^{3/4}\left(\frac{\mu\kappa H}{\Delta\rho g}\right)^{1/4}, \tag{5.2}$$

where $S_m = L/[C_p(T_0 - T_f)]$, $S_\infty = L/[C_p(T_f - T_\infty)]$, L is the latent heat of the magma, C_p is its specific heat capacity, T_0, T_f and T_∞ are the initial magmatic temperature, the magma freezing temperature and the far-field temperature of the crust, respectively, μ is the viscosity of the flowing magma, κ is its thermal diffusivity, $\Delta\rho$ is the difference between the density of the host rocks and that of the magma, and g is the gravitational acceleration (Petford et al., 1993). Considering flow as laminar and driven by buoyancy within a dyke of thickness w and horizontal extent B, magma flows with an average velocity $\overline{u} = (\Delta\rho g w^2)/(12\mu)$ and thus an average volumetric flow rate $\overline{Q} = (\Delta\rho g w^3 B)/(12\mu)$. Combining this latter expression with equation (5.2) gives a critical minimum magma supply rate

$$Q_c = \frac{9}{32}\left(\frac{S_m}{S_\infty^2}\right)^{9/4}\left(\frac{\Delta\rho g\kappa^3 H^3}{\mu}\right)^{1/4} B. \tag{5.3}$$

This is the minimum influx of magma a buoyant dyke needs in order to propagate over a distance H without freezing. Therefore, a pluton that grows by a single and continuous injection of magma would need to be fed with at least this magma supply rate Q_c, otherwise its feeder dyke would freeze before it could reach the crustal emplacement level of that pluton; Q_c can be envisaged as a minimum pluton filling rate.

Considering magma viscosities in the range of 10^4 to 10^8 Pa s, a minimum supply rate Q_c of 0.1 to 10 km^3/yr is required to feed plutons that are 5 to 30 km away from their source. Fig. 5.2 compares these minimum magma fluxes with estimates of the maximum long-term-averaged filling rates for 33 different plutons as compiled by de Saint-Blanquat et al. (2011). All but four of the reported plutons had too low a magma supply rate to have formed by a single episode of continuous magma injection; their feeder dyke would have frozen before reaching their emplacement level. This finding holds irrespective of the emplacement depth of the plutons, the composition of their magmas and the tectonic setting. Of the four remaining plutons, three involve small magma volumes (< 30 km^3), but small

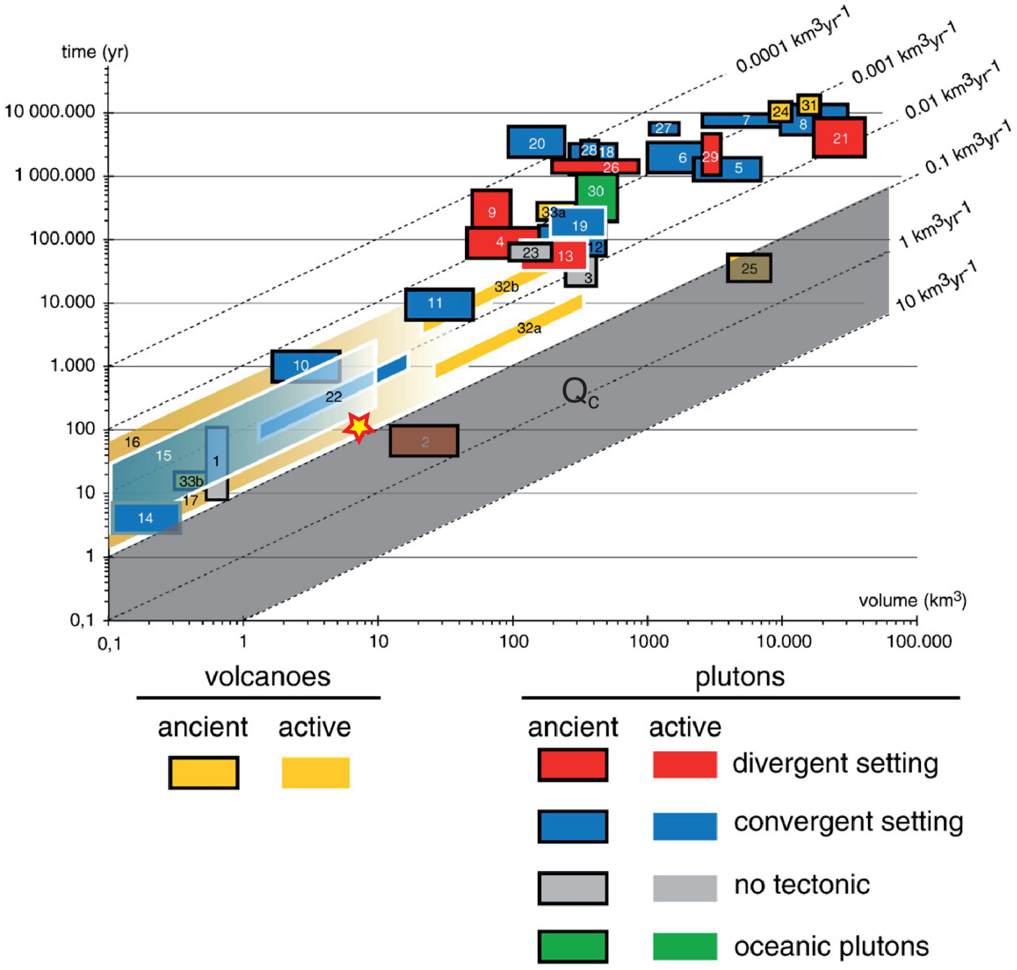

Figure 5.2: Comparison of Q_c (grey area) with estimates of the maximum, long-term-averaged filling rates for 33 different plutons as compiled by de Saint-Blanquat et al. (2011). The yellow start represents estimates for the volume (6–9 km^3) and rate (0.05 km^3/yr) of the magma recharge that preceded the Minoan eruption that occurred at Santorini volcano around 1600 BC (Druitt et al., 2012). The current activity at Nea Kameni involves similar flux but too small a volume (10^{-2} km^3) to appear in the graph.

plutons are precisely those that most convincingly exhibit field evidence of growth by incremental emplacement of magma sheets (de Saint-Blanquat et al., 2001, 2006; Horsman et al., 2010; Miller et al., 2011). Thus the formation of large plutons must involve the injection of successive, discrete magma pulses with a minimum flux of ~ 0.1 km^3/yr. This flux must also be the minimum flux associated with the recharge of magma chambers such as that of Santorini volcano. Yet, this is two to ten times larger than the recharge rates estimated for the Minoan eruption or the current activity at Nea Kameni (Fig. 5.2). However, these latter rates are not instantaneous fluxes related to magma intrusions but rather integrate also intervening repose periods. Instantaneous recharge rates would thus likely be larger and thus consistent with the minimum flux required for magma migration between deep hot zones and shallower reservoirs.

This thermal analysis would thus suggest that volcanoes like Santorini are regularly fed by magmas that originate from a deep source where they can differentiate prior to recharging its shallow reservoir. This feeding would occur only when the flux is high enough to prevent magmas from solidifying before reaching the shallow reservoir level, that is with a minimum flux of ~ 0.1 to 10 km^3/yr. However, their shallow reservoir can only develop into a potentially active magma chamber with a sizeable amount of eruptible magma when the time-averaged feeding flux exceeds 10^{-3}–10^{-2} km^3/yr (Annen, 2009). For lower average fluxes, the volume of eruptible magma available at anyone time would be, at best, that of a single magmatic recharge, hence with a more limited potential for eruption. This model is not restricted to Santorini and is applicable to other volcanoes.

Pushing and testing this model further require high precision age dating. Diffusion chronometry provides access to timescales that are commensurate with the instantaneous emplacement of magma intrusions such as dykes (Druitt et al., 2012). Additionally, continuous geodetic measurements of volcano surface deformation provide a means to calculate and follow the recharge volumes and rates through time. In principle this should enable us to discriminate between magmatic intrusions bound to crystallise because they involve too low magma fluxes from those recharging a reservoir with fluxes that are high enough to develop a potential for eruption.

5.1.3 Relating geodetic surface signals to magma accumulation in the crust

(Potential Funding: *ClerVolc*)

The arguments presented above raise also the question of our ability to read geodetic surface signals: can we differentiate between surface deformation produced by an influx of magma bound to form a frozen pluton from one associated with the recharge of a magma chamber? Perhaps a more useful question would be: which parameters do we need to properly determine in order to make such a distinction?

Interferometric Synthetic Aperture Radar (InSAR) provides a remarkable geodetic tool for the remote monitoring of volcano surface deformation with high spatial precision and a repeat time down to a few days (e.g. Prittchard and Simmons, 2002; Froger et al., 2004, 2007). However, if most eruptions are preceded by days to months, and perhaps even years, of subtle seismic activity caused by the ascent of magma and ground uplift due to the pressurisation of magma reservoirs (e.g. Dzurisin, 2003), the significance of this uplift remains difficult to interpret. Indeed, there are many observations of edifice inflation without eruptions as well as eruptions without precursory inflation. For instance, Chaussard and Amelung (2012) recently used InSAR data gathered between 2006 and 2009 over the entire west Sunda arc, Indonesia, to show evidence of inflation at six volcanoes with an average uplift of 3–8 cm/yr. Remarkably, three of these six volcanoes erupted a few months to two years after the observation period, but whether the other three volcanic centres will erupt, in relation with observed uplift, remains uncertain.

When surface deformation is interpreted as reflecting magmatic activity, InSAR data are usually inverted in order to constrain the geometry, depth and volume of the magmatic source. Perhaps more importantly, InSAR data can also inform on the recharge rate of the magmatic system (Parks et al., 2012); this is an important constraint on whether the magmatic system could develop an active magma chamber with a sizeable amount of eruptible magma (Annen, 2009). The solutions to the inverse problem are notoriously non unique but they can be tested and discriminated against one another. It is commonly assumed in these inversions that the crust behaves elastically, but it sometimes fails to explain the observed surface deformation or leads to solutions that are physically unrealistic, such as an implausible geometry or rate of volume change, or a source location too deep that the assumption of purely elastic deformation becomes invalid (Fialko and Pearse, 2012). When this happens, it is necessary to assume a more realistic rheology for the crust, for instance viscoelasticity or a power-law rheology. But this usually leads to the further assumption that the selected rheology applies to a prescribe portion of the crust or to a finite region around the inferred igneous body only (e.g. Newman et al., 2001). Instead, the rheology and the region over which it applies should stem from its thermal history and not be prescribed a priori. These assumptions currently limit our ability to interpret surface deformation as measured by InSAR. A telling example is the 2–3 cm/yr surface uplift that has been continuously measured at the Lastarria - Cordon del Azufre Complex, Chile, over the last decade: we are still unable to tell the extent to which this uplift truly reflects magma accumulation within the crust (Remy et al., 2011).

In collaboration with Jean-Luc Froger (LMV) and Catherine Annen (Bristol University), I intend to develop a numerical model that combines the thermal evolution of the crust, and its resulting rheology as it is repeatedly intruded by magma, with a Finite Element Method (FEM) model of crustal deformation. Such a model would enable us to relate the intrusive history of the crust with the surface deformation. We intend to use the thermal model of Catherine Annen: for a given composition of the crust and intruding magma, this model determines the thermal evolution of the entire system in both time and space. This would then enable the rheology of the crust and the intruded region to be also determined as a function of time and space as more magma, hence heat, is accumulated. This time- and space-dependent rheology could then be input into the FEM Comsol Multiphysics software available at LMV (and Bristol) to calculate the deformation field around the intruded region, and more specifically that at surface, through time. The overall approach will be to test different crustal rheologies and intrusive scenarii (intrusion geometry and magma influx), and determine whether and under which conditions geodetic surface signals associated with pluton formation differ from those associated with magma chamber recharge. The model outputs would then be compared to those measured at the Lastarria - Cordon del Azufre Complex as a first test target, and for which we have an extensive coverage of InSAR data. In the longer term, by determining the rheology and temperature of the intruded body itself, such a model should also enable us to conduct the same analysis with other expected geophysical signals (gravimetry, MT...) and their evolution through time.

Although this project will focus in the first place on the deformation of volcanic edifices, it is also relevant to quantifying the mechanisms and timescales for the long-term accumulation of magma in the crust.

5.2 Magma transport and degassing

5.2.1 Dyke interactions with tectonic faults and their role on monogenetic basaltic volcanism

(Potential Funding: *AXA*)

The following proposal has been submitted to the AXA Research Fund for a two-year post-doctoral grant. Nicolas Le Corvec is the applicant. If successful the project will start early 2013.

Monogenetic basaltic volcanism is a peculiar type of volcanism, where most new eruptions lead to the formation of new volcanic centre, ultimately creating fields of tens to hundreds of volcanic centres. Their formations remain unclear and pose major concern for densely populated areas or nuclear facilities nearby. Monogenetic basaltic fields require direct magma ascent from mantle to surface via dykes and are associated with major fault systems, suggesting an interplay between dykes and pre-existing faults. Both crustal faults and propagating dykes influence, independently, their local stress field, and interact with each other. Dyke intrusions promote or restrict displacement along pre-existing faults (Le Corvec and Walter, 2009), and faults can modify dyke trajectories and be used by dykes as conduits, thus facilitating magma ascent to the surface and increasing the probability of an eruption (Le Corvec et al., submitted). The theoretical conditions for dykes to propagate via pre-existing faults have recently been described, but we still do not understand why a dyke would interact with a fault nearby, nor what the role of these interactions is in the development of monogenetic volcanic fields.

Using analogue modelling to understand dyke-fault interaction, Le Corvec et al. (submitted) show that buoyancy-driven dykes are expected to intersect pre-existing faults if they are separated by less than $\sim$ 200 m, and that the ascent velocity of dykes whose volume is less than~ 0.01 km^3 would decrease due to the surrounding faults. Thus, on the one hand, faults could be exploited by dykes and facilitate magma eruption, but on the other hand, faults could also impede the dynamics of magma transport and decrease the likelihood of eruptions. Although these results do not explain the exact mechanism that modifies dyke dynamics or controls whether a dyke intersects a pre-existing fault, they suggest the ambient stress field plays a key role. This project proposes to quantify this role using numerical modelling.

Numerical models allow the detailed computation of strain and stress within an elastic medium, and enable to control and vary its mechanical parameters, such as its rigidity, pre-existing faults, their geometry and orientation. Thus numerical models provide a complementary approach to the analogue experiments of Le Corvec et al. (submitted) for quantifying interactions between propagating dykes and pre-existing faults. This will be achieved by using two complementary boundary element analyses, Poly3D and the model developed by Maccaferri et al. (2010); Poly3D can account for the presence of faults but not for a moving dyke, whereas the model of Maccaferri et al. (2010) calculates dyke trajectories but cannot deal with faults. Boundary element methods are renowned for their computational efficiency. Additionally, we are in contact with Laurent Maerten (Manager at IGEOSS Europe and Consultant in Montpellier, France) and his group who developed Poly3D (academic licence costs 100 euros per annum), and we are also collaborating with Francesco Maccaferri's group at the GFZ Potsdam, Germany. Both groups are continuously developing their model, and so the project could benefit from potential updates. Both models will be integrated as follows:

1. Poly3D will be used to create a 3D elastic model with a single fault, subject the model to a remote stress field and analyse how the fault modifies this stress field. The applied stress field will be either lithostatic or extensional, and the physical parameters of the model will be systematically varied, including the geometry and friction of the fault.

2. The computed modified stress field will be used as input parameter for the model of Maccaferri et al. (2010). This model will then compute how this perturbed stress field affects dyke trajectories. It will also reveal the additional stress induced by the dyke itself, and so help resolve the respective role of fault-induced and dyke-induced stress perturbations in dyke propagation.

3. More complex models will be designed by including additional pre-existing faults. These models will be tested against the experimental results of Le Corvec et al. (submitted), and will provide constraints on the stress-field evolution in space and time as more dykes and faults are included.

Finally, the models will be applied to the Chaine des Puys, accounting for the regional topography (the Limagne graben) and the location of major tectonic faults (the Limagne Fault on the East and the Sillon Houiller on the West). The initial dyke conditions will be systematically varied (zone of injection and volume) as well as the stress field, lithostatic or extensional. The aim is to elucidate the role of the major faults in the formation and evolution of the Chaine des Puys, and to identify the conditions that lead to its location on the horst rather than inside the Limagne graben.

The ultimate goal is to provide a generic model for understanding the role of crustal faults in the evolution of monogenic volcanic fields, and an additional tool for assessing their associated volcanic and seismic hazards.

5.2.2 Magma ascent through dykes and degassing

(Potential Funding: *ANR*)

I am currently taking an active part in the development of a 4-year research project entitled "Magma Ascent through Dykes (MAD)" that will be submitted to ANR in January 2013. The Principal Investigator of this project is Nicole Métrich from IPGP. The project is based on the close collaboration between four partner laboratories in France: IPG-Paris, LMV-Clermont-Ferrand, ISTerre-Chambéry/Grenoble, and CRPG-Nancy.

Most eruptions of basaltic volcanoes are fed by magmatic dykes that propagate to the surface and give rise to lava flows and explosive activity (lava fountains, Strombolian explosions). These dyke-fed eruptions, occurring at low altitude on a volcano flank or along simple volcano-tectonic fault systems, are very common and constitute one major threat to densely inhabited volcanic regions over the world. Improved understanding and modeling of the processes that govern these eruptions is thus crucial for hazard assessment. This is the heart of MAD project.

Magma ascent and dyke propagation are complex processes which depend on various parameters: (i) the magma source depth and pressure, (ii) the magma physical properties, degassing path and decompression rate, (iii) the physical properties of country rocks and how these accommodate the pressure induced by magma intrusion, and (iv) the regional and local stress field. Until now, little efforts have been done to integrate measurements or assessments of all these parameters into a numerical and physical modeling of basaltic dyke propagation. The aim of MAD project is to fill in this gap. By gathering researchers with different areas of expertise (petrology, geochemistry, structural geology and geophysical modeling) we plan to build a conceptual model of basaltic magma transfer through dykes, able to explain the range of observed eruptive phenomena, across the following steps:

1. Measurement/modeling of the pressure-dependent magma volatile content, degassing path, crystallization, decompression rate and physical properties of basaltic magmas; equilibrium versus kinetic processes.

2. Assessment/modeling of the stress state in the volcano and of the stress perturbations induced by magma dyking, by integrating inversions of both seismic and geodetic (GPS, InSAR) data.

3. Integration of the results above into new dynamic numerical models of dyke propagation that have the ability to interpret jointly the temporal evolution of the recorded geophysical/geochemical signals and to be predictive by providing dyke path, velocity and eruptive vent location.

MAD project will be primarily focused on Piton de la Fournaise (PdF) basaltic volcano on Reunion Island, which typically displays recurrent dyke-fed eruptions and for which we dispose of a large geophysical and observational dataset collected by the dense local monitoring network. PdF is one most suitable target volcano for building improved numerical models of basaltic dyke propagation. This project will provide a fantastic opportunity to relate degassing processes with magma properties (essentially its viscosity) as well as magma movements and mingling within dykes and conduit as revealed by texture analyses. This will improve our understanding of the intimate relationship between magma movement and degassing within volcanic plumbing system.

Bibliography

Annen, C. (2009). From plutons to magma chambers: thermal constraints on the accumulation of eruptible silicic magma in the upper crust. *Earth and Planetary Science Letters 284*(3-4), 409–416.

Annen, C., B. Scaillet, and R. S. J. Sparks (2006). Thermal constraints on the emplacement rate of a large intrusive complex: The Manaslu leucogranite, Nepal Himalaya. *J. Petrol. 47*, 71–95.

Chaussard, E. and F. Amelung (2012). Precursory inflation of shallow magma reservoirs at west Sunda volcanoes detected by InSAR. *Geophysical Research Letters 39*(L21311), doi: 10.1029–2012GL053817.

de Saint-Blanquat, M., G. Habert, E. Horsman, S. S. Morgan, B. Tikoff, P. Launeau, and G. Gleizes (2006). Mechanisms and duration of non-tectonically assisted magma emplacement in the upper crust: the Black Mesa pluton, Henry Mountains, Utah. *Tectonophysics 48*, 1–31.

de Saint-Blanquat, M., E. Horsman, G. Habert, S. Morgan, O. Vanderhaeghe, R. Law, and B. Tikoff (2011). Multiscale magmatic cyclicity, duration of pluton construction, and the paradoxical relationship between tectonism and plutonism in continental arcs. *Tectonophysics 500*, 20–33.

de Saint-Blanquat, M., R. Law, J. Bouchez, and S. Morgan (2001). Internal structure and emplacement of the Papoose Flat pluton: An integrated structural, petrographic, and magnetic susceptibility study. *Bulletin of the Geological Society of America 113*, 976–995.

Druitt, T. H., F. Costa, E. Deloule, M. Dungan, and B. Scaillet (2012). Decadal to monthly timescales of magma transfer and reservoir growth at a caldera volcano. *Nature 482*, 77–80.

Dzurisin, D. (2003). A comprehensive approach to monitoring volcano deformation as a window on the eruption cycle. *Reviews of Geophysics 41*(1001), doi:10.1029–2001RG000107.

Fialko, Y. and J. Pearse (2012). Sombrero Uplift Above the Altiplano-Puna Magma Body: Evidence of a Ballooning Mid-Crustal Diapir. *Science 338*, 250–252.

Froger, J. L., Y. Fukushima, P. Briole, T. Staudacher, T. Souriot, and N. Villeneuve (2004). The deformation field of the August 2003 eruption at Piton de la Fournaise, Reunion Island, mapped by ASAR interferometry. *Geophysical Research Letters 31*(L14601), doi: 10.1029–2004GL020479.

Froger, J. L., D. Remy, S. Bonvalot, and D. Legrand (2007). Two scales of inflation at Lastarria-Cordon del Azufre volcanic complex, central Andes, revealed from ASAR-ENVISAT interferometric data. *Earth Planet. Sci. Lett 255*, 148–163.

Galland, O., P. Cobbold, E. Hallot, J. de Bremond d'Ars, and G. Delavaud (2006). Use of vegetable oil and silica powder for scale modelling of magmatic intrusion in a deforming brittle crust. *Earth and Planetary Science Letters 243*, 786–804.

Horsman, E., S. Morgan, M. De Saint-Blanquat, G. Habert, A. Nugent, R. A. Hunter, and B. Tikoff (2010). Emplacement and assembly of shallow intrusions from multiple magma pulses, Henry Mountains, Utah. *Earth and Environmental Science Transactions of the Royal Society of Edinburgh 100*, 117–132.

Kavanagh, J. L., T. Menand, and R. S. J. Sparks (2006). An experimental investigation of sill formation and propagation in layered elastic media. *Earth Planet. Sci. Lett. 245*, 799–813.

Le Corvec, N. and T. R. Walter (2009). Volcano spreading and fault interaction influenced by rift zone intrusions: Insights from analogue experiments analyzed with digital image correlation technique. *J. Volcanol. Geotherm. Res. 183*, 170–182.

Leuthold, J., O. Müntener, L. P. Baumgartner, B. Putlitz, M. Ovtcharova, and U. Schaltegger (2012). Time resolved construction of a bimodal laccolith (Torres del Paine, Patagonia). *Earth and Planetary Science Letters 325-326*, 85–92.

Maccaferri, F., M. Bonafede, and E. Rivalta (2010). A numerical model of dyke propagation in layered elastic media. *Geophysical Journal International 180*, 1107–1123.

Martin, V. M., D. J. Morgan, D. A. Jerram, M. J. Caddick, D. J. Prior, and J. P. Davidson (2008). Bang! Month-Scale Eruption Triggering at Santorini Volcano. *Science 321*, 1178.

Menand, T. (2008). The mechanics and dynamics of sills in elastic layered media and their implications for the growth of laccoliths. *Earth Planet Sci. Lett. 267*, 93–99.

Menand, T. (2011). Physical controls and depth of emplacement of igneous bodies: A review. *Tectonophysics 500*, 11–19.

Menand, T., M. de Saint-Blanquat, and C. Annen (2011). Emplacement of magma pulses and growth of magma bodies. *Tectonophysics 500*, 1–2.

Michel, J., L. Baumgartner, B. Putlitz, U. Schaltegger, and M. Ovtcharova (2008). Incremental growth of the Patagonian Torres del Paine laccolith over 90 ky. *Geology 36*(6), 459–462.

Miller, C. F., D. J. Furbish, B. A. Walker, L. L. Claiborne, G. C. Koteas, H. A. Bleick, and J. S. Miller (2011). Growth of plutons by incremental emplacement of sheets in crystal-rich host: Evidence from Miocene intrusions of the Colorado River region, Nevada, USA. *Tectonophysics 500*.

Newman, A. V., T. H. Dixon, G. Ofoegbu, and J. E. Dixon (2001). Geodetic and seismic constraints on recent activity at Long Valley Caldera, California: evidence for viscoelastic rheology. *J. Volcanol. Geotherm. Res. 105*, 183–206.

Parks, M. M., J. Biggs, P. England, T. A. Mather, P. Nomikou, K. Palamartchouk, X. Papanikolaou, D. Paradissis, B. Parsons, D. M. Pyle, C. Raptakis, and V. Zacharis (2012). Evolution of Santorini Volcano dominated by episodic and rapid fluxes of melt from depth. *Nature Geoscience 5*, 749–754.

Petford, N., R. C. Kerr, and J. R. Lister (1993). Dike transport of granitoid magmas. *Geology 21*, 845–848.

Prittchard, M. E. and M. Simmons (2002). A satellite geodetic survey of large-scale deformation of volcanic centres in the central Andes. *Nature 418*, 1–5.

Remy, D., J.-L. Froger, H. Perfettini, S. Bonvalot, G. Gabalda, V. Cayol, T. Souriot, and F. Albin (2011). Joint inversion of insar and gps times series: Application to monitoring ground motions related to volcanic or tectonic. *Fringe conference , Rome*, 19 Sep.–23 Sep.

Schaltegger, U., P. Brack, M. Ovtcharova, I. Peytcheva, B. Schoene, A. Stracke, M. Marocchi, and G. M. Bargossi (2009). Zircon and titanite recording 1.5million years of magma accretion, crystallization and initial cooling in a composite pluton (southern Adamello batholith, northern Italy). *Earth and Planetary Science Letters 286*, 208–218.

Taisne, B. and S. Tait (2011). Effect of solidification on a propagating dike. *Journal of Geophysical Research 116*(B01206), doi: 10.1029/2009JB007058.

Traversa, P., V. Pinel, and J. R. Grasso (2010). A constant influx model for dike propagation: Implications for magma reservoir dynamics. *Journal of Geophysical Research 115*, B01201.